I. R. IRAN

ISSN: 1728-144X
e-ISSN: 1735-9244

International Journal of Engineering

Journal Homepage: www.ije.ir

MERC

TRANSACTIONS B: Appliations

Volume 34, Number 11, November 2021

Materials and Energy Research Center

In the Name of God

INTERNATIONAL JOURNAL OF ENGINEERING
Transactions A: Basics

DISCLAIMER

The publication of papers in International Journal of Engineering does not imply that the editorial board, reviewers or publisher accept, approve or endorse the data and conclusions of authors.

International **J**ournal of **E**ngineering *Transactions A: Basics* (ISSN 1728-1431) (EISSN 1735-9244)
International **J**ournal of **E**ngineering *Transactions B: Applications* (ISSN 1728-144X) (EISSN 1735-9244)
International **J**ournal of **E**ngineering *Transactions C: Aspects* (ISSN 2423-7167) (EISSN 1735-9244)
Web Sites: www.ije.ir & www.ijeir.info E-mails: ije.editor8@gmail.com, Tel: (+9821) 88771578, Fax: (+9821) 88773352
Materials and Energy Research Center (MERC)

ISSN: 1728-144X, e-ISSN: 1735-9244

International Journal of Engineering, Volume 34, Number 11, November 2021

CONTENTS:

ISSN: 1728-144X, e-ISSN: 1735-9244

International Journal of Engineering, Volume 34, Number 11, November 2021

International Journal of Engineering

Journal Homepage: www.ije.ir

Design and Optimization of Halbach Permanent Magnet Array with Rectangle Section and Trapezoid Section

N. Song[a], M. Zhu*[a], G. Zhou[a], L. Guo[a], Y. Mu[a], J. Gao[a], J. Ma[a], K. Zhang[b]

[a] *Institute of Automation, Qilu University of Technology (Shandong Academy of Sciences), Shandong Provincial Key Laboratory of Automotive Electronics Technology, Jinan, Shandong, China*

[b] *Rongcheng Rongjia Power Co., LTD, Rongcheng, Shandong, China*

PAPER INFO

Paper history:
Received 25 April 2021
Received in revised form 21 June 2021
Accepted 29 July 2021

Keywords:
Magnetic
Halbach Array
Surface Current Method
Genetic Algorithm
Optimization

ABSTRACT

In this work, a novel Halbach permanent magnet array with rectangle section and trapezoid section is proposed and optimized. The analytical model of the Halbach array is established based on the surface current method, which is numerically efficient and can be utilized to evaluate the magnetic field of the Halbach array caused by varying magnet segment's configurations. The fundamental component of the magnetic flux density and the sinusoidal distortion rate are chosen as the optimization object and the optimization is executed by the genetic algorithm in global scale. The effectiveness of the optimization is validated by the finite element analysis in Comsol. Compared to the traditional Halbach array with rectangle section, the magnetic field created by the proposed Halbach array in this paper owns better performance.

***doi**: 10.5829/ije.2021.34.11b.01*

NOMENCLATURE

l	length of one magnetic period	N	total number of permanent magnets in one Halbach array
ω	width of each magnet segment	n	the nth magnet segment
h	height of the smaller magnet segment with rectangle section	k_v	the linear current density of the surface current
θ	angle between the hypotenuse and the horizontal line in the magnet segment with trapezoid section	μ_0	the permeability of vacuum
I	equivalent surface current	B_{δ_1}	fundamental component of the magnetic flux density
B	magnetic flux density	B_{r_i}	ith harmonic component
K_{BD}	sinusoidal distortion rate of the magnetic flux density	Z	objective function
p	the weighting coefficient of the K_{BD}	k	the weighting coefficient of the B_{δ_1}

1. INTRODUCTION

Klaus Halbach found a special permanent magnet array arrangement that owns stronger magnetic field on one side of the array because of the overlap and cancel out of the tangential and radial magnetic field, which is called the Halbach permanent magnet array [1]. Figure 1(a) shows the traditional regular Halbach permanent magnet array. Now, the Halbach array has been widely used in high-energy physics, high-speed motor, maglev train system, magnetic bearing and medical area [2, 3]. The ideal Halbach array is one permanent magnet whose magnetization direction varies continuously sinusoidal along the array direction, as shown in Figure 1(b). In this way, the magnetic field generated by the array can be consistent with the standard sinusoidal distribution. But due to the technical limitations and cost constraints, the ideal Halbach array cannot be manufactured.

*Corresponding Author Institutional Email: zmm2021@163.com (M. Zhu)

Please cite this article as: N. Song, M. Zhu, G. Zhou, L. Guo, Y. Mu, J. Gao, J. Ma, K. Zhang, Design and Optimization of Halbach Permanent Magnet Array with Rectangle Section and Trapezoid Section, International Journal of Engineering, Transactions B: Applications, Vol. 34, No. 11, (2021) 2379-2386

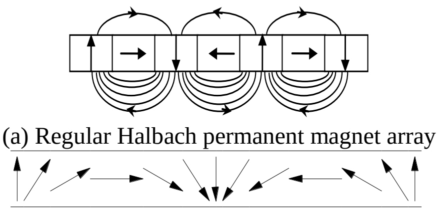

(a) Regular Halbach permanent magnet array

(b) Ideal Halbach permanent magnet array

Figure 1. Schematic diagram of Halbach permanent magnet array

In some occasions such as the linear motors that provide power for nanoscale positioning mechanisms, magnetic field with high performance is needed [4]. Sine there exists disparity between the magnetic field generated by traditional Halbach array and the sinusoidal, researches focused on the optimal design of permanent magnets (PM), such as unequal thickness of PM, PM with triangle section, trapezoid section or other shapes have been investigated [5-14]. Different optimization and modeling approaches were applied on the Halbach arrays' improvements. Zhang Kunlun established analytical model for linear permanent Halbach array with trapezoidal shape permanent magnets based on the theory of magnetic charge. According to kriging method, the double-sided structure motor is demonstrated to have better performance in the thrust ripple and the average thrust than single-sided structure [15]. Ren et al. [16] proposed a ring-pair permanent magnet array and the magnetic field was modeled by equivalent currents. By applying a genetic algorithm [17-19], magnetic field with high field homogeneity and high field strength was achieved [16].

A novel Halbach permanent magnet array with rectangle section and trapezoid section is presented in this paper. The surface current method is chosen to model magnetic flux density because of its closely connection with PM's configuration, which is of vital importance for optimization. The optimization method used in this paper is genetic algorithm, which is an intelligent algorithm with nonlinear, high computational efficiency and global optimization. The fundamental component of the magnetic flux density and the sinusoidal distortion rate with changeable weight coefficient compose the fitness function. Then, the better performance of the optimized Halbach array is verified by the comparison of optimized Halbach array with the traditional array and the finite element model.

2. STRUCTURE AND MODELING OF HALBACH ARRAY WITH RECTANGLE SECTION AND TRAPEZOID SECTION

2. 1. Geometrical Model As shown in Figure 2, Halbach permanent magnet array proposed in this paper is composed of magnet segments with rectangle section and trapezoid section. The dotted lines represent the beginning and ending of one magnetic period, and every five magnet segments form one magnetic period, described as l. There are two magnetic periods in Figure 2. The magnetization direction of magnet segments in this paper is parallel to *x* or *y* axis.

The magnet segment in the middle of one magnetic period owns bigger rectangle section. In contrast, magnet segments at the ends of one magnetic period own smaller rectangle section. Magnet segments with trapezoid section located in between the bigger and smaller magnet segments with rectangle section. Arrows on the magnet segments stand for magnetization direction, which are 90° rotated in clockwise of adjacent magnets. Residual magnetic flux density of each magnet segment is the same.

To reduce the processing costs, the width of each magnet segment is the same, expressed as ω, as shown in Figure 3. The height of the smaller magnet segment with rectangle section is expressed as h, as shown in Figure 3(a). Figure 3(b) shows the configuration of the magnet segment with trapezoid section. The angle between the hypotenuse and the horizontal line is described as θ. The height of the side, adjacent to the smaller magnet segment with rectangle section, is still h. According to the geometrical relationship, the height of the other side is $h+\omega\cdot\tan\theta$. In this way, the height of the bigger magnet segment with rectangle section is $h+\omega\cdot\tan\theta$.

2. 2. Mathematical Model In the surface current method, which is based on the Ampere's hypothesis of molecular current, the effect of the molecular electric current can be cancelled out when a permanent magnet

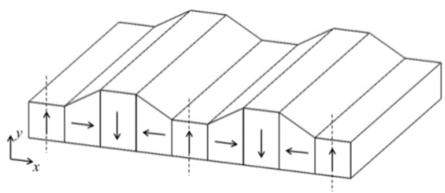

Figure 2. Halbach permanent magnet array with rectangle section and trapezoid section

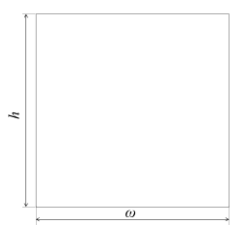

(a)Smaller magnet segment with rectangle section

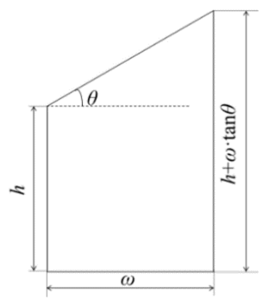

(b) Magnet segment with trapezoid section

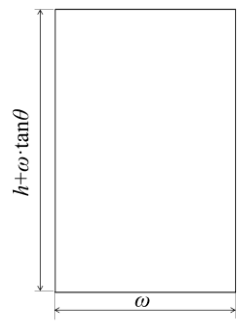

(c) Bigger magnet segment with rectangle section

Figure 3. Diagram of cross-section size

segment is magnetized uniformly. So, the magnetic field created by one magnet segment at any point in the outer space is equivalent to that stimulated by the surface current [20-21].

Figure 4 shows the equivalent surface current model of the smaller magnet segment with rectangle section. Coordinate system $X_1O_1Y_1$ is established in the geometric center of the cross-section, and the magnetization direction of the magnet segment shown in Figure 4 is in positive Y axis. The equivalent surface currents I_1, I_2 are on the sides, and the symbols stand for the direction of currents.

According to the surface current method, the magnetic flux density stimulated by surface currents I_1, I_2 at point $\mathrm{P}(x,y)$ can be expressed as Equations (1) and (2):

$$\begin{cases} B_{I_{1x}}(x,y,k_v)=\dfrac{\mu_0 k_v}{4\pi}\ln\dfrac{\left(y+\dfrac{h}{2}\right)^2+\left(x-\dfrac{\omega}{2}\right)^2}{\left(y-\dfrac{h}{2}\right)^2+\left(x-\dfrac{\omega}{2}\right)^2} \\ B_{I_{1y}}(x,y,k_v)=\dfrac{\mu_0 k_v}{2\pi}\left(\arctan\dfrac{y-\dfrac{h}{2}}{x-\dfrac{\omega}{2}}-\arctan\dfrac{y+\dfrac{h}{2}}{x-\dfrac{\omega}{2}}\right) \end{cases} \tag{1}$$

$$\begin{cases} B_{I_{2x}}(x,y,k_v)=-\dfrac{\mu_0 k_v}{4\pi}\ln\dfrac{\left(y+\dfrac{h}{2}\right)^2+\left(x+\dfrac{\omega}{2}\right)^2}{\left(y-\dfrac{h}{2}\right)^2+\left(x+\dfrac{\omega}{2}\right)^2} \\ B_{I_{2y}}(x,y,k_v)=-\dfrac{\mu_0 k_v}{2\pi}\left(\arctan\dfrac{y-\dfrac{h}{2}}{x+\dfrac{\omega}{2}}+\arctan\dfrac{y+\dfrac{h}{2}}{x+\dfrac{\omega}{2}}\right) \end{cases} \tag{2}$$

where k_v is the linear current density of the surface current.

Similarly, the equivalent surface current models of the bigger magnet segment with rectangle section and the magnet segment with trapezoid section are established, as shown in Figures 5 and 6. The coordinate system $X_2^{'}O_2^{'}Y_2^{'}$ is established in the geometric center of the bigger rectangle section. The magnetization direction of the magnet segment shown in Figure 5 is in negative Y axis. The equivalent surface currents I_3, I_4 are on the sides, and the symbols stand for the direction of currents, in the opposite direction compared with that in Figure 4. Based on the surface current method, the magnetic flux density stimulated by surface currents I_3, I_4 at point $\mathrm{P}'(x',y')$ in coordinate system $X_2^{'}O_2^{'}Y_2^{'}$ can be expressed.

In the Halbach array，the coordinate system $X_2^{'}O_2^{'}Y_2^{'}$ is $(\omega\cdot\tan\theta)/2$ away from the coordinate system

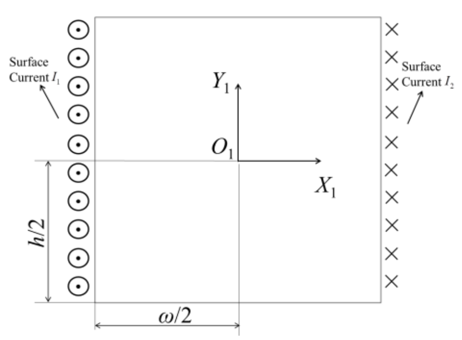

Figure 4. Equivalent surface current model of the smaller magnet segment with rectangle section

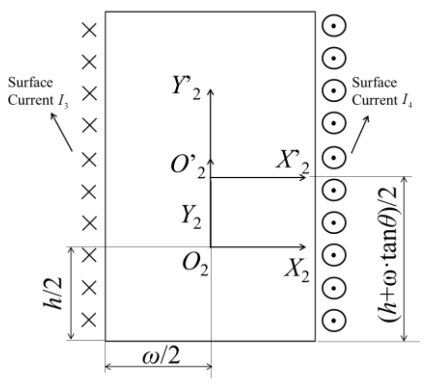

Figure 5. Equivalent surface current model of the bigger magnet segment with rectangle section

$X_1O_1Y_1$ on the Y axis, which will bring inconformity to the expression of the magnetic field at the same point away from the working face. So, coordinate system $X_2O_2Y_2$ is established by translating coordinate system $(\omega \cdot \tan\theta)/2$ downward on Y axis. According to the coordinate translation principle, the magnetic flux density stimulated by surface currents I_3, I_4 at point $\mathrm{P}(x, y)$ in coordinate system $X_2O_2Y_2$ can be expressed.

The coordinate system $X_3O_3Y_3$ is established in the magnet segment with trapezoid section, where the origin is located $h/2$ away from the base, $\omega/2$ away from the left side, as shown in Figure 6. The magnetization direction of the magnet segment shown in Figure 5 is in positive X axis. The equivalent surface current I_5 is on the hypotenuse, and the surface current I_6 is on the base. The symbols stand for the direction of currents. In the same way, the magnetic flux density stimulated by surface currents I_6 at point $\mathrm{P}(x, y)$ in coordinate system $X_3O_3Y_3$ can be expressed.

To describe the magnetic flux density stimulated by surface current I_5, coordinate system $X_3'O_3'Y_3'$ is obtained by rotating the coordinate system $X_3O_3Y_3$ counterclockwise by an angle of θ, whose coordinate axis X_3' is parallel to the hypotenuse. The magnetic flux density stimulated by surface current I_5 at point $\mathrm{P}'(x', y')$ in coordinate system $X_3'O_3'Y_3'$ can be expressed based on the surface current method. According to the coordinate rotation theory, the magnetic flux density stimulated by surface current I_5 at point $\mathrm{P}(x, y)$ in coordinate system $X_3O_3Y_3$ can be expressed.

Based on the above and the superposition principle, the analytical model of the Halbach array at point can be expressed as Equation (3).

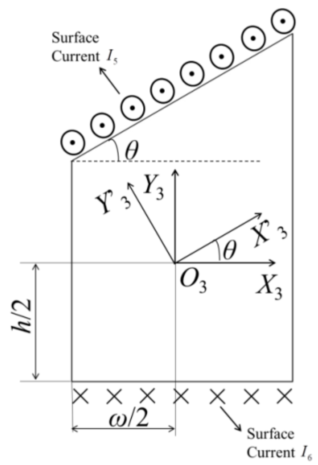

Figure 6. Equivalent surface current model of the magnet segment with trapezoid section

$$\begin{cases} B_x(x,y) = \sum_{n=0}^{N} \sum_{i=1}^{5} B_{ix}\left(x - \left(n + \frac{\omega}{2}\right), y, k_v\right) \\ B_y(x,y) = \sum_{n=0}^{N} \sum_{i=1}^{5} B_{iy}\left(x - \left(n + \frac{\omega}{2}\right), y, k_v\right) \end{cases} \tag{3}$$

where: N is the total number of permanent magnets in one Halbach array; n represents the nth magnet segment; B_x is the magnetic flux density on X axis, B_y is the magnetic flux density on Y axis.

3. OPTIMAL DESIGN OF THE HALBACH ARRAY

Based on the above, the magnetic flux density of the Halbach array is described closely related with the magnet segment's configurations, which lays a good foundation for optimization.

3. 1. Optimization Problem

The fundamental component of the magnetic flux density B_{δ_1} indicates the magnetic energy, and the sinusoidal distortion rate K_{BD} can measure the sinusoid of the magnetic flux density. By executing Fourier transformation on the mathematical model of the magnetic flux density deduced from the above, harmonic components of the magnetic flux density can be obtained. B_{δ_1} is the first order of the harmonic component and K_{BD} can be described as:

$$K_{\mathrm{BD}} = \sqrt{\sum_{i \neq 1} \left(\frac{B_{r_i}}{B_{\delta_1}} \right)^2} \tag{4}$$

where B_{r_i} is the ith harmonic component.

Both the fundamental component of the magnetic flux density and the sinusoidal distortion rate are the main performance indices of the motors. In this way, the objective function for pursuing the optimal design of motors can be defined as:

$$Z = \frac{K_{\mathrm{BD}}^{p}}{B_{\delta_1}^{k}} \tag{5}$$

where: p , k are the weighting coefficients. Optimization with different focus can be conducted by changing values of p, k .

3. 2. Genetic Algorithm

Genetic algorithm simulates the biological genetic process. The natural selection of eliminating the poor gene is operated by the fitness evaluation on the initial group resulting from the initial coding, as shown in Figure 7. In this paper, the fitness function is expressed as Equation (5), which contains the fundamental component of the magnetic flux density and the sinusoidal distortion rate, and the maximum fitness value is to be sought. The populations with strong magnetic flux density and low sinusoidal distortion rate are selected to produce offspring. To bring diversity to the population, crossovers and mutations are applied to the produced offspring. Then the fitness value of the evolved population is calculated and compared. The optimal solution of the objective function can be searched by evolution of multiple generations.

As one of the cases, take $l = 24mm, \omega = 6mm$ as the configuration of the traditional Halbach array, and the magnetic flux density 0.5mm away from the working face is studied. To get the Halbach array with higher performance, the angle θ and the height h are optimized, while other magnet segment's configurations are fixed. Considering the costs, the area of the Halbach array should be controlled, so the growth of the area is limited to 10%. It is expected that the performance of the magnetic flux density can be improved while the area decreases, so the minimum area is limited to 90% of the traditional area due to the working condition. The constraint is nonlinear because the calcualtion of the area is related with the trigonometric operation of varialbles. The angle θ is global searched in $(0, \pi/2)$ and the height h is global searched in $(4\text{mm}, 8\text{mm})$. In this optimization problem, $p = k = 1$ is chosen to define the objective function.

Figure 8 shows the variation of the magnetic flux density along x and y axis throughout a certain amount of iterative searches. It is obvious that the peak part of the magnetic flux density is gradually close to the trigonometric function curve, which indicates the effectiveness of the optimization. The reasonable variables that can be satisfied with strong magnetic flux density and low sinusoidal distortion rate is 9.688° and 6mm.

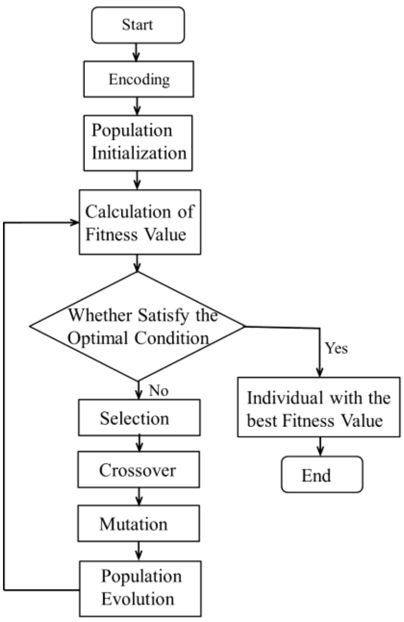

Figure 7. Flowchart of the GA

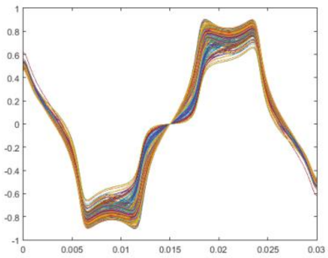

(a) *x* axis

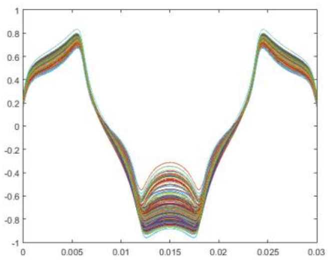

(b) *y* axis

Figure 8. Variation of the magnetic flux density

4. RESULT AND DISCUSSION

The parameters of the optimized Halbach permanent magnet array are listed in Table 1, and the structure diagram of the optimized Halbach permanent magnet array in one magnetic period is shown in Figure 9. The traditional Halbach permanent magnet array composed of smaller magnet segment with rectangle section is proposed for comparison, as shown in Figure 10. According to calculation, the area of the traditonal Halbach array is $1.8\times10^{-4}\,\text{m}^2$ and the optimized is $1.92\times10^{-4}\,\text{m}^2$.

Comparing the magnetic flux density 0.5mm away from the working face generated by the optimized array in Figure 9 and those of the traditional array in Figure 10, the optimized magnet array has the sinusoidal distortion rate K_{BD} of 0.1813 and the fundamental component of

TABLE 1. Parameters of Halbach array

	Fixed			Variable	
Parameters	Magnetic Period/ (l)	Width (ω)	Residual Magnetism (B_r)	Angle (θ)	Height (h)
Value	24 mm	6 mm	1.35T	9.688°	6mm

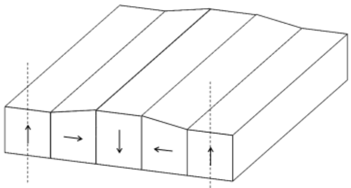

Figure 9. Schematic diagram of the specific Halbach permanent magnet array

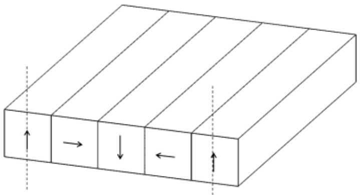

Figure 10. Schematic diagram of the traditional Halbach permanent magnet array

the magnetic flux density of 0.9672T, whereas the traditional magnet array has the sinusoidal distortion rate K_{BD} of 0.2057 and the fundamental component of the magnetic flux density of 0.9772T. As can be seen, the optimization reduces the sinusoidal distortion rate by 11.86% with a sacrifice of the field strength of 1.02% and the area of 6.82%. The optimization offers significant improvement in sinusoidal while still maintains a similar field strength. Also, the added cost can be beared. The solid lines represent the magnetic flux density of the optimized magnet array along *x* and *y* axis in Figure 11, and the dotted lines represent those of the traditional array. Specific value of the main performance indices are shown in Table 2.

In order to verify the feasibility of the modeling method, the magnetic flux density 0.5mm away from the working face generated by the optimized array are evaluated by the finite element model. The dotted line in Figure 12 represents the magnetic flux density in finite element method and the solid line represents the

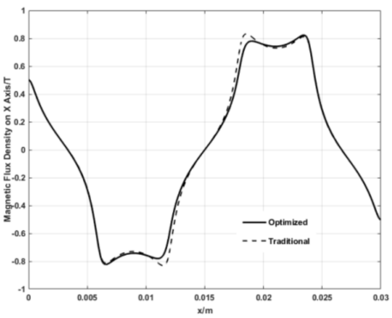

(a) *x* axis

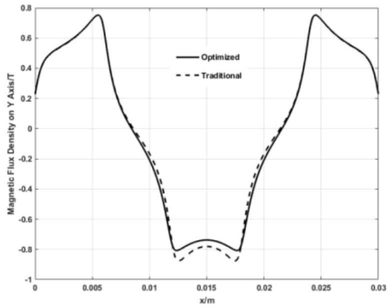

(b) *y* axis

Figure 11. Comparison of the magnetic flux density of the optimized and traditional magnet array

TABLE 2. Comparison of the Evaluation Indexes of Halbach Magnet Arrays

Index	**Type**	
	Traditional	**Optimized**
$B_{\delta_{1x}}$ (T)	0.6481	0.6412
$B_{\delta_{1y}}$ (T)	0.7313	0.7241
B_{δ_1} (T)	0.9772	0.9672
K_{BDx}	0.1629	0.1411
K_{BDy}	0.1256	0.1138
K_{BD}	0.2057	0.1813
Area	$1.8\times10^{-4}\mathrm{m}^2$	$1.92\times10^{-4}\mathrm{m}^2$

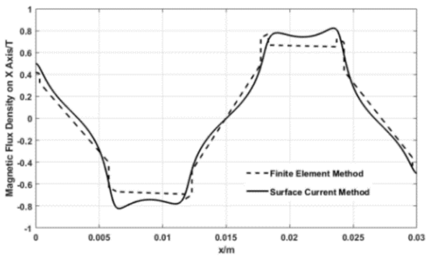

(a) *x* axis

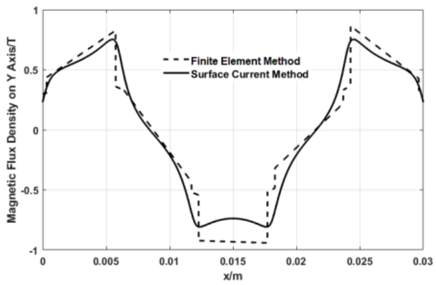

(b) *y axis*

Figure 12. Comparison of the magnetic flux density of surface current method and finite element method

magnetic flux density by the surface current method. It can be seen that lines follow the same trend and the magnetic flux density described by the surface current method contain more details.

5. CONCLUSION

The design and optimization of a novel Halbach permanent magnet array with rectangle section and trapezoid section is proposed. The magnetic flux density of the array is modeled according to the surface current method, which is closely related with the magnet segment's configurations. The feasibility of the modeling method is validated in the finite element method. To achieve better magnetic flux density performance, the genetic algorithm is applied based on the above. As the main performance indices, the fundamental component of the magnetic flux density and the sinusoidal distortion rate are chosen to construct the fitness function. Compared with the traditional Halbach array, the optimized Halbach array owns significant improvement in sinusoidal while still maintains similar field strength.

6. ACKNOWLEDGMENTS

This work was supported by the Natural Science Foundation of Shandong Province (Grant No. ZR2019BEE038), the Youth Foundation of Shandong Academy of Sciences (2020QN0031), the Collaborative Innovation Fund of Shandong Academy of Sciences (2019CXY25), the Major Science and Technology Innovation Project of Shandong Province (2019JZZY010912), and the Special Construction Project of Engineering Technology Research Center of Shandong Province (2019JZP014).

7. REFERENCES

1. Halbach K., "Design of permanent multipole magnets with oriented rare earth cobalt materials" ***Nuclear Instruments and Methods***, Vol. 169, No. 1, (1980), 1-10. doi.org/10.1016/0029-554X(80)90094-4
2. Zhang L., Kou B., Xing F., Jin Y., Zhang H., Zhu J., "Magnetically levitated synchronous permanent magnet planar motor with concentric structure winding used for lithography machine" ***Journal of Applied Physics***, Vol. 11, No. 7, (2015), 15-25. doi.org/10.1063/1.4917332
3. Zhu H., Pang C. K., Teo T. J., "Analysis and control of a 6 DOF maglev positioning system with characteristics of end-effects and eddy current damping" ***Mechatronics***, Vol. 47, (2017), 183-194. doi.org/10.1016/j.mechatronics.2016.12.004
4. Song N. R., Ma S.Y., Zhang Z.Q., "A numerical study of forces for sandwiched maglev stage", ***International Journal of Applied Electromagnetics and Mechanics***, Vol. 55, (2017), 89-100. DOI: 10.3233/JAE-160152
5. Fang, S. H., Xue, S. H., Pan, Z. B., et al. "Torque ripple optimization of a novel cylindrical arc permanent magnet synchronous motor used in a large telescope", ***Energies***, Vol. 12, (2019), 362-377. doi.org/10.3390/en12030362
6. Li Z. J., Yan Z. J., Luo J. T., "Performance comparison of electromagnetic energy harvesters based on magnet arrays of alternating polarity and configuration", ***Energy Conversion and Management***, Vol. 179, (2019), 132-140. doi.org/10.1016/j.enconman.2018.10.060
7. Arish N., Teymoori V., "Development of Linear Vernier Hybrid Permanent Magnet Machine for Wave Energy Converter", ***International Journal of Engineering, Transactions B: Applications***, Vol. 33, No. 5, (2020), 805-813. DOI: 10.5829/IJE.2020.33.05B.12
8. Arish N., Marignetti F., "Evaluation of Linear Permanent Magnet Vernier Machine Topologies for Wave Energy Converters", ***International Journal of Engineering, Transactions B: Applications***, Vol. 34, No. 2, (2021), 403-413. DOI: 10.5829/IJE.2021.34.02B.12
9. Uberruck T., Blumich B., "Variable magnet arrays to passively shim compact permanent-yoke magnets", ***Journal of Magnetic Resonance***, Vol. 298, (2019), 77-84. doi.org/10.1016/j.jmr.2018.11.011
10. Zhang Y., Cao J. Y., Zhu H. Y., "Design, modeling and experimental verification of circular Halbach electromagnetic energy harvesting from bearing motion", ***Energy Conversion and Management***, Vol. 180, (2019), 811-821. doi.org/10.1016/j.enconman.2018.11.037
11. Meribout M., Sonowan S., "Optimal Halbach magnet array design for portable NMR targeting multiphase flow metering applications", ***IEEE Transactions on Magnetics***, Vol. 1, No. 55, (2019). DOI: 10.1109/TMAG.2018.2877603
12. Zhang Y. Q., Yu M.H., "Field and thrust analysis of linear servo motor with permanent-magnet of different shapes", in Proceedings of IEEE ICEM conference, Kuala Lumpur, Malaysia, (2010), 1516-1519.
13. Zhang Y. Q., Yu M.H., "Analysis and design of double-sided air core linear servo motor with trapezoidal permanent magnets", ***IEEE Transactions on Magnetics***, Vol. 47, No. 10, (2011), 3236–3239. DOI: 10.1109/TMAG.2011.2156398
14. Meessen K. J., Gysen B. L., "Halbach permanent magnet shape selection for slotless tubular actuators", ***IEEE Transactions on Magnetics***, Vol. 44, No. 11, (2008), 4305-4308. **DOI:** 10.1109/TMAG.2008.2001536
15. Duan J. H., Xiao S., Zhang K. L., Jing Y.Z., "A novel 3-D analytical modeling method of trapezoidal shape permanent magnet Halbach array for multi-objective optimization", ***Journal of Electrical Engineering & Technology***, Vol. 14, (2019), 635-643.
16. Ren Z. H., Mu W. C., Huang S. Y., "Design and optimization of a ring-pair permanent magnet array for head imaging in a low-field portable MRI system", ***IEEE Transactions on Magnetics***, Vol. 1, No. 55, (2019) 1-8. DOI: 10.1109/TMAG.2018.2876679
17. S. Mohammadi, M. Babagoli. "A Hybrid Modified Grasshopper Optimization Algorithm and Genetic Algorithm to Detect and Prevent DDoS Attacks". ***International Journal of Engineering, Transactions A: Basics***, Vol. 34, No. 4, (2021), 811-824. doi.org/10.5829/ije.2021.34.04a.07
18. L. Izadi, F. Ahmadizar, J. Arkat. "A Hybrid Genetic Algorithm for Integrated Production and Distribution Scheduling Problem with Outsourcing Allowed". ***International Journal of Engineering, Transactions B: Applications***, Vol. 33, No. 11, (2020), 2285-2298. DOI: 10.5829/IJE.2020.33.11B.19
19. M. Parvane, E. Rahimi, F. Jafarinejad. "Optimization of Quantum Cellular Automata Circuits by Genetic Algorithm". ***International Journal of Engineering, Transactions B:***

Applications, Vol. 33, No. 2, (2020), 229-236. doi.org/10.5829/ije.2020.33.02b.07

20. Luo C., Zhang K. L., Zhang W. L., Jing Y. Z., "3D analytical model of permanent magnet and electromagnetic hybrid Halbach array electrodynamic suspension system", ***Journal of Electrical Engineering & Technology***, Vol. 15, (2020), 1713-1721.

21. Luo C., Zhang K. L., Zhang W. L., Jing Y. Z., "Study of permanent magnet electrodynamic suspension system with a novel Halbach Array", ***Journal of Electrical Engineering & Technology***, Vol. 15, (2020), 969-977.

Persian Abstract

چکیده

در این مقاله ، یک آرایه آهنربای دائمی Halbach با بخش مستطیل و بخش ذوزنقه ای پیشنهاد و بهینه شده است. مدل تحلیلی آرایه Halbach بر اساس روش جریان سطحی ایجاد شده است ، که از لحاظ عددی کارآمد است و می تواند برای ارزیابی میدان مغناطیسی آرایه Halbach ناشی از تنظیمات مختلف بخش آهنربایی مورد استفاده قرار گیرد. جزء اساسی چگالی شار مغناطیسی و میزان اعوجاج سینوسی به عنوان شیء بهینه سازی انتخاب شده و بهینه سازی توسط الگوریتم ژنتیک در مقیاس جهانی اجرا می شود. اثربخشی بهینه سازی با تجزیه و تحلیل اجزای محدود در Comsol تأیید می شود. در مقایسه با آرایه سنتی Halbach با بخش مستطیل ، میدان مغناطیسی ایجاد شده توسط آرایه Halbach پیشنهادی در این مقاله دارای عملکرد بهتری است.

International Journal of Engineering

Journal Homepage: www.ije.ir

Non-linear Forced Vibration Analysis of Piezoelectric Functionally Graded Beams in Thermal Environment

Y. El khouddar*[a], A. Adri[a], O. Outassafte[a], S. Rifai[a], R. Benamar[b]

[a] *Laboratoire de Mécanique Productique et Génie Industriel, Ecole Supérieure de Technologie, Hassan II University of Casablanca, Oasis, Casablanca, Morocco*
[b] *Mohammed V University in Rabat, EMI-Rabat, LERSIM, Agdal, Rabat, Morocco*

PAPER INFO

Paper history:
Received 29 January 2021
Received in revised form 13 March 2021
Accepted 31 March 2021

Keywords:
Geometrical Non-linearity
Functionally Graded Beams
Thermo-piezoelectric
Forced Vibrations
Multimode Approch

ABSTRACT

This work proposes a geometrically non-linear vibratory study of a functional gradation beam reinforced by surface-bonded piezoelectric fibers located on an arbitrary number of supports, subjected to excitation forces and thermoelectric changes. The non-linear formula is based on Hamilton's principle combined with spectral analysis and developed using Euler-Bernoulli's beam theory. In the case of a non-linear forced response, numerical results of a wide range of amplitudes are given based on the approximate multimodal method close to the predominant mode. In order to test the methods implemented in this study, examples are given and the results are very consistent with those of the literature. It should also be noted that the thermal charge, the electrical charge, the volume fraction of the structure, the thermal properties of the material, the harmonic force and the number of supports have a great influence on the forced non-linear dynamic response of the piezoelectrically functionally graded structure.

***doi**: 10.5829/ije.2021.34.11b.02*

1. INTRODUCTION

Functionally graded piezoelectric structures are heterogeneous composite materials with excellent mechanical and electrical properties, making them potentially useful for many applications in structural mechanics, electronics and other engineering fields. These structures are mainly composed of functionally graded materials (FGMs) and piezoelectric materials and are very useful in practice as they are related to structural vibration control and thermoelectric stress control. FGM is an advanced composite material that can change continuously between surfaces according to a certain distribution law. In general, FGM consists of a mixture of metal and ceramics. Refractory ceramics have a heat-insulating effect due to their low thermal conductivity, while ductile metals have higher mechanical properties and reduce the risk of fracture. This gives FGMs the following advantages: they can withstand harsh streets in high-temperature environments while maintaining their structural integrity, as dmenstrated by Hosseini Hashemi et al. [1]. Piezoelectric structures are another class of advanced materials: they are smart structures that can be used as actuators for piezoelectric transformers and sensors to control structural vibrations. The main advantage of piezoelectric materials is that they can affect the mechanical state of the structure by changing the electric field applied to the material, as shown in the document of Tadi Beni et al. [2]. Therefore, the piezoelectric FGM structure has the advantage of combining the characteristics of the FGM material and the piezoelectric material.

In recent years, research activities related to this topic have been carried out. Demir et al. [3] have committed to solve the problem of bending nano/micro beams under concentrated and dispersed loads, and target various boundary conditions, i.e. cantilevered, tight, cantilevered and simply supported. Habibi et al.

*Corresponding Author's Email: yassine.elkhouddar@ensem.ac.ma (Y. El khouddar)

Please cite this article as: Y. El khouddar, A. Adri, O. Outassafat, S. Rifai, R. Benamar, Non-linear Forced Vibration Analysis of Piezoelectric Functionally Graded Beams in Thermal Environment, International Journal of Engineering, Transactions B: Applications, Vol. 34, No. 11, (2021) 2387-2397

[4] developed the size dependent non-linear formulation for the Euler-Bernoulli nano-beam using the size dependent coherent piezoelectric theory. In this analysis, the properties of the FGM piezoelectric beam on bending, buckling, and free vibration responses were obtained and discussed. Samani and Beni [5] studied the static behavior and nonlinear free vibrations of Timoshenko's piezoelectric nanobeams under mechanical and electrical loads. In this analysis, they found that the size-dependent derivative formulation and the results of the formula were compared with the results of the linear torque stress theory and the classical linear and non-linear theories [5]. Tadi Beni [6] studied the mechanical and thermal buckling of the flexoelectric nanobeam. The results of this study indicate that as the thickness and length scale parameter increased the critical load and the critical temperature change increased. In addition, the results showed that a decrease in flexoelectric coefficient related to beam softening, critical load and critical temperature is generally reduced. Tadi Beni [7]. studied the high-order electromechanical coupling of free-vibrating nanoparticles based on Euler-Bernoulli beams in a thermal environment. In this study, the influence of parameters (such as size, length and temperature) on the natural frequencies of isotropic and anisotropic nanobeams were investigated. Tadi Beni et al. [8] used the coherent torque stress theory to study the non-linear analysis of the free and forced vibration of isotropic piezoelectric/viscoelastic nanobeams in a piezoelectric process. Nowadays, FGM structures that couple with piezoelectric materials are one of the most important engineering elements that are used in various types of systems. They also play an important role in the field of active control and intelligent detection. Li and Cheng [9] have proposed a vibration analysis method used to reinforce the static thermal post-bending of FGM stamped beams with a piezoelectric layer bonded to the surface. Use of numerical methods to solve ordinary differential equations. Li et al. [10] studied the static bending and free vibration of the cantilevered piezoelectric FGM beam using the modified stress gradient theory and Timoshenko's beam theory. Kiani and Eslami [11] studied the buckling of FGM beams. In this analysis, they assumed that the buckling surface of the beam has several piezoelectric layers and is affected by the temperature changes and constant tension. Rafiee and coworkers [12] studied the non-linear free vibration of carbon nanotube-reinforced FGM materials with a piezoelectric layer on the surface, which can withstand the combined effects of heat and electric charge. The results showed that the ratio between non-linear and linear frequencies increased with increasing the volume fraction and temperature. In another study, the same authors investigated the nonlinear thermal bifurcation buckling of carbon nanotube-reinforced composites, in which a piezoelectric layer is bonded to the surface of a carbon nanotube structure [13]. Yuan [14] proposed an active vibration and sound control law based on an intelligent panel structure of dynamic vibration damper (DVA) type. Tang and Ding [15] analyzed the non-linear dynamic response of the coupling of transverse and longitudinal deformations of a functional gradient bi-directional beam. In this investigation, they assumed that material properties, moisture and heat distribution change progressively in the thickness and length directions. Their results showed that the non-linear frequency increased with increasing temperature and humidity concentration. They also showed that moisture concentration has a great influence on the thermal vibration of the FGM beam. More recently, Liu and coworkers [16] have studied the non-linear vibration of piezoelectric nanoplate materials subjected to thermal loading under various boundary conditions. The analysis is based on the theory of non-native Mindlin Patch Theory. However, it should be noted that the proposed literature review reveals the following conclusions: most research on the geometric non-linearity of FGM beams with surface-bound piezoelectric layers is limited to the use of numerical methods to solve the guiding equations. In addition, we have noticed that there are few studies on the forced vibration of piezoelectric FGM beams in thermal environments, and most research is based on linear theory.

In this paper, for the first time, attempts are made to exploit the approximate multimodal method that is close to the dominant mode to solve the guiding equations of the forced vibration of geometrically non-linear FGM piezoelectric beams. The paper also aims to carry out a numerical study of the free and forced non-linear vibrations of FGM beams reinforced with surface-fixed piezoelectric layers. The latter is placed on any number of supports and subjected to mechanical, thermal and electrical loads. In addition, the research covers a wide range of thermal loads ($300 \leq T \leq 500$), electrical loads ($-400 \leq V \leq +400$) and volume fractions ($0 \leq n \leq 5$).

2. FUNDAMENTAL EQUATIONS

Consider the piezoelectric FGM beam shown in Figure 1. The length of the rectangular cross-section of the beam is L and the thickness is H. It consists of an FGM core of thickness h and a layer of piezoelectric material of thickness hp. It is assumed that the piezoelectric actuator is symmetrical and perfectly adhered to the upper and lower surfaces of the FGM beam. The effective characteristics of the FGM beam are defined by the Voigt mixing rule [17], and the volume fraction is distributed using the power law [18], a technique commonly used by researchers because of its high

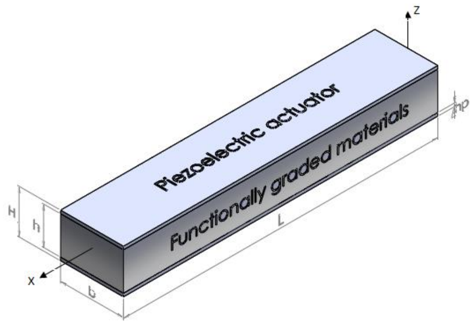

Figure 1. Coordinate system and schematic diagram of a piezoelectric functionally graded beams

accuracy. The characteristics of FGMs are illustrated below [19]:

$$P(z,T)=P_m+(P_c-P_m)\left(\frac{1}{2}+\frac{z}{h}\right)^n \tag{1}$$

Most FGMs are used at high-temperature environments, and the characteristics of the constituent materials depend on temperature, which can be written according to the definition in the literature [20]:

$$P=P_0(P_{-1}T^{-1}+1+P_1T+P_2T^2+P_3T^3) \tag{2}$$

The piezoelectric material is assumed to have temperature-independent characteristics, where C_{11} and α_p are the reduced elastic constant and thermal expansion coefficient, respectively, as summarized in Table 1. P is the temperature correlation coefficient of the FGM layer stated in Table 2. In this analysis, it is assumed that Young's modulus E_f and coefficient of thermal expansion α_f are temperature dependent and can be evaluated at any temperature. However, the density ρ_f, thermal conductivity k_f and Poisson's ratio are independent of temperature [21].

2. 1. Linear Formulation The linear vibration equation of the piezoelectric FGM beam can be obtained:

$$\left(D_{11}-\frac{B_{11}^2}{A_{11}}\right)\frac{\partial^4 w}{\partial x^4}+\left(N_x^T+N_x^P\right)\frac{\partial^2 w}{\partial x^2}+\mathrm{I}_0\frac{\partial^2 w}{\partial t^2}=0 \tag{3}$$

N_x^T and N_x^P are the thermal resultant and the electrical force, respectively. They are calculated using the relations given in documents [22-23]:

$$N_x^T=\int_{-H/2}^{H/2}E\alpha\Delta T dz, N_x^P=\int_{-H/2}^{H/2}Ed_{31}E_z dz \tag{4}$$

A_{11}, B_{11} and D_{11} are extension-extension, flexion-extension-flexion and flexion-flexion coupling coefficients, respectively; which can be evaluated using the classical FMS beam theory, as reported in the literature [24-25]. Their definitions are as follows:

$$A_{11}=\int_{-\frac{H}{2}}^{\frac{H}{2}}Edz, B_{11}=\int_{-\frac{H}{2}}^{\frac{H}{2}}E(z-z_0)dz,$$
$$D_{11}=\int_{-\frac{H}{2}}^{\frac{H}{2}}E(z-z_0)^2dz \tag{5}$$

Equation (3) can be written in a slightly more complicated way, and the result is:

$$w''''+\lambda w''-\beta^4 w=0 \tag{6}$$

In formula (6), the new symbol represents the following functional relationship:

$$\lambda=\frac{N^T+N^P}{\left(D_{11}-\frac{B_{11}^2}{A_{11}}\right)},\ \beta^2=\frac{\omega}{c}, c^2=\frac{\left(D_{11}-\frac{B_{11}^2}{A_{11}}\right)}{\mathrm{I}_0} \tag{7}$$

The lateral displacement of the beam can be defined as the correlation between several functions [26]. We can write the general solution of equation (6) at the jth support as follows:

$$\begin{aligned}w_{ji}(x^*)=&A_j\sin\left(\sqrt{\frac{1}{2}\lambda+\frac{1}{2}\sqrt{\lambda^2+4\beta_i^4}}\left(x^*-\xi_{j-1}\right)L\right)+\\&B_j\cos\left(\sqrt{\frac{1}{2}\lambda+\frac{1}{2}\sqrt{\lambda^2+4\beta_i^4}}\left(x^*-\xi_{j-1}\right)L\right)+\\&C_j\sinh\left(\sqrt{-\frac{1}{2}\lambda+\frac{1}{2}\sqrt{\lambda^2+4\beta_i^4}}\left(x^*-\xi_{j-1}\right)L\right)+\\&D_j\cosh\left(\sqrt{-\frac{1}{2}\lambda+\frac{1}{2}\sqrt{\lambda^2+4\beta_i^4}}\left(x^*-\xi_{j-1}\right)L\right)\end{aligned} \tag{8}$$

x^* is the dimensionless coordinate, which can be written $x^*=\frac{x}{L}$ and $\xi_j=\frac{x_j}{L}$ is the dimensionless position of the support. The index i changes from 1 to n, where n is the number of functions. The constants A_j, B_j, C_j and D_j are determined by the boundary and continuity conditions of the beam. We point out that due to the applied thermoelectric axial loading, this system of equations allows us to obtain the natural frequency which is solved iteratively using the Newton-Raphson algorithm and the shape of the vibration mode.

2. 2. Non-linear Formulation Taking into account von-Karman's geometrical non-linearity (explaining the tension of the beam in the median plane), the relationship between deformation and displacement can be written as follows:

$$\varepsilon_{xx} = \frac{\partial u}{\partial x} - (z - z_0)\frac{\partial^2 w}{\partial x^2} + \frac{1}{2}\left(\frac{\partial w}{\partial x}\right)^2 \tag{9}$$

The Von-Karman geometric non-linearity considered in Equation (9) is applicable to displacement amplitudes of the order of the thickness of the rolled beam. This hypothesis is generally considered in the literature and mentioned in literature [27]. Therefore, the kinetic energy T_e of the piezoelectric FGM beam is equal to [28]:

$$T_e = \frac{I_0}{2}\int_0^L \left(\frac{\partial w}{\partial t}\right)^2 dx \tag{10}$$

For our case, the total elastic deformation energy of the Euler-Bernoulli beam is defined as follows:

$$V = \frac{1}{2}\int_0^L N_x\left(\frac{\partial u}{\partial x} + \frac{1}{2}\left(\frac{\partial w}{\partial x}\right)^2\right) + M_x\left(-\frac{\partial^2 w}{\partial x^2}\right)dx \tag{11}$$

The forces generated by the stresses N_x and M_x are the internal axial force and the bending moment acting on the median plane of the beam, respectively [29]. The lateral displacement function develops into a series of basic spatial functions, while the time function is considered as harmonics, as shown in literature [30]:

$$w(x,t) = a_i w_i(x)\sin\omega t \tag{12}$$

The expressions of kinetic energy and potential energy that vary with the lateral displacement defined above can be expressed as follows:

$$T_e = \frac{1}{2}\omega^2 a_i a_j m_{ij}\cos^2\omega t \tag{13}$$

$$\begin{aligned} V &= \frac{1}{2}a_i a_j a_k a_l b_{ijkl}\sin^4\omega t + \frac{1}{2}a_i a_j k_{ij}\sin^2\omega t \\ &+ \frac{1}{2}a_i a_j a_k V_{ijk}\sin^3\omega t \end{aligned} \tag{14}$$

m_{ij}, k_{ij}, b_{ijkl} and V_{ijk} are mass tensor, linear and non-linear stiffness tensors. For the piezoelectric FGM beam excited by the force $F(x,t)$, non-linear vibration equations are studied. The physical force $F(x,t)$ excites the transverse mode of the structure by a set of generalized forces $F_i(t)$. These forces depend on the expression of $F(x,t)$, the point of excitation of the concentrated force, the repair in the range S representing the length of the beam or part of the beam, and the mode considered. The generalized force $F_i(t)$ is given by:

$$F_i(t) = \int_S F(x,t)w_i(x,t)dx \tag{15}$$

In our case, the force $F(x,t)$ can be considered as the distributed harmonic force $F^d(x,t)$ or the concentrated harmonic force $F^c(x,t)$ acting on the point x_f. We can write [31]:

$$\begin{aligned} F_i^d(t) &= F^d\sin\omega t\int_S w_i(x)dx = f_i^d\sin\omega t \\ F_i^c(t) &= F^c\sin(\omega t)w_i(x_f) = f_i^c\sin\omega t \end{aligned} \tag{16}$$

According to Hamilton's principle, the dynamic behavior of the structure is expressed as follows:

$$\partial\int_0^{\frac{2\pi}{\omega}}\left(V - T_e + W_T\right)dt = 0 \tag{17}$$

Given the symmetry of the matrices, the non-linear algebraic equations are calculated using tensor notation:

$$a_i k_{ir} + \frac{3}{2}a_i a_j a_k b_{ijkr} - \omega^2 a_i m_{ir} = f_r^d, r = 1,...,n \tag{18}$$

$$a_i k_{ir} + \frac{3}{2}a_i a_j a_k b_{ijkr} - \omega^2 a_i m_{ir} = f_r^c, r = 1,...,n \tag{19}$$

In order to carry out a general parametric study, we used a non-dimensional formulation by setting up:

$$x^* = \frac{x}{L},\ w_i(x) = r\,w_i^*(x^*),\ r^2 = \frac{\int_{-H/2}^{H/2} z^2 dz}{\int_{-H/2}^{H/2} dz} \tag{20}$$

where m_{ij}^*, k_{ij}^* and b_{ijkl}^* are the general non-dimensional matrices which are defined by:

$$\begin{aligned} m_{ij}^* &= \int_0^1 w_i^* w_j^* dx^*, \\ k_{ij}^* &= \int_0^1\left(\frac{\partial^2 w_i^*}{\partial x^{*2}}\right)\left(\frac{\partial^2 w_j^*}{\partial x^{*2}}\right)dx^* + \\ &\alpha_2\int_0^1\left(\frac{\partial^2 w_i^*}{\partial x^{*2}}\right)\left(\frac{\partial^2 w_j^*}{\partial x^{*2}}\right)dx^* + \alpha_3\int_0^1\left(\frac{\partial w_i^*}{\partial x^*}\right)\left(\frac{\partial w_j^*}{\partial x^*}\right)dx^* \\ b_{ijkl}^* &= \alpha_1\int_0^1\left(\frac{\partial w_i^*}{\partial x^*}\right)\left(\frac{\partial w_j^*}{\partial x^*}\right)dx^*\int_0^1\left(\frac{\partial w_k^*}{\partial x^*}\right)\left(\frac{\partial w_l^*}{\partial x^*}\right)dx^* \end{aligned} \tag{21}$$

$$\begin{aligned} \alpha_1 &= \frac{A_{11}^2}{48\left(D_{11}A_{11} - B_{11}^2\right)}H^2, \alpha_2 = \frac{B_{11}^2}{\left(D_{11}A_{11} - B_{11}^2\right)}, \\ \alpha_3 &= \frac{\left(N^T + N^P\right)A_{11}}{2\left(D_{11}A_{11} - B_{11}^2\right)}L^2 \end{aligned} \tag{22}$$

The generalized dimensionless force f_i^{*d} corresponds to the uniformly distributed force in the range of $S^*(0 \le S^* \le 1)$ on one side, and the generalized dimensionless force f_i^{*c} on the other side corresponds to the force concentrated at any point of the beam, defined in literature [32] as follows:

$$f_i^{*d} = \frac{L^4 F^d}{r\left(D_{11} - \frac{B_{11}^2}{A_{11}}\right)} \int_{S^*} w_i^*(x^*) dx^*, \qquad f_i^{*c} = \frac{L^3 F^c}{r\left(D_{11} - \frac{B_{11}^2}{A_{11}}\right)} w_i^*(x^*) \tag{23}$$

The numerical solutions of Equations (18) and (19) are obtained using the approximate method described by El Kadiri et al. [33]. This approximation consists of ignoring the second-order terms provided by the relevant mode. As mentioned in the literature, in the non-linear $a_i a_j a_k b_{ijkr}$ expression of Equations (18) and (19), the second order term of ε_i will be ignored, resulted in:

$$a_i a_j a_k b_{ijkr} = a_1^3 b_{111r} + a_1^2 \varepsilon_i b_{11ir} \tag{24}$$

Formulas (18) and (19) can be expressed as matrices:

$$\left(\left[K_R^*\right] - \omega^{*2}\left[M_R^*\right]\right)\left\{A_R\right\} + \frac{3}{2}\left[\alpha^*\right]\left\{A_R\right\} = \left\{f_i^{*d} - \frac{3}{2} a_1^3 b_{i111}{}^*\right\} \tag{25}$$

$$\left(\left[K_R^*\right] - \omega^{*2}\left[M_R^*\right]\right)\left\{A_R\right\} + \frac{3}{2}\left[\alpha^*\right]\left\{A_R\right\} = \left\{f_i^{*c} - \frac{3}{2} a_1^3 b_{i111}{}^*\right\} \tag{26}$$

The index i changes from 2 to n, where $\left[\alpha^*\right]$ is the matrix defined by $a_1^2 b_{11ir}^*$, and the vector $\left\{A_R\right\} = \left[\varepsilon_2, \varepsilon_3, ..., \varepsilon_{10}\right]$ is a vector modeling the contribution coefficient, which can be determined by solving approximate linear Equations (25) and (26).

3. PRESENTATION AND DISCUSSION OF NUMERICAL RESULTS

In this numerical analysis, we consider that the length of the beam is L = 200 mm, the thickness H = 10 mm and the thickness of the FGM layer is h = 8 mm. The piezoelectric fibers are manufactured on the basis of PZT 5A, assuming that they are not affected by temperature, their characteristics are defined in Table 1 according to literature [34]. The FGM layer is based on silicon nitride (Si_3N_4) and stainless steel (SUS304). Their Young's modulus and coefficient of thermal expansion are temperature dependent and are therefore listed in Table 2 according to literature [35-36]. Unless otherwise stated, we assume that the reference temperature is the same as the temperature of the lower surface of the piezoelectric FGM beam, while the temperature of the upper surface is variable and the Poisson's ratio of the FGM layer is a constant equal to 0.28. In addition, in order to ensure the accuracy and validity of the results obtained from this analysis and approximation, verification and validation studies will be conducted in the following section. Subsequently, a comprehensive parameter study was conducted to evaluate the influence of different parameters on the non-linear vibratory behaviour of the piezoelectric FGM beam.

3. 1. Comparison with Previous Results

The first application presents a non-linear vibratory analysis of the results of a homogeneous isotropic beam which is compared to the predictions reported in literature [37-40]. Table 3 shows the ratio of the non-linear frequency to the linear frequency of the isotropic beam under different vibration amplitudes Wmax/r. The results presented in Table 3 show that there is a good agreement between the predicted value of the current method and the other published data in the literature.

In another verification study, under the conditions corresponding to a thermal load $T_c = 300K$ and the absence of electric charge ($V = 0V$), the Backbone Curves of the piezoelectric FGM beam with different volume fractions of n were considered in Figure 2. The figure shows that the results of this study are consistent with those obtained by Fu et al. [37]. Moreover, Figure 3 clearly shows that the influence of the volume fraction index n significantly affects the frequency ratio, and the non-linear frequency increases with increasing vibration amplitude. According to Figure 3, when the volume fraction remains constant $n = 1$, the voltage

TABLE 3. Comparisons of non-linear and linear frequency ratios of a homogeneous isotropic beam

Wmar/r	Present	Ref [37]	Ref [38]	Ref [39]	Ref [40]
1	1.0222	1.0231	1.0222	1.0252	1.0222
2	1.0868	1.0892	1.0857	1.0899	1.0857
3	1,1880	1.1902	1.1831	1.1885	1.1833
4	1,3187	1.3178	1.3064	1.3140	1.3065
5	1.4723	1.4647	1.4488	1.4597	1.4477

variations V are respectively equal to $V = 400V$, $0V$ and $-400V$ have little influence on the backbone curves. Figure 4 shows the effect of temperature changes ($T_c = 300, 400, 500K$) when the volume fraction is kept constant at $n = 1$. The influence of temperature and volume fraction on the amplitude-frequency response curve is more severe than that of electrical charge. This can be predicted by formula (4), the value of the piezoelectric deformation constant is much less than the thermal expansion coefficient. At the same time, the difference in thickness between the piezoelectric layer and the FGM layer is another factor. It can also be seen that the results of this study are consistent with those of the literature. It should also be noted that an increase in temperature causes an increase in the ratio of the non-linear frequency to the linear frequency.

TABLE 1. Properties of PZT 5A

Properties	E_p **(Gpa)**	ρ_p **(Kg/m3)**	κ_p **(W/mK)**	ν_p	α_p **(1/K)**	d_{31} **(m/V)**
Values	63	7600	2.1	0.3	0.9e-6	2.54e-10

TABLE 2. Coefficients material properties as a function of temperature for Si_3N_4 and SUS304

Materials	**Properties**	P_0	P_{-1}	P_1	P_2	P_3
Si_3N_4	$E_c(Pa)$	348.43e+9	0	-3.07e-4	2.160e-7	-8.964e-11
	$\alpha_c(1/K)$	5.8723e-6	0	9.095e-4	0	0
SUS304	$E_m(Pa)$	201.04e+9	0	3.079e-4	-6.534e-7	0
	$\alpha_m(1/K)$	12.33e-6	0	8.086e-4	0	0

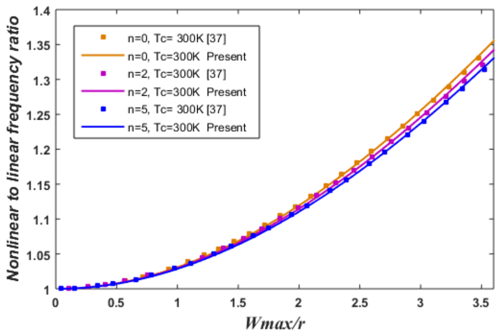

Figure 2. Comparison of the frequency ratio of the piezoelectric FGM beam with variation of the volume fraction n

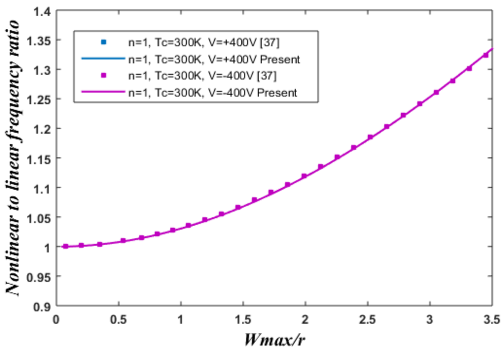

Figure 3. Comparison of the frequency ratio of the piezoelectric FGM beam under electrical load

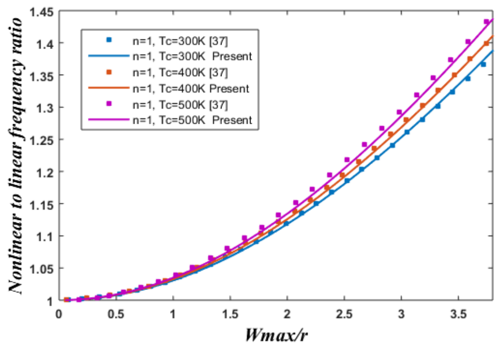

Figure 4. Comparison of the frequency ratio of the piezoelectric FGM beam under thermal load

3. 2. Numerical Results and Discussion The numerical results presented in this section are obtained for embedded beams resting on two supports. The positions of the supports are chosen as follows: $\zeta_1 = \frac{1}{3}$, $\zeta_1 = \frac{2}{3}$. Figure 5 shows the typical shape of the first four modes of an isotropic beam. However, Figure 6 uses the current formula to present the shape of the first non-linear mode of the piezoelectric FGM, where the volume fraction of $n = 1$, the thermal charge of $T_c = 300K$ and the electrical charge of $V = 0V$. It can be clearly seen in Figure 6 that for different vibration

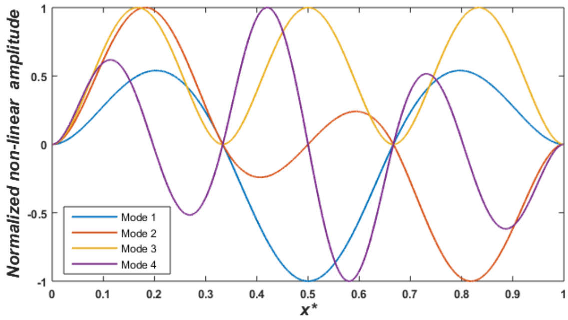

Figure 5. The first normalized linear modes of a clamped beam resting on two simple supports

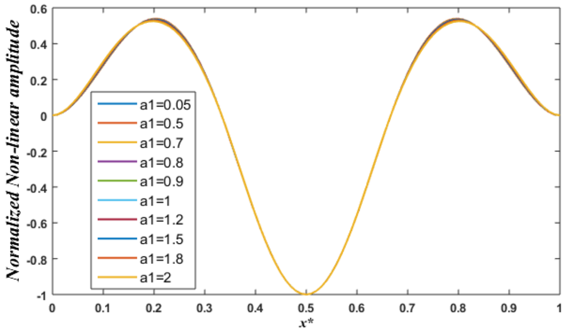

Figure 6. The first normalized non-linear mode of piezoelectric FGM beam, which rests on two simple supports and has several vibration amplitudes values

amplitudes, the effect of geometrical non-linearity can be observed.

As shown in Figures 7-10, in the case of a non-linear forced-vibration system, the resonance curve shows the jump phenomenon [40]. This behavior indicates that as the excitation frequency increases or decreases, the amplitude of the vibration may increase or decrease. This leads to the creation of a frequency range in which there are three amplitudes for a given frequency, resulting in frequency jumps. In this part of the numerical analysis, two typical excitations are verified, namely that the harmonic force uniformly distributed along the length of the beam is given by (a), while (b) presents the case of a force concentrated in the center of the beam. All frequency response curves show that the resonance area of the concentrated harmonic force is wider than that of the uniformly distributed harmonic force. In fact, this behavior indicates that the way to widen the resonance band is to add stiffness characteristics. A hardening or softening stiffness can produce the wider resonant frequency band [41]. As shown in Figures 7-10, the action of the concentrated harmonic force causes the widening of the resonant frequency band. In other words, beams subjected to concentrated harmonic forces exhibit a softening behavior compared to beams subjected to uniformly distributed harmonic forces. For the three excitation levels corresponding to F = 50, 500 and 1000, Figures 7a and 7b show the influence of the uniformly distributed harmonic excitation and the concentrated harmonic force on the amplitude-frequency response curve of the beam, respectively. In these figures, we can see that the peak amplitude increases with excitation. In addition, for higher excitation values, the frequency range of the solution is wider. Figure 8 shows the effect of thermal loading on the amplitude-frequency response curve when the force is set to F = 500. The results show that as the thermal load increases, the amplitude of the frequency response decreases, while the amplitude-frequency curve tends to the right. In fact, this behavior indicates that the presence of non-linear terms can bend the amplitude-frequency response curve. In addition, as the temperature decreases, the hardening effect is greatly enhanced. Therefore, it can be deduced that thermal loading has a significant influence on the frequency response and the hardening of the beam. Figure 9 shows the effect of the volume fraction on the resonance response when the force is set at F=500. As shown in Figures 9a and 9b, for both types of excitation, an increase in the volume fraction index leads to an increase in the dimensionless frequency and a decrease in the maximum amplitude. Figure 10 shows the effect of the electrical voltage on the forced dynamic response of the beam when the force is set at F = 500 and the volume fraction is set at $n=1$.

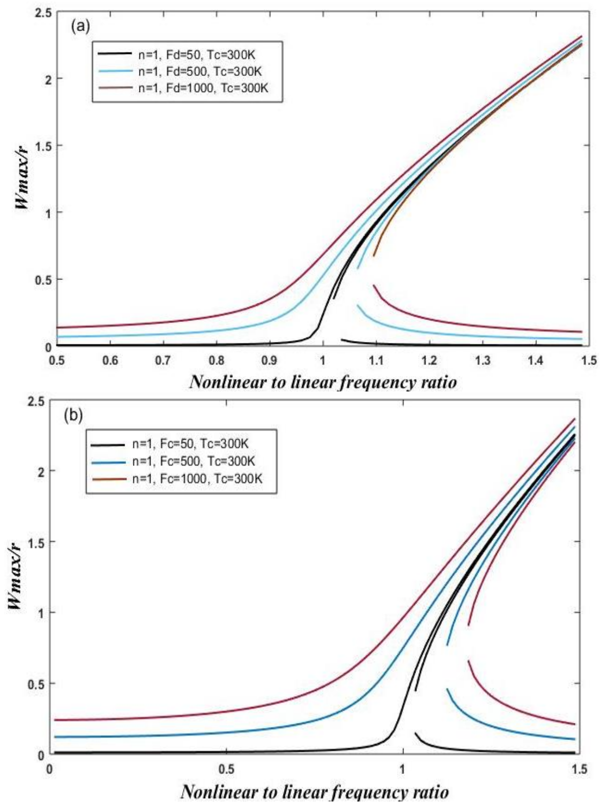

Figure 7. Resonance curves of three levels of excitation

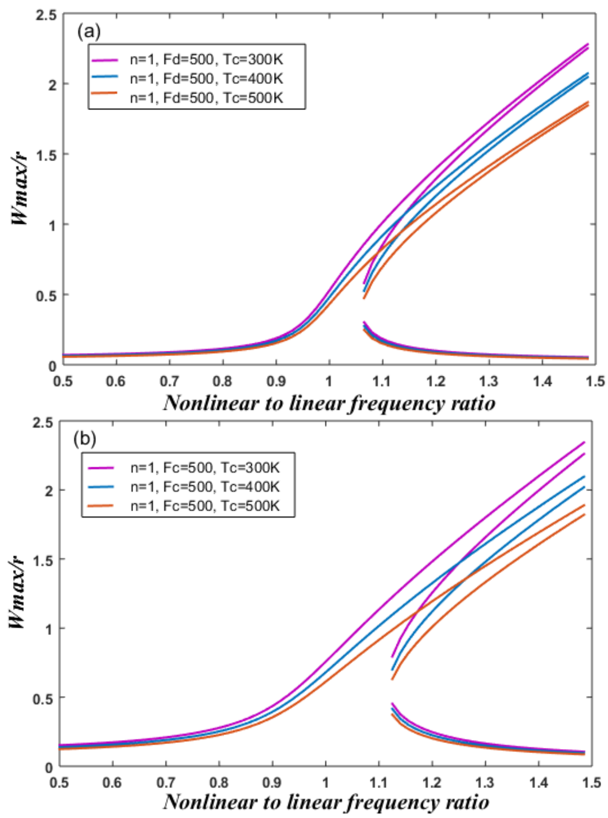

Figure 8. Resonance curves of thermal loads

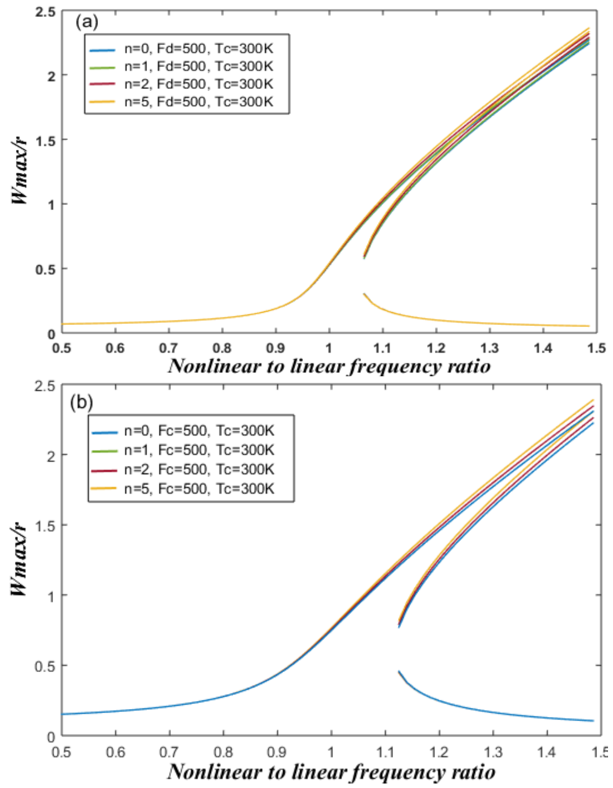

Figure 9. Resonance curves with different volume fraction values

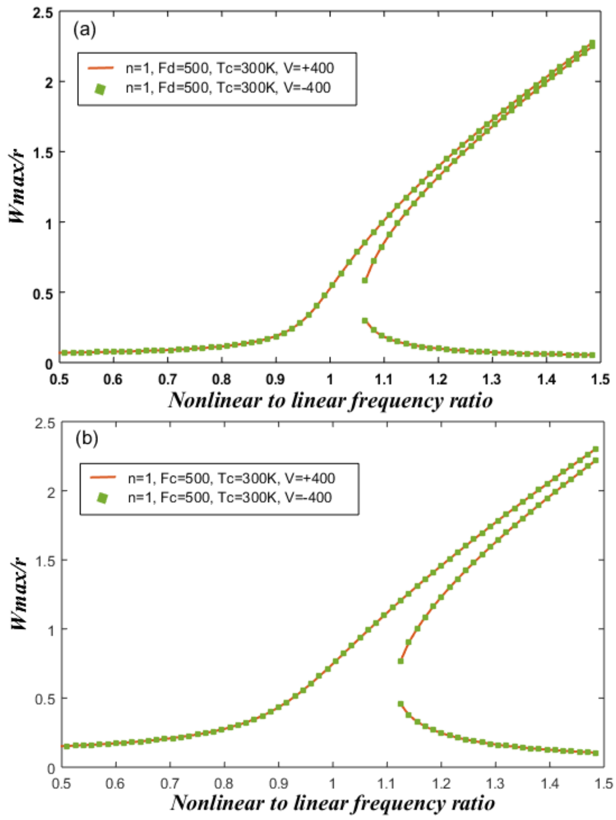

Figure 10. Resonance for different values of the electric charge

Obviously, since the value of the piezoelectric strain constant is much smaller than the coefficient of thermal expansion, the variation of the electric voltage has little effect on the resonance response curve, and the same phenomenon is observed in Figure 3. In addition, Figure 10 shows the unstable region of the non-linear forced vibration, in which the discontinuous part is the unstable boundary, the solution between the boundaries is unstable and the other regions are stable. In fact, this behavior indicates that the amplitude number varies with the type and value of the external excitation frequency. According to the forced non-linear response, the presence of regions with multiple values will cause a jump phenomenon. In the case of uniformly distributed external excitation, the unstable region is offset from the concentrated excitation.

4. CONCLUSIONS

On the basis of Euler-Bernoulli's beam theory and von Kármán's displacement-deformation relationship, we have studied the free vibration and the geometrically non-linear forced vibration of the piezoelectric FGM beam under the action of a thermoelectric field. The Hamiltonian principle and spectral analysis are used to obtain the guiding equations that control the free and forced non-linear behavior. The latter was adopted for the case of a uniform distribution over the length of the beam and also for the case of a force concentrated in the center of the beam. In addition, the analytical response of the non-linear forced vibration is obtained by introducing an approximation function based on the multimode method close to the main mode. This approximation makes it possible to obtain the dynamic behavior of beams resting on several supports. Then, the methods used in this study are verified by referring to the results of the literature. Finally, the numerical results revealed an impact on the resonance curve through several variances: the volume fraction index, the thermal load, the effect of the beam supports and the thermal characteristics of the constituent materials. The above analysis clearly highlights the following points:

- In the resonance response curve, an increase in the distributed or concentrated harmonic excitation force applied to the piezoelectric FGM beam causes the curve to gradually increase as the frequency increases, and this increase in force also widens the resonance curve.
- As the temperature decreases, the ratio of non-linear to linear frequency increases, and the amplitude-frequency response curve shows an improvement in peak amplitude.
- As the volume fraction increases, the amplitude of the forced vibration system gradually increases.
- Compared to the thermal load, the electrical load has little effect on the behavior of free and forced non-linear vibrations. The results also confirmed that the addition of reinforcing mounts has an important influence on the non-linear vibration behavior of the piezoelectric FGM beam.

5. REFERENCES

1. Bakhshi Khaniki, H., Hosseini Hashemi, S. and Bakhshi Khaniki, M., "Free Vibration Analysis of Functionally Graded Materials Non-Uniform Beams", ***International Journal of Engineering*, *Transactions C: Aspects,*** Vol. 29, No. 12, (2016), 1734-1740, DOI: 10.5829/idosi.ije.2016.29.12c.12.
2. Tadi Beni, Z., Hosseini Ravandi, S. and Tadi Beni, Y., "Investigation of the Size Effect on the Nano-Beam Type Piezoelectric Low Power Energy Harvesting", ***International Journal of Engineering, Transactions C: Aspects***, Vol. 31, No. 9, (2018), 1585-1592, DOI: 10.5829/ije.2018.31.09c.15.
3. Demir, Ç. and Civalek, Ö., "On the Analysis of Microbeams", ***International Journal of Engineering Science***, Vol. 121, (2017), 14-33, DOI: 10.1016/j.ijengsci.2017.08.016.
4. Habibi, B., Beni, Y.T., Mehralian, F., "Free Vibration of Magneto-Electro-Elastic Nanobeams Based on Modified Couple Stress Theory in Thermal Environment", ***Mechanics of Advanced Materials and Structures***, Vol. 26, No. 7, (2019), 601-613, DOI: 10.1080/15376494.2017.1410902.
5. Samani, M.S.E. and Beni, Y.T, "Size Dependent Thermo-Mechanical Buckling of the Flexoelectric Nanobeam", ***Materials Research Express***, Vol. 5, No. 8, (2018), 085018, DOI: 10.1088/2053-1591/aad2ca.
6. Tadi Beni, Y., "Size-Dependent Analysis of Piezoelectric Nanobeams Including Electro-Mechanical Coupling", ***Mechanics Research Communications***, Vol. 75, (2016), 67-80, DOI: 10.1016/j.mechrescom.2016.05.011.
7. Tadi Beni, Y., "Size-Dependent Electromechanical Bending, Buckling, and Free Vibration Analysis of Functionally Graded Piezoelectric Nanobeams", ***Journal of Intelligent Material Systems and Structures***, Vol. 27, No. 16, (2016), 2199-2215, DOI: 10.1177/1045389X15624798.
8. Tadi Beni, Z., Hosseini Ravandi, S., Tadi Beni, Y., "Size-Dependent Nonlinear Forced Vibration Analysis of Viscoelastic/Piezoelectric Nano-Beam", ***Journal of Applied and Computational Mechanics***, (2020), DOI: 10.22055/jacm.2020.32044.1958.
9. Li, S.-r., Cheng, C.-j., "Free Vibration of Functionally Graded Material Beams with Surface-Bonded Piezoelectric Layers in Thermal Environment", ***Applied Mathematics and Mechanics***, Vol. 30, No. 8, (2009), 969-982, DOI: 10.1007/s10483-009-0803-7.
10. Li, Y., Feng, W. and Cai, Z., "Bending and Free Vibration of Functionally Graded Piezoelectric Beam Based on Modified Strain Gradient Theory", ***Composite Structures***, Vol. 115, (2014), 41-50, DOI: 10.1016/j.compstruct.2014.04.005.
11. Kiani, Y., Eslami, M., "Thermal Buckling Analysis of Functionally Graded Material Beams", ***International Journal of Mechanics and Materials in Design***, Vol. 6, No. 3, (2010), 229-238, DOI: 10.1007/s10999-010-9132-4.
12. Rafiee, M., Yang, J. and Kitipornchai, S., "Large Amplitude Vibration of Carbon Nanotube Reinforced Functionally Graded Composite Beams with Piezoelectric Layers", ***Composite Structures***, Vol. 96, (2013), 716-725, DOI: 10.1016/j.compstruct.2012.10.005.
13. Rafiee, M., Yang, J., Kitipornchai, S., "Thermal Bifurcation Buckling of Piezoelectric Carbon Nanotube Reinforced Composite Beams", ***Computers & Mathematics with Applications***, Vol. 66, No. 7, (2013), 1147-1160, DOI: 10.1016/j.camwa.2013.04.031.
14. Yuan, M., "Compact and Efficient Active Vibro-Acoustic Control of a Smart Plate Structure", ***International Journal of Engineering, Transactions B: Applications,*** Vol. 29, No. 8, (2016), 1068-1074.
15. Tang, Y. and Ding, Q., "Nonlinear Vibration Analysis of a Bi-Directional Functionally Graded Beam under Hygro-Thermal Loads", ***Composite Structures***, Vol. 225, (2019), 111076, DOI: 10.1016/j.compstruct.2019.111076.
16. Liu, C., Ke, L.-L., Yang, J., Kitipornchai, S., Wang, Y.-S., "Nonlinear Vibration of Piezoelectric Nanoplates Using Nonlocal Mindlin Plate Theory", ***Mechanics of Advanced Materials and Structures***, Vol. 25, No. 15-16, (2018), 1252-1264, DOI: 10.1080/15376494.2016.1149648.
17. WANI, S.B., "Influence of Bi-Directional Fibreglass Grid Reinforcement on Drying Shrinkage and Mechanical Properties of Lightweight Foamed Concrete", ***International Journal of Engineering, Transactions A: Basics,*** Vol. 34, No. 1, (2021), DOI: 10.5829/ije.2021.34.01a.02.
18. Rahnavard, M., "Hot Corrosion Behavior of Functional Graded Material Thermal Barrier Coating (Research Note)", ***International Journal of Engineering, Transactions A: Basics,*** Vol. 30, No. 1, (2017), 101-108, DOI: 10.5829/idosi.ije.2017.30.01a.13.
19. Sherafatnia, K., Farrahi, G. and Faghidian, S.A., "Analytic Approach to Free Vibration and Buckling Analysis of

Functionally Graded Beams with Edge Cracks Using Four Engineering Beam Theories", ***International Journal of Engineering*, *Transactions C: Aspects*** Vol. 27, No. 6, (2014), 979-990. DOI: 10.5829/idosi.ije.2014.27.06c.17

20. Mirzavand, B. and Eslami, M.J., "Thermal Buckling of Simply Supported Piezoelectric Fgm Cylindrical Shells", ***Journal of Thermal Stresses***, Vol. 30, No. 11, (2007), 1117-1135, DOI: 10.1080/01495730701416036.
21. Huang, X.-L., Shen, H.-S., "Vibration and Dynamic Response of Functionally Graded Plates with Piezoelectric Actuators in Thermal Environments", ***Journal of Sound and Vibration***, Vol. 289, No. 1-2, (2006), 25-53 DOI: 10.1016/j.jsv.2005.01.033.
22. Zhang, D.-G. and Zhou, Y.-H., "A Theoretical Analysis of Fgm Thin Plates Based on Physical Neutral Surface", ***Computational Materials Science***, Vol. 44, No. 2, (2008), 716-720, DOI: 10.1016/j.commatsci.2008.05.016.
23. Emam, S.A. and Nayfeh, A.H., "Postbuckling and Free Vibrations of Composite Beams", ***Composite Structures***, Vol. 88, No. 4, (2009), 636-642, DOI: 10.1016/j.compstruct.2008.06.006.
24. Tian, Y., Fu, Y., Wang, Y., "Nonlinear Dynamic Response and Vibration Active Control of Piezoelectric Elasto-Plastic Laminated Plates with Damage", ***Journal of Vibration***, Vol. 15, No. 10, (2009), 1463-1492, DOI: 10.1177/1077546309103265.
25. Kitipornchai, S., Ke, L., Yang, J., Xiang, Y., "Nonlinear Vibration of Edge Cracked Functionally Graded Timoshenko Beams", ***Journal of Sound and Vibration***, Vol. 324, No. 3-5, (2009), 962-982, DOI: 10.1016/j.jsv.2009.02.023.
26. Maiz, S., Bambill, D.V., Rossit, C.A., Laura, P.A.A., "Transverse Vibration of Bernoulli–Euler Beams Carrying Point Masses and Taking into Account Their Rotatory Inertia: Exact Solution", ***Journal of Sound and Vibration***, Vol. 303, No. 3-5, (2007), 895-908, DOI: 10.1016/j.jsv.2006.12.028.
27. Adri, A. and Benamar, R., "Linear and Geometrically Non-Linear Frequencies and Mode Shapes of Beams Carrying a Point Mass at Various Locations. An Analytical Approch and a Parametric Study", ***Diagnostyka***, Vol. 18, No. 2, (2017).
28. Zhang, Z. and Zhang, C., "Mechanical Properties Analysis of Bilayer Euler-Bernoulli Beams Based on Elasticity Theory", ***International Journal of Engineering, Transactions B: Applications***, Vol. 33, No. 8, (2020), 1662-1667, DOI: 10.5829/ije.2020.33.08b.25.
29. Ansari, R., Gholami, R. and Sahmani, S., "Free Vibration Analysis of Size-Dependent Functionally Graded Microbeams Based on the Strain Gradient Timoshenko Beam Theory", ***Composite Structures***, Vol. 94, No. 1, (2011), 221-228, DOI: 10.1016/j.compstruct.2011.06.024.
30. Benamar, R., Bennouna, M., White, R., "The Effects of Large Vibration Amplitudes on the Mode Shapes and Natural Frequencies of Thin Elastic Structures Part I: Simply Supported and Clamped-Clamped Beams", ***Journal of Sound and Vibration***, Vol. 149, No. 2, (1991), 179-195, DOI: 10.1016/0022-460X(91)90630-3.
31. Azrar, L., Benamar, R., White, R., "A Semi-Analytical Approach to the Non-Linear Dynamic Response Problem of Beams at Large Vibration Amplitudes, Part Ii: Multimode Approach to the Steady State Forced Periodic Response", ***Journal of Sound and Vibration***, Vol. 255, No. 1, (2002), 1-41, DOI: 10.1006/jsvi.2000.3595.
32. Fakhreddine, H., Adri, A., Chajdi, M., Rifai, S. and Benamar, R., "A Multimode Approach to Geometrically Non-Linear Forced Vibration of Beams Carrying Point Masses", ***Diagnostyka***, Vol. 21, (2020), DOI: 10.29354/diag/128603.
33. El Kadiri, M., Benamar, R., White, R., "Improvement of the Semi-Analytical Method, for Determining the Geometrically Non-Linear Response of Thin Straight Structures. Part I: Application to Clamped–Clamped and Simply Supported–Clamped Beams", ***Journal of Sound and Vibration***, Vol. 249, No. 2, (2002), 263-305, DOI: 10.1006/jsvi.2001.3808.
34. Rafiee, M., Mohammadi, M., Aragh, B.S. and Yaghoobi, H., "Nonlinear Free and Forced Thermo-Electro-Aero-Elastic Vibration and Dynamic Response of Piezoelectric Functionally Graded Laminated Composite Shells, Part I: Theory and Analytical Solutions", ***Composite Structures***, Vol. 103, No., (2013), 179-187 DOI: 10.1016/j.compstruct.2012.12.053.
35. Reddy, J. and Chin, C., "Thermomechanical Analysis of Functionally Graded Cylinders and Plates", ***Journal of Thermal Stresses,*** Vol. 21, No. 6, (1998), 593-626, DOI: 10.1080/01495739808956165.
36. Babaee, A., Sadighi, M., Nikbakht, A. and Alimirzaei, S., "Generalized Differential Quadrature Nonlinear Buckling Analysis of Smart Sma/Fg Laminated Beam Resting on Nonlinear Elastic Medium under Thermal Loading", ***Journal of Thermal Stresses,*** Vol. 41, No. 5, (2018), 583-607, DOI: 10.1080/01495739.2017.1408048.
37. Fu, Y., Wang, J. and Mao, Y., "Nonlinear Analysis of Buckling, Free Vibration and Dynamic Stability for the Piezoelectric Functionally Graded Beams in Thermal Environment", ***Applied Mathematical Modelling***, Vol. 36, No. 9, (2012), 4324-4340, DOI: 10.1016/j.apm.2011.11.059
38. Ke, L.-L., Yang, J. and Kitipornchai, S., "An Analytical Study on the Nonlinear Vibration of Functionally Graded Beams", ***Meccanica,*** Vol. 45, No. 6, (2010), 743-752, DOI: 10.1007/s11012-009-9276-1
39. Shooshtari, A. and Rafiee, M., "Nonlinear Forced Vibration Analysis of Clamped Functionally Graded Beams", ***Acta Mechanica***, Vol. 221, No. 1, (2011), 23. DOI: 10.1007/s00707-011-0491-1
40. Azrar, L., Benamar, R. and White, R. G., "Semi-analytical approach to the non-linear dynamic response problem of s–s and c–c beams at large vibration amplitudes part i: general theory and application to the single mode approach to free and forced vibration analysis", ***Journal of Sound and Vibration***, Vol. 224, No. 2, (1999), 183-207, DOI: 10.1006/jsvi.1998.1893.
41. Rubes, O., and Hadas, Z., "Designing, Modelling and Testing of Vibration Energy Harvester with Nonlinear Stiffness, Smart Sensors, Actuators, and MEMS VIII, Smart Sensors, Actuators, and MEMS VIII", ***International Society for Optics and Photonics***, Vol. 10246, (2017), 102460W.

Persian Abstract

چکیده

این کار یک مطالعه ارتعاشی غیر خطی هندسی از یک پرتو درجه بندی عملکردی را تقویت می کند که توسط الیاف پیزوالکتریک پیوندی روی سطح واقع در تعداد دلخواه پشتیبانی ، تحت نیروهای تحریک و تغییرات ترموالکتریک تقویت شده است. فرمول غیر خطی بر اساس اصل همیلتون همراه با تجزیه و تحلیل طیفی و با استفاده از نظریه پرتو اویلر-برنولی ساخته شده است. در مورد پاسخ اجباری غیر خطی ، نتایج عددی طیف گسترده ای از دامنه ها بر اساس روش چند مدی تقریبی نزدیک به حالت غالب داده می شود. به منظور آزمایش روشهای پیاده سازی شده در این مطالعه ، مثالهایی آورده شده است و نتایج با داده های گزارش شده بسیار مطابقت دارد. همچنین باید توجه داشت که بار حرارتی ، بار الکتریکی ، کسر حجمی سازه ، خصوصیات حرارتی ماده ، نیروی هارمونیک و تعداد تکیه گاه ها تأثیر زیادی در پاسخ دینامیکی غیر خطی دینامیکی ساختار پیزوالکتریک دارای درجه بندی عملکردی است.

IJE TRANSACTIONS B: Applications Vol. 34, No. 11, (November 2021) 2398-2407

International Journal of Engineering

Journal Homepage: www.ije.ir

Designing Exponentially Weighted Moving Average Control Charts under Failure Censoring Reliability Tests

P. Mohammadipour[a], H. Farughi*[a], H. Rasay[b], J. Arkat[a]

[a] *Department of Industrial Engineering, University of Kurdistan, Sanandaj, Iran*
[b] *Department of Industrial Engineering, Kermanshah University of Technology, Kermanshah, Iran*

PAPER INFO

Paper history:
Received 22 June 2021
Received in revised form 15 August 2021
Accepted 16 August 2021

Keywords:
Control Chart
Statistical Process Control
Lifetime Testing
Failure Censoring
Quality Characteristic
Average Run Length

A B S T R A C T

One of the most important quality characteristics in a production process is the product lifetime. The production of highly reliable products is a concern of manufacturers. Since it is time-consuming and costly to measure lifetime data, designing a control chart seems difficult. To solve the problem, lifetime tests are employed. In the present study, one-sided and two-sided exponentially weighted moving average (EWMA) control charts are designed under a type II censoring (failure censoring) life test. Product lifetime is a quality characteristic dealt with in this study. It is assumed to follow the Weibull distribution with a fixed shape parameter and a variable scale parameter. In order to design a control chart, first, the control chart limits are calculated for different parameters, and then the Average Run Length (ARL) in the out-of-control state is used to evaluate the performance of the proposed control chart. Next, a comprehensive sensitivity analysis is performed for the different parameters involved. The computational results show that the one-sided control chart has better performance to detect the shift of lifetime data than the two-sided control chart. The average run length curve of the two-sided control chart is biased, while that of the one-sided control chart is unbiased. A very effective parameter that increases the performance of a control chart is found to be the number of failures in the failure censoring process. Finally, simulated and real examples are provided to show the performance of the proposed control chart.

doi: *10.5829/ije.2021.34.11b.03*

NOMENCLATURE

m	Shape parameter	UCL	Upper control limit
Θ	Scale parameter	LCL	Lower control limit
c	Shift constant	α	Probability of type I errors for the control chart
r	Number of failures	β	Probability of type II errors for the control chart
n	Sample size in the life test	ARL0	In-control average run length
$V(i)$	Statistic of the life test censoring	ARL1	Out-of-control average run length
$Q(i)$	Statistic of the EWMA chart	λ	Smoothing constant in the EWMA chart
Γ	Gamma function	ϕ	Cumulative distribution function of the normal distribution

1. INTRODUCTION[1]

Nowadays, many products of different brands are introduced in markets, but consumers consistently demand only a small number of them due to their quality characteristics [1]. In this regard, statistical process control (SPC) is widely used as a method of statistical quality control (SQC). As a very powerful tool for monitoring a process in SPC, a control chart is used mainly to maintain the statistical stability of the process. A control chart has a center-line (CL) and two control limits, including the lower control limit (LCL) and the upper control limit (UCL) [2]. Based on the sample statistics, the process status is divided into in-control and out-of-control states. If the drawn points are between the LCL and the UCL, the process is assumed to be in control; otherwise, it is assumed to be out of control [3].

* Corresponding Author's Email: h.farughi@uok.ac.ir (H. Farughi)

Please cite this article as: P. Mohammadipour, H. Farughi, H. Rasay, J. Arkat, Designing Exponentially Weighted Moving Average Control Charts under Failure Censoring Reliability Tests, International Journal of Engineering, Transactions B: Applications, Vol. 34, No. 11, (2021), 2398-2407

A serious weakness of the control charts designed by Shewhart is in the use of the information of the last sample rather than that of the old samples. Unlike Shewhart control charts, memory-type control charts use the information of both the old and the previous samples. So, if the goal is to detect small changes in a process, it is a memory-type control chart to use. Another popular and widely-used memory-type control chart is the EWMA control chart, first introduced by Roberts [4] in 1959.

To design a control chart for process monitoring, there is a need for enough data about the quality characteristics to be examined. However, collecting enough data for this purpose is not practical in some industries or processes. The problem is attributed to product lifetime as an important quality characteristic; data collection is difficult, time-consuming, and costly. In this case, reliability lifetime tests are used to obtain the required data on lifetime [5].

The application of control charts is now widespread in various fields of engineering, management, services, biology, healthcare, and finance. Kabiri and Bayati [6] used control charts as important tools of statistical process control in combination with modern tools such as artificial neural networks. Fattahzadeh and Saghaei [7] monitored their processes using image sensors and control charts. Rasay et al. [8] showed the application of multivariate control charts in condition-based maintenance. Sadeghi et al. [9] proposed a control method based on Shewhart control charts to monitor financial processes.

In general, the research performed so far has been on the type of control charts and life tests in various distributions. For example, a Shewhart variable control chart was designed by Khan et al. [10] through failure censoring, assuming that lifetime follows the Weibull distribution with a fixed shape parameter and a variable scale parameter. Adebayo and Ogundipe [11] assumed that product lifetime follows a generalized exponential distribution with a fixed shape parameter and a variable scale parameter. They then designed an attribute control chart using truncated life tests. Balamurali and Jeyadurga [12] designed an attribute NP control chart to monitor the mean lifetime of type-II Pareto distribution through truncated life tests and multiple deferred state sampling.

Aslam et al. [13] presented a mixed control chart through the accelerated hybrid censoring that monitors variable and attribute quality characteristics. Rao et al. [14] designed an attribute NP control chart via truncated life tests and assumed that the product lifetime follows a Dagmu distribution with a fixed shape parameter and a variable scale parameter.

Xu and Daniel [15] presented a WEWMA chart to monitor lifetime with the Weibull distribution using type I censored data. In the research by Faraz et al. [16], the shape and scale parameters of the Weibull distribution were assumed to be unknown, and then the control charts of S^2 and $\bar{Z}$ were proposed to monitor the shifts in the shape and scale parameter of the Weibull distribution. One-sided and two-sided t-control charts were presented by Rasay and Arshad [17] using a failure censoring test to monitor lifetime when it followed exponential distribution. Table 1 summarizes the most relevant studies in this area.

A literature review shows that the design of control charts with life tests and monitoring lifetime data is of great importance. In addition, most of the studies conducted in this area are related to two-sided control charts; there has been only a little research on designing one-sided control charts and memory-based control charts. To the best of the authors' knowledge, no research has been conducted on designing one-sided EWMA control charts using failure censoring life tests.

Hence, in the present study, the one-sided and two-sided EWMA control charts are designed through a Type II censoring life test to monitor the average lifetime of the Weibull distribution. For this purpose, first, the relationships among one-sided and two-sided control limits, type II error, and the average run length in the out-of-control state are identified. Then, the performance of the control chart is evaluated by ARL in the out-of-control mode. Finally, a comprehensive sensitivity analysis is performed based on the problem parameters.

TABLE 1. Research summary

Lifetime distribution	Life test	Control chart	Year	Author
Weibull	failure censoring	Variable control chart	2018	Nasrullah Khan et al. [10]
Weibull	Truncated life test	np	2018	Balamurali & Jeyadurga [12]
Weibull	-	Shewhart control chart ($\bar{X}$ and s)	2014	Faraz et al. [16]
Generalized Exponential	Trancated life test	np	2020	Adebayo & Ogundipe [11]
Weibull	hybrid censoring life test	Mixed control chart	2020	Muhammad Aslam et al. [13]
Pareto distribution of the second kind	Truncated life test	np	2019	Balamurali & Jeyadurga [12]
Dagmu	Trancated life test	np	2019	Rao et al. [14]
Exponential	failure censoring	t control chart	2020	Rasay & Arshad [17]
Weibull	type I censored	WEWMA chart	2018	Xu & Daniel [15]

The rest of the paper is organized into several sections. First, the problem for which the control charts are designed is described. The next section discusses how to design one-sided and two-sided control charts. Section 4 is devoted to the computation of the average run length of the control charts. In section 5, several simulated examples are presented. Using simulation studies, a case study is presented in section 6. Finally, section 7 concludes the paper.

2. DESCRIPTIONS

Consider the lifetime of an item, which is denoted by X, as its concerned quality characteristic. In the current study, it is assumed that X follows the Weibull distribution with the following cumulative distribution function:

$$F_x(x) = 1 - exp[-(x\theta)^m] \tag{1}$$

In Equation (1), θ and *m* are the scale and the shape parameters of the distribution, respectively. The mean lifetime of the Weibull distribution has the following form:

$$\mu = \frac{\Gamma\left(\frac{1}{m}\right)}{\theta m} \tag{2}$$

In Equation (2), it is supposed that variable *m* has a stable shape parameter, but the scale parameter needs to be monitored using a suitable control chart. In the following section, some control charts are proposed for this purpose.

It is to be noted that the distribution of the data on lifetime is determined according to historical data and by statistical tests such as the goodness of fit test. Lifetime is one of the characteristics that often follow non-normal distributions; a normal distribution has limited application in longevity data. Weibull, exponential, normal log, gamma, and Pareto distributions are the most important distributions used to model quality characteristics in reliability.

To monitor the scale parameter of the Weibull distributed items, a failure censoring reliability test is conducted. More specifically, first, n items are randomly selected and put on the test simultaneously. The test continues until r failures ($r \leq n$) are observed. During the test, the failure time of each item is recorded to obtain $x_{(1)}, x_{(2)}, \dots, x_{(r)}$ as the order statistic data. Accordingly, the following statistic is computed:

$$V_i = \sum_{i=1}^{r} \left(\frac{x_i}{\mu_0}\right)^m + (n-r)\left(\frac{x_r}{\mu_0}\right)^m \tag{3}$$

where μ_0 is the specified mean time and x_i is the failure time of the i'th item.

According to Jun et al. [18], V_i follows a gamma distribution with parameters W0 and r. W_0 is computed as follows:

$$W_0 = (\theta_0\mu_0)^m = \left(\frac{\Gamma(1/m)}{m}\right)^m \tag{4}$$

According to Jun et al. [18], $2VW_0$ follows a chi-square distribution with 2r degrees of freedom.

It is desirable to monitor the scale parameter θ, or the alternative process mean μ, using an appropriate control chart. As it is known, indeed, at each sampling point, there is a statistical hypothesis test to conduct. Let's assume θ_0 and μ_0 as the target values of the scale parameter and the mean, respectively. In this regard, the following hypothesis tests are conducted:

$$\text{A:}\begin{cases} H_0: \mu = \mu_0 \\ H_0: \mu > \mu_0 \end{cases}, \quad \text{B:}\begin{cases} H_0: \mu = \mu_0 \\ H_0: \mu \neq \mu_0 \end{cases}$$

Hypothesis test A leads to a one-sided control chart, while B leads to a two-sided control chart.

3. DESIGNING THE CONTROL CHARTS

In this section, first, the design of a one-sided control chart is discussed, and then a two-sided control chart is presented.

As $2VW_0$ follows a chi-square distribution with 2r degrees of freedom, the following equations can be obtained for the mean and the variance of V_i:

$$E(V_i) = \frac{r}{w_0} \tag{5}$$

$$var(V_i) = \frac{r}{w_0^2} \tag{6}$$

At the i'th sampling time, the following EWMA statistic is computed and plotted on an EWMA control chart:

$$Q_i = \lambda V_i + (1-\lambda)Q_{i-1} \tag{7}$$

where λ is the smoothing parameter of the EWMA control chart.

The central limit theorem is used to obtain the control limits of the EWMA chart. According to theorem, if the variables $x_1, x_2, x_3, \dots, x_n$ are independent of one another, it can be concluded that the sum or mean of x_i follows a normal distribution for large 'i's. Now, the values are inserted in Equation (7) instead of all Q_{i-1}, and the following equation is obtained:

$$Q_i = \lambda \sum_{j=0}^{i-1} (1-\lambda)^j V_{i-j} + (1-\lambda)^i Q_0 \tag{8}$$

Based on Equation (8), the values of Q_i depend only on the initial value of Q_0 and the values of V_i. Therefore, Q_i values will be independent of each other. According to the central limit theorem, it can be concluded that the mean and variance of Q_i for a large value of I are as follows:

$$E(Q_i) = E(V_i) = \frac{r}{w_0} \tag{9}$$

$$Var(Q_i) = Var(V_i) \times \left(\frac{\lambda}{2-\lambda}\right) = \frac{r}{w_0^2} \times \frac{\lambda}{2-\lambda} \tag{10}$$

In the following, the relationships of control limits, β error and ARL_1 are presented for one-sided and two-sided EWMA control charts.

3. 1. One-sided Control Chart

Suppose that a process is only concerned with monitoring the deterioration of quality characteristic. In this case, one-sided control charts are used with LCL.

The Equation of LCL, based on the results of the central limit theorem and the mean and variance of Q_i, is as follows:

$$LCL = \mu_{Q_i} - k\sigma_{Q_i}$$
$$= \frac{r}{W_0} - Z_\alpha \left(\frac{\lambda}{2-\lambda} \times \frac{r}{W_0^2}\right)^{0.5} \tag{11}$$

where k is the coefficient of control limits, which is considered equal to Z_α, and Z_α is a certain percentage of the distribution *N* (0,1). So, P $\{Z \geq Z_\alpha\} = \alpha$.

3. 2. Two-sided Control Chart

The one-sided control chart cannot show the improvement of the process. To monitor both the improvement and the deterioration of the process, a two-sided control chart is used. Like in most two-sided control charts, let's assume type I error is equally divided for both sides of the control chart.

The control limits of a two-sided control chart are as follows:

$$UCL = \mu_{Q_i} + k\sigma_{Q_i} = \frac{r}{W_0} + Z\alpha_{/2} \left(\frac{\lambda}{2-\lambda} \times \frac{r}{W_0^2}\right)^{0.5} \tag{12}$$

$$LCL = \mu_{Q_i} - k\sigma_{Q_i} = \frac{r}{W_0} - Z\alpha_{/2} \left(\frac{\lambda}{2-\lambda} \times \frac{r}{W_0^2}\right)^{0.5} \tag{13}$$

Equations (12) and (13) serve to calculate the values of LCL and UCL, respectively. If a point falls between the two limits, it means that the process is probably in-control. On the other hand, the occurrence of a point below the LCL can be a sign of the process deterioration, while its being above the UCL is suggestive of the process improvement. With a flowchart, Figure 1 shows the stages of the proposed control chart.

4. COMPUTING THE ARL OF THE CONTROL CHARTS

An important indicator of the performance of a control chart is the Average Run Length (ARL). Every control chart has two ARLs; one corresponds to the in-control state (ARL_0), and the other to the out-of-control state (ARL_1).

The value of ARL_0 is the inverse of type I error; that is, $ARL_0 = 1/\alpha$. The value of ARL_1, however, depends on the values of the shift and the other characteristics of the control chart.

Let's consider a case in which the scale parameter of the distribution shifts from θ_0 to $c\theta_0$ and value c determines the magnitude of the shift. For a one-sided control chart, β can be obtained as follows:

$$\beta = P(Q_i > LCL | \theta_1 = c\theta_0) = 1 - \phi\left(LCL - \frac{r}{w_1} \middle/ \sqrt{\frac{\lambda}{2-\lambda} \times \frac{r}{w_1^2}}\right) \tag{14}$$

Similarly, for a two-sided control chart, β is calculated as follows:

$$\beta = P(LCL < Q_i < UCL | \theta_1 = c\theta_0) = \phi\left(\frac{UCL - \frac{r}{W_1}}{\sqrt{\frac{\lambda}{2-\lambda} \times \frac{r}{W_1^2}}}\right) - \phi\left(\frac{LCL - \frac{r}{W_1}}{\sqrt{\frac{\lambda}{2-\lambda} \times \frac{r}{W_1^2}}}\right) \tag{15}$$

To obtain the ARL_1 values, first, the β values are obtained, and then the values of ARL_1 are calculated with Equation (16).

$$ARL_1 = \frac{1}{1-\beta} \tag{16}$$

For example, the values of ARL1 for a two-sided control chart are given in Table 2. The following results can be inferred from comparing the tables together and examining the trend of ARL_1 shifts for different parameters.

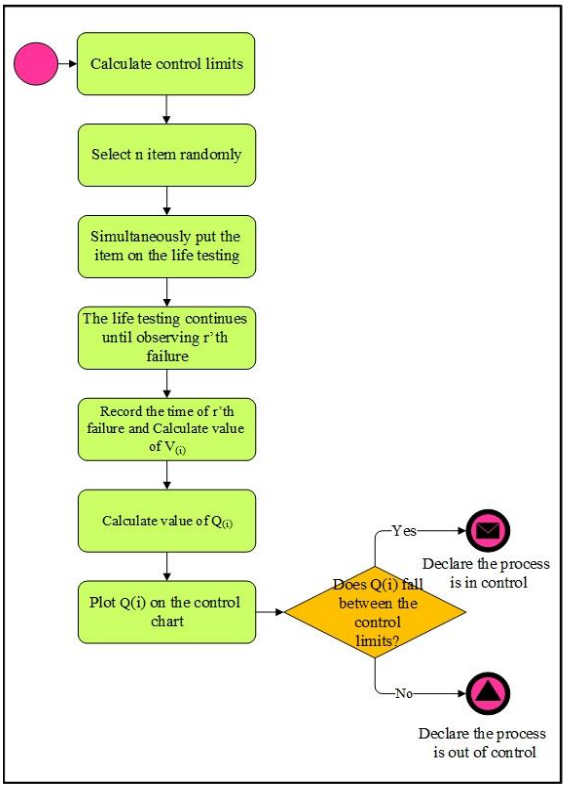

Figure 1. The flowchart of the proposed control chart

TABLE 2. The ARL for a two-sided control chart

m=0.5 λ=0.2						
ARL_0=370						
r	1	2	3	4	5	6
c	ARL_1					
0.2	1.60	1.19	1.07	1.02	1.01	1.00
0.4	4.66	2.72	1.98	1.61	1.40	1.27
0.6	19.58	11.59	8.01	6.03	4.80	3.96
0.8	96.83	73.71	58.80	48.44	40.85	35.09
1	370	370	370	370	370	370
1.2	655	478.2	369.0	295.5	243.0	203.9
1.4	729.60	358.3	212.9	140.1	98.47	72.53
1.6	739.5	264.2	128.2	72.90	45.84	30.96
1.8	740.6	199.7	81.74	41.44	24.08	15.39
2	740.7	154.5	54.66	25.36	13.97	8.67
2.5	740.80	87.97	23.60	9.57	5.02	3.14
3	740.8	54.66	12.21	4.75	2.58	1.75
m=0.5 λ=0.2						
ARL_0=200						
r	1	2	3	4	5	6
c	ARL_1					
0.2	1.52	1.16	1.06	1.02	1.01	1.00
0.4	3.96	2.41	1.81	1.50	1.32	1.22
0.6	14.44	8.89	6.32	4.86	3.94	3.31
0.8	60.73	47.37	38.49	32.18	27.49	23.87
1	200	200	200	200	200	200
1.2	329.53	247.33	194.85	158.68	132.38	112.51
1.4	351.79	181.81	112.10	76.07	54.92	41.43
1.6	340.91	131.24	67.35	40.11	26.27	18.40
1.8	326.54	97.43	43.01	23.22	14.24	9.56
2	313.02	74.24	28.92	14.53	8.56	5.64
2.5	284.05	41.22	12.82	5.86	3.39	2.31
3	260.38	25.29	6.90	3.13	1.93	1.43
m=1.5 λ=0.2						
ARL0=370						
r	1	2	3	4	5	6
c	ARL1					
0.2	1.01	1.00	1.00	1.00	1.00	1.00
0.4	1.07	1.01	1.00	1.00	1.00	1.00
0.6	1.71	1.23	1.09	1.04	1.01	1.01
0.8	10.07	5.74	3.97	3.03	2.46	2.09
1	370	370	370	370	370	370
1.2	740.52	220.34	95.55	50.32	29.98	19.49
1.4	740.80	69.09	16.78	6.61	3.50	2.26
1.6	740.80	23.80	4.42	1.89	1.27	1.08
1.8	740.80	9.33	1.84	1.12	1.01	1.00
2	740.80	4.29	1.18	1.01	1.00	1.00
2.5	740.80	1.34	1.00	1.00	1.00	1.00
3	740.80	1.01	1.00	1.00	1.00	1.00
m=1.5 λ=0.2						
ARL0=200						
r	1	2	3	4	5	6
c	ARL1					
0.2	1.01	1.00	1.00	1.00	1.00	1.00
0.4	1.07	1.01	1.00	1.00	1.00	1.00
0.6	1.61	1.20	1.08	1.03	1.01	1.00
0.8	7.93	4.72	3.35	2.62	2.17	1.88
1	200	200	200	200	200	200
1.2	331.67	108.11	50.22	28.00	17.53	11.90
1.4	271.94	32.13	9.28	4.19	2.48	1.76
1.6	220.55	11.04	2.78	1.47	1.13	1.03
1.8	177.35	4.57	1.40	1.05	1.00	1.00
2	141.65	2.34	1.06	1.00	1.00	1.00
2.5	79.14	1.08	1.00	1.00	1.00	1.00
3	43.68	1.00	1.00	1.00	1.00	1.00

According to Figure 2, with an increase in the value of *r*, the values of ARL_1 decrease. This is because the higher the number of failures in a process, the longer the test time, and the greater the chance of detecting a shift. Therefore, the probability of β error and the value of ARL_1 are reduced.

According to Figure 3, the value of ARL_1 increases as the value of ARL_0 rises. Also, as the value of ARL_0 increases, the control limits become wider. This means that if a shift occurs in the process, the delay of the chart to detect the shift increases.

According to Figure 4, the value of ARL_1 decreases with an increase in the value of *m*. Indeed, an increase in the value of *m* decreases the probability of β error; consequently, ARL_1 decreases too.

According to Figure 5, ARL_1 value decreases with an increase in the value of *c*. The larger the shift constant in a process, the larger the shift, and the sooner the shift is detected by the chart. Therefore, the probability of β error and ARL_1 is reduced. In addition, referring to the charts presented, it is quite clear that the ARL_1 chart is asymmetric. The values of ARL_1 for $c > 1$ are greater than those for $c < 1$. So, the chart can detect $c < 1$ shifts faster.

According to Figure 6, the value of ARL_1 increases as the value of λ rises. This is because the distance between the control limits increases when λ rises; therefore, the chance of detecting shifts in the process decreases.

As Figure 7 suggests, an increase in the value of α causes a decrease in the values of ARL_1 decrease, which is because the increase of α decreases the probability of β error and, consequently, ARL_1.

The best performance of a control chart is achieved when ARL_1 has its maximum value, ARL_0, when the process is in control, i.e., c = 1. The ARL_1 value decreases as soon as a shift occurs in the process. In the EWMA control chart, the ARL_1 chart is biased in some cases; that is, in some cases and for some parameter values, the maximum amount of ARL_1 does not occur at $c = 1$, as shown in the charts and tables. The *r* parameter is one of the most important factors that increase the ability of the control chart to detect deviations. This increase greatly improves the chart performance. In other words, as *r* increases, the biased ARL curve problem is relieved.

In a one-sided EWMA control chart, the ARL_1 values are always lower than the ARL_1 values of a two-sided control chart. This is because the LCL of the one-sided control chart is larger than that of the two-sided control chart. Therefore, in the event of a shift in the process, the one-sided control chart will detect the deviation faster, as illustrated in Figure 8. Moreover, because the one-sided control chart has only one control limit, it monitors the process only on one side, and its ARL_1 chart has a uniform behavior. This is unlike the ARL_1 chart of the two-sided control chart, which is biased.

5. SIMULATION STUDY

To show the performance of the control charts, two examples are presented here. A two-sided control chart is used in the first one, and the second one is about a one-sided control chart.

5. 1. Example 1 A simulation study is conducted to show the performance of the proposed control charts. First, 20 sample points are generated while $\theta_0 = 1$. Then, 30 sample points are generated while the scale parameter

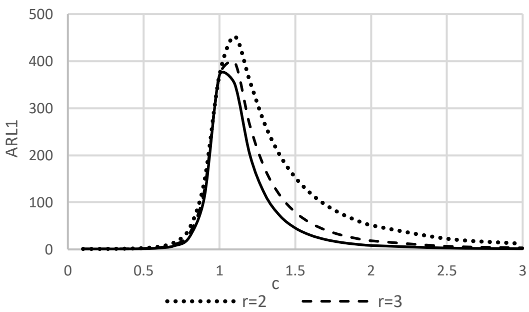

Figure 2. ARL1 of the two-sided control charts for different values of *r*

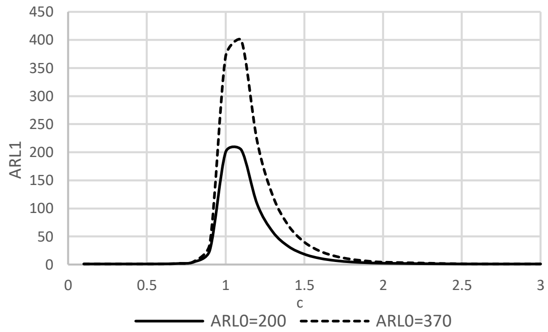

Figure 3. ARL_1 of the two-sided control charts for different values of ARL_0

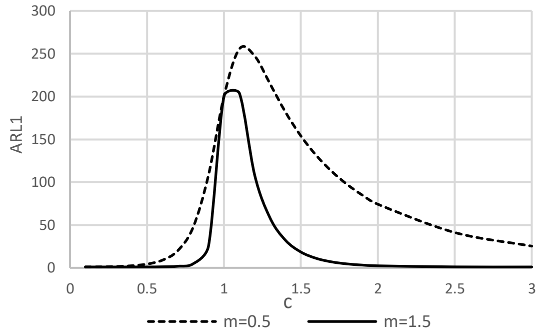

Figure 4. ARL_1 of the two-sided control charts for different values of *m*

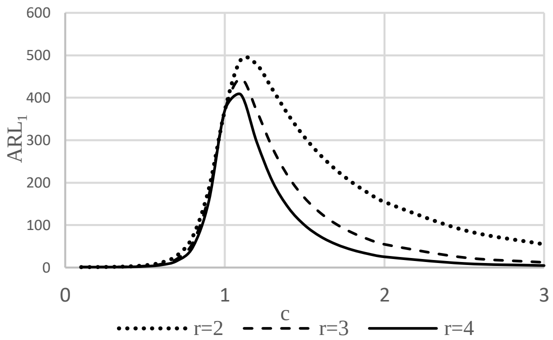

Figure 5. ARL_1 of the two-sided control charts for different values of *c*

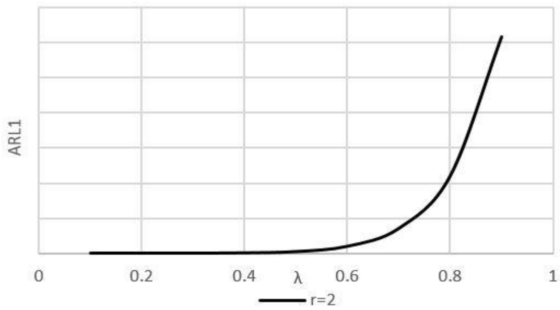

Figure 6. ARL_1 of the two-sided control charts for different values of λ

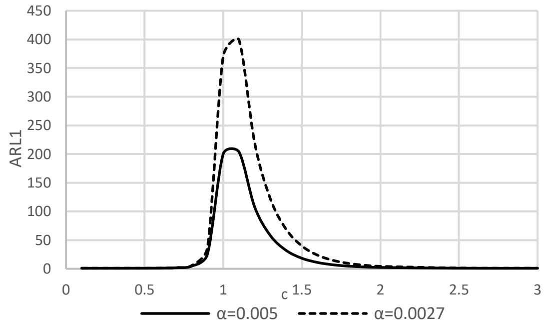

Figure 7. ARL_1 of the two-sided control charts for different values of α

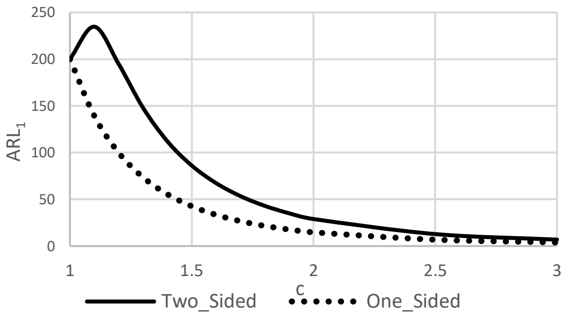

Figure 8. Comparison of the ARLs for one-sided and two-sided control charts

shifts from $\theta_0 = 1$ to $\theta = 0.7$. The other inputs of the control charts include $ARL_0 = 370, m = 2, n = 5, r = 3$, and $\lambda = 0.2$. Table 3 presents the limits of the control charts. The values of the control statistic Q_i and the failure times are also provided in Table 4. The values of Q_i are plotted on the control chart in Figure 9. The figure clearly shows the changes in sample 26.

5. 2. Example 2 In this example, First, 15 sample points are generated while $\theta_0 = 1$. Then, 25 sample points are generated while the scale parameter shifts from $\theta_0 = 1$ to $\theta = 1.5$. The other inputs of the control charts include $ARL_0 = 200, m = 1.5, n = 5, r = 3$, and $\lambda = 0.3$. Table 3 shows the limits of the control charts. The values of Q_i are also plotted on the control chart in Figure 10. The changes in sample 21 are evident in this figure.

6. CASE STUDY

As a case study, the real data of a car manufacturer in Korea are used to design control charts [10]. The data are about the operational time of a part of the machine until failure occurs in a period of one month.

The data follow the Weibull distribution with the shape parameter $m = 2.5$ and the scale parameter $\theta_0 = 1$. The assumptions are $ARL_0 = 370$, $r = 3$, and $\lambda = 0.4$. The values of V_i and Q_i are shown in Table 5.

TABLE 3. The control limits of the control charts

Two-sided	ARL0 = 370				*m* = 2		
	r	1	2	3	4	5	6
λ = 0.2	UCL	2.5	4.3	6.02	7.63	9.21	10.7
	LCL	0	0.7	1.61	2.54	3.51	4.5
Two-sided	ARL0 = 370				*m* = 2.5		
	r	1	2	3	4	5	6
λ = 0.4	UCL	3.3	5.5	7.54	9.43	11.2	13.1
	LCL	-	-	0.54	1.34	2.21	3.13
One-sided	ARL0 = 200				*m* = 1.5		
	r	1	2	3	4	5	6
λ = 0.3	LCL	-	0.5	1.31	2.14	3.01	3.91

TABLE 4. The simulated data and the statistical values

	Sample	1	2	3	V(i)	Q(i)
m = 2 θ = 1	1	0.2628	0.5986	0.6132	1.9805	2.344
	2	0.4414	0.5978	0.6632	2.3829	2.375
	3	0.1498	0.5276	0.6336	1.9163	2.008
	4	0.2392	0.6305	0.8709	3.4758	3.182
	5	0.0070	0.7756	0.8070	3.2532	3.239
	6	0.3620	0.7147	0.8360	3.4869	3.437
	7	0.1189	0.3033	0.8309	2.7722	2.905
	8	0.6604	0.7968	0.9688	4.9490	4.540
	9	0.2778	0.6529	0.6851	2.4337	2.855
	10	0.4840	0.4872	1.0616	4.9056	4.495
	11	0.1327	0.5609	0.6965	2.2762	2.720
	12	0.4462	0.9839	1.1461	6.5036	5.746
	13	0.2706	0.8077	1.0214	4.9088	5.076
	14	0.4985	0.8817	1.0024	5.1446	5.130
	15	0.1296	0.7848	0.9160	4.0106	4.234
	16	0.4138	0.6800	1.0789	5.2533	5.049
	17	0.3106	0.6931	0.9753	4.3677	4.504
	18	0.4366	0.7921	0.9658	4.6046	4.584
	19	0.3282	0.8221	0.9708	4.5978	4.595
	20	0.4358	0.6012	0.7467	2.8316	3.184
	Sample	1	2	3	V(i)	Q(i)
m = 2 θ = 0.7	21	0.8891	0.9600	1.0611	6.4804	5.821
	22	0.2434	0.8434	1.0434	5.1393	5.275
	23	0.4128	0.8442	0.9277	4.4119	4.584
	24	0.2443	0.7908	1.1481	5.9073	5.642
	25	0.4036	0.4172	0.4844	1.3250	2.188
	26	0.8674	1.4280	1.4397	11.4710	9.614
	27	0.2146	0.4567	0.8865	3.3258	4.583

28	0.5578	1.0281	1.4927	10.2532	9.119
29	0.6363	1.0198	1.2363	7.6773	7.965
30	0.4170	0.5209	1.0497	4.7758	5.413
31	1.4443	0.9263	1.2582	9.7957	8.919
32	0.5874	0.8391	0.9157	4.5383	5.414
33	0.3551	0.8920	1.2037	6.7077	6.449
34	0.1578	0.7775	1.3584	7.8497	7.569
35	1.0975	1.1039	1.1934	8.5247	8.333
36	0.6039	1.2403	1.6447	12.757	11.87
37	0.9551	1.0658	1.8941	16.317	15.42
38	0.4016	0.6704	0.9525	4.231	6.479
39	1.3108	1.3249	1.4853	12.848	11.57
40	0.4727	0.8110	0.8543	3.909	5.442
41	0.1710	0.9366	1.8650	14.443	12.64
42	0.3562	0.6444	0.8107	3.200	5.088
43	0.4010	0.4344	1.5475	9.592	8.691
44	0.5393	0.6582	0.9561	4.413	5.269
45	0.6136	1.1168	1.2072	7.633	7.160
46	0.9505	1.6125	1.8332	17.291	15.27
47	1.0844	1.0919	1.2606	9.080	10.322
48	0.6196	0.7171	1.2194	6.821	7.522
49	0.1140	0.9953	1.2717	7.450	7.468
50	0.4324	0.4668	0.5071	1.497	2.691

The process is monitored with the EWMA control chart. The control limits are shown in Table 3. The values of Q_i are plotted on the control chart (Figure 11).

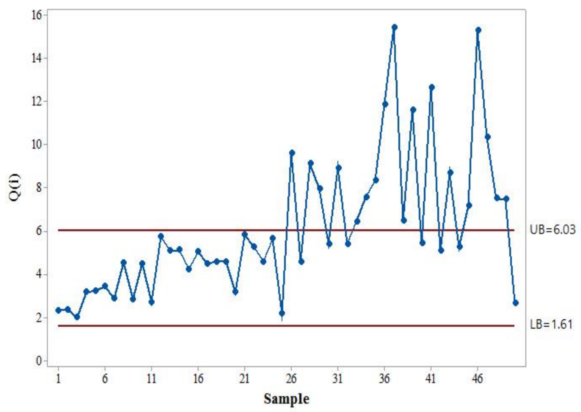

Figure 9. The proposed control chart for the simulated data while the process improves

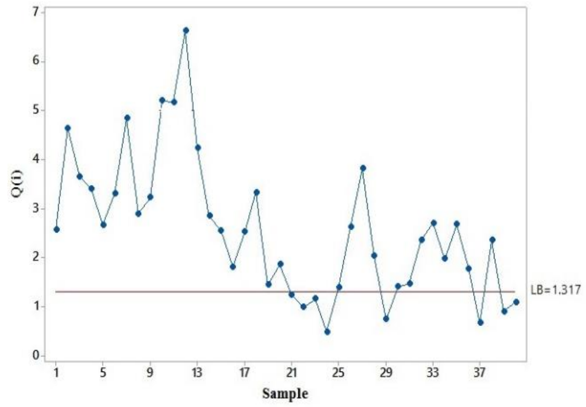

Figure 10. The proposed control chart for the simulated data while the process deteriorates

TABLE 5. The simulated data and the statistical values

Sample	1	2	3	4	5	6	7
V(i)	8.26	9.68	3.22	3.75	5.14	1.30	2.97
Q(i)	7.14	8.92	4.93	4.10	4.83	2.36	2.79
Sample	8	9	10	11	12	13	14
V(i)	5.92	3.42	4.71	4.59	7.99	9.76	5.39
Q(i)	4.98	3.88	4.46	4.55	6.96	8.92	6.45
Sample	15	16	17	18	19	20	21
V(i)	2.40	3.80	3.86	1.65	1.10	3.11	4.23
Q(i)	3.61	3.75	3.82	2.30	1.46	2.62	3.75
Sample	22	23	24	25	26	27	28
V(i)	3.12	7.10	5.56	6.44	4.18	3.44	7.26
Q(i)	3.31	5.96	5.68	6.21	4.79	3.85	6.24
Sample	29	30	31	32	33	34	35
V(i)	4.66	0.69	1.93	2.96	5.09	5.30	10.22
Q(i)	5.13	2.02	1.96	2.66	4.36	5.02	8.66
Sample	36	37	38	39	40	41	42
V(i)	4.68	3.21	2.68	4.64	10.51	2.52	1.11
Q(i)	5.88	4.01	3.08	4.17	8.61	4.35	2.08
Sample	43	44	45	46	47	48	49
V(i)	4.05	8.87	3.25	2.09	5.23	1.36	4.59
Q(i)	3.46	7.25	4.45	2.79	4.50	2.30	3.90
Sample	50						
V(i)	3.17						
Q(i)	3.39						

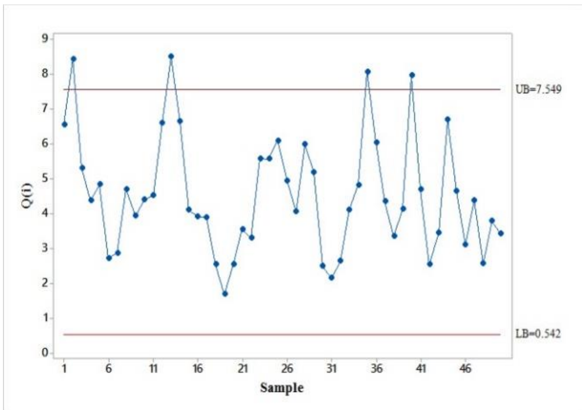

Figure 11. The control chart proposed for real data

The EWMA chart shows that the process is sometimes out of control, and corrective action is needed immediately.

7. CONCLUSION

In this study, one-sided and two-sided EWMA control charts were designed under Type II censoring life tests. As a quality characteristic of products, it was assumed that lifetime would follow the Weibull distribution with a fixed shape parameter and a variable scale parameter. First, the relationships of control limits, β error and ARL_1 were presented. Then, the control limits were calculated for different parameters while ARL_1 were used to evaluate the performance of the control charts. The ARL_1 values of those parameters were also obtained and presented in tables. As the numerical analyses showed, the ARL_1 values would decrease with an increase in *r* and *m* and increase as the ARL_0 values increased. Moreover, as the *r* parameter increased, the ability of the control chart to detect out-of-control states also increased. Similarly, the ARL_1 values were found to rise with an increase in the value of λ. In the two-sided control chart, the ARL_1 curve varied up and down uniformly. The examination of the ARL_1 curves and values of the charts proved that the one-sided control chart outperforms the two-sided control chart in detecting shifts. Compared to the Shewhart type control chart, the proposed control chart has a significantly better capability of detecting out-of-control states in production processes to avoid producing low-quality items. Using the proposed control chart, it is possible to have continual improvement in lifetime as an important quality characteristic of products. The mangers of manufacturing companies can also significantly reduce their costs and improve the competitiveness of their businesses. Moreover, since the EWMA control chart is designed based on efficient failure censoring life testing, it can decrease the cost of the life testing involved in the application of control charts. Designing EWMA control charts for hybrid censoring life tests and unbiased EWMA control charts under failure censoring is a recommendation for future studies.

8. REFERENCES

1. Tsekouras, K., Dimara, E. and Skuras, D., "Adoption of a quality assurance scheme and its effect on firm performance: A study of greek firms implementing iso 9000", ***Total quality management***, Vol. 13, No. 6, (2002), 827-841, doi: 10.1080/0954412022000010163.
2. Siraj, I. and Bharti, P.S., "Reliability analysis of a 3d printing process", ***Procedia Computer Science***, Vol. 173, (2020), 191-200, doi: 10.1002/j.1538-7305.1926.tb00125.x.
3. Montgomery, D.C., "Introduction to statistical quality control, John Wiley & Sons, (2020).
4. Roberts, S., "Control chart tests based on geometric moving averages", ***Technometrics***, Vol. 42, No. 1, (2000), 97-101, doi: 10.1080/00401706.2000.10485986.
5. Barlow, R.E. and Proschan, F., *Statistical theory of reliability and life testing: Probability models*. 1975, Florida State Univ Tallahassee.
6. Bayati, N. and Kabiri Naeini, M., "Pattern recognition in control chart using neural network based on a new statistical feature", ***International Journal of Engineering***, Vol. 30, No. 9, (2017), 1372-1380, doi: 10.5829/idosi.ije.2017.30.09c.10.
7. Fattahzadeh, M. and Saghaei, A., "A statistical method for sequential images–based process monitoring", ***International Journal of Engineering***, Vol. 33, No. 7, (2020), 1285-1292, doi: 10.5829/IJE.2020.33.07A.15.
8. Rasay, H., Fallahnezhad, M. and ZareMehrjardi, Y., "Application of multivariate control charts for condition based maintenance", ***International Journal of Engineering***, Vol. 31, No. 4, (2018), 597-604, doi: 10.5829/ije.2018.31.04a.11.
9. Sadeghi, H., Owlia, M.S., Doroudyan, M.H. and Amiri, A., "Monitoring financial processes with arma-garch model based on shewhart control chart (case study: Tehran stock exchange)", ***International Journal of Engineering***, Vol. 30, No. 2, (2017), 270-280, doi: 10.5829/idosi.ije.2017.30.02b.14.
10. Khan, N., Aslam, M., Raza, S.M.M. and Jun, C.H., "A new variable control chart under failure-censored reliability tests for weibull distribution", ***Quality and Reliability Engineering International***, Vol. 35, No. 2, (2019), 572-581, doi: 10.1002/qre.2422.
11. Adeoti, O.A. and Ogundipe, P., "A control chart for the generalized exponential distribution under time truncated life test", ***Life Cycle Reliability and Safety Engineering***, Vol. 10, No. 1, (2021), 53-59, doi: 10.1007/s41872-020-00146-9.
12. Balamurali, S. and Jeyadurga, P., "An attribute np control chart for monitoring mean life using multiple deferred state sampling based on truncated life tests", ***International Journal of Reliability, Quality and Safety Engineering***, Vol. 26, No. 01, (2019), 1950004, doi: 10.1142/S0218539319500049.
13. Aslam, M., Raza, M.A., Sherwani, R.A.K., Farooq, M., Jeong, J.Y. and Jun, C.-H., "A mixed control chart for monitoring failure times under accelerated hybrid censoring", ***Journal of Applied Statistics***, Vol. 48, No. 1, (2021), 138-153, doi: 10.1080/02664763.2020.1713060.
14. Gadde, S.R., Fulment, A. and Josephat, P., "Attribute control charts for the dagum distribution under truncated life tests", ***Life Cycle Reliability and Safety Engineering***, Vol. 8, No. 4, (2019), 329-335, doi: 10.1007/s41872-019-00090-3.

15. Xu, S. and Jeske, D.R., "Weighted ewma charts for monitoring type i censored weibull lifetimes", ***Journal of Quality Technology***, Vol. 50, No. 2, (2018), 220-230, doi: 10.1080/00224065.2018.1436830.

16. Faraz, A., Saniga, E.M. and Heuchenne, C., "Shewhart control charts for monitoring reliability with weibull lifetimes", ***Quality and Reliability Engineering International***, Vol. 31, No. 8, (2015), 1565-1574, doi: 10.1002/qre.1692.

17. Rasay, H. and Arshad, H., "Designing variable control charts under failure censoring reliability tests with replacement", ***Transactions of the Institute of Measurement and Control***, Vol. 42, No. 15, (2020), 3002-3011, doi: 10.1177/0142331220938206.

18. Jun, C.-H., Lee, H., Lee, S.-H. and Balamurali, S., "A variables repetitive group sampling plan under failure-censored reliability tests for weibull distribution", ***Journal of Applied Statistics***, Vol. 37, No. 3, (2010), 453-460, doi: 10.1080/02664760802715914.

Persian Abstract

چکیده

طول عمر محصولات یکی از مهم‌ترین مشخصه‌های کیفی مد نظر در تولید می‌باشد. از این رو تولیدکنندگان به دنبال تولید محصولات با قابلیت اطمینان بالا هستند. داده‌های طول عمر به علت اینکه اندازه‌گیری آنها صرف زمان و هزینه بالایی می‌باشد، طراحی یک نمودار کنترل را مشکل می‌کنند. برای حل این مشکل از آزمون‌های طول عمر استفاده می‌شود. در این تحقیق به طراحی نمودار کنترل EWMA یک طرفه و دو طرفه تحت آزمون طول عمر سانسورشده خرابی پرداخته شده است. مشخصه کیفی که قرار است تحت نظارت قرار بگیرد طول عمر محصول می‌باشد که فرض شده از توزیع وایبول با پارامتر شکل ثابت و پارامتر مقیاس متغیر پیروی خواهد کرد. جهت طراحی نمودار کنترلی ابتدا حدود کنترل نمودار به ازای پارامترهای مختلف بدست آمده و در جداولی ارائه شده است. سپس جهت ارزیابی عملکرد نمودار کنترل پیشنهادی، از میانگین طول دنباله در حالت خارج از کنترل استفاده شده و مقادیر آن به ازای پارامترهای مختلف بدست آمده و تحلیل حساسیت صورت گرفته است. نتایج محاسباتی نشان می‌دهد که نمودار کنترل یک طرفه نسبت به نمودار کنترل دو طرفه عملکرد بهتری در تشخیص کاهش طول عمر دارد. منحنی متوسط طول دنباله نمودار کنترل دو طرفه به صورت اریب و نمودار کنترل یک طرفه هیچ اریبی نسبت به متوسط طول دنباله ندارد و به صورت یکنواخت افزایش و یا کاهش می‌یابد. یکی از مهمترین پارامترهای تاثیر گذار که عملکرد نمودار کنترل را افزایش می‌دهد، تعداد خرابی مورد نظر در آزمون سانسورشدگی خرابی می‌باشد. در نهایت جهت نشان دادن عملکرد نمودار کنترل پیشنهادی مثال های شبیه سازی شده و واقعی ارائه شده است.

IJE TRANSACTIONS B: Applications Vol. 34, No. 11, (November 2021) 2408-2417

International Journal of Engineering

Journal Homepage: www.ije.ir

Development of a Non-Iterative Macromodeling Technique by Data Integration and Least Square Method

M. Sedaghat[a], Z. H. Firouzeh*[a], H. Aliakbarian[b]

[a] Department of Electrical and Computer Engineering, Isfahan University of Technology, Isfahan, Iran
[b] Department of Electrical Engineering, KN Toosi University of Technology, Tehran, Iran

P A P E R   I N F O

Paper history:
Received 03 April 2021
Received in revised form 19 August 2021
Accepted 11 September 2021

Keywords:
Data Integration
Least Square Method
Macromodeling

A B S T R A C T

In this paper, a new method is introduced to synthesize the original data obtained from simulation or measurement results in the form of a rational function. The integration of the available data is vital to the performance of the proposed method. The values of poles and residues of the rational model are determined by solving the system of linear equations using conventional Least Square Method (LSM). To ensure the stability condition of the provided model, a controller coefficient is considered. Also, using this parameter, the designer can increase the stability margin of a system with poor stability conditions. The introduced method has the potential to be used for a wide range of practical applications since there is no specific restriction on the use of this method. The only requirement that should be considered is Dirichlet condition for the original data, usually the case for physical systems. To verify the performances of the proposed method, several application test cases were investigated and the obtained results were compared with those gathered by the well-known vector fitting algorithm. Also, the examinations showed that the method is efficient in the presence of noisy data.

doi: *10.5829/ije.2021.34.11b.04*

1. INTRODUCTION

Full detail modeling of many practical structures in engineering fields, such as solving Maxwell's equations at the system level, is very difficult based on the first principle [1]. This is because the complete simulation of these structures is highly time-consuming and needs a large amount of memory [2, 3]. In some cases, the complexity is due to the electrical size of the structure leading to an unreasonable number of unknowns. Especially with increasing frequency, fully detailed analysis has become the main requirement for all state-of-the-art circuit design and simulations [4, 5]. Furthermore, simulators face trouble in simulating the structures in the presence of nonlinear components due to mixed frequency/time problems as well as CPU inefficiency [6, 7]. It is well-known that characteristics of understudying structures are governed by Telegrapher's equations of Partial Differential Equations (PDEs) considered to be best solved in the frequency domain, while nonlinear elements are described in the time domain using Ordinary Differential Equations (ODEs) [8-9]. The mentioned problems could be observed in various cases such as on-chip, packaging structures, power systems, printed circuit boards (PCB) and etc. In such situations, a common technique is to divide this complexity into two cases. In the first case, physical characteristics of the structure are known and modeling is based on the most appropriate method. In the second case, where a physical structure is unknown or any analytic solution is hard to derive, rational macromodeling approximation from full-wave electromagnetic simulation or port-port measured data are used to the model system [7].

Several types of black-box macromodeling are done using known physical characteristics of the system [10]. These models are established following many different methods, depending on the available data from the understudying system [11]. These methods lead to three general flows including macromodeling via model order reduction, macromodeling from field solver data, and macromodeling from measured responses. Also, rational

*Corresponding Author Institutional Email: zhfirouzeh@iut.ac.ir (Z. H. Firouzeh)

Please cite this article as: M. Sedaghat, Z. H. Firouzeh, H. Aliakbarian, Development of a Non-Iterative Macromodeling Technique by Data Integration and Least Square Method, International Journal of Engineering, Transactions B: Applications, Vol. 34, No. 11, (2021), 2408-2417

approximation modeling can be constructed from tabulated data responses, as it may also be obtained by a full-wave simulation or through measured data in the frequency domain often existing in the form of impedance, hybrid, scattering, or admittance parameters data. To this end, several methods are proposed, including Vector Fitting (VF) algorithm [12, 13], brute force lumped segmentation modeling [14], the Loewner framework [15, 16], Passive Reduced-Order Interconnect Macromodeling Algorithm (PRIMA) [17], Matrix Rational Approximation (MRA) [18, 19], compact difference [20], integral congruent transformation [21, 22] and so on.

In terms of efficacy, accuracy, and complexity, all the above mentioned methods have their own advantages and disadvantages. For example, vector fitting is currently one of the most popular pole-residue based system identification tools formulated as a linear least-squares problem, depending on an iterative pole relocation approach to improve the approximation. Some advantages to this algorithm include high computational efficiency, high model accuracy, and a relatively simple formulation. Unlike vector fitting, Loewner Method is very efficient in identifying the system from the tabulated data with fewer state-space equations [15, 23]. In Loewner Matrix modeling, the order of the system could be identified from the Singular Value Decomposition (SVD) of Loewner Matrix [23].

In this work, a mathematical method for developing a rational-based transfer function model for practical applications is introduced; addressing the challenges of low complexity. This method is developed based on the integration of the original simulated or measurement data at several specified intervals to decrease data losses and increase the accuracy of the final outcome. For the number of integration intervals, a number of equations are obtained. The result is a system of linear equations. Then, using the Least Square Method (LSM), the required values, including poles and residues of the rational form of the model are determined. To ensure the stability condition of the final response, a closed-loop model is attributed to the understudying system. This goal will be met through defining a stability controller coefficient for the closed-loop model. Several practical examples are provided to evaluate the performance of the proposed method. We tried herein to first present the mathematical formulation of the proposed method in section 2. Then to investigate several examples and comparing the obtained results of the vector fitting algorithm in section 3. Finally, reaching a conclusion in section 4.

2. MATHEMATICAL FORMULATION

Practical structures are modeled using simulation or measured data from frequency-dependent scattering, impedance, or admittance parameters. It is common to acquire a rational function to approximate the obtained data as follows [1].

$$H(x) = \sum_{n=1}^{N} \frac{r_n}{x-p_n} + r_0 \tag{1}$$

where r_n, p_n correspond to residues and poles respectively, while the value r_0 is optional; x can be considered as frequency f or Laplace variable s (complex frequency), and N is the number of poles and residues or the order of the rational function. The other common notation of rational transfer functions $H(x)$ is described as the ratio of two polynomials

$$H(x) = \frac{P(x)}{Q(x)} = \frac{b_{N_P}x^{N_P} + b_{N_P-1}x^{N_P-1} + \ldots + b_1 x + b_0}{a_{N_Q}x^{N_Q} + a_{N_Q-1}x^{N_Q-1} + \ldots + a_1 x + 1} \tag{2}$$

In which, the degree of the prescribed numerator and denominator polynomials $P(x)$ and $Q(x)$ are N_P and N_Q, respectively. In most cases, it is assumed that $N_P=N_Q=N$. One of the simplest assumptions in the underlying model structure is using the linear least square method. Multiplying by $Q(x)$ both sides of equation (2) and some simplification leads to:

$$\begin{aligned} &b_0 + b_1 x - a_1 H(x)x + b_2 x^2 - a_2 H(x)x^2 \\ &+ \ldots + b_n x^N - a_n H(x)x^N = H(x) \end{aligned} \tag{3}$$

Samples of the desired transfer function at each $x=x_m$; $m=1, 2, \ldots, M$ are available. Using these samples, the above equation can be rewritten as a linear system of M equations in $2N+1$ unknown, where M is the total number of samples [1].

$$\mathbf{\Phi u} = \mathbf{v} \tag{4}$$

$$\boldsymbol{u} = [b_0 \quad \cdots \quad b_N \quad a_1 \quad \cdots \quad a_N]^T \tag{5a}$$

$$\boldsymbol{v} = [H(x_1) \quad H(x_2) \quad \cdots \quad H(x_M)]^T \tag{5b}$$

$$\boldsymbol{\Phi} = \begin{bmatrix} 1 & \cdots & x_1^N & -x_1 H(x_1) & \cdots & -x_1^N H(x_1) \\ \vdots & & & \ddots & & \vdots \\ 1 & \cdots & x_M^N & -x_M H(x_M) & \cdots & -x_M^N H(x_M) \end{bmatrix} \tag{5c}$$

It is assumed that coefficient matrix $\boldsymbol{\phi}$ is not a zero matrix. Typically, equations number M is greater than the unknown number $2N+1$. Therefore, by assuming that the coefficient matrix is left-invertible, the following equation is the unique solution to the least-squares problem (4) [24].

$$\tilde{\boldsymbol{u}} = (\boldsymbol{\Phi}^T\boldsymbol{\Phi})^{-1}\boldsymbol{\Phi}^T\boldsymbol{v} \tag{6}$$

It is clear that the above solution is not an exact answer for any choice of $\mathbf{u}$. The solution defined by (6) is the vector that minimizes the sum of squares of the error vector $\mathbf{E}$ defined as the Euclidean norm as follows [25].

$$\boldsymbol{E} = \|\boldsymbol{\Phi}\tilde{\boldsymbol{u}} - \boldsymbol{v}\|^2 \tag{7}$$

This method is affected by several issues. First, the coefficient matrix $\boldsymbol{\phi}$ known as the Vandermond matrix, becomes seriously ill-conditioned when order of numerator and/or denominator polynomials increases. Second, solution (6) will be successful, whereas there is a linear relationship between variable x and the desired transfer function $H(x)$. However, in practical applications, this condition is not provided [25, 26]. Furthermore, this method suffers from local control over the unshaped area of the desired data [27]. In other words, in this method, information between two adjacent samples is not used. If the goal is to use all the information, the number of unknowns, being the degree of the numerator and the denominator polynomials of (2), increases dramatically. This problem could be solved by integrating both sides of the equation (3) over an interval $[x_i, x_f]$.

$$\begin{aligned}&\int\{b_0 + b_1x - a_1H(x)x + b_2x^2\}dx + \\ &\int\{-a_2H(x)x^2 + \ldots + b_nx^N - a_nH(x)x^N\}dx = \\ &\int H(x)\,dx\end{aligned} \tag{8}$$

Some simplifications could also be made as follows.

$$\begin{aligned}&b_0x + \frac{b_1}{2}x^2 + \ldots + \frac{b_n}{N+1}x^{N+1} - a_1\int H(x)xdx - \\ &a_2\int H(x)x^2dx \ldots - a_n\int H(x)x^Ndx = \int H(x)dx\end{aligned} \tag{9}$$

For a given desired data, the integration result for both left and right-hand sides of the above equation could be calculated. The unknown numbers are $2N$+1. Hence, at least $2N$+1 independent equations are required. In practical application, it is assumed that the desired data are available from frequency interval $f \in [f_{min}, f_{max}]$. As mentioned before, x could be considered as a frequency f or Laplace variable s. Hence, x is varying over the interval $x \in [x_{min}, x_{max}]$, where x_{min} and x_{max} correspond to a minimum and maximum frequency, respectively. By dividing the distance $x_{min} \le x \le x_{max}$ to M equal segments, the required number of equations will be obtained.

$$x\begin{cases}x1_{min} \\ xM+1_{max}\{\end{cases}\Bigg| \xrightarrow{\text{Integ. Interval}} x\,m+1 \quad _m\,max_{min} \tag{10}$$

By specifying upper and lower limits of the integration interval, only the coefficient's a_i, b_i remains unknown. As a result, a linear system of M equations and $2N$+1 unknown is made. This equation system and its solution are as follows.

$$\boldsymbol{\Psi u} = \boldsymbol{w} \tag{11a}$$

$$\widetilde{\boldsymbol{u}} = (\boldsymbol{\Psi^T\Psi})^{-1}\boldsymbol{\Psi^T w} \tag{11b}$$

where $\boldsymbol{\Psi}$ is M×$2N$+1 coefficient matrix, $\mathbf{u}$ is $2N$+1×1 column vectors, in which holds the unknowns, and $\mathbf{w}$ is M×1 column vectors that include the desired data.

$$\boldsymbol{u} = [b_0 \quad \cdots \quad b_N \quad a_1 \quad \cdots \quad a_N]^T \tag{12a}$$

$$\boldsymbol{w} = \left[\int_{x_1}^{x_2} H(x)dx \quad \cdots \quad \int_{x_M}^{x_{M+1}} H(x)dx\right]^T \tag{12b}$$

$$\boldsymbol{\Psi} = \begin{bmatrix} \int_{x_1}^{x_2} dx & \cdots & \int_{x_1}^{x_2} x^N dx & -\int_{x_1}^{x_2} xH(x)dx & \cdots & -\int_{x_1}^{x_2} x^N H(x)dx \\ \vdots & & & \ddots & & \vdots \\ \int_{x_M}^{x_{M+1}} dx & \cdots & \int_{x_1}^{x_2} x^N dx & -\int_{x_1}^{x_2} xH(x)dx & \cdots & -\int_{x_M}^{x_{M+1}} x^N H(x)dx \end{bmatrix} \tag{12c}$$

In some practical cases, using equation (11b) is not a good solution, especially when $\boldsymbol{\Psi}$ is an ill-conditioned matrix, and it may cause a low accuracy in the final answer. In these cases, using of a modified QR factorization technique leads to an increase in computational efficiency, where $\mathbf{P}$ is the permutation matrix [1].

$$\widetilde{\boldsymbol{u}} = \boldsymbol{PR^{-1}Q^T w} \tag{13a}$$

$$\boldsymbol{\Psi P} = \boldsymbol{QR} \tag{13b}$$

It could be seen that the integral responses in Equation (12) are independent of variable x. This ensures that the proposed method is less affected by any unwanted noise or disturbance. In other words, the integral operator is resistant to noise. As mentioned before, the typical least square method suffers from a nonlinear feature understudying systems while the integral operator solves this problem. In many former researches in literature, they use only samples of the available data. This means that, in these methods, all observable output of the system is not used properly and there is a data loss problem, while in the proposed technique, all available data are used in the integration process, and there is not any data loss.

According to equation (12), three conditions should be met. First, available data should be absolutely integrable over any interval. Second, available data should be of bounded variation in any given bounded interval. Third, available data should have a finite number of discontinuities in any given bounded interval, and the discontinuities cannot be infinite. In summary, Dirichlet condition should be met as follows [28].

$$\int_x |H(x)|dx < \infty \tag{14a}$$

$$\int_x |H(x)x^n|dx < \infty;\ n \text{ is integer} \tag{14b}$$

The computational complexity of Equation (11) is dependent on the value of M. The Nyquist theorem can be helpful to determine the sampling rate Δ. For an arbitrary available data, the following equation can be used to the first approximation of M [26].

$$\Delta \le \frac{|x_{\max} - x_{\min}|}{4N} \tag{15a}$$

$$M \ge \frac{8N}{|xmin_{max}|} \tag{15b}$$

In other words, the number of integration intervals is considered equal to the number of samples. It should be noted that the above equations are obtained, assuming that the integration intervals have equal lengths. In some cases, intervals of equal length may not produce acceptable results. For these cases, the number of integral intervals of a range of x that are more important could be increased. Correspondingly, for regions of x that the original data is less important, less number of integral intervals could be considered. For example, if the original data is the frequency response of a bandpass filter, the number of integral intervals in the passband range will be considered greater than the number of integral intervals in the stopband range.

After determining the unknown coefficients a_i, b_i using Equation (11), poles, and zeros of Equation (2) should be determined. The poles and zeros are Eigen-values of the following matrixes [29].

$$\boldsymbol{T_P} = \begin{bmatrix} -\frac{b_{N-1}}{b_N} & -\frac{b_{N-2}}{b_N} & \cdots & -\frac{b_0}{b_N} \\ 1 & 0 & \cdots & 0 \\ \vdots & \ddots & & \vdots \\ 0 & 0 & 1 & 0 \end{bmatrix}_{N\times N} \tag{16a}$$

$$\boldsymbol{T_Q} = \begin{bmatrix} -\frac{a_{N-1}}{a_N} & -\frac{a_{N-2}}{a_N} & \cdots & -\frac{1}{a_N} \\ 1 & 0 & \cdots & 0 \\ \vdots & \ddots & & \vdots \\ 0 & 0 & 1 & 0 \end{bmatrix}_{N\times N} \tag{16b}$$

By specifying the poles and zeros of the system, available data could be expressed in poles-residues form as (1). As mentioned before, in physical problems, x is some independent variable such as real frequency f or complex frequency s in order of GHz. To avoid the computational complexity, before incoming the process, variable x can be normalized to its maximum value. After specifying the poles and residue, the rational form can be easily rescaled to its normal case.

In some cases, the obtained poles may be placed in an unstable region. In the following, a simple technique will be introduced to overcome this problem. The general form of a closed-loop system with forward transfer function $G(x)$ and feedback transfer function $F(x)$ is presented in Figure 1. The transfer function of the closed-loop system is as follows.

$$TF(x) = \frac{G(x)}{1+G(x)F(x)} \tag{17}$$

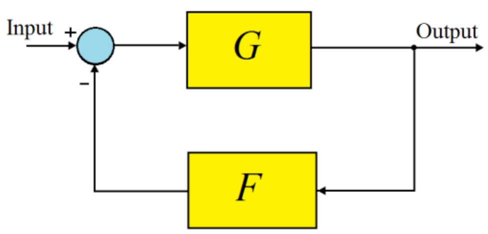

Figure 1. Block diagram of a closed-loop system

For simplicity, it is assumed that the feedback transfer function is equal to one and the forward transfer function could be expressed as a ratio of two polynomials. This system is considered as a macromodel to the understudying system as follows.

$$TF(x) = \frac{G(x)}{1+G(x)F(x)} \xrightarrow{F(x)=1\,G(x)=k\frac{B(x)}{A(x)}} \\ TF(x) = \frac{kB(x)}{A(x)+kB(x)} \tag{18}$$

Therein, parameter k is a stability controller coefficient, using which the stability of the model could be controlled. By comparing Equation (18) with Equation (2), we have:

$$H(x) = \frac{kB(x)}{A(x)+kB(x)} = \frac{kB(x)}{C(x)} = \\ k\,\frac{b_N x^N + b_{N-1}x^{N-1} + \ldots + b_1 x + b_0}{c_N x^N + c_{N-1}x^{N-1} + \ldots + c_1 x + c_0} \tag{19a}$$

$$\begin{cases} c_n = a_n + kb_n \\ c_0 = 1 + kb_0 \end{cases}, n = 1,2,\ldots,N \tag{19b}$$

In this situation, the proposed procedure is applied to a new case. In other words, Equation (12c) should be rewritten for a new case.

$$\boldsymbol{\Psi} = [\boldsymbol{\Psi_b} \quad \boldsymbol{\Psi_a}] \tag{20a}$$

$$\boldsymbol{\Psi_b} = k \begin{bmatrix} \int_{x_1}^{x_2} h(x)dx & \cdots & \int_{x_1}^{x_2} h(x)x^N dx \\ \vdots & \ddots & \vdots \\ \int_{x_M}^{x_{M+1}} h(x)dx & \cdots & \int_{x_M}^{x_{M+1}} h(x)x^N dx \end{bmatrix} \tag{20b}$$

$$\boldsymbol{\Psi_a} = \begin{bmatrix} -\int_{x_1}^{x_2} xH(x)dx & \cdots & -\int_{x_1}^{x_2} x^N H(x)dx \\ \vdots & \ddots & \vdots \\ -\int_{x_M}^{x_{M+1}} xH(x)dx & \cdots & -\int_{x_M}^{x_{M+1}} x^N H(x)dx \end{bmatrix} \tag{20c}$$

$$h(x) = 1 - H(x) \tag{20d}$$

As a result, by changing the parameter k, the stability condition could be met. In other words, unstable poles could be moved toward the stable region. Another solution is to plot the root locus of the system and determining the acceptable value of k that guarantees the stability condition.

Passivity can be achieved through the conventional two-step methods introduced in literature [1]. In this way, first step comprises of approximation with stable poles. Then, using the method of repetition and perturbation in the residues, we can achieve the condition of being passive. More details are available in literature [1]. Also, the proposed method could be easily extended for Multi-Input-Multi-Output systems (MIMO) using the introduced procedure by Grivet-Talocia et al. [1].

3. RESULTS AND DISCUSSIONS

In this section, the performance of the proposed method will be demonstrated using several examples. It should be noted that the purpose of this paper is not to show the overall superiority of the proposed method over the VF algorithm; although, this is obvious in some examples. Here, the realxed VF algorithm version 3 is used as a known method to compare the results [31].

3. 1. Single Trace PCB A single trace PCB, as shown in Figure 2 with a length of 10 cm is considered as the first example. The width of the strip and substrate height is about 1.55 mm, 0.8 mm, respectively. The applied substrate is FR4 with a relative permittivity of 4.3. This structure is simulated using CST microwave studio in time domain. The corresponding scattering parameters ranged between 0 and 5 GHz are considered as the input of the problem. The magnitude and phase of rational approximation of S21 using the proposed method with 6 poles (N=6) and vector fitting algorithm with N=8, 10 poles for the first example are shown in Figures (3a) and (3b). It can be seen that VF with N=8 shows a small deviation in magnitude, but by increasing the poles number to N=10, the synthesized error is decreased. A comparison of the results shows that the proposed method has a better performance with a lower number of poles.

3. 2. MultiLayer Structure The second example is a multilayer structure shown in Figure 4. In this structure, a microstrip trace with width and length of 1.18 mm, 8.49 mm, respectively, in signal layer is connected to a stripline trace in the third layer with width and length 0.47 mm, 22.64 mm, respectively. The copper planes in layers 2 and 4 are regarded as ground. A FR4 substrate with relative permittivity, loss tangent and height 4.3, 0.02 and 0.6 mm, is used for this example. The structure is terminated matched load (50 Ohms impedance). The simulated scattering parameters in frequency ranged from 0 to 5GHz are considered as the available data to the synthesis procedure. Figure 5 shows the rational approximation results of the example for the proposed method with two different poles numbers N=3, 8 and vector fitting algorithm with N=6. Although the vector fitting algorithm and the proposed method with N=8 have an acceptable accuracy, the VF was able to synthesize the problem with a smaller number of poles.

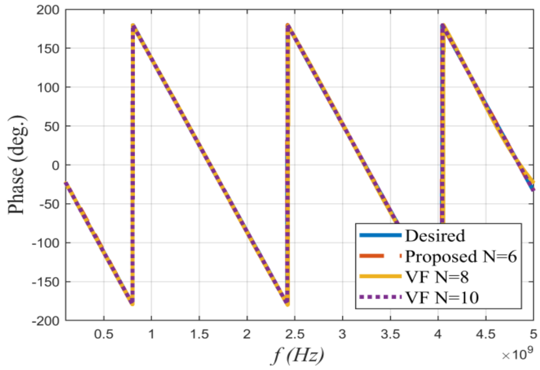

Figure 3b. Magnitude of the synthesized S_{21} of single trace PCB

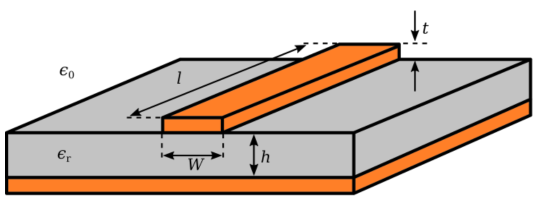

Figure 2. The geometry of a single trace PCB

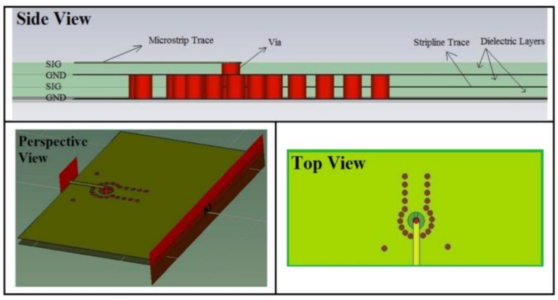

Figure 4. The structure geometry of multilayer microstrip

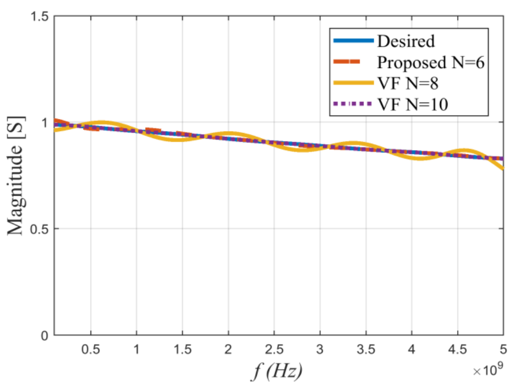

Figure 3a. Magnitude of the synthesized S_{21} of single trace PCB

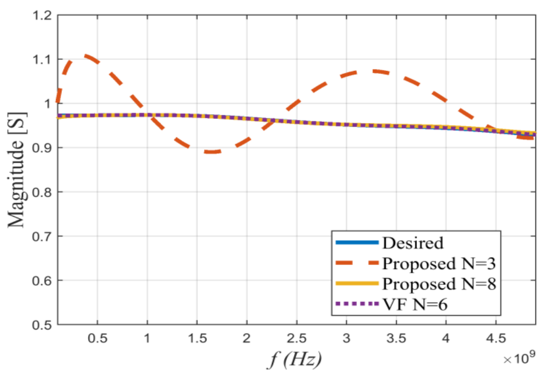

Figure 5a. Magnitude of synthesized S_{21} of multilayer microstrip

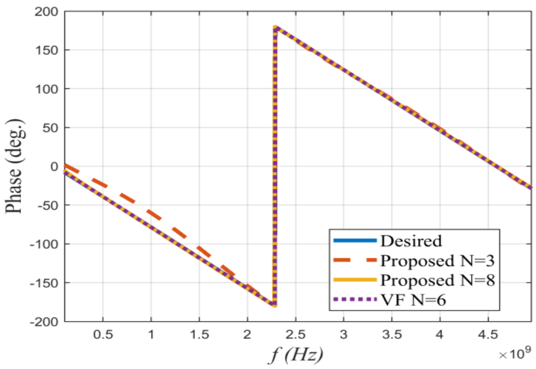

Figure 5b. Phase of synthesized S_{21} of multilayer microstrip

3. 3. Noise-Infected Data

The third test case is a theoretical example in which the goal is to assess the performance of the proposed method for noise-infected data in frequency ranged from 0 to 10 GHz. This example includes a synthetic transfer function with 16 poles described in Table 1 [30]. First, the synthetic transfer function is considered to be noise-free. Figure 6 shows the obtained results of the proposed method with N=12 and VF algorithm with *N*=16. The performance of the proposed method is clearly better than the VF.

TABLE 1. Poles and residues of the TF of theoretical example

Poles (GHz)	Residues (GHz)
-0.6132±j3.4551	-0.9877±j0.0809
-0.3940±j7.3758	-0.2067±j0.0131
-0.0880±j14.3024	-0.1382±j0.0145
-0.4097±j17.7864	-0.1182±j0.0166
-0.2991±j28.4622	-0.2426±j0.0145
-0.6447±j35.2669	-0.4043±j0.0297
-1.0135±j37.9655	-0.6787±j0.1465
-0.5711±j57.4748	-0.2626±j0.1037
r_0=0.1	

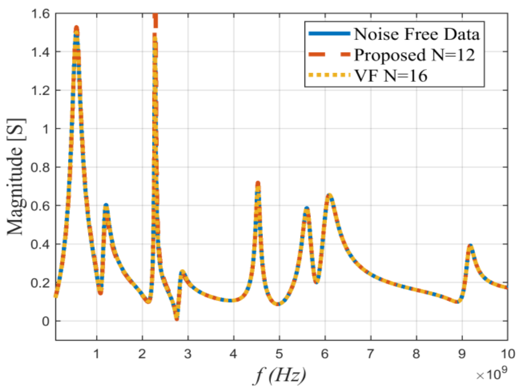

Figure 6a. Magnitude of synthesized TF of theoretical example in the absence of noise

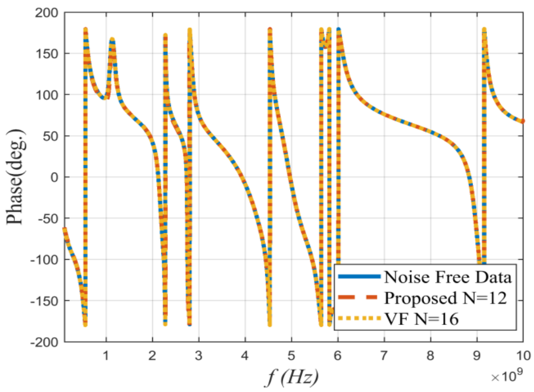

Figure 6b. Phase of synthesized TF of theoretical example in the absence of noise

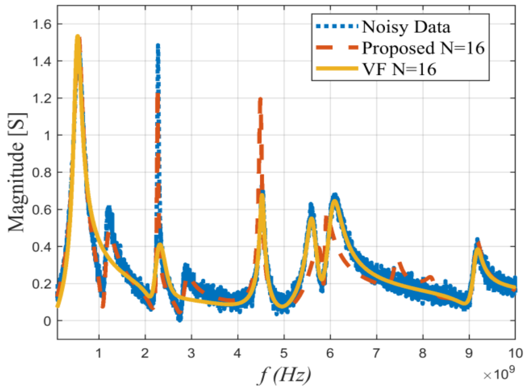

Figure 7a. Magnitude of synthesized TF of theoretical example in the presence of noise

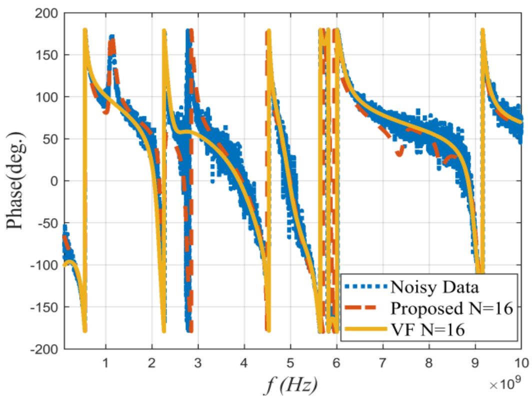

Figure 7b. Phase of synthesized TF of in the presence of noise

Now, consider the same transfer function in the presence of noise. Both real and imaginary parts of the transfer function are infected by white Gaussian noise. The noise level considered for this example is set to 20 dB signal-to-noise ratios (SNRs). The synthesized results of both VF and the proposed method with noisy data are depicted in Figure 7. Due to numerous fluctuations, it is not

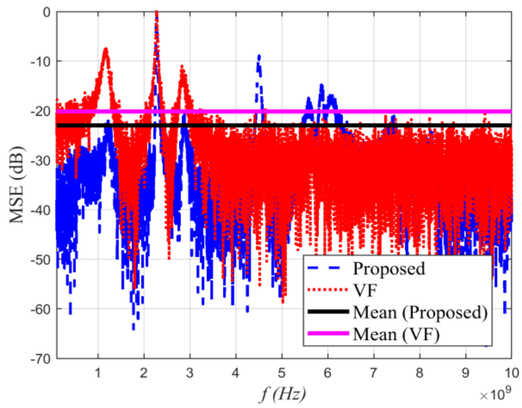

Figure 7c. Mean square error of TF vs. frequency for theoretical example

possible to compare the results from the figures correctly. For this reason, the diagram of the Mean Squares Error (MSE) in dB for both methods is also shown. It is observed that the proposed method has a lower MSE than VF, for about 2.8 dB averagely. In other words, the proposed method has more immunity with respect to noise. It should be noted that the noisy transfer function does not show smooth behavior and includes several sudden jumps versus frequency.

3. 4. Coupled Structure The coupled structures are widely used in microwave engineering [32-33]. As the fourth example, a coupled microstrip line using TLY062 substrate with relative permittivity of 2.2, the thickness of 1.56 mm, and loss tangent 0.009 is considered [34]. The length and width of the board is 50 mm. The culprit and victim strip width are set to 4.8 mm, and the distance between two traces is about 0.5 mm. The measured far-end crosstalk is regarded as original data [34]. The fabricated of the understudying structure is shown in Figure 8 [34]. The magnitude and phase of rational approximation using the proposed method with N=9, 10, and vector fitting algorithm with N=14 poles are shown in Figure 9. It can be seen that the proposed method with N=9 shows a small deviation in magnitude in low frequencies. However, through increasing the poles number to N=10, the synthesized error is decreased. Although the accuracy of VF and the proposed method for N=10 is almost acceptable, the proposed method with a smaller number of poles shows better performance.

The relative error signals of all examples can be seen in Figures 10(a) to 10(c). It should be noted that the error signal of the third example (assumed TF with noise-infected data) is available in Figure 7c. It can be seen that in all examples except the second structure, the error value of the proposed method is lower than VF. Although in the second structure the error of VF is lower than the proposed method, the error value of the proposed method is less than 1%, and it is acceptable.

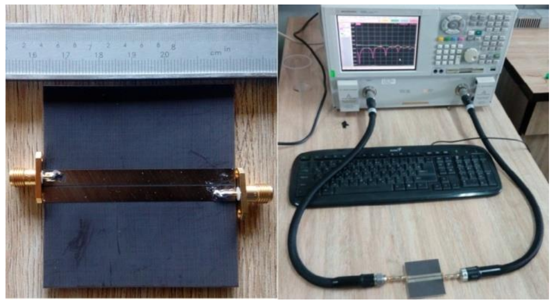

Figure 8. The fabricated structure of coupled microstrip line [34]

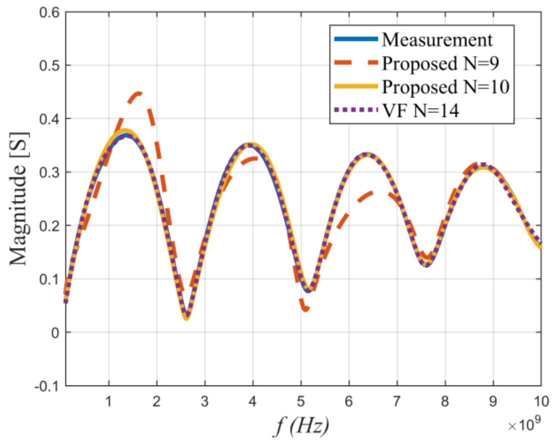

Figure 9a. Magnitude of synthesized, far-end crosstalk of coupled microstrip line

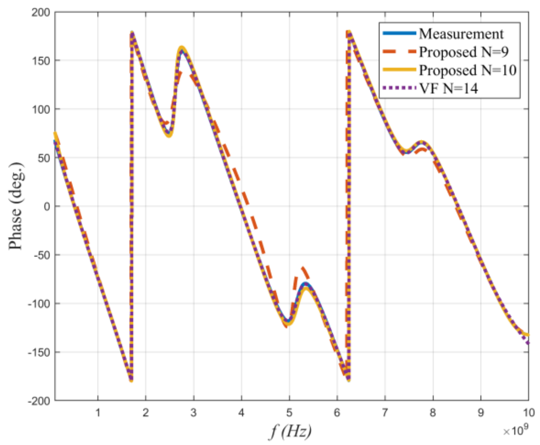

Figure 9b. Phase of synthesized far-end crosstalk of coupled microstrip line

The condition numbers of coefficient matrix of Equations (5c) and (12c) (or (20a)) for all examples are reported in Table 2. It can be seen that the condition numbers of the coefficient matrix of Equations (5c) are very large in comparison to Equation (12c). Large condition numbers mean numerical difficulties in the

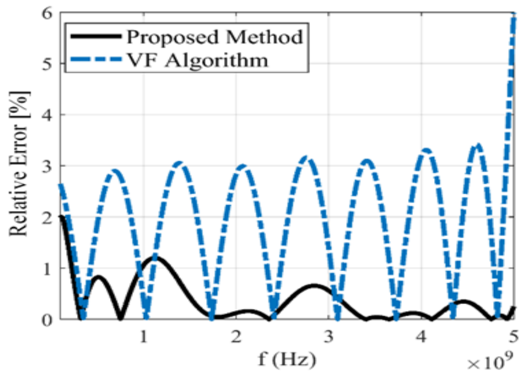

Figure 10a. The relative error signal of single trace PCB

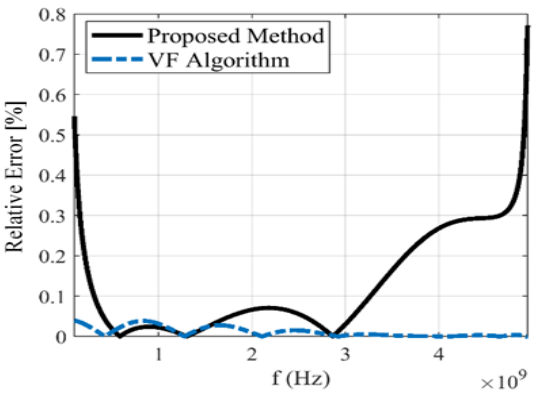

Figure 10b. The relative error signal of multilayer structure

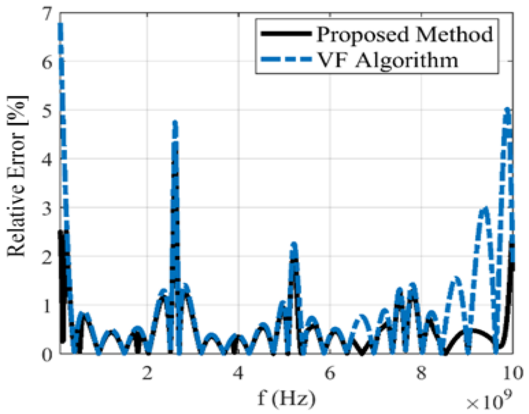

Figure 10c. The relative error signal of coupled structure

computation of the poles and residues of the final model [1]. Table 2 shows that the proposed method has created an extreme improvement in the condition number of coefficient matrix compared to the LSM method. This has led to a significant reduction in the computational error of the introduced method.

TABLE 2. Condition number of coefficients matrix for all examples

	N	**Cond (5c)**	**Cond (12c) or (20a)**
Example I	6	2.6542e+62	1.2724e+06
Example II	8	6.2741e+81	2.1412e+09
Example III	16	3.4643e+163	6.1996e+13
Example IV	10	9.6081e+103	3.4439e+09

4. CONCLUSION

In this paper, a mathematical method is presented to approximate the simulation or measurement data in the poles-residue form. The integration of the original data at several specified intervals, produces a system of linear equations that could be solved using the least square method. The stability condition of the provided model is guaranteed through defining a controller coefficient. To evaluate the performance of the proposed method, several practical examples were investigated and obtained results were compared with those obtained by the well-known vector fitting algorithm. The comparison showed that, in some cases, the proposed method could model the original data with a smaller number of poles than the VF algorithm. Also, the obtained results demonstrated that the performance of the method was less affected by noise. This is a very important point to notice since the measurement data is usually contaminated with noise.

5. ACKNOWLEDGMENTS

This project is supported by the Iran National Science Foundation (INSF) under Grant No. 97013228.

6. REFERENCES

1. Grivet-Talocia S, Gustavsen B, Passive Macromodeling: Theory and Applications. New York, NY, USA: Wiley, 2016.
2. Alijani M, G, H, Sheikh. S, Kishk. Ahmed, "Development of Closed-Form Formula for Quick Estimation of Antenna Factor", 15th European Conference on Antennas and Propagation (EuCAP), (2021), 1-5. doi: 10.23919/EuCAP51087.2021.9411008
3. Contreras. A, "Objective Functions for the Optimization of an Ultra Wideband Antenna", ***International Journal of Engineering, Transaction A: Basics,*** Vol. 34, No. 7, (2021), 1743-1749. doi: 10.5829/ije.2021.34.07a.19
4. Gupta. P, Pandey. R, "Dual Output Voltage Differencing Buffered Amplifier Based Active -C Multiphase Sinusoidal Oscillator", ***International Journal of Engineering Transaction C: Aspects,*** Vol. 34, No. 6, (2021), 1438-1444. doi: 10.5829/ije.2021.34.06c.07
5. Niasar. M, M, Molaei. M, J, Aghaei. A, "Electromagnetic Wave Absorption Properties of Barium Ferrite/Reduced Graphene

Oxide Nanocomposites", ***International Journal of Engineering, Transaction C: Aspects,*** Vol. 34, No. 6, (2021), 1503-1511. doi: 10.5829/ije.2021.34.06c.14

6. Yang. C, Bruns. H, D, Liu. P, Schuster. C, "Impulse response optimization of band-limited frequency data for hybrid field-circuit simulation of large-scale energy-selective diode grids", ***IEEE Transaction Electromagnetic Compatibility,*** Vol. 58, No. 4, (2016), 1072–1080. doi: 10.1109/TEMC.2016.2540921

7. Beygi. A, Time-domain macromodeling of high speed distributed networks. Ph.D. dissertation, The University of Western Ontario, 2011.

8. Alijani. M, G, H, Neshati. M, H, "A new non-iterative method for pattern synthesis of unequally spaced linear arrays", ***International Journal of RF and Microwave Computer-Aided Engineering,*** Vol. 29, No. 11, (2019), 740-771. doi: 10.1002/mmce.21921

9. Dounavis. A, Achar. R, Nakhla. M, S, "Addressing transient errors in passive macromodels of distributed transmission-line networks", ***IEEE Transaction Microwave Theory Technique,*** Vol. 50, No. 12, (2002), 2759-2768. doi: 10.1109/TMTT.2002.805130

10. Grivet-Talocia. S, Acquadro. S, Bandinu. M, Canavero. F, G, Kelander. I, Rouvala. M, "A parameterization scheme for lossy transmission line macromodels with application to high speed interconnects in mobile devices", ***IEEE Transaction Electromagnetic Compatibility,*** Vol. 49, No. 1, (2007), 18-24. doi: 10.1109/TEMC.2006.888179

11. Ferranti. F, Knockaert. L, Dhaene. T, "Guaranteed passive parameterized admittance-based macromodeling", ***IEEE Transaction on Advanced Packag*ing,** Vol. 33, No. 3, (2010), 623-629. doi: 10.1109/TADVP.2009.2029242

12. Gustavsen. B, Semlyen. A, "Rational approximation of frequency domain responses by vector fitting", ***IEEE Transactions on Power Delivery,*** Vol. 14, No. 3, (1999), 1052-1061. doi: 10.1109/61.772353

13. Deschrijver. D, Mrozowski. M, Dhaene. T, De-Zutter. D, "Macromodeling of multiport systems using a fast implementation of the vector fitting method", ***IEEE Microwave Wireless Component Letter,*** Vol. 18, No. 6, (2008), 383-385. doi: 10.1109/LMWC.2008.922585

14. Dhaene. T, De-Zutter. D, "Selection of lumped element models for coupled lossy transmission lines", ***IEEE Transaction Computer-Aided Design Integrated Circuits System,*** Vol. 11, No. 7, (1992), 805-815. doi: 10.1109/43.144845

15. Kabir. M, Khazaka. R, "Macromodeling of distributed networks from frequency domain data using the Loewner matrix approach", ***IEEE Transaction Microwave Theory Technique,*** Vol. 60, No. 12, (2012), 3927-3938. doi: 10.1109/TMTT.2012.2222915

16. Rergis. C, M, Kamwa. I, Khazaka. R, Messina. A, R, "A Loewner Interpolation Method for Power System Identification and Order Reduction", ***IEEE Transactions on Power Systems,*** Vol. 34, No. 3, (2019), 1834-1844. doi: 10.1109/TPWRS.2018.2884655

17. Odabasioglu. A, Celik. M, Pileggi. L, T, "PRIMA: passive reduced-order interconnect macromodeling algorithm", ***IEEE Transaction Computer-Aided Design Integrated Circuits System,*** Vol. 17, No. 8, (1998), 645-654. doi: 10.1109/43.712097

18. Dounavis. A, Achar. R, Nakhla. M, S, "Efficient passive circuit models for distributed networks with frequency-dependent parameters", ***IEEE Transaction Advanced Packaging,*** Vol. 23, No. 3, (2000), 382-392. doi: 10.1109/6040.861551

19. Dounavis. A, Achar. R, Nakhla. M, "A general class of passive macromodels for lossy multi-conductor transmission lines", ***IEEE Transaction Microwave Theory Technique,*** Vol. 49, No. 10, (2001), 1686-1696. doi: 10.1109/22.954772

20. Cangellaris. A, C, Pasha. S, Prince. J, L, Celik. M, "A new discrete transmission line model for passive model order reduction and macromodeling of high-speed interconnections", ***IEEE Transaction Advanced Packaging,*** Vol. 22, No. 3, (1999), 356-364. doi: 10.1109/6040.784485

21. Yu. Q, Wang. J, M, L, Kuh. E, S, "Passive multipoint moment matching model order reduction algorithm on multiport distributed interconnect networks", ***IEEE Transaction Circuits System I: Fundamental Theory and Applications,*** Vol. 46, No. 1, (1999), 140-160. doi: 10.1109/81.739262

22. Gad. E Nakhla. M, "Efficient simulation of non-uniform transmission lines using integrated congruence transform", ***IEEE Transactions on Very Large Scale Integration (VLSI) Systems,*** Vol. 12, No. 12, (2004), 1307-1320. doi: 10.1109/TVLSI.2004.837988

23. Lefteriu. S, Antoulas. A, C, "A new approach to modelling multiport systems from frequency-domain data", ***IEEE Transactions Computed-Aided Design Integrated Circuits System,*** Vol. 29, No. 1, (2010), 14-27. doi: 10.1109/TCAD.2009.2034500

24. Alijani. M, G, H, Neshati. M, H, "A New Closed-Form Expression for Dispersion Characteristics of Fundamental Mode of SIW by Least Squares Method", ***Journal of Applied Computational Electromagnetic Society,*** Vol. 30, No. 8, (2015), 930-933.

25. Mendel. J, M, Lessons in Estimation Theory for Signal Processing, Communications, and Control. Prentice Hall PTR, 1995.

26. Alijani. M, G, H, Neshati. M, H, "Development a New Technique Based on Least Square Method to Synthesize the Pattern of Equally Space Linear", ***International Journal of Engineering, Transaction B: Applications,*** Vol. 32, No. 11, (2019), 1620-1626. doi: 10.5829/ije.2019.32.11b.13

27. Alijani. M, G, H, Neshati. M, H, "Development A New Array Factor Synthesizing Technique by Pattern Integration and Least Square Method", ***IEEE Transaction Antennas and Propagation,*** Vol. 66, No. 12, (2018), 6869-6874. doi: 10.1109/TAP.2018.2871715

28. Courant. R, Hilbert. D, Methods of Mathematical Physics. John Wiley & Sons, 1989.

29. Pan. V, Y, "Solving a Polynomial Equation: Some History and Recent Progress", ***SIAM Review,*** Vol. 39, No. 2, (1997), 187-220. doi: 10.1137/S0036144595288554

30. Beygi. A, Dounavis. A, "An instrumental variable vector-fitting approach for noisy frequency responses", ***IEEE Transaction Microwave Theory Technique,*** Vol. 60, No. 9, (2012), 2702-2712. doi: 10.1109/TMTT.2012.2206399

31. http://www.energy.sintef.no/Produkt/VECTFIT/index.asp.

32. Rashtian. M, Vafapour. M, "Gain Boosted Folded Cascade Op-Amp with Capacitor Coupled Auxiliary Amplifiers", ***International Journal of Engineering, Transaction B: Applications,*** Vol. 34, No. 5, (2021), 1233-1238. doi: 10.5829/ije.2021.34.05b.16

33. Sobouti. M, A, Azizian. D, Bigdeli. M, Gharehpetian. G, B, "Multi-Conductor Transmission Line Model of Split-Winding Transformer for Frequency Response and Disk-to-Disk Fault Analysis", ***International Journal of Engineering, Transaction C: Aspects*** Vol. 34, No. 6, (2021), 1486-1492. doi: 10.5829/ije.2021.34.06c.12

34. Soleimani. N, Alijani. M, G, H, Neshati. M, H, "Crosstalk Analysis of Multi-Microstrip Coupled Lines Using Transmission Line Modeling", ***International Journal of RF and Microwave Computer-Aided Engineering,*** Vol. 22, No. 6, (2019), 1-7. doi: 10.1002/mmce.21677

Persian Abstract

چکیده

در این مقاله ، یک روش جدید برای سنتز داده های به دست آمده از نتایج شبیه سازی یا اندازه گیری در قالب یک تابع کسری معرفی شده است. انتگرال گیری از داده های موجود نقش مهمی در عملکرد روش پیشنهادی دارد. مقادیر قطب ها و مانده های مدل کسری با حل سیستم معادلات خطی با روش حداقل مربعات (LSM) تعیین می شود. برای اطمینان از شرایط پایداری مدل ارائه شده، ضریب کنترل کننده در نظر گرفته شده است. همچنین، با استفاده از این پارامتر، طراح می تواند حاشیه پایداری سیستم را با شرایط پایداری ضعیف افزایش دهد. روش معرفی شده امکان استفاده در طیف گسترده ای از کاربردهای عملی را فراهم می کند زیرا محدودیت خاصی در استفاده از این روش وجود ندارد. تنها موردی که باید در نظر گرفته شود شرط دیریچله برای داده های اصلی است که معمولاً در مورد سیستم های فیزیکی برقرار است. برای تأیید عملکرد روش پیشنهادی، چندین مورد مثال کاربردی بررسی شده و نتایج بدست آمده با نتایج بدست آمده توسط الگوریتم برازش برداری مقایسه می شود. همچنین، نتایج شبیه سازی نشان می دهد که این روش در حضور داده های نویزی کارآمد است.

IJE TRANSACTIONS B: Applications Vol. 34, No. 11, (November 2021) 2418-2423

International Journal of Engineering

Journal Homepage: www.ije.ir

Mode-I Fracture Toughness Investigation on Carbon/Glass Hybrid Composites

M. S. EL-Wazery*

Department of Production Engineering and Mechanical Design, Faculty of Engineering, Menoufia University, Shebin El-Kom, Egypt

PAPER INFO

Paper history:
Received 16 Augest 2021
Received in revised form 9 September 2021
Accepted in 18 September 2021

Keywords:
Fracture Toughness
Hybrid Composites
Hand Lay-up Technique
Single Edge Notch Bending

ABSTRACT

Mode-I fracture toughness of carbon/glass reinforced polyester hybrid composites was experimentally and numerically investigated by using the COSMOS/M 2.6 finite element software after manufactured by utilizing the hand lay-up technique. The single edge notch-bending test was developed to evaluate the mode-I fracture toughness of the carbon composites, glass composites and hybrid composites at various fiber configurations. Scanning electron microscope was used to examine the fractured surfaces of hybrid composites under the effect of mode-I loading. The experimental results showed the stress intensity factor was reached to 882.34 MPa.mm$^{1/2}$ for the hybrid composites with stacking sequences [C/G/G/C] during the mode-I loading compared to the other stacking sequences. Glass fiber enhanced the stress intensity factors of the hybrid composite when the glass fibers are placed at the middle portion between the carbon layers. In addition, the experimental results are in good agreement with the finite element modeling.

***doi**: 10.5829/ije.2021.34.11b.05*

1. INTRODUCTION

Hybrid Composites are considered one of the most developed materials due to the light weight, high rigidity, low manufacturing costs and good corrosion resistance so they are used in automotive parts, aerospace, aircraft and wind turbines [1-3]. The hybrid composites consisting of polymer matrix such as polyester or epoxy and glass, carbon and Kevlar fiber which are used as a reinforcement in the matrix resin [4]. Fracture toughness is one of the most important tools of the material that can be used to measure the resistance to crack propagation. In addition, the enhancement in the fracture toughness and crack arresting of a composite material attributed to the hybridization. Number of the researchers investigated on the fracture behavior of the hybrid composites under the effect of mode-I loading conditions. Damage deformation mechanisms are instrumental in redistributing the overstresses around the notch; therefore, improving their fracture behavior [5-7]. In addition, various specimen types such as compact tension specimens (CTS), end notch flexure (ENF) specimens and single edge notch bending (SENB) were used to evaluate the mode-I fracture toughness [8-10]. Jung and Kim [11] investigated the fracture toughness of carbon-glass/epoxy hybrid composites after fabricate by using vacuum assisted resin transfer molding and found that the fracture toughness reduced with increasing in glass fiber content. In addition, Arasan et al. [12] studied the influences of the crack length and position on the fracture strength of the hybrid and non-hybrid composite plates. They concluded that the fracture toughness of hybrid and non-hybrid composites increased with the crack length increased. The CT specimen was used to evaluate the mode-I fracture behavior of glass-carbon/epoxy hybrid composites experimental and numerically. For mode I, the stress intensity factors of the tensile sample was larger along with fiber orientation [13]. The stress intensity factor (K_{IC}) was 24% error in results compared to the experimental work. The fracture strength of carbon-basalt/ epoxy hybrid composites was studied under the effect of Mode I fracture test by using CT specimen and found that the fracture toughness of hybrid composites decreased with an increase in the basalt fiber percent at the core between the carbon fabrics [14]. Santhanam et

*Corresponding Author Institutional Email: eng_mahmoudsamir@yahoo.com (M. S. EL-Wazery)

al. [15] performed the compact tension test to determine the Mode I fracture toughness for banana fiber and Glass fiber reinforced polyester matrix composites. The fracture toughness of banana fiber reinforced composite is in close agreement with glass fiber. In addition, Harikrishnan et al. [16] used jute/glass fibre hybrid composite to evaluate the fracture toughness experimental and numerically. The glass fiber composites exhibited maximum fracture toughness was 131.90 $MPa.mm^{1/2}$. Abdel Ghafaar et al. [17] established three different types of woven fibers in the epoxy resin and prepared by hand lay-up method to evaluate the mechanical properties under the effect of bending loads and observed that the maximum values of the flexural strength and modulus at CFRP compared to the hybrid composites and GFRP were 360 MPa, 17.11 MPa, respectively. In addition, Chinta et al. [18] carried out the single edge notch bending (SENB) to study the mode-I fracture toughness for non-hybrid woven carbon/epoxy (C20), and hybrid carbon core composite (G5C10G5), experimentally and finite element modeling (ANSYS). The non-hybrid carbon composite exhibited higher fracture toughness than that the other laminates. Kaleemulla et al. [19] reported the various notch configurations to evaluate the fracture behavior of glass- textile satin /epoxy hybrid composites and found that fracture toughness increase with an increasing in the glass fabric. The effect of displacement rates on the mode I of the carbon/epoxy composites fracture using double cantilever beam (DCB) test were experimentally and numerically investigated. For all displacement rates (1, 10, 100, 500 mm/min), it was found that there is no fibre bridging and the experimental work is in a good agreement with the numerical analysis with maximum error (15%) [20]. The maximum principle stress (MPS) theory was used to evaluate the crack propagation angle of CLS, MMF specimens of the epoxy/ glass composites and found that the fiber/ matrix interface plays an important role in determination of the crack propagation path direction [21].

The paper aimed to study the effect of the fiber configurations of the carbon/glass reinforced polyester hybrid composites on the fracture toughness after utilizing the single edge notch bending (SENB) test. The critical stress intensity factor K_{IC} for the various fiber configurations experimentally and by finite element modeling (COSMOS/M 2.6) for the GFRP, CFRP, and glass-carbon/polyester hybrid composites was investigated. Fracture analyses of the hybrid and non-hybrid specimens were examined by scanning electron microscope (SEM).

2. EXPERIMENTAL WORK

2. 1. Materials and Specimens Fabrication

In this paper, two types of fabrics are used as reinforcement for fabrication the hybrid composites, twill weaves (2x2) carbon fabric (C120-3K) and E-glass fabric (biaxial weave 300 g/sqmt). Beside, the unsaturated polyester resin was used as a matrix. The manual hand layup technique was developed for manufacturing the non-hybrid and hybrid composites as a form of four layers. The details about the used technique and properties of the reinforcement and polyester resin are reported in previous publications [22-24]. The designation and stacking configuration of hybrid and non-hybrid composites are listed in Table 1 and Figure 1.

2. 2. Mode-I Fracture Test

According to ASTM D5045-99, Mode-I fracture toughness test for non-hybrid and carbon/glass reinforced polyester hybrid composites with different fiber configurations was conducted on SENB specimens with a thickness of 4 mm, as shown in Figure 2 [25]. Fracture test were carried out on the universal testing machine (INSTRON 8801) at a cross speed of 0.05 mm/min. The pre-crack length was 1 ± 0.01mm and cut by disc saw along the mid-span of each specimen of hybrid and non-hybrid composites. Five samples were tested for each laminate.

Mode-I stress intensity factor can be determined by Equation (1):

TABLE 1. Designation of hybrid and non-hybrid composites

Laminates	***Stacking sequences***	**Carbon and glass contents (wt.%)**	**Volume fraction of carbon/glass (vt.%)**
C	[C/C/C/C]	60/0	50.15/0
G	[G/G/G/G]	0/60	0/40.37
L1	[C/G/G/C]	30/30	27.31/18.37
L2	[G/C/C/G]	30/30	27.31/18.37
L3	[C/G/C/G]	30/30	27.31/18.37
L4	[G/C/G/C]	30/30	27.31/18.37

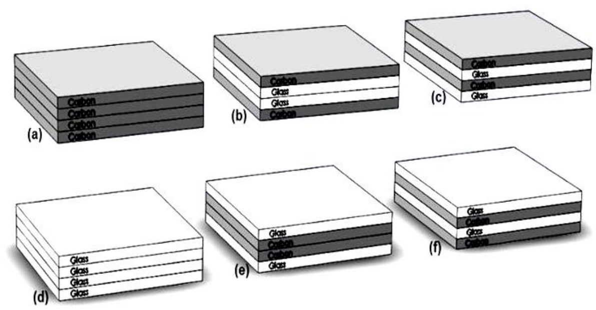

Figure 1. Stacking configuration of a) 4 C, b) C/2G/C, c) C/G/C/G, d) 4 G, e) G/2C/G, f) G/C/G/C structure of the hybrid and non-hybrid composites

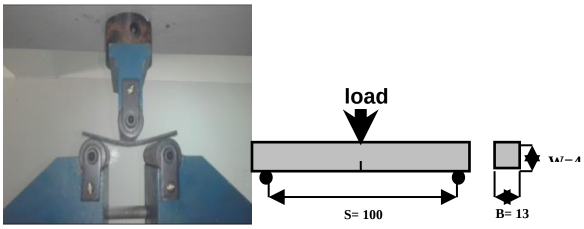

Figure 2. Universal testing machine showing the SENB during the fracture toughness test, (Dimensions in mm)

$$K_{IC} = \left(\frac{P}{BW^{\frac{1}{2}}}\right) f\left(\frac{a}{w}\right) \quad (1)$$

where B, w and a are the sample thickness (mm), width (mm) and crack length (mm), P and KIC are the fracture load and the mode-I stress intensity factors and F (a/w) is the correlation factors. The ratio between a and w was 0.25, where a is the pre-crack length, w is the thickness, and B is the width of the specimen. The applied load was vertically affected at the center of the specimen. The maximum load Pmax was experimentally estimated by using load displacement curve of each laminate .The crack geometry factors f (a/w) can be estimated as follows by Equation (2) [26, 27].

$$f\left(\frac{a}{w}\right) = 6x^{\frac{1}{2}}\left(\frac{[1.99-x(1-x)(2.15-3.93+2.7x^2]}{(1+2x)(1-x)^{3/2}}\right) \quad (2)$$

3. FINITE ELEMENT MODELING

Finite element modelling was employed to investigated the fracture parameters such as the stress intensity factor (KIC) and the crack propagation angle specially aroud the crack edge region under the plain strain condition. COSMOS/M 2.6 finite element package was used to perform the linear elastic stress analysis of the SENB specimen [28]. The non-hybrid and hybrid composites at variuos stacking sequenes were anlyzed by using the SENB sample under the effect of mode-I loading. COSMOS/M 2.6 mesh is the element type which used in the present numerical anlysis. The conditions for the front and real edges were (Uy = 0), where the meshing of the SENB specimen is consist of 28823 element and 45486 nodes, as shown in Figure 3.

4. RESULTS AND DISCUSSIONS

4. 1. Mode-I Fracture Behavior

The SENB test was used to predict the critical stress intensity factor and the crack path at the tip of crack of hybrid and non-hybrid composites at varuos configuations under the effect of Mode-I loading. However, the critical stress intensity factor (K_I) was determined by using the analytical formulas Equations (1) and (2). Figures 4a and 4b show the load displacement curves after the fracture test of the carbon/ glass reinforced polyester hybrid composites with variuos stacking sequences [C/G/G/C] and [C/C/C/C]. In addition, the load dispacement curves have an initially linear behaviuor (stable crack) then the load drops until reached to the maximum value (un stable crack). As shown in Figure 3a. It was observed that the maximum load was 5.77 KN ocured at the hybrid composite with stacking sequence [C/G/G/C]. While, for the glass composites (non-hybrid), Figure 4b, reached to 4.40 KN.

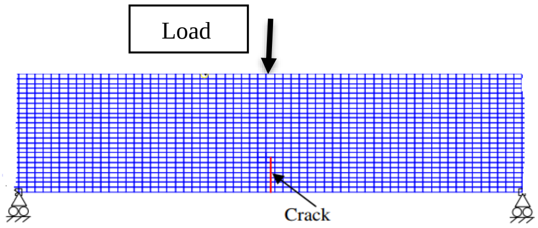

Figure 3. Load and boundry conditions of SENB specimen

Figure 5 shows the principle stress contours of hybrid composites with stacking sequences [C/G/G/C] under the effect of Mode-I loading to MPS criteria around the crack tip. The stress field at the crack tip varies with $1/\sqrt{r}$, where r is the radial distance. For carbon-glass/polyester hybrid composite, it can be observed that the stresses are high theoretically tending to infinite at the tip of crack. Therefore, this region called stress singularity due to the reduction of radial distance to its minimum value. As shown in this figure, the maximum stresses are noticed at the region of crack tip and on this basis, the internal stresses developed here often exceed the yield stress of the used hybrid material, which makes it soften, and then crack easily propagated.

Expermental and numerical results of the critical stress intensity factor (K_{IC}) of the hybrid and non-hybrid composites at various stacking sequences under the mode I loading are sumerized in Table 2.

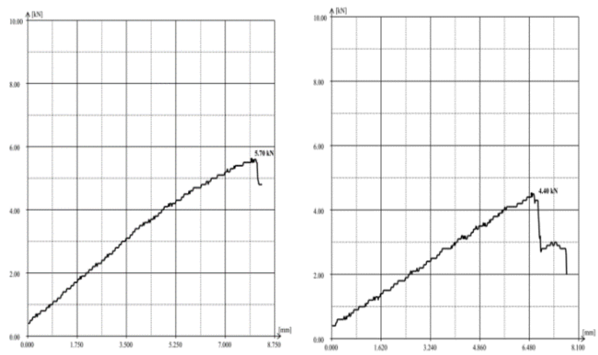

Figure 4. Load displacement curves of hybrid and non- hybrid composites with stacking sequence a) Laminate [C/G/G/C], b) Laminate [G/G/G/G]

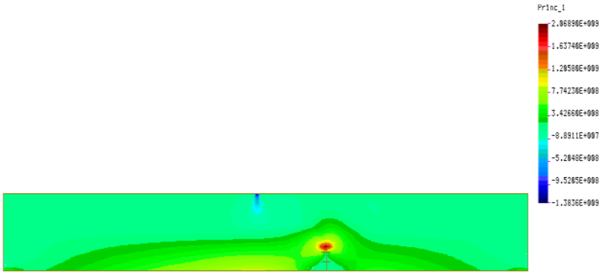

Figure 5. Principle stress concentration of SENB specimen under mode I loading of laminate L1 with stacking sequences [C/G/G/C], numerically

It can be evidented that, the hybrid composites with outer carbon layers [C/2G/C] has highest stress intensity factor value (881.34 MPa. mm$^{1/2}$) compared to the stress intensity factor (686.60 MPa. mm$^{1/2}$) with outer glass layers (G/2C/G). However, the critical stress intensity factor was affected by the different fiber arrangement and the equal number of carbon and glass layers of the all hybrid composites. The maximum value of the stress intensity factor of laminate L3 with stacking sequence [C/2G/C] due to the high stiffness of carbon fiber at the core (center). This is leads to the highest resistance of crack propagation at the tipe of crack. In addition, the glass composites (G) with stacking sequence [G/G/G/G] exhibited minimum value of the stress intemsity factor (672.84 MPa. mm$^{1/2}$). The reduction in stress intensity factor of this composite was attributed to a lower resistance to crack initiation and propagation among to the other laminates. The difference in stress intensity factor between fiber configurations [C/G/G/C], [C/G/C/G is not large. This is due to the reinforcing position of glass fiber may affect the fracture resistance of the hybrid composites. The numerical modeling results have a good agreement with experimental results. The maximum error in the numerical and experimental results of the stress intensity factor was 5.16% in the hybrid and non-hybrid composites specimen. The crack propagation was determined according to the maximum principle stress criterion. In this criterion, the crack was propagated in normal direction to the maximum principle stress criterion (MPSC). The stress distribution around the crack tip of the laminate L1 with stacking sequences [C/G/G/C] is shown in Figure 6. As the seen in this figure, it was noted that the value of the principle stress is high, theoretically tending to infinite (stress singularity) at the crack tip and decreases as the redial distance is increased. From the stress distributions at the crack tip, it can be seen that the point of the maximum principle was tangent to the crack tip.

TABLE 2. Experimental and numerical results of the stress intensity factor

Laminates	*Stacking sequences*	Max force (KN)	$K_{IC\ Exp}$ (MPa. mm$^{1/2}$)	$K_{IC\ Nn}$ (MPa. mm$^{1/2}$)	Error (%)
C	[C/C/C/C]	4.98	761.52	765.34	3.82
G	[G/G/G/G]	4.40	672.84	677.65	4.81
L1	[C/G/G/C]	5.77	882.34	885.21	2.87
L2	[G/C/C/G]	4.49	686.60	691.76	5.16
L3	[C/G/C/G]	5.70	871.63	874.69	3.06
L4	[G/C/G/C]	5.72	874.69	879.27	4.58

4. 2. Fracture Surface

Figures 7 and 8 show the fractographs of mode-I fractured surface of the hybrid composites with laminates L1 and L2, sequentially. For hybrid composite with laminate L1 as shown in Figure 7, it was clearly that there is good bonding between carbon and glass fibers and matrix phase. In addition, minimum fiber pull-out may be observed. In this case, stable and homogenous by distributes voids are created upon fiber-matrix debonding under state loading.

As shown in Figure 8, there are, some fibers were peeled out. In addition to, the traces of fibers in the polyester resin regions mixed with the pores, voids and debonded fibers. This is leads to the reduction in stress intensity factors of laminate L1 with stacking sequences [G/C/C/G].

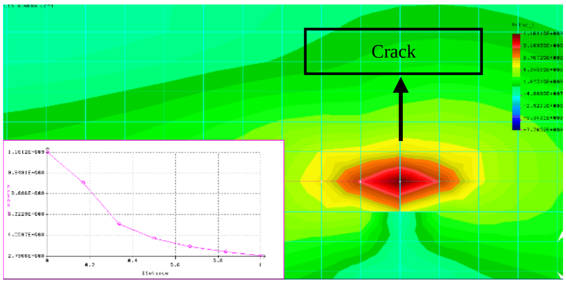

Figure 6. Crack propagation direction for mode I loading with stacking sequences [C/G/G/C], numerically

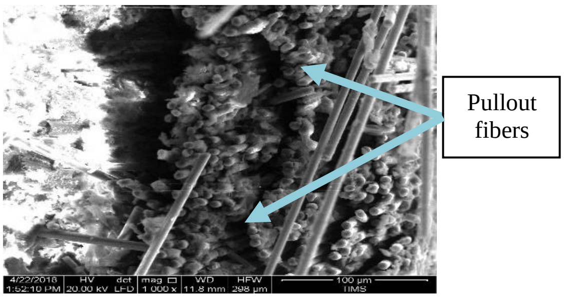

Figure 7. Fracture surface of the hybrid composites with combinations L1 [C-G-G-C]

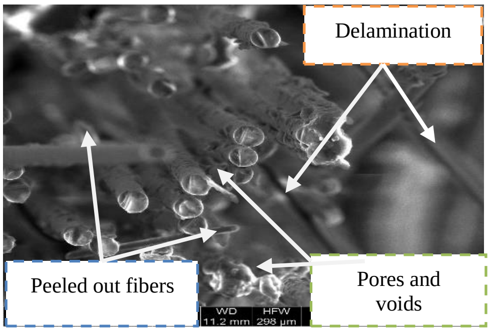

Figure 8. SEM image of the hybrid composite with L2 with stacking sequence [G/C/C/G]

5. CONCLUSIONS

The influences of fiber configurations of the glass/carbon reinforced polyester hybrid composites on the mode-I fracture toughness experimentally by using the SENB test and the finite element modeling were investigated. In the experimental results, it was observed that the hybrid composite with stacking sequence [C/G/G/C] exhibited maximum value of stress intensity factor (16.35 MPa. $mm^{1/2}$), while the minimum stress intensity factor was (12.18 MPa. $mm^{1/2}$), obtained in the glass composites [4G]. For hybrid composites with fiber configurations [C/G/G/C], The position of the glass fiber is affect the stress intensity factor. Glass fiber leads to an improving in the stress intensity factor of the hybrid composite when the glass fibers are placed at the middle portion. The maximum principle stress criterion (MPSC) was effective to predict the crack propagation path for the mode I fracture toughness. The finite element results of the stress intensity factors (KIC) are a good agreement with the experimental results.

6. REFERENCES

1. Artemenko, S.E. and Kadykova, Y.A., "Hybrid composite materials", ***Fibre Chemistry***, Vol. 40, No. 6, (2008), 490-492, doi.
2. Vanu Madhav, V., Gupta, A. and More, S., "Study of the fracture behavior under the effect of cross-ply and angle-ply arrangement of frp composite laminate subjected to central circular cut-out with mechanical and thermal loading conditions", ***International Journal of Engineering, Transactions C: Aspects,*** Vol. 34, No. 6, (2021), 1523-1529, doi: 10.5829/ije.2021.34.06c.16.
3. El-wazery, M., "Mechanical characteristics and novel applications of hybrid polymer composites-a review", ***Journal of Materials and Environmental Sciences***, Vol. 8, No. 2, (2017), 666-675, doi.
4. Gururaja, M. and Rao, A.H., "A review on recent applications and future prospectus of hybrid composites", ***International Journal of Soft Computing and Engineering***, Vol. 1, No. 6, (2012), 352-355.
5. Zhu, X.-K. and Joyce, J.A., "Review of fracture toughness (g, k, j, ctod, ctoa) testing and standardization", ***Engineering Fracture Mechanics***, Vol. 85, (2012), 1-46, doi: org/10.1217/j.korsoceng.404.03.001.
6. Park, H.-S., Lee, W.-H., Keum, J.-H., Choi, J.-H., Koo, J.-M. and Seok, C.-S., "The evaluation of fracture toughness for woven carbon fibered reinforced composite materials", ***Journal of the Korean Society for Precision Engineering***, Vol. 27, No. 10, (2010), 69-76, doi: org/10.1217/j.korsoceng.404.03.001.
7. Nasuha, N., Azmi, A. and Tan, C., "A review on mode-i interlaminar fracture toughness of fibre reinforced composites", in Journal of Physics: Conference Series, IOP Publishing. Vol. 908, No. 1, (2017), 012024.
8. Moore, D.R., Williams, J. and Pavan, A., "Fracture mechanics testing methods for polymers, adhesives and composites, Elsevier, (2001).
9. Zhang, J., Chaisombat, K., He, S. and Wang, C.H., "Hybrid composite laminates reinforced with glass/carbon woven fabrics for lightweight load bearing structures", ***Materials & Design (1980-2015)***, Vol. 36, (2012), 75-80, doi: org/10.1016/j.matdes.2011.11.006.
10. Huddhar, A., Desai, A., Sharanaprabhu, C., Kudari, S.K. and Gouda, P.S., "Studies on effect of pre-crack length variation on inter-laminar fracture toughness of a glass epoxy laminated composite", in IOP Conference Series: Materials Science and Engineering, IOP Publishing. Vol. 149, No. 1, (2016), 012161.
11. Jung, H. and Kim, Y., "Mode i fracture toughness of carbon-glass/epoxy interply hybrid composites", ***Journal of Mechanical Science and Technology***, Vol. 29, No. 5, (2015), 1955-1962, doi: 10.1007/s12206-015-0416-3.
12. Arasan, Ş., Aktaş, M. and Balcıoğlu, H.E., "Fracture toughness of woven glass and carbon reinforced hybrid and non-hybrid composite plates", ***Polymer Composites***, Vol. 39, No. 3, (2018), 783-793, doi: 10.1002/pc.23999.
13. Gouda, P.S., Kudari, S., Prabhuswamy, S. and Jawali, D., "Fracture toughness of glass-carbon (0/90) s fiber reinforced polymer composite–an experimental and numerical study", ***Journal of Minerals and Materials Characterization and Engineering***, Vol. 10, No. 08, (2011), 671.
14. Subagia, I.A., Tijing, L.D. and Atmika, K.A., "Mode i fracture toughness of interply hybrid epoxy composite reinforced with carbon-basalt fibers", ***Composites Part B: Engineering***, Vol. 58 (2014) 611-617.
15. Santhanam, V., Chandrasekaran, M., Venkateshwaran, N. and Elayaperumal, A., "Mode i fracture toughness of banana fiber and glass fiber reinforced composites", in Advanced Materials Research, Trans Tech Publ. Vol. 622, (2013), 1320-1324.
16. Harikrishnan, K. and Deviprasad, V., "Mode i fracture toughness of jute/glass fiber hybrid composite—an experimental and numerical study", ***International Journal of Engineering Trends and Technology***, Vol. 28, No. 6, (2015), 307-310, doi: 10.14445/22315381/IJETT-V28P259.
17. Ghafaar, M.A., Mazen, A. and El-Mahallawy, N., "Behavior of woven fabric reinforced epoxy composites under bending and compressive loads", ***JES. Journal of Engineering Sciences***, Vol. 34, No. 2, (2006), 453-469.
18. Raj, S.S., Reddy, P.R. and Vincent, E., "Numerical and experimental investigation of effect of stacking sequence on the fracture parameters of composite materials".
19. Kaleemulla, K.M. and Siddeswarappa, B., "Plane strain fracture behaviour of fabric reinforced hybrid composites under varied notch configurations", ***Journal of Minerals and Materials Characterization and Engineering***, Vol. 8, No. 06, (2009), 495, doi: 10.4236/jmmce.2009.86043.

20. Low, K., Teng, S., Johar, M., Israr, H. and Wong, K., "Mode i delamination behaviour of carbon/epoxy composite at different displacement rates", ***Composites Part B: Engineering***, Vol. 176, (2019), 107293, doi: org/10.1016/j.compositesb.2019.107293.
21. Szekrényes, A. and Uj, J., "Analysis of the interlaminar crack initiation in mixed-mode i+ ii composite fracture specimens", ***Periodica Polytechnica Mechanical Engineering***, Vol. 47, No. 2, (2003), 103-118.
22. El-Menshawy, O., El-Sissy, A., El-Wazery, M. and Elsad, R., "Electrical and mechanical performance of hybrid and non-hybrid composites", ***International Journal of Engineering***, Vol. 32, No. 4, (2019), 580-586, doi: 10.5829/ije.2019.32.04a.16
23. El-Wazery, M., El-Elamy, M. and Zoalfakar, S., "Mechanical properties of glass fiber reinforced polyester composites", ***International Journal of Applied Science and Engineering***, Vol. 14, No. 3, (2017), 121-131, doi: 10.6703/IJASE.2017.14 (3).121.
24. EL-Wazery, M., EL-Kelity, A. and Elsad, R., "Effect of water absorption on the tensile characteristics of natural/synthetic fabrics reinforced hybrid composites", ***International Journal of Engineering***, Vol. 33, No. 11, (2020), 2339-2446, doi: 10.5829/ije.2020.33.11b.24.
25. ASTM, I., "Standard test methods for plane-strain fracture toughness and strain energy release rate of plastic materials", ***ASTM D5045-99***, (2007).
26. Chow, W. and Atluri, S., "Stress intensity factors as the fracture parameters for delamination crack growth in composite laminates", ***Computational Mechanics***, Vol. 21, No. 1, (1998), 1-10.
27. Prasad, M.S., Venkatesha, C. and Jayaraju, T., "Experimental methods of determining fracture toughness of fiber reinforced polymer composites under various loading conditions", ***Journal of Minerals and Materials Characterization and Engineering***, Vol. 10, No. 13, (2011), 1263.
28. Divaka, M., Lashkari, M. and Cosmos, M., *Structural research and analysis corporation*. 1993, Santa Monica, CA.

Persian Abstract

چکیده

چقرمگی شکست حالت کامپوزیت های ترکیبی پلی استر تقویت شده با کربن/شیشه به صورت تجربی و عددی با استفاده از نرم افزار اجزای محدود COSMOS/M ۲.۶ پس از ساخت با استفاده از تکنیک چیدمان دستی مورد بررسی قرار گرفت. آزمون پرتوی تک لبه برای ارزیابی چقرمگی شکست حالت کامپوزیت های کربن ، کامپوزیت های شیشه ای و کامپوزیت های ترکیبی در پیکربندی های مختلف الیاف توسعه داده شد. میکروسکوپ الکترونی روبشی برای بررسی سطوح شکسته کامپوزیت های ترکیبی تحت تأثیر بارگذاری حالت I استفاده شد. نتایج تجربی نشان داد حداکثر ضریب شدت تنش ۸۸۲.۳۴ MPa.mm۱/۲ بود که در کامپوزیت های ترکیبی با توالی انباشته [C/G/G/C] در طول بارگذاری حالت I در مقایسه با سایر توالی های انباشته به دست آمد. این به سطحی مناسب بین کربن و الیاف شیشه و فاز ماتریسی نسبت داده می شود. از نتایج بدست آمده، نشان داده است که نتایج تجربی با مدل سازی عناصر محدود مطابقت خوبی دارد.

IJE TRANSACTIONS B: Applications Vol. 34, No. 11, (November 2021) 2424-2432

International Journal of Engineering

Journal Homepage: www.ije.ir

Carbon Nanotube Field Effect Transistors Based Digitally Reconfigurable Single Differential Voltage Current Conveyor based Analog Biquadratic Multifunctional Filter at 32nm Technology Node

S. Chandra, V. Gupta*, A. Imran

Zakir Husain College of Engineering & Technology, Aligarh Muslim University, Aligarh, India

PAPER INFO

Paper history:
Received 25 April 2021
Received in revised form 27 August 2021
Accepted 08 September 2021

Keywords:
Biquadratic Multifunctional Filter
Carbon Nanotube Field Effect Transistors
Current Conveyor
Current Summing Network
Differential Voltage Current Conveyor
Digitally Programmable Differential Voltage

ABSTRACT

As the scaling continues, Carbon Nanotube Field Effect Transistors (CNFET) are considered to be the potential candidates for overcoming the shortcomings associated with the scale of the art Complementary metal–oxide–semiconductor (CMOS) transistors. In this paper a digitally reconfigurable CNFET based biquadratic multifunctional filter employing a CNFET based single Differential Voltage Current Conveyor (DVCC) at 32nm technology node is presented. The circuit utilizes a single CNFET based DVCC block along with the arrangement of few resistors and capacitors. The proposed digitally reconfigurable multifunctional filter circuit is able to obtain programmable low pass, high pass and band pass filter configurations using the same topology. The designed CNFET based multifunctional filter obtains a resonant frequency of the order of GHz. Furthermore, a 3-bit digital control of the designed multifunctional filter parameters i.e. Quality Factor (Qo) and resonant frequency has been made possible using the Current Summing Network (CSN). Sensitivity and comparative analysis has also been performed. The circuit has been simulated at a low voltage supply of 0.9V using Hewlett Simulation Program with Integrated Circuit (HSPIC) environment at 32nm technology node. The simulation results obtained are in sync with the theoretical analysis.

***doi**: 10.5829/ije.2021.34.11b.06*

NOMENCLATURE

D_{CNT}	Diameter of CNT	G	Conducatnce
V_{th}	Threshold Voltage	V_X	Potential at X terminal of DVCC
S	Inter-CNT pitch	I_{Y1} & I_{Y2}	Currents entering the Y_1 and Y_2 terminals of DVCC respectively
N	Number of CNT's in the channel	Q	Qulaity Factor
q	Electronic Charge	ω_0	Resonant Angular frequency
N_1, N_2	Chiral Vector	R	Resistance
V_π	Carbon bond energy (π-π)	C	Capacitance
a	Lattice Constant	k	Current transfer gain parameter

1. INTRODUCTION

For the last 30-40 years, CMOS technology has played a quintessentially important role in the advancements observed within the fields of computation, telecommunications, electronics, mechatronics, and instrumentation. Miniaturizations, or scaling down the size of the basic device has been the blueprint, which allowed for higher speed, lower power dissipation, lesser costs and higher integration density. However, as the CMOS transistors continues to scale down, various non-idealities like tunneling phenomenon, process variations, random dopant fluctuations, leakage currents etc. hinder its exemplary performance, thereby making it indispensable to look for alternatives that could continue to revolutionize the advancements. Off late a lot of

*Corresponding Author Institutional Email: *ale.imran23@gmail.com* (A. Imran)

Please cite this article as: S. Chandra, V. Gupta, A. Imran, Carbon Nanotube Field Effect Transistors Based Digitally Reconfigurable Single Differential Voltage Current Conveyor based Analog Biquadratic Multifunctional Filter at 32nm Technology Node, International Journal of Engineering, Transactions B: Applications, Vol. 34, No. 11, (2021) ... 2424-2432

research has been ongoing, in designing and developing new Nano-electronic devices, and various substitutes like Quantum FETs, FinFETs, Nano-sheet transistors have appeared. Carbon Nano Tube Field Effect Transistor (CNFET) is also considered among one of the potential candidates for extending the already saturated Moore's law and providing a platform for the next generation electronic circuits [1-5]. A CNFET is a molecular device, having three terminals namely drain, source and gate. It uses a semiconducting carbon nano tube (CNT) acting as a channel, bridging the contact between two electrodes i.e. source and drain. CNFET's are considered as potential candidates, in the post Silicon era owing to its exceptional electrical and structural characteristics. It offers high mobility, greater current carrying capacity, better transconductances, low intrinsic capacitances, improved subthreshold slope etc. among various improved parameters over the state of the art CMOS transistors [6, 7].

Second generation current conveyor, a well known current mode device (CC-II) was introduced by Sedra and Smith in 1970. It is a versatile analog building block, used to implement variety of voltage and current mode circuits like amplifiers, oscillators, multifunctional filters etc. [8, 9]. However, the design of various new circuits and topologies requires two high input impedance terminals or the usage for differential input signals; thereby restricting the utilization of the conventional Current Conveyor. Differential voltage Current conveyor (DVCC) is a relatively new analog building block, coming from the family of current conveyors. DVCC utilizes the concept of differential inputs and is widely used for the implementation of various voltage and current mode analog signal processing circuits. It also offers high signal bandwidth and greater linearity, therby making it an attractive proposition for the researchers and designers [10, 11].

In this work, the single input multi output voltage mode multi-functional proposed by Chen et al. [12] has been redesigned using optimized CNFETs. Furthermore the circuit is digitally controlled using a 3-bit current summing network. Introduction of digital control to the DVCC based multifunctional filter provides flexibility in reconfiguring the circuit while helping to adapt specifically to the requirements of different modern analog system applications. The outline of the paper is as follows: After introduction in section 1, Carbon Nanotubes Field Effect Transistors (CNFET) have been discussed briefly in Section 2, followed by the discussions around Differential Voltage Current Conveyor (DVCC) and the design of CNFET based DVCC biquadratic multifunctional filter in section 3 and 4, respectively. Section 5 highlights digitally reconfigurable DVCC followed by the design of CNFET based Digitally reconfigurable multunctional filter in section 6. Section 7, 8 and 9 of the paper, discuss the obtained simulation results (in sync with the theory), sensitivity analysis and comparative analysis respectively; which is followed by conculsion.

2. CARBON NANOTUBE FIELD EFFECT TRANSISTORS

Carbon Nanotubes (CNT's), a promising nanostructured material was initially discovered by Iijima [13]. It is basically a group of carbon atoms; arranged hexagonally and rolled up into a seamless cylindrical shape with length of the order of few microns and diameter of few nanometers. CNT's can be of following types i.e. armchair, chiral or zig-zag in nature, depending upon the chiral vector (n_1 , n_2). A CNT is called Zigzag if n_1=o or n_2=o. If n_1 & n_2 are unequal and non-zero, CNT is said to be of chiral type and if n_1 =n_2 , then it's called Armchair configuration [14]. Carbon Nanotube Field Effect Transistors (CNFET) utilize the semiconducting CNT's for the transport of electrons in the channel region. Depending upon the current requirement in the designed circuit, maybe one or usually multiple semiconducting CNTs are arranged in parallel configurations between the drain and source regions. The transport of charge carriers (electrons or holes) between the highly doped drain/source regions takes place through these semicinducting CNT's which expedite intrinsic ballistic transport properties associated with the CNTs. The Ballistic transport ensures that the mobility of the charge carriers is comparatively much higher as compared to the silicon CMOS devices. The top end view of CNFET device, incorportaing the design parameters is shown in Figure 1. The number of CNT's in the channel (N), the Diameter of CNT (D_{CNT}) and the Inter CNT Pitch (S) are the important parameters associated with the design of CNFET based circuits [15]. The equations co-relating the important parameters of chiral vector (m, n), threshold voltage (Vth) , diameter of CNT (D_{CNT}), Inter- CNT Pitch (S), Number of CNTs in the channel (N) and Energy Gap ($\sum$g) are as follows :

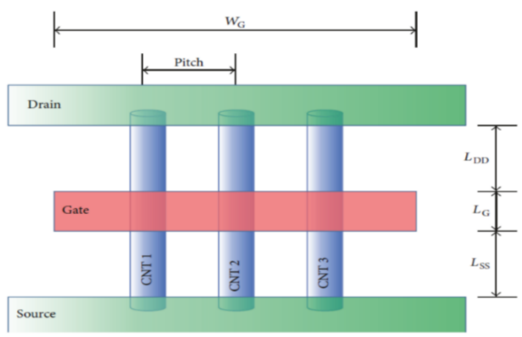

Figure 1. Top-End View of CNFET

$$D_{CNT} = \frac{\sqrt{{N_1}^2 + {N_2}^2 + N_1 N_2}}{\pi} \quad (1)$$

$$V_{th} = \frac{a\,V_\pi}{\sqrt{3} q D_{CNT.}} \quad (2)$$

$$W = (N\text{-}1)^* S + D_{CNT} \quad (3)$$

$$\Sigma g = \frac{0.84 eV}{D_{CNT}} \quad (4)$$

where q is the electronic charge, a= 2.49 is the lattice constant and V_π is the carbon bond energy (π-π) and is equal to 3.033eV. Furthermore, the working principle of CNFET device is similar to the CMOS in which electrons flow from source to drain terminal and the gate terminal is used for controlling the current intensity in the semi-conducting CNT channel [16]. However, unlike CMOS, where there is a standard convention of keeping the transistor's width usually 2X-4X transistor's length; no such constraints exist for CNFETs, since in CNFETs both the n and p type of devices have equal current carrying capabilities, and the device is optimized in terms of number of CNT's (N), Inter-CNT Pitch (S) and diameter of CNT (D_{CNT}). The circuit compataible Stanford CNFET Model developed by Deng and Wong [17, 18] have used for carrying out the simulation using HSPICE environment at 32nm technology node. The model has been experimentally validated and accounts for the non-idealities like channel length dependence of current drive, source drain series resistance, inter-CNT charge screening effects etc. along with the device parasitics associated with more than 90% accuracy.

3. DIFFERENTIAL VOLTAGE CURRENT CONVEYOR

Differential Voltage Current Conveyor (DVCC) is one of the widely used blocks for analog signal processing. It is basically a current mode device and can be used for the design of various analog circuits like integrators, amplifiers oscillators, filters etc. The block diagram of DVCC is shown in Figure 2 and its terminal characteristics is described by the matrix given in equation 5, where V_X is the potential at X terminal ; I_{Y1} and I_{Y2} are the currents entering the Y_1 and Y_2 terminals, respectively. Furthermore I_{Z+} is the positive type current. It is to be noted tthat at terminal X, DVCC shows (ideally) zero input resistance, whereas at both terminals Y and Z, it exhibits (infinite) high resistance [19].

$$\begin{bmatrix} V_X \\ I_{Y1} \\ I_{Y2} \\ I_{Z+} \end{bmatrix} = \begin{bmatrix} 0 & 1 & -1 & 0 \\ 0 & 0 & 0 & 0 \\ 0 & 0 & 0 & 0 \\ 1 & 0 & 0 & 0 \end{bmatrix} \begin{bmatrix} I_X \\ V_{Y1} \\ V_{Y2} \\ V_{Z+} \end{bmatrix} \quad (5)$$

Significant amount of research, off-late has been carried out using DVCC building block. Upadhyayand Pal [20] proposed an Op-Amp based on DVCC, capable of operating at higher frequencies as compared to the conventional op-amp. Vavra [21] designed a capacitance multiplier employing a single DVCC, whereas Jain and Bharti [22] realized LNA for wireless receivers using CMOS based DVCC. The basic modules of intgegrators and differentiators have also been implemented using the same DVCC block incorporating a few passive elements by Minaei [23]. Furthermore numerous universal and multifunctional filters, based on voltage and current mode have also been designed, implemented and verified using the same DVCC thereby making it an extremely significant building block of interest for researchers [24-29].

4. DESIGN OF CNFET BASED DVCC MULTIFUNCTIONAL FILTER

The circuit diagram of Voltage Mode Multifunctional filter realized by Chen et al. [12] using TSMC 0.18 um CMOS technology is shown in Figure 3 and has been used in this work for redesigning as digitally reconfigurable CNFET based filter. It is to be noted that, the circuit has been completely re-designed using optimized CNFET transistors at 32 nm techology node. Number of CNT's (N), Inter-CNT Pitch (S) and diametre of CNT (D_{CNT}) have been carefully chosen to provide an optimum DVCC performance and then the circuit has

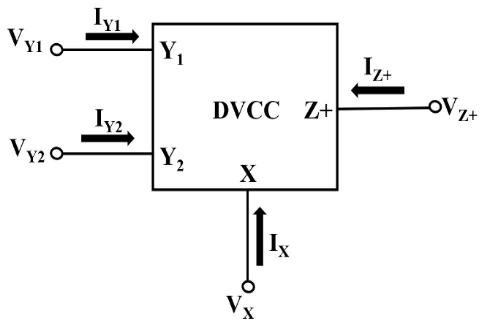

Figure 2. Block Diagram of DVCC based on Z+ node

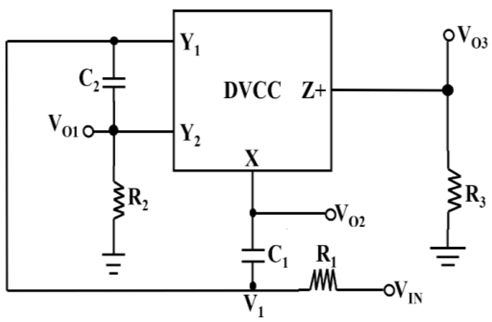

Figure 3. Circuit diagram of DVCC Multifunctional Filter [12]

been digitally programmable using Current Summing Network (CSN). The configuration of the used circuit [12] gives the band-pass, low-pass and high-pass filters as signified by Equations (6), (7) and (8), respectively.

$$\frac{V_{O1}}{V_{IN}} = \frac{sC_2G_1}{s^2C_1C_2+sC_2(G_1+G_2)+G_1G_2} \tag{6}$$

$$\frac{V_{O2}}{V_{IN}} = \frac{G_1G_2}{s^2C_1C_2+sC_2(G_1+G_2)+G_1G_2} \tag{7}$$

$$\frac{V_{O3}}{V_{IN}} = \frac{-G_1}{G_3}\frac{s^2C_1C_2}{s^2C_1C_2+sC_2(G_1+G_2)+G_1G_2} \tag{8}$$

where $G_1 = \frac{1}{R_1}, G_2 = \frac{1}{R_2}, G_3 = \frac{1}{R_3}$

The quality factor(Q) and resonant angular frequency (ω_0) is given below:

$$Q = \frac{1}{G_1+G_2}\sqrt{\frac{C_1G_1G_2}{C_2}} \tag{9}$$

$$\omega_0 = \sqrt{\frac{G_1G_2}{C_1C_2}} \tag{10}$$

The circuit employed realizes the biquadratic band pass (V_{O1}), low pass (V_{O2}) and high pass filters (V_{O3}) simultaneously without changing the values of passive components. The DVCC multifunctional filter is simulated at supply voltages of V_{DD}=-V_{SS}=0.9V using the 32nm Stanford CNFET model at HSPICE simulation environment. The circuit is re-designed for fo=1.06 GHz and Q=0.5 by selecting the value of R_1=R_2=R_3=10kΩ C_1=C_2=15ff. The CNFET technology parameters used for the simulation have been listed in Table 1, whereas the optimized parameters of Number of CNT's (N), Inter-CNT Pitch (S) and Diameter of CNT (D_{CNT}) used for simulation have been discussed as a part of design in Section 5. Figure 4 shows the obtained amplitude frequency response of the multifunctional filter. It is to be noted that since CNFET technology has been used the obtained frequency response is having the 3-dB cut off frequency of the order of 1.08 GHz, which is significantly of the higher order. The 3-dB frequency of the designed filter in-fact could be further enhanced, by changing the optimized parameters of CNFET particularly the Diameter of CNT (D_{CNT}), however the same is achieved at the cost of increased power dissipation.

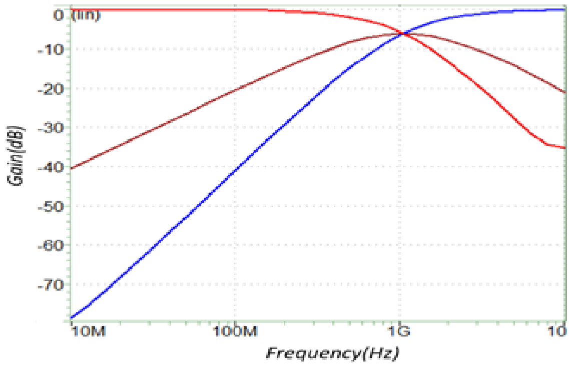

Figure 4. Simulated amplitude frequency response of MF

TABLE 1. technology parameters of CNFET

Parameters	Value[a]
Oxide Thickness	4 nm
Physical Channel Length	32 nm
Gate Dielectric & Dielectric Constant	HfO_2 & 16
Mean Free path (Intrinsic CNT)	200 nm
Mean Free Path (Doped CNT)	12.5 nm

5. DIGITALLY PROGRAMMABLE CNFET DVCC

The terminal characteristics of digitally reconfigurable/programmable differential voltage current conveyor (DP-DVCC) is determined by the matrix given below in Equation (11) [30].

$$\begin{bmatrix} V_X \\ I_{Y1} \\ I_{Y2} \\ I_{Z+} \end{bmatrix} = \begin{bmatrix} 0 & 1 & -1 & 0 \\ 0 & 0 & 0 & 0 \\ 0 & 0 & 0 & 0 \\ k & 0 & 0 & 0 \end{bmatrix} \begin{bmatrix} I_X \\ V_{Y1} \\ V_{Y2} \\ V_{Z+} \end{bmatrix} \tag{11}$$

where, $k = \frac{I_Z}{I_X}$

Digitally programmable DVCC is used to inculcate the factor of re-configurability in DVCC multifunctional filter. A Digital control word is generated by the use of Current Summing Network (CSN) which is added at the Z+ terminal and it varies from 1 to 2^n-1 where *n* is number of transistor arrays connected in parallel. CSN is employed to control the current transfer gain parameter-*k* [31]. Therefore, Current at the Z+ terminal assumed to be flowing out of DP-DVCC is shown in Equation (12) and the current transfer gain parameter-*k* is given by Equation (13):

$$I_Z = \sum_{i=0}^{n-1} d_i 2^i (I_7 - I_{10}) \tag{12}$$

$$k = \frac{I_Z}{I_X} = \frac{\sum_{i=0}^{n-1} d_i 2^i (I_7 - I_{10})}{(I_7 - I_{10})} = \sum_{i=0}^{n-1} d_i 2^i \tag{13}$$

where d_i is the digital code bit applied to the i^{th} branch of the CSN. Depending upon the value of di, whether it's a logic 1 or logic 0 the current flow in a particular branch is either enabled or disabled [32]. The implementation of DP-DVCC using CNFETs is shown in Figure 5 and the dimensions of the individual designed optimized CNFETs have been enlisted in Table 2. The CNFET transistors of DP-DVCC have been individually optimized in terms of design parameters i.e. Number of CNT's, Inter-CNT Pitch and Diameter of CNT to obtain an improved high frequency response. While designing, it has been ensured that the inherent port characteristics of the DVCC reflect near to ideal behavior. The

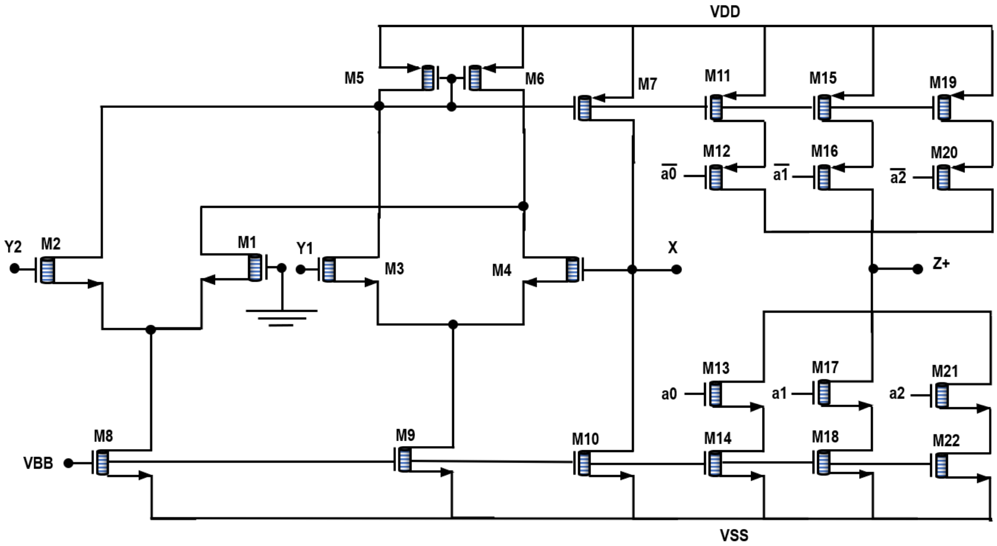

Figure 5. CNFET based implementation of DP-DVCC on Z+ node only

simulated obtained input resistances at Port Y_1 (R_{Y1}) and Port Y_2 is (R_{Y2}) 6.2 MΩ, whereas the value obtained at Port X (R_X) is 275Ω.

6. OPTIMIZED CNFET BASED DP-DVCC MULTIFUNCTIONAL FILTER

The designed DP-DVCC is now employed as the basic building block for the programmable multifunctional filter. The proposed circuit of DP-DVCC multifunctional filter with the help of CNFET technology; that incorporates the tunability factor using current summing network is shown in Figure 6. The circuit besides realizing the filter functions of low-pass, high pass and bandpass also includes the feature of varying the quality factor and resonant frequency with the help of the applied digital control word (k). There is a significant change in the transfer function of the tunable biquadratic multifunctional filter responses which is given below as follows:

$$\frac{V_{O1}}{V_{IN}} = \frac{ksC_2G_1}{s^2C_1C_2+skC_2(G_1+G_2)+kG_1G_2} \tag{14}$$

$$\frac{V_{O2}}{V_{IN}} = \frac{kG_1G_2}{s^2C_1C_2+skC_2(G_1+G_2)+kG_1G_2} \tag{15}$$

$$\frac{V_{O3}}{V_{IN}} = \frac{-G_1}{G_3}\frac{ks^2C_1C_2}{s^2C_1C_2+skC_2(G_1+G_2)+kG_1G_2} \tag{16}$$

Equations (12), (13) and (14) depicts the transfer response of the digitally programmable band pass, low pass and high pass filters respectively. The modified expressions of quality factor (Q) and resonant angular frequency(ω_0) is shown is as:

$$Q = \frac{1}{G_1+G_2}\sqrt{\frac{C_1G_1G_2}{kC_2}} \tag{17}$$

$$\omega_0 = \sqrt{\frac{kG_1G_2}{C_1C_2}} \tag{18}$$

The theoretical analysis hereby highlight the fact that the quality factor $Q \propto \frac{1}{\sqrt{k}}$ and the resonant frequency $\omega_0 \propto \sqrt{k}$ of the proposed multifunctional filter.

7. SIMULATION RESULTS AND DISCUSSION

The proposed digitally programmable optimized CNFET based multifunctional biquadratic filter comprises of a block of DP-DVCC, three resistors and two capacitors. The simulations results obtained have been verified on HSPISCE. The obtained resultant waveform of the simulated multifunctional filter for different control words of [011] and [111] is shown in Figures 7 and 8, respectively. The obtained simulation results are in accordance to the theoretical results obtained in the previous section, where ω_0 is directly proportional to $k^{1/2}$ and for reference the variation of the resonant/cut-off

TABLE 2. design of cnfet based digitally programmable dvcc

Transistor	Number of CNT's	Inter CNT Pitch	Chiral Vector (*m*,*n*)	Diameter of CNT	Column 3 [a]
M1-M14	4	75nm	(19,0)	1.5 nm	zzz1
M15-M18	8	32nm	(19,0	1.5nm	zzz2
M19-M22	16	15nm	(19,0	1.5nm	zz3

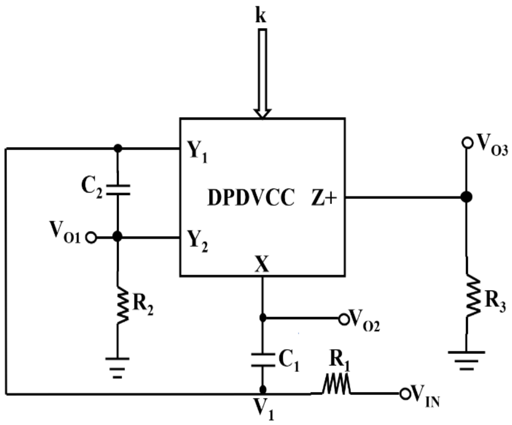

Figure 6. Circuit diagram of CNFET based DP-DVCC Multifunction filter

frequency with the digital control word for band-pass, low-pass and high-pass filters is depicted in Figures 9-11, respectively. The effect of the variation of quality factor with the digital control word has also been studied and is reflected in Figure 12, which shows that the quality factor is inversely proportional to the applied digital control word. It is to be further impressed that besides being programmable the circuit exhibits excellent high frequency response of the order of Gigahertz range that makes it useful for wideband, radio-frequency and Bluetooth applications.

8. SENSITIVITY ANALYSIS

This section deals with the sensitivity analysis of the programmable multifunctional filter circuit parameter's such as quality factor, resonant frequency and bandwidth with reference to the passive components of resistance and capacitance. Table 3 depicts the results of sensitivity analysis of the circuit. The results obtained in Table 3 depicts the fact that the variations in the circuit parameters of the proposed programmable multifunctional filter with respect to the passive components is below 1; thereby affirming that tolerances in the values of passive elements won't degrade the performance of the circuit.

9. COMPARATIVE ANALYSIS

Table 4 summarizes the comparison of the designed CNFET based biquadratic multifunctional filter, with other circuits of similar nature available in literature. The 3-dB cut off frequency, port resistances at input and output, number of active and passive components used, the realizations possible with the topology and sensitivity analysis have been chosen as the parameters of comparison among various realized multifunctional filters. The comparative analysis clearly indicates the improved performance of the circuit, owing to the superior performance of the optimized CNFET transistors in terms of better cut-off and resonant frequencies, near to ideal port resistances and lower sensitivity issues.

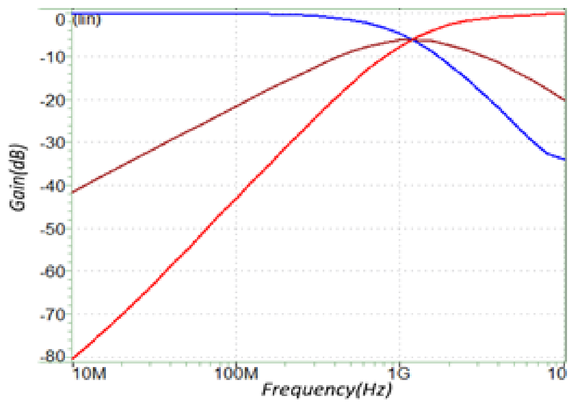

Figure 7. Simulated Gain Frequency response (in dB) for band pass , low pass and high pass filter with control word (k) [a2 a1 a0] = [0 1 1]

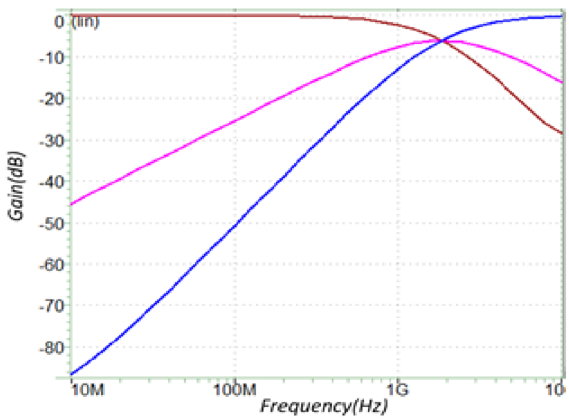

Figure 8. Simulated Gain Frequency response (in dB) for band pass , low pass and high pass filter with control word (k) [a2 a1 a0] = [1 1 1]

TABLE 3. Results of Sensitivity Analysis

Sensitivity	Value	Sensitivity	Value
$S^{\omega_0}_{C1}$	-0.5	S^{Q}_{C1}	+0.5
$S^{\omega_0}_{C2}$	-0.5	S^{Q}_{C2}	-0.5
$S^{\omega_0}_{G1}$	+0.5	S^{Q}_{G1}	+0.5
$S^{\omega_0}_{G2}$	+0.5	S^{Q}_{G2}	+0.5

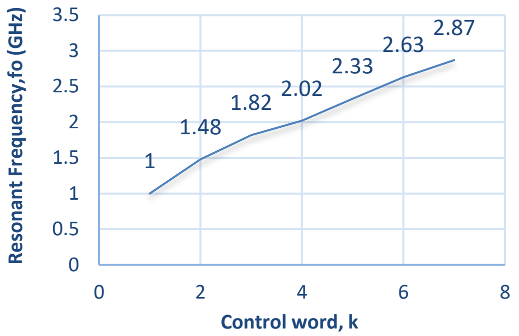

Figure 9. Variation in resonant frequency with digital control word of BPF

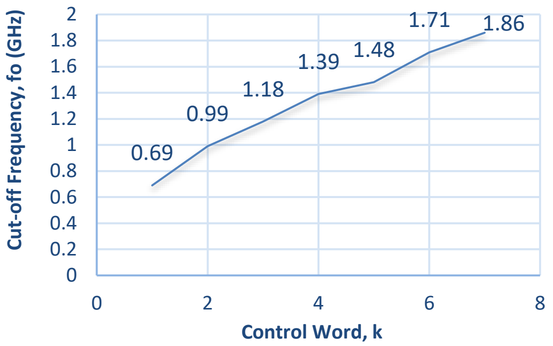

Figure 10. Variation of Cut-off frequency with digital control word of LPF

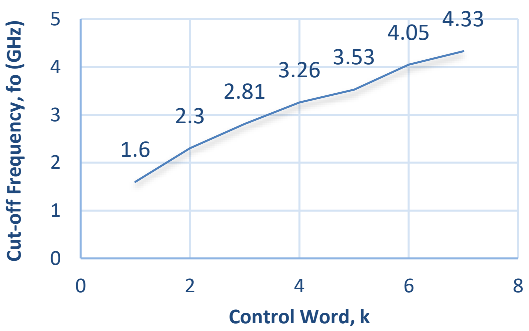

Figure 11. Variation of cut-off frequency with digital control word of HPF

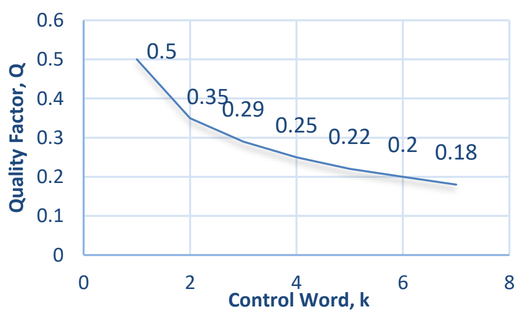

Figure 12. Variation in Quality factor with digital control word

TABLE 4. Comparative analysis with other circuits

Parameters	CNFET based multifuntional filter	Reference No. 24	Reference No. 25	Reference No. 26
Realizations	LPF, HPF, BPF	LPF, HPF, BPF, BRF, APF	LPF, HPF, BPF, BRF	LPF, HPF, BPF, BRF
Cut-off Frequency	1.08 Ghz	100 KHz	8.0025 MHz	100 KHz
Number of DVCC used	One	Two	One	One
Number of passive components	Five	Five	Four	Five
Resistance at port Y_1 and Y_2	6.2 Ohms	NA	NA	NA
Resistance at port X	275 Ohms	NA	NA	NA
Sensitivity	<1	<1	NA	<1

10. CONCLUSION

This paper proposes a digitally reconfigurable CNFET based multifunctional filter. The paper contributes by designing a filter using optimized carbon nanotube field effect transistors, which results in a resonant frequency of much higher order (GHz range). Furthermore the tunability factor has also been incorporated using Current Summing Network (CSN) and the simulation results are in accordance to the theory. The cut off frequencies of Band pass, Low pass and High pass is varied by varying the control word from [0 0 1] to [1 1 1]. It can be seen that cut off frequency of the filter is changed without changing any passive component present in the circuit. Due to control word the cut off frequency is varies from (1 GHz to 2.87 GHz) for band pass filter, (0.69 GHz to 1.86 GHz) for low pass filter and (1.6 GHz to 4.33 GHz). For practical considerations sensitivity analysis has also been performed on the circuit parameters with reference to passive components and the results lie well within the tolerant ranges. The comparative analysis with other similar circuits available in literature has also been performed. The circuit is expected to found use in the domain of high frequency low voltage analog signal processing.

11. REFERENCES

1. Ali, M., Ahmed, M.A. and Chrzanowska-Jeske, M., "Logical effort framework for cnfet-based vlsi circuits for delay and area optimization", ***IEEE Transactions on Very Large Scale Integration (VLSI) Systems***, Vol. 27, No. 3, (2018), 573-586, doi: 10.1109/TVLSI.2018.2880322.
2. Ho, R., Lau, C., Hills, G. and Shulaker, M.M., "Carbon nanotube cmos analog circuitry", ***IEEE Transactions on Nanotechnology***, Vol. 18, (2019), 845-848, doi: 10.1109/TNANO.2019.2902739.

3. Keshavarzi, A., Raychowdhury, A., Kurtin, J., Roy, K. and De, V., "Carbon nanotube field-effect transistors for high-performance digital circuits—transient analysis, parasitics, and scalability", ***IEEE Transactions on Electron Devices***, Vol. 53, No. 11, (2006), 2718-2726, doi: 10.1109/TED.2006.883813.

4. Awano, Y., Sato, S., Nihei, M., Sakai, T., Ohno, Y. and Mizutani, T., "Carbon nanotubes for vlsi: Interconnect and transistor applications", ***Proceedings of the IEEE***, Vol. 98, No. 12, (2010), 2015-2031, doi: 10.1109/JPROC.2010.2068030.

5. Pable, S., Imran, A. and Hasan, M., "Performance optimization of cnfet based subthreshold circuits", in 2010 Annual IEEE India Conference (INDICON), IEEE. (2010), 1-4.

6. Imran, A., Hasan, M., Islam, A. and Abbasi, S.A., "Optimized design of a 32-nm cnfet-based low-power ultrawideband ccii", ***IEEE Transactions on Nanotechnology***, Vol. 11, No. 6, (2012), 1100-1109, doi: 10.1109/TNANO.2012.2212248.

7. Wong, H.-S., Appenzeller, J., Derycke, V., Martel, R., Wind, S. and Avouris, P., "Carbon nanotube field effect transistors-fabrication, device physics, and circuit implications", in 2003 IEEE International Solid-State Circuits Conference, 2003. Digest of Technical Papers. ISSCC., IEEE. (2003), 370-500.

8. Sedra, A.S., "The current conveyor: History and progress", in IEEE International Symposium on Circuits and Systems, IEEE. (1989), 1567-1571.

9. Wilson, B., "Recent developments in current conveyors and current-mode circuits", ***IEE Proceedings G-Circuits, Devices and Systems***, Vol. 137, No. 2, (1990), 63-77.

10. Hassan, T.M. and Mahmoud, S.A., "New cmos dvcc realization and applications to instrumentation amplifier and active-rc filters", ***AEU-International Journal of Electronics and Communications***, Vol. 64, No. 1, (2010), 47-55, doi. https://doi.org/10.1016/j.aeue.2008.11.002

11. Ma, M., Li, Z. and Yao, Z., "Current-mode cmos active inductor with applications to low-voltage oscillators", ***Engineering, Technology & Applied Science Research***, Vol. 3, No. 6, (2013), 540-543, doi. https://doi.org/10.48084/etasr.317

12. Chen, H.-P., Chiu, Y.-L., Chung, C.-K. and Chou, C.-C., "Voltage-mode multifunction filter with single input and three outputs based on single plus-type dvcc", in 2014 International Conference on Information Science, Electronics and Electrical Engineering, IEEE. Vol. 3, (2014), 1828-1841.

13. Iijima, S., "Helical microtubules of graphitic carbon", ***Nature***, Vol. 354, No. 6348, (1991), 56-58, doi: 10.1038/354056a0.

14. Dixit, A. and Gupta, N., "A compact model of gate capacitance in ballistic gate-all-around carbon nanotube field effect transistors", ***International Journal of Engineering***, Vol. 34, No. 7, (2021), 1718-1724, doi: 10.5829/IJE.2021.34.07A.16.

15. Imran, A., Pable, S. and Hasan, M., "A comparative study of cmos & cnfet based current conveyor at 32nm technology node", in 2010 International Conference on Computer and Communication Technology (ICCCT), IEEE. (2010), 276-281.

16. Ghabri, H., Issa, D.B. and Samet, H., "Performance optimization of 1-bit full adder cell based on cntfet transistor", ***Engineering, Technology & Applied Science Research***, Vol. 9, No. 6, (2019), 4933-4936, doi. https://doi.org/10.48084/etasr.3156

17. Deng, J. and Wong, H.-S.P., "A compact spice model for carbon-nanotube field-effect transistors including nonidealities and its application—part i: Model of the intrinsic channel region", ***IEEE transactions on Electron Devices***, Vol. 54, No. 12, (2007), 3186-3194, doi: 10.1109/TED.2007.909030.

18. Deng, J. and Wong, H.-S.P., "A compact spice model for carbon-nanotube field-effect transistors including nonidealities and its application—part ii: Full device model and circuit performance benchmarking", ***IEEE Transactions on Electron Devices***, Vol. 54, No. 12, (2007), 3195-3205, doi: 10.1109/TED.2007.909043.

19. Imran, A., Arora, D. and Kumar, R., "Dual dvcc based voltage-mode digitally programmable biquadratic filter", ***Circuits and Systems***, Vol. 2014, (2014), doi: 10.4236/cs.2014.51001.

20. Upadhyay, A. and Pal, K., "Realisation of dvcc based operational amplifier and its bandpass filter application", in 2016 International Conference on Advances in Computing, Communication, & Automation (ICACCA)(Spring), IEEE. (2016), 1-5.

21. Vavra, J., "Floating capacitance multiplier based on dvcc", in 2018 41st International Conference on Telecommunications and Signal Processing (TSP), IEEE. (2018), 1-4.

22. Jain, M. and Bharti, R., "Simulation of low power dvcc based lna for wireless receiver", in 2021 Devices for Integrated Circuit (DevIC), IEEE. (2021), 455-460.

23. Minaei, S., "Dual-input current-mode integrator and differentiator using single dvcc and grounded passive elements", in Proceedings of the 12th IEEE Mediterranean Electrotechnical Conference (IEEE Cat. No. 04CH37521), IEEE. Vol. 1, (2004), 123-126.

24. Dixit, V.K., "Dvcc based voltage-mode multifunctional biquadratic filter", in 2009 International Conference on Emerging Trends in Electronic and Photonic Devices & Systems, IEEE. (2009), 128-131.

25. Goel, N., "Dtmos based dvcc with multifunction filter application", in 2015 4th International Conference on Reliability, Infocom Technologies and Optimization (ICRITO)(Trends and Future Directions), IEEE. (2015), 1-6.

26. Gupta, S. and Arora, T.S., "Novel current mode universal filter using single dvcc", in 2016 International Conference on Signal Processing and Communication (ICSC), IEEE. (2016), 437-442.

27. Khan, M.Z., Ansari, M.S. and Siddiqui, M.J., "Digitally programmable second-order current mode continuous-time filters", in 2013 Saudi International Electronics, Communications and Photonics Conference, IEEE. (2013), 1-4.

28. Ansari, M.S. and Khan, M.Z., "Digitally programmable first-order current mode continuous-time filters", in 2012 2nd International Conference on Power, Control and Embedded Systems, IEEE. (2012), 1-6.

29. Imran, A., Arora, D. and Kumar, R., "Versatile digitally reconfigurable current-mode multifunctional biquadratic filter and quadrature oscillator", ***Journal of Active & Passive Electronic Devices***, Vol. 12, (2017).

30. Ghallab, Y.H., Badawy, W., Kaler, K.V. and Maundy, B.J., "A novel current-mode instrumentation amplifier based on operational floating current conveyor", ***IEEE Transactions on Instrumentation and Measurement***, Vol. 54, No. 5, (2005), 1941-1949, doi: 10.1109/TIM.2005.854254.

31. Gift, S.J., "An enhanced current-mode instrumentation amplifier", ***IEEE Transactions on Instrumentation and Measurement***, Vol. 50, No. 1, (2001), 85-88, doi: 10.1109/19.903882.

32. Lee, C.-N., "Independently tunable mixed-mode universal biquad filter with versatile input/output functions", ***AEU-International Journal of Electronics and Communications***, Vol. 70, No. 8, (2016), 1006-1019, doi: 10.1016/j.aeue.2016.04.006.

Persian Abstract

چکیده

با ادامه مقیاس بندی ، ترانزیستورهای اثر نانولوله کربنی (CNFET) به عنوان کاندیداهای احتمالی برای رفع نقایص مربوط به مقیاس ترانزیستورهای تکمیلی فلز اکسید – نیمه هادی (CMOS) در نظر گرفته می شوند. در این مقاله یک فیلتر چند منظوره دو کاره مبتنی بر CNFET با قابلیت تنظیم مجدد دیجیتالی با استفاده از یک نوار نقاله جریان ولتاژ دیفرانسیل مبتنی بر CNFET (DVCC) در گره فناوری ۳۲ نانومتر ارائه شده است. این مدار از یک بلوک DVCC مبتنی بر CNFET به همراه آرایش مقاومت ها و خازن های کمی استفاده می کند. مدار فیلتر چند منظوره پیکربندی مجدد دیجیتالی با استفاده از یک توپولوژی می تواند پیکربندی فیلترهای کم گذر ، بالا گذر و باند گذر قابل برنامه ریزی را بدست آورد. فیلتر چند منظوره مبتنی بر CNFET فرکانس طنینی از مرتبه گیگاهرتز را بدست می آورد. علاوه بر این ، کنترل دیجیتالی ۳ بیتی پارامترهای فیلتر چند منظوره طراحی شده یعنی عامل کیفیت (Qo) و فرکانس تشدید با استفاده از شبکه جمع بندی فعلی (CSN) امکان پذیر شده است. حساسیت و تجزیه و تحلیل مقایسه ای نیز انجام شده است. مدار با منبع ولتاژ پایین ۰.۹ ولت با استفاده از برنامه شبیه سازی Hewlett با محیط مدار مجتمع (HSPIC) در گره فناوری ۳۲ نانومتر شبیه سازی شده است. نتایج شبیه سازی به دست آمده با تجزیه و تحلیل نظری همگام است.

IJE TRANSACTIONS B: Applications Vol. 34, No. 11, (November 2021) 2433-2441

International Journal of Engineering

Journal Homepage: www.ije.ir

Design and Modeling of a High-speed Permanent Magnet Synchronous Generator with a Retention Sleeve of Rotor

H. Parivar*, A. Darabi

Department of Electrical Engineering, Shahrood University of Technology, Shahrood, Iran

PAPER INFO

Paper history:
Received 31 May 2021
Received in revised form 14 September 2021
Accepted 23 September 2021

Keywords:
high-speed Permanent Synchronous Machine
Retention Sleeve
Taguchi Optimization Method
Titanium Sleeve

ABSTRACT

In this paper, the authors present a novel approach to design a high-speed permanent magnet synchronous generator (HS-PMSG) with a retention sleeve. The importance of the retention sleeve becomes conspicuous when the rotor suffers from the radial and tangential stresses derived from a high speed say 60 krpm. With respect to the mechanical property of Titanium. This material has been demonstrated that it could be a proper material for the retention sleeve. The investigations in this paper concentrated on the electromagnetic coupled with mechanical design of a 2-poles, 18-slots, 40 KW HS-PMSG which is carried out through FEM analysis using JMAG 17.1 and ABAQUS CAE and optimized through the well-known Taguchi optimization method. The obtained results assure the robust mechanical behaviour of the HS-PMSG at a rotational speed of about 60 krpm meanwhile the cogging torque, the Joule loss, and the total weight of the optimally designed HS-PMSG were reduced 44.71, 27.87, and 2.78%, respectively compared with the initial design.

doi: *10.5829/ije.2021.34.11b.07*

1. INTRODUCTION

In the last century, electrical energy has become an undeniable part of human life. Without electrical energy, our world drowns in the darkness, modernization would be stopped and numerous consequences would threaten the life of the earth. The generation of electrical energy plays a vital role in power systems. Among all generator units, PMSGs have been utilized as a significant part of generation units. Due to the important role of PMSGs, multi1ple studies have dedicated their effort to analyze the behavior, modelling, simulation, and operation improvement of these devices [1]. They have drawn massive attention exceedingly in both low speed and high-speed industrial applications as a generator or motor. High-power density, low manufacturing costs, which is a consequence of the overall weight and the size reduction, are the advantages of the mentioned machines. Two kinds of interior PM (IPM) and surface-mounted PM (SPM) machines are becoming candidates in high-speed applications. Figure 1 represents the most important advantages and disadvantages of the PMSGs [2-6]. In the last decade and along with the discovery of new PMs, these types of generators have drawn lots of attention, not only in academic papers but also in the power engineering world [7]. Among high-speed machines, the HS-PMSGs have been utilized more widely than others. Thus, the proper design of these machines is an inevitable step in the utilization of them. The main issue in the design of such generators is to design the exact mechanical behavior of rotors considering electrical, magnetic, mechanical, thermal, and even economic aspects [8]. Protection of the PMs against the massive induced centrifugal forces of the rotor is the main objective of the design of HS-PMSGs which is dealt with by taking the advantage of retention sleeves. The aforementioned sleeves should not only have a proper mechanical resistance, suitable thermal conductance, and low electromagnetic loss but also should be thin enough [9]. The design procedure of HS-PMSG faces numerous challenges and hindrances. The mechanical stresses of the rotor, temperature

*Corresponding Author Institutional Email: hosseinparivar72@yahoo.com (H. Parivar)

Please cite this article as: H. Parivar, A. Darabi, Design and Modeling of a High-speed Permanent Magnet Synchronous Generator with a Retention Sleeve of Rotor, International Journal of Engineering, Transactions B: Applications, Vol. 34, No. 11, (2021), 2433-2441

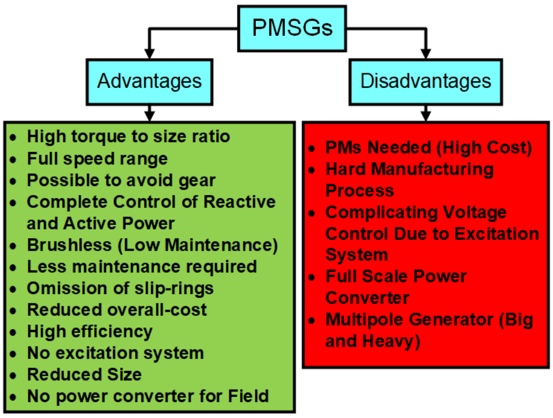

Figure 1. Advantages and disadvantages of the PMSGs [2-6]

considerations, and losses are the most significant challenges [10-11]. All the parameters affecting the mechanical and electromagnetic performance of the HS-PMSG can be determined optimally by the Taguchi optimization method. Moreover, the Taguchi optimization method is generally preferred to others such as trial and error due to faster response. In this regard, the Taguchi optimization approach is employed in this paper for designing an HS-PMSG optimally getting started from an initial design with numerous parameters. In fact, without using this optimization method, in the design process of the HS-PMSG, it is necessary to suggest various and infinite parameters for the thicknesses of the retention sleeve and the PM, while in this approach, the proper and optimum value is determined with fewer steps.

In this paper, the authors try to propose an optimum design of the HS-PMSG with a retention sleeve. The optimization process is conducted based on the well-known Taguchi optimization method which is accomplished to designate the proper thickness of PMs and retention sleeve.

The rest of this paper includes sections 2 and 3, which covered the HS-PMSG electromagnetic and mechanical modelling, respectively. The subject of section 4 is the thicknesses of the sleeve and PM. Section 5 involves results and discussions. Section 6 presents the final electromagnetic and mechanical design of HS-PMSG, and the conclusion are expressed in section-7.

2. HS-PMSG ANALYTICAL MODELING

In this section, the design approach of a HS-PMSG is presented. At first, let us start to design an instance HS-PMSG which is presented by Damiano et al. [12]. It is a 40^{KW}, 60^{krpm}, 2-pole, and 18-slot with material properties summarized in Table 1. Determining the air gap sizes can be a starting point of the machine design. In the electromagnetic design of the HS-PMSG, the retention sleeve plays a role as an extra air gap. So, the physical air gap is considered 1^{mm} which for a machine with the stated size and power, regarding previous experiences, this value of the air gap is reasonable. Analytical design of the HS-PMSG start by assuming initial design parameters like as: D: stator diameter on the airgap side $= 77^{mm}$, L: machine axial length $= 80^{mm}$, h_m: PM thickness in the radial direction $= 3^{mm}$. These extents are taken from a similar size and power rating machine. Owing to Figure 2, the effective air gap (g') is defined as:

$$g' = g_1 + g_2 = g + (h_m/\mu_r) = 1 + (3/1.05) = 3.85^{mm} \quad (1)$$

where μ_r is the permeability of the PM. Owing to the considered air gap size (g), the rotor radius on the air gap side (R_m) and the rotor core outer radius (R_r) are defined [13]:

$$R_m = (D/2) - g = (77/2) - 1 = 37.5^{mm} \quad (2)$$

$$R_r = R_m - h_m = 37.5 - 3 = 34.5^{mm} \quad (3)$$

The slot pitch (τ_t) and the Karter coefficient (K_c) could be conducted by Say [13]:

$$\tau_t = (2\pi R_s)/(N_s) \quad (4)$$

$$K_c = (\tau_t)/(\tau_t - \gamma g') \quad (5)$$

where R_s is the stator core inner radius and N_s is the number of stator slots. Experience shows which for a medium-sized machine (1^{KW} to 100^{KW}), the stator slot opening at the slot tip parameter (B_{s0}) is usually 2^{mm} to 3^{mm}, and the γ constant is defined as follows [13]:

$$\gamma = \frac{4}{\pi}\left(\frac{B_{s0}}{2g'}\right)\tan^{-1}\left(\frac{B_{s0}}{2g'}\right) - \ln\sqrt{\left(1 + \left(B_{s0}/2g'\right)^2\right)} \quad (6)$$

Therefore, according to Equations (4) and (5) τ_t and K_c are 13.43^{mm} and 1.012, respectively. The effective stator inner radius is 38.54^{mm} evaluated by [13]:

$$R_{se} = R_s + (K_c - 1)g' \quad (7)$$

The fundamental component of back EMF (E_1) for the number of turns per phase of the stator winding given as $Nc=30$ is 292.5^{V} [13]:

$$E_1 = 4.44\, f N_c B_1 k_{w1} (2/\pi)(\pi D/p\, L) \quad (8)$$

B_1 is the fundamental spatial harmonic component of the airgap flux density produced by the PM (T), k_{w1} is the fundamental winding factor and p is the number of the poles. Therefore, the winding current is

TABLE 1. HS-PMSG Parameters

Type	Material
Stator Core	VACOFLUX-48
PMs	NdFeB NEOREC 50H (TDK)
Windings	Copper
Insulation Class	Class-F
Sleeve	Titanium

$I_{ph}=P_{out}/n_{phase}\times E_1=26.31^A$. The stator tooth width (T_{sw}), the stator core thickness (T_{sc}), and the rotor core thickness (T_{rc}) which are shown in Figure 2 are equal to 12.5^{mm}, 12.5^{mm}, and 3.11^{mm}, respectively [13].

$$T_{sc}=\Phi/\left(2B_{sc}Ll_f\right) \tag{9}$$

$$T_{rc}=\Phi/\left(2B_{rc}Ll_f\right) \tag{10}$$

$$T_{sw}=\Phi_{tm}/\left(B_{st}Ll_f\right) \tag{11}$$

where Φ is the flux per pole (Wb), and Φ_{tm}, B_{sc}, B_{rc}, B_{st}, and l_f are the maximum stator tooth flux (Wb), flux density in the stator core (T), flux density in the rotor core (T), flux density in the stator tooth (T) and lamination

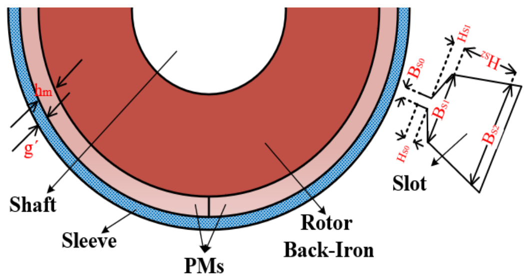

Figure 2. The design parameters of HS-PMSG

TABLE 4. The PM and sleeve thicknesses

Number of Case Study	PM	Sleeve
1	2	1
2	2.5	1
3	3	1
4	2	1.5
5	2.5	1.5
6	3	1.5
7	2	2
8	2.5	2
9	3	2

factor, respectively. The rotor inner diameter (D_{ri}) can be expressed as [13]:

$$D_{ri}=D-2(g+h_m+T_{rc}) \tag{12}$$

The armature reaction inductance (L_m) is equal to 1.54^{mH} evaluated by [13]:

$$L_m=\frac{3}{\pi}\left(\left(k_{w1}N_c\right)/\left(p/2\right)\right)^2\times\left(\mu_0\times DL\right)/\left(g'K_c\right) \tag{13}$$

Both height of the stator slot wedge (H_{s1}) and the height of the stator tooth tip (H_{s0}) parameters cannot be calculated at the first step, so are assumed to be equal to 1^{mm} which is based on experience. So, the stator slot opening at the slot wedge (B_{s1}) is 11.02^{mm} owing to [13]:

$$B_{s1}=\pi\left(D+2\left(H_{s0}+H_{s1}\right)\right)/N_s-T_{sw} \tag{14}$$

The stator slot area per slot (A_s) is calculatable as 102.81^{mm2} by [13]:

$$A_s=\left(B_{s1}+B_{s2}\right)/2\times H_{s2}=102.81^{mm^2} \tag{15}$$

And, the end winding leakage inductance can be calculated by [13]:

$$L_{sle}=0.5\times pq\mu_0\left(T_{sw}+B_{s1}+B_{s2}/2\right)\left(3N_c/N_s\right)^2 \times\log\left(\left(T_{sw}+B_{s1}+B_{s2}/2\right)\sqrt{\pi}/\sqrt{2A_s}\right) \tag{16}$$

H_{s2} is the height of the stator from the wedge to the slot bottom, q is the number of slots per pole per phase, B_{s1} is the stator slot opening at the slot wedge, B_{s2} is the stator slot opening at the slot bottom, N_s is the number of stator slots. Another geometric parameter like the stator slot opening at the slot bottom ($B_{s2new}=13.19^{mm}$) and the height of stator from the wedge to the slot bottom ($H_{s2new}=13.63^{mm}$) are specified by [13]:

$$B_{s2new}=\left[\pi\left(D+2\left(H_{s0}+H_{s1}+H_{s2}\right)\right)/N_s\right]-T_{sw} \tag{17}$$

$$H_{s2new}=A_s/\left(\left(B_{s1}+B_{s2}\right)/2\right) \tag{18}$$

Finally, the current density (J_{snew}) is $3.93^{A/mm2}$ evaluated by [13]:

$$J_{snew}=J_s\times A_{cui}/A_{cu} \tag{19}$$

The stator outer diameter (D_o) is 133.26^{mm} as [13]:

$$D_o=D+2\left(H_{s0}+H_{s1}+H_{s2new}+T_{rc}\right) \tag{20}$$

According to the yield strength ($\sigma_{yield}=190^{MPa}$) and the expected maximum shaft torque (approximately equal to 4 times the rated torque) of the machine ($T_{max}=50.4^{N.m}$) and with respect to the safety factor of $n_s=50$, the frame thickness is 1.47^{mm} as [13]:

$$\frac{\pi}{2}\left(\left(\left(\frac{D_o}{2}\right)+t_f\right)^4-\left(\frac{D_o}{2}\right)^4\right)=\frac{(T_{\max}\times n_s\times\left(\frac{D_o}{2}\right)+t_f)}{\sigma_{yield}} \quad (21)$$

The calculated HS-PMSG volume and weights are stated in Table 2. At 15ºC, the copper resistivity is 2.52×10^{-8} Ωm so, the DC resistance (R_{DC}) is 0.05Ω and finally, the copper loss (P_{cu}) is 103.83W. The core loss (P_{core}) in the rated condition is *5289.6W*. Another loss such as the windage and the friction loss (P_{wf}) is assumed to be *200W* for a machine with this size and power is reasonable. The maximum flux density in the stator teeth (B_{st}) is calculated and is *1.09T*. In the steady-state, the permissible stator current regarding the PMs' demagnetization (I_{dmgrm}) is *124.56A*. The rated phase current (I_{ph}) is *26.31A* therefore, the PMs' demagnetization is not probable to occur.

3. MECHANICAL MODELING

The HS-PMSG rotor is assumed as a rotational cylinder and the inner stress is due to the radial ε_r and the tangential strains ε_θ. Concerning Hook's law and the isotropic and homogenous cylinder material assumptions, the radial strain ε_r can be calculated by [13]:

$$\varepsilon_r = 1/E_Y\left(\sigma_r-\upsilon\sigma_\theta\right)+\alpha_T\Delta T \quad (22)$$

where σ_r and σ_θ are the radial and tangential stress, E_Y and υ are young's modulus and Poisson's ratio respectively, α_T is the thermal expansion coefficient and ΔT is the variation between actual and reference temperatures and the tangential strain ε_θ is [13]:

$$\varepsilon_\theta=-\left(1/E_Y\right)\left(\upsilon\sigma_r+\sigma_\theta\right)+\alpha_T\Delta T \quad (23)$$

Equations (22) and (23) should satisfy the following equality [13]:

$$\sigma_r+r\left(d\sigma_r/dr\right)-\sigma_\theta+\rho\omega_m^2r^2=0 \quad (24)$$

TABLE 2. HS-PMSG weights and valume

Type	Weight (Kg) and Volume (m³)
Stator Core	30.8
Stator tooth	5.68
Rotor Core	14.41
PMs (3ᵐᵐ)	3.42
Sleeve (2.85ᵐᵐ)	2.16
Windings	2.64
Frame	5.25
Total Weights	64.34
Total Volume	1500

where ω_m is the rotational speed and r is the radius of the infinitesimal portion of the cylinder with the mass density of ρ. The radial stress σ_r is accessible by solving the differential equation given by [13]:

$$\frac{d^2\sigma_r}{dr^2}+\frac{3d\sigma_r}{rdr}+(3+\upsilon)\rho\omega_m^2+(\frac{\alpha_T E_Y}{r})\frac{d\Delta T}{dr}=0 \quad (25)$$

The radial σ_r and the tangential σ_θ stresses play a role in Von Mises equivalent stress σ_{eq} defined as [13]:

$$\sigma_{eq}=\left(\sigma_r^2+\sigma_\theta^2-\sigma_r\sigma_\theta\right)^{1/2} \quad (26)$$

The values of mechanical parameters of the retention sleeve and the PM materials needed for the above equations are given in Table 3.

4. THICKNESS OF THE SLEEVE AND PM

The Taguchi optimization method is a statistical method developed by Genichi Taguchi for quality improvement, which is mostly employed in the engineering world. The objective functions are the thicknesses of the PM and the retentions sleeve. As been described, the aforementioned optimization method is implemented in MINITAB software which is an important software in this field. Hence, to avoid extending the optimization process, only the optimization results are given and these results are compared and optimized in the following sections. The orthogonal arrays (OA) reduce significantly the number of iterations and experiments of this optimization approach. In this algorithm, the ratio of Signal to Noise (S/N) is calculated by:

$$(S/N)_i=-10\log\left[\frac{1}{n}\sum_{j=1}^{n}\frac{1}{Y_{ij}^2}\right] \quad (27)$$

where i is the number of case studies and Y_{ij} is the measured value of quality for *i-th* and *j-th* case studies, and parameter n is the number of iterations for each case studies combination. The Taguchi optimization method often uses a two-step process. In the first stage, the (S/N) ratio is used to identify controlling factors to reduce changes. In the second stage, the control factors that have

TABLE 3. Mechanical Properties of the Sleeve and PM

Type	PM	Sleeve
Mass Density (g/mm³)	0.0075	0.0045
Young Modulus (MPa)	170000	120000
Poisson Ratio (-)	0.24	0.34
Residual Magnetism (T)	1.37	-
Maximum Temperature (C)	80	-
Thermal Expansion Coefficient (10^{-6}/C)	4	9

a negligible effect on the (S/N) ratio are identified to achieve the goal. The response for each (S/N) ratio for any surface factor is Γ and ᐯ. Γ is the difference between the maximum and minimum response (S/N ratio) for any factors and ᐯ is each Γ rank. To using the optimization process, both the sleeve and the PM thicknesses are considered in Table 4. According to the Taguchi method the influences of PMs and sleeve on the sleeve centrifugal force **(State 1)**, on the PMs centrifugal force **(State 2)**, the maximum stress on the sleeve **(State 3)**, the maximum stress on the PMs **(State 4)**, the maximum strain on the sleeve **(State 5)**, the maximum strain on the PMs **(State 6)** all are given in Table 5. The Γ and ᐯ changes according to Table 6.

5. RESULTS AND DISCUSSIONS

5. 2. Taguchi Optimization Method

Results obtained from the Taguchi method is as : The sleeve thickness has a major impact on the sleeve centrifugal force, while the PM thickness has a minor influence. With an increase in PM thickness, the PM centrifugal force also increases, and the influence of the sleeve thickness is insignificant. The sleeve thickness affects the sleeve maximum stress directly via Γ while the PM thickness impresses the sleeve maximum stress up to 2.5mm. Variation of sleeve thickness from 1 to 2mm yields to 1.13% increase in the maximum stress of PM while the PM thickness varies from 2 to 3mm, the maximum stress in the PM rises 0.82%. It can be concluded that in comparison with PM thickness, the sleeve thickness variation has much influence on the maximum stress of the PM. For maximum strain in the sleeve, the impact of sleeve thickness is 10.25% more than the PM. From the sleeve thickness of 1 to 1.5mm, the maximum strain in PM decreases 2.28% and from 1.5 to 2mm increases 1.92% and for the PM thickness, from 2 to 2.5mm, the maximum strain in PM decreases 1.43% and from 2.5 to 3mm, increases 1.18%. So, the sleeve thickness has significant effects on the maximum strain of PM rather than the PM thickness.

In these 6 states, the thickness of the sleeve was the most important factor in calculating the centrifugal force in the sleeve, the maximum stress on the sleeve and the PM, and the maximum strain in the sleeve and the PM. The thickness of the sleeve is considered to be a vital factor.

5. 2. Electromagnetic Analysis

According to Figures 3 and 4, the obtained results are as following:
The maximum cogging torque from the 1^{st} to 4^{th} case study is constant and is 0.39N.m. It increases at the 9^{th} case study, which has a maximum value of 1.23N.m. The increase in sleeve thickness does not affect the voltage of the HS-PMSG at the 1^{st} to 3^{rd} case study. This parameter increases 18.75% in the 4^{th} case study and with a 47.37% increase, the maximum voltage becomes 227V. With a 31.11% increasing in the current of the HS-PMSG, the maximum value occurs in the 9^{th} case study. The Joule loss in the 1^{st} case study is 12.31W and with respect to

TABLE 5. The Effect of The Thicknesses of the Sleeve and PM on Various Parameters

Sleeve Thickness	PM Thickness	State 1	State 2	State 3	State 4	State 5	State 6
1	2	19.86	111.84	2746	3448	0.01583	0.0161
2	2.5	19.86	139.84	2806	3486	0.01595	0.01549
3	3	19.86	167.81	2861	3540	0.01635	0.01635
4	2	29.11	111.84	2803	3541	0.01613	0.01595
5	2.5	29.11	139.84	2929	3548	0.01637	0.0159
6	3	29.11	167.81	2808	3481	0.01649	0.01561
7	2	39.2	111.84	2849	3523	0.01647	0.01619
8	2.5	39.2	139.84	2877	3501	0.01618	0.01616
9	3	39.2	167.81	2915	3576	0.01665	0.01604

TABLE 6. (S/N) Ratio Resulted From Taguchi Method

Type	State 1		State 2		State 3		State 4		State 5		State 6	
	ST	PMT	ST	PMT	ST	PMT	ST	PMT	ST	PMT	ST	PMT
Γ	19.34	0	0	56	76	72	41	29	0.00039	0.00035	0.00037	0.00023
ᐯ	1	2	2	1	1	2	1	2	1	2	1	2

ST = Seeve Thickness PMT = PM Thickness

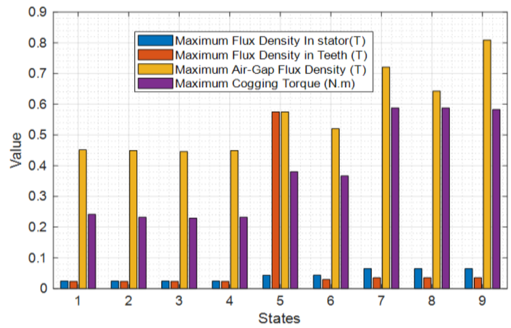

Figure 3. Changes on the maximum flux density in the stator, the maximum flux density in teeth, the maximum air-gap flux density, and the maximum cogging torque of HS-PMSG

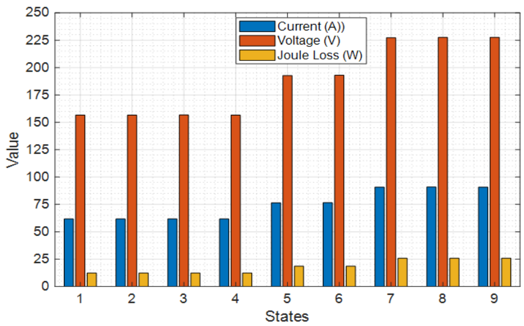

Figure 4. Changes in the stator current, the stator voltage, and the Joule loss of HS-PMSG

0.16% reduction, the minimum valve occurs in the 2^{nd}, 3^{rd}, and 4^{th} case studies. For the maximum flux density in the teeth and the stator, from 1^{th} to 4^{th} case study, a state equal to 0.02T occurs. A maximum value for the maximum flux density in teeth occurs for the 5^{th} case study. For the maximum flux density in the stator with a 68.75% increase, the maximum value takes place in the 9^{th} case study. In this case study, the maximum flux density in teeth is equal to 0.5T. According to the results of the previous sections, the optimum thickness for the PM is *2.5mm* and for the retention sleeve is *2mm*.

6. FINAL DESIGN

One of the possible methods to find the proper and optimal thickness for the sleeve and the PM is to utilize the trial and error method. In this method, first, a set of various values for these two parameters is guessed. Then, various FEM analyses and simulations are performed to get closer to the optimal point. Obviously, this method is time-consuming and long. The proposed method in this manuscript is more accurate than the trial and error method and responds to variables faster. Another point that distinguishes the Taguchi optimization method is that in this method, the electromagnetic and mechanic variables affecting the performance of the HS-PMSG can be found and modified.

6. 1. Electromagnetic Design In this section, the electromagnetic design of HS-PMSG based on the above-discussed Taguchi optimization method has been accomplished. The electromagnetic design of the HS-PMSG is done using the JMAG that provides a variety of features to efficiently support optimized design. This is a popular and famous software among the designers of electrical machines and is mostly used in articles as design and simulation software. More, by using the JMAG, the results and sensitivity analysis offer functions where can improve the design. Figure 5 shows the HS-PMSG structure and geometrical property of HS-PMSG design is tabulated in Table 7. These parameters which are named geometric dimensions are based on the initial design of the HS-PMSG with respect to literature [13] which presented a design algorithm for PM machines. Due to a large number of equations in the design algorithm, only a number of them is described in the initial design of the HS-PMSG (Equations (1) to (21)) and others are categorized as Table 7. Figure 6 illustrates the FEM analysis of the HS-PMSG.

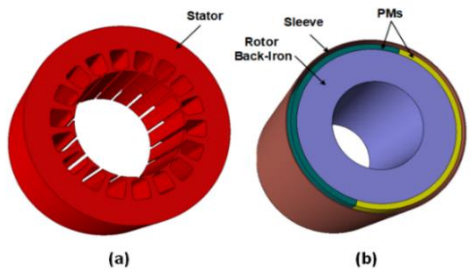

Figure 5. 3D-View of the designed HS-PMSG. a: stator, b: rotor

TABLE 7. Geometric Properties of HS-PMSG

Type	Value (mm)	Type	Value (mm)
Rotor Core Thickness	12.5	PM Thickness	2.5
Stator Core Thickness	12.5	Sleeve Thickness	1.5
Stator Teeth Width	3.11	Air-Gap	1
Slot Height	13.63	Stator Inner Diameter	76.31
Opening Slot	2	Stator Outer Diameter	132.26
Bottom Slot Length	11.02	Active Length	82
Top Slot Length	13.19	Frame Thickness	1.47
Shaft Radius	32	Wire Thickness	1.45

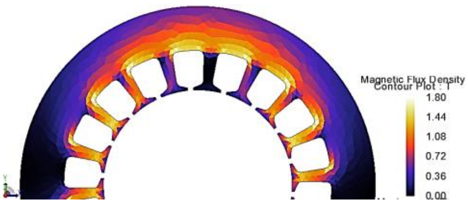

Figure 6. The no-load magnetic flux density of HS-PMSG

6. 2. Mechanical Design Figure 7 illustrates the 2-D view of the designed HS-PMSG rotor. Figure 8, displays the Von Mises stress and strain distribution on the HS-PMSG rotor. According to Figure 9, in the worst-case scenario, the amount of the Von Mises stress is equal to 682.167MPa in 60krpm. Similarly, for the Von Mises strain, the maximum value has been shown in Figure 10. The maximum shear stress of the titanium is equal to 729MPa. Therefore, for the worst condition in 60krpm, failure does not occur. Figure 11, shows the Hoop and radial stress in the sleeve. With a 0.5mm increasing, the Hoop and the radial stress increase 1.15 and 2.07%, responsively. The maximum valve occurs in 2mm which the Hoop stress is 277.19MPa and the radial stress is 275.05MPa. The maximum radial and the Hoop stress in PMs occurs in 1mm of the sleeve thickness that is equal to 355.34MPa and 337.42MPa, responsively. According to Figure 12, by 2.5mm increase in the thickness of PM, the radial stress is reduced by 0.55%, and also, the Hoop stress is reduced by 0.54%.

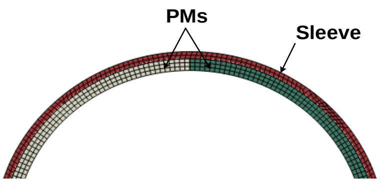

Figure 7. 2-D View of HS-PMSG rotor

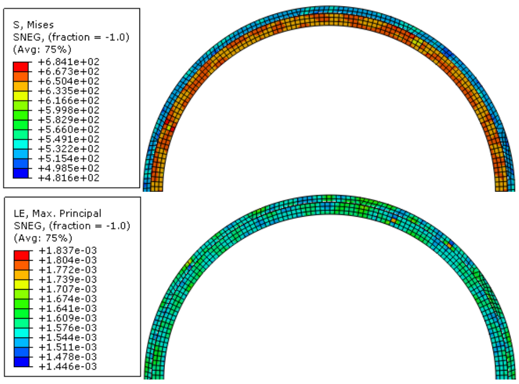

Figure 8. Von Mises stress (Top) and strain (Bottom) distribution on HS-PMSG rotor

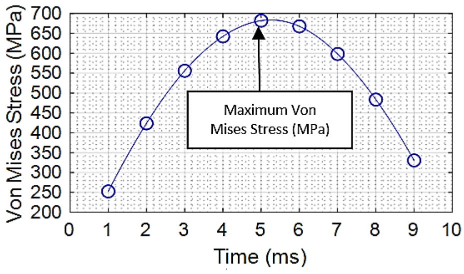

Figure 9. Maximum Von Mises stress

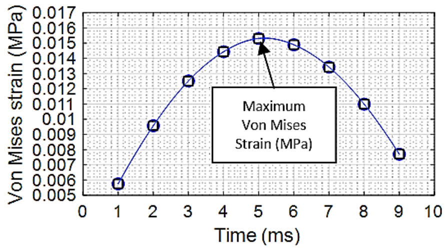

Figure 10. Maximum Von Mises strain

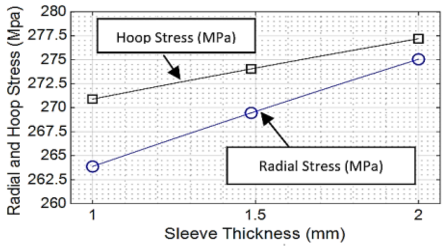

Figure 11. Sleeve's Hoop stress and the radial stress of PM

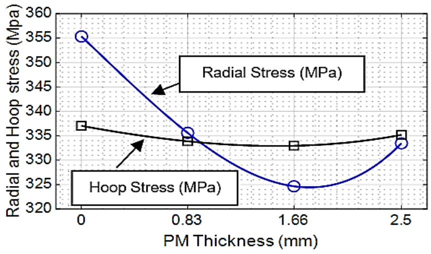

Figure 12. PM's Hoop stress and the radial stress of PM

7. CONCLUSION

In this paper, not only the proposed optimization method aims to improve the electromagnetic performance of the HS-PMSG but also the simulations sought to provide the proper mechanical conditions for the designed HS-PMSG. The result shows that: In the worst-case scenario of the rotational speed of 60krpm, the PM is safe against mechanical stresses and centrifugal forces. The Taguchi optimization method is utilized with a fast response to select the optimum thickness of the PM and the sleeve and also, by utilizing the Taguchi optimization method, the cost reduction of the practical experiments and simulations is accessible. Compared with the initially designed HS-PMSG, in the optimum design, the following results are obtained: The cogging torque is reduced by 44.71%. The Joule loss is reduced by about 27.87%. The maximum flux density in teeth is reduced by approximately 37.5%. The PM and the sleeve weight are reduced 16.67 and 30.09% responsively, and the total weight of HS-PMSG is reduced by 2.78%.

8. REFERENCES

1. B. Poudel, E. Amiri, P. Rastgoufard and B. Mirafzal, "Toward Less Rare-Earth Permanent Magnet in Electric Machines: A Review," ***IEEE Transactions on Magnetics***, Vol. 57, No. 9, 1-19, (2021), DOI: 10.1109/TMAG.2021.3095615.
2. Tenconi, A., S. Vaschetto, and A.J.I.T.o.I.E. Vigliani, "Electrical machines for high-speed applications: Design considerations and tradeoffs", ***IEEE Transactions on Industrial Electronics***, Vol. 61, No. 6, (2013), 3022-3029, DOI: 10.1109/TIE.2013.2276769
3. H. Parivar, S. M. Seyyedbarzegar, A. Darabi, "An Improvement on Slot Configuration Structure of a Low-speed Surface-mounted Permanent Magnet Synchronous Generator with a Wound Cable Winding", ***International Journal of Engineering, Transactions C: Aspects***, Vol. 34, No. 9, (2021), 2045-2052, DOI: 10.5829/ije.2021.34.09c.01
4. Y. Gu, X. Wang, P. Gao and X. Li, "Mechanical Analysis With Thermal Effects for High-Speed Permanent-Magnet Synchronous Machines," ***IEEE Transactions on Industry Applications***, Vol. 57, No. 5, 4646-4656, (2021), DOI: 10.1109/TIA.2021.3087120.
5. R. Nasiri-Zarandi, A. Mohammadi Ajamloo, K. Abbaszadeh "Cogging Torque Minimization in Transverse Flux Permanent MagnetGenerators using Two-step Axial Permanent MagnetSegmentation for Direct Drive Wind Turbine Application", ***International Journal of Engineering, Transactions A: Basics***, Vol. 34, No. 04, (2021), 908-918, DOI: 10.5829/ije.2021.34.04a.17
6. M. A. Rahman, "History of interior permanent magnet motors [History]," in ***IEEE Industry Applications Magazine***, Vol. 19, No. 1, 10-15, (2013), DOI: 10.1109/MIAS.2012.2221996.
7. Z. Kolondzovski, a. Belahcen, and a. Arkkio, "Comparative thermal analysis of different rotor types for a high-speed permanent-magnet electrical machine,"***IET Electric Power Applications***, Vol. 3, No. 4, 279-288, (2009). DOI: 10.1049/iet-epa.2008.0208
8. M. Arehpanahi, E.Kheiry, "A New Optimization of Segmented Interior Permanent Magnet Synchronous Motor Based on Increasing Flux Weakening Range and Output Torque" ***International Journal of Engineering, Transactions C: Aspects***, Vol. 33, No. 6, (2020), 1122-1127, DOI: 10.5829/ije.2020.33.06c.09
9. T. Han, Y. Wang and J. -X. Shen, "Analysis and Experiment Method of Influence of Retaining Sleeve Structures and Materials on Rotor Eddy Current Loss in High-Speed PM Motors," ***IEEE Transactions on Industry Applications***, Vol. 56, No. 5, (2020), 4889-4895, DOI: 10.1109/TIA.2020.3009909
10. Kurvinen E, Di C, Petrov I, Nerg J, Liukkonen O, Jastrzebski RP, Kepsu D, Jaatinen P, Aarniovuori L, Sikanen E, Pyrhonen J. "Design and Manufacturing of a Modular Low-Voltage Multi-Megawatt High-Speed Solid-Rotor Induction Motor." ***IEEE Transactions on Industry Applications***, (2021), 1-10 DOI: 10.1109/TIA.2021.3084137
11. Q. Zhang, S. Cheng, D. Wang, Z. Jia, "Multiobjective design optimization of high-power circular winding brushless DC motor," ***IEEE Transactions Industrial Electronics***, Vol. 65, No. 2, (2018), 1740-1750, DOI: 10.1109/TIE.2017.2745456
12. Damiano, A. Floris, G. Fois, M. Porru and A. Serpi, "Modelling and design of PM retention sleeves for High-Speed PM Synchronous Machines," 2016 6th International Electric Drives Production Conference (EDPC), (2016), 118-125. DOI: 10.1109/EDPC.2016.7851323
13. K. M. G. Say, Performance and design of AC machines: Pitman, London, 1970, ISBN: 273 40199 8
14. Damiano, A. Floris, G. Fois, M. Porru and A. Serpi, "Modelling and design of PM retention sleeves for High-Speed PM Synchronous Machines," 2016 6th International Electric Drives Production Conference (EDPC), (2016), 118-125. DOI: 10.1109/EDPC.2016.7851323

9. APPENDIX

The proposed flowchart is as shown in Figure A1.

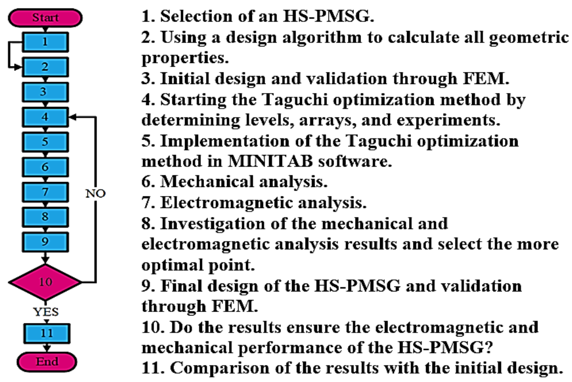

Figure A1. Proposed Flowchart

Persian Abstract

چکیده

در این مقاله، نویسندگان یک روش جدید برای طراحی ماشین سنکرون مغناطیس دائم سرعت بالا (HS-PMSG) مجهز به روکش محافظ ارائه داده اند. اهمیت استفاده از روکش محافظ زمانی حیاتی می‌شود که روتور در معرض تنش‌های شعاعی و مماسی ناشی از سرعت‌های بالا در حدود ۶۰ هزار دور بر دقیقه قرار می‌گیرد. با توجه به ویژگی‌های مکانیکی تیتانیوم، این ماده می‌تواند یک ماده مناسب برای استفاده در روکش HS-PMSG باشد. با استفاده از نظریه مکانیک الاستیگ، این ماده می‌تواند از نظر مکانیکی از روتور HS-PMSG محافظت کند. محور تحقیقات این مقاله بر روی طراحی الکترومغناطیسی و مکانیکی HS-PMSG که دارای ۲ قطب، ۱۸ شیار و توان ۴۰ کیلووات است متمرکز شده است. ماده آهنربای دائم استفاده شده در این ماشین NdFeB (نئودیمیوم) می‌باشد. نتایج بدست آمده با استفاده از دو نرم افزار JMAG و ABAQUS CAE می‌باشد که با استفاده از روش المان محدود اعتبار سنجی شده است. در بخش بعدی این مقاله، ضخامت‌های آهنربای دائم و روکش محافظ با استفاده از روش تاگوچی، بهینه‌سازی شده اند. نتایج بدست آمده از این روش پیشنهادی، عملکرد الکترومغناطیسی و مکانیکی HS-PMSG را در سرعت ۶۰ هزار دور بر دقیقه تضمین می‌کند و همچنین گشتاور دندانه‌ای، تلفات ژول، و وزن کلی HS-PMSG نسبت به طرح اولیه به ترتیب ۴۴.۷۱ درصد، ۲۷.۸۷ درصد و ۲.۷۸ درصد کاهش یافته‌اند.

IJE TRANSACTIONS B: Applications Vol. 34, No. 11, (November 2021) 2442-2451

International Journal of Engineering

Journal Homepage: www.ije.ir

Numerical Simulation of a Heavy-duty Diesel Engine to Evaluate the Effect of Fuel Injection Duration on Engine Performance and Emission

B. Alizadeh Kharkeshi, R. Shafaghat*, M. Mohebbi, S. Talesh Amiri, M. Mehrabiyan

Sea-Based Energy Research Group, Babol Noshirvani University of Technology, Babol, Iran

PAPER INFO

Paper history:
Received 7 August 2021
Received in revised form 28 August 2021
Accepted 27 September 2021

Keywords:
Heavy-Duty Engine
Power Density
Injection Duration
Pressure Gradient

ABSTRACT

Due to limited space in transport vehicles, compression ignition (CI) engines with high power density have always been a priority. In heavy-duty diesel engines, direct injection results creation of the lean region in the space of the combustion chamber. Increasing the fuel penetration by changing injection duration is an effective solution to achieve a homogenous mixture. In this paper, the impact of changing injection duration in upgraded MTU-4000-R43L diesel engine on power characteristics, rate of heat release (RoHR), combustion phasing, emission and, most importantly, the gradient of pressure changes as a characteristic of the vibration and knocking of the engine, has been studied numerically. Numerical simulation is performed in AVL Fire which is coupled with reduced detail chemical kinetics. The fuel injection duration was varying from 14.6 to 35.6 ºCA, the in-cylinder mean pressure, the IMEP decreases, and the ISFC increases; however, as the fuel injection duration decreases, the pressure gradient rises; from the range of 30.6 degrees onwards, the reduction of the fuel injection duration leads to a severe knock of the engine and as a result reduces its engine life. Emission results also showed that CO_2 and NOx increased and CO reduced with decreasing fuel decreasing injection duration.

***doi**: 10.5829/ije.2021.34.11b.08*

NOMENCLATURE

3D	Three Dimensional	IMEP	Indicated Mean Effective Pressure
aBDC	After Bottom Dead Center	ISFC	Indicated Specific Fuel Consumption
aTDC	After Top Dead Center	IVC	Intake Valve Closing
BDC	Bottom Dead Center	LHV	Low Heating Value
CAD	Crank Angle	PFI	Port Fuel Injection
CFD	Computational Fluid Dynamics	RoHR	Rate of Heat Release
EVO	Exhaust Valve Opening	TDC	Top Dead Center

1. INTRODUCTION

Diesel engines can be used in a variety of applications due to their high power density and efficiency; also, among the types of internal combustion engines, diesel engines have a high compression ratio; therefore, mentioned engines have the highest heat efficiency among internal and external combustion engines [1]. Therefore, diesel engines are applicable in different sizes and applications [2]. One of the most important applications of heavy diesel engines is their applicant as the driving force of transportation systems [3]; however, it is important to note that in heavy diesel engines, due to the high volume of the combustion chamber, a homogeneous air-fuel mixture of fuel and air is not normally formed before the combustion process begins; This creates lean areas inside the combustion chamber, and by reducing the combustion quality, part of the fuel is exhausted from the engine unburned. This will reduce the thermal efficiency of the engine in different operating conditions [4]. Different methods have been proposed to solve this problem, all of which are based on increasing the level of homogenization of the fuel-air

*Corresponding Author Institutional Email: *rshafaghat@nit.ac.ir* (R. Shafaghat)

Please cite this article as: B. Alizadeh Kharkeshi, R. Shafaghat, M. Mohebbi, S. Talesh Amiri, M. Mehrabiyan, Numerical Simulation of a Heavy-duty Diesel Engine to Evaluate the Effect of Fuel Injection Duration on Engine Performance and Emission, International Journal of Engineering, Transactions B: Applications, Vol. 34, No. 11, (2021) 2442-2451

mixture by earlier fuel injection [5]. The main problem of implementing this type of strategy is the impossibility of precise control of the start of combustion and, of course, control of engine performance at different speeds and high loads [6]. On the other hand, changing the injection duration may cause a change in the flow regime and collide the fuel spray with the edge of the piston bowl rim edge [7]. Therefore, this set of scientific strategies for internal combustion engines have so far been used only in laboratory conditions and light applications. In addition, focusing on fuel injection characteristics can greatly help improve the performance of compression ignition engines in injection duration conditions. In evaluating engine performance, it is necessary to consider the fuel injection strategy to control combustion. It is noteworthy that the momentary change of fuel injection along with the momentary change of combustion start will have different effects on engine power and performance [8-10]. The use of the EUI (Electronic Injector Control Unit) system is one of the significant advances in diesel engines that has had a remarkable impact on fuel consumption, durability as well as emission standards. EUI technology, with better performance than traditional technologies, allows precise adjustment of fuel injection in terms of fuel injection duration, pressure and injection volume [8, 11]. Homogenization of fuel-air mixture in a heavy diesel engine depends on two characteristics of fuel penetration and diffusion in the combustion chamber [12]. Various factors such as fuel type and physical properties, nozzle hole diameter, in-cylinder pressure during the injection process, fuel droplet diameter, and fuel evaporation rate on fuel permeability in air mass inside the cylinder have an effect [12-14]. But the most effective factor on fuel penetration is the spray interval and pressure. At a constant mass flow rate, as the fuel injection duration decreases, it is predicted that the penetration into the combustion chamber will increase due to the rise in droplet velocity [15]. Vamankar and Morgan investigated the effect of fuel injection scheduling on the performance of a direct-injection (DI) single-cylinder diesel engine with a combined fuel. In this study, synthetic fuel with a volume composition of 10% CB and 90% diesel (Carbodiesel10) was applied. Studies have shown that with the consume of Carbodiesel10, the thermal efficiency increased by about 6.4% in some injection times and the specific fuel consumption decreased by about 11.9%; also, NOx emission increased by about 23% and smoke decreased by about 13.5% at 26° CA bTDC injection [16]. Malbec et al. [17] showed that, compared to conventional diesel combustion, abnormal operating conditions can cause further combustion delays. If these long delays are longer than the injection time, the combustion quality is significantly affected by the end of injection (EOI). Ignition delays were investigated through cylinder pressure analysis and lamp chemistry imaging. At TDC temperature of 850K or higher, injection time is longer than combustion delay. Therefore, EOI has no effect on combustion delay. At TDC temperature of 800K or lower, for a short injection time, ignition occurs after EOI, and combustion delay decreases as injection time decreases [17]. Koten and Paralagit [18] investigated the effect of diesel engine parameters on ignition delay. They showed that although there are many parameters that affect each other such as fuel consumption, greenhouse gas emissions and engine noise, the results are more related to the quality of combustion. In this regard, control of combustion start and ignition delay should be well analyzed. Turkan et al. [19] studied the fuel injection time in a diesel engine. They showed that injection time is a parameter that directly affects engine performance and emissions. Injection time can be varied by considering fuel characteristics, inlet air pressure and temperature, compression ratio, injection systems, engine speed, and combustion chamber design. In a numerical study using GT-POWER software, Abu Ahmad et al. [20] investigated the effect of instantaneous fuel injection on engine performance and emissions and found the optimum operating point for a six-cylinder diesel engine by the turbocharger. The simulations were performed at four separate injection times (5, 10, 20 and 25ºCA bTDC) and constant engine speed (1800 rpm). Delay in injection time along with reduction of NO_2 and CO_2 pollutants increased HC and CO_2 emissions. The results also showed that early injection time (20◦ CA bTDC and 25◦ CA bTDC) reduces CO_2, emissions of unburned hydrocarbons and also increases the thermal efficiency of the engine. Biramoglu and Nouran [21] studied the effect of fuel injection duration (injection duration) on diesel engine performance and emissions. In their study, the effects of different injection times on diesel engine performance and exhaust emissions were investigated using computational fluid dynamics (CFD). Numerical study was performed on a four-stroke single-cylinder engine. In this study, combustion chamber velocity profiles, fuel mass change, temperature, pressure, heat release rate were determined for standard operating conditions. Rosa et al. [22] used a single-cylinder research engine to experimentally determine the effect of different strategies and fuel injection duration on combustion, emission characteristics and engine performance. They found that advanced injection time increased the RoHR in the early stages of combustion. by decreasing SOI and BMEP increased and BSFC and exhaust gas temperature decreased significantly; also, the emissions of carbon dioxide and unburned hydrocarbons were significantly reduced. Long et al. [23] conducted a study on knock intensity due to non-uniform temperature distribution in the engine in the form of two and three-dimensional simulations with regular temperature changes. Gikwad et al. [24], in the form of an experimental and numerical study of a piston engine, investigated the effects of peak pressure on the occurrence of knock in the engine. They showed that with increasing peak pressure values, the potential for knock occurrence increases. In heavy-duty diesel engines, due to the high volume of the cylinder, the fuel does not fully combine with the air inside the cylinder; earlear fuel injection is one of the new methods to increase the homogenization of the fuel-air mixture. However, considering this strategy in heavy diesel engines, it is not possible to control the engine at different loads. In the present paper, the possibility of increasing engine efficiency by increasing the amount of fuel penetration in the air mass in the cylinder has been investigated. In this regard, an attempt has been made to carry out investigations during a combustion cycle by constantly considering the mass of the injection fuel by changing the fuel injection duration. For this purpose, the fuel injection duration at maximum speed and load in the upgraded MTU4000 R43L heavy diesel engine as the target engine has been numerically evaluated. Numerical simulation in the AVL Fire software environment is performed in the form of a coupling with a detailed chemical kinetics code. The important point in this study is to consider the engine performance limitation by changing the fuel injection duration, which can cause knocking and the possibility of damage to the engine.

2. METHODOLOGY

2. 1. Governing Equations and Solution Method

AVL Fire software is applied to numerically simulate the closed cycle of the engine. The governing equations in this section include the equation of continuity, momentum, energy, and equations of the turbulence model by k-ζ-f model have implemented [25]. In studying the performance of an internal combustion engine, solving chemical equations is necessary to evaluate fuel oxidation and heat release. During the fuel oxidation process, in addition to the temperature and pressure of the combustion chamber, it is crucial to be aware of the production and consumption of some species, including free radicals of hydrogen [26]. According to the objectives of this study, the accuracy of calculations is very important to investigate the effect of fuel injection duration on the combustion process. Therefore, in this work, detailed chemical kinetics code has been used to solve chemical equations and raise the accuracy of the results. The flowchart shown in Figure 1 shows the simultaneous simulation steps of AVL Fire software as a coupling with chemical coupled kinetics code. According to the figure, after executing and checking the geometry and mesh, considering the boundary conditions and thermodynamic conditions in the software, a numerical simulation based on mass and momentum survival equations is performed. Kelvin-Helmutz and Riley-Taylor models were applied to simulate fuel injection. After completing the calculations related to computational fluid dynamics, combustion calculations are carried out. Suppose the computational cell temperature is above 600 K. In that case, the data from the kinetic code of combined combustion of diesel and gasoline fuels, which include 77 species and 457 reactions, were applied to modify data such as species concentrations and heat release. These steps were repeated until the crank angle reaches the moment of opening the exhaust valve. It should also be noted that the Zeldovich method was implemented to calculate the amount of NOx in the chemical coupled kinetics code (Figure 1) [7].

2. 2. Validation

The engine studied in this research is MTU-4000 R43L, the specifications of which are presented in Table 1. In this engine, a common rail system is applied for the direct injection of fuel into the combustion chamber. Table 2 summarizes the specifications of the direct fuel injection system. For validation, numerical results are compared with experimental data. In this regard, the performance of MTU4000 R43L engine was studied in an experimental test. Figure 2 shows a schematic diagram of the engine and other equipment required in the experimental test room.

According to the objectives of the present study, experimental tests were performed at 1800 rpm and maximum load. To apply the defined load, the HORIBA hydraulic dynamometer model DT3600-2 is used (Table 3). The pressure inside the cylinder is also measured by the piezoelectric pressure sensor KISTLER 6613CA and

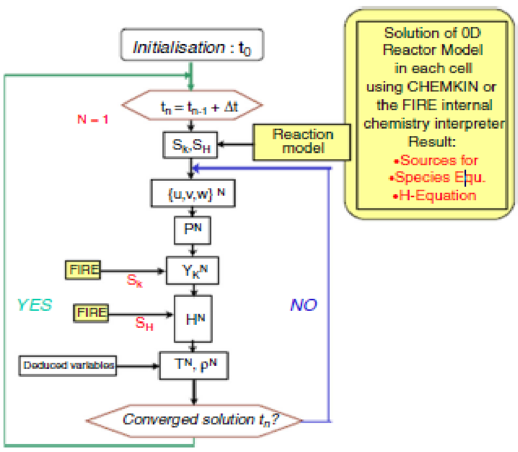

Figure 1. The strategy of coupling AVL fire and detailed chemical kinetics [7]

TABLE 1. Engine Characteristics [27]

Item	Specification
Type	Heavy-Duty Diesel Engine MTU4000-R43L
Bore (mm)	170
Stroke (mm)	190
Displacement (cc)	51.7
Compression ratio	18
Intake valve closing (CAD aBDC)	5
Exhaust valve opening (CAD bBDC)	50
Number of cylinders	16

TABLE 2. Specifications of the direct fuel injection system and fuel injection in port [27]

Items	Common-rail injection system
Number of holes	8
Hole diameter (mm)	3.5
Spray angle	6
Injection pressure (bar)	1600

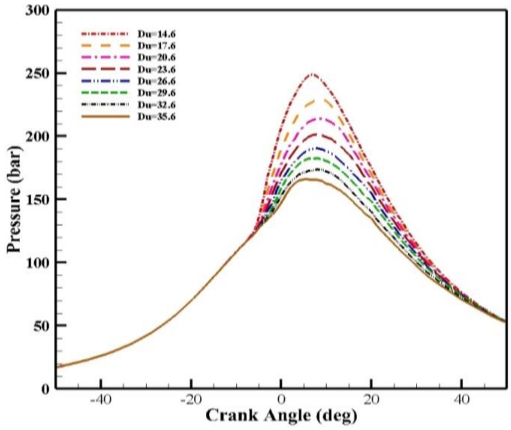

Figure 2. In-cylinder mean pressure change by engine crank angle

the amplifier KISTLER 5018. The measured pressure data were compared with similar numerical results In order to validate the simulation. To derive numerical results, the MTU4000 R43L heavy-duty diesel engine is first simulated in a closed cycle between the time the air valve closes and the smoke valve opens. According to the available information from the laboratory study and considering the number of nozzle holes, for numerical simulation in AVL fire software environment, one-eighth of the piston geometry has been used for modeling and meshing. According to the size and geometry of the solution field, the number of computational cells was considered to be about 31,400 (Figure 3).

TABLE 3. Specifications of HORIBA DT3600-2 hydraulic dynamometer

Item	Unit	Specification
P_{nom}	kW	3600
Maximal Speed n_{max}	1/min	3000
Rated Torque M_{nom}	Nm	30000
max. Share of Coupling Mass at n_{max} /Distance from the coupling flange	Kg	280/114
Θ Rotor	kgm^2	18.4
Torsion-spring constant up to middle of dynamometer	10^6 Nm/rad	11.9
Weight	kg	3200

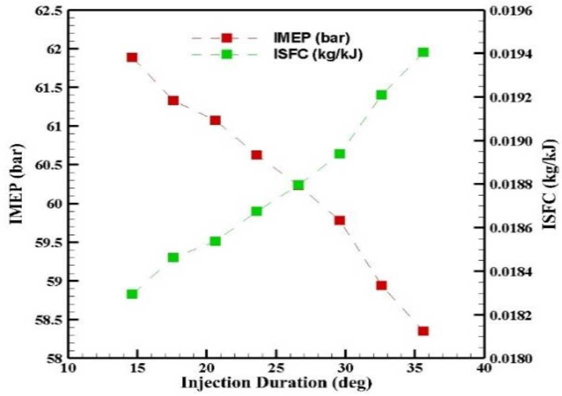

Figure 3. Varying IMEP and ISFC by injection duration

It is observed that the mean pressure inside the cylinder is very well coordinated with the experimental data. In practice, numerical simulation and solving the problem by computational fluids dynamics reached a good agreement with experimental data. Port and diesel fuel characteristics are shown in Table 4.

3. RESULTS AND DISCUSSIONS

One of the key characteristics that significantly affect the performance of a CI engine is the fuel injection

TABLE 4. Diesel fuel charctristics [7]

Items	Diesel
Chemical formula	C12-C25
Cetane number	52.1
Octane number	-
Density (gr/mL)	0.845
Low Heating Value (Mj/kg)	42.8
Latent heat of vaporization (kJ/kg)	301
Viscousity (Mpa.s)	3.995

strategy. In CI engines, to increase the level of homogenization, the reduction of lean areas in the combustion chamber is implemented in different strategies, which are based on increasing fuel penetration and more diffusion, and thus, enriching the mixture. Fuel and air enter the engine cylinder in different areas. Increasing fuel penetration is possible by increasing the velocity of the fuel droplets sprayed from the injector. It is necessary to raise the fuel injection pressure. Therefore, in this research, by keeping the mass of the injection fuel constant in a heavy diesel engine, the effect of changes in the fuel injection duration is investigated. Figure 2 shows the changes in the average pressure inside the combustion chamber at different fuel injection duration. As the fuel injection duration decreases, so do the maximum pressure inside the engine cylinder, since as the fuel injection duration declined, the fuel penetration naturally increases, and as the leaner areas decrease, a better homogeneous mixture of fuel and air is formed, which causes more mass of fuel to participate in the combustion process, therefore at each stage, with decreasing fuel injection duration, the maximum average pressure inside the cylinder is increased. One of the important points in studying the pressure inside the cylinder is to study the trend of maximum pressure changes in different fuel injection duration. As can be seen in Figure 2, the step of increasing the maximum pressure in the injection duration less than 20.6 CA is significantly more than the injection duration less than this value, so that by reducing the fuel injection duration from 26.6 degrees to 14.6 CA, the maximum pressure has increased by about 11.5 percent, if this characteristic reduced from 35.6 to 32.6 CA around it has increased by 6.3%.

Figure 4 shows the indicated mean effective pressure (IMEP) change rate with respect to the change in fuel injection duration. As can be seen, with decreasing fuel injection duration from 14.6 to 35.6, the amount of IMEP has been continuously increasing.

Considering that reducing the fuel injection duration, if fuel mass keeps constant increases the penetration of fuel droplets in the combustion chamber during the fuel injection process, which results in a reduction of lean areas and the participation of more mass of fuel in the combustion process. It is also worth noting that the reduced the fuel injection duration, the more volume of fuel is injected in a shorter period of time, the combustion process will start at a smaller volume of the combustion chamber. This will increase the indicator mean effective pressure value, which is one of the characteristics of the output power.

Indicator-specific fuel consumption is one of the efficient characteristics of the internal combustion engine. This characteristic shows how much output power is generated in relation to the fuel consumed. As can be seen in Figure 2, by decreasing the fuel injection duration, the value of this characteristic has reduced, which is due to the constant mass of the fuel in the injector and the increase of the maximum pressure inside the cylinder and, consequently, the output power by reducing the fuel injection duration.

Figure 4 shows the changes in the heat release rate; in this figure, the starting of heat release rate and its process for different injection duration is shown. According to the marked part of the figure, it can be seen that the combustion conditions in different duration are divided into two parts; in the injection duration, less than 23.6° CA, heat release rate at the starting point is much more than the others. At injection duration greater than 29.6° CA, is heat release rate has lower gradient, but one of the most thought-provoking points in this figure is the injection duration of 26.6 °CA. As can be seen, the heat release rate gradient is similar to the other durations up to 70 Joules, but it can be seen that in the continuation of the heat release process, the gradient of the same heat release increases with injection duration. In fact, Du = 26.6 is an injection duration of transition between two combustion processes. Also, in Figure 5,

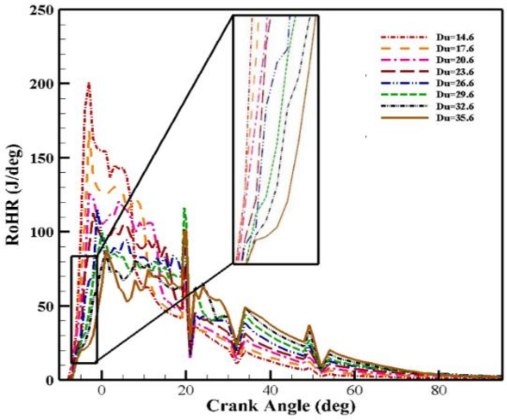

Figure 4. Varying RoHR by crank angle

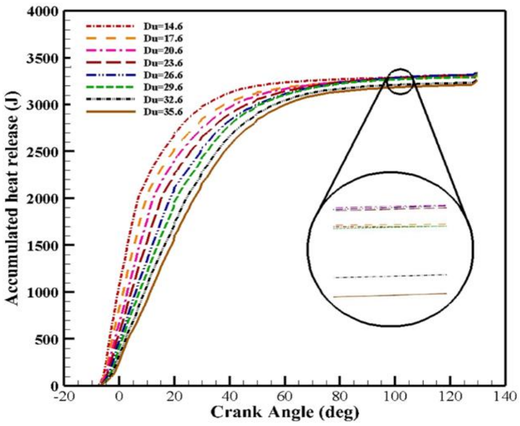

Figure 5. Varying cumulative heat release rate by the crank angle

the accumulated heat release is shown. In this figure, the total accumulated of heat released in the injection duration of 32.6º CA and 35.6 º CA is less than other fuel injection duration, which injection duration, that by reducing the injection duration, more fuel mass participates in the combustion process due to the reduction of lean areas.

Combustion duration (CD) is the duration which 5 to 90% of the total heat release. Ignition delay is also characterized by the duration between the fuel injection and 5% of the total heat release. One of the most important performance characteristics of CI engines is ID and CD, on the basis of which the fuel injection duration is set. As can be seen in Figure 6, as the fuel injection duration decreases, the ignition delay rate decreases continuously, since as the fuel injection duration reduced, the start of fuel injection is considered fixed. The whole mass of fuel is injected into the engine closer to the start of injection, which causes combustion to start earlier due to the higher volume of fuel and reduce the ignition delay; but according to the diagram of changes in the combustion duration, a different process takes place. In the injection duration between 35.6 to 29.6 degrees, as the injection duration decreases, the fuel is injected in a shorter duration, so the total combustion process takes less time; however, in the injection duration of 26.6, the combustion duration is suddenly decreased. As shown in Figure 4, it was observed that this injection duration is in fact, a transition between different combustion processes. In low injection durations, the combustion process started with a larger gradient due to the higher volume of fuel compared to other injection durations, and then the combustion process gradient has decreased since the injection penetration velocity is lower than the combustion development. On the other hand, the greater portion of the fuel participated in combustion; therefore, combustion duration increased in comparison with the injection duration of 29.6 CA, then combustion duration decreased as the injection duration reduced.

Figure 7 shows the CA50 (the moment which half of the heat of the entire combustion process is released). As the fuel injection duration decreases, the CA50 reduced continuously. This means that as the fuel injection duration decreases, the entire fuel combustion process takes place at a distance closer to the TDC and naturally in a smaller volume of the combustion chamber. This will have two consequences; the first consequence is an increase in engine power due to the increase in maximum pressure inside the combustion chamber, which leads to an increase in thermal efficiency, as shown in Figure 8, the ISFC reduced. But, the second consequence of this event is the early formation of combustion and start of combustion before the TDC and the application of negative work in the piston and combustion chamber. Due to the fact that in

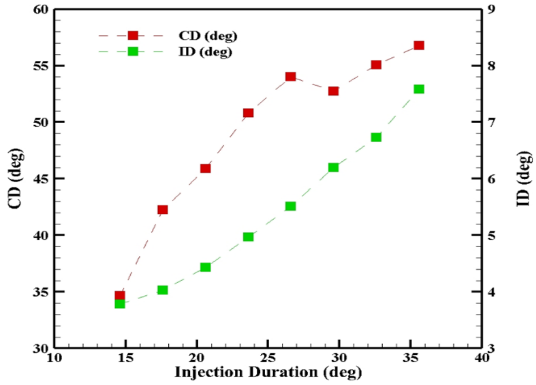

Figure 6. Varying ID and CD by injection duration

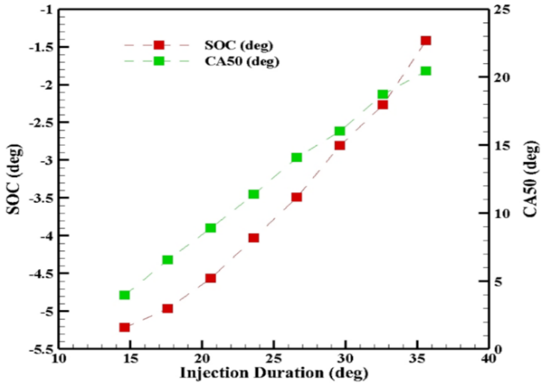

Figure 7. Varying start of combustion and CA50 by injection duration

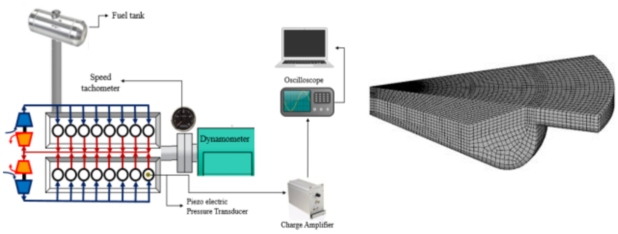

(a)

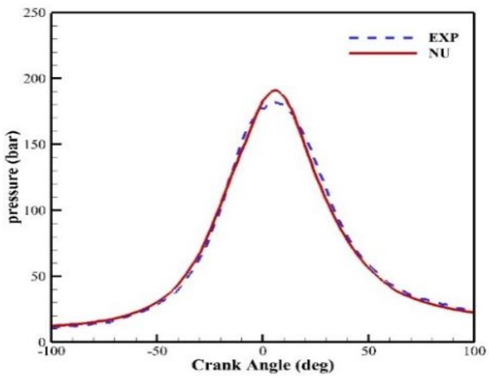

(b)

Figure 8. Validation of numerical simulation process by considering the diagram of the mean pressure inside the chamber

this particular engine, the start time of fuel injection is 9 degrees before the TDC, so the second consequence does not have a significant impact on the engine power and the total work.

Figure 9 shows the maximum gradient of the pressure diagram and the moment of maximum pressure increase in the combustion chamber. The maximum gradient of the actually injection durationicates the vibration and noise of the engine which cause serious damages to the cylinder body, cylinder head, connecting rod and engine crankshaft. According to the figure, the maximum gradient of the pressure diagram decreases with increasing fuel injection duration. In the duration range of 35.6 to 32.6, the maximum gradient of the pressure diagram does not increase slightly, but from Du = 32.6 to Du = 35.6 because a larger portion of the fuel is involved in the combustion process, the value of this characteristic increases dramatically. In the injection duration of 26.6, which was introduced as a transition mode in the previous sections, up to the duration of 20.6, the maximum gradient of the pressure diagram has not increased significantly. In the injection duration between 20.6 and 14.6 degrees, the value of this characteristic has increased sharply. As can be seen in these cases, the point at which the amount of pressure reaches its maximum change is 4 degrees before the TDC, which means that in addition to the fact that the pressure suddenly increases, the volume of the combustion chamber is decreasing. This causes a sudden increase in pressure inside the cylinder, and in fact, the reason for the change in the maximum pressure changes mentioned in Figure 8 is the occurrence of this phenomenon. This event, which is an injection duration of knocking process, will cause severe damage to the engine, as well as increase the noise and vibration of the engine, so reducing the fuel injection duration is not so desirable, but to increase power and efficiency can be reduced the duration to 20.6 degrees.

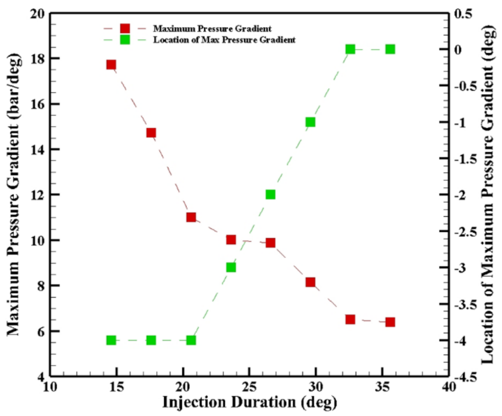

Figure 9. Varying the pressure gradient maximum and the location by injection duration

Figure 10 shows the effect of fuel injection duration on carbon monoxide and carbon dioxide greenhouse gas emissions. The more homogeneous a mixture of fuel and air is formed, and the more oxygen is introduced into the chemical process, the lower amount of carbon monoxide. By reducing the fuel injection duration, the fuel penetration increases, and in different areas of the combustion chamber space, the fuel-air composition becomes more homogeneous. It can be said that the lean areas are reduced, participates in the combustion process, and causes the combustion process of the fuel to move towards complete combustion, which increases CO_2 (which is in fact the product of combustion and a sign of complete combustion). At injection duration of fewer than 35.6 degrees, the value of these two species does not change significantly, which injection duration that in this case, the mixture has reached its most homogeneous state, and as shown in Figure 11. The most amount of fuel has participated in the combustion process, which injection duration the high condition of combustion conditions and increased engine efficiency. It can also be seen in Figure 11 that the amount of NOx pollution has increased continuously with decreasing injection duration. This is studied in Figure 8; however, in increasing the injection duration from 32.6 to 35.6, the increase in this pollution is very significant, because in this interval. According to Figure 9, the sudden increase in pressure coincides with a decrease in volume and causes an excessive increase in pressure and its nature. The temperature has risen, which is the most important reason for the increase in NOx. On the other hand, by reducing the fuel injection duration, the unburned hydrocarbon in the engine decreases to the injection duration of 23.6.6 degrees, which injection duration increase in IMEP and engine temperature due to the reduction of the fuel injection duration. Up to this point, due to better penetration and distribution of fuel and reduction of lean areas in the engine. But, by reducing the fuel injection duration to less than 23.6 degrees, and the reason for increasing performance

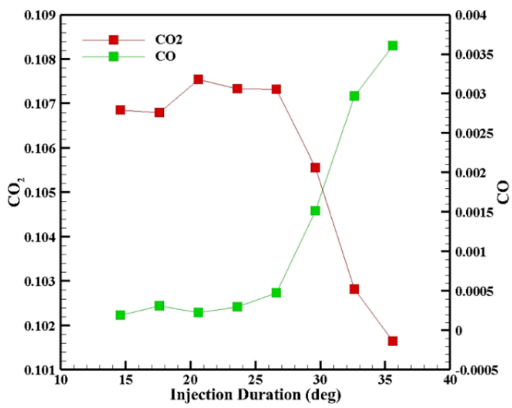

Figure 10. Varying CO_2 and CO by injection duration

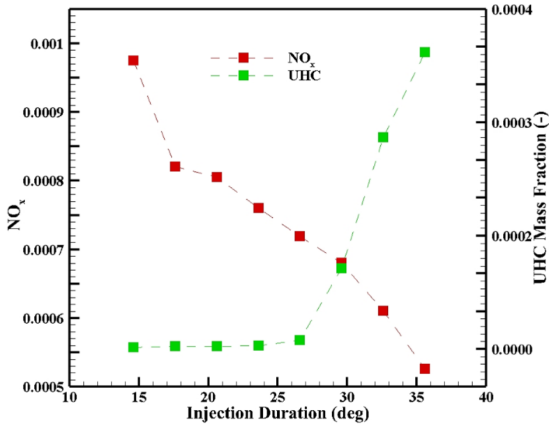

Figure 11. Varying NO_x and UHC by injection duration

parameters is not better and more fuel consumption, it should be considered in the engine phase change of combustion.

Table 5 shows the concentration of diesel fuel in a different piston position for different fuel injection duration. Studying the trend of changing the contours in the position 4 degrees before the TDC, it is clearly seen that by reducing the fuel injection duration, the penetration and diffusion of fuel has increased, and even more volume of fuel has been injected up to that point. As can be seen, when the piston is at the TDC, it is evenly distributed over the entire dead volume in the shortest injection duration, and this results in the condition that the combustion chamber has its lowest volume, the volume of lean areas reaches its lowest

TABLE 5. Fuel concentration contour inside the chamber at different positions

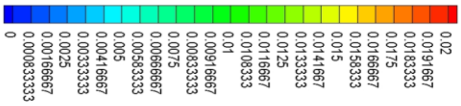

Injection Duration	-4˚CA	0˚CA	10˚CA
14.6	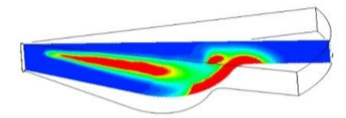	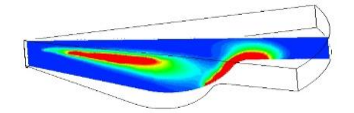	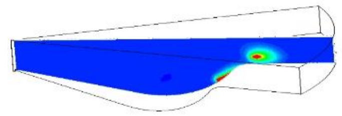
17.6	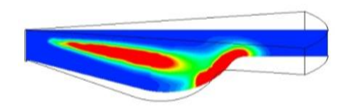	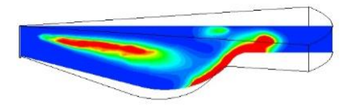	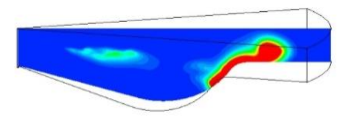
20.6	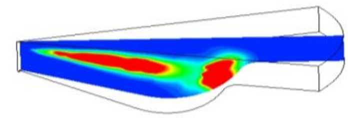	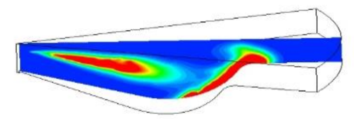	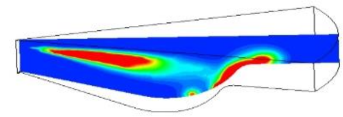
23.6	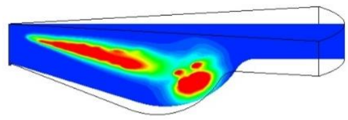	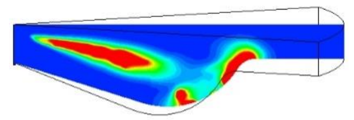	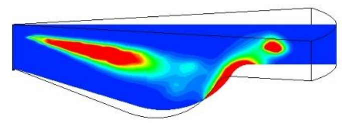
26.6	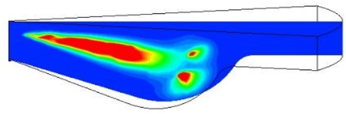	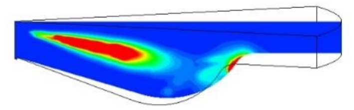	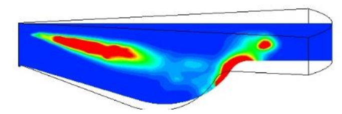
29.6	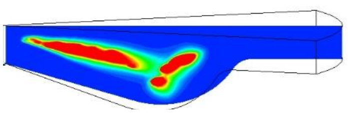	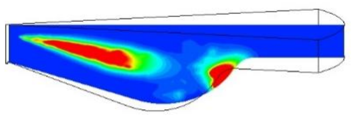	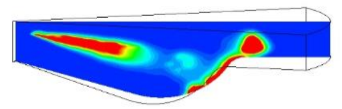
32.6	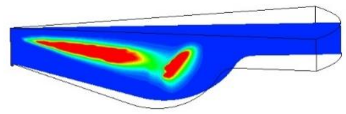	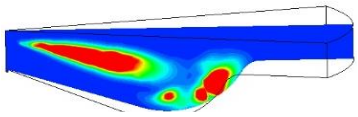	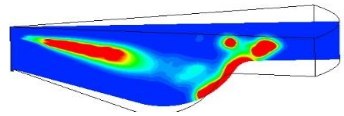
35.6	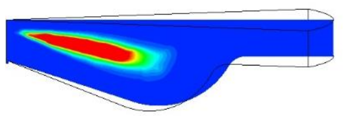	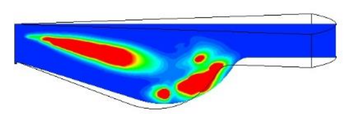	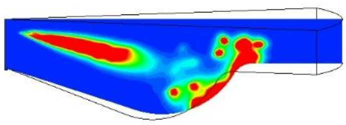

level. On the other hand, in the position of 10 degrees after the TDC in the lowest fuel injection duration, a large volume of fuel is consumed. Gradually, with increasing the fuel injection duration, the volume of the unconsumed fuel has increased increases.

4. CONCLUSIONS

An upgraded version of the MTU-4000 R43L engine has been used to investigate the feasibility of increasing the power density of the heavy diesel engine (with the set of changes that have been made in the study phase, it has the ability to provide more power than the base engine). In this study, the effect of changing the fuel injection duration on the performance of an upgraded, heavy-duty 16-cylinder MTU4000-R43L diesel engine was numerically studied. In this regard, to numerically simulate the engine, AVL Fire software was implemented by coupling with chemical joint kinetics code. In order to evaluate the effect of these conditions on combustion, important parameters such as in-cylinder pressure, temperature, released heat rate, IMEP, ISFC, combustion duration, combustion delay, combustion start, and pollutants have been investigated. The results obtained show:

- Reducing the duration of fuel injection leads to an increase in pressure and temperature of the combustion chamber, and also the gradient of this increase in temperature and pressure increases with decreasing fuel injection duration. Increasing the fuel injection duration also reduces the rate of heat released into the chamber.
- Increasing the duration of fuel injection duration leads to a decrease in the pressure inside the chamber, and the IMEP and an increase in the injection duration ISFC, or in other words, it can be said power increase by reducing injection duration.
- As the fuel injection duration decreases, the pressure gradient increases, which can cause the knock and vibration of the engine, so that the duration decreases from 20.6 °CA fuel injection will result in severe engine knock and thus reduce its service life.
- Increasing the fuel injection duration can increase the lean areas inside the chamber. However, the better the fuel penetration, the more complete the combustion. The results showed that the higher
- The carbon dioxide (Injection duration better combustion) increases with decreasing fuel injection duration decreases carbon monoxide (injection duration incomplete combustion). The temperature of the combustion chamber increases so does the production of NO_x.

5. REFERENCES

1. Pulkrabek, W.W., *Engineering fundamentals of the internal combustion engine*. 2004. https://doi.org/10.1115/1.1669459
2. Kirkpatrick, Allan, Yuan Li, Charles Mitchell, and Bryan Willson. "Analytical and Computational Modeling of High Pressure Gas Injection.", Internal Combustion Engine Division Fall Technical Conference, Vol. 80142, 25-32. (2001), American Society of Mechanical Engineers,. https://doi.org/10.1115/2001-ICE-410.
3. Kasper, A., Aufdenblatten, S., Forss, A., Mohr, M. and Burtscher, H., "Particulate emissions from a low-speed marine diesel engine", ***Aerosol Science and Technology***, Vol. 41, No. 1, (2007), 24-32. https://doi.org/10.1080/02786820601055392
4. Buchwald, R., Brauer, M., Blechstein, A., Sommer, A. and Kahrstedt, J., "Adaption of injection system parameters to homogeneous diesel combustion", ***SAE Transactions***, (2004), 551-562. https://www.jstor.org/stable/44723530
5. Shim, E., Park, H. and Bae, C., "Comparisons of advanced combustion technologies (hcci, pcci, and dual-fuel pcci) on engine performance and emission characteristics in a heavy-duty diesel engine", ***Fuel***, Vol. 262, (2020), 116436. https://doi.org/10.1016/j.fuel.2019.116436
6. Jain, A., Singh, A.P. and Agarwal, A.K., "Effect of fuel injection parameters on combustion stability and emissions of a mineral diesel fueled partially premixed charge compression ignition (pcci) engine", ***Applied Energy***, Vol. 190, (2017), 658-669. https://doi.org/10.1016/j.apenergy.2016.12.164
7. Talesh Amiri, S., Shafaghat, R., Jahanian, O. and Fakhari, A., "Numerical investigation of reactivity controlled compression ignition engine performance under fuel aggregation collision to piston bowl rim edge situation", ***Iranian (Iranica) Journal of Energy & Environment***, Vol. 12, No. 1, (2021), 10-17. https://dx.doi.org/10.5829/ijee.2021.12.01.02
8. Ghaedi, A., Shafaghat, R., Jahanian, O. and Hasankola, S.S.M., "Comparing the performance of a ci engine after replacing the mechanical injector with a common rail solenoid injector", ***Journal of Thermal Analysis and Calorimetry***, Vol. 139, No. 4, (2020), 2475-2485. https://doi.org/10.1007/s10973-019-08760-1
9. Fakhari, A.H., Shafaghat, R., Jahanian, O., Ezoji, H. and Hasankola, S.S.M., "Numerical simulation of natural gas/diesel dual-fuel engine for investigation of performance and emission", ***Journal of Thermal Analysis and Calorimetry***, Vol. 139, No. 4, (2020), 2455-2464. https://doi.org/10.1007/s10973-019-08560-7
10. Hasankola, S.S.M., Shafaghat, R., Jahanian, O. and Nikzadfar, K., "An experimental investigation of the injection timing effect on the combustion phasing and emissions in reactivity-controlled compression ignition (rcci) engine", ***Journal of Thermal Analysis and Calorimetry***, Vol. 139, No. 4, (2020), 2509-2516. https://doi.org/10.1007/s10973-019-08761-0
11. Verma, G., Prasad, R.K., Agarwal, R.A., Jain, S. and Agarwal, A.K., "Experimental investigations of combustion, performance and emission characteristics of a hydrogen enriched natural gas fuelled prototype spark ignition engine", ***Fuel***, Vol. 178, (2016), 209-217. https://doi.org/10.1016/j.fuel.2016.03.022
12. Zhou, X., Li, T., Wei, Y. and Wang, N., "Scaling liquid penetration in evaporating sprays for different size diesel engines", ***International Journal of Engine Research***, Vol. 21, No. 9, (2020), 1662-1677. https://doi.org/10.1177/1468087419889835
13. Pickett, L.M., Genzale, C.L. and Manin, J., "Uncertainty quantification for liquid penetration of evaporating sprays at

diesel-like conditions", ***Atomization and Sprays***, Vol. 25, No. 5, (2015). 10.1615/AtomizSpr.2015010618

14. Du, J., Mohan, B., Sim, J., Fang, T. and Roberts, W.L., "Macroscopic non-reacting spray characterization of gasoline compression ignition fuels in a constant volume chamber", ***Fuel***, Vol. 255, (2019), 115818. https://doi.org/10.1016/j.fuel.2019.115818
15. Yontar, A.A., "Injection parameters and lambda effects on diesel jet engine characteristics for jp-8, fame and naphtha fuels", ***Fuel***, Vol. 271, (2020), 117647. https://doi.org/10.1016/j.fuel.2020.117647
16. Wamankar, A.K. and Murugan, S., "Effect of injection timing on a di diesel engine fuelled with a synthetic fuel blend", ***Journal of the Energy Institute***, Vol. 88, No. 4, (2015),406-413. https://doi.org/10.1016/j.joei.2014.11.003
17. Malbec, L.-M., Eagle, W.E., Musculus, M.P. and Schihl, P., "Influence of injection duration and ambient temperature on the ignition delay in a 2.34 l optical diesel engine", ***SAE International Journal of Engines***, Vol. 9, No. 1, (2016), 47-70. https://www.jstor.org/stable/26284796
18. Köten, H. and Parlakyiğit, A.S., "Effects of the diesel engine parameters on the ignition delay", ***Fuel***, Vol. 216, (2018), 23-28. https://doi.org/10.1016/j.fuel.2017.11.136
19. Turkcan, A., Altinkurt, M.D., Coskun, G. and Canakci, M., "Numerical and experimental investigations of the effects of the second injection timing and alcohol-gasoline fuel blends on combustion and emissions of an hcci-di engine", ***Fuel***, Vol. 219, (2018), 50-61. https://doi.org/10.1016/j.fuel.2018.01.061
20. Ahmed, S.A., Zhou, S., Zhu, Y., Feng, Y., Malik, A. and Ahmad, N., "Influence of injection timing on performance and exhaust emission of ci engine fuelled with butanol-diesel using a 1d gt-power model", ***Processes***, Vol. 7, No. 5, (2019), 299. https://doi.org/10.3390/pr7050299
21. Bayramoğlu, K. and Nuran, M., "Analyzing the effect of fuel injection timing and injection duration on performance and emissions in diesel engines", ***Journal of ETA Maritime Science***, Vol. 8, No. 1, (2020), 38-52. https://doi.org/10.5505/jems.2020.99705
22. Rosa, J.S., Martins, M.E.S., Telli, G.D., Altafini, C.R., Wander, P.R. and Rocha, L.A.O., "Exploring the effects of diesel start of injection and water-in-ethanol concentration on a reactivity controlled compression ignition engine", ***Fuel***, Vol. 281, (2020), 118751. https://doi.org/10.1016/j.fuel.2020.118751
23. Luong, M.B., Desai, S., Pérez, F.E.H., Sankaran, R., Johansson, B. and Im, H.G., "A statistical analysis of developing knock intensity in a mixture with temperature inhomogeneities", ***Proceedings of the Combustion Institute***, Vol. 38, No. 4, (2021), 5781-5789. https://doi.org/10.1016/j.proci.2020.05.044
24. Gaikwad, P.U., Gnanamani, S. and Subramani, N., "Experimental and numerical simulation of the piston engine fueled with alternative fuel blends: Cfd approach", ***Aircraft Engineering and Aerospace Technology***, (2021). https://doi.org/10.1108/AEAT-12-2020-0291
25. Hanjalić, K., Popovac, M. and Hadžiabdić, M., A robust near-wall elliptic-relaxation eddy-viscosity turbulence model for CFD. ***International Journal of Heat and Fluid Flow,*** Vol. 25, No. 6, (2004), 1047-1051. https://doi.org/10.1016/j.ijheatfluidflow.2004.07.005
26. Jahanian, O. and Jazayeri, S.A., "A comprehensive study on natural gas hcci engine response to different initial conditions via a thermo-kinetic engine model", in ASME 2009 Internal Combustion Engine Division Fall Technical Conference, American Society of Mechanical Engineers Digital Collection. (2010), 127-135. https://doi.org/10.1115/ICEF2009-14084
27. Kech, J., Schmidt, G., Philipp, C. and Rall, H., "Exhaust gas recirculation: Internal engine technology for reducing nitrogen oxide emissions", Engine Technology, MTU Friedrichshafen GmbH, www. mtu-online. com (2011), (2011). https://www.mtu-solutions.com/content/dam/mtu/download/technical-articles/131218_WhitePaper_Abgasrueckfuehrung_EN.pdf/_jcr_content/renditions/original./131218_WhitePaper_Abgasrueckfuehrung_EN.pdf

Persian Abstract

چکیده

با توجه به فضای محدود در وسایل نقلیه حمل و نقل ، موتورهای احتراق تراکمی (CI) به‌علت چگالی قدرت بالا همیشه در اولویت بوده اند. در موتورهای دیزلی سنگین، تزریق مستقیم باعث ایجاد ناحیه‌ی فقیر در فضای محفظه احتراق می شود. افزایش نفوذ سوخت با تغییر مدت زمان تزریق یک راه حل موثر برای دستیابی به مخلوط همگن است. در این مقاله ، تأثیر تغییر مدت تزریق در موتور دیزلی MTU-4000-R43L ارتقا یافته بر ویژگی های قدرت ، نرخ آزاد سازی حرارت، فاز احتراق ، آلایندگی و مهمتر از همه ، شیب تغییرات فشار به عنوان ویژگی ارتعاش و ضربه موتور، به صورت عددی مورد مطالعه قرار گرفته است. شبیه سازی عددی درنرم افزار AVL Fire با کوپل سینتیک شیمیایی کاهش یافته صورت پذیرفته است. مدت زمان تزریق سوخت از ۱۴.۶ تا ۳۵.۶ °CA تغییر داده شده است، میانگین فشار درون سیلندر، IMEP کاهش می یابد و ISFC افزایش می یابد. با این حال، با کاهش مدت زمان تزریق سوخت ، گرادیان فشار افزایش می یابد. از محدوده ۳۰.۶ درجه به بعد، کاهش مدت زمان تزریق سوخت منجر به ضربه شدید موتور و در نتیجه کاهش عمر موتور می شود. همچنین نتایج انتشار آلایندگی نشان داد که با کاهش مدت زمان تزریق، CO_2 و NOx افزایش یافته و CO کاهش می یابد.

IJE TRANSACTIONS B: Applications Vol. 34, No. 11, (November 2021) 2452-2466

International Journal of Engineering

Journal Homepage: www.ije.ir

High-contribution of Strip Glass Waste in Strengthening Slender Glass Reinforced Concrete Columns under Axial Compressive Load

Sumardi, T. Rochman*, I. R. Riskiyah

Civil Engineering Department, State Polytechnic of Malang, Indonesia

P A P E R   I N F O

Paper history:
Received 5 April 2021
Received in revised form 19 August 2021
Accepted 13 September 2021

Keywords:
Glass Reinforced Concrete
Buckling Failures
Axially Loaded Column Test
Glass-Reinforced Concrete Slim Columns
Alkali Silica Reaction Problem

A B S T R A C T

The important thing about axially loading slender columns is buckling stability. However, very limited researches were found, especially using glass-reinforced concrete. An alkali silica reaction (ASR) deterioration problem only occurs when particles are very fine. The utilization of glass as a particle was avoided, and bigger dimension of glass strip waste was utilized instead because cement cannot penetrate deep into the glass piece. A series of axial loading tests of glass-reinforced concrete (GLARC) slim columns were carried out on arrangement types; glass strips, homogenous and randomly pieces reinforced to explore their buckling performance. All axial GLARC columns capacity results were better than glassless columns reinforcement. The best reinforcement was longitudinal horizontal strip arrangement since they have consistent strength contribution hence allow the GLARC columns to resist higher axial loads to avoid buckling failures. The tests results in a good performance and hence GLARC columns have potential chances to be used extensively as structural compression members.

***doi**: 10.5829/ije.2021.34.11b.09*

NOMENCLATURE

EI	Flexural rigidity of column cross section	P_E	Euler buckling load
y	Deflection to the y-axis	N_E	Axial force for slender column
P_c	Critical axial load	$w(x)$	Lateral deflection in x-distance
ℓ	Length of the column	$e(x)$	Imperfection buckling in x-distance
n	number of half-sine waves in the deformed geometry of the column	π	3.14159265359

1. INTRODUCTION

Waste glass contributes significantly to environmental degradation, owing to the inconsistency in waste glass sources. With mounting environmental demand to eliminate solid waste and recycle as much as practicable, the concrete industry has implemented a variety of strategies to accomplish this aim. Research examined the properties of concretes comprising waste glass as fine aggregate was explored by Ismail and Al-Hashmi [1]. Indonesia is expected to generate 64 million tons of waste per year. According to statistics from the Ministry of Environment and Forestry (KLHK), glass waste accounted for 1.7% of overall waste in 2017 [2].

Nearly any form of building involves the use of concrete. Traditionally, concrete was made mainly of cement, water, and aggregates [3]. Additionally, coarse aggregate may be substituted with incinerator bottom ash aggregate and sintered fly ash pellets. The use of recycled glass aggregates (RGA), bottom ash from thermal power plants, and quarry dust as fine aggregates in concrete has considerable potential. RGA has significant potential for the use as a fine aggregate in concrete, including high performance concrete. Research has shown that concrete made with RGA as fine aggregate develops comparable or slightly higher strength and modulus of elasticity than concrete made with natural sand of the same grading, whereas flexural strength, creep, and shrinkage are essentially unaffected. RGA can also be used as a filler

*Corresponding Author Email: *taufiq.rochman@polinema.ac.id* (T. Rochman)

Please cite this article as: Sumardi, T. Rochman, I. R. Riskiyah, High-contribution of Strip Glass Waste in Strengthening Slender Glass Reinforced Concrete Columns under Axial Compressive Load, International Journal of Engineering, Transactions B: Applications, Vol. 34, No. 11, (2021), 2452-2466

aggregate in concrete to increase its strength and stiffness [4]. Some of the studies on glass materials, such as that conducted by Martens et al. [5], resulted in the creation of strengthened and prestressed glass beams. Despite fundamental variations in output and methods, the majority demonstrate superior behaviour, which results in increased substantial post-failure strength.

As a concrete composite, Feldmann and Langosch [6] investigated the behavior of structural concrete incorporating glass powder when added to reinforced concrete columns. The results indicated that substituting glass powder for 20% of the cement in a column measured at 28 days postponed cover cracking and marginally improved load-bearing capability and post-peak response.

In contrast to the findings above, a study conducted by Rosso et al. [7] on the properties of concrete incorporating recycled glass aggregates made from exploded lamp materials found that the greater the amount of recycled glass aggregate added, the less benefits the concrete features received from glass involvement. Microscopic research performed to understand this phenomena demonstrates the detrimental impact of the aggregate grain shape produced.

Yu et al. [8], on the other hand, investigated the durability of concrete constructed from steel slag and waste glass. Compressive power, flexural strength, and modulus of elasticity of steel slag concrete are equal to or perhaps greater than those of limestone aggregate concrete. As coarse aggregate was supplemented with up to 17.5% waste glass, there was just a minor influence on the concrete's mechanical properties. Steel slag and waste glass, due to their superior thermal and/or mechanical properties, have the potential to improve the fire resistance of concrete. However, researchers who have studied glass materials, have been left out of the way of applying glass piece reinforcement to concrete structures. This research focuses on the application of reinforcing broken glass piece in columns, which has not been studied well.

2. LIRERATURE REVIEW

2. 1. Column Buckling

Columns are classified as struc-tural members that suffer the majority of their loads in compression. Columns typically include bending moments along one or both of the cross section's axes, and the bending behavior can generate tensile forces across a portion of the cross section. Except in these situations, columns are commonly referred to as compression members due to their predominant action under compression powers. Columns are classified into two different categories: short columns, whose strength is determined by the material's strength and the cross section geometry, and slender columns, whose strength may be greatly diminished by lateral deflections [5]. The majority of structures of slim or slender dimensions that are subjected to compressive force can exhibit buckling instability. Buckling occurs when a structure is unable to retain its initial geometry and must adjust geometry to rebalance. Buckling is essentially a geometric problem in which there is a significant deflection that alters the form of the structure. Equilibrium states occur for the axially loaded column depicted in Figure 1 (left side). When a column is forced laterally at midheight and released, it returns to its original position; and so on. Figure 1 (right side) illustrates a section of a column in neutral equilibrium [5]. The differential equation for this column is:

$$EI\,\frac{d^2y}{dx^2} = -Py \tag{1}$$

In 1744, Leonhard Euler derived Equation (2) and its solution, where:

$$P_c = \frac{n^2\pi^2 EI}{\ell^2} \tag{2}$$

Figure 1 (right side) illustrates the cases of n = 1,2, and 3. For n = 1,0, the lowest value of Pc occurs. This results in what is known as the Euler buckling load:

$$P_E = \frac{\pi^2 EI}{\ell^2} \tag{3}$$

The equation for slender glass columns under an axial force N_E, using sinusoidal imperfection also developed by Feldmann and Langosch [6] as:

$$w''(x) + \frac{N_E}{EI}\cdot w(x) = -\frac{N_E}{EI}e(x)$$

Feldmann and Langosch [6] also derived the theory of imperfection buckling column. Therefore, buckling behaviour is critical to investigate, ever more so when the column geometry is slender and exhibits wall-like behavior, and even more so when subjected to cyclic or seismic loads, as earthquakes such stated in literature [7-10]. While several observation regarding column element or axial member in many research also can be seen in literature [11-15].

Figure 1. Imperfection buckling of a pin-ended column Source: [5]

2. 2. Glass Waste As seen from the lens of physics, glass is a very cold substance. Thus named due to the arrangement of the constituent particles being as far separated as they are in a liquid, but the glass itself being solid. This is because the cooling mechanism is so rapid that the silica particles do not have enough time to assemble themselves properly. Glass is composed of a variety of non-volatile inorganic oxides that are formed through the decomposition and fusion of alkaline and alkaline earth compounds, sand, and numerous other constituents. Glass's distinctive properties are determined by the uniqueness of silica (SiO_2) and the mechanism by which it is formed [10].

The roughness of the glass imparts an abrasion resistance to the concrete that only a few natural aggregates possess. In comparison to other ceramic types, glass exhibits unique characteristics. Typically, the glass is ground first to remove the rough points. Glass powders are generated during the grinding process as a consequence of scraping the outer side of the crushed glass. Typically, glass powder is discarded straight onto the ground, rather than being recycled, since shattered glass may be burned and reprinted [10].

A mix design preparation approach that is suitable is required to create a concrete mix design that satisfies quality standards and has a strong economic benefit [7]. There are several techniques for designing concrete mixes, including the following: (1) the trial and error process, which involves comparing concrete mixtures of varying composing materials in order to achieve a composition of a desired workability; and (2) the fineness modulus scheme. (3) The Department of Environment (DOE) process originated in the United Kingdom and is based on the basic compressive strength of concrete measuring 15 x 15 x 15 cm; (4) American Concrete Institute (ACI) method 61354. This process of developing concrete mixes originated in America and is focused on the compressive power of cylindrical concrete with a diameter of 15 cm and a height of 30 cm; (5) Shacklock's method of high strength concrete mix design, which is used for high strength concrete (> K.350 kg/cm^2).

Environmentally friendly concrete (green concrete) is a kind of concrete that is made from products that are not harmful to the environment. The erosion of rugged hills is an indicator of environmental degradation caused by the use of natural resources. The growing demand for concrete supply results in widespread extraction of rock, one of the constituent materials of concrete in the form of coarse aggregate, reducing the amount of natural resources usable for concrete purposes [16]. Coarse aggregate is the primary component of concrete. In environmentally sustainable concrete (green concrete), broken stone (split) may be substituted for broken tile aggregate derived from clay, synthetic aggregate derived from clay, or aggregate derived from crushed concrete waste [17]. Another research that utilizing waste or recycled glass in concrete was reported in literature [18-21].

2. 3. Alkali-Silica Reaction However, when glass sand or powder is used as a particle aggregate in reinforced concrete, alkali silica reaction (ASR) issues such as those depicted in Figure 2 often occurred in many researches [22-29].

However, an ASR alkali issue exists only with extremely fine particles. To prevent this problem, the use of glass as a particle was avoided; thus, the reinforcement proposed was structural in nature and therefore not material in nature. When the horizontal strip waste remains in the glass shop cutter, the dimension of glass strip waste is large enough. As a result, ASR would not occur here, as cement cannot penetrate deeply into the glass fragment, partial or complete substitution of cement with more environmentally sustainable products during the concrete manufacturing phase is a choice. Green concrete is a movement that seeks to empower building professionals such that while concrete is manufactured, what matters is that the concrete is environmentally safe, in compliance with its status, does not waste natural resources, and is forward-thinking in order to provide an atmosphere conducive to sustainable growth (sustainable development) [22].

3. AXIAL TEST METHODOLOGY

In this study, continuing the previous reseach regarding flexural loads [30, 31], five column specimens of varying glass waste arrangement were used, as shown in Figure 3.

In Figure 3, the first GLARC column specimen was namely as column without glass (CWG), and the second was random glass pieces (RGP), and the third was vertically strip longitudinal (VSL) cut, and the fourth was horizontally strip longitudinal (HSL) cut as uniform 1-2 cm long, and finally was uniformly homogeneous pieces (UHP). While the glass waste and columns specimens were depicted in Figure 4.

Figure 2. View of alkali silica reaction phenomenon

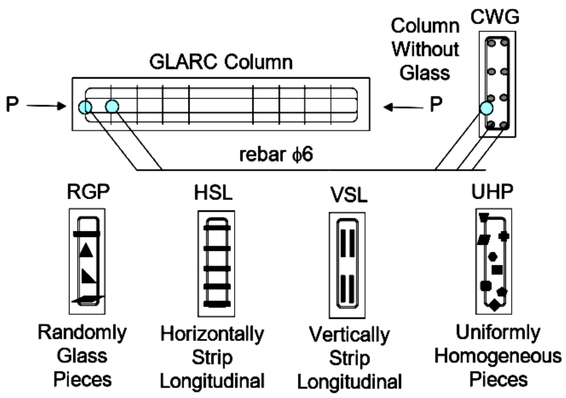

Figure 3. Variation of GLARC column specimens

Figure 4 (a) Glass-waste (b) Slim column specimens

Hydraulic jacking devices such as those depicted in Figure 5(a) and the loading dials are depicted in Figure 5(b), while the holder and clamp for dial mounting, as well as the dial gauge for calculating load and deflection, are depicted in Figure 5(c).

The loading frame used to validate the above structure is a 4m long I-profile steel frame, the details of which are shown in Figure 6(a) and support for dial gauges in Figure 6(b).

The data acquisition device was used to monitor the strain amplifiers' observed values automatically. The PCI expansion board interface used is the PCI-3126 with a 12 bit analog input board that comes with the GPF-3100 driver software. The limitations and requirements apply

Figure 5. (a). Hand pump (b) hydraulic jack, (c) Dial gauge, dial holder and clamp

Figure 6. (a) Loading frame; (b) dial gauge support

to relative humidity levels of 20%-90% (non-condensing). Figure 7(a) illustrates the way two wires for this system was mounted, and Figure 7(b) illustrates a PCI-3126 card in a PC machine slot to install.

The auxiliary software is used to configure the test, and all necessary information such as the strain gauge factor, calibration coefficient, and channel gain is input into the software.

A strain gauge is mounted axially on the tensile part (bottom) of the girder in the center section of the flexural test girder specimen, and the strain data is connects by data acquisition that recorded 6 channels simultaneously to the AS1803 strain amplifier shown in Figure 8, followed by a cable that connects to PCI-3126 12 bit analog input board embedded in a PC drivered by GPF-3100, where each line has its own processing unit that can take 8 data per second with a resolution of 16 bits and has 8 different input settings in range 10 V. When the input is increased, the measurement sensitivity rises proportionately, resulting in a smoother curve. Additionally, the strain gauge can be adjusted between + 5V and + 10V.

Strain gauges were used in Figure 9 to determine the strain, which has a factor of 2.09± 1%. This strain gauge

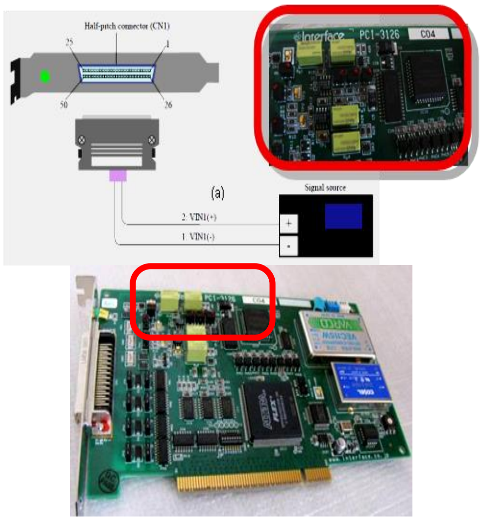

Figure 7. (a) Installation of cables using the two wires connection method; (b) PCI-3126 card that is installed in the computer slot and its inzet

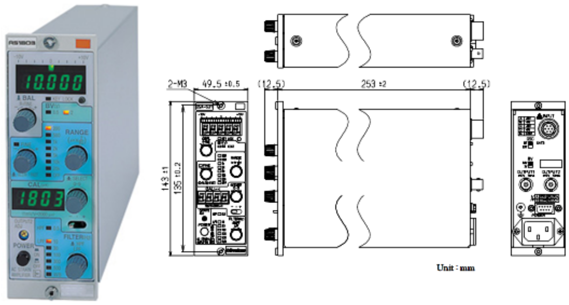

Figure 8. Strain amplifier AS-1803 connected to the PCI-3126 using the GPF-3100 driver software

is designed specifically for plastic materials and operates between 20˚C-80˚ C. It has a gauge length of 3 mm and a resistance of 120±0.3Ω. The strain gauge composite is a Cu-Ni alloy with a strain limit of 3%.

The hydraulic jack was positioned on the upper GLARC column with respect to the compression test specimen. The static load is then applied gradually before ultimate failure occurs (quasi-static). Figure 10 illustrates the configuration of the GLARC column specimen in the loading frame.

4. RESULTS AND DISCUSSION

The compressive axial load test results for CWG or glassless column specimens shown in Figure 11 reflect the initial loads before buckling, as well as the strain gauge location in the center of the glassless column length.

Figure 9. Strain gauge with a resistance of 120 ± 0.3 Ω

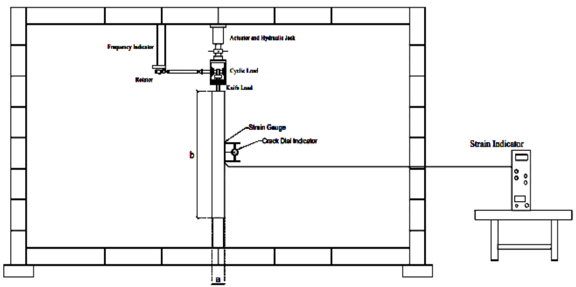

Figure 10. Setup of compressive test on GLARC column

Figure 11. (a) CWG as column without glass due to axial load before buckling occurs (b) position of the glassless column strain gauge

Owing to the large load on the support, the damage was localized. The failure area could not be exactly in the center of the column due to some imperfection in the column during testing.

As shown in Figure 12 a), a local failure occurred at the column support location. As illustrated in Figure 12 b), the location of failure in a CWG or unreinforced glass concrete column seems not on the strain gauge position. The axial test with a GLARC column of RPG or a column of random glass specimen is seen in Figure 12b. The results indicate that buckling is the most common type of failure in concrete columns, followed by tensile and progressive compressive failure such depicted in Figures 13 and 14. RPG specimens tends more ductile than CWG specimens.

The results obtained by the GLARC column with the strengthening of broken glass, RGP (random glass pieces) showed better results, it does not behave brittle but contrary it is more ductile as indicated by the lateral deflection that is larger than the CWG specimen (column without glass), at load 52 kN is 1.15 mm, 4.62 mm, 1.24 mm, 10.40 mm, and 1.2 mm for CWG, RGP-1, RGP-2, RGP-3, and RGP-4, respectively. Additionally, the majority of RGP specimens with corresponding above deflection showed higher peak loads than CWG 59 kN, 79 kN, 102 kN, 52 kN, and 72 kN, respectively.

Figure 12. (a) local collapse on the RPG column support (b) upper RPG column spalling at peak load

The results of axial test for CWG-1 (column without glass) and UHP-1 to UHP-4 (uniformly homogeneous piece) specimens can be seen in Figures 15 and 16, respectively.

Figure 13. RPG column: (a) Buckling failure (b) tensile cracks (c) Progressive compression failure

Figure 14. (a) Loading begin at UHP column before buckling (b) Behaviour of specimen collapse (c) joint support (d) local compressive failure

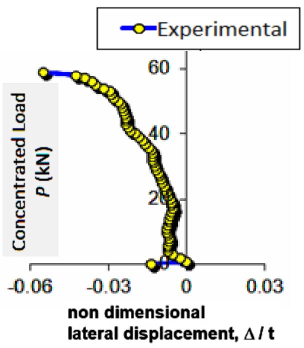

Figure 15. Lateral deflection – axial load relationship of CWG column

(a) UHP-1 specimen of GLARC column

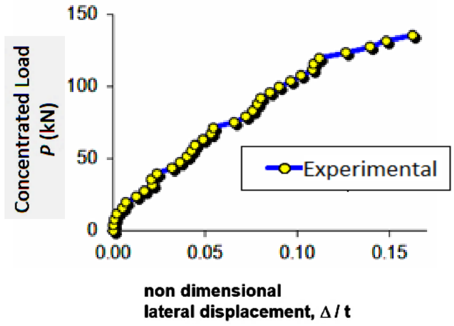

(b) UHP-2 specimen of GLARC column

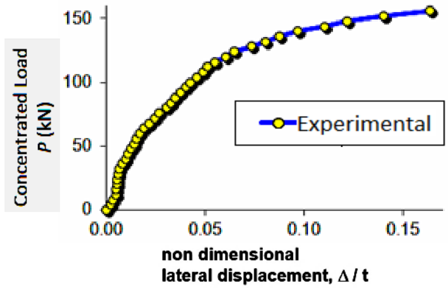

(c) UHP-3 specimen of GLARC column

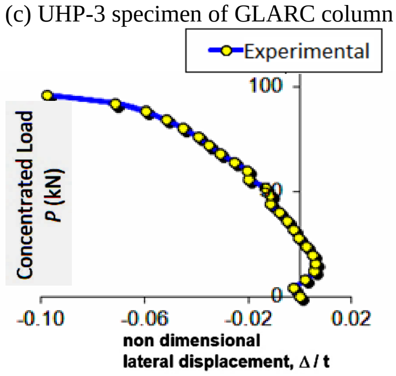

(d) UHP-4 specimen of GLARC column

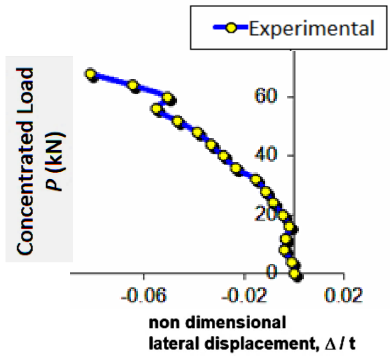

Figure 16. Lateral deflection – axial load relationship of UHP-1 to UHP-4 column specimens

The results of buckling lateral deflection for CWG specimen (column without glass), UHP (uniform glass column) at 56 kN load were 0.92 mm, 2.23 mm, 0.82 mm, 0.88 mm, 2.37 mm and 2.15 mm, for CWG, UHP- 1, UHP-2, UHP-3, UHP-4, and UHP-5, respectively.

The results of the lateral deflection are slightly larger, indicating that the UHP column is more ductile as well as all the compressive capacity is better than the CWG which has a peak load of only 59 kN while the peak load values are 136 kN, 156 kN, 96 kN, 68 kN and 80 kN for UHP-1, UHP- 2, UHP-3, UHP-4, and UHP-5, respectively.

This is probably due to the increased stiffness of the GLARC concrete column due to the glass-concrete composite action. When compared to RGP, UHP is also stiffer hence has less deformation and importantly has higher compressive axial capacity than RGP.

CWG specimens are more brittle than UHP-3 specimens, and the non-dimensional lateral deflection, Δ /t, for CWG column specimens at a load of 56 kN is greater than those UHP-3 column specimens, which are 0.0365 and 0.02 mm, respectively. In addition, the UHP-3 column specimen has a higher peak load of 96 kN than the of CWG's peak load, which is 59 kN.

The GLARC column lateral deflection results of uniformly homogeneous piece UHP-5 and random glass pieces of the RGP-1 specimen can be seen in Figures 17 and 18, respectively.

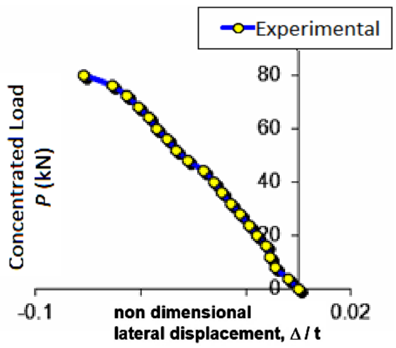

Figure 17. Lateral deflection – axial load relationship of specimen UHP-5 GLARC column

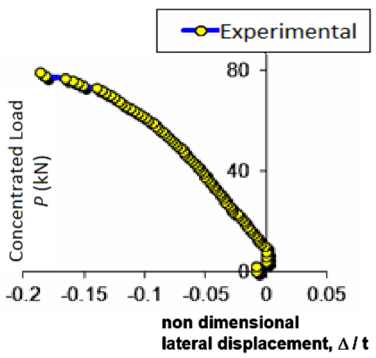

Figure 18. Lateral deflection – axial load relationship of specimen RGP-1 of GLARC column

The results of GLARC column specimens with uniform glass reinforcement results in more ductile behavior, even the Δ/t value could be more than 0.15. The UHP-4 specimen showed slightly larger value than CWG-1 for both lateral deflection and load. The effect of uniform glass seems good for the compressive case, this is understandable because the compressive strength of glass specimens is larger than those of non-glass reinforced concrete.

While the results of random glass pieces GLARC column RGP-2, RGP-3 and RGP-4 specimens are depicted in Figure 19.

(a) RGP-2 specimen of GLARC column

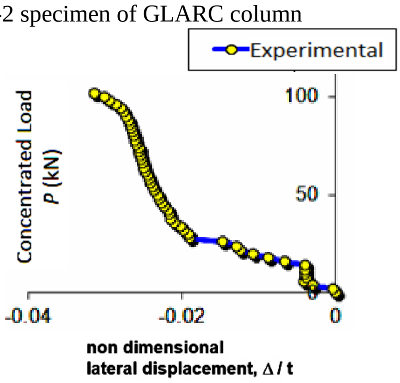

(b) RGP-3 specimen of GLARC column

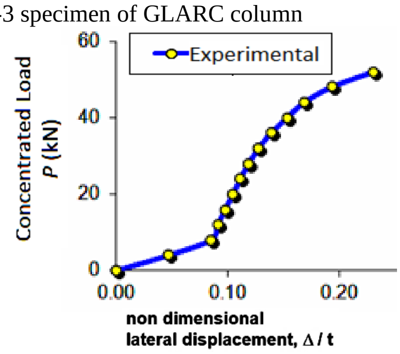

(c) RGP-4 specimen of GLARC column

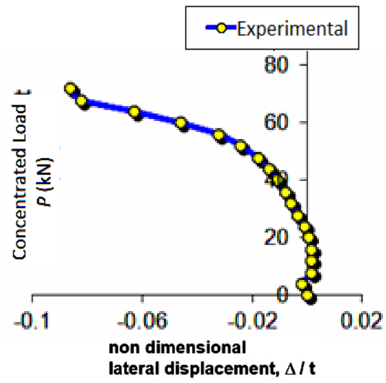

Figure 19. Lateral deflection and axial load on random GLARC column (a) RGP-1; (b) RGP-2 (c) RGP-3; (d) RGP-4

The random glass piece GLARC column specimens showed relatively random results due to the inhomogeneous dispersion even at the same glass amount and the distribution of the direction of the pieces is also very random, that is, the effect of slip on the glass surface is greater, but on the other hand, the sharp edges of the glass give an enough bite, which is more monolithic to ensure a composite action with concrete. These reasons can give an irregular slope of the curve to the column lateral deflection results.

The results of axial compression test for glassless column specimens (CWG-2) and HSL-1 horizontal strip glass GLARC column can be figured out in Figure 20.

The results of the lateral deflection of the HSL-1 column specimens were about three times better in ductility than the CWG-2 specimens, namely 0.06 and 0.018, respectively, meaning that the glassless CWG-2 specimen could deform further than the HSL-1 specimen. But contrary with that, the peak load that the HSL-1 specimen was able to withstand was almost twice as good as that of the CWG-2 specimen, which as 128 kN and 72 kN, respectively.

The results of the GLARC column with horizontal strip glass reinforcement for specimens of HSL-2, HSL-3, HSL-4 and HSL-5 can be seen in Figure 21.

It can be seen in Figure 21 that the GLARC column specimens with horizontal strip glass (HSL) reinforcement shows the best results, with a very significant increase in stiffness as well as excellent ductility.

(a) Column without glass (CWG-2)

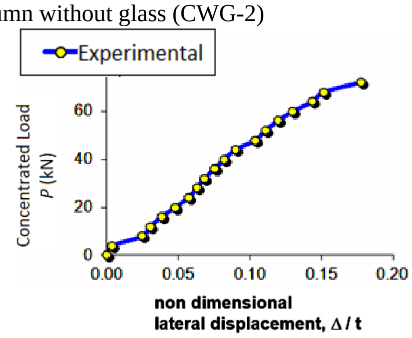

(b) Horizontal strip glass column (HSL-1)

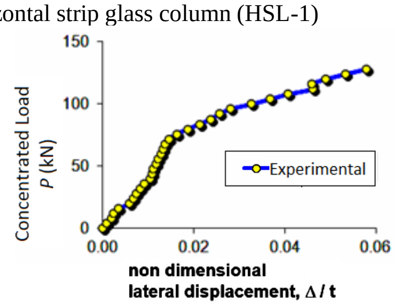

Figure 20. Lateral deflection and axial load on the column (a) CWG-2 column; (b) Column HSL-1

These excellent horizontal strip glass HSL specimens arise due to the higher inertia moment of the horizontal strip glass stiffened the weak axis (thin column geometry in lateral direction). These are not occur in other glass arrangements.

(a) Horizontal glass GLARC column (HSL-2)

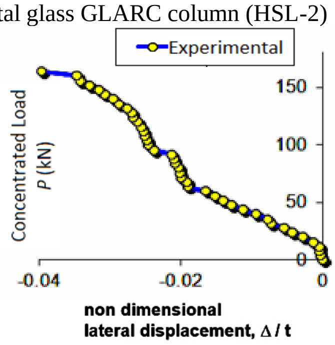

(b) Horizontal glass GLARC column (HSL-3)

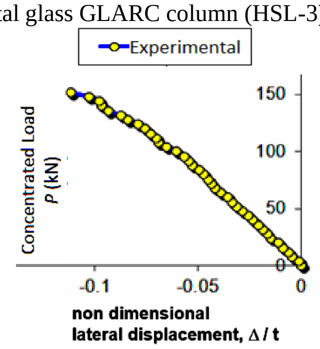

(c) Horizontal glass GLARC column (HSL-4)

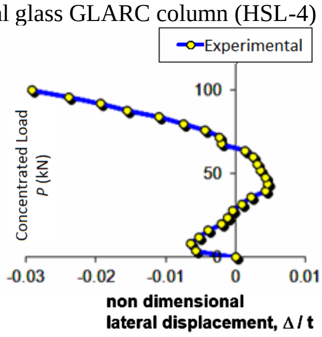

(d) Horizontal glass GLARC column (HSL-5)

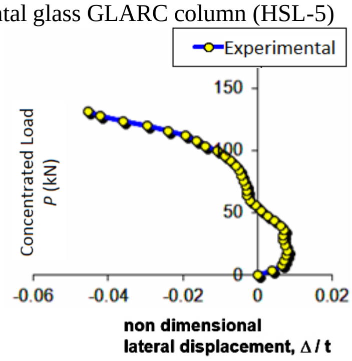

Figure 21. Lateral deflection and axial load on GLARC column with horizontal strip glass (a) HSL-2; (b) HSL-3 (c) HSL-4; (d) HSL-5

(a) Vertical glass GLARC column (VSL-1)

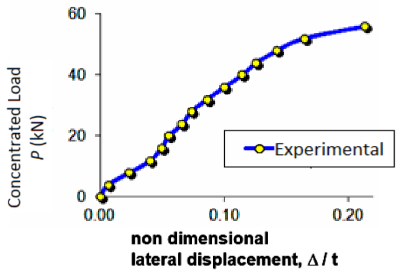

(b) Vertical glass GLARC column (VSL-2)

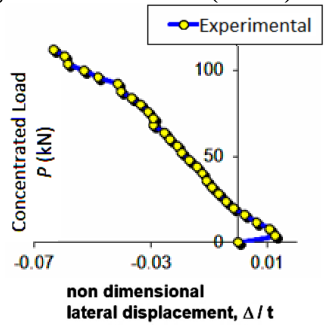

(c) Vertical glass GLARC column (VSL-3)

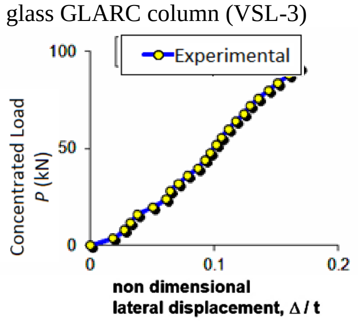

(d) Vertical glass GLARC column (VSL-4)

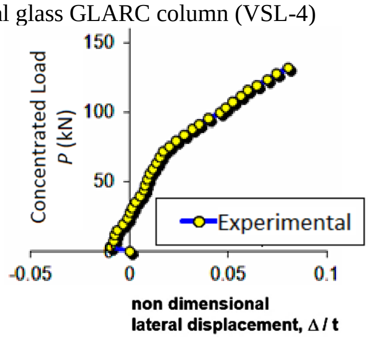

Figure 22. Lateral deflection and axial load on GLARC column with vertical striped glass (a) VSL-1; (b) VSL-2 (c) VSL-3; (d) VSL-4

Above in Figure 22 can be seen the results of the GLARC column with the vertical strip glass reinforcement of the VSL-1, VSL-2, VSL-3 and VSL-4 specimens.

With the exception of VSL-1 which has a peak load of only 60 kN, in general the results of GLARC column specimens with vertical glass strip reinforcement from VSL-2 to VSL4 show good results, with high peak loads, some even more than 100 kN. All VSL specimens had good ductility, even the non-dimensional lateral deflection of VSL-1 specimens was more than 0.2. Figure 23 depicts the lateral deflection versus axial load results among the glass piece arrangement HSL, VSL and UHP specimens.

As for all CWG column specimens and GLARC column specimens, namely RGP specimens can be seen in Figure 24.

In general, the results of GLARC column RGP specimens with random glass reinforcement show higher peak load results than those in CWG specimens, some even more than 100 kN, at almost the same lateral deflection as 0.2. In other words RGP tends to show more ductile behavior than CWG.

(a) Uniform homogen GLARC column (UHP)

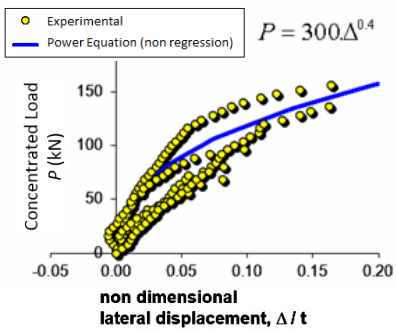

(b) Horizontal strip GLARC column (HSL)

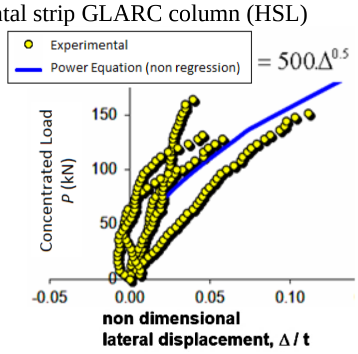

(c) Vertical strip glass GLARC column (VSL)

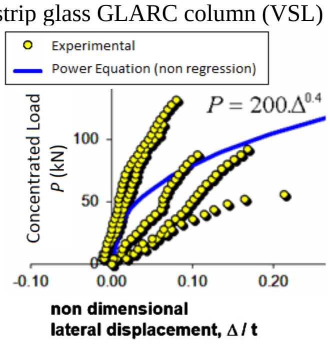

Figure 23. Lateral deflection and axial load on GLARC column of (a) UHP (b) HSL; (c) VSL specimens

Overall, both in detail can be presented in Figure 24 and in the results resumed in Figure 25, GLARC column specimens with any glass reinforcement show better results than CWG or glassless specimens.

It can be seen in Figure 25 that the best results for peak load were obtained specimens of HSL, UHP, VSL, RGP, and CWG respectively from the largest to lowest order. Then for the non-dimensional lateral deflection or ductility, namely Δ/t from the largest value is VSL, RGP, CWG, UHP and HSL respectively.

However, the bending capacity due to axial compressive forces is more important than ductility in the column due to their buckling resistance. They are not like a beams or girders where the ductility is important for their safety because in serviceability of girder structural deflection seems to be more considered.

While buckling failure in the columns seem more abrupt, especially in slim or thin slender columns [13, 14]; therefore, their resistance to buckling is more crucial to be take into account. Hence, both the highest compressive load capacity and the smallest lateral deflection is the best consideration for columns, while – surely in all research conducted under flexural loads –the highest bending capacity and the largest ductility are the best consideration for the beams or girders.

While the stress and strain relationship results can be seen for UHP-1 to UHP-4 (uniformly homogeneous piece) and CWG (column without glass) specimens can be seen in Figures 26 and 27, respectively.

As UHP specimen depicted in Figure 26, almost of them reach high enough critical stress due to capability to experience snap-buckling, hence their rigidity avoid them to reach both displacement and strains. They behave snap buckling rather than enlarge the strain. They

(a) Column without glass (CWG)

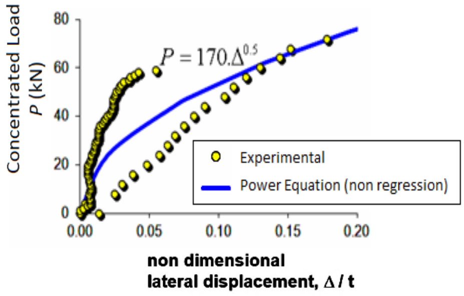

(b) Random glass GLARC column (RGP)

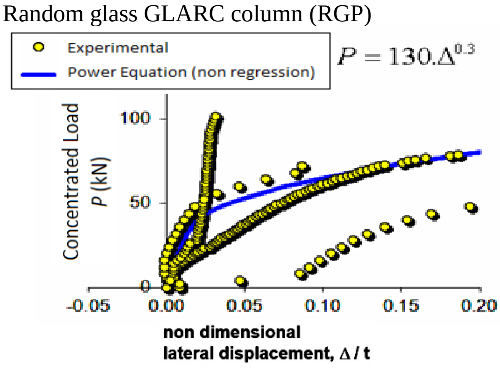

Figure 24. Lateral deflection and axial load on the column (a) CWG; (b) RGP

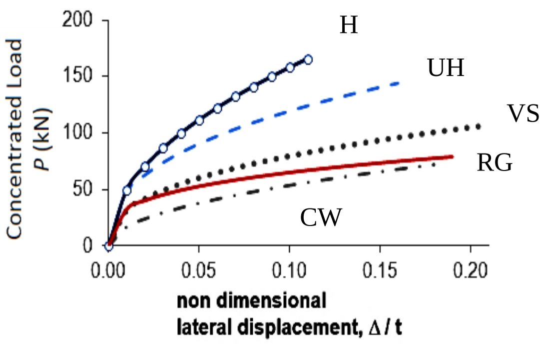

Figure 25. Lateral deflection and axial load in all specimens of glassless columns and GLARC columns in various arrangement of glass reinforcement

(a) UHP-1 specimen of GLARC column

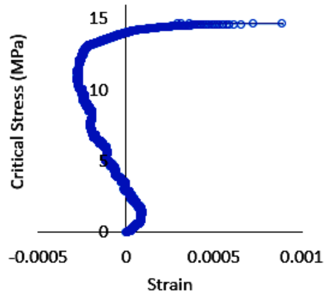

(b) UHP-2 specimen of GLARC column

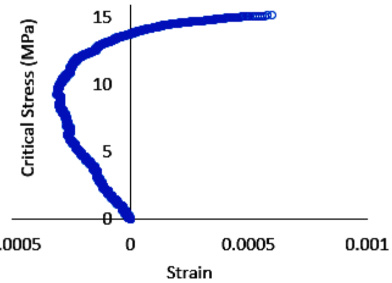

(c) UHP-3 specimen of GLARC column

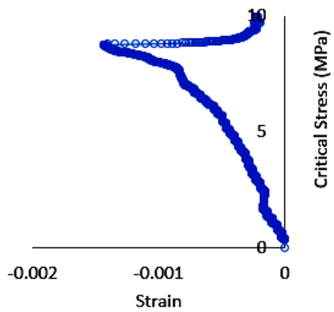

(d) UHP-4 specimen of GLARC column

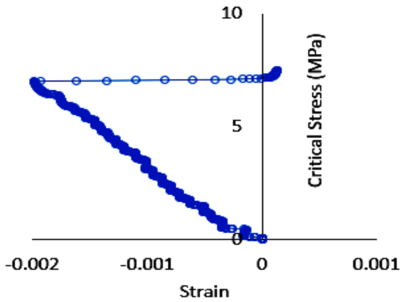

Figure 26. Strain versus critical buckling stress relationship of UHP-1 to UHP-4 column specimens

have quite small strain below 0.002 even some less than 0.001. It can be stated that UHP specimens have certain capability to restore to their original positions.

As seen in CWG (column without glass) as control column buckling test, CWG-1 tends to buckle at the strain of 0.002 before reach concrete failure strain which is around 0.003.

The GLARC column strain versus stress results of random glass pieces of the RGP-1 to RPG-2 specimen can be seen in Figure 28.

While the strain-stress results of random glass pieces GLARC column RPG-3 to RGP-4 specimens can be depicted in Figure 29.

As RGP specimen depicted in Figures 28 and 29, almost of them reach low critical stress below 10 MPa, except RGP-2 little bit larger which is more than 10 MPa. The have no capability to perform snap-buckling. Half of them enlarge the strain approach 0.003 although half result less than 0.0015. It can be stated that RGP specimens have lowest stiffness and tend to get much higher in both of their deflections and strains.

The stress versus strain results for HSL-1 horizontal strip glass GLARC column can be found in Figure 30 and the other HSL in Figure 31.

As seen in HSL-1, it tends very hard to buckle as it have very low strain less than 0.00025 very far from0.003 concrete failure strain. This phenomenon show very high rigidity due to the glass strip direction that strengthen the weak axis.

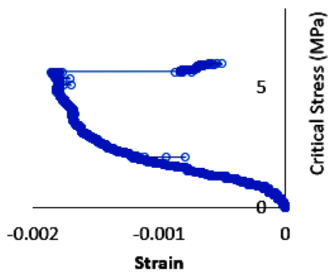

Figure 27. Strain versus critical buckling stress relationship of CWG-1 column

(a) RGP-1 specimen of GLARC column

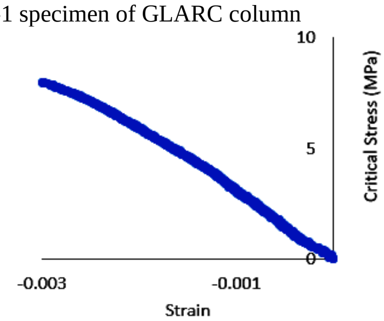

(b) RGP-2 specimen of GLARC column

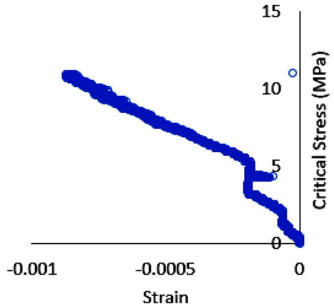

Figure 28. Strain versus critical buckling stress of specimen RGP-1 and RGP-2 of GLARC column

(a) RGP-3 specimen of GLARC column

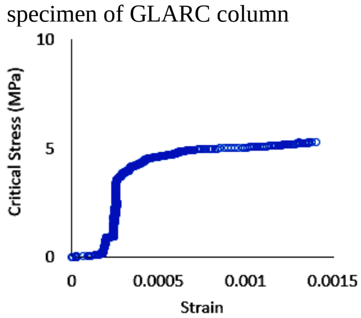

(b) RGP-4 specimen of GLARC column

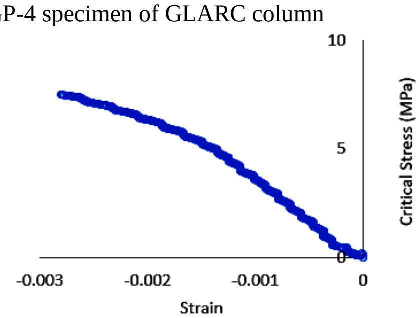

Figure 29. Strain versus critical buckling stress of specimen RGP-3 and RGP-4 of GLARC column

Below in Figure 32 can be seen the strain-stress relationship results of the GLARC column with the vertical strip glass reinforcement of the VSL-1, VSL-2, VSL-3 and VSL-4 specimens.

It can be seen in Figure 33 that the lowest stress are in specimen CWG, the second lowest were RPG due to its random arrangements. The VSL specimens were in medium and moderate results among all.

(a) Horizontal strip glass column (HSL-1)

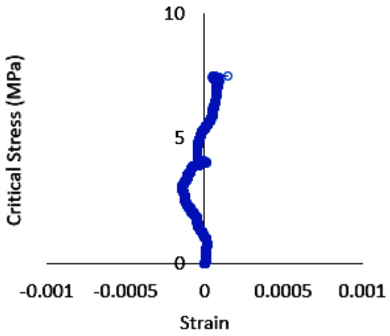

Figure 30. Strain versus critical buckling stress relationship in (a) Column HSL-1

(a) Horizontal glass GLARC column (HSL-2)

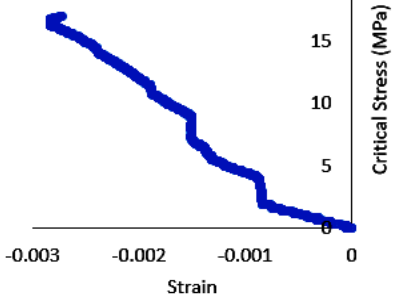

(b) Horizontal glass GLARC column (HSL-3)

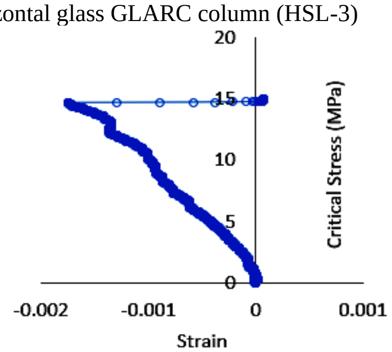

(c) Horizontal glass GLARC column (HSL-4)

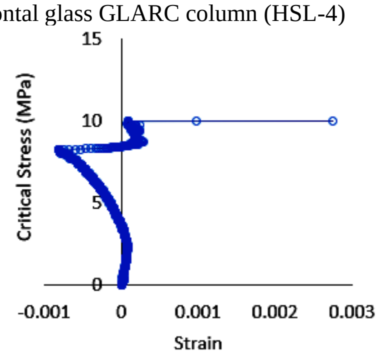

(d) Horizontal glass GLARC column (HSL-5)

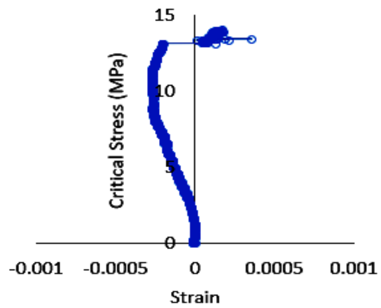

Figure 31. Strain versus critical buckling stress on GLARC column with horizontal strip glass (a) HSL-2; (b) HSL-3 (c) HSL-4; (d) HSL-5

The UHP specimens were read not in consistent stress, but also quite high critical stress due to their capability to snap-buckling and their lowest strain show their excellent rigidity. Finally, the best results for peak critical stress were obtained by HSL specimens from the lowest to largest order.

(a) Vertical glass GLARC column (VSL-1)

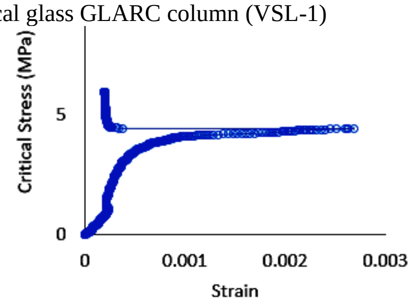

(b) Vertical glass GLARC column (VSL -2)

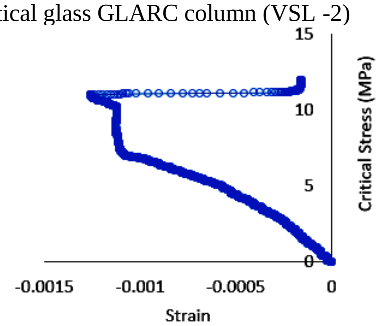

(c) Vertical glass GLARC column (VSL -3)

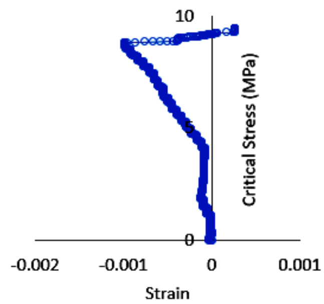

(d) Vertical glass GLARC column (VSL -4)

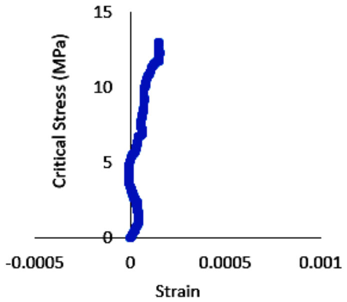

Figure 32. Strain versus critical buckling stress relationships on GLARC column with vertical striped glass (a) VSL-1; (b) VSL-2 (c) VSL-3; (d) VSL-4

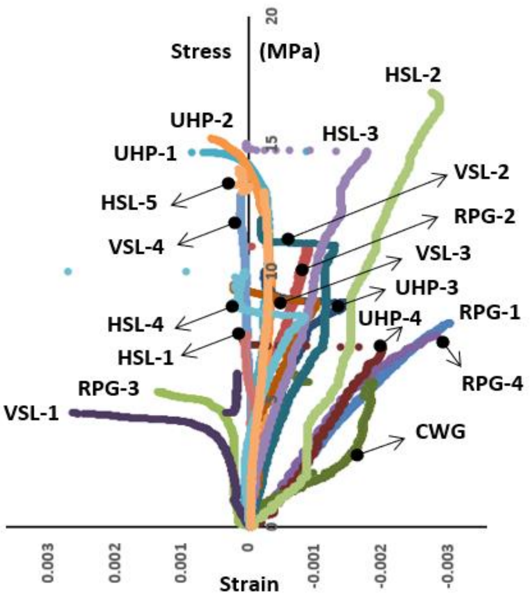

Figure 33. Strain versus critical buckling stress relationships in all specimens of GLARC columns in various arrangement of glass reinforcement

4. CONCLUSION

This discussion demonstrates the influence of the glass waste addition on axial behaviour of reinforced concrete columns. As a result, the following outcomes are obtained:

1. The results describe that compressive test of GLARC (glass reinforced concrete) columns from recycled glass waste, showed good results both in terms of their strength and stiffness over the CWG, glassless one, especially HSL arrangement.
2. Glass waste can be used as an alternative to strengthening reinforced concrete structures, especially precast beams and columns hence that it can overcome glass waste and eventually solved environmental problems. UHP arrangement of glass waste is quite good as a reinforcement material due to cheap and easily to installed and have the lowest strain as below 0.0005, hence to be the stiffest column of GLARC specimen.
3. HSL with a horizontal strip longitudinal arrangement achieved highest peak axial compressive load around 100-150 kN and axial stresses 10-15 MPa under relatively low strain as 0.0005-0.001. This HSL arrangement is the best configuration glass reinforced due to cheap, easy and have the largest compressive capacity and the second most stiffer among others.
4. With roughly neglected parameter such thickness, glass arrangement, glass amount, slenderness ratio and imperfection behaviour the P_{cr} of GLARC column in this dimension is said to be around 60 kN – 150 kN, and considering snap through buckling this P_{cr} value is tend to be lower as 40-60 kN.

The following can be noted to enhanced and give a deeper understanding regarding GLARC columns:

1. The use of glass in GLARC columns have not been done according to certain regulations or valid protocol and codes. This is due to the lack of reinforced concrete design code containing glass waste utilization. These recommendations should be underlined for non-structural column applications for the sake of waste management term.
2. The calculation of critical buckling load and allowable load of GLARC columns have not been conveyed expressly yet because it contain many parameter that should be examined further by another research such as thickness, weight of glass waste, the glass arrangement angle, etc.
3. The structures with stands bending momentum have already investigated but surely concrete and glass alone can not withstand tensile stresses independently cause all specimens containing steel rebar in a small amount and hence, glass, can not replace steel in concrete but indeed they have large contribution under axial compressive loading.
4. The glass amount is set to be constant, because this research focuses on the arrangement on the same amount. Further research is needed to explore how much an optimal glass amount for reinforcement.

5. REFERENCES

1. Ismail, Z. Z., Al-Hashmi, E. A., "Recycling of waste glass as a partial replacement for fine aggregate in concrete", ***Waste Management***, Vol. 29 No. 2, (2009), 655-659. https://www.sciencedirect.com/science/article/abs/pii/S0956053X0800281X
2. Hidup, K. L., Indonesia, K. R. "Sistem Informasi Pengelolaan Sampah Nasional". ***Dipetik March***, Vol. 13, (2019).
3. Subramanian, N. "Design of reinforced concrete structures". Oxford University Press, (2013)

https://global.oup.com/academic/ product/design-of-reinforced-concrete-structures-9780198086949? cc=us&lang=en&

4. Dhir, R. K., Paine, K. A. "Value added sustainable use of recycled and secondary aggregates in concrete", ***Indian Concrete Journal***, Vol. 84, No. 3, (2010), 7-26. https://researchportal.bath.ac.uk/en/publications/value-added-sustainable-use-of-recycled-and-secondary-aggregates-

5. Martens, K., Caspeele, R., Belis, J., "Development of reinforced and posttensioned glass beams: review of experimental research". ***Journal of Structural Engineering***, Vol. 142, No. 5, (2016), 04015173.https://ascelibrary.org/doi/10.1061/%28ASCE%29ST.1943-541X.0001453

6. Feldmann, M., Langosch, K. "Buckling resistance and buckling curves of pane-like glass columns with monolithic sections of heat strengthened and tempered glass". In Challenging Glass Conference Proceedings, Vol. 2, (2010), 319-330. https://doi.org/10.7480/cgc.2.2420

7. Rosso, A., Almeida, J. P., Beyer, K. "Stability of thin reinforced concrete walls under cyclic loads: state-of-the-art and new experimental findings". ***Bulletin of Earthquake Engineering***, Vol. 14 No. 2, (2016), 455-484. https://link.springer.com/article/10.1007/s10518-015-9827-x

8. Parra, P. F., Moehle, J. P. "Stability of slender wall boundaries subjected to earthquake loading", ***ACI Structural Journal,*** Vol. 114, No. 6, (2017), 1627-1636. https://structurae.net/en/literature/journal-article/stability-of-slender-wall-boundaries-subjected-to-earthquake-loading

9. Parra, P. F., Moehle, J. P. "Effects of strain gradients in the onset of global buckling in slender walls due to earthquake loading", ***Bulletin of Earthquake Engineering,*** Vol. 18, (2020), 3205-3221, https://link.springer.com/article/10.1007/s10518-020-00821-3

10. Niang, A., Roy, N., Tagnit-Hamou, A. "Structural behavior of concrete incorporating glass powder used in reinforced concrete columns", ***Journal of Structural Engineering***, Vol. 141 No. 3, (2015), B4014007. https://ascelibrary.org/doi/10.1061/%28ASCE%29ST.1943-541X.0000986

11. Margaretta, D. O., Amalia, N., Utami, F. D., Viridi, S., Abdullah, M. "Second-order phase transition and universality of self-buckled elastic slender columns", ***Journal of Taibah University for Science***, Vol. 13 No. 1, (2019), 1128-1136. https://www.tandfonline.com/doi/full/10.1080/16583655.2019.1688542

12. Seif, M., Schafer, B. "Design of locally slender structural steel columns", ***Journal of Structural Engineering***, Vol. 140, No. 4, (2014), 04013086. https://ascelibrary.org/doi/abs/10.1061/%28ASCE%29ST.1943-541X.0000889

13. Sirimontreea, S., Keawsawasvong, S., Thongchom, C., Jongvivatsakul, P., Noroozinejad Farsangi, E. "Experimental Investigations on Strengthened Reinforced Concrete Columns under Monotonic Axial Loading", ***International Journal of Engineering, Transactions B: Applications***, Vol. 34 No. 5, (2021), 1124-1131. doi: 10.5829/ije. 2021.34.05b.06

14. Shahbazi, N., Tariverdilo, S., Amani Dashlejeh, A. "Effects of Radial Imperfection on the Load Capacity of Round HSS Columns", ***International Journal of Engineering, Transactions A: Basics***, Vol. 32 No. 1, (2019), 36-45. doi: 10.5829/ije.2019.32.01a.05

15. Ahmadi, M., Naghipour, M., Nematzadeh, M. "Numerical and Experimental Investigations on the Behavior of Steel-reinforced Concrete Columns Subjected to Eccentric Loading", ***International Journal of Engineering, Transactions B: Applications***, Vol. 33 No. 8, (2020), 1529-1543. doi: 10.5829/ije.2020.33.08b.11

16. Drzymała, T., Zegardło, B., Tofilo, P. "Properties of Concrete Containing Recycled Glass Aggregates Produced of Exploded Lighting Materials", ***Materials***, Vol. 13, No. 1, (2020), 226. https://www.mdpi.com/1996-1944/13/1/226

17. Yu, X., Tao, Z., Song, T. Y., Pan, Z. "Performance of concrete made with steel slag and waste glass". ***Construction and Building Materials***, Vol. 114, (2016), 737-746. https://www.sciencedirect.com/science/article/abs/pii/S0950061816305219

18. Marandi, S. M., Ghasemi, M. "Laboratory studies of the effect of recycled glass powder additive on the properties of polymer modified asphalt binders". ***International Journal of Engineering, Transactions A: Basics***, Vol. 26 No. 10, (2013), 1183-1190. doi: 10.5829/ idosi.ije.2013.26.10a.08

19. Mohsenzadeh, S., Maleki, A., Yaghin, M. A. "Experimental and Numerical Study of Energy Absorption Capacity of Glass Reinforced SCC Beams", ***International Journal of Engineering, Transactions C: Aspects***, Vol. 32 No. 12, (2019), 1733-1744. doi: 10.5829/ ije.2019.32.12c.06

20. Rath, B., Deo, S., Ramtekkar, G. "Durable glass fiber reinforced concrete with supplementary cementitious materials. ***International Journal of Engineering***, Vol. 30 No. 7, (2017), 964-971. doi: 10.5829/ije.2017.30.07a.05

21. Yasin Mousavi, S., Tavakkoli, A., Jahanshahi, M., Dankoub, A. "Performance of High-strength Concrete Made with Recycled Ceramic Aggregates" (Research Note), ***International Journal of Engineering, Transactions C: Aspects***, Vol. 33 No. 6, (2020), 1085-1093. doi: 10.5829/ije. 2020.33.06c.05

22. Jin, W. "Alkali-silica reaction in concrete with glass aggregate: A chemo-physico-mechanical approach", (1999), Columbia University. https://ui.adsabs.harvard.edu/abs/1998PhDT........88J/abstract

23. Dhir, R. K., Dyer, T. D., Tang, M. C. "Expansion due to alkali-silica reaction (ASR) of glass cullet used in concrete". In 2003 International Symposium Advances in Waste Management and Recycling, Thomas Telford, (2003), 751-760 https://discovery.dundee.ac.uk/en/publications/expansion-due-to-alkali-silica-reaction-asr-of-glass-cullet-used-

24. Dhir, R. K., Dyer, T. D., Tang, M. C. "Alkali-silica reaction in concrete containing glass", ***Materials and Structures***, Vol. 42 No. 10, (2009), 1451. https://link.springer.com/article/10.1617/s11527-008-9465-8

25. Rajabipour, F., Maraghechi, H., Fischer, G. "Investigating the alkali-silica reaction of recycled glass aggregates in concrete materials", ***Journal of Materials in Civil Engineering***, Vol. 22 No. 12, (2010), 1201-1208. https://ascelibrary.org/doi/abs/10.1061/(ASCE)MT.1943-5533.0000126

26. Islam, M.S., Akhtar, S. "A critical assessment to the performance of alkali–silica reaction (ASR) in concrete", ***Canadian Chemical Transactions,*** Vol. 1 No. 4, (2013), 253-266. http://citeseerx.ist.psu.edu/viewdoc/download?doi=10.1.1.707.7455&rep=rep1&type=pdf

27. Yang, S., Cui, H., Poon, C. S. "Assessment of in-situ alkali-silica reaction (ASR) development of glass aggregate concrete prepared with dry-mix and conventional wet-mix methods by X-ray computed micro-tomography", ***Cement and Concrete Composites***, Vol. 90, (2018), 266-276. https://doi.org/10.1016/j.cemconcomp.2018.03.027

28. Hay, R., Ostertag, C. P. "On utilization and mechanisms of waste aluminium in mitigating alkali-silica reaction (ASR) in concrete", ***Journal of Cleaner Production***, Vol. 212, (2019), 864-879.https://agris.fao.org/agrissearch/search.do?recordID=US201900105719

29. Yang, S., Lu, J. X., Poon, C. S. "Recycling of waste glass in dry-mixed concrete blocks: Evaluation of alkali-silica reaction (ASR) by accelerated laboratory tests and long-term field monitoring", ***Construction and Building Materials***, Vol. 262, (2020), 120865. https://www.sciencedirect.com/science/article/abs/pii/S0950061820328701

30. Sumardi, Bisri, M., Munawir, A. "On the Simplification of Flexural Failure Prediction of Glass Reinforced Concrete: An Eco-friendly Beam Structure-under 4 Point Bending Loads", ***Research Journal of Applied Sciences, Engineering and Technology***, Vol. 13 No. 11, (2016), 815-824. https://maxwellsci.com/jp/mspabstract.php?jid=RJASET&doi=rjaset.13.3423

31. Sumardi, Bisri, M., Soemarno, Munawir, A. "An environmental-structural utilization of glass waste: An assessment of glass tensile to initial prediction of GLARC-beam flexural strength". ***ARPN Journal of Engineering and Applied Sciences***, Vol. 11 No. 19, (2016), http://www.arpnjournals.org/jeas/research_papers/rp_2016/jeas_1016_5141.pdf

Persian Abstract

چکیده

نکته مهم در بارگذاری محوری ستون های باریک ثبات کمانش است. با این حال ، تحقیقات بسیار محدودی موجود است به ویژه با استفاده از بتن تقویت شده با شیشه. مشکل خرابی واکنش سیلیس قلیایی (ASR)تنها زمانی رخ می دهد که ذرات بسیار ریز باشند. از استفاده شیشه به عنوان ذره اجتناب شد و بجای آن از ابعاد بزرگتری از ضایعات نوار شیشه ای استفاده شد زیرا سیمان نمی تواند به عمق قطعه شیشه نفوذ کند. مجموعه ای از آزمایشهای بارگذاری محوری ستونهای باریک شیشه ای (GLARC)بر روی انواع آرایش انجام شد. نوارهای شیشه ای ، قطعات همگن و تصادفی تقویت شده تا عملکرد کمانش آنها را بررسی کند. همه نتایج ستونهای محوری GLARC بهتر از تقویت ستونهای بدون شیشه بود. بهترین تقویت ، چیدمان نوار افقی طولی بود ، زیرا آنها دارای استحکام ثابتی هستند ، بنابراین به ستون های GLARC اجازه می دهد تا در برابر بارهای محوری بیشتر مقاومت کنند تا از خرابی کمانش جلوگیری شود. نتایج آزمایش ها عملکرد خوبی دارد و بنابراین ستون های GLARC شانس بالقوه ای برای استفاده گسترده به عنوان اعضای فشرده سازی ساختاری دارند.

IJE TRANSACTIONS B: Applications Vol. 34, No. 11, (November 2021) 2467-2475

International Journal of Engineering

Journal Homepage: www.ije.ir

Development of Open-pit Mine Reclamation Cost Estimation Models: A Regression-based Approach

S. Amirshenava[a], M. Osanloo*[a], A. Esfahanipour[b]

[a] *School of Mining Engineering, Amirkabir University of Technology, Tehran, Iran*
[b] *Department of Industrial Engineering & Management Systems, AmirKabir University of Technology, Tehran, Iran*

PAPER INFO

Paper history:
Received 11 Septamber 2021
Received in revised form 30 Septamber 2021
Accepted 02 October 2021

Keywords:
Mine Reclamation
Mine Reclamation Cost Estimation
Regression Analysis
Sustainable Mining

ABSTRACT

In the recent decade, very few studies have been done on mine reclamation cost estimation and no study has been conducted on proposing mine reclamation cost estimation models based on historical data. This study aims to develop predictor models for mine reclamation costs. To this end, after collecting the historical cost data of 41 open-pit mine reclamation projects, a comprehensive data set of 16 mine reclamation costs groups and the extent of the disturbed mined land corresponding to each group was prepared. Given the advantage of the regression method in developing a reliable predictor model with few data, the proposed cost models are developed based on the regression analysis technique. The R square for all and more than 87% of the developed models was more significant than 85% and 90%, respectively, indicating the proper fits on the data sets. Also, the root mean square error ratio to the standard deviation of observed cost data (RSR) was lower than 0.7 for all developed models, indicating the predictor models' good performance on reliably estimating mine reclamation costs. These efficient and simple general models can help make the right decisions by mine reclamation planners and pave the way to achieve sustainable mining by considering mine reclamation cost in the mine planning and design process.

doi: *10.5829/ije.2021.34.11b.10*

1. INTRODUCTION

Mine reclamation is an accepted stage in the Modern Mining Life Cycle (MMLC) to keep mining in a Sustainable Development (SD) path by performing the responsible mining [1]. Given that the mine reclamation is a progressive activity, much of which is carried out in the last years of the MMLC, the primary concern of government agencies overseeing the reclamation plan is to ensure its successful implementation [2,3]. Estimation of mine reclamation costs to determine the amount of financial resources required is the key element of the successful implementation of the mine reclamation project. According to the World Bank report, mine reclamation costs range from less than $1 million for small-scale mines to hundreds of millions of dollars for giant mines [4].

Failure to finance the mine reclamation expenditures is synonymous with the inability to deploy the Post-Mining Land-Use (PMLU) option successfully. It will have consequences such as remaining the abandoned mines or bankruptcy of the mining company [2]. Therefore, to successfully implement the reclamation plan, its costs should be incorporated into the mine planning and design. Besides, considering these costs in the mine planning and design is one of the main requirements for achieving SD and performing responsible mining [5-10]. To this end, mine reclamation costs should be estimated at an acceptable level of confidence at the preliminary stages of the MMLC [11].

Mine reclamation costs are affected by PMLU option, mining method, mined land condition, mine waste and tailings characteristics, and the most important, the extent of earthworks required. Earthworks account for more than 70% of the mine reclamation costs [11, 12]. In a

*Corresponding Author Email: morteza.osanloo@gmail.com (M. Osanloo)

Please cite this article as: S. Amirshenava, M. Osanloo, and A. Esfahanipour, Development of Open-pit Mine Reclamation Cost Estimation Models: A Regression-based Approach, International Journal of Engineering, Transactions B: Applications, Vol. 34, No. 11, (2021), 2467-2475

general classification, mine reclamation expenses can be divided into common and specific costs. Common costs are related to the activities that need to be performed according to the mine reclamation objectives for preparation operations before deploying the PMLU option. They are similar between reclamation projects regardless of the type of PMLU option. These cost items are generally affected by the extent of earthworks required in each mine. In the other group, specific costs are related to implementing the PMLU option selected [11,13].

Cost estimation is an essential part of all levels of studies for mining projects. There are several methods for cost estimation, such as the comparative method, unit cost method, detailed estimate, artificial intelligence-based methods, and regression-based methods. The appropriate estimation method is determined based on the amount and type of data required and the desired accuracy of the estimate [14-16]. Regression analysis and artificial intelligence-based methods are the most famous techniques for cost estimation purposes. Using artificial intelligence-based methods requires much historical data for training, validation, and testing the model [17]. In comparison, regression analysis techniques provide good results with a fairly small data set [18].

Despite the importance of the mine reclamation cost estimation, very few studies have addressed this issue, especially in the recent decade. Many of these studies [19-26] focus on reclamation cost estimation of United States (US) surface coal mines based on the unit costs of activities. Catlett and Boehlje [27] developed a multivariate regression model to estimate the reclamation costs of surface coal mines. This model considers only parameters related to slope, overburden height, and coal layer thickness. The US Office of Surface Mining Reclamation and Enforcement (OSMRE) [12] proposed a handbook for the calculation of reclamation bond amounts. The proposed model in this guide is based on detailed cost estimation by defining all reclamation cost items in detail. The main advantage of this study is the identification and classification of the types of mine reclamation direct and indirect costs based on the Surface Mining Control and Reclamation (SMCR) Act of 1977. The US Environmental Protection Agency (EPA) modified the OSMRE classification by aggregating similar detail cost items into some general items [3]. Some researchers [28-31] focus on developing simulation-based approaches to estimate mine closure and reclamation costs. In these studies, by defining different scenarios and using the Monte Carlo simulation method, a probabilistic distribution diagram of mine reclamation costs is presented, determining mine reclamation costs at varying levels of risk. Kaźmierczak et al. [11] and Ignatyeva et al. [32] proposed an approach for cost estimation of mine reclamation activities based on the unit cost method. Environmental organizations in some countries developed mine reclamation cost estimation models for reclamation bond calculation purposes in a standardized process. These models include the US Standardized Reclamation Cost Estimator (SRCE) model [33], the Australian Estimated Rehabilitation Cost Calculator (ERC) model [34], and the Canadian RECLAIM model [35].

Based on the literature review, there is no universal and perfect study in developing estimation models for common costs of open-pit mine reclamation projects by considering all activities required for different parts of the mined land. In the most of reviewed studies, it is not clear what type of mine reclamation activities are included in each cost item. For example, about earthworks costs, only grading has been considered in some studies, and in others, other operations such as topsoiling and cover placement have been considered. Therefore, it is required to specify the reclamation operations for each cost item based on a standard classification such as OSMRE handbook [12]. Besides, so far, no algebraic formula with a reliable range of error has been proposed to estimate the costs of different mine reclamation activities.

The aim of this study is to develop cost estimation models for cost items that are common in all mine reclamation plans. In this regard, after determining and classifying the mine reclamation cost items, the related historical cost data will be collected to develop reliable predictor models. Then, the regression analysis will be applied to develop estimation models for mine reclamation expenses. Finally, the reliability of models will be investigated and reported.

2. METHODOLOGY AND DATA SOURCES

Due to the lack of legal requirements in most countries (especially under development countries) to perform progressive mine reclamation activities, there is little data on mine reclamation costs. Therefore, the shortage of historical data existed on mine reclamation costs is the main limitation in developing cost predictors models. Given the limited number of available historical data and the advantage of regression-based methods in developing a reliable predictor model with a small number of data, in this study, the regression analysis technique is applied to develop the predictor models for mine reclamation cost estimation.

Statistical regression analysis is one of the best and most commonly used methods to develop a predictor model. This method generates the predictor model by establishing a relationship between independent input and dependent output variables. This model can estimate the target value based on the input value regarding the independent variables [18]. In the current study, the dependent variable in each model is the cost of mine reclamation activity, and the independent variable is the unit value of this activity (i.e., the extent of the disturbed area).

2. 1. Mine Reclamation Cost Classification Given the variety of mine reclamation costs, one of the most important issues in developing predictor models is providing a standard classification of these costs. In this study, the mine reclamation costs were classified based on the OSMRE's handbook [12]. Mine reclamation costs are classified into direct and indirect costs. The direct cost includes the costs associated with beginning a mine reclamation plan into production through site preparation and other activities. The classification of direct costs is given in Table 1. Indirect costs summarized in administration, engineering, and non-itemized services are classified into seven groups: mobilization/ demobilization, engineering design and redesign, contingency, contractor profit and overhead, contractor liability insurance, payment and performance bonds, and agency direct costs [12].

According to Table 1, there are five types of direct common costs for mine reclamation activities. Among these five cost groups, E & R is the major reclamation cost. Mine reclamation would require considerable earthwork activities, which its implementation requirements are different for different parts of the mined land. Therefore, it is needed to develop the cost predictor model separately for different parts of mined land include open-pit, waste rock dump, tailings facility, heap/dump leach, and process pond and reservoir. It is worth noting that depending on the type of mineral, an open-pit mine may not have all of these facilities. Therefore, in the cost estimation process of an open-pit mine reclamation project, only cost estimation models related to the facilities that exist in the mine will be used.

2. 2. Data Set Description Due to the long history of mine reclamation law in the US (SMCR Act of 1977), this country is one of the leading countries in mine reclamation. Accordingly, most of the available historical data on mine reclamation cost items are related to the US In this study, the reclamation cost data according to the extent of the disturbed areas of 41 open-pit mines were collected to construct the estimator models (Table 2). According to Table 2, this data set is related to different states of the US and has a wide variation range. These data have been gathered and reported by US EPA [3]. Given that the collected cost data were for different years (from 2007 to 2014), in this study, using the cost index provided by Engineering News-Record (ENR) Construction Cost Index [36], total costs were normalized to the 2020 US dollar. The descriptive statistics of the collected data are given in Table 3. It is worth noting that the cost data reported in Table 3 were normalized to the 2020 US dollar according to the ENR cost index. According to Table 3, the number of data collected varies for each reclamation cost group. Because, in none of the studied mines, all categories of mine reclamation costs have been reported. Thus, the number of data in each cost category depends on the number of mines, which reported that cost item. Accordingly, in this study, cost estimation models were developed separately for each mine reclamation cost category.

3. COST MODELS DEVELOPMENT

In the data set reported in Table 3, except for the water treatment cost, which depends on the volumetric flow rate (Q) of water treatment, other reclamation costs are a function of the extent of the disturbed areas considered in the reclamation plan. Therefore, the cost predictor regression models' independent variable is the area of part or all mined land (depending on the cost category). After collecting the cost data (Table 3), there is sufficient data to generate a numerical relationship between data on

TABLE 1. Mine reclamation direct costs classification [3, 12]

Num.	Direct cost	Reclamation acitivities
1	Earthworks & Revegetation (E & R)	Backfilling, grading, cover placement, ripping/scarifying, topsoiling, revegetation
2	Solid and hazardous waste disposal	Solid waste, hazardous material, contaminated soils, and organic solutions removal, haulage and disposal; structure, building and equipment demolition and disposal (i.e., buildings, haul access roads, crusher, foundation, fences, powerlines, etc.)
3	Surface water drainage	Diversion channels construction to collect and convey stormwater from the reclaimed land to prevent contamination through run-on or run-off
4	Annual water treatment	Minimize the toxicity of mine-influenced waters with chemicals (e.g., lime), Water management (prevent the release of contaminated water), process fluid stabilization, neutralization, and solution disposal, and seepage capture
5	Annual Operation & Maintenance (O & M) and monitoring	Groundwater and surface water monitoring, geotechnical stability monitoring, erosion and vegetation monitoring, fish and wildlife monitoring, road, stormwater, and revegetation repairs and maintenace

TABLE 2. General specifications of collected cost data

Num.	Mine Reclamation Cost item		Num. of Data	Type of Mineral (NUM.)	Country (NUM.)
1	Open-pit E & R Cost		17	Au (10), Cu (4), Fe (1), Ag (1), Au-Ag (1)	**USA**: Nevada (12), Arizona (1), California (1), Minnesota (1), New Mexico (1), Utah (1)
2	Waste rock dump E & R Cost		20	Au (8), Cu (4), Fe (3), Mo (2), Rare Earth (1), Au-Ag (1), Zn-Pb (1)	**USA**: Nevada (6), Alaska (3), Minnesota (3), Arizona (2), California (2), Colorado (1), Idaho (1), South Carolina (1), Utah (1)
3	Tailings facility E & R Cost		12	Au (7), Au-Ag (2), Cu (2), Mo (1)	**USA**: Nevada (5), Alaska (2), Arizona (2), Colorado (1), Montana (1), New Mexico (1) South Carolina (1)
4	Heap/dump leach E & R Cost		8	Cu (4), Au (2), Au-Ag (2)	**USA**: Nevada (5), Arizona (2), Montana (1)
5	Process pond & reservoir E & R Cost		14	Cu (7), Au (5), Au-Ag (1), P (1)	**USA**: Nevada (8), Arizona (3), Idaho (1), New Mexico (1), Utah (1)
6	Surface water drainage cost		8	Au (5), Cu (2), P (1)	**USA**: Nevada (4), Alaska (1), Arizona (1), Idaho (1), Utah (1)
7	Solid & hazardous waste disposal cost		7	Au (6), Cu (1), Au-Ag (1)	**USA**: Nevada (6), California (1)
8	Annual O & M and mointoring cost		15	Au (8), P (2), Cu (1), Rare Earth (1), Ag (1), Mo (1), Zn-Pb (1)	**USA**: Nevada (7), Alaska (4), Idaho (2), California (1), Colorado (1)
9	Annual water treatment cost		7	Au-Ag (4), Cu (2), Au (1)	**USA**: Colorado (2), Montana (2), New Mexico (2), Alaska (1)
10	Indirect costs	Mobilization/demobilization cost	12	Au (6), Cu (4), Ag (1), Mo (1)	**USA**: Nevada (7), New Mexico (2), Arizona (1), California (1), Colorado (1)
11		Engineering design and redesign cost	11	Au (7), Cu (3), Au-Ag (1)	**USA**: Nevada (6), Montana (2), Alaska (1), Arizona (1), New Mexico (1)
12		Contingency cost	16	Cu (6), Au (4), Fe (2), Mo (1), P (1), Rare Earth (1), Au-Ag (1)	**USA**: Nevada (4), Arizona (2), California (2), Idaho (2), Minnesota (2), New Mexico (2), Alaska (1), Utah (1)
13		Contractor profit and overhead cost	13	Au (9), Cu (2), MO (1), P (1)	**USA**: Nevada (6), Arizona (2), California (2), Idaho (2), Alaska (1)
14		Contractor liability insurance cost	9	Au (5), Cu (2), Ag (1), P (1), Mo (1)	**USA**: Nevada (4), Colorado (2), Alaska (1), Idaho (1), New Mexico (1)
15		Payment and performance bonds	12	Au (10), Mo (1), P (1)	**USA**: Nevada (6), Alaska (2), Colorado (2), New Mexico (1)
16		Agency direct costs	15	Au (9), Cu (3), Mo (1), Rare Earth (1), P (1)	**USA**: Nevada (6), Alaska (2), Idaho (2), California (1), Montana (1), New Mexico (1), South Carolina (1)

TABLE 3. Descriptive statistics of collected data

Variable	Unit	Acronym	NUM.	Mean	Median	StDev	Minimum	Maximum
Open-pit E & R cost	US$ 1000	$E \& R_{(O\text{-}P)}C$	17	234.58	90.78	380.73	1.82	1458.36
Waste rock dump E & R cost	US$ 1000	$E \& R_{(WRD)}C$	20	5046	3785.84	5188.08	307.73	22241.45
Tailing's facility E & R cost	US$ 1000	$E \& R_{(TF)}C$	12	11542.71	6676.25	12689.78	1171.15	44650.05
Heap/dump leach E & R cost	US$ 1000	$E \& R_{(HL)}C$	8	4551.59	4042.59	2770.72	910.45	8371.62
Process pond & reservoir E & R cost	US$ 1000	$E \& R_{(PR)}C$	14	634.6	423.98	817.25	23.33	3229.47
Surface water drainage cost	US$ 1000	*SWDC*	8	55.85	17.25	68.07	3.45	165.23
Solid & hazardous waste disposal cost	US$ 1000	*WDC*	7	170.98	43.67	238.39	5.25	652.04
Annual O & M and monitoring cost	US$ 1000	*O & MC*	15	366.61	266.15	434.35	57.08	1764.49
Annual water treatment cost	US$ 1000	*WTC*	7	3768.9	2859.82	2177.52	1918.86	7694.57
Mobilization/demobilization cost	US$ 1000	*MobC*	12	664.25	366.01	697.89	77.45	2181.82
Engineering design and redesign cost	US$ 1000	*EngC*	11	2727.61	2022.42	2375.49	716.85	8929.34

Contingency cost	US$ 1000	*ContC*	16	1698.29	1296.59	1462.66	175.32	4136.69
Contractor profit and overhead cost	US$ 1000	*P & OC*	13	4855.68	3301.50	4744.25	501.58	15815.64
Contractor liability insurance cost	US$ 1000	*LIC*	9	671.66	253.11	744.04	21.5	2115.82
Payment and performance bonds	US$ 1000	*PBC*	12	1312.36	934.6	1418.38	59.29	4744.69
Agency direct costs	US$ 1000	*AgenC*	15	3425.27	2716.52	3165.64	158.35	9918.01
Open Pit disturbed area	ha	$A_{(O\text{-}P)}$	17	120.81	45.32	185.37	1.62	647.50
Waste rock dump disturbed area	ha	$A_{(WRD)}$	20	386.43	278.02	405.68	17.00	1605.79
Tailings facility disturbed area	ha	$A_{(TF)}$	12	429.03	235.32	474.93	54.63	1711.42
Heap/dump leach disturbed area (ha)	ha	$A_{(HL)}$	8	233.76	223.18	143.85	52.61	442.32
Process pond & reservoir disturbed area	ha	$A_{(PR)}$	14	10.55	7.08	14.46	0.4	57.06
Total site-wide disturbed area	ha	$A_{(S\text{-}w)}$	41	823.66	491.29	879.92	5.26	3305.07
Volumetric flow rate of water treatment	l/min	*Q*	7	3374.42	2649.79	1732.26	1483.88	6056.66

each mine reclamation cost category and the variable related to the extent of mine reclamation activities in that category. The purpose is to select the regression model to achieve the best fit possible for the data with the lowest estimation error. To this end, the R square (R2) and Root Mean Square Error (RMSE) of each type of regression model were evaluated. Accordingly, the model with the highest R^2 and the lowest RMSE was selected. Equations (1) to (16) show regression functions to predict mine reclamation costs. The variables of these equations and their unit of measurement are described in Table 3. Also, the regression relationships and their R^2 are expressed as graphs in Figure 1.

$$E\,\&\,R_{(O-P)}C = 0.0018 \times {A_{O-P}}^2 + 0.8925 \times A_{O-P} + 41.174 \quad (1)$$

$$E\,\&\,R_{(WRD)}C = 0.0021 \times {A_{WRD}}^2 + 9.2605 \times A_{WRD} + 825.17 \quad (2)$$

$$E\,\&\,R_{(TF)}C = 26.19 \times A_{TF} + 303.76 \quad (3)$$

$$E\,\&\,R_{(HL)}C = -0.0144 \times {A_{HL}}^2 + 25.263 \times A_{HL} - 303 \quad (4)$$

$$E\,\&\,R_{(PR)}C = 0.0623 \times {A_{PR}}^2 + 51.918 \times A_{PR} + 67.788 \quad (5)$$

$$SWDC = 0.0666 \times A_{S-w} + 6.8855 \quad (6)$$

$$WDC = 8.9128 \times e^{0.0017 \times A_{S-w}} \quad (7)$$

$$O\,\&\,MC = 0.6309 \times A_{S-w} + 60.723 \quad (8)$$

$$WTC = 1.161 \times Q - 148.66 \quad (9)$$

$$MobC = 0.7266 \times A_{S-w} - 1.252 \quad (10)$$

$$EngC = 0.0002 \times {A_{S-w}}^2 + 1.8552 \times A_{S-w} + 656.75 \quad (11)$$

$$ContC = -0.0002 \times {A_{S-w}}^2 + 1.9076 \times A_{S-w} + 97.839 \quad (12)$$

$$P\,\&OC = 0.0008 \times {A_{S-w}}^2 + 5.4103 \times A_{S-w} + 66.825 \quad (13)$$

$$LIC = 2.1065 \times A_{S-w} + 66.211 \quad (14)$$

$$PBC = 0.0006 \times {A_{S-w}}^2 + 0.7689 \times A_{S-w} + 171.76 \quad (15)$$

$$AgenC = 3.3302 \times A_{S-w} + 529.27 \quad (16)$$

4. MODELS EVALUATION

After developing the cost models, the goodness of models fitness should be evaluated. The R^2 coefficient obtained from regression analysis is a good measure for explaining the model's capability. The R^2 values more than 0.5 are acceptable, and values greater than 0.75 are good for representing the accuracy. The high R^2 coefficients show that the developed cost models can properly estimate the mine reclamation costs [37]. Although the R^2 coefficient is widely used for model evaluation, this statistic is insensitive to proportional differences between observed and predicted values according to the developed model. Therefore, it is required to apply some of the error indices for model evaluation. The RMSE is the main error index for regression model evaluation. The RMSE value close to zero indicates a perfect fit in the regression model. Therefore, it is necessary to calculate the RMSE value based on Equation (17).

$$RMSE = \sqrt{\frac{\sum_{i=1}^{n}(y_{obs} - y_i)^2}{n}} \quad (17)$$

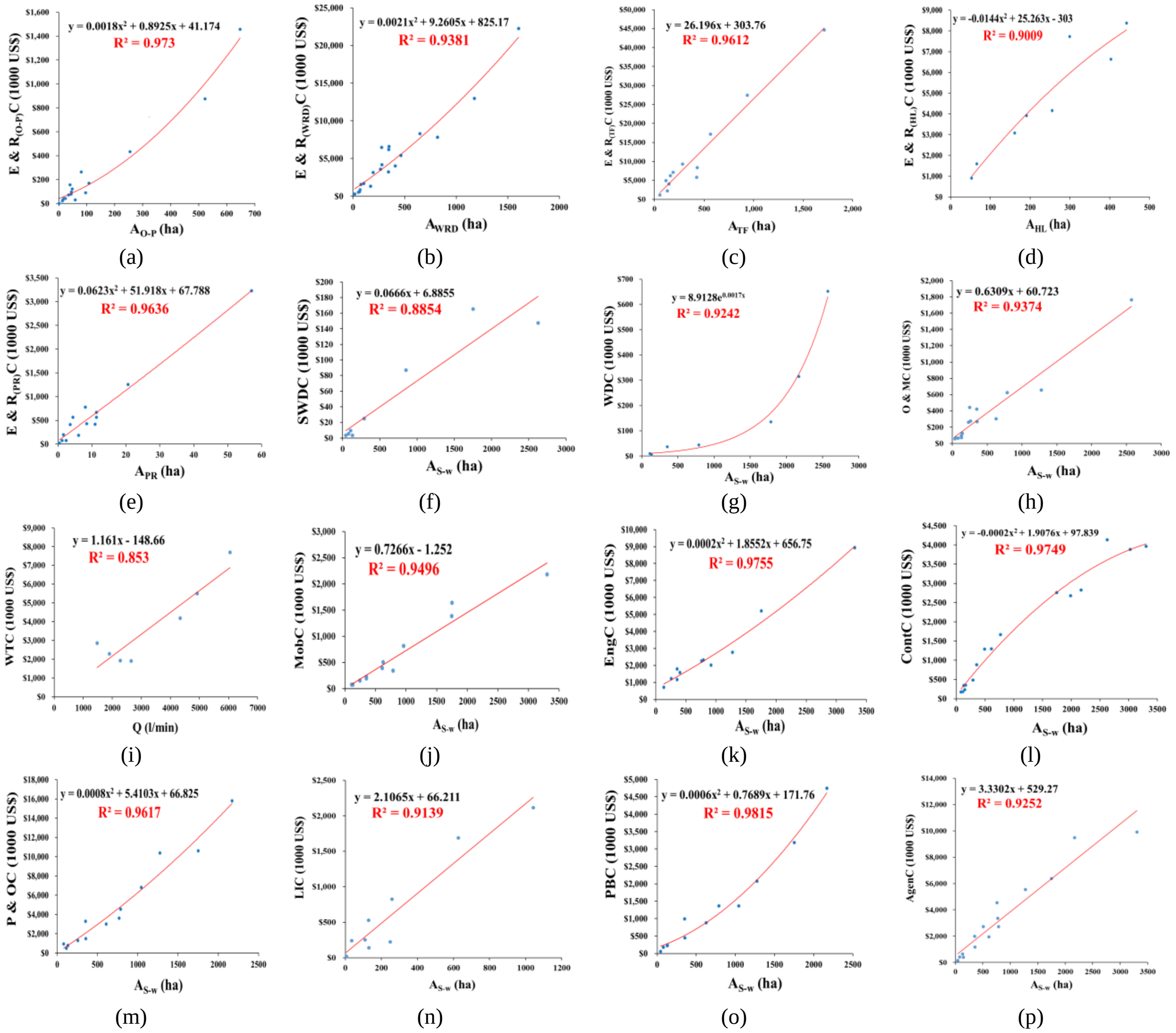

Figure 1. Univariable regression results for mine reclamation costs

where y_{obs} is the input value, y_i is the predicted value, and n is the number of data. Although the RMSE is the most commonly used index to evaluate the model's error, it alone cannot represent the model's accuracy and depends on the data's average value and Standard Deviation (StDev). To this end, the RMSE-observations standard deviation ratio (RSR) is applied to evaluate the model's performance. RSR is calculated as the ratio of RMSE to StDev of measured data according to Equation (18) [37].

$$RSR = \frac{RMSE}{StDev_{obs}} = \frac{\sqrt{\sum_{i=1}^{n}(y_{obs} - y_i)^2}}{\sqrt{\sum_{i=1}^{n}(y_{obs} - y_{mean})^2}} \tag{18}$$

where y_{mean} and $StDev_{obs}$ are the average value and standard deviation of the observed data, respectively.

After calculating the RSR ratio, the model's performance is evaluated according to the performance rating presented in Table 4. The amounts of the RMSE and RSR of the proposed cost estimation models are given in Table 5. The values of RSR for developed cost models show the good performance of these models in estimating mine reclamation costs.

TABLE 4. Model's performance rating based on the *RSR* [37]

Performance Rating	RSR
Very good	$0 \leq RSR \leq 0.5$
Good	$0.5 < RSR \leq 0.6$
Satisfactory	$0.6 < RSR \leq 0.7$
Unsatisfactory	$RSR > 0.7$

TABLE 5. RMSE and RSR of the cost models

Cost Model	RMSE	RSR	Performance
$E \& R_{(O\text{-}P)}C$	60.735	0.16	Very good
$E \& R_{(WRD)}C$	1258.315	0.24	Very good
$E \& R_{(TF)}C$	2393.06	0.188	Very good
$E \& R_{(HL)}C$	816.031	0.29	Very good
$E \& R_{(PR)}C$	562.315	0.68	Satisfactory
SWDC	21.556	0.31	Very good
WDC	33.049	0.14	Very good
O & MC	105.026	0.241	Very Good
WTC	773.015	0.354	Very Good
MobC	149.98	0.214	Very good
EngC	354.74	0.14	Very good
ContC	946.25	0.64	Satisfactory
P & OC	3215.66	0.67	Satisfactory
LIC	205.893	0.276	Very good
PBC	642.88	0.45	Very good
AgenC	836.676	0.264	Very good

5. DISCUSSIONS

This study developed the predictor models for mine reclamation cost estimation based on the statistical regression analysis. These new and general models, developed for different parts and facilities of the open-pit mines separately, cover all direct and indirect common costs of open-pit mine reclamation projects. Since the input variable of these models is based on the extent of the disturbed land area, these models can be used at any stage of MMLC by entering the extent of disturbed land area under reclamation operations. This study's main novelty is developing algebraic formulas for different mine reclamation cost groups based on a data set of mine reclamation costs. These novel generic models are responsible for calculating mine reclamation costs in a simple and systematic manner. Data collection from 41 open-pit mine reclamation projects and accordingly preparation of a comprehensive data set of mine reclamation costs and the extent of the disturbed area of the mined land corresponding to each cost group are the other superior aspects of the current study.

According to Figure 1, the R^2 amounts for all and more than 87% of the developed models was more significant than 85% and 90%, respectively, indicating the proper fits on the data sets. According to Table 5, the *RSR* values of all 16 developed models are at an acceptable level (lower than 0.7) that represents the acceptable performance of predictor models. It is worth noting that the *RSR* values for more than 81% of the proposed models was lower than 0.5, indicating very good performance of these models. The high amounts of R^2 and low values of *RSR* appear that the proposed models have a suitable capability for mine reclamation costs estimation with a reliable error range.

It is worth noting that each type of mineral has its own requirements for reclamation operations. Some of these requirements are related to specific mining facilities for that type of mineral. In a gold mine, for example, there is the heap leach and process pond. While in an iron ore mine, there are no such mining facilities. Therefore, the mine reclamation planner will not consider the cost estimation models related to these facilities in the cost estimation process of this mine's reclamation project. However, it is essential to note that much of the reclamation work in an open-pit mine is related to earthworks (more than 70% of reclamation costs), which can be considered common in all mines. For example, earthworks for waste rock dump in a gold mine is not much different from this type of operation in an iron or copper mine.

PMLU profoundly affects the mine reclamation cost. On the other hand, the main criterion for measuring the completion of the mine closure operation is the successful establishment of the PMLU option, which requires funding its related costs. Therefore, to calculate the final cost of the mine reclamation project, which is equal to the sum of common and specific costs, it is required to estimate the cost of establishing the PMLU option. However, the frontier of this research is the development of estimating models for the common costs of reclamation operations, and providing models to estimate the cost of implementing each of the PMLU options can be the subject of future researches. Nevertheless, the cost of establishing the desired PMLU option can be calculated based on unit cost method.

6. CONCLUSION

Mine reclamation cost estimation is the main prerequisite for successfully implementing the mine reclamation project and achieving sustainable mining by incorporate this cost in the mine planning and design. In this study, 16 predictor models for estimation of mine reclamation costs were developed based on the regression analysis. To this end, a comprehensive data set of 16 mine reclamation cost groups and the extent of the disturbed area of the mined land corresponding to each group was prepared based on the data collected from 41 open-pit mine reclamation projects. These new and general models, developed for different parts and facilities of the open-pit mines separately, cover all direct and indirect common cost categories of open-pit mine reclamation projects. The results show that developed algebraic models are suitable for estimating mine reclamation costs with a reliable error range. These novel generic models are responsible for calculating mine reclamation costs in a simple and systematic manner. Developing algebraic formulas for different mine reclamation costs based on a comprehensive data set of 16 mine reclamation cost groups gathered from cost data of 41 open-pit mine reclamation projects is the main superiority and novelty of this study. These efficient and simple general models can help make the right decisions by mine reclamation planners and also can be a helpful tool for mine reclamation bond calculation required for government agencies. This work contributes to establishing a paradigm for future studies related to incorporating mine reclamation cost in the mine planning and design process.

7. REFERENCES

1. Amirshenava, S., and Osanloo, M., "Mine closure risk management: An integration of 3D risk model and MCDM techniques", ***Journal of Cleaner Production***, Vol. 184, (2018), 389-401, DOI: 10.1016/j.jclepro.2018.01.186.
2. Amirshenava, S., and Osanloo, M., "Mined Land Suitability Assessment: A Semi-Quantitative Approach based on a New Classification of Post-Mining Land Uses", ***International Journal of Mining, Reclamation and Environment***, Published online, (2021), DOI: 10.1080/17480930.2021.1949864.
3. "US Environmental Protection Agency | US EPA." https://www.epa.gov/ (accessed Sep. 03, 2021).
4. Sassoon, M., "Financial Surtey: Guidelines for the Implementation of Financial Surety for Mine Closure," Extractive Industries for Development Series #7, The World Bank, (2009), Accessed online: https://openknowledge.worldbank.org/handle/10986/18386.
5. Burgher, K. E., and Erickson, E., "The optimization of coal mine production schedules using linear programming: an example that determines the effects of reclamation costs and interest rates", ***Mining Science and Technology***, Vol. 2, (1984), 69-78, DOI: 10.1016/S0167-9031(84)90223-8.
6. Jafarpour, A., and Khatami, S., "Analysis of Environmental Costs' Effect in Green Mining Strategy Using a System Dynamics Approach: A Case Study", ***Mathematical Problems in Engineering***, Published online, (2021), DOI: 10.1155/2021/4893776.
7. Baidowi, N., Rosyidi, C.N., and Aisyati, A, "A Cut-Off Grade Optimization Model in Open Pit Mining Considering Reclamation Cost and Revenue", IOP Conference Series: Materials Science and Engineering, (2021), DOI: 10.1088/1757-899x/1096/1/012021.
8. Narrei, N., and Osanloo, M., "Optimum cut-off grade's calculation in open pit mines with regard to reducing the undesirable environmental impacts", ***International Journal of Mining, Reclamation and Environment***, Vol. 29, No. 3, 2015, 226-242, DOI: 10.1080/17480930.2014.994734.
9. Muttaqin, B. I. A., Rosyidi, C. N., and Pujiyanto, E., "A cut-off grade optimization model in the open pit mining considering reclamation and valuable waste materials", In Proceedings of the IEEE International Conference on Industrial Engineering and Engineering Management, (2018), 45-49, DOI: 10.1109/IEEM.2017.8289848.
10. Amirshenava, S., and Osanloo, M., "A hybrid semi-quantitative approach for impact assessment of mining activities on sustainable development indexes", ***Journal of Cleaner Production***, Vol. 218, (2019), 823-834, DOI: 10.1016/j.jclepro.2019.02.026.
11. Kaźmierczak, U., Malewski, J., and Strzałkowski, P., "The concept of forecasting the reclamation cost in rock mining", ***Gospodarka Surowcami Mineralnymi/ Mineral Resources Management***, Vol. 35, No. 4, (2019), 163-176, DOI: 10.24425/gsm.2019.128537.
12. OSMRE (Office of Surface Mining Reclamation and Enforcment), "Handbook for calculation of reclamation bond amounts", (2000), Accessed online: https://www.osmre.gov/LRG/docs/directive882.pdf.
13. Sweigard, R.J., and Ramani, R.V., "Economic Aspects of Postmining Land Use Planning", In Proceedings of the Society of Mining Engineers Fall Meeting Conference, Albuquerque, NM, USA, (1985), 1801-1808.
14. Nourali, H., and Osanloo, M., "Mining capital cost estimation using Support Vector Regression (SVR)", ***Resources Policy***, Vol. 62, (2019), 527-540, 10.1016/J.RESOURPOL.2018.10.008.
15. Gentry, D.W., O'Neil, T.J., "Mine Investment Analysis", Book (SME), New York, (1984). ISBN: 978-0895204295.
16. Gilson, N.K., and Vanreyk, A.J., "Review of Cost Estimation Models", ***International Journal of Scientific Engineering and Research***, Vol. 4, (2014), 42-44, Accessed online: https://www.ijser.in/archives/v4i3/IJSER15714.pdf.
17. Nourali, H., and Osanloo, M., "A regression-tree-based model for mining capital cost estimation," ***International Journal of Mining, Reclamation and Environment***, Vol. 34, No. 2, (2020), 88-100, DOI: 10.1080/17480930.2018.1510300.
18. Nourali, H., and Osanloo, M., "A new cost model for estimation of open pit copper mine capital expenditure," ***International Journal of Engineering, Transactions B: Applications***, Vol. 32, No. 2, (2019), 184-191, DOI: 10.5829/ije.2019.32.02b.21.
19. Xu, X.C, Gu, X.W., Wang, Q., Gao, X.W., Liu, G.P., Wang, Z.K., and Wang, X.H., "Production scheduling optimization considering ecological costs for open pit metal mines," ***Journal of Cleaner Production***, Vol. 180, (2018), 210-221, DOI: 10.1016/j.jclepro.2018.01.135.
20. Lin, W., Spore, R.L., and Nephew, E.A., "Land Reclamation and Strip-mined Coal Production in Appalachian", ***Journal of Environmental Economics and Management***, Vol. 3, (1976), 236-252, DOI: 10.1016/0095-0696(76)90023-1.
21. Gronhovd, D. E., and Scott, D. F., "Reclamation Costs of strip-mined land in Western North Dakota", ***Farm Research***, Vol. 37, No. 1, (1979), 7-11.
22. K. L. Leathers, "Costs of Strip Mine Reclamation in the West," Technical Report: United States Department of Agriculture, Report No. 19, (1980), Accessed online: https://naldc.nal.usda.gov/download/AGE81916922/PDF.
23. Misiolek, W. S., and Noser, T. C., "Coal Surface Mine Land Reclamation Costs", ***Land Economics***, Vol. 58, No. 1, (1982), 67-85, DOI: 10.2307/3146077.
24. Baker, K., Sullivan, J., Burger, J. A., and Amacher, G., "Coal mine reclamation in the southern appalachains: costs of forestry versus hayland/pasture", ***Journal American Society of Mining and Reclamation***, Vol. 2008, No. 1, (2008), 78-96, DOI: 10.21000/JASMR08010078.
25. Sullivan, J., and Amacher, G. S., "Private and social costs of surface mine reforestation performance criteria," ***Environmental Management***, Vol. 45, No. 2, (2010), 311-319, DOI: 10.1007/s00267-009-9395-4.
26. Mishra, S. K., Hitzhusen, F. J., Sohngen, B. L., and Guldmann, J., "Costs of abandoned coal mine reclamation and associated recreation bene fi ts in Ohio," ***Journal of Environmental Management***, Vol. 100, (202), 52-58, DOI: 10.1016/j.jenvman.2012.01.021.

27. Catlett L., and Boehlje, M., "Strip-Mine Reclamation Laws and Regional Cost Implications," ***Journal of Agricultural and Applied Economics***, Vol. 11, No. 1, (1979), 157-161, DOI: 10.1017/S0081305200014898.

28. Du Plessis, A., and Brent, A. C., "Development of a risk-based mine closure cost calculation model", ***Journal of the Southern African Institute of Mining and Metallurgy***, Vol. 106, No. 6, (2006), 443-450.

29. Hutchison, I., and Dettore, R., "Statistical and Probabilistic Closure Cost Estimating," ***In Proceedings Tailings and Mine Waste***, Vancouver, BC., (2011), DOI: 10.14288/1.0107717.

30. Pavloudakis, F., Roumpos, C., and Galetakis, M., "Public acceptance of surface mining projects and the determination of the marginal environmental cost", ***International Journal of Mining, Reclamation and Environment***, Vol. 26, No. 4, (2012), 292-308, DOI: 10.1080/17480930.2011.613568.

31. Paricheh, M., and Osanloo, M., "A simulation-based framework for estimating probable open-pit mine closure time and cost," ***Journal of Cleaner Producti***, Vol. 167, (2017), 337-345, DOI: 10.1016/j.jclepro.2017.08.202.

32. Ignatyeva, M., Yurak, V., and Pustokhina, N., "Recultivation of post-mining disturbed land: Review of content and comparative law and feasibility study", ***Resources***, Vol. 9, No. 6, (2020), DOI: 10.3390/resources9060073.

33. "Standardized Reclamation Cost Estimator (SRCE)| NDEP," 2021. https://nvbond.org/ (accessed Sep. 03, 2021).

34. "Estimated Rehabilitation Cost (ERC)." https://environment.des.qld.gov.au/ (accessed Sep. 03, 2021).

35. "RECLAIM Model." https://www.enr.gov.nt.ca/en (accessed Sep. 03, 2021).

36. "Construction Economics." https://www.enr.com/economics (accessed Sep. 05, 2021).

37. Moriasi, D. N., Arnold, J. G., Van Liew, M. W., Bingner, R. L., Harmel, R. D., and Veith, T. L., "Model Evaluation Guidelines for Systematic Quantification of Accuracy in Watershed Simulations," ***Transactions of the ASABE***, Vol. 50, No. 3, (2007), 885-900, DOI: 10.13031/2013.23153.

Persian Abstract

چکیده

در دهه اخیر، مطالعات بسیار محدودی در زمینه تخمین هزینه‌های بازسازی معدن انجام شده است و تا کنون هیچ مطالعه‌ای در زمینه ارائه مدل‌های تخمین‌گر هزینه‌های بازسازی بر اساس داده‌های تاریخی انجام نشده است. هدف این مطالعه توسعه مدل‌های تخمین‌گر برای هزینه‌های بازسازی معدن است. بدین منظور ، پس از جمع آوری داده‌های مرتبط با هزینه‌های تاریخی پروژه بازسازی ۴۱ معدن روباز، مجموعه داده‌های جامعی از ۱۶ گروه هزینه‌های بازسازی معدن و مساحت زمین تخریب شده مربوط به هر گروه تهیه شد. با توجه به مزیت روش رگرسیون در توسعه یک مدل تخمین‌گر با تعداد داده تاریخی کم، مدل‌های ارائه شده در این مطالعه بر اساس روش آنالیز رگرسیون توسعه یافته‌اند. مقدار ضریب همبستگی به دست آمده از فرایندهای مدل‌سازی، نشان می‌دهد که مدل‌های توسعه یافته در این مطالعه به خوبی بر داده‌ها برازش یافته‌اند. همچنین نسبت جذر میانگین مربعات خطا به انحراف از معیار داده‌های هزینه ورودی در تمامی مدل‌های توسعه یافته، مقدار کمتر از ۰/۷ است که معرف عملکرد مناسب این مدل‌ها در تخمین قابل اعتماد هزینه‌های بازسازی معدن است. این مدل‌های کارآمد و ساده می‌توانند به تصمیم‌گیری صحیح توسط برنامه‌ریزان بازسازی کمک کرده و راه دستیابی به معدنکاری پایدار را با لحاظ کردن هزینه‌های بازسازی در فرایند طراحی و برنامه‌ریزی معدن هموار کند.

IJE TRANSACTIONS B: Applications Vol. 34, No. 11, (November 2021) 2476-2493

International Journal of Engineering

Journal Homepage: www.ije.ir

Probabilistic Seismic Assessment of Moment Resisting Steel Buildings Considering Soft-story and Torsional Irregularities

M. H. Razmkhah[a], H. Kouhestanian[b], J. Shafaei*[b], H. Pahlavan[c], M. Shamekhi Amiri[b]

[a] *Department of Civil Engineering Faculty, University of Semnan, Semnan, Iran*
[b] *Department of civil engineering, Shahrood University of Technology, Shahrood, Iran*

PAPER INFO

Paper history:
Received 03 August 2021
Received in revised form 19 September 2021
Accepted 23 September 2021

Keywords:
Incremental Dynamic Analysis
Probabilistic Seismic Assessment
Soft-story
Steel Moment Resisting Frame
Torsional Irregularity

ABSTRACT

In this study, the fragility curves were developed for three-, five-, and eight-story moment resisting steel frame structures with considering soft story and torsional irregularities during the earthquake mainshock to assess the probabilistic effects of irregularities in plan and height of steel structures. These models were designed according to Iranian seismic codes. 3D analytical models of steel structures were created in the OpenSees software platform and Incremental Dynamic Analysis (IDA) was conducted to plot the IDA curves. The maximum value of inter-story drift was selected as the demand parameter and the capacity is determined according to the HAZUS-MH limit states; finally, the corresponding fragility curves were developed. The results of the 3D nonlinear dynamic analysis indicated that the damage state of the structure due to soft story irregularity was decreased with increasing stories. On the other hand, the damage caused by torsional irregularity in plan was increased by increasing the height of the structure. For example, in the 3-story structure, soft-story effect on damage probability was more dominant than torsional irregularity.

doi: *10.5829/ije.2021.34.11b.11*

NOMENCLATURE

E	Steel module of elasticity (N/m^2)	PGA	Peak ground acceleration of ground motion (m/s^2)
I	Moment of inertia (m^4)	Δ	Lateral displacement (m)
K	Lateral stiffness (N/m)		

1. INTRODUCTION

Earthquake is one of the most destructive natural phenomena that can cause severe damages to the building structures, leading to huge economic damages and casualties. The disastrous economic and social consequences, which are resulting from inappropriate design and poor execution of buildings along with the expansion of the construction businesses, has highlighted the significance of proper design of structures, improvements and strengthening the buildings against earthquakes. Many buildings suffer from sudden changes to structural stiffness of stories because of including parking spaces, using buildings for commercial purposes and inappropriate usage of masonry infill walls, all of which create a soft or an extremely soft story condition that can lead to the vulnerability of buildings during earthquakes (Figure 1).

On the other hand, any irregularity in a plan like "mass eccentricity" may create torsion in the buildings which can cause the frame, on one side of building. This study focuses on examining the extent of damages to the structures with torsional irregularity in plan and soft story irregularity in height. Moreover, this study also examines the simultaneous effects of these two irregularities on the steel moment-resisting frame buildings.

The probabilistic seismic assessment of the existing steel buildings with the soft story and torsional irregularity is of great importance for presenting retrofitting plans and evaluating the vulnerability for

*Corresponding Author Institutional Email: j.shafaei@shahroodut.ac.ir (J. Shafaei)

Please cite this article as: M. H. Razmkhah, H. Kouhestanian, J. Shafaei, H. Pahlavan, M. Shamekhi Amiri, Probabilistic Seismic Assessment of Moment Resisting Steel Buildings Considering Soft-story and Torsional Irregularities, International Journal of Engineering, Transactions B: Applications, Vol. 34, No. 11, (2021) 2476-2493

Figure 1. Damages caused by soft-story irregularity in Kermanshah Earthquake, 2017

these types of structures. As a first step, the extent of damage to these types of structures should be detected and examined. Several studies have focused on the probabilistic seismic assessment of steel and reinforced concrete structures. The main focus of this study is to examine the effects of earthquakes on fragility curves of steel structures and to perform the probabilistic seismic assessment of steel structures constructed with regard to Iranian construction practice, according to Iranian Standard No. 2800, with soft story and plan torsional irregularities.

The increasing damages to the structures, caused by large and severe earthquakes such as 1994 Northridge earthquake in California, 1995 Kōbe earthquake in Japan and 2003 Bam earthquake in Iran, have highlighted the weaknesses of the existing codes of practice that are used for seismic design of buildings. In the current codes of practice, the structural designs are mainly performance-based and the displacement is regarded as the main criterion for designing the structures and detecting the magnitude of damage [1].

Initially, the fragility curves were used for analyzing the vulnerability of the nuclear power plants because the performance of these structures is of paramount importance and even the slightest defect may lead to disastrous incidents during earthquakes [2]. Therefore, the fragility curves were developed for the nuclear power plants with regard to different factors like Peak Ground Acceleration (PGA). These fragility curves were developed by Kircher and Martin [3]. After 1994 Northridge earthquake that caused huge financial damages to buildings, the engineering community majorly realized (focused on) the importance of assessing the extent of damages to the structures after severe earthquakes.

Anagnos and Rojahn [4] conducted several studies based on load distribution in ATC, all of which led to the development of a new type of fragility curve. In their study, all seismic calculations were conducted based on ATC-13. The horizontal axis of the fragility curves was the modified Mercalli values because it was a more scientific method for analyzing the fragility. Moreover, Log-normal distribution function was assumed in their study through which useful ideas were provided for future research regarding using earthquake records. They used the results of log-normal distribution for extracting the fragility curves.

Ozturk et al. [5] obtain seismic performance assessment for precast concrete industrial buildings using the fragility curves.

Naseri and Ghodrati [6] applied the fragility curves to examine the reinforced concrete structures without considering the effect of infilled frame and the structural vulnerability. The results indicated that the slope of fragility curve was higher at slight and moderate damage states and at low PGA. As PGA values increased, the slope of the fragility curve decreased i.e. the probability of damage was higher at lower PGA values [7].

In 2017, Ouzturk [8] estimated the seismic behavior of two monumental buildings in the historical Cappadocia region of Turkey, and It was observed that slab discontinuities on the first floors constitute a major element in the expected structural damage for both buildings. In addition, upon application of certain ground motions, destructive levels of drift were observed, another element contributing to the expected damage.

Hwang and Lee [9] examined the effect of assigned risk category on the earthquake performance of low- to mid-rise, steel special moment-resisting frame (MRF) buildings. The results indicated that the collapse risk of the steel special MRF buildings of an ordinary occupancy used showed in earthquake much higher than that of the higher risk buildings.

Moufid Kassem et al. [10] used Group of National Defense against earthquake (GNDT) approach for seismic performance assessment and the results indicated that there is a good correlation between the analytical modeling approach and the observed fragility features during in-situ field investigations.

Fattahi and Gholizadeh [11] assessed the seismic performance of the reinforced Steel Moment Frames (SMFs) under performance-based design (PBD) framework. For this purpose, SMFs were optimized. Then the optimized SMFs were analyzed using incremental non-linear dynamic analysis (IDA). Later, the fragility curves were plotted to examine the damage states. The results indicated that the design optimization could only be efficient before the structure faced the complete collapse state.

Taiyari et al. [12] investigated on damage-based optimal design of friction dampers in multistory chevron braced steel frames. The performance of proposed method was illustrated using three steel moment-resisting frames models with friction damper systems such as chevron braces and damper devices. According to the results, the largest damage probability in every structural model was associated with higher slip force and the lower stiffness ratio, where the undesirable buckling failure occurred before the friction damper was fully activated.

The main purpose of this study is to examine the effects of soft-story and torsional irregularities of steel moment-resisting frames on the four damage states during earthquakes, with respect to HAZUS-MH MR-5 code [13]. Therefore, fragility curves are developed for four damage states to examine the effect of soft-story irregularity on the lateral load stiffness of the first-story and to investigate the effect of the torsional irregularity in plan on the 3, 5, and 8 story steel moment-resisting frame models during the earthquake.

The soft-story irregularity can occur for several reasons such as inappropriate usage of masonry infill walls, increasing the height of the structure or removing a structural element (column or beam) to create parking spaces. In this study, the main reason for soft-story irregularity was attributed to the increase of height in buildings which in turn led to the reduction of Lateral Load Stiffness. Moreover, torsional irregularity can occur as a result of asymmetric usage of lateral load resisting systems, the existence of large openings in the diaphragm, plan asymmetry and excessive concentration of gravity load on one side of plan, etc. The irregularity caused by the asymmetry in the lateral load resisting systems is also examined in this study.

2. INTRODUCTION OF THE MODELS (BUILDING STRUCTURES) OF THE STUDY

The 3D models used in this study have consisted of three-, five- and eight-story buildings with medium steel moment frames as their lateral load resisting systems, the characteristics of which are as follows:

A) Structures with regularity in plan and height (Figure 2(a))
B) Structures with regularity in plan and soft-story irregularity
C) The structure with simultaneous soft-story irregularity and torsional irregularity in plan (Figure 2(b))

The buildings were designed in accordance with the existing standard codes of Iran. The characteristics of the model that is used in this study are as follows:

- The structure is built on relatively high seismic hazard zones.
- The soil of construction site is considered to be Type III.
- The height of the first story is considered to be 2.8 and 3.8 m for the structure with regular height and soft story irregularity, respectively. The heights of other stories are considered as 3.2 m.
- The steel's yield stress which is used in the beam and column equals 240 MPa.
- The steel's ultimate stress that is used in the beam and column equals 370 MPa.

3. DETECTING SOFT STORY AND TORSIONAL IRREGULARITY

According to Iranian Standard No. 2800, the soft story condition occurs when the lateral stiffness of one story of the building is 70% lower than the upper stories. Torsional irregularity occurs when the ratio of maximum story displacement is 1.2 times greater than the average story displacement of the structure. In this study, the lateral stiffness of the first story is calculated using the Etabs software program. Moreover, the stiffness of the first and other stories was compared to detect soft-story irregularity.

In Etabs, a unit load (F) was applied on the diaphragm of the first story and the drift of the first story was calculated to estimate the story's stiffness using Equation (1). The value of K is equal to the lateral stiffness of the structure and Δ the lateral displacement of the structure.

Then, the stiffness of the second story was computed. In order to detect the existence of soft stories in the first story, the stiffness of the first and second stories was compared by considering the fact that soft-story condition occurs when the stiffness of the first story is 60 to 70% lower than the second story.

In order to determine the torsional irregularity of the structure, firstly, the maximum and average displacement of the structure were separately calculated. Then, the ratio of the maximum and average displacement was estimated. Torsional

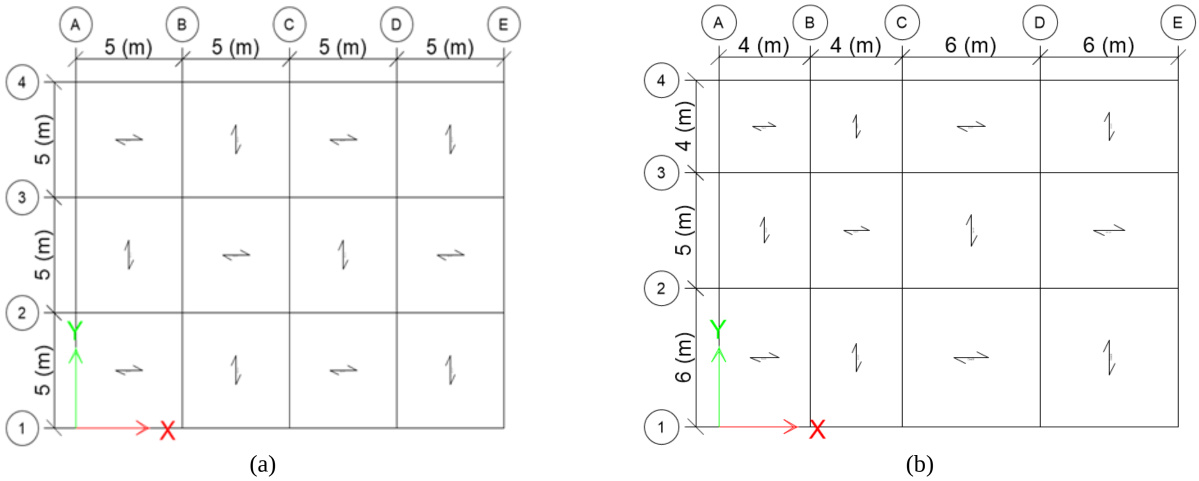

Figure 2. The plan of different types of modeled structures: (a) Structure with regular plan; (b) Structure with an Irregular plan

irregularity occurs if the ratio of maximum story displacement is 1.2 times greater than the average story displacement of the structure (Standard No. 2800 of Iranian code [14]).

In addition to utilize Etabs to calculate the lateral stiffness of the structure, Equation (2) can be used to estimate the lateral stiffness of each story. In this relation E is the modulus of elasticity and I is the moment of inertia as well as L is the length of the column.

$$F = K\Delta \tag{1}$$

$$K = \sum \frac{12EI}{L^3} \tag{2}$$

After calculating the lateral stiffness of the models under this study, it can be concluded that if the height of the first story is 3.8 m, the stiffness of the first story will be 61% lower than that of the second story; and consequently, the first story has soft story irregularity.

4. OPENSEES SOFTWARE VERIFICATION WITH EXPERIMENTAL RESULTS

The first step in modeling software is to validate the results obtained through software with the actual behavior of the structure. Figure 3 shows a 4-story, 2-span frame prototype model of an office building in the Los Angeles area. The structural system of this prototype model consisted of the lateral load system of special moment-resisting frame (SMRF) with reduced beam sections (RBS). The soil type D was used in the construction site. This model was comprised of two spans, columns axis-to-axis length of 9100 mm, first story height of 4600 mm and other stories are of 3700 mm high.

This model was designed based on IBC [15]. The gravity loads and lateral load are calculated and applied on the structure based on ASCE-7 [16] and AISC [17], respectively.

The beam sections that were used in the first and second stories and also in the third and fourth stories were W27X102 and W21X93, respectively. The column's sections which were used in the first and second stories and also in the third and fourth stories were W24X131 and W24X76, respectively. A992 steel Grade 50 was used in all elements of this model. The lateral loads that were applied on the first three stories and on the fourth story were assumed as 4600N and 5300 N (1200 Kips), respectively [18]. As can be seen in Figure 4, in order to compare the results that were obtained by the experimental and software models, the load-drift curves were developed for both models. For analytical model, Uniaxial Materials Command is used to define steel materials [8]. In this study, the Steel02 materials with isotropic' hardening are used; because these materials also take rupture and the drop resistance conditions into consideration as well [19]. Fiber Section was used to define the beam and column cross-sections in OpenSees and can be used to apply

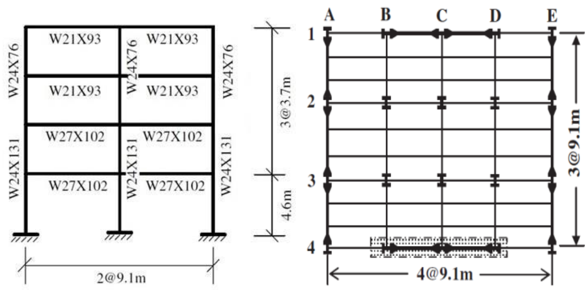

Figure 3. The details of 2D frame used for verification [19]

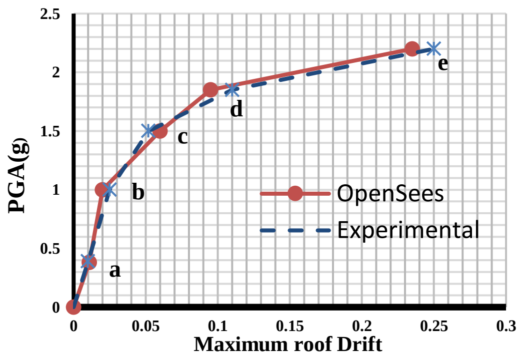

Figure 4. The comparison between Load-displacement curves of experimental and OpenSees samples

different characteristics of the materials to every cross-section of the element.

Since the non-linear analysis was applied in this study, Nonlinear Beam-Column Element command was used to define the elements. The elements are modeled non-linearly by using this command. Moreover, this command is also used to distribute the inelastic effects throughout the model. The experimental sample was modeled in OpenSees after selecting and examining the behavior model of the material in this software. The gravity and lateral loads were applied on the OpenSees sample with respect to the experimental sample. Accordingly, the roof displacement of OpenSees sample that was obtained from PGA, was extracted. Figure 4 illustrates the load-displacement curves of experimental and OpenSees samples.

As shown in Figure 4, relatively similar results, with high level of accuracy, were obtained for both experimental and modeled results.

5. ACCELEROGRAPH SELECTION

One of the most significant steps in the non-linear dynamic analysis is determined the ground-motion records because the results obtained by incremental dynamic analysis (IDA) are mainly dependent on these records. The records must be selected in such a way as to include all seismic behaviors of the structure. In this study, 20 ground-motion records are selected from "Peer" website while considering the soil type of the site and Li et al. [20] suggestions as follows:

- The shear velocity of the soil must be 175-375 m/s, with regard to the site's soil type.
- The Peak Ground Acceleration (PGA) must be greater than 0.4 g.

The selected records are summarized in Table 1.

TABLE 1. Selected Records

Record No	Record name	Site name	Soil type	Earthquakes Magnitude (Richter)	PGA(g)
1	Chalfant valley	Zack Brothers Ranch	III	6.19	0.447
2	Coalinga	Oil-City	III	5.77	0.398
3	Northridge	Sun Valley - Roscoe Blvd	III	6.69	0.604
4	Imperial Valley	El Centro Array #11	III	6.53	0.37
5	Coalinga	14Th & Elm (Old CHP)	III	5.77	0.84
6	Imperial Valley	Bonds Corner	III	6.53	0.776
7	Mammoth lakes	Convict Creek	III	6.06	0.444
8	Mammoth lakes	Fish & Game (FIS)	III	5.94	0.376
9	Mammoth lakes	Mammoth Lakes H. S	III	5.69	0.44
10	Managua-Nicaragua	Managua-Esso	III	6.24	0.371
11	Northridge	Northridge - 17645 Saticoy St	III	6.69	0.459
12	Northridge	Canoga Park - Topanga Can	III	6.69	0.392
13	Northridge	Jensen Filter Plant Administrative Building	III	6.69	0.617
14	Northridge	La - Sepulveda Va Hospital	III	6.69	0.93
15	Northridge	Newhall - Fire Sta	III	6.69	0.59
16	Northridge	Rinaldi Receiving Sta	III	6.69	0.87
17	Imperial Valley	El Centro Array #4	III	6.53	0.48
18	Imperial Valley	El Centro Array #5	III	6.53	0.53
19	Imperial Valley	El Centro Array #7	III	6.53	0.57
20	Imperial Valley	El Centro Array #8	III	6.53	0.61

In this study, in order to develop the fragility curves and to also compare the damages to the structures, all accelerograph records of the main-shock were scaled up to 1g. A sample of motion records recovered from the Mammoth Lakes-Convict Creek earthquake is shown in Figure 5.

6. HYSTERESIS CURVE

The moment-rotation hysteresis curve was examined to investigate the performance of the model and cross-sections built in OpenSees. The selected beam's hysteresis curve is shown in Figure 6. The hysteresis curve of the beam in the first story under the Chalfant valley earthquake in Zack Brothers Ranch site is shown in Figure 7 while the hysteresis curve of the column in the first story under the earthquake that was scaled up to 1g.

Figure 8 shows the column hysteresis curves along the C-2 axis, in the first story under Chalfant valley earthquake in Zack Brothers Ranch site; and also under the earthquake that was scaled up to 1g, which are shown in Figure 9. As shown in Figure 9, there is a slight difference in the amount of energy absorption for the column specified in the five-story structure with the soft story and with the soft story and torsional irregularity for the specified record.

After examining the hysteresis curves, it was observed that beam and column elements entered in the inelastic region which highlights the capability of the analysis model in estimating the structural non-linear response.

7. COMPARISON OF BASE SHEAR OF THE MODELS

One of the most important curves of the seismic behaviors of the structures is known as the base

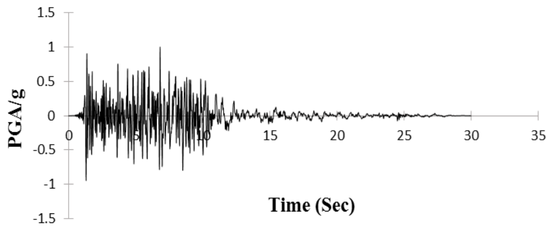

Figure 5. The scaled accelerographs of Mammoth Lakes-Convict Creek earthquake

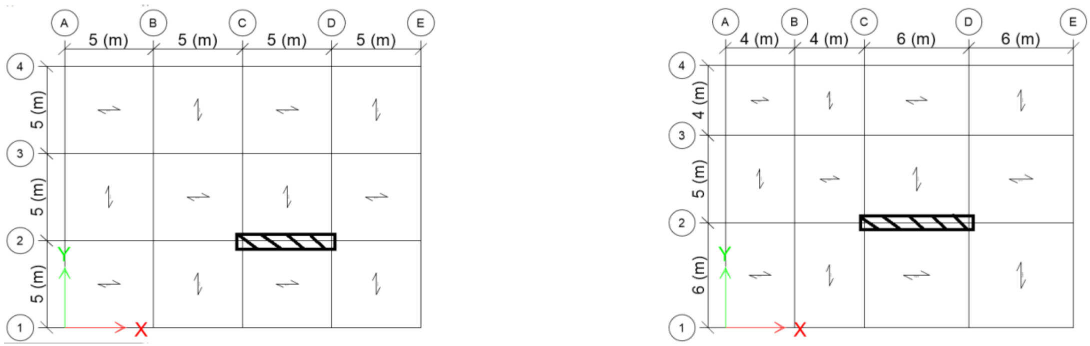

(a) (b)

Figure 6. The beam selected for plotting hysteresis curve: (a) The 5-story structure with soft story irregularity (b)The 5-story structure with soft story and torsional irregularity

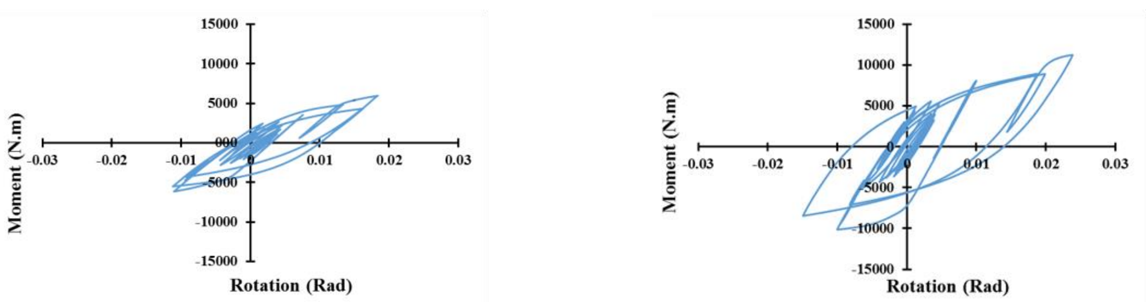

(a) (b)

Figure 7. The moment-rotation hysteresis curve of beam in the 5-story structure: (a) Structure with soft story irregularity; (b) Structure with soft story and torsional irregularity

shear-roof displacement curve, through which the stiffness variations of the structure, the structure strength, and ductility are demonstrated. Figure 10 represents the base shear-roof displacement curves of 3, 5 and 8-story structures. There is little difference between the base shear-roof displacement curve of the three-story structure with a soft story and the three-story structure with simultaneous a soft story and torsional irregularity. The reason for this phenomenon can be stated in the fact that due to the low height of the structure, the amount of displacement of the roof of the structure to the base shear force is not sensitive to the existence of soft story and torsional irregularities in the structure. After comparing the effects of torsional and soft-story irregularities on the base shear-roof

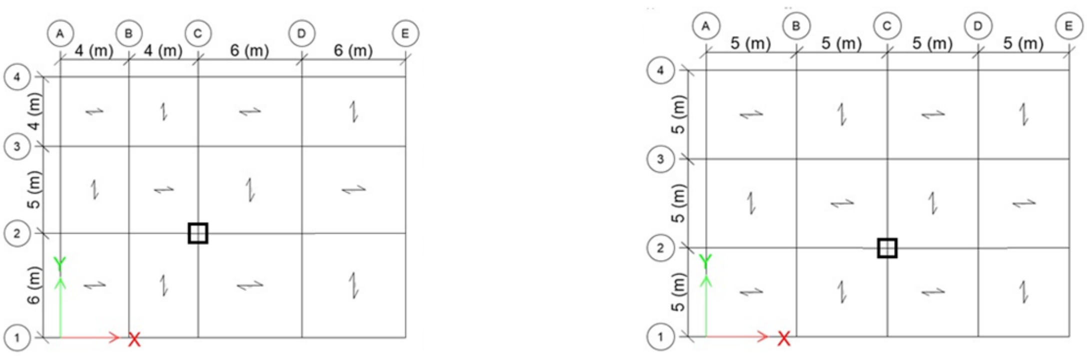

(a) (b)

Figure 8. The column selected for plotting hysteresis curve: (a) The 5-story structure with soft story irregularity; (b) The 5-story structure with soft story and torsional irregularity

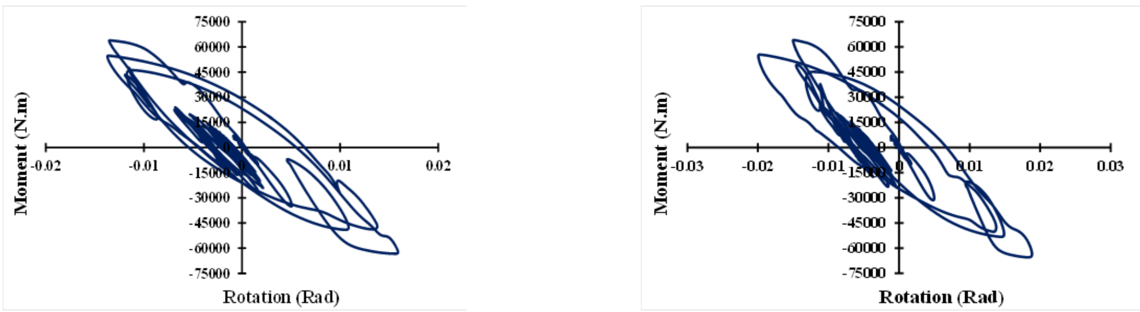

(a) (b)

Figure 9. The moment-rotation hysteresis curve of column in the 5-story structure**:** (a) Structure with soft story irregularity; (b) Structure with soft story and torsional irregularity

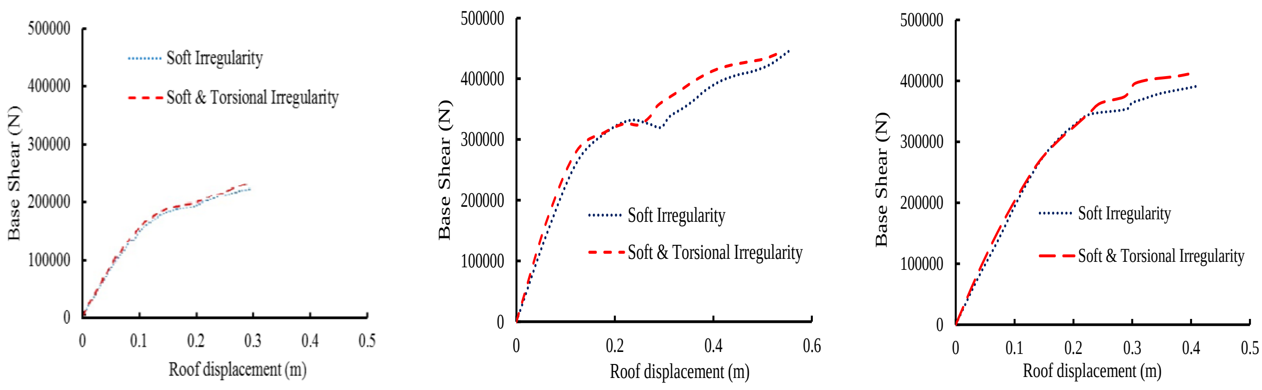

(a) (b) (c)

Figure 10. The base shear-roof displacement graph: (a) 3-story structures (b) 5-story structures (c) 8-story structures

displacement graphs, it was indicated that the shear-base increased in equal displacements in the structures with torsional irregularity. In fact, the shear-base values increased up to 7, 9 and 11% in the 3, 5 and 8-story structures, respectively.

8. COMPARING THE INCREASE OF DRIFTS AMONG THE STRUCTURES

The building structures may be affected by the earthquakes with different magnitudes during over different periods of time. Therefore, Figure 11 represents the comparison among the drifts of the structures in this study for three different PGA values, 0.1g, 0.2g, 0.3g, under Chalfant valley earthquake in Zack Brothers Ranch site (See Figures 11, 12 and 13).

After comparing the drift graphs of 3, 5 and 8-story structures, it was observed that on the roof level, the drift in the structures with simultaneous soft story and torsional irregularities was greater than that of the structures with only soft-story irregularity. The drift evidently increased with an increasing the number of stories, (The increase in drift became more evident with increasing number of stories).

The effects of the earthquakes on the drifts of different stories and various movement modes of the structures can be observed after comparing the story drifts of the structures with different heights. The movement mode was similar in the structure with the same number of stories but different types of irregularities. Although the movement mode of the structure is dependent on the number of stories, but it is not affected by different types of regularities.

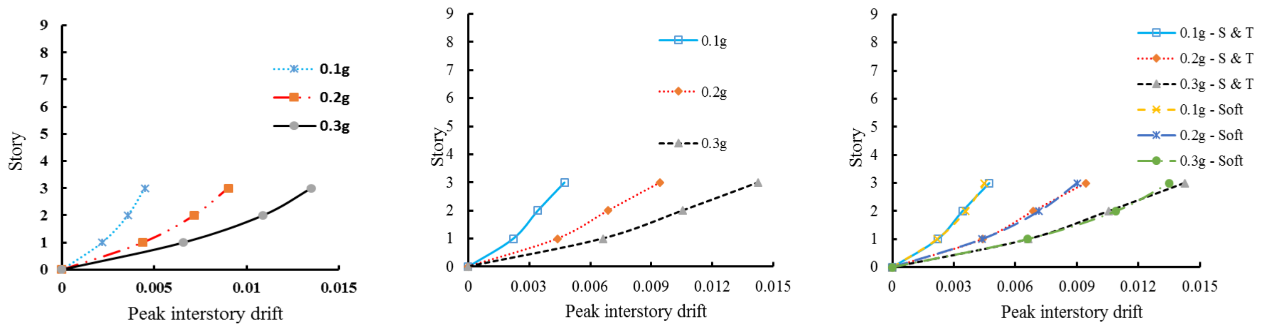

(a) (b) (c)

Figure 11. The drift graph of 3-story structures: (a) only the soft-story irregularity (b) Simultaneous soft story and torsional irregularities (c) The drift graph of 3-story structures with only the soft-story irregularity and also simultaneous soft story and torsional irregularities

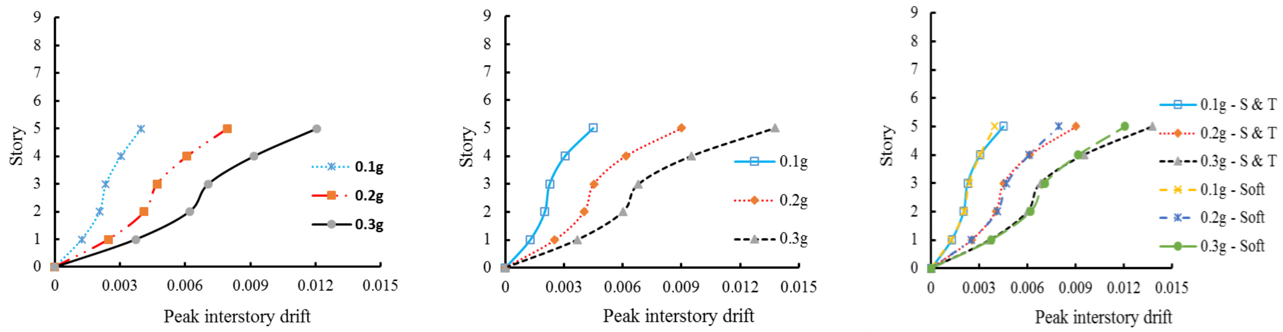

(a) (b) (c)

Figure 12. The drift graph of 5-story structures: (a) only the soft-story irregularity (b) Simultaneous soft story and torsional irregularities (c) The drift graph of 5-story structures with only the soft-story irregularity and also simultaneous soft story and torsional irregularities

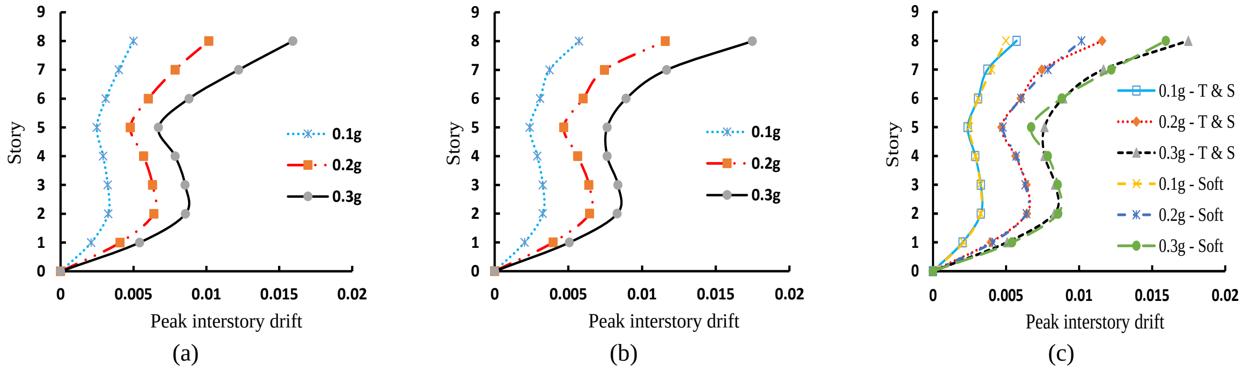

Figure 13. The drift graph of 8-story structures: (a) only the soft-story irregularity (b) Simultaneous soft story and torsional irregularities (c) The drift graph of 8-story structures with only the soft-story irregularity and also simultaneous soft story and torsional irregularities

9. COMPARISON AMONG THE ROOF DISPLACEMENT OF STRUCTURES DURING EARTHQUAKES

In order to compare the displacement of structures in this study during earthquakes and also observe their permanent displacements, these structures were examined under Chalfant valley records in Zack Brothers Ranch site.

As can be seen in Figure 14, since relatively identical roof displacements were observed in the three-story structures with different irregularities, their permanent displacements were also similar to one another. However, in five-story structures (Figure 15), a small roof displacement was observed in structures with simultaneous soft story and torsional irregularity. Therefore, the permanent displacement of the five-story structure with simultaneous soft story and torsional irregularity was smaller than that of with soft story irregularity. On the other hand, identical permanent displacements were observed in eight-story structures with both soft story irregularity and simultaneous soft story and torsional irregularity (Figure 16).

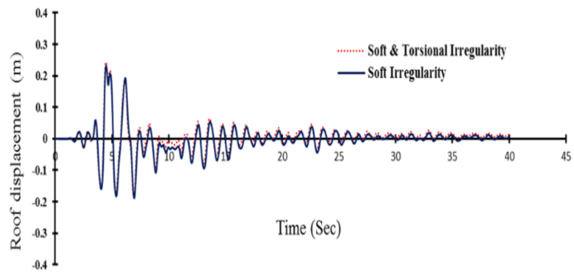

Figure 14. The roof displacement graph during earthquake in two 3-story structures with soft story irregularity and simultaneous soft story and torsional irregularities

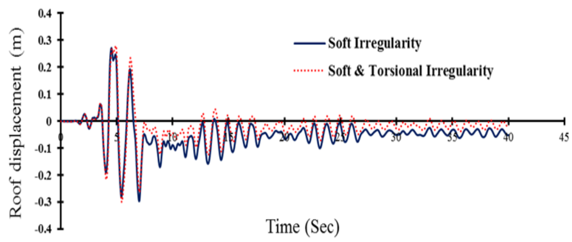

Figure 15. The roof displacement graph during earthquake in two 5-story structures with soft story irregularity and simultaneous soft story and torsional irregularities

10. THE INTRODUCTION OF DAMAGE STATES

Four damage states including slight, moderate, extensive and complete collapse are introduced for the structure with respect to HAZUS-MHMR-5. Table 2 shows the maximum displacement of each damage state. According to HAZUS-MHMR-5, the point at which the materials reach the softening region to achieve the complete dynamic instability is considered as the best point in which the structure can withstand until the complete collapse occurs.

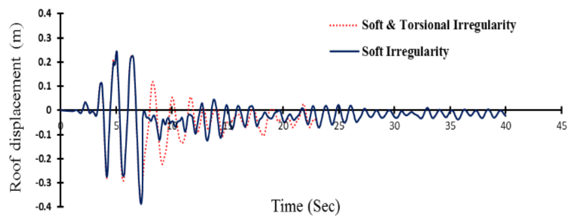

Figure 16. The roof displacement graph during earthquake in two 8-story structures with soft story irregularity and simultaneous soft story and torsional irregularities

This point has the slightest damage state among other points. Another damage criterion is known as the maximum drift among the stories. Table 2 shows the maximum drifts of low-, mid- and high-rise structures with respect to HAZUS-MH MR-5 code.

11. IDA CURVES FOR SOME MODELS IN THIS STUDY

Incremental dynamic analysis is a seismic analysis method based on the structures' performances. The structures' behaviors with different intensity levels are also identified by IDA. Unlike pushover analysis, IDA can be successfully used to determine the structural capacity, the collapse probability and the percentage of reaching a particular damage limit. IDA provides more precise analyses, compared to the pushover method due to have some capabilities such as introducing the materials with non-linear behaviors and performing dynamic analyses [21].

TABLE 2. The amount of drift at different damage states considering the damage type considering HAZUS-MHMR-5

Structure type	Drift at the Threshold of damage state			
	Slight damage	**Moderate damage**	**Extensive damage**	**Complete damage**
Low-rise	0.006	0.00104	0.0235	0.06
Mid-rise	0.004	0.0069	0.0157	0.04
High-rise	0.003	0.0052	0.0118	0.03

In this study, IDA was used to examine the models in such a way that the maximum PGA, applied on the structure, was scaled up to 0.1g. Then, IDA curves were developed after analyzing the structure at each incremental PGA value. In this study, IDA curves were developed for three, five and eight-story structures, under the main-shock and also the main-shock-aftershock sequence under 20 accelerographs in Figures 17, 18 and 19.

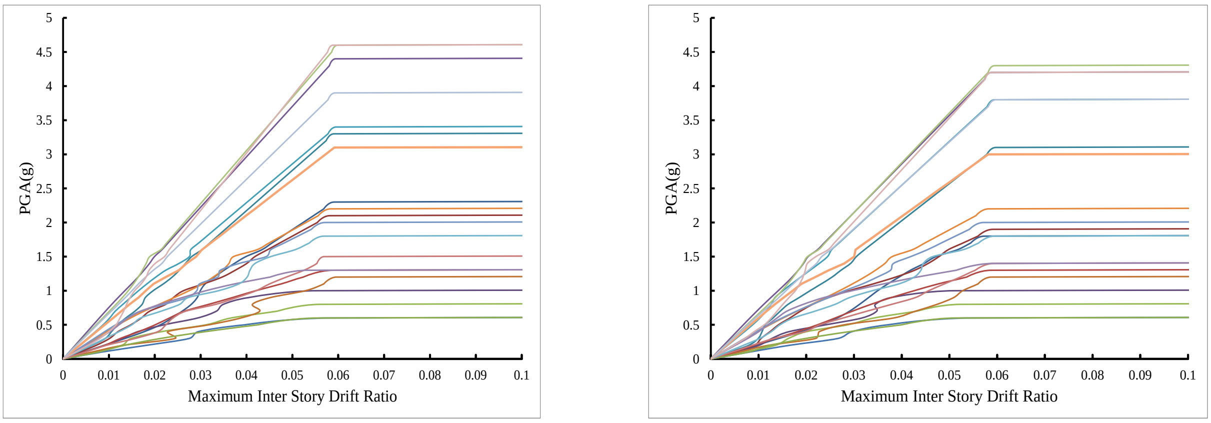

(a) (b)

Figure 17. IDA graph (curve) for 3-story structure: (a) With soft story irregularity (b) With soft story and torsional irregularity

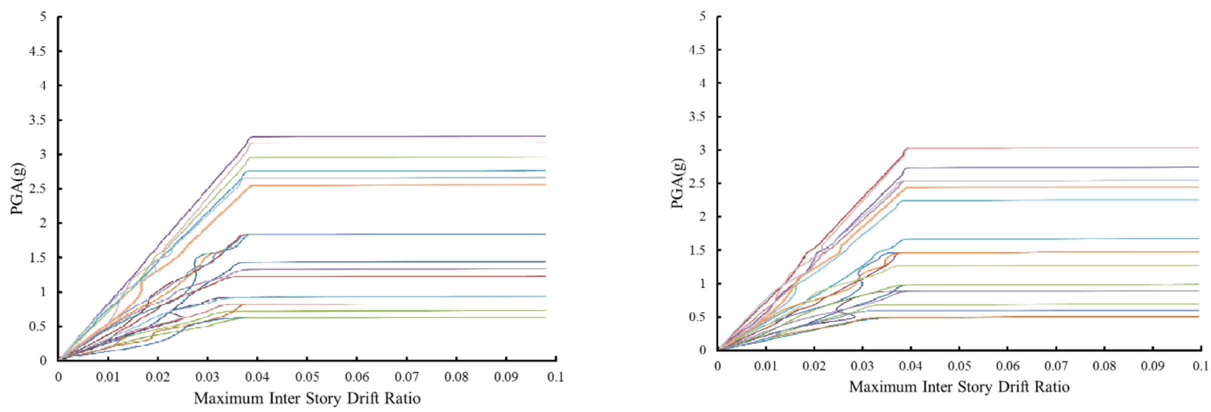

(a) (b)

Figure 18. IDA graph (curve) for 5-story structure: (a) With soft story irregularity (b) With soft story and torsional irregularity

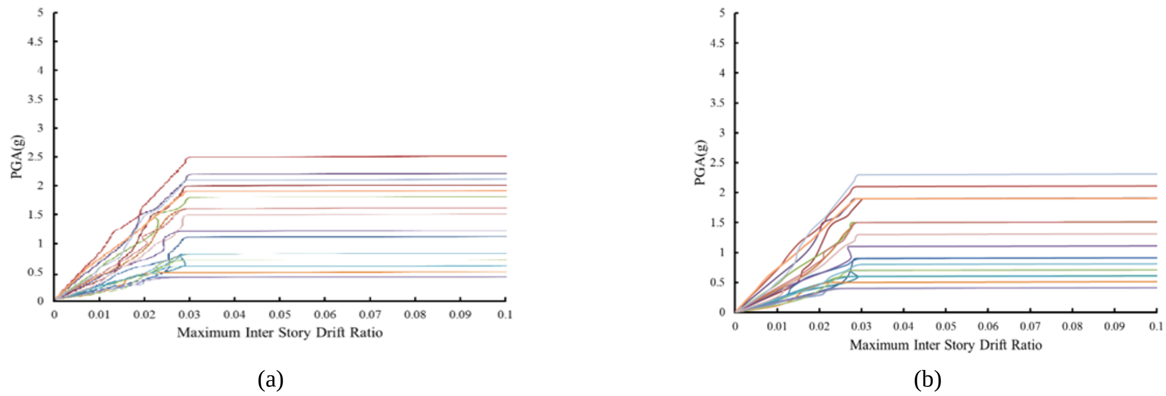

Figure 19. IDA graph (curve) for 8-story structure: (a) With soft story irregularity(b) With soft story and torsional irregularity

Considering the IDA graphs, it can be concluded that the structures exhibited extreme load resistance behavior under accelerographs, indicating that the displacement hardly occurred in the structure and mostly appeared around the slope of the elastic region. Moreover, a relatively constant increase was observed in the relative drift of three-story structures. However, as the number of stories increased, the drift of some stories led to the complete collapse of the structure.

12. DEVELOPING AND PLOTTING THE FRAGILITY CURVE

The fragility curves are considered as one of the useful tools for analyzing the damage probability of the structures. The probability of exceedance from a particular damage state against seismic parameters of the structure is determined through fragility curves. While developing the fragility curves, it should be noticed that the characteristics of the structures are different in every country. Therefore, the specific characteristic of every structure should be taken into consideration for analysis process. A probability distribution for engineering demand parameter, obtained from IDA, was used to develop a fragility curve.

This study used the Log-normal distribution to develop the fragility curves. Every structure was analyzed under 20 ground motion records, the PGA values of which varied from 0.1g to 1.5g. Then, the fragility probability of the structure was examined using OpenSees. Since the structural capacity and seismic demand are the two parameters that follow the log-normal distribution. Therefore, the fragility curves can be developed as a cumulative lognormal distribution function, based on Equation (3):

$$P(:\leq D)=\Phi\left[\left(\frac{\mathrm{Ln}\left(S_d/S_c\right)}{\beta_{sd}}\right)\right] \tag{3}$$

P is considered as the probability of reaching to or exceeding the *damage state (D) (the maximum inter-story displacement)*, β_{sd} is the standard deviation of Log-normal distribution, s_c is the mean value of capacity limit state and S_d is the median value of seismic demand.

Figure 20 shows the fragility curves of four damage states in the three-story structure with regularity in plan and height, with simultaneous soft story and torsional irregularity, and with only soft story irregularity under ground motion records.

Figure 21 illustrates the fragility curves of four damage states in the five-story structure with regularity in plan and height, with simultaneous soft story and torsional irregularities, and with only soft story irregularity under ground motion records.

Figure 22 depicts the fragility curves of four damage states in the for eight-story structure with regularity in plan and height, with simultaneous soft story and torsional irregularity, and with only soft story irregularity under ground motion records.

13. THE COMPARISON AMONG THE FRAGILITY CURVES OF THE STRUCTURES

In this section, the fragility curves of three-, five- and eight-story structures are investigated.

13. 1. Comparison among the Fragility Curves of the three-story Structure

Firstly, the fragility curves of 3, 5 and 8-story structures with regularity in plan and height, with simultaneous soft story and torsional irregularity, and with only soft story irregularity during the earthquake were separately calculated and developed. Then, the fragility curves of the structure with regularity in plan and height were compared with that of the structure with soft story irregularity. Later, the fragility curves of structures with only soft story irregularity were compared with that of the structures with simultaneous soft story and

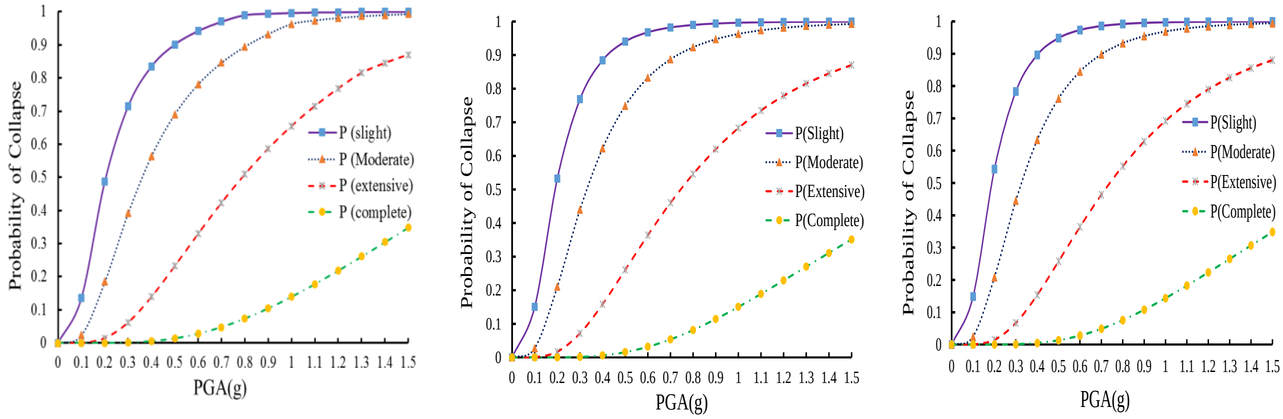

(a) (b) (c)

Figure 20. Fragility curve of 3-story structure: (a) Structure with regularity in plan and height (b) Structure with soft story irregularity (c) Structure with simultaneous soft story and torsional irregularity

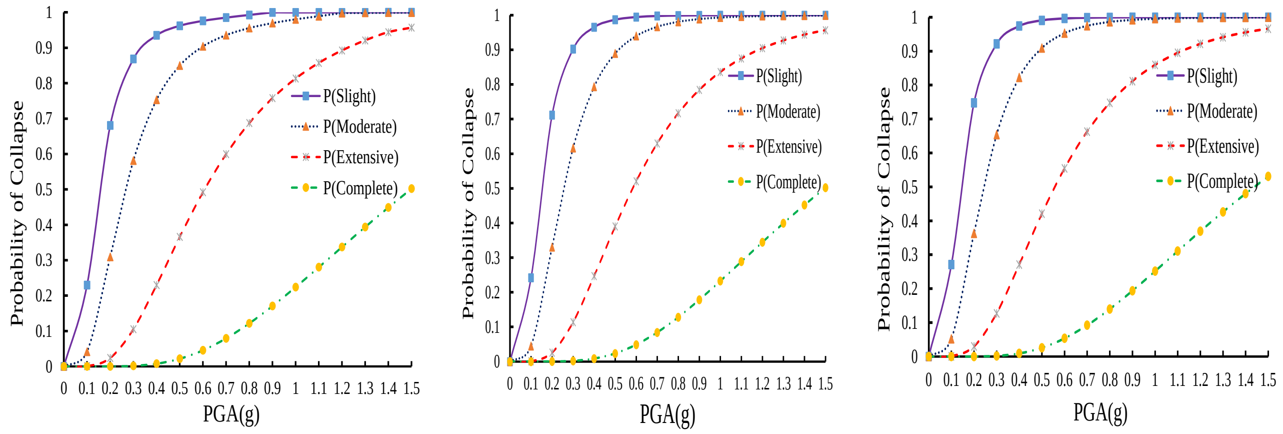

(a) (b) (c)

Figure 21. Fragility curve of 5-story structure: (a) Structure with regularity in plan and height (b) Structure with soft story irregularity (c) Structure with simultaneous soft story and torsional irregularity

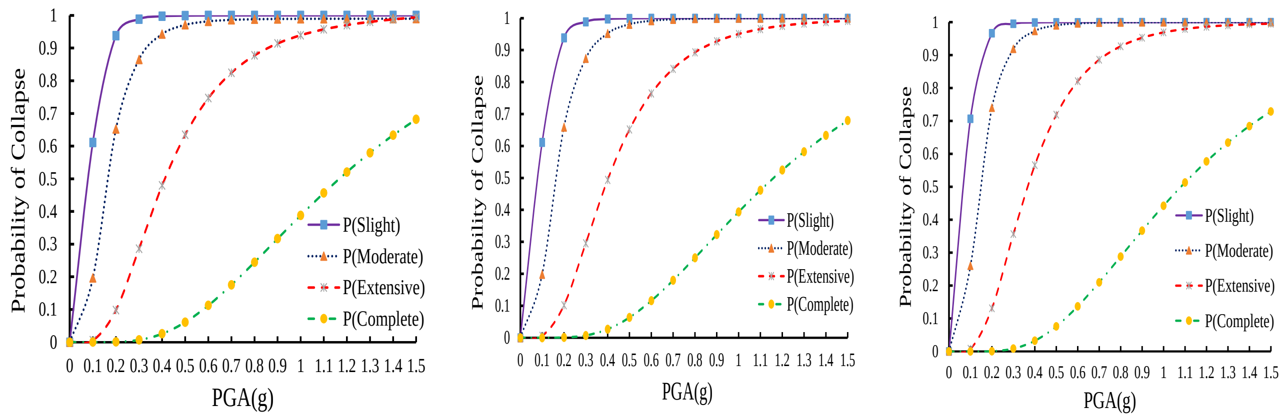

(a) (b) (c)

Figure 22. Fragility curve of 8-story structure: (a) Structure with regularity in plan and height (b) Structure with soft story irregularity (c) Structure with simultaneous soft story and torsional irregularity

torsional irregularity under the given earthquake. Firstly, Figure 23 demonstrates the comparison among 3-story structure with different irregularities.

After comparing the 3-story structure with soft story irregularity and with regularity in plan and height, it was concluded that when the structure was put under ground motion records, the PGA values of structure with soft-story irregularity decreased to almost 5, 8 and 9% to the midpoint of slight, moderate, extensive damage states, respectively; compared to structure with regularity in plan and height. As for the complete collapse state, the PGA value of the structure with soft-story irregularity decreased to 4%, compared to the structure with regularity in plan and height which led to 20 % probability of the complete collapse of the structure.

After comparing the 3-story structure with soft-story irregularity and with simultaneous soft-story and torsional irregularity, it was observed that in both models, the midpoint fragility values occurred at relatively equal PGAs. Therefore, the fragility curve of the structure with soft-story irregularity was relatively compatible with that of the structure with simultaneous soft-story and torsional irregularity.

13. 2. Comparison among the Fragility Curves of the Five-story Structure This part focused on comparing the fragility curves of the 5-story structure under ground motion records (Figure 24).

After comparing the 5-story structure with soft story irregularity and with regularity in plan and height, it was observed that when the structure was put under different ground motion records, the PGA of the structure with soft-story irregularity decreased to almost 3, 4 and 5% to the midpoint of slight, moderate, extensive damage states; respectively; compared to structure with regularity in plan and height. As for the complete collapse state, the PGA value of the structure with soft-story irregularity decreased to 3%, compared to that of the structure with regularity in plan and height which led to 20% probability of complete collapse of the structure.

After comparing the 5-story structure with soft-story irregularity and with simultaneous soft-story and torsional irregularity, when the structure was put under different ground motion records, the PGA of structure with simultaneous soft-story and torsional irregularity decreased to almost 3, 4, 5 and 6% to the midpoint of slight, moderate, extensive damage states and complete collapse, respectively; compared to that of the structure with only soft-story irregularity.

13. 3. Comparison among the Fragility Curves of the 8-story Structure After developing and comparing the fragility curves of 3 and 5-story structures under different ground motion records, finally, the fragility curves of 8-story structures under ground motion records were also compared (Figure 25).

After comparing the 8-story structure with soft story irregularity and with regularity in plan and height, it was observed that when the structure was put under different ground motion records, the two structures had relatively equal PGAs to the midpoints of slight and moderate damage states. As a result, the fragility curve of the 8-story structure with soft story irregularity was compatible with that of the structure with regularity in plan and height. Moreover, the PGA of the structure with soft story irregularity decreased to 2 and 3% to the midpoint of the extensive and complete collapse, respectively; compared to that of the structure with regularity in plan and height.

After comparing the 8-story structure with soft-story irregularity and with simultaneous soft-story and torsional irregularity, it was concluded that when the structure was put under different ground motion

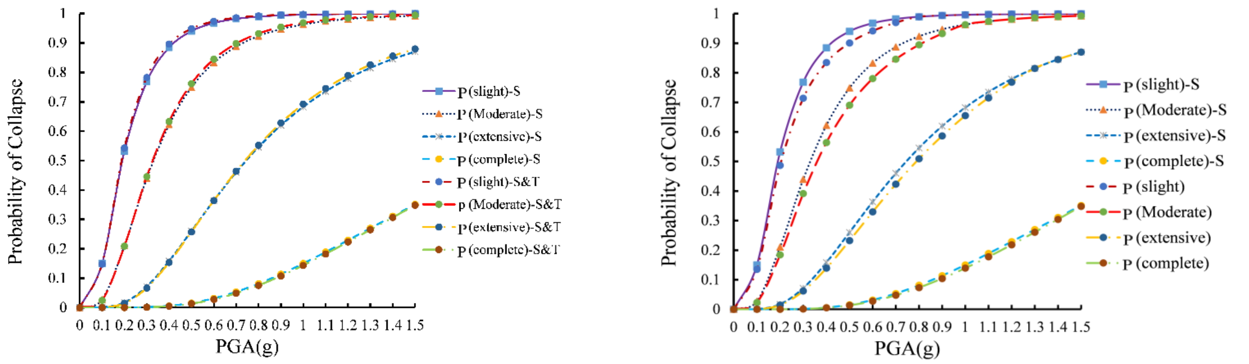

(a) (b)

Figure 23. Fragility curve of 3-story structure: (a) With soft story irregularity (b) With simultaneous soft story and torsional irregularity

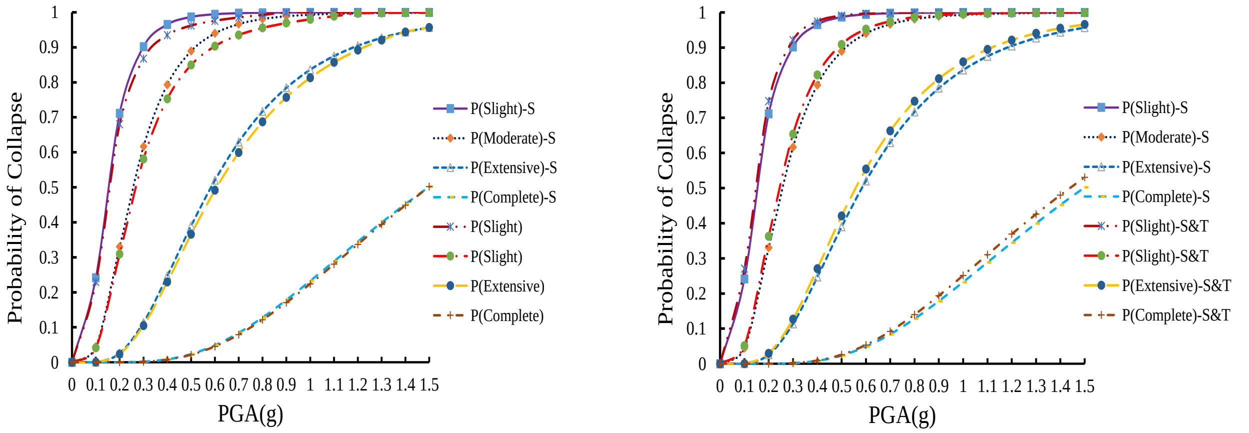

(a) (b)

Figure 24. Fragility curve of 5-story structure: (a) With soft story irregularity (b) With simultaneous soft story and torsional irregularity

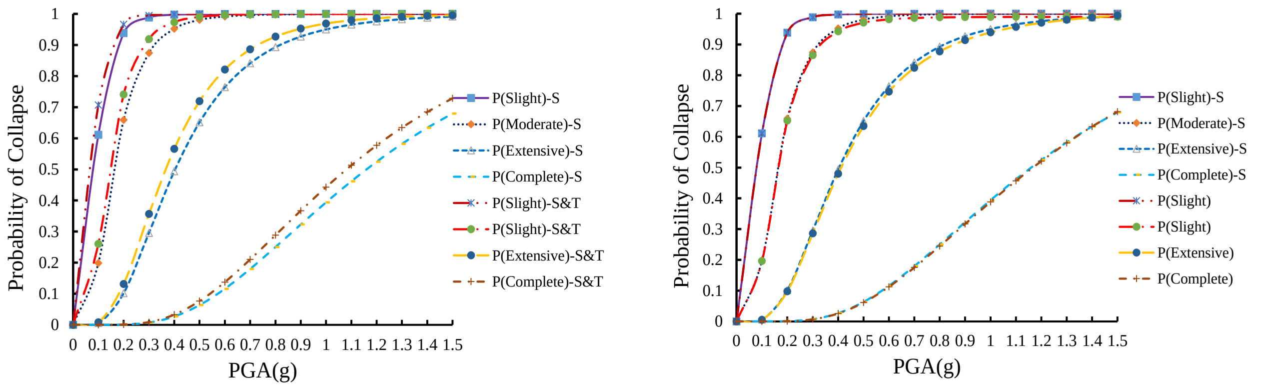

(a) (b)

Figure 25. Fragility curve of 8-story structure: (a) With soft story irregularity (b) With simultaneous soft story and torsional irregularity

records, the PGA of structure with simultaneous soft-story and torsional irregularity decreased to almost 15, 12, 10 and 9% to the midpoint of slight, moderate, extensive damage states and complete collapse, respectively; compared to that of the structure with soft-story irregularity.

14. CONCLUSIONS

After analyzing the three, five and eight-story steel structures with regularity in plan and height, with only soft-story irregularity and with simultaneous soft-story and torsional irregularities, it was concluded that the soft-story irregularity of the structure had relatively no significant effect on reaching the slight and moderate damage states. However, the extensive damage state and complete collapse of the structure were significantly affected by soft-story irregularity. Moreover, the soft-story irregularity has less effect on the 4 damage states of the buildings by increasing the number of stories. The numerical results regarding the effects of increased height on the damage extent of 3, 5 and 8-story structures are as follows:

- Damages to low-rise buildings were more affected by soft story irregularity. As the number of stories increased, the effect of soft-story irregularity on the damage state decreased. In other words, in low-rise buildings (three-story structures) the slight, moderate, extensive and complete collapse states increased to 5, 8, 9 and 4%, respectively. In mid-rise buildings (five-story structures), the slight, moderate, extensive and complete collapse states increased to 3, 4, 5 and 3%, respectively. As for the high-rise buildings (eight-story structures), the extensive and complete collapse states increased to 2 and 3%, respectively.

After examining the soft-story irregularity, the effects of torsional irregularity on the damage state of structures were examined, the results of which are summarized as follows: Torsional irregularity had no significant effect on the damage states in low-rise buildings. However, as the number of stories increased, the effect of torsional irregularity on all four damage states increased as well. Therefore, it can be said that the high-rise structures were significantly affected by torsional irregularity.

After examining the fragility curves of structures, the following numerical results were obtained:
The low-rise structures were not affected by torsional irregularity in such a way that the damage curves of the structures with torsional irregularity were completely compatible with that of the structures with regularity in plan. However, the damages to the high-rise structures were mainly attributed to the torsional irregularity. In the 8-story structure, the slight, moderate, extensive and complete collapse states increased up to 15, 12, 10 and 9%, respectively by increasing the height.

After comparing the fragility curves of 3, 5 and 8-story structures under the earthquake effects, it was concluded that the damages to the low-rise structures increased due to soft story irregularity. However, the effect of soft-story irregularity on damage states of buildings decreased by increasing the number of stories in such a way that the high-rise structures were not affected by soft-story irregularity. On the other hand, low-rise structures were not affected by torsional irregularity. But, as the number of stories increased, the damages to the structures were mostly attributed to the torsional irregularity.

The effects of soft story and torsional irregularity on the base shear-roof displacement of the structures were compared. The results indicated that in equal base shear, the extent of displacement increased 7, 9 and 11% in 3, 5 and 8 structures with torsional irregularity, respectively.

This study examined the damage states of structures with soft-story irregularity and torsional irregularity. Although some findings of previous studies especially the ones indicating that other irregularities that were mentioned in international building codes such as cutting off the lateral load system, the soft story, etc. could cause damages the buildings under earthquakes, can be considered as interesting subjects for future research, the soft-story irregularity can occur due to various reasons such as the increasing the height of the story, inappropriate usage of masonry infill walls, cutting off or removing structural elements (column or beam). In this study, the soft story irregularity was mainly attributed to the increase of height of the story. However, other factors involved in creating soft-story irregularity can be examined in future research.

15. REFERENCES

1. Pahlavan, H., Zakeri, B. and Ghodrati Amiri, G., "Probabilistic performance assessment of retrofitted horizontally curved multi-frame rc box-girder bridges", ***Journal of Earthquake and Tsunami***, Vol. 11, No. 04, (2017), 1750010, https://doi.org/10.1142/S1793431117500105
2. Kennedy, R.P., Cornell, C.A., Campbell, R., Kaplan, S. and Perla, H., "Probabilistic seismic safety study of an existing nuclear power plant", ***Nuclear Engineering and Design***, Vol. 59, No. 2, (1980), 315-338, https://doi.org/10.1016/0029-5493(80)90203-4
3. Kircher, C.A., Nassar, A.A., Kustu, O. and Holmes, W.T., "Development of building damage functions for earthquake loss estimation", ***Earthquake spectra***, Vol. 13, No. 4, (1997), 663-682, https://doi.org/10.1193/1.1585974
4. Anagnos, T., Rojahn, C. and Kiremidjian, A.S., "Nceer-atc joint study on fragility of buildings", (1995), http://hdl.handle.net/10477/700
5. Ozturk, B., Sahin, H.E. and Yildiz, C., "Seismic performance assessment of industrial structures in turkey using the fragility curves", in 15th World Conference on Earthquake Engineering, Lisbon, Portugal. (2012), 1-7.
6. Naseri, A., Pahlavan, H. and Ghodrati Amiri, G., "Probabilistic seismic assessment of rc frame structures in north of iran using fragility curves", ***Journal of Structural and Construction Engineering***, Vol. 4, (2018), 58-78, doi: 10.22065/JSCE.2017.78827.1095. .
7. Pahlavan, H., Shaianfar, M., Ghodrati Amiri, G. and Pahlavan, M., "Probabilistic seismic vulnerability assessment of the structural deficiencies in iranian in-filled rc frame structures", ***Journal of Vibroengineering***, Vol. 17, No. 5, (2015), 2444-2454, https://www.jvejournals.com/article/15794
8. Ozturk, B., "Seismic behavior of two monumental buildings in historical cappadocia region of turkey", ***Bulletin of Earthquake Engineering***, Vol. 15, No. 7, (2017), 3103-3123, https://doi.org/10.1007/s10518-016-0082-6
9. Hwang, S.-H. and Lee, K., "Probabilistic seismic demand assessment of steel moment-resisting frame buildings with ordinary and essential occupancy uses", ***International Journal of Steel Structures***, Vol. 20, (2020), 1230-1240, https://doi.org/10.1007/s13296-020-00354-0
10. Kassem, M.M., Nazri, F.M., Farsangi, E.N. and Ozturk, B., "Improved vulnerability index methodology to quantify seismic risk and loss assessment in reinforced concrete buildings", ***Journal of Earthquake Engineering***, (2021), 1-36, doi. https://doi.org/10.1080/13632469.2021.1911888
11. Fattahi, F. and Gholizadeh, S., "Seismic fragility assessment of optimally designed steel moment frames", ***Engineering Structures***, Vol. 179, (2019), 37-51, https://doi.org/10.1016/j.engstruct.2018.10.075
12. Taiyari, F., Mazzolani, F.M. and Bagheri, S., "Damage-based optimal design of friction dampers in multistory chevron braced steel frames", ***Soil Dynamics and Earthquake Engineering***, Vol. 119, (2019), 11-20, https://doi.org/10.1016/j.soildyn.2019.01.004
13. County, C., "Federal emergency management agency", ***F***EMA Community, No. 170132, (2013).
14. Abkar, G. and Lorki, A.A., "Evaluation of progressive collapse in steel structures designed based on iranian code of practice for seismic resistant design buildings (standard no. 2800), and iranian national building code'inbc', part 10", ***Journal of civil Engineering and Materials Application***, Vol. 2, No. 4, (2018), 192-200.
15. Trombly, B., "The international building code (ibc)", CMGT 564-Term Paper, (2006),.

16. ASCE, "Minimum design loads for buildings and other structures, American Society of Civil Engineers. Vol., No., (2005).
17. Malley, J.O., "The 2005 aisc seismic provisions for structural steel buildings", ***Engineering Journal-American Institute of Steel Construction***, Vol. 44, No. 1, (2007).
18. Lignos, D.G., Krawinkler, H. and Whittaker, A.S., "Prediction and validation of sidesway collapse of two scale models of a 4-story steel moment frame", ***Earthquake Engineering & Structural Dynamics***, Vol. 40, No. 7, (2011), 807-825, https://doi.org/10.1002/eqe.1061
19. Mander, J.B., Priestley, M.J. and Park, R., "Theoretical stress-strain model for confined concrete", ***Journal of Structural Engineering***, Vol. 114, No. 8, (1988), 1804-1826, doi. https://doi.org/10.1061/(ASCE)0733-9445(1988)114:8(1804)
20. Li, Y., Song, R. and Van De Lindt, J.W., "Collapse fragility of steel structures subjected to earthquake mainshock-aftershock sequences", ***Journal of Structural Engineering***, Vol. 140, No. 12, (2014), 04014095, https://doi.org/10.1061/(ASCE)ST.1943-541X.0001019
21. Banazadeh, M. and Jalali, S.A., "Probabilistic seismic demand assessment of steel moment frames with sideplate connections", ***Amirkabir Journal of Civil Engineering***, Vol. 44, No. 2, (2013), 47-64, https://doi.org/10.1016/j.scient.2011.11.036

16. APPENDIX

The specifications of the sections used in this research for three-, five-, and eight-story structures are specified in Tables 3 to 11(The beam sections are I-shaped and the column sections are box-shaped). For example, a beam with dimensions of 20 * 18 * 1 means a beam with a height of 20 and a width of 18 and a thickness of 1 cm, and a column with dimensions of 20 * 20 * 1 means a column with dimensions of 20 by 20 and a thickness It is 1 cm. Figure 26 shows the plan of the structures, that the type of beams is specified by color.

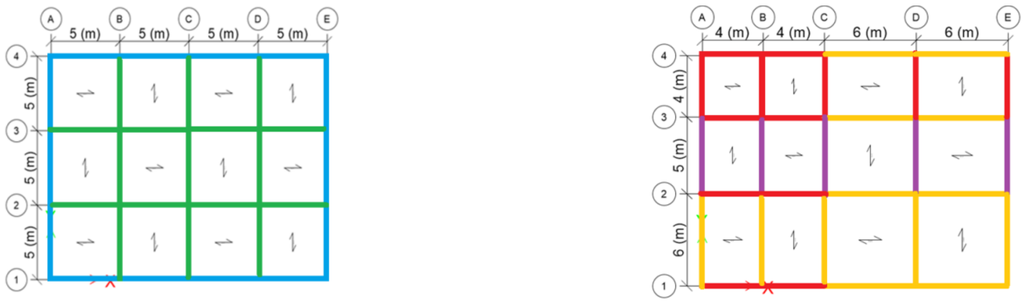

(a) (b)

Figure 26. The plan of different types of modeled structures: (a) Structure with regular plan; (b) Structure with an Irregular plan

TABLE 3. The specifications of the sections for three-story with soft story

Number of story	Beam selected by green color	Beam selected by blue color	column 1-A, 1-B, 1-C, 1-D, 1-E 2-A, 2-D 3-A, 3-D 4-A, 4-B, 4-C, 4-D, 4-E	column 2-B, 2-C, 2-D 3-B, 3-C, 3-D
1	20*18*1	20*16*0.8	27*27*1	22*22*1
2	20*18*1	20*16*0.8	25*25*0.8	20*20*0.8
3	20*18*1	20*16*0.8	25*25*0.8	20*20*0.8

TABLE 4. The specifications of the sections for three-story with torsional irregularity in plane

Number of story	Beam selected by red color	Beam selected by yellow color	Beam selected by purple color	Column 1-A, 1-B, 1-C, 1-D, 1-E	Column 2-A, 2-B, 2-C, 2-D, 2-E 3-A, 3-B, 3-C, 3-D, 3-E	Column 4-A, 4-B, 4-C, 4-D, 4-E
1	15*15*0.5	20*15*0.8	15*15*0.8	30*30*0.8	25*25*0.8	25*25*0.5
2	15*15*0.5	20*15*0.8	15*15*0.8	30*30*0.8	25*25*0.8	25*25*0.5
3	15*15*0.5	20*15*0.8	15*15*0.8	25*25*0.8	20*20*0.8	15*15*0.5

TABLE 5. The specifications of the sections for three-story with simultaneous soft story and torsional irregularity

Number of story	Beam selected by red color	Beam selected by yellow color	Beam selected by purple color	Column 1-A, 1-B, 1-C, 1-D, 1-E	Column 2-A, 2-B, 2-C, 2-D, 2-E 3-A, 3-B, 3-C, 3-D, 3-E	Column 4-A, 4-B, 4-C, 4-D, 4-E
1	15*15*0.5	20*15*0.8	15*15*0.8	32*32*1	30*30*1	28*28*0.8
2	15*15*0.5	20*15*0.8	15*15*0.8	30*30*0.8	25*25*0.8	25*25*0.5
3	15*15*0.5	20*15*0.8	15*15*0.8	25*25*0.8	20*20*0.8	15*15*0.5

TABLE 6. The specifications of the sections for five-story with soft story

Number of story	Beam selected by green color	Beam selected by blue color	column 1-A, 1-B, 1-C, 1-D, 1-E 2-A, 2-D 3-A, 3-D 4-A, 4-B, 4-C, 4-D, 4-E	column 2-B, 2-C, 2-D 3-B, 3-C, 3-D
1	22*20*1	20*16*1	30*30*1.2	32*32*1.2
2	22*20*1	20*16*1	28*28*1	30*30*1
3	20*16*0.8	18*16*0.8	22*22*1	26*26*1
4	20*16*0.8	18*16*0.8	22*22*1	26*26*1
5	18*16*0.8	16*16*0.8	18*18*0.8	20*20*0.8

TABLE 7. The specifications of the sections for five-story with torsional irregularity in plane

Number of story	Beam selected by red color	Beam selected by yellow color	Beam selected by purple color	Column 1-A, 1-B, 1-C, 1-D, 1-E	Column 2-A, 2-B, 2-C, 2-D, 2-E 3-A, 3-B, 3-C, 3-D, 3-E	Column 4-A, 4-B, 4-C, 4-D, 4-E
1	20*15*0.8	25*20*1	20*15*0.8	40*40*1.4	36*36*1.2	30*30*1
2	20*15*0.8	25*20*1	20*15*0.8	40*40*1.4	36*36*1.2	30*30*1
3	18*15*0.8	22*18*0.8	18*15*0.8	32*32*1.4	30*30*1.2	25*25*1
4	18*15*0.8	22*18*0.8	18*15*0.8	32*32*1.4	30*30*1.2	25*25*1
5	16*15*0.8	20*16*0.8	16*15*0.8	20*20*0.8	20*20*0.8	20*20*0.8

TABLE 8. The specifications of the sections for five-story with simultaneous soft story and torsional irregularity

Number of story	Beam selected by red color	Beam selected by yellow color	Beam selected by purple color	Column 1-A, 1-B, 1-C, 1-D, 1-E	Column 2-A, 2-B, 2-C, 2-D, 2-E 3-A, 3-B, 3-C, 3-D, 3-E	Column 4-A, 4-B, 4-C, 4-D, 4-E
1	20*15*0.8	25*20*1	20*15*0.8	44*44*1.6	40*40*1.4	32*32*1.2
2	20*15*0.8	25*20*1	20*15*0.8	40*40*1.4	36*36*1.2	30*30*1
3	18*15*0.8	22*18*0.8	18*15*0.8	32*32*1.4	30*30*1.2	25*25*1
4	18*15*0.8	22*18*0.8	18*15*0.8	32*32*1.4	30*30*1.2	25*25*1
5	16*15*0.8	20*16*0.8	16*15*0.8	20*20*0.8	20*20*0.8	20*20*0.8

TABLE 9. The specifications of the sections for eight-story with soft story

Number of story	Beam selected by green color	Beam selected by blue color	column 1-A, 1-B, 1-C, 1-D, 1-E 2-A, 2-D 3-A, 3-D 4-A, 4-B, 4-C, 4-D, 4-E	column 2-B, 2-C, 2-D 3-B, 3-C, 3-D
1	40*20*1	40*20*0.8	44*44*1.2	44*44*1.4
2	40*20*1	40*20*0.8	40*40*1.2	40*40*1.4
3	32*18*1	32*16*0.8	40*40*1.2	40*40*1.4
4	32*18*1	32*16*0.8	35*35*0.8	35*35*1
5	32*18*1	32*16*0.8	35*35*0.8	35*35*1
6	20*15*0.8	20*15*0.6	35*35*0.8	35*35*1
8	20*15*0.8	20*15*0.6	16*16*0.8	16*16*1
9	20*15*0.8	20*15*0.6	16*16*0.8	16*16*1

TABLE 10. The specifications of the sections for eight-story with torsional irregularity in plane

Number of story	Beam selected by red color	Beam selected by yellow color	Beam selected by purple color	Column 1-A, 1-B, 1-C, 1-D, 1-E	Column 2-A, 2-B, 2-C, 2-D, 2-E 3-A, 3-B, 3-C, 3-D, 3-E	Column 4-A, 4-B, 4-C, 4-D, 4-E
1	40*20*0.8	40*20*1	40*20*0.8	44*44*1.4	40*40*1.4	40*40*1
2	40*20*0.8	40*20*1	40*20*0.8	44*44*1.4	40*40*1.4	40*40*1
3	40*20*0.8	40*20*1	40*20*0.8	44*44*1.4	40*40*1.4	40*40*1
4	32*18*0.8	36*18*0.8	32*18*0.8	36*36*1	35*35*1	32*32*1
5	32*18*0.8	36*18*0.8	32*18*0.8	36*36*1	35*35*1	32*32*1
6	32*18*0.8	36*18*0.8	32*18*0.8	36*36*1	35*35*1	32*32*1
7	20*0.6*15*0.6	20*15*0.8	20*0.6*15*0.6	20*20*1	18*18*1	16*16*1
8	20*0.6*15*0.6	20*15*0.8	20*0.6*15*0.6	20*20*1	18*18*1	16*16*1

TABLE 11. The specifications of the sections for eight-story with simultaneous soft story and torsional irregularity

Number of story	Beam selected by red color	Beam selected by yellow color	Beam selected by purple color	Column 1-A, 1-B, 1-C, 1-D, 1-E	Column 2-A, 2-B, 2-C, 2-D, 2-E 3-A, 3-B, 3-C, 3-D, 3-E	Column 4-A, 4-B, 4-C, 4-D, 4-E
1	40*20*0.8	40*20*1	40*20*0.8	44*44*1.6	44*44*1.4	44*44*1
2	40*20*0.8	40*20*1	40*20*0.8	44*44*1.4	40*40*1.4	40*40*1
3	40*20*0.8	40*20*1	40*20*0.8	44*44*1.4	40*40*1.4	40*40*1
4	32*18*0.8	36*18*0.8	32*18*0.8	36*36*1	35*35*1	32*32*1
5	32*18*0.8	36*18*0.8	32*18*0.8	36*36*1	35*35*1	32*32*1
6	32*18*0.8	36*18*0.8	32*18*0.8	36*36*1	35*35*1	32*32*1
7	20*0.6*15*0.6	20*15*0.8	20*0.6*15*0.6	20*20*1	18*18*1	16*16*1
8	20*0.6*15*0.6	20*15*0.8	20*0.6*15*0.6	20*20*1	18*18*1	16*16*1

Persian Abstract

چکیده

در این پژوهش، منحنی‌های شکنندگی برای سازه‌های فولادی قاب خمشی با تعداد طبقات سه، پنج و هشت که نماینده سازه کوتاه، متوسط و بلندمرتبه است و همچنین دارای نامنظمی طبقه نرم و نامنظمی پیچشی در پلان می‌باشد، توسعه داده‌شده است. این مدل‌ها بر اساس آیین‌نامه ایران طراحی‌شده‌اند و به‌صورت سه‌بعدی در نرم‌افزار OpenSees تحت تحلیل دینامیکی افزایشی (IDA) گرفته و منحنی‌های IDA برای آن‌ها محاسبه‌شده است. مقدار حداکثر نسبت دیریفت به‌عنوان پارامتر تقاضا بر اساس آیین‌نامه HAZUS-MH انتخاب شد و درنهایت، منحنی‌های شکنندگی مربوطه توسعه داده شد. نتایج تجزیه و تحلیل دینامیکی غیرخطی نشان داد که با افزایش تعداد طبقات، آسیب ناشی از نامنظمی طبقه نرم کاهش می‌یابد. از طرف دیگر، آسیب ناشی از نامنظمی پیچشی در پلان با افزایش تعداد طبقات افزایش می‌یابد.

IJE TRANSACTIONS B: Applications Vol. 34, No. 11, (November 2021) 2494-2507

International Journal of Engineering

Journal Homepage: www.ije.ir

A Hidden Markov Model for Morphology of Compound Roles in Persian Text Part of Tagging

H. Rezaei[a], H. Motameni*[a], B. Barzegar[b]

[a] *Department of Computer Engineering, Sari Branch, Islamic Azad University, Sari, Iran*
[b] *Department of Computer Engineering, Babol Branch, Islamic Azad University, Babol, Iran*

PAPER INFO

Paper history:
Received 16 April 2021
Received in revised form 30 July 2021
Accepted 23 August 2021

Keywords:
Hidden Markov Model
Morphology
Independent Roles
Dependent Roles
Tri Gram

ABSTRACT

Nowadays, data mining has become significant given the popularity of social networks as well as the emergence of abbreviated words, foreign terms and emoticons in Persian language. Meanwhile, numerous studies have been conducted to identify the type of words. Identifying the role of each word in a sentence is far more important than identifying the type of word in the sentence. Meanwhile, the spelling-grammatical similarity of Persian to Arabic has enabled the newly proposed method in this paper to be applied to Arabic. In this paper, we adopted the Hidden Markov Model (HMM) and Tri-gram tagging with the aim of identifying the morphology of composition roles in Persian sentences. Then, a comparison was made between the technique developed in this paper and the Hidden Markov Model, Uni-gram and Bi-gram tagging. The proposed method supports the results obtained by the word role identification through "independent" and "dependent" roles and several factors that have a contribution to the words roles in sentences. In fact, the simulation results show that the average success rates of independent composition roles with HMM and Tri-gram tagging were 20.56% and 17.67% compared to Uni-gram and Bi-gram methods, respectively. Regarding the dependent composition role, there were improvements by 24.67% and 32.62%, respectively.

doi*: 10.5829/ije.2021.34.11b.12*

1. INTRODUCTION

Nowadays, the expansion and popularity of social networks among the public has led the divergence of writing and speech styles in every language, turning phrases into a rather abridged, colloquial form. For that reason, it becomes increasingly crucial to conduct research into linguistics essential to numerous functions such as machine translation [1], smart filtering [2] speech recognition [3, 4], text processing and summarization. Persian is a language officially spoken in many countries including Iran, Afghanistan, Tajikistan and unofficially in certain regions of Uzbekistan. Furthermore, Persian is akin to Arabic in terms of alphabet, and in some extent grammar. This in turn explains the significant contribution of Persian to morphology of other languages. On the other hand, Persian language experts have more frequently investigated the processing of word types in sentences. Nevertheless, the word roles in machine translation or speech recognition tend to be more effective than word types for achievement of better results. Widely applied by many scholars in language processing, Hidden Markov Model (HMM) [5] with N-gram tagging is a key statistical measure in identification of words [6]. Due to insufficient investigation into the semantic aspect of words in sentences (i.e. compounds), there has been a significant gap in morphology through HMM with a focus on the scope of word roles in a Persian sentence. Raising the success rate in sentence role identification in any language will help to achieve better results in practical areas. The morphology of compound roles in Persian sentences is carried out through HMM with Tri-gram tagging given 1) the importance of identifying word roles in a sentence based on the word type, 2) the significant dispersion of Persian language across several countries, and 3) expansion of Persian usage [7-9].

To solve the above problems, this paper makes three

* Corresponding Author Institutional Email: motameni@iausari.ac.ir (H. Motameni)

Please cite this article as: H. Rezaei, H. Motameni, B. Barzegar, A Hidden Markov Model for Morphology of Compound Roles in Persian Text Part of Tagging, International Journal of Engineering, Transactions B: Applications, Vol. 34, No. 11, (2021) 2494-2507

contributions:

- The output of this research can be used in all data mining projects mentioned above.
- The method of this research can be used in all Persian-speaking countries and in Arabic-speaking countries.
- Morphology using fuzzy Hidden Markov Model Within the role of words in Persian sentences.

The remainder of this paper is organized as follows. Section 2 introduces background and literature review. Section 3 introduces the problem description. In Section 4, the proposed algorithm is described and its performance is evaluated. Section 5 gives the performance study with simulation. Finally, Section 6 concludes the paper.

2. LITERATURE REVIEW

This investigates the fundamental concepts in lingusitics and morphology. Furthermore, the related prelimineries are discussed in detail.

2. 1. Linguistics Scientists belive that language is a generic term interacting with wide array of issues including social factor, regional class, language acquisition, neurolinguistics, application of linguistic knowledge to the forensic context of law which is known as forensic linguistic, analysis of language disabilities, and language usage. Literature also shows that computer sicence and analytical techniques have great impacts on linguistics along with the aforementioned concept in recent years.

Linguistics includes the fields of reflecting the various dimensions of linguistics [12, 13]. Generally speaking, language is the study of language and its structure, and a linguist should be expert in one of the specific branches in linguisitc including dialectology, computational linguisitcs, applied linguistics, and etc [14]. Although lingusitcs is a legacy field of studying developed by Indian Panini during fifth century, the modern linguisitcs dates from the beginning of 20th century. The famous linguists in the beginning era of linguistics are Ferdinand de Saussure and Noam Chomsky. Ferdinand de Saussure trusted in theory of structuralism in linguistics while Chomsky identified that sentence as the unit of study in linguistics. The theories of Noam Chomsky have still strong followers and fans in North America today. In contrast, there exists a method called discourse approach that do not recognize sentence as the unit of study in linguistics.

Three semantic levels are identified for every text basically which examine three distinguished concepts namely, content, interaction within equation of this content, the level of sentence impact in formulation of the content. A discourse approach does not restrict the text to have pre-specified length as it even recognizes a word as a text [15]. The Iranian Linguistics Foundation proposed the initial Persian grammer and later advanced by Bateni through introducing new structures within Persian grammar. One of the main achievments of Bateni was formulating the conversion between different types of sentence. According to Meghdari et al. computational linguistic is an interdisciplinary field relating to two branch of knowledge namely, computer science and linguistics in which the natural lanuage is evaluated using statistical and machine learning techniques [16, 17]. This method includes grammar for making sentences and making words. One of the researchers on using Grammar in Natural Language Processing (NLP) in non-Persian-Arabic languages is Chomsky. He was a pioneer in this research.The aim of computational linguistic is to implement and build artifacts which improve the relationship between computer and the language. The initial applicability of computational linguistics was in machine translation using machine learning and data analytical techniques. The first journal publishes the machine translation related issues was Mechanical Translation in 1954 (renamed later as computational linguistics) prior to establish the Association for Computational Linguistics in 1962 [18]. The appliability of computational linguistics is not restricted to machine translation and is used wide range of IT-related issues [19, 20]. Literature also reveals many researches regarding Persian computational linguistics [2, 21-23].

With the establishment of a web technology research laboratory in recent years at Ferdowsi University of Mashhad [24] and the Linguistics Research Institute at Sharif University, extensive research has been done in this regard [16, 19]. They show the concentration and direction of computational linguistics research in Iran.

Fuzzy intelligent systems deal with fuzzy rules to describe vague, inaccurate concepts. In recent research, fuzzy theory has been used in Persian linguistics as well as its combination with Arabic [26]. In another study [6, 25, 34], the fuzzy method was adopted to identify composition roles in Persian sentences. Considering all advances in fuzzy data mining it seems that fuzzy morphology [34], especially in Persian and Arabic, and in particular the combination of words in the sentence, which deals with the meaning of words in sentences, has been paid less attention by the researchers.

2. 2. Morphology The literature offers various definitions for the term ‘Morphology’. Among them, the most commonly-referred definition indicats that morphology is the study of words and morphemes so that morphemes refer to the stem of words. Morphology is kind of complex since different languages involve different phonemes, alphabet, grammar, and speech. For example, English morphology meaningfully differs from Arabic and Persian morphology [27-29]. Buckwalter [33] implemented morphological analysis of Arabic and applied rule-based method to improve root search and clarification of Arabic words, and performed system evaluating root search of Arabic by that grammar and the relevant rules. Arab and Azimazadeh [35] used HMMs to predict the tags of unknown words. Tri-grams were used in their model and they tried to solve the ambiguity problem. Okhovvat and Minaiee [36] applied HMMs for Part-of-Speech (POS) tagging. They trained a model by both homogenous and heterogeneous corpora. They determined the sentence boundaries to make the model more precise. Another study was designing a dependency parser for Persian language and discovering the linguistic dependencies to ease NLP tasks [37]. Kardan and Imani [38] used maximum entropy as a classifier for POS tagging. They chose those types of features that can show the most important characteristics of a word. Pakzad and Minaee [39] also used dependency grammar and joint probability for Persian and English annotation. Table 1 compares the most important studies in the field of Persian morphology.

3. PROBLEM DESCRIPTION

In this section, we explore the HMM, N-gram tagging (particularly Tri-gram) and sentence roles in Persian prior to presenting our new method.

TABLE 1. Comparison of morphological research

Ref.	Methodology	Advantages	Disadvantages
Bijankhan el al. [21]	Eagles standard	One of the basic Persian morphological corpora	Tagging words and constructing corpora merely based on word types, nonstandard corpora textual documents, eagles-based methodology
Assi and Abdolhosseini [23]	Manual	One of the basic Persian colloquial morphological corpora	Tagging words and constructing corpora merely based on word types, nonstandard corpora textual documents, manual methodology
Motameni and Peykar [8]	Fuzzy HMM	Using fuzzy system to determine word roles	Tagging standard sentences, high computational complexity
Motameni et al. [25]	Classified fuzzy	Low computational complexity, determining word roles, using fuzzy system	Only tagging standard sentences
Motameni [34]	Deep Learning Fuzzy Neural Network	memory of the fuzzy GRU method allows to select irregular values relative to the input states	Tagging standard sentences, high computational complexity

3. 1. Hidden Markov Model In HMM, observations are probabilistic functions of states. The output is a stochastic model involving an underlying random hidden process observable only to a set of random processes that generate the sequence of observations [32]. As can be seen in this scenario, the observation time (t) is defined by variable Y_t. This model has been demonstrated in Equation (1), where S_1 is the initial probability value, $P(Y_t \mid S_t)$ is the extent of observation probability, and $P(S_t \mid S_{t-1})$ specifies the level of state transition.

$$P(S_{1:T}, Y_{1:T}) = P(S_1)P(Y_1 \mid S_1)\prod_{t=2}^{T} P(S_t \mid S_{t-1})P(Y_t \mid S_t) \tag{1}$$

The HMM consists of forward and backward models. The forward model computes the probability of a state according to subsequent states. Meanwhile, the backward model computes the probability of a state according to previous states. The newly proposed method adopts the forward model [5].

3. 2. N-gram Tagging This model was presented at the IBM linguistics lab for the first time in an effort to recognize speech through the Tri-gram model and roughly 20000 dictionaries with over 8 trillion modeling parameters [4].

Note that an N-gram in the fields of computational linguistics and probability is in fact a contiguous order of *N* items from a certain speech or text sample. Depending on the application in use, the items could be phonemes, syllables, letters, words, or base pairs. In general, researchers gather the N-grams searching in a text or speech corpus. In cases where the items are in the form of words, the N-grams might also be termed 'shingles'.

In this model, an increased level of n leads to higher accuracy, whereas it may decrease the reliability of parameters fulfilled from a peace of limited training text. The HMM is used as a decision-making model in N-gram tagging.

3. 3. Uni-gram The Uni-gram tagging is the primary level of N_gram. Uni-gram is not dependent on any of previous or subsequent words/letters. Meanwhile, all calculations are made through Equation (2) based on occurrences independent from other words/letters. In this scenario, M represents the number of words/letters, while *i* represents the number of current words/letters [11].

$$p(w) = \sum_{i=1}^{M} (Fi) \tag{2}$$

3. 4. Bi-gram The Bi-gram tagging method examines the occurrence probability of a role according to the previous or subsequent word/letter. The word weights are obtained through Bi-gram method according to Equation (3), where *M* indicates the number of words/letters, and *i* indicates the number of current words/letters.

$$p(w) = \sum_{(i=1)}^{(M-1)} (Fi \quad after \quad Fi + 1) \quad (3)$$

3. 5. Tri-gram In this paper, the Tri-gram tagging has been employed for the letters composing each word, as well as for the occurrence probability of each sentence role. Therefore, the word weights and the occurrence probability of roles can be obtained through Tri-gram tagging according to Equation (4), where M indicates the number of words/letters, and i indicates the number of current words/letters [11].

$$p(w) = \sum_{(i=1)}^{(M-2)} (Fi \quad after \quad Fi + 1 \ and \ after \ Fi+) \quad (4)$$

3. 6. Independent and Dependent Roles Roles in the Persian language are classified into two categories of independent and dependent. Given the two categories, the compound roles will be as follows.

- Totally independent of other roles, primary roles are significant in terms of word type and position in a sentence. These roles include subject (agent), predicate, object, complement and verb.

Dependent roles generally come in four classes, namely adjective, governing genitive, apposition and bending. A precise examination of dependent compound roles reveals more than four classes, extending the number to nine, including noun, genitive, governing genitive, apposition, retroactive exclamation, governing transducer, dependent adverb, annunciator, bending, etc. [21].

4. PROPOSED METHOD

The new method is composed of various elements. This section first discusses the essential elements for the newly proposed method and then offers the general algorithm for sentence processing. Finally, a practical example explains all processing stages.

4. 1. Input In this system, inputs are represented by words or phrases that are seprated by space characters "؟،!", sentences separated by "." as well as parsed Persian sentences. The sentence parsing can be completed by Pars Pardaz [7] or any other similar software.

4. 2. HMM Parameters The HMM involves two types of probability distributions namely discrete and continuous. Since this research intends to obtain the roles of individual words, this paper adopts the discrete probability distribution through Equation (5).

$$\lambda = (A.B.\pi) \quad (5)$$

The triad set in discrete HMM is the main parameter directly involved in HMM's decision-making. The rest of parameters indirectly participate in HMM's decision-making. Therefore, it is crucial to first obtain the required parameters in order to engage the HMM computations as well as to achieve the best possible solution to the role of each word in Persian sentences. These risks include:

- Number of possible states: In independent roles, $11^{(\text{number of words})}$ is true, where 11 is the number of compound roles in primary roles (subject, predicate, object, complement, verb) + letters in sentences + three spacing characters "؟،!". In addition, in each sentence, the number of words will be variable. In spite of the fact that predicate may contain subject and other items in our observations, in cases where the new system decides that the word in the sentence is predicate while failing to detect the type of predicate, the role will only be reported to be predicate. Moreover, the dependent compound roles are explored separately. In this section, the number of possible states is $17^{(\text{number of words})}$, where the value of 17 is made of 11 dependent compound roles (noun, adjective, bending, genitive, governing genitive, dependent adverb, apposition, governing transducer, exclamation and annunciator), three spacing characters "؟،!", one unspecified, one verb and one letter. However, the number of words in this number of states will vary according to each input sentence.
- The number of observations depends on the number of words in a sentence. Therefore, the possible outputs that may be accepted by each words in the input sentence will appear as subject, predicate, object, complement, verb, noun, adjective, bending, genitive, governing genitive, dependent adverb, apposition, governing transducer, unspecified, letter, exclamation and annunciator.
- There are specific symbols to the number of all roles and even the type of words. Moreover, the states in each input sentence can be observed with more difficulty. Hence, the sequence of observations is achieved through Equation (6).

$$O = \{o_1 \ldots . o_t\} \quad (6)$$

4. 3. Initial Probability Distribution π={π_i } This distribution is stored by a single-dimensional matrix with one line of information, indicating the probability of each role starting a sentence among all 194 training sentences. The initial value of each Persian sentence role is obtained according to Equation (7).

$$\pi_i = p\{q_1 = i\}. 1 \leq i \leq N \quad (7)$$

The values of initial probability distribution have been displayed in Table 2. Since sentences are not likely to begin with certain roles, the phrasing states initiated by these roles do not require HMM calculation, since they are excluded from the set of possible states.

TABLE 2. Initial probability distribution (π)

Percentage of being a first word	Role	Percentage of being a first word	Role
4.895	Adjective	0.34	Verb
0	Governing genitive	4.545	Letter
0.349	Genitive	4.545	Adverb
0	Genitive	0	N.A.
1.748	Governing transducer	18.531	Subject
0	Bending	0.349	Subject
5.244	Retroactive	4.895	Predicate
1.398	Exclamation	0	Object
0.699	Annunciator	0	Complement
		0.699	Noun

4. 4. State Transition Matrix A=[a_ij] This matrix comprises a set of transition probabilities between states, which is called MatrixA in this paper. Having determined different types of possible states, the percentage of transition in possible states is calculated through forward Tri-gram according to Equation (8), where *N* is the number of words, a_ij is the percentage of presence for each role after another role and then another role. Moreover, *i* is the number of matrix rows, which is equal to q_t followed by $q\_(t+1)$, i.e. current role, while *j* is the corresponding number of columns, which is equal to $q\_(t+2)$, i.e. two roles after the current role.

$$
\begin{aligned}
&A = [a\_ij] \\
&a\_ij = p\{j = q\_(t+2) \mid i = q\_t.\, q\_(t+1)\},\ \ 1 \le i.j \le N. \\
&a\_ij \ge 0.\ \ 1 \le i.j \le N \\
&\sum\_(j=1)\text{^}N ⬚〖a\_ij = 1.\ \ 1 \le i \le N〗
\end{aligned}
\tag{8}
$$

Since this method calculates the possibility of one or two subsequent roles, a large matrix is created with dimensions of 26×703. Furthermore, another reason behind the large size of matrix is the number of word types and roles, as well as three spacing characters in the matrix, which have led a total of 26 rows.

On the other hand, two possible states are assumed in rows equivalent to 26×26 since the Tri-gram model is involved. In addition, the Bi-gram method is explored for 2-word sentences adding 26 more items. As for 1-word sentences, one row covers Uni-gram, leading to a total of 703 matrix rows. The values of this matrix are derived from 194 sentences which are used to train the new system.

4. 5. Probability Distribution of Observations/ Matrix B The individual letters composing each word in a sentence are examined to determine the weight of each word and the probability distribution of observations through Tri-gram tagging. For that reason, each role is distinguished in the database, followed by adoption of Tri-gram method, which displays the percentage of three letters occurring together in words larger than two letters.

As for 2- and 1-letter words, Bi-gram and Uni-gram are used respectively to calculate the weights of words corresponding to the number of letters. The dimensions of this matrix are 44×1936 for each of the roles. The reason behind the large number of matrix rows is that the table involves a possible compound of two Persian letters together, in addition to 1- and 2-letter words, making it a total of 1936 rows and 44 columns, including the Persian alphabet as well as the Arabic alphabets such as “ء، إ، أ، ي، ؤ، ة”, letters “آ، (،)” and the spacing character. Therefore, Equations (9) and (10) are employed to calculate the distribution in each role.

$$
\begin{aligned}
&B = \{b\_j(k)\} \\
&b\_j(k) = p\{v\_k = o\_ + \mid j = q\_t\}.\ \ 1 \le j \le N.\ 1 \le \\
&k \le M
\end{aligned}
\tag{9}
$$

where, v_k represents the *k*th symbol observed in the alphabet, o_+ is the vector of current input parameters, N is the number of words, J is the word counter, M is the number of letter in each word, and k is the letter count for each word [6, 10].

$$
\begin{aligned}
&b\_j(k) \ge 0.\ \ 1 \le j \le N.\ 1 \le k \le M \\
&\sum\_(k=1)\text{^}M ⬚〖b\_j(k) = 1.\ \ 1 \le j \le N〗
\end{aligned}
\tag{10}
$$

4. 6. Output Calculation and Viterbi Algorithm The Viterbi algorithm is the final decision-maker in this research. In fact, the independent roles and $17\text{^}(Number\ of\ character)$ possible states of dependent roles at this stage determine which state provides the best possible solution. In the best possible state, given the values, the initial probability distribution, transition state matrix, and observations probability distribution are calculated by HMM method, where the largest value is obtained with the Viterbi algorithm.

4. 7. Tri-gram Morphology General Algorithm

1. In the first stage, various word types in each of the roles are extracted separately.
2. Various types of possible sentence phrasing are obtained in Persian grammar.
3. State transition matrix (A): The value of Tri-gram tagging in the structure of sentence obtained in Stage 2 is calculated through level 3 N-gram. In fact, this stage statistically analyses what roles fall in t+1 and t+2 positions after/before each role at *t* the position. Equation (11) displays how the state transition matrix is calculated.

$$A = [a_{ijk}]$$

$$a_{ijk} = p\{k = q_{(t+2)} \mid j = q_{(t+1)} \mid i = q_t\}.\ a_{ijk} \geq 0.\ 1 \leq i.j \leq N. \quad (11)$$

$$A(ijk) = \sum_{k=1}^{No\ roles} \sum_{j=1}^{No\ roles} \sum_{i=1}^{No\ roles} [\![\text{roles } i \text{ after } j \text{ after } k]\!]$$

4. Initial probability distribution (π): In order to calculate the initial probability distribution for the sentences obtained from Stage 2, we find out the percentage of cases where one of the roles occurred in the starting position of a sentence. Equation (12) shows how to calculate the initial probability matrix as one of the components required in HMM computations.

$$\pi = \{\pi_i\},\ \pi_i = p\{q_1 = i\}. 1 \leq i \leq N \quad (12)$$

5. Observations probability distribution matrix (B): At this stage, Tri-gram tagging is adopted to weigh the words. These calculations serve to obtain the word weights in each role, covering the letters of each word. In this matrix, the values of word weights in each role are obtained based on the percentage of cases where and what letters in *t*th position fall in t+1 and t+2. Hence, Equation (13) is used at this stage.

$$B(ijk) = \sum_{k=1}^{No\ char} \sum_{j=1}^{No\ char} \sum_{i=1}^{No\ char} [\![\text{word } i \text{ after } j \text{ after } k]\!] \quad (13)$$

6. After completing the statistical calculations from Stages 1 to 5, the HMM is employed to specify the role of each word for each possible state in the sentence. Given the role of each word, the letters composing each word, and the possibility of presence for each role as the first word in a sentence, HMM can obtain values to determine whether each state is true as follows. These calculations are completed through Equation (14), where *n* represents the number of input sentence words.

$$MA = \sum_{i=1}^{n} [\![\text{Frequency percentage of roles after } i \text{ and } i+1 \text{ and } i+2]\!] \quad (14)$$

In Equation (15), the weight of each word in the input sentence is obtained through Matrix B, where the frequency percentage of letters is extracted and *m* is the number of letters in each word.

$$MB = \sum_{i=1}^{m} [\![(\text{Frequency percentage of word } i\ after\ i+1\ after\ i+2)]\!] \quad (15)$$

The occurrence probability of each phrasing state might be obtained through HMM according to Equation (16).

MB: The level of transition state for each possible phrasing, MA is the level of observations probability for input sentence, and π: is the level of initial probability distribution for each phrasing.

$$P = \pi \times [\![MB]\!]_{(1..N)} \times [\![MA]\!]_{(1..N)} \quad (16)$$

7. Once the occurrence probability of each sentence is calculated through Equation (17), the largest P is sent as the largest possible occurrence, indicating the role of each word in the sentence. Where, *s* indicates the number of phrasing states, and P is the occurrence probability of each state.

$$OutPut = \max_{\top s}(P\ s) \quad (17)$$

8. Due to using defuzzifier y Max (product), the effect of any lower value is less and the effect values are more [6].

4. 8. An Example of the Newly Proposed Morphology Tri-gram Algorithm

At first, the state transition matrix (A) is calculated according to Table 3 using Tri-gram tagging, statistical calculations and tables obtained from these calculations in Stages 1 and 2.

As noted in Stage 2 of the algorithm, possible phrasing states are created as many as possible for each sentence. The value of state transition matrix should be calculated for all states. For instance, the value of transition matrix for input Persian sentence "او به مدرسه رفت" literally translated into "he to school went" will be according to Table 3 for the possible state of "subject, preposition, complement, verb".

Following the state transition matrix calculations, the initial probability distribution of statistical calculations obtained from 194 different sentence phrasing types is calculated as training data in the system at Stage 4. Table (2) provides the possibility of each role starting a sentence (i.e. initial probability distribution).

In Stage 5, the probability distribution matrix (B) is computed according to Table 4. As noted earlier, however, Uni-gram and Bi-gran tagging methods are adopted in words where the number of letters is fewer than 3. Table 4 displays hypothetical sentence "او به مدرسه رفت" and hypothetical state "subject, preposition, complement, verb".

TABLE 3. Example of state transition matrix calculations for hypothetical state (A)

I	Tri-gram words	Tri-gram roles	Tri-gram occurrence value
0	مدرسه به، او،	Subject → preposition → complement	0.236
1	رفت مدرسه، به،	preposition → complement → verb	0.367
Conclusion:			0.236+0.367 = 0.603

TABLE 4. Example of Calculations for probability distribution matrix (B)

I	Tri-gram word	Tri-gram role	Tri-gram calculations of word in role	Tri-gram occurrence value
0	او	Subject	Occurrence value "ا" and then "و" as subject role	0.333
1	به	Article	Occurrence value "ب" and then "ه" as preposition role	0.9
2	مدرسه	Complement	Occurrence value "م" and then "د" and then "ر" + occurrence values of "س"و"ر"د" + occurrence values of "ه" و"س"و"ر" as complement role	0.742+0.456+0.389=1.587
3	رفت	Verb	Occurrence value "ر" and then "ف" and then "ت" as sentence verb role	0.649

Depending on the spacing characters, the type of words and the zero initial probability distribution are filtered to reduce the number of possible states and curtail the computation time of the project. Then, the HMM calculations are completed. The overall occurrence calculated for sentence "او به مدرسه رفت" and the value of hypothetical state "Subject, preposition , Complement, Verb" is calculated by Equation (18). Then, Tri-gram state transition is calculated for phrasing state "subject-proposition-complement-verb" according to Equation (18) using Table 3.

$$\mathrm{P(Subject, preposition\ , Complement, Verb)} \\ = \mathrm{P(subject, preposition\ , complement)} \\ * \mathrm{P(preposition\ , Complement, Verb)} * \mathrm{P(subject)}$$

Given the values in Tables 1 to 3 and Equations (18) to (19), the value of HMM for input sentence "او به مدرسه رفت" and hypothetical state "subject, preposition, complement, verb" will be according to Table 5.

As shown in Table 5, the calculations of Equations (18) and (19) are performed similar to Table 5 for each input sentence and all phrasing states. Moreover, the largest result is indicated as the input sentence compound.

5. PERFORMANCE STUDY WITH SIMULATION

In addition to the roles provided in previous section, there are "verb-letter" roles, which were discarded because of their shared decomposition and composition.

$$\text{Success percentages} = (\text{Success } \times 100)/(\,Total\,) \quad (18)$$

Relying on Equation (18), we obtained the success rate in each section. Parameter *Total* in Equation (18) changes in each section. In addition, parameter *Success* in this regard varies according to each section.

Also the main software used to exploit the proposed method of visual studio 2019- visual basic software, for primary statistical work from the office 2019 collection Excel 2019 software was used and then in the programming environment the results obtained from Excel to SQL server 2017 is used.

This section makes a comparison between the simulation results obtained by the proposed method and those of other methods. Accordingly, the success rate of the new method is comparatively examined with the HMM Uni-gram and Bi-gram tagging techniques.

TABLE 5. Final HMM calculations for sentence "او به مدرسه رفت". (rows 1, 2, 3, 4 total of percentage of occurrence for letters, and 5, 6, 7 percentage of occurrence probability of the state).

No.	Phrase	Matrix name	Percentage value
1	P(او ،subject)	Observations probability distribution matrix (B):	0.333
2	P(به ،preposition)	Observations probability distribution matrix (B):	0.9
3	P(مدرسه ،complement)	Observations probability distribution matrix (B):	1.587
4	P(رفت ،verb)	Observations probability distribution matrix (B):	0.649
5	P(subject, preposition, complement)	State transition matrix (A):	0.236
6	P(preposition, complement, verb)	State transition matrix (A):	0.367
7	P(subject)	Initial probability distribution (π):	0.634
8	P(Subject, preposition, Complement, Verb)	With values of rows 5, 6 and 7	0.236×0.367×0.634= 0.054
Result	P(او،به،مدرسه،رفت|Subject, preposition, Complement, Verb)	Using rows 1 to 8	0.333×0.9×1.587×0.649× 0.054= 0.016

5. 1. Results of Tri-gram Tagging with HMM The average success rate of this method is 73.34608 percent in identifying the roles in Persian sentences.

As displayed in Table 6, the success rates of both categories of roles are less than 1%, which indicates the approximate equality of success rate in calculating the word roles in Persian sentences. According to Table 6, this difference has been demonstrated in Figure 1.

As displayed in Table 7, the success percentage lies within interval 40-98.55343, where the success rate follows an ascending order "complement, object, predicate, proposition, verb and subject".

According to Figure 2, the highest and lowest success rates were achieved by "subject" and "complement", respectively. It is worth noting that in reality, however, "agent and pronoun" are two roles categorized as "subject", the average success rate of which is 82.5%.

TABLE 6. Average success rates for both categories of compound roles through HMM and Tri-gram tagging

Category	Value %
Independent roles	73.9816
dependent roles	73.34608

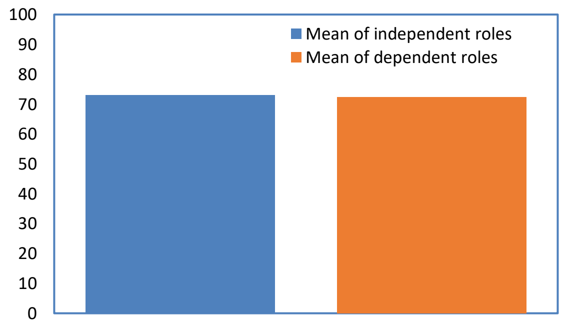

Figure 1. Average success in finding compound roles in two separate categories

TABLE 7. Average success rates for independent compound roles through HMM and Tri-gram tagging

No.	Role	Value %
1	Verb	91.64355
2	Predicate	67.76667
3	Subject	98.55343
4	Subject	79.567995
5	Object	56.98756
6	Complement	40
7	Letter	86.97294

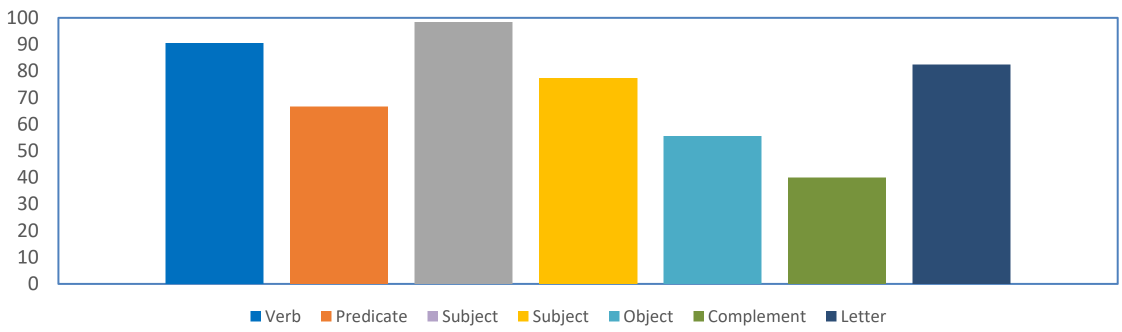

Figure 2. Success rate of each primary role with Tri-gram tagging and HMM

TABLE 8. Average success rates for dependent compound roles through HMM and Tri-gram tagging

No.	Role	Value in terms of %
1	Adjective	22.22222
2	Noun	72.72727
3	Adverb	55.17241
4	Unspecified	77.55102
5	Governing genitive	20
6	Genitive	20
7	Apposition	100
8	Governing transducer	100
9	Bending	100
10	Retroactive	100
11	Exclamation	100
12	Annunciator	100

Among these 12 roles in Table 8, the 4th role (unspecified) indicates the percentage of words without any specific dependent roles in the sentence. Table 8 provides the success rates of dependent role tagging in third-order N-gram and HMM. The range of variations in the success rate of tagging is 80% for HMM. Since these roles are overlapping, it is difficult to determine the success rate of dependent compound roles.

As can be seen in Figure 3, the success rate in dependent roles “apposition, governing transducer, bending, retroactive, exclamation, annunciation”,

which are basically rare roles in Persian sentences, is 100%. One reason is that filtering is used to alleviate the computational load in the new method. Meawhile, the lower frequency of such roles affects the results. According to Figure 3, however, the smallest values are related to "genitive, governing genitive and adjective".

600 dpi and without borders, with capital first letter of axis titles and write its unit (all the Figures and Tables should be placed on the top or in the bottom of the page; not in the middle of text).

5. 1. Comparative Overview of Uni-gram, Bi-gram and Tri-gram Tagging Techniques with HMM

One of the most important advantages of the proposed method is its improvement in tagging. Considering that previous studies have already calculated these values through Uni-gram and Bi-gram tagging methods, the current paper focused on Tri-gram tagging.

Table 9 displays the difference in improvement of success in detection of roles in Persian sentences through HMM. The shift from first-order to second-order N-gram is about 5.7%. However, there is approximately 20% improvement in the success of detecting compound roles from second to third order.

Figure 4 demonstrates the difference in success rates of tagging styles in an ascending trend. Table 10 displays the average success of independent roles by three tagging styles of Uni-gram, Bi-gram and Tri-gram in the HMM.

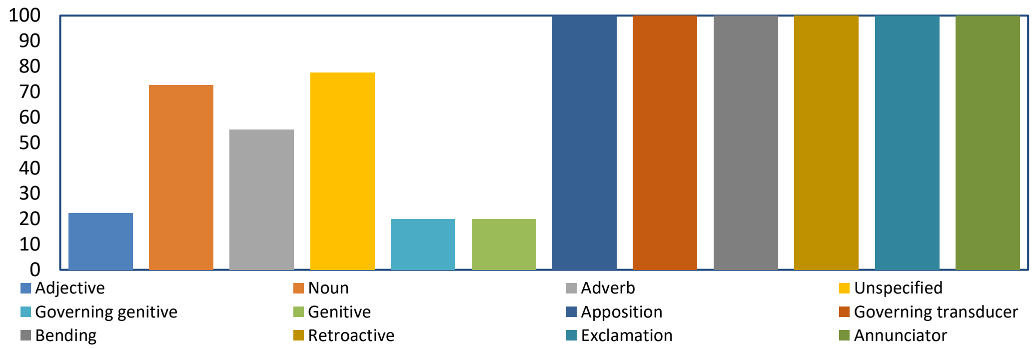

Figure 3. Success rate of each dependent role with Tri-gram tagging and HMM

TABLE 9. Average success rates of Uni-gram, Bi-gram, and Tri-gram tagging techniques through HMM

Tagging Method	Value
Uni-gram	45.49315
Bi-gram	50.02104
Tri-gram	73.84364

TABLE 10. Comparison of average success rates for independent roles through HMM and Uni-gram, Bi-gram and Tri-gram

Tagging style	Independent roles
Uni-gram	55.3028
Bi-gram	52.4129
Tri-gram	73.9816

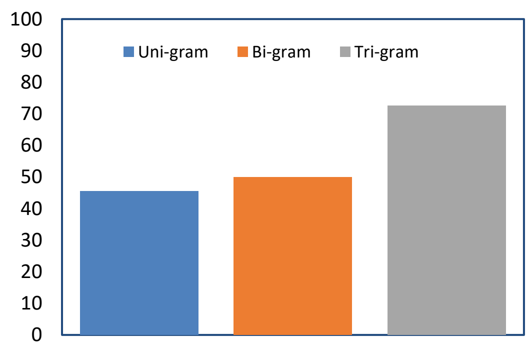

Figure 4. Comparison of overall results from Uni-gram, Bi-gram and Tri-gram tagging techniques

As can be observed, there is a slight difference between the independent roles for Uni-gram and Bi-gram tagging styles, whereas the difference from Tri-gram is roughly 20%.

As shown in Figure 5, the slope of variations in independent roles is not identical in each stage. In addition, the lowest average values were found in Bi-gram. As displayed in Table 11, comparison of success rates for Uni-gram, Bi-gram, and Tri-gram tagging techniques in dependent roles reveals a difference of approximately equal from 11% to 20% in each stage. Nevertheless, these values arise from dependent roles, the detail of which do not indicate such difference in success rates.

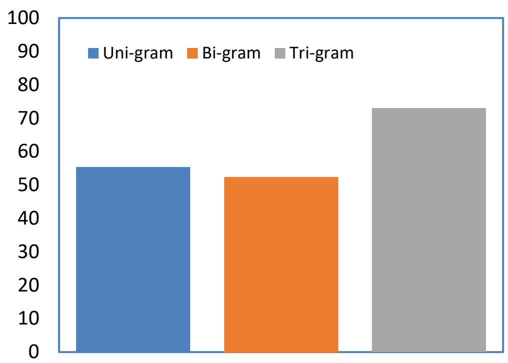

Figure 5. Average success rates for independent compound roles in Uni-gram, Bi-gram and Tri-gram

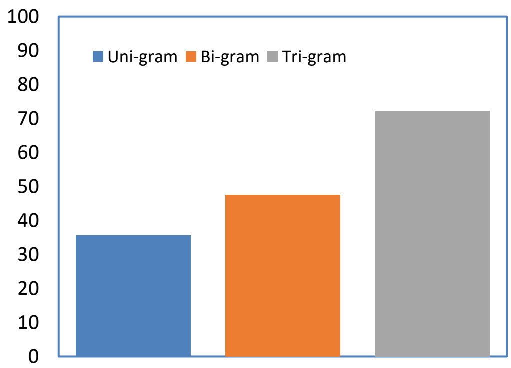

Figure 6. Average success rates for independent compound roles in Uni-gram, Bi-gram and Tri-gram

TABLE 11. Comparison of average success rates for dependent roles through HMM and Uni-gram, Bi-gram and Tri-gram

Tagging style	dependent roles
Uni-gram	35.683907
Bi-gram	47.629573
Tri-gram	73.34608

As shown in Table 7, the lowest and highest success rates in this category of roles were found in Uni-gram to Tri-gram, respectively. Average success rates for dependent roles through HMM and Uni-gram, Bi-gram and Tri-gram have been shown in Table 12.

The values of verb and letter, however, have been excluded since they were extracted from decomposition. The minimum value is for object in Uni-gram tagging, while the maximum value is for subject in Tri-gram tagging. As shown in Table 8, the highest value was found in "subject" while the lowest value was found in "complement", except Uni-gram tagging where the lowest value was found in "object".

TABLE 12. Average success rates for independent roles through HMM and Uni-gram, Bi-gram and Tri-gram

No.	Role	Uni-gram tagging %	Bi-gram tagging %	Tri-gram tagging %
1	Predicate	24.39	60.975	67.66667
2	Subject	51.162	88.37	98.93333
3	Subject	51.351	48.648	77.511935
4	Object	18.818	31.818	55.65556
5	Complement	33.333	8.33	40

Since "apposition" is rarely found in a Persian sentence, it was not calculated in Uni-gram and Bi-gram tagging styles. Nonetheless, rows 7 to 12 indicate rare roles because there is a little statistical population. In case of no value is identified, a large percentage is lost.

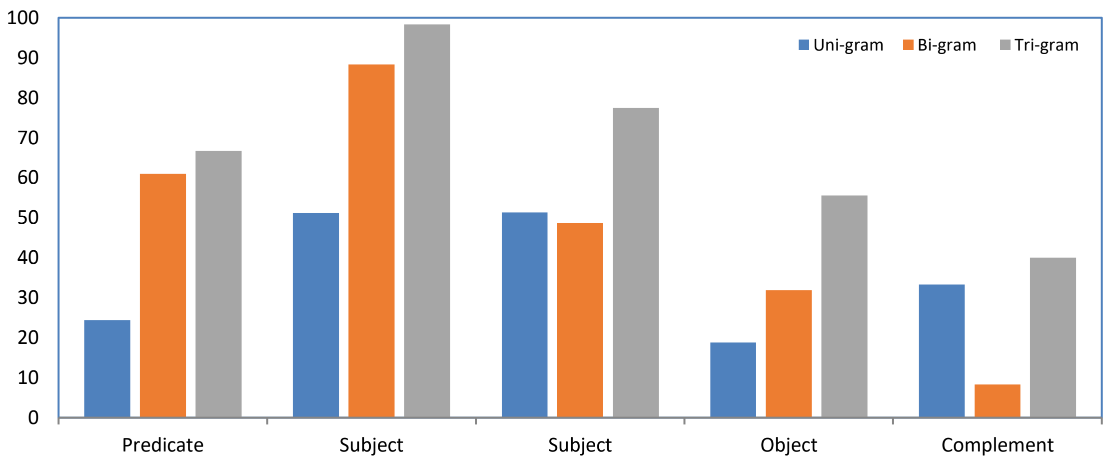

Figure 7. Success rates for independent compound roles in Uni-gram, Bi-gram and Tri-gram

Table 13 shows the smallest values were found in "genitive" following "exclamation, annunciator, apposition", indicating 0% in the two tagging techniques of the first stage. As can be seen from the results in Figure 8, the smallest values were found in "genitive" following "exclamation, annunciator, apposition", indicating 0% in the two tagging techniques of the first stage. Moreover, the highest values were found in “bending, retroactive and unspecified” [30, 31].

TABLE 13. Average success rates for dependent roles through HMM and Uni-gram, Bi-gram and Tri-gram

No.	Role	Uni-gram tagging by %	Bi-gram tagging by %	Tri-gram tagging by %
1	Adjective	60	30	23.22222
2	Noun	25	66.66	74.72728
3	Adverb	96.299	81.482	56.17242
4	Unspecified	100	75	79.55103
5	Governing genitive	29.413	35.295	20
6	Genitive	14.281	21.429	20
7	Apposition	-	-	100
8	Governing transducer	33.333	66.666	100
9	Bending	75	100	100
10	Retroactive	75	100	100
11	Exclamation	100	0	100
12	Annunciator	0	0	100

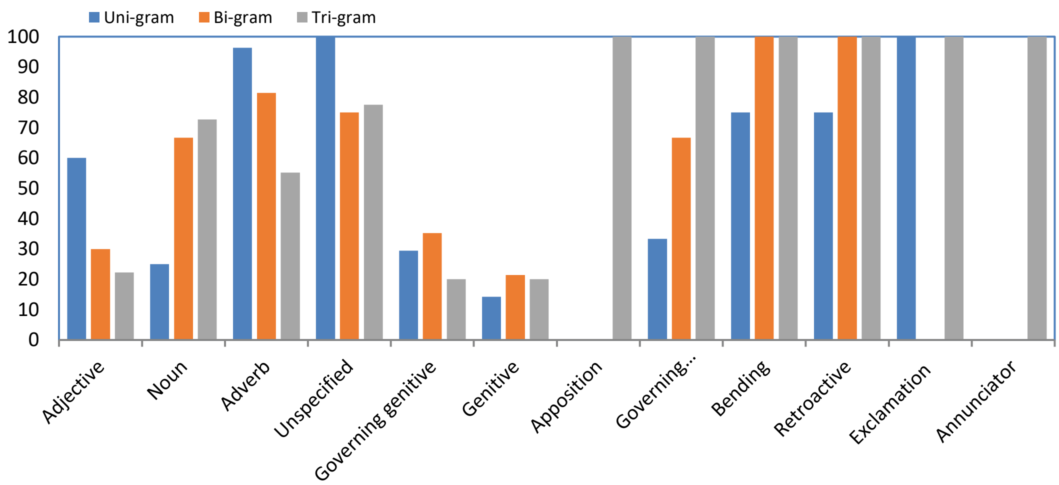

Figure 8. Average success rates for dependent compound roles in Uni-gram, Bi-gram and Tri-gram

6. CONCLUSIONS AND FUTURE WORK

The results of simulation in the proposed method suggest that Tri-gram tagging achieved improvement about 20% higher than Bi-gram tagging. The same amount of improvement was found in both independent roles and dependent roles. The results of Tri-gram tagging indicated that the lowest success rate is 40%, whereas success rates in Uni-gram and Bi-gram are 18% and 8%, respectively. Moreover, there are very different values for independent roles associated with rare roles. Nevertheless, these roles have been greatly improved by Tri-gram tagging method. There are several explanations for improvement by the new method: 1) high accuracy in matrices applied in HMM under Tri-gram tagging style, 2) the filtering applied on possible states making a key contribution to the calculations. In fact, calculations can be lightened through filtering according to Persian grammar. In addition to reducing the computational load in this scenario, this type of calculations shifts from statistical to rule-based or hybrid.

Future studies can focus on the new method in combination with other morphology techniques in an effort to compare its effects on success rate. Finally, different methods can be investigated to curtail the computational load of the statistical procedure.

7. REFERENCES

1. Yoonseok, H., Sangwoo, K. and Donghyun, Y., "Multimodal Neural Machine Translation with Weakly Labeled Images," ***IEEE Access***, Vol. 7, 54042-54053, (2019), doi: 10.1109/ACCESS.2019.2911656.
2. Alshammari, M., Nasraoui, O., and Sanders, S., "Mining Semantic Knowledge Graphs to Add Explainability to Black Box Recommender Systems," ***IEEE Access***, Vol. 7, 110563-110579,(2019),doi: 10.1109/ACCESS.2019.2934633.
3. Wu, B., Kehuang, L., Fengpei, G., Zhen, H., Minglei, Y., Chin, L., and Chin-H, L., "An End-to-End Deep Learning Approach to Simultaneous Speech Dereverberation and Acoustic Modeling for Robust Speech Recognition," ***IEEE Journal of Selected Topics in Signal Processing***, Vol. 11, No. 8, (2017), 1289-1300. DOI: 10.1109/JSTSP.2017.2756439.
4. Vani, H., Anusuya, M., "Fuzzy Speech Recognition: A Review," ***International Journal of Computer Applications***, Vol. 177, No. 47, (2020), 39-54. DOI:10.5120/ijca2020919989.
5. Xia, T., Chen, X. (2020). A Discrete Hidden Markov Model for SMS Spam Detection. ***Applied Sciences***. 10. 5011. 10.3390/app10145011.
6. Motameni, H., Peykar, A., "Morphology of Compounds as Standard Words in Persian through Hidden Markov Model and Fuzzy Method, 2015.," ***Journal of Intelligent & Fuzzy Systems***, Vol. 30, No. 10.3233/IFS-151865, (2016), 1567-1580. DOI: 10.3233/IFS-151865.
7. Peykar, A., Motameni, H., Aboutalebi, M. "Application of fuzzy identification method depends on the synthesis of the Persian language," in Conference iran data mining Iran, Tehran, 2014.
8. Peykar, A., Motameni, H., Aboutalebi, M. "Comparison of fuzzy and hidden Markov model to identify independent of synthesis words in Persian," in Conference iran data mining Iran, Tehran, 2014.
9. Asghari, R. "Application of N-gram modeling in language statistical modeling. (Persian)," in International Conference on Nonlinear Modeling & Optimization, Amol, Iran, 2012.
10. Keysers, D., Deselaers, T., Rowley, H., Wang, L. and Carbune, V., "Multi-Language Online Handwriting Recognition," ***IEEE Transactions on Pattern Analysis and Machine Intelligence***, Vol. 39, No. 6, (2017), 1180-1194. DOI: 10.1109/TPAMI.2016.2572693
11. Peykar, A., Motameni, H., Aboutalebi, M. "study of the role of labeling N_Gram, terminology and phrases in Farsi, hidden Markov models," in third national conference on computational linguistics, Tehran, 2014.
12. Obin, N., Lanchantin, P., "Symbolic Modeling of Prosody: From Linguistics to Statistics," ***IEEE/ACM Transactions on Audio, Speech, and Language Processing***, Vol. 23, No. 3, (2015), 588 - 599. DOI: 10.1109/TASLP.2014.2387389.
13. Sahraee Juybari, M., Bozorgian, H., "Cultural Linguistics and ELT curriculum: The case of ‘Prospect’ English textbooks in Iran",Vol.30,Issue3, (2020),https://doi.org/10.1111/ijal.12301.
14. Lücking, A., Driller, C., Stoeckel, M., Abrami, G., Pachzelt, A. and Mehler, A., "Multiple annotation for biodiversity: developing an annotation framework among biology, linguistics and text technology", ***Language Resources & Evaluation***, (2021). https://doi.org/10.1007/s10579-021-09553-5.
15. Fang, K. L., "A Short History of Linguistics R. H. Robins," American Anthropologist, Vol. 70, (2009), 1186-1186.
16. Moniri, M., "Fuzzy and Intuitionistic Fuzzy Turing Machines.," ***Fundamenta Informaticae***, Vol. 123, No. 3, (2013), 305-315. DOI: 10.3233/FI-2013-812.
17. Meghdari, A., Alami, M., "Phrases from well-known social robotics," in Symposium on gateways to the field of cognitive science, Tehran, (2015).
18. Abid, M., Habib, A., Ashraf, J., Shahid, A., "Urdu word sense disambiguation using machine learning approach". ***Cluster Comput***, Vol. 21, (2018), 515-522 https://doi.org/10.1007/s10586-017-0918-0.
19. Austin, P. "Theory of language: a taxonomy". ***SN Soc Sci*** 1, 78 (2021). https://doi.org/10.1007/s43545-021-00085-x.
20. Bijankhan, M., Sheykhzadegan, J., Bahrani, M. and Ghayoomi, M., "Lessons from Building a Persian Written Corpus: Peykare," ***Language Resources and Evaluation***, Vol. 45, (2011), 143-164. DOI: 10.1007/s10579-010-9132-x
21. Baghaei P., Khoshdel-Niyat, F. & Tabatabaee-Yazdi, M."The Persian adaptation of Baddeley’s 3-min grammatical reasoning test", ***Psicologia: Reflexão e Crítica*** Vol. 30, No. 16, (2017), https://doi.org/10.1186/s41155-017-0070-z.
22. Yusupov, A., Yusupova, N., Sibgatullina, A. Grammatical Absorption and Functioning of Arab and Persian Conjunctions in Old Tatar Language in the 19th Century. ***International Journal of Society, Culture & Language***, 8, 3 (Special Issue on Russian Culture and Language)) (2020), 80-88.
23. Web, A. F., "Natural Language Processing Software of Ferdowsi University of Mashhad Version 1.3.(persian)," Web Technology Lab of Ferdowsi University of Mashhad, Mashhad, (2012).
24. Sadeghi, H., Motameni, H., Ebrahimnejad, A. and Vahidi, J., "Morphology of composition functions in persian sentences through a newly proposed classified fuzzy method and center ofgravity defuzzification method," ***Journal of Intelligent & Fuzzy Systems***, Vol. 36, No. 6, (2019), 5463-5473. DOI: 10.3233/JIFS-181330
25. Safari, A., Mazinani, M. and Hosseini, R., "A Novel Type-2 Adaptive Neuro Fuzzy Inference System Classifier for Modelling Uncertainty in Prediction of Air Pollution Disaster", ***International Journal of Engineering, Transactions B: Applications***, Vol. 30, No. 11, (2017), 1746-1751. doi: 10.5829/ije.2017.30.11b.16
26. Gardani, F. "Borrowing matter and pattern in morphology. An overview". ***Morphology***, Vol. 30, (2020), 263-282, https://doi.org/10.1007/s11525-020-09371-5.
27. Alexis Amid, N., Éric, L., "Pattern-and-root inflectional morphology: the Arabic broken plural". ***Language Sciences***, Vol. 40, (2013), 221-250, https://doi.org/10.1016/j.langsci.2013.06.002.
28. Pakendorf, B. "Lamunkhin Even evaluative morphology in cross-linguistic comparison". ***Morphology,*** Vol. 27, (2017), 123-158 https://doi.org/10.1007/s11525-016-9296-1.
29. Sagot, B., Walther, G. "A Morphological Lexicon for the Persian Language," in LREC 2010, Valletta, Malta, 2010.
30. Megerdoomian, K. "Finite-State Morphological Analysis of Persian," in Proceedings of the Workshop on Computational Approaches to Arabic Script-based Languages., Stroudsburg, 2004.

31. Mor, B., Garhwal, S., Kumar, A. "A Systematic Review of Hidden Markov Models and Their Applications". ***Archives Computational Methods in Engineering,*** Vol. 28, No. 3 1429–1448, (2021). https://doi.org/10.1007/s11831-020-09422-4.

32. T. Buckwalter, "Buckwalter Arabic Morphological Analyzer.," the Linguistic Data Consortium,, Pennsylvania, 2002, https://doi.org/10.35111/050q-5r95.

33. Motameni, H. Determining the Composition Functions of Persian Non-standard Sentences in Terminology using a Deep Learning Fuzzy Neural Network Model. ***International Journal of Engineering, Transactions C: Aspects***, (2020); 33(12): 2471-2481. doi: 10.5829/ije.2020.33.12c.06

34. Azimizadeh, A., Arab, M., Quchani, S. Persian part of speech tagger based on Hidden Markov Model. In JADT 2008 : 9th international conference on textual data statistical analysis, pages 121–128, March 2008.

35. Okhovvat, M, Minaei Bidgoli, B, "A hidden Markov model for Persian part-of-speech tagging", ***Procedia Computer Science***, Vol. 3, (2011), 977-981, https://doi.org/10.1016/j.procs.2010.12.160.

36. Seraji, M., Megyesi, B., Nivre, J. "Dependency parsers for Persian". In Proceedings of the 10th Workshop on Asian Language Resources, (2012), 35-44.

37. Kardan, A., Imani, M. "Improving Persian POS tagging using the maximum entropy model". In 2014 Iranian Conference on Intelligent Systems (ICIS), (2014), 1-5, doi:10.1109/IranianCIS.2014.6802567.

38. Nourian, A., Rasooli, M., Imany, M., Faili, H. "On the importance of ezafe construction in Persian parsing". In Proceedings of the 53rd Annual Meeting of the Association for Computational Linguistics and the 7th International Joint Conference on Natural Language Processing (Vol. 2: Short Papers), Vol. 2, (2015), 877-882.

39. Pakzad, A., Minaei Bidgoli, B., "An improved joint model: POS tagging and dependency parsing". ***Journal of AI and Data Mining***, Vol. 4, No. 1, (2016), 1-8, ISSN 2322-5211. doi:10.5829/idosi.JAIDM.2016.04.01.01.

Persian Abstract

چکیده

امروزه به دلیل محبوبیت شبکه های اجتماعی و نیز ورود کلمات مختصر، کلمات خارجی و شکلک‌ها در زبان فارسی، اهمیت داده‌کاوی افزایش یافته و پژوهش هایی در رابطه با شناسایی نوع کلمات انجام شده است. این در حالی است که تشخیص نقش کلمه در جمله مهمتر از تشخیص نوع کلمه در جمله می باشد. از طرفی تشابه املایی- دستوری زبان فارسی به زبان عربی، موجب شده تا بتوان از روش پیشنهادی این مقاله در زبان عربی نیز استفاده کرد. در این مقاله، جهت واژه شناسی نقش‌های ترکیب جملات زبان فارسی از روش آماری مدل مخفی مارکوف و برچسب گذاری Tri-gram استفاده شده و با روش مدل مخفی مارکوف و برچسب‌گذاری Uni-gram و Bi-gram مقایسه شده است. در روش پیشنهادی با استفاده از دو دسته نقش‌های "مستقل" و "وابسته"، و عوامل پذیرش نقش کلمات در جملات، نتایج شناسایی نقش کلمات را بهبود می‌بخشد. به طوری که نتایج شبیه سازی نشان می دهد که میانگین موفقیت نقش های مستقل ترکیب با مدل مخفی مارکوف و برچسب گذاری Tri-gram نسبت به روش Uni-gram و Bi-gram به ترتیب ۲۰.۵۶ و ۱۷.۶۷ درصد و برای نقش های وابسته ترکیب به ترتیب ۲۴.۶۷ و ۳۲.۶۲ درصد، بهبود داشته است.

IJE TRANSACTIONS B: Applications Vol. 34, No. 11, (November 2021) 2508-2516

International Journal of Engineering

Journal Homepage: www.ije.ir

A Joint Optimization Model for Production Scheduling and Preventive Maintenance Interval

S. Babaeimorad[a], P. Fattahi*[a], H. Fazlollahtabar [b]

[a] *Department of Industrial Engineering, Faculty of Engineering, Alzahra University, Tehran, Iran*
[b] *Department of Industrial Engineering, School of Engineering Damghan University, Damghan, Iran*

PAPER INFO

Paper history:
Received 14 August 2021
Received in revised form 17 September 2021
Accepted 19 September 2021

Keywords:
Adapted Branch and Bound Algorithm
Joint Optimization
Preventive Maintenance
Production Scheduling

ABSTRACT

Machine maintenance is performed in production to prevent machine failure in order to maintain production efficiency and reduce failure costs. Due to the importance of maintenance in production, it is necessary to consider an integrated schedule for production and maintenance. Most of the literature on machine scheduling assumes that machines are always available. However, this assumption is unrealistic in many industrial applications. Preventive maintenance (PM) is often performed in a production system to prevent premature machine failure in order to maintain production efficiency. Machine maintenance plan is often performed in a production system to prevent premature machine failure in order to maintain production efficiency In this paper, a parallel machine scheduling problem with individual maintenance operations is considered. Then, a mathematical model is formulated including scheduling and maintenance operation optimization. The objective is to assign all jobs to machines so that the completion time and the average cost are minimized, jointly. Maintenance is considered in time intervals. To solve the proposed problem, a branch and bound (B&B) algorithm is adapted and proposed. The results showed the applicability of the mathematical model in production systems and efficiency of the adapted B&B in compare with Gams optimization software.

***doi**: 10.5829/ije.2021.34.11b.13*

NOMENCLATURE

Indices	
i	index of jobs, $i = 0,1,2, \dots, n$;
k	index of machines, $k = 1,2, \dots, K$;
m_k	index of maintenance operations, $m_k = 1,2, \dots, m$;

Parameters	
p_{ik}	Processing time of the ith job on machine k
M	A large positive number
M_k	Number of maintenance activities on machine k
C_{ik}	Completion time of the ith job on machine k
L_{mk}	The latest maintenance start time for the mth maintenance activity on machine k
C_{ik}	Completion time of the ith job on machine k
C_{pm}	Cost of a PM action
C_{Cm}	Cost of a CM action
B	A positive number between 0 and 1
μ_{pmk}	Average time for executing a PM action
μ_{cmk}	Average time for executing a CM action
$g_{pm}(t_{mk})$	Probability density function associated with the duration of a PM action
$g_{cm}(t_{mk})$	Probability density function associated with the duration of a CM action
ε	Instant of failure in the machine
$F(t)$	Probability distribution function for time to failure of machines
$R(t)$	Machine reliability$R(m) = 1 - F(t)$

Decision Variables	
x_{ijk}	1 if job *i* precedes job *j* on machine *k*
Y_{imk}	1 if the m^{th} maintenance activity is performed prior to the i^{th} job on machine *k*
C_{max}	Completion time of the last job$C_{max} = \max\{C_{jk}\}$
t_{mk}	Start time of maintenance operations on the machine *k*

1. INTRODUCTION

Determining the schedule and sequence of operations in a production cycle is utmost important and plays a substantial and effective role as one of the key success factors in any production system. Production scheduling minimizes the accumulation of capital, reduces waste, reduces or eliminates machine downtime and tries to

*Corresponding Author Institutional Email: P.fattahi@alzahra.ac.ir (P. Fattahi)

Please cite this article as: S. Babaeimorad, P. Fattahi, H. Fazlollahtabar, A Joint Optimization Model for Production Scheduling and Preventive Maintenance Interval, International Journal of Engineering, Transactions B: Applications, Vol. 34, No. 11, (2021) 2508-2516

make better use of the resources leading to satisfying customer orders in a timely manner. Time-based production and manufacturing have been proposed as a rational approach to production and operations management that also established a time-based orientation in manufacturing companies. Manufacturing companies need to transfer the elements of this concept to their operations management. An organization that can provide a variety of products to its customers in a shorter period of time with a desirable level of competitive price will be a successful organization. Time-based systems with a focus on shortening process time will lead to a reduction in overall delivery time. As a result, the inventory level will decrease and it will be possible to increase the responsiveness.

In many manufacturing industries, equipment failure is one of the main reasons for reduced production efficiency [1]. Various examples can be found in the real world, such as thermoplastic industry (such as molds in hydraulic presses), the semiconductor industry [2], cutting tools in drilling (machines, cooling systems), and sensors [1]. In some cases, equipment and machinery can be repaired and maintenance is an effective strategy to maintain machine performance and improve production efficiency.

Maintenance schedule is one of the most important issues in the manufacturing industry [3]. Despite the importance of maintenance in production, maintenance activities may interfere with production timing and cause conflicts during the execution of jobs and maintenance. Irregular maintenance may cause a complete shutdown of the production unit and reduce its availability.

There are two challenges in a production system. The first one is the production planning problem, which determines the optimal production lots, the accumulated size and evaluates the required production capacity; and the second is the scheduling and sequence of production operations, which allocate the existing production capacity to the jobs, determine the sequence of production operations and their start time. Maintenance in a production system is basically of two types. In the first type, there is no control over the condition of the machine meaning that the machines are repaired only in case of failure. Therefore, in this type of maintenance, practically no planning is done for maintenance. In the second type of maintenance, there is a partial control over the condition of the machine meaning that the maintenance includes both corrective and preventive tasks. In PM, it is possible to repair the machines to prevent the occurrence of failure. Therefore, in this situation, optimal maintenance planning is important with the aim of minimizing maintenance costs or maximizing the availability or reliability of the production system [1]. However, ignoring maintenance planning may lead to a complete stoppage of machines and the whole production system. Therefore, using machine failure information to simultaneously optimize production and maintenance schedules is a challenging problem.

The number of researches dedicated to single-machine production units is more than any other production unit. There are several reasons for this focus in single-machine environments. The first reason is the simplicity of the single-machine production unit, and the second reason is that some studies focus on bottlenecks when analyzing production lines. That is, according to the machine which failure has a great impact on the level of efficiency and operational strength of the production line [4].

From the above discussion, it can be concluded that in a production system, decisions are divided into two general groups. The first group is decisions related to the production and the second one is related to the maintenance. PM models can be broadly classified into two types: time-based and condition-based models [5]. Numerous studies have addressed the issue of integrating maintenance planning and production scheduling with time based maintenance activities. For example, in a two-machine flow shop environment with the aim of minimizing production completion time, a precautionary maintenance is planned on one of the two machines in the first period [6]. The integration of corrective maintenance (CM) and PM based on time and production schedule on a single machine production system was studied by Wang and Liu [7]. Also, the issue of fixed and flexible preventive maintenance in a job shop scheduling problem with fuzzy processing time has been discussed by Li and Pan [8]. Integration of maintenance and production scheduling has been investigated in the periodic mode, in which a single machine scheduling problem was considered and maintenance activities were performed periodically over predetermined periods [9]. The previous problem is scheduling a single machine with periodic maintenance and random processing and repair time that was developed by Shen and Zhu [10]. Mosheiov and Sidney [11] reached a similar point, that is, the problem of scheduling for a single machine with maintenance activities, but assuming that maintenance activities decline and if it is done later, it will take frailer and more time. Yazdani et al. [12] addressed the issue of scheduling of tool replacement activities in a multi-factor machine production system. Similarly, the tool was replaced after a predetermined period of time. Numerous articles have been published in the field of joint optimization of parallel machine production schedule and maintenance, which are briefly reviewed in the following.

Wang and Liu [13] investigated a multi-objective parallel machine scheduling problem with two kinds of resources (machines and moulds) and with flexible PM activities on resources. The objective was to simultaneously minimize the makespan for the production, the unavailability of the machine system, and the unavailability of the mould system for the maintenance. A multi-objective integrated optimization method with NSGA-II adaption was proposed to solve this problem. Gara-Ali et al. [14] considered a general model for scheduling jobs on unrelated parallel-machines with maintenance interventions. The processing times deteriorated with their position in the production sequence and the goal of the maintenance was to help to restore good processing conditions. The maintenance duration was dependent on the time elapsed since the last maintenance intervention. Lee [15] considered a problem of scheduling on parallel machines where each machine required maintenance activity once over a given time window. The objective was to find a coordinated schedule for jobs and maintenance activities to minimize the scheduling cost represented by either one of several objective measures including makespan, (weighted) sum of completion times, maximum lateness and sum of lateness. Zhang et al. [16] studied linear deteriorating jobs and maintenance activities under the potential disrupted parallel machines. Potential disruption means that there exists an unavailable interval at a particular time under a certain probability on some machines. Shen and Zhu [17] studied a parallel-machine scheduling problem with PM. Because of the existence of indeterminacy phenomenon, the processing and maintenance times were assumed to be uncertain variables. Branda et al. [18] have examined a flow shop scheduling problem in which machines are not available during the whole planning horizon and the periods of unavailability are due to random faults. To solve their problem, proposed two novel meta-heuristic algorithms obtained modifying a standard Genetic Algorithm (GA) and Harmony Search (HS).

Kalay and Caner [19] investigated a tactical level production planning problem in process industries under costly sequence dependent family setups, which drives the need for manufacturing of product families in campaigns. They investigated the question by implementing a multidimensional Global Optimization branch and bound algorithm with the help of three frameworks with a different level of abstraction. Daneshamooz et al. [20] proposed exact methods are based on branch and bound (B&B) approach to minimize the total completion time of products. Some numerical examples are used to evaluate the performance of the proposed methods.

Rahimi et al. [21] presented a mathematical model to address the integrated cell formation and cellular rescheduling problems in a cellular manufacturing system. As a reactive model, the model is developed to handle the arrival of a new job as a disturbance to the system. They used Gams software to solve their model. Abtahi and Sahraeian [22] presented a predictive robust and stable approach for a two-machine flow shop scheduling problem with machine disruption and uncertain job processing time. A general approach is proposed that can be used for robustness and stability optimization in an m-machine flow shop or job shop scheduling problem. A method based on decomposing the problem into sub-problem and solving each sub-problem, and a theorem-based method. The extensive computational results indicated that the second method has a better performance in terms of robustness and stability, especially in large-sized problems.

In this paper, a new mathematical model is formulated for the problem of parallel machine production scheduling and preventive maintenance (PM). In addition to preventive maintenance, corrective maintenance (CM) is also included when machines experience accidental failures. To prevent these failures, reliability has been considered for each machine, which is another major contribution of this paper.

2. PROPOSED MODEL

2. 1. Proposed Optimization Model

The description of the problem under study is given as follows: There are n independent jobs in the job set $\mathrm{N} = \{\mathrm{J}_1, \dots . \mathrm{J}_\mathrm{n}\}$ which are going to be processed on K identical parallel machines, over a scheduling period. All the n jobs are available for processing at time zero. Each job needs to be processed only on one machine and each machine is capable of processing any job but at most one job at a time. Also, it is assumed that two parallel machines are similar and independent. Maintenance operations are performed periodically. After each maintenance operation, the machine returns to its original state. Maintenance operations are not performed at time zero. If the system fails between maintenance intervals, it will undergo repair work. In this model, maintenance can be performed on both machines simultaneously.

2. 2. The Proposed Model

The objective function of the model consists of two parts. The first is to minimize the completion time and the second is to minimize the average cost of maintenance and repairs per unit of time. The model is formulated as follows:

$$\min \mathrm{Z}_1 = C_{max} \tag{1}$$

$$\min \mathrm{Z}_2 = \sum_{k=1}^{2} \frac{C_{pm} * R_k(t_{mk}) + C_{cm} * F_k(t_{mk})}{\mu_{pmk} * R_k(t_{mk}) + \mu_{cmk} * F_k(t_{mk}) + \int_{m-1}^{m} R_k(u)du} \tag{2}$$

$$\min Z : \; W_1 (\frac{Z_1 - Z_1^*}{Z_1^*}) + W_2 (\frac{Z_2 - Z_2^*}{Z_2^*}) \tag{3}$$

$$C_{\max} \geq \mathrm{C_{jk}} \quad \forall\, K \in \{1,2, \dots, n\}, \quad \forall \;\; j \in \{0,1,2, \dots, N\} \tag{4}$$

$$\sum_{k=1}^{n}\sum_{i=0}^{N} x_{ijk} = 1 \quad \forall\ i \neq j\ and\ j \in \{1,2,\ldots,N\} \tag{5}$$

$$\sum_{k=1}^{n}\sum_{j=1}^{N} x_{ijk} \leq 1\ \ \forall\, i \neq j\ \ and\ \ i \in \{0,1,2,\ldots,N\} \tag{6}$$

$$\sum_{h=0}^{N} x_{hik} \geq x_{ijk} \quad \forall\, i \neq j, i \neq h\ \ and\ \ i,j, \in \{1,2,\ldots,N\} \quad K \in \{1,2,\ldots,n\} \tag{7}$$

$$C_{0k} = 0 \qquad \forall \in \{1,2,\ldots,n\} \tag{8}$$

$$C_{jk} + M(1-\mathrm{x}_{ijk}) \geq C_{ik} + \mathrm{p}_{jk} + (t_{m_K k} + g_{pm}(t_{m_K k}) * R(t_{m_K k}) + g_{cm_K}(t_{m_K k}) * F(t_{m_K k}) * Y_{im_k k} \tag{9}$$

$$i \in \{0,1,..,N\}\ i \neq j\ \ \forall\, j \in \{1,2,\ldots,N\}\ ,$$

$$\forall\, K \in \{1,2,\ldots,n\}, and\ \forall\, m_k \in \{1,2,\ldots,m\}$$

$$\sum_{m_k=1}^{m} Y_{im_k k} \leq 1\ \ \forall\, K\ \in \{1,2,\ldots,n\}, i \in \{0,1,..,N\} \tag{10}$$

$$\sum_{m_k=1}^{m} Y_{im_k k} \leq \sum_{j=1}^{N} x_{ijk}\ \ \forall\, K \in \{1,2,\ldots,n\},\ i \in \{0,1,2,\ldots,N\}, i \neq j\ and\ j \in \{1,2,\ldots,N\} \tag{11}$$

$$\sum_{i=1}^{N} Y_{im_k k} = 1\ \ \forall\, K\ \in \{1,2,\ldots,n\}, m_k \in \{1,..,m\} \tag{12}$$

$$t_{mk} = L_{mk}\ \forall\, K \in \{1,2,\ldots,n\},\ \ m_K \in \{1,2,\ldots,m\} \tag{13}$$

$$L_{m+1,k} = t_{m,k} + g_{p(m)}(t_{(m)k}) * R(t_{(m)k}) + L_k \quad \forall\, K \in \{1,2,\ldots,n\},\quad m_K \in \{1,2,\ldots,M_K-1\} \tag{14}$$

$$p(\varepsilon \geq L_k) = \beta \tag{15}$$

$$x_{ijk}\ and\ Y_{imk} \in \{0,1\}\ \ t_{m,k} \geq 0\ \forall\, K \in \{1,2,\ldots,n\},\ m \in \{1,2,\ldots,M_K\}\ \forall\, i,j\ \in \{1,2,\ldots,N\} \tag{16}$$

Equation (4) defines the maximum completion time. Equation (5) ensures that every job is assigned to only one machine and has exactly one predecessor. Equation (6) ensures that the maximum number of successors of every job to be one. Equation (7) limits the number of successors of each job to a maximum of one on each machine. Equation (8) indicates the completion time of the job zero. Equation (9) is used to calculate the completion times of the jobs on machines. Basically, if the job j is assigned to the machine k after the job i (i.e., $\mathrm{x}_{ijk} = 1$), its completion time C_{jk}must be greater than the completion time of the job i, i.e., C_{ik}. If $\mathrm{x}_{ijk} = 0$, as the constant M is a large positive number, the constraint will become redundant and can be removed. Equation (10) ensures that the m^{th} maintenance task must be performed on each machine exactly after the job i. Equation (11) shows that the m^{th} maintenance task after the job i will be done on the machine k when the job i is assigned to the machine k. Equation (12) indicates that only one maintenance task is performed on each machine at a time. Equations (13) and (14) show how to obtain the latest start time for maintenance tasks. Equation (15) shows how to obtainL_k, which indicates the upper limit of the maximum time that the machine can operate without performing preventive maintenance. Equation (16) indicates decision variables.

3. NUMERICAL SOLUTION ALGORITHM

The following is a numerical method for determining decision variables that minimize completion time and minimize total maintenance costs per unit time. Initially, according to the definition of reliability, the value of $L_k$which indicates the working time of the machine without performing maintenance operations, is calculated to be in the constraint (10); in other words, the latest start time of maintenance operations, then the latest start time and the earliest start time of maintenance operations are calculated. After assigning each job to each machine, the latest start time and the earliest start time for maintenance operations are calculated. If the processing time of the jobs does not intersect with the time of maintenance operations, the jobs will be assigned to the machine; otherwise, that job will not be allocated and maintenance operations will be performed. This operation continues until no jobs are left. The values of the objective functions are then calculated. The branch and bound algorithm is adapted to assign jobs to machines and the solution steps are given. Figure 1 shows the solution algorithm.

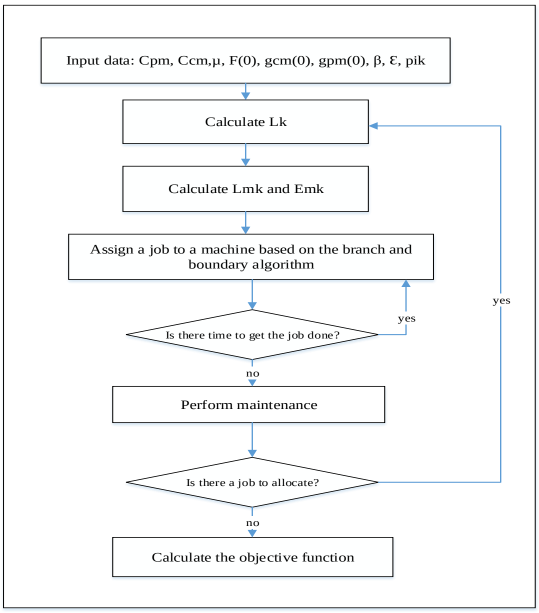

Figure 1. Algorithm for solving the proposed model

3. 1. Adapted Branch and Bound Design The branch and bound algorithm is a well-known exact algorithm for solving an optimization problem, especially combinational optimization. This algorithm was introduced by Land and Doig [23] to solve discrete optimization problems for the first time. This method finds possible answers to the problem in a state space search. Here the set of probabilistic answers is considered as a tree whose root corresponds to all the answers and its branches are subsets of probabilistic answers. Before navigating the set of answers of a sub-branch, the algorithm checks the set of answers of the branch with the lower and upper bounds of the optimization problem in general, and if the sub-branch is not able to generate a more optimal answer to the problem, it scans the whole sub-branch discard.

3. 1. 1. Features of the Method To solve optimization problems for which a polynomial time algorithm has not been found, algorithms with exponential complexity are used that have low execution time, branching and bounding method in this style of problems is a good option. The complexity of these algorithms is usually exponential.

3. 1. 2. Proposed Branching Strategy In each node, one job is assigned to one machine**.** The sequence of jobs is determined by the parent-child relationship in the search tree. The children in this search tree include members of jobs that have not been assigned to any machine up to that node (node *N*).That is, all cases of assigning jobs to machines are considered, for each allocation, a child node is created in *N*. Suppose that node *N* assigns job *i* to machine *k* (*N (i, k)*). Given the path from root to node, which represents a partial scheduling scheme, start time of job *i* is equal to the earliest time when both the machine is available and no maintenance is performed on the machine. Profile-machine shows the busy times of the machine for processing job. In other words, it shows the history of the jobs performed by the machine until the moment of assigning another job, which shows both the to-do list and the maintenance performed up to that moment. And these values are calculated according to the path from the root node to the parent when assigning the job.

$$\textbf{Profile} - \textbf{machine} = \begin{cases} 1 & \text{When the machine is processing jobs or maintenance operations} \\ 0 & \text{otherwise} \end{cases}$$

The start time of job *i* in machine *k* is then calculated as follows. And is equal to the earliest time the first machine is released.

$$\boldsymbol{min\ start\ time\ job\ i} = \left\{\{start\ time\ job\ i \mid \text{Profile} - \text{machine} = 0;\ \mathrm{C}_{i-1,1}, \mathrm{C}_{i-1,2}\}\right\}$$

The symbol in Figure 2 is used to display nodes in the search tree.

3. 1. 3. Boundary Strategy To avoid duplicate nodes or the development of nodes that we know do not improve the best answer found, rules must be designed for boundaries. In the following, 3 features are presented as boundary strategies.

Feature 1: If we are in node *N* and the moment of arrival of job i on the machine is *k*, it should be checked that if during the processing of job *i*, the time for maintenance operations is reached, job *i* should not be assigned to that machine. And that branch is removed. See Figure 3 for clarity. Suppose the machine is at time 28 and it is time to assign job 7 to machine 1, which has a processing time of 14. If Job 7 is done, the end time of Job 7 is 42, while the machine must be maintained at 38.Therefore, in that node, Job 7 is not assigned to machine 1 and that branch is deleted.

Feature 2: If we are in node *N* and the moment of entry of job *i* is on machine k, and at that moment the machine has a corrective failure, job *i* may not be assigned to machine *k*, in which case the branch will be deleted, or job *i* may wait for the maintenance operation to be completed and then perform it on the same machine,

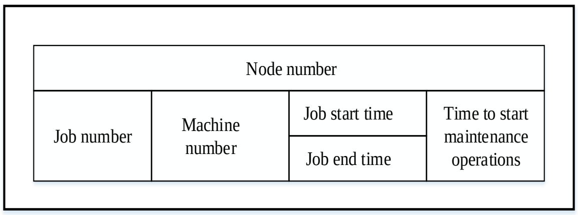

Figure 2. Nodes in the search tree

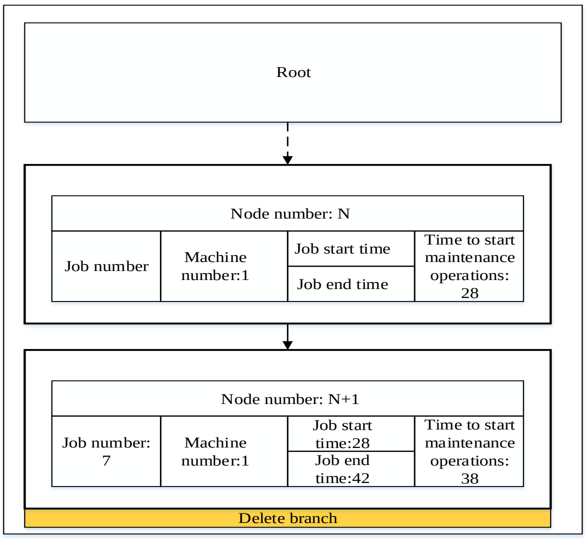

Figure 3. The branch according to feature 1

in which case the start time will be delayed as much as the maintenance operation (See Figure 4).

Feature 3: At the beginning of assigning tasks to machines, we consider the time to complete the jobs infinitely, and then we assign all the jobs to one machine. We get the maximum completion time of jobs by taking into account the processing time of works and maintenance operations which is specified as the upper bound, jobs are then assigned to both machines. If the job is completed in a branch longer than this value, the branch is removed. In addition, if a branch has been completed and a value is obtained for the time of completion, and in another branch that has not yet been completed, the completion time is longer than that branch, the branch that has not been completed will be removed (See Figure 5).

3. 1. 4. General Structure of the Method If we want to present an algorithm that minimizes the function

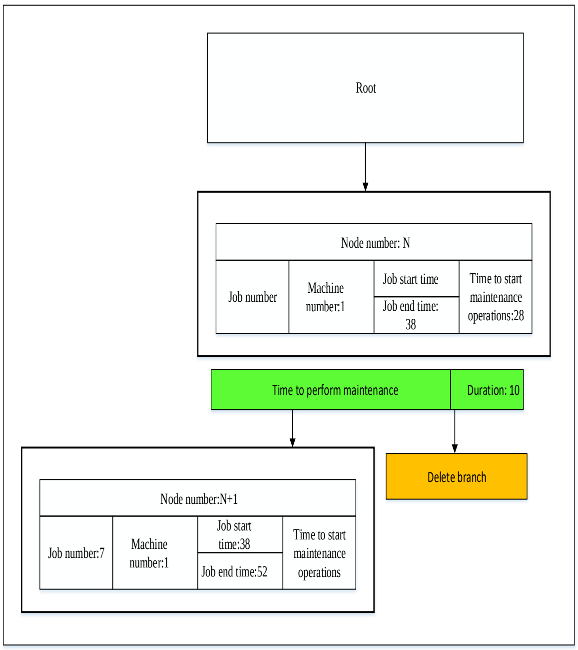

Figure 4. The branch according to feature 2

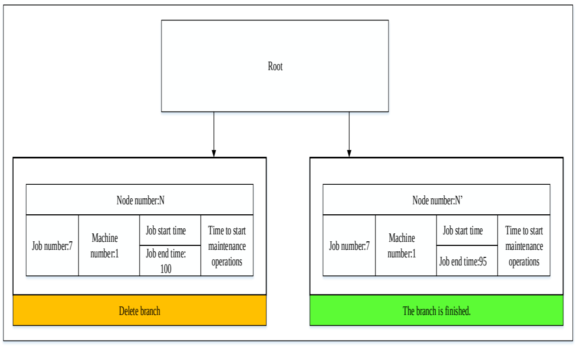

Figure 5. The branch according to feature 3

f and the function g is the lower bound for the value of f at the vertices of a sub tree of state space. The general structure of this method will be as follows:

1) First find an arbitrary answer x and set the value of B to *f (x)*, from now on, the value B will indicate the best answer found up to this point.
2) Consider a row of vertices of the state space and add the root of the state space tree to it.
3) Repeat the next steps until the queue is empty.

- A vertex is pulled out of the queue.
- If this vertex represents a specific answer to the problem such as *x* and *f (x) <B*, this answer is the best answer ever found, so the value *f (x)* is placed inside B.
- Otherwise for all branches of this vertex, for example *Ni*.

4) If *g (Ni) <B:*

- This branch may lead to a better answer, so we add *Ni* to the list.
- Otherwise this branch has no value because the lower limit of its answers is larger than the upper limit of the problem answer. Return to command 3.

3. 2. Numerical Examples In this section, the input data for solving the model by the proposed algorithm is given. This model is solved by 10 problems with the same dimensions and different processing times. An example of an issue is given below. The results for comparing 10 problems are given in Table 1.

- Costs: Cost of PM = 2, Cost of CM = 4;
- The duration of PM task ~LogNorm (mean μ_P=10, standard deviation $\delta_P = 1.5$);
- The duration of CM task ~LogNorm (mean μ_C=20, standard deviation $\delta_C = 2$);
- The time to machine failure ~ Weibull distribution (shape parameter = 2, scale parameter = 100), i.e., the average lifetime is μ =8.86 time units;
- β = 90%
- Number of machines =2;
- The number of jobs and their processing times, as well as the start time and duration of CM tasks are given in Tables 2, 3, and 4, respectively.
- In this example, the jobs are assigned to machines and there are different sequences between the jobs of each machine.

4. COMPUTATIONAL RESULTS

The proposed algorithm is implemented in MATLAB software. By studying several articles in this field, random data is generated to evaluate the algorithm. In this model assumed in the worst case, all jobs are assigned to one of the machines, and after each job,

TABLE 1. Processing time for 10 jobs in 10 problems

Job	Problem number	1	2	3	4	5	6	7	8	9	10
	1	5	8	12	9	18	14	14	-	-	-
	2	6	10	7	12	18	17	5	-	-	-
	3	6	20	7	19	8	19	20	-	-	-
	4	11	8	5	6	10	6	13	-	-	-
	5	18	20	18	9	12	14	5	8	18	16
p_{ik}	6	6	11	8	12	6	7	14	12	17	5
	7	5	10	16	20	17	15	15	14	6	14
	8	13	12	15	15	15	17	20	15	16	10
	9	19	10	9	5	12	19	15	14	19	8
	10	11	13	7	9	17	5	5	15	20	14

there is a need for preventive maintenance, so there are 10 maintenances for each machine. The numerical algorithm first determines the required time interval of machine reliability, In fact, the upper limit of this interval, L_k, indicates the maximum useful life of some parts that must be replaced after 90% operation because if they are not replaced, the machine may fail and lead to many breakdowns. After determining L_k, the earliest and latest time for maintenance operations is determined. Jobs are then assigned to machines, and this continues until the first maintenance operation is completed. It then stops and undergoes maintenance.

The important point is that if the job time to be allocated to a machine interferes with the time of preventive maintenance, the machine may be idle and not in production until the end of the maintenance operation or the machine may perform the desired job and then preventive maintenance. However, delays are not allowed for corrective maintenance, and the machine must be stopped at any time according to the schedule. After the maintenance operation, for each machine again L_k, the earliest and latest time for maintenance operations is determined and jobs are reassigned, and this continues until no jobs are left and the maximum time of the machines is set to C_{max}.

The results of solving one of the problems by the proposed algorithm and assigning jobs to two machines are given in Tables 2 and 3. In these tables, (*pcm*) indicates corrective maintenance operations; (*pm*) indicates preventive maintenance operations.

TABLE 2. Schedule on the machine 1

Job	7	Pm	2	Pm	5	pm	8	Pcm	4
Start time	0	14	14.45	23	23.61	42	42.55	57.24	58.23
End Time	14	14.45	22.45	23.61	41.61	42.55	54.55	58.23	63.55

TABLE 3. Schedule on the machine 2

Job	1	3	Pm	6	Pm	10	Pcm	9
Start time	0	5	17	17.68	32	32.73	48.23	49.36
End Time	5	17	17.68	31.68	32.73	40.73	49.36	66.36

TABLE 4. Results of solving problems

Problem Number	Objective Function	Cmax Gams	Cmax Matlab	Solution Time Matlab	Solution Time Gams
1	20.623	41.05	41.05	121.18	524.12
2	19.713	39.23	39.23	99.89	335.92
3	26.273	52.35	52.35	101.22	529.32
4	15.723	31.25	31.25	133.37	658.18
5	33.995	-	66.53	143.269	-
6	37.043	-	72.58	187.191	-
7	47.478	-	93.45	135.594	-
8	48.373	-	95.24	258.427	
9	33.328	-	65.15	227.686	-
10	40.448	-	79.39	167.517	-

4. SENSITIVITY ANALYSIS

In order to perform the sensitivity analysis, by keeping the other parameters constant, the costs are reduced and the objective function is evaluated. According to Figure 3, as the corrective maintenance cost decrease, the value of the objective function decreases more than preventive maintenance cost. Because the amount of maintenance costs was higher than preventive maintenance and the amount of objective function was more sensitive to it. The results of Figure 4 show that by increasing the value of *w* the objective function increases from 0.197 to 66.53. It can be concluded that if the completion time of the jobs

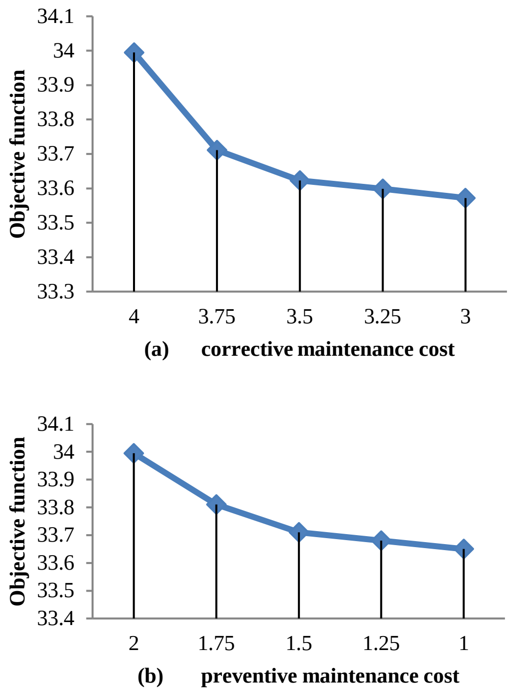

Figure 3. Diagram of changes in the objective function by reducing corrective and preventive maintenance costs

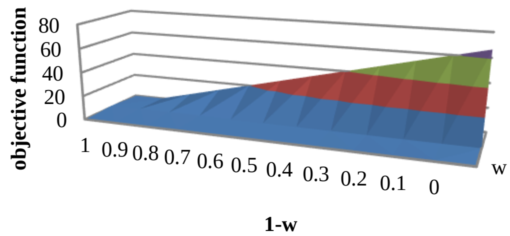

Figure 4. Variation of objective function problem 5 with changes in the value of w

is more important than the cost, the amount of the objective function will be higher.

5. CONCLUSION

In this paper, a model for scheduling a parallel machine production system and an exact solution algorithm is presented. In this case, considering maintenance operations in the schedule complicates the issue. The objective function consists of two parts, the first part is to minimize the maximum completion time of the jobs and the second part is to minimize the cost of maintenance. After presenting the model, in order to check the accuracy of its performance, several sample problems with a size of 10 jobs were solved by Gams software. Following combined branch and bound algorithm are presented. The resulting algorithm is a exact solution algorithm and the answers obtained from it on a small scale are the same as the answers obtained from Gams software. With the difference that the solution time in Gams software is much longer than the proposed algorithm. In the section of sensitivity analysis, it can be concluded that the objective function is more sensitive to the cost of corrective maintenance and decreases to a greater extent by reducing it.

Maintenance for future studies can be considered to be based on the conditions or quality control can be used to detect the maintenance operation. By changing (reducing) the parameter value of preventive maintenance costs and running the algorithm, the value of the objective function from 33.995 to 33.651 and by changing (reducing) the value of the parameter of the cost of corrective maintenance of the algorithm, the value of the objective function from 33.995 to 33.572 decreases, which indicates the correct operation of the algorithm.

6. REFERENCES

1. Bajestani. M. A, Banjevic. D, and Beck. J. C, "Integrated maintenance planning and production schedulingwith Markovian deteriorating machine conditions", ***International Journal of Production Research***, Vol. 52, No. 24, (2014), 7377-7400, doi: 10.1080/00207543.2014.931609.
2. Sloan. T. W, Shanthikumar, J. G, "Combined production and maintenance scheduling for a multipleproduct single- machine production system", ***Production and Operations Management***, Vol. 9, No. 4, 379-399, doi: 10.1111/j.1937-5956.2000.tb00465.
3. Xiao. L, Song. S, Chen. X, Coit. D.W, "Joint optimization of production scheduling and machine group preventive maintenance", ***Reliability Engineering & System Safety***, Volume 146, (2016), 68 78, doi:10.1016/j.ress.2015.10.013.
4. Taghipour. S, Azimpoor. S, "Joint Optimization of Jobs Sequence and Inspection Policy for a Single System with Two-Stage Failure Process", ***in IEEE Transactions on Reliability***, Vol. 67, No. 1, (2018), 156-169, doi: 10.1109/TR.2017.2775958.
5. Fitouhi. M. C, Nourelfath. M, Gershwin. S. B,"Performance evaluation of a twomachine line with afnite buffer and condition-based maintenance", ***Reliability Engineering & System Safety***, Vol. 166, (2017), 61-72, doi: 10.1016/j.ress.2017.03.034.
6. Allaoui. H, Lamouri. S, Artiba.A, Aghezzaf. E, "Simultaneously scheduling n jobs and the preventive maintenance on the two-machine flow shop to minimize the makespan", ***International Journal of Production Economics***, Vol. 112, (2008), 161-167, doi: 10.1016/j.ijpe.2006.08.017.
7. Wang. S, and Liu. M, "A branch and bound algorithm for single-machine production scheduling integratedwith preventive maintenance planning", ***International Journal of Production Research***, Vol. 51, (2012), 847-868, doi: 10.1080/00207543.2012.676683.
8. Li. J, Pan. Q, "Chemical-reaction optimization for solving fuzzy job-shop scheduling problem with flexible maintenance activities", ***International Journal of Production Economics***, Vol. 145, (2013), 4-17, doi: 10.1016/j.ijpe.2012.11.005.

9. Yazdani. M, Jolai. F, Taleghani. M, and Yazdani. R, "A modifed imperialist competitive algorithm for atwo-agent single-machine scheduling under periodi maintenance consideration", ***International Journal of Operational Research***, Vol. 32, (2018), 127, doi: 10.1504/IJOR.2018.092011.
10. Shen. J, Zhu. K, "An uncertain single machine scheduling problem with periodic maintenance", ***Knowledge-Based Systems,*** Vol. 144, (2018), 32-41, doi: 10.1016/j.knosys.2017.12.021.
11. Mosheiov. G. Sidney. J. B, "Scheduling a deteriorating maintenance activity on a single machine", Journal of the Operational Research Society, Vol. 65, (2010), 882-887, doi: 10.1057/jors.2009.5.
12. Yazdani. M, Khalili. S. M, Jolai. F, "A parallel machine scheduling problem with two-agent and tool change activities: An efcient hybrid metaheuristic algorithm", ***International Journal of Computer Integrated Manufacturing***, Vol. 26, (2016), 1075-1088, doi:10.1080/0951192X.2015.1130261.
13. Wang. S, Liu. M, "Multi-objective optimization of parallel machine scheduling integrated with multi resources preventive maintenance planning", ***Journal of Manufacturing Systems,*** Vol. 37, (2015), 182-192, doi: 10.1016/j.jmsy.2015.07.002.
14. Gara-Ali. A, Finke. G, Espinouse, M.L, "Parallel-machine scheduling with maintenance: praising the assignment problem", ***European Journal of Operational Research,*** Vol. 252, (2016), 90-97, doi: 10.1016/j.ejor.2015.12.047.
15. Lee. I.S, "Parallel Machine Scheduling with Maintenance Activities", ***Computers & Industrial Engineering,*** Vol. 101, (2016), 361-371, doi:10.1016/j.cie.2016.09.020.
16. Zhang. X, Liu. S, Lin. W, Wu. G, "Parallel-machine scheduling with linear deteriorating jobs and preventive maintenance activities under a potential machine disruption", ***Computers & Industrial Engineering,*** Vol. 145, (2020), 106482, doi:10.1016/j.cie.2020.106482.
17. Shen. J., Zhu. Y, "A parallel-machine scheduling problem with periodic maintenance under uncertainty", ***Journal of Ambient Intelligence and Humanized Computing***", Vol. 10, (2019), 10, 3171-3179, doi:10.1007/s12652-018-1032-8.
18. Branda. A, Castellano. D, Guizzi. G, Popolo. V, "Metaheuristics for the flow shop scheduling problem with maintenance activities integrated", ***Computers & Industrial Engineering,*** Vol. 151, (2021), 0360-8352, doi: 10.1016/j.cie.2020.106989.
19. Kalay. T, Caner. Z, "A branch-and-price algorithm for parallel machine campaign planning under sequence dependent family setups and co-production", ***Computers & Operations Research***, Vol. 135, (2021), 105430, doi: 10.1016/j.cor.2021.105430.
20. Daneshamooz. F, Fattahi. P, Hosseini. S.M.H, " Mathematical modeling and two efficient branch and bound algorithms for job shop scheduling problem followed by an assembly stage", ***Kybernetes***, (2021), doi:10.1108/K-08-2020-0521.
21. Rahimi.V, Arkat. J, Farughi. H, "Reactive Scheduling Addressing Unexpected Disturbance in Cellular Manufacturing System", ***International Journal of Engineering, Transactions A: Applications*** Vol. 34, No. 01, (2021) 162-170, doi: 10.5829/IJE.2021.34.01A.18.
22. Abtahi. z, Sahraeian. R, "Robust and Stable Flow Shop Scheduling Problem under Uncertain Processing Times and Machines' Disruption", ***International Journal of Engineering, Transactions A: Basics,*** Vol. 34, (2021), 935-947, doi: 10.5829/IJE.2021.34.04A.20.
23. Land. A. H, Doig. A. G, "An automatic method of solving discrete programming problems", ***Econometrica***, Vol. 28, (1960), 497-520, doi:10.2307/1910129.

Persian Abstract

چکیده

نگهداری و تعمیرات ماشین در تولید برای جلوگیری از خرابی ماشین به منظور حفظ کارایی تولید و کاهش هزینه های خرابی انجام می‌شود. با توجه به اهمیت نگهداری و تعمیرات در تولید، لازم است یک برنامه یکپارچه برای تولید و نگهداری و تعمیرات در نظر گرفته شود. اکثر پیشینه تحقیق مربوط به زمانبندی ماشین فرض می‌کنند که ماشین‌ها همیشه در دسترس هستند. با این حال، این فرض در بسیاری از کاربردهای صنعتی غیر واقعی است. نگهداری و تعمیرات پیشگیرانه (PM) اغلب در سیستم تولید برای جلوگیری از خرابی زودرس ماشین به منظور حفظ کارایی تولید انجام می شود. در این مقاله، یک مساله زمان بندی ماشین موازی با عملیات نگهداری و تعمیرات در نظر گرفته شده است. سپس، یک مدل ریاضی شامل زمانبندی و بهینه‌سازی عملیات نگهداری و تعمیرات تدوین می‌شود. هدف این است که همه کارها به گونه‌ای به ماشین‌آلات اختصاص داده شود تا زمان اتمام و هزینه متوسط به طور مشترک به حداقل برسد. نگهداری و تعمیرات در فواصل زمانی منظم در نظرگرفته می‌شود. برای حل مساله پیشنهادی، یک الگوریتم شاخه و کران (B&B) پیشنهاد شده است.

IJE TRANSACTIONS B: Applications Vol. 34, No. 11, (November 2021) 2517-2524

International Journal of Engineering

Journal Homepage: www.ije.ir

Dry Sliding Behavior of Carbon-based Brake Pad Materials

U. V. Saindane*, S. Soni, J. V. Menghani

Mechanical Engineering Department, Sardar Vallabhbhai National Institute of Technology, Surat, India

PAPER INFO

Paper history:
Received 11 September 2021
Received in revised form 28 September 2021
Accepted 05 October 2021

Keywords:
Brake Materials
Dry Sliding
Friction Coefficient
Friction Materials
Pin on Disc
Wear

ABSTRACT

The brake pad plays a crucial role in the control of vehicle and machinery equipment and subsequent safety. There is always a need for a new functional material with improved properties than existing ones. The present research study was carried out to develop a new brake pad material made up of polymer nanocomposite for enhanced physical, mechanical, and frictional characteristics in comparison to existing brake pad materials. In this study, polymer nanocomposite samples were developed and their physical properties namely density, water-oil absorption, and porosity were evaluated. Mechanical hardness of developed samples was estimated with Vicker's hardness tester. Frictional characteristics of samples and wear values determined with pin or disc apparatus. Dry sliding behavior was examined by conducting multiple trials with sliding speed in the span of 2-10 m/s and load were changed from 20 N to 100 N to discuss the effect of velocity, the effect of nominal contact pressure and the effect of sliding distance on friction and temperature parameters. Morphology of prepared brake pad samples was characterized with the scanning electron microscope. Scanning electron micrographs of brake pad surfaces showed different shape wear debris and plateaus significantly affecting the friction characteristics. Developed samples along with commercial specimens show excellent resistance to water and oil absorption. Thus obtained results for evaluated polymer nanocomposite brake pad samples demonstrate their potential for brake pad applications.

doi: *10.5829/ije.2021.34.11b.14*

NOMENCLATURE

FBP	Fabricated brake pad	POD	Pin on Disc
CBP	commercial brake pad	SCF	short carbon fibers
COF	Coefficient of friction	CNT	carbon nanotubes
MWCNT	Multiwall carbon nanotubes	WA	Water absorption
CI	Cast iron	OA	Oil absorption

1. INTRODUCTION

The braking mechanism is a critical part of cars and machinery equipment. As opposed to drum brakes, most cars now use disc brakes because they escape heat faster and thus reduce fade. Brake pads transform the vehicle's kinetic energy to thermal energy. The brake pad is making contact with the disk to provide force for stopping, it gets heated up as a result minor quantities of friction compounds are transferred to the disc or pad [1]. However, no particular material could meet the expected performance-related requirements like safety and reliability under different brake conditions in a disc brake system. The friction materials must provide a stable COF and high wear resistance at different operating pressures, speeds, environmental conditions and temperatures, Additionally, these materials should be compliant with the material of the rotor to minimize wear of rotor, friction, and braking noise [2].

Some of the unique benefits of hybrid composites over traditional composites are balanced strength and stiffness, balanced bending and membrane mechanical characteristics, balanced thermal distortion stability, and decreased cost and weight. Various hybrid composite

*Corresponding Author Institutional Email: *ds17me002@med.svnit.ac.in* (U. V. Saindane)

Please cite this article as: U. V. Saindane, S. Soni, J. V. Menghani, Dry Sliding Behavior of Carbon-based Brake Pad Materials, International Journal of Engineering, Transactions B: Applications, International Journal of Engineering, Transactions B: Applications, Vol. 34, No. 11, (2021), 2517-2524

materials have been investigated and used as brake pads for automobiles in recent years [3]. Brake pads consist of more than 10 different ingredients, reinforcing fibers, resin as a binder, solid lubricants, abrasives, wear-resistant and friction modifiers are often used in these components. The type and quantity of these constituents are often decided by practice, empirical observation or a trial-and-error approach for developing a new combination. Asbestos has been a common ingredient in brake pads for the past twenty years because of its resilience, heat resistance, and fire resistance. Since asbestos emits toxic substances that can cause lung cancer and affect health adversely, it has been banned from being used as a component in the manufacture of brake pads since 1980s. Therefore, asbestos was replaced with non-asbestos materials such as Kevlar (aramid fiber), glass fiber, and graphite [4, 5]. However alternatives such as Kevlar, glass fiber and graphite did not compete with the friction performance of materials containing carbon fibers [6]. Carbon fibers provide a stable coefficient of friction (0.4-0.5) throughout the braking operation [7]. An attempt has been made in this paper to manufacture the composite samples with short carbon fibers as the main reinforcement.

Considering the advantage of carbon fibers as brake pad additive material, recently [8] has developed short carbon fiber reinforced epoxy composites. The use of SCF additive in epoxy composite significantly reduced the immediate contact between the counterpart and composite. While the use of CNT and graphene powder in brake pad epoxy composite, also improved the mechanical characteristics and thermal conductivity of the composite [9].

In consistency with the latest efforts for the development of new and effective brake pad materials, [10] have designed and developed two polymer nanocomposites made up of epoxy polymer, multiwalled carbon nanotubes, graphene and carbon fibers.

The present study compares a possibly modern fabricated non-asbestos carbon-based brake pad (FBP) to a non-asbestos commercial brake pad (CBP) to test and examine their tribological properties. Both FBP and CBP were tested by measuring hardness, density, water and oil absorption. Pin on Disc type tribe test machine was used to carry out tribal tests. Grey cast iron rotor disc was used to test the friction materials. The test was conducted under the effect of load (20-100 N), sliding speed (2-10 m/s) and sliding distance up to (2.7 km).

2. EXPERIMENTAL PROCEDURE

Jai Rubber Enterprises, Pune has supplied the woven carbon fabric and epoxy resin of grade 650 and hardener form from Adnano technologies pvt. ltd., Shimoga, Karnataka. Molybdenum disulfide powder was obtained from Premier industrial corporation Ltd., Mumbai.

2. 1. Preparation of Pad Specimens FBP samples were manufactured using the hand lay method in this work. The detailed procedure was explained in the work [10]. The ingredients and their proportion were represented in Table 1. The fabricated sample was made by mixing powdered and epoxy resin materials. Epoxy resin, multi-wall carbon nanotubes and graphite nanopowder were manually mixed for 20 minutes to achieve a homogenous solution. Tiny, 5-10 mm long carbon fibers are then mixed with a combination of epoxy and nanocomposites. This blend is then mixed manually for a further ten minutes. The plastic mold measuring 50 mm x 50 mm x 15 mm was used to prepare the fabricated brake pad. Wax was added to the mold's inner surface before pouring to make the composite easy to remove. The mixture was subsequently poured into a 12 mm deep open mold. The mix was permitted to cure for two days at room temperature in the mold. After two days of proper curing, the composite mixture was removed, Sample was polished to a smooth surface finish. Figure 1 depicts a polished sample. Commercial brake pad sample was chosen from brake pad samples available in the market. The fabricated brake pad sample was compared with chosen commercial brake pad sample. The chosen brake pad sample was used in the Bajaj Pulsar two- wheeler automobile shown in Figure 2.

2. 2. Hardness and Density Test Vickers hardness tester was used to conduct the hardness test. Because the Vickers technique covers the full hardness

Figure 1. Fabricated brake pad sample (FBP)

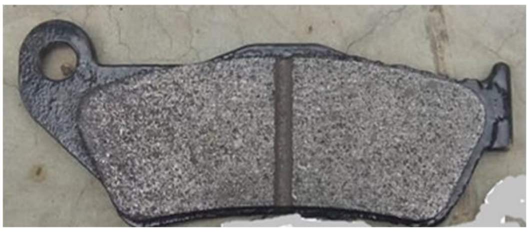

Figure 2. Commercial brake pad sample (CBP)

TABLE 1. Physical properties of ingredients

Sr. No.	Ingredient	Density (g/cm^3)	Viscosity (mPas)	Size	Colour
1	Epoxy Resin (650)	1.13	800-1000	-	Semi transparent
2	Hardner (651)	1.019	650	-	Yellow
3	Short carbon fibers	2	-	L=5-10 mm	
4	MWCNT	0.14	-	L=1-20 µm, D=10-30 nm	Black
5	Graphene	1-2.39	-	D=<100 nm	Iron black
6	Molybdenum disulfide	5.06	-	D=10-30 µm	Grey

range, it could be used on all materials and test specimens, from soft to hard [11]. Each sample was indented three times with a diamond indenter, and the average of the diagonals in all three indentations was used to calculate the results, as shown in Figure 5. Equation (1) was used for hardness calculation.

$$HV = 1.854 \times \left(\frac{F}{d^2} \right) \tag{1}$$

Where, F= Load in kgf, $d = \left(\frac{(d_1 + d_2)}{2} \right)$

The Archimedean technique was used to determine the density of the composites. The difference in water level between samples was measured after they have been fully immersed in water. According to the concept, 1 ml of water displaced equals 1 cm^3 of body volume submerged in that water. Finally, the density of samples was determined by the mass to volume ratio [12].

2. 3. Water and Oil Absorption Test The test was done in accordance with the ASTM D 570-98 test specification [13]. To disperse heat generated during braking, porosity is necessary. The samples were thoroughly immersed in the engine oil of grade 10W-30 from the Mak 4t Zipp brand of Bharat Petroleum Corporation Ltd. for the oil absorption test. The initial and end weights of the samples were determined, and the percent oil absorption was computed using Equation (2).

$$\%Oil\ Absorption = \left(\frac{Final\ weight - Initial\ weight}{Initial\ weight} \times 100 \right) \tag{2}$$

2. 4. Porosity Test Standard JIS D 4418-1996 was used to measure porosity [14]. The specimens were sliced to 15 × 15 × 5 mm^3 each and weighed (M_1). The sliced samples were then placed in a desiccator for 24 hours at ambient temperature. The samples were then kept in an oil container and heated to 85°C for 7 hours. The samples were then put into the oil tank for the next 12 hours to achieve room temperature. After removing the samples from the oil tank, the oil had been removed using a cloth. Finally the samples were weighed (M_2). The density (ρ) and volume (V) of the samples were also determined. The porosity (P) in percent was calculated using the following Equation (3).

$$P(\%) = \left(\frac{M_2 - M_1}{\rho} \right) \times \left(\frac{1}{V} \right) \times 100 \tag{3}$$

2. 5. Counter Disc Material To assess the wear, grey cast iron of grade 4 E was utilized. The disc has a hardness rating of 190 HV. The disc had an average surface roughness of $2.2 \pm 0.2\ \mu$m.

2 .6. Test Set up and Procedures POD type apparatus was utilized to perform tribo test as seen in Figure 3 to study the work in progress at and medium nominal contact pressure (upto1 Mpa) and high speed (up to 10 m/s). Specimen of fabricated brake pad sample was prepared in the form of the pin shown in Figure 4. Dry sliding tests were carried out at room temperature and ambient humidity, with sliding speed in the span of 2-10 m/s and the load were changed from 20 N to 100 N. 10 dry tests were performed on 10 different specimens prepared of fabricated brake pad for various speeds (2 - 10 m/s) and various load conditions (20 -100 N). The next 10 run of dry tests were performed on 10 distinct specimens prepared of commercial brake pad sample under the same velocity and load conditions [15]. To ensure that the two rubbing surfaces make excellent, consistent contact, rubbing of pad specimens was carried out with a silicon abrasive paper before the tests. i. e. contacting surfaces. The frictional force was measured using a strain guage present at the level arm that holds the specimen. The coefficient of friction value was calculated using the ratio of frictional force to normal load. Wear was determined in the form of weight loss

Figure 3. Pin on Disc tribo tester

Figure 4. Specimen Pins

during the test [16]. The microstructures of worn-out surfaces were determined using scanning electron microscope Hitachi S- 3400 N.

2. 7. Temperature Measurement STANLEY STHT0-77365 high accuracy industrial digital infrared thermometer was used to know the temperature during surface interaction. The infrared thermometer was kept approximately 12 cm away from the trailing edge of the brake pad specimen.

3. RESULTS AND DISCUSSION

The values of characterization for both brake materials are tabulated. The measured values of physical and mechanical characteristics of both the samples are lies in the range of acceptable limits (Table 2).

3. 1. Physical and Mechanical Properties An Increase in hardness of FBP was found significant compare to the CBP sample. The strength of short carbon fibers and multi-wall carbon nanotubes increased the hardness. The presence of carbon fiber content in the composite decreased the FBP sample's density [12]. This may be due to void formation due to carbon fibers, as a result porosity has increased (2.1%) [17]. The absorption of the heat generated mainly depends on porosity. High porosity leads to enhanced friction coefficient and high wear rate as contact area increases for FBP than CBP in the current study. Water and Oil absorption values were representing the moisture content for FBP and CBP. High values of water and oil absorption were observed for FBP as compared to CBP due to the carbon-based ingredients used in FBP, which may detoriate the fiber-matrix interface and change the sample dimensions.

3. 2. Wear Test The surface films developed due to friction between the disc and pad interface. Some authors claimed that this can lead to a steady friction pattern, but their precise function in braking is still tendentious [18]. Addition of abrasive additives in friction materials is used to control the growth of friction film developed on the rotor disc surface and to improve the grip between pad and disc [19]. The mechanism of steady friction using the third body system remain to be expressive. The driver's key worry was the brake pad's effective functioning under various braking conditions. It was therefore necessary to present changes in COF as a function of the speed of sliding and load applied or contact pressure.

3. 3. Effect of Sliding Speed Figure 5 shows the effect of the speed of sliding on friction and wear properties under a continuous load of 45 N, corresponding to 0.4 MPa nominal contact pressure, over a test duration of 300 seconds. The impact of speed of sliding on friction, thermal and wear rate performance was seen in Figure 5, when tested at a constant normal load 45 N i.e. contact pressure (nominal) of 0.4 MPa for 300 seconds. The friction coefficient shows a 'increasing-steady state decreasing' pattern in Figure 5 (a) for both friction materials namely fabricated brake pad and commercial brake pad. The generation of cold welding and breakup of asperities on the fresh friction surface must have caused the rising trend in COF i.e. from 0.31 to 0.38 for CBP and 0,36 to 0.44 for FBP at the start of the dry sliding test.

As a result, the temperature of the interfaces increased throughout the test, which later was verified by a visual inspection of Figure 5 (b). Illustrating that as the sliding speed increases, the temperature rises linearly ie from 48 ^{o}C to 68 ^{o}C for CBP and from 60 ^{o}C to 89 ^{o}C for FBP. A similar trend was reported by Österle et al. [20]. It was discovered that the test specimen's uneven surface can lead to the formation of a separate body between the pad and disc surfaces. These third entities can help with film transfer onto the sliding counterface by moving between the interfaces in a circular or linear motion [21]. During the adhesive dry test, this raised the friction coefficient, resulting in a considerably higher contact temperature. When the contact temperature reached 6 m/s, the COF of all brake pad samples started to fall as a result of loss of

TABLE 2. Physical and mechanical properties

	Hardness (HV 70)	Density (gm/cc)	WA (%)	OA (%)	Porosity (W) %	Porosity (O) %
FBP	195	0.8591	0.0277	0.0094	2.1	0.113
CBP	177	1.8667	0.0324	0.01022	1.16	0.086

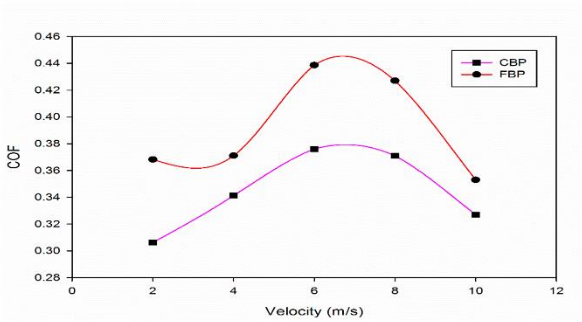

(a)

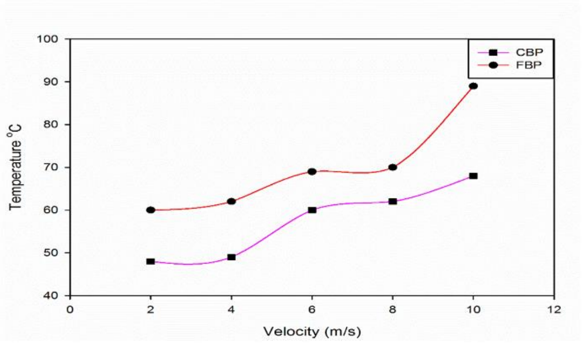

(b)

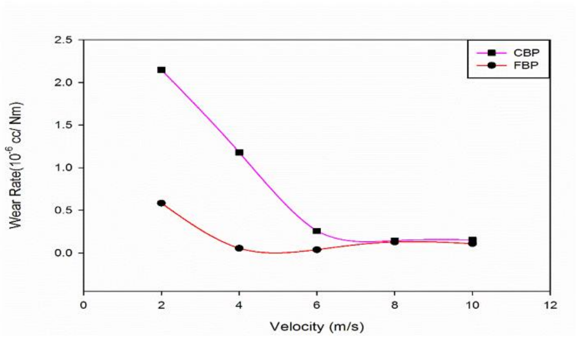

(c)

Figure 5. Changes in (a) friction, (b) interface temperature, and (c) wear for FBP and CBP materials exposed to a constant nominal load of 45 N for a test duration of 300 seconds

friction owing to frictional heating, When the contact temperature reached 8 m/s, the COF of all brake pad materials started to fall as a result of frictional heating, called as fade.

Alternatively, for both brake pad compositions, there was evidence of a ‘running in' phase of wear rate, as shown in Figure 5(c). When the wear rate was raised to 6 m/s, the variations in wear characteristics between the two friction materials were no longer as evident as they had been in the 'running in' area i.e. reduced from 0.018 to 0.012 gm. When the speed of sliding was more than 6 m/s, the COF also began to decline till further decline up to the value 0.327 which was seen in Figure 5(a). This might be owing to the fast layer transfer to the counterface, which resulted in the development of a thin shield film that prevents the brake pad material’s wear rate from increasing any further [22].

3. 3. Effect of Normal Load The impact of normal load on friction and wear characteristics for two distinct friction materials subjected to constant velocity 4 m/s for the duration of test 300 s is presented in Figure 6.

Friction and temperature profiles of both brake pads show a general upward tendency with increasing normal load, Figures 6(a) and 6(b). This leads to a considerable temperature increase as well as an increase in COF i.e. from 60 ºC to 84 ºC and from 0.33 to 0.40 for temperature and COF respectively. The current study's findings are consistent with finding reported by Österleet al. [20] who showed that in a wide variety of operating conditions, a reliable brake pad material must retain good stability of friction except at load 100 N decrease in temperature from 84ºC to 79ºC was attributed to uncertainties and errors during experiments [23].

The wear rate of both friction materials, on the contrary, showed a non-linear gradual decline as contact pressure increased, as shown in Figure 6(c). Wear rate decline from 0.84 10^{-6} ml/Nm to 0.11 10^{-6} ml /Nm for CBP and from 2.57 10^{-6} ml /Nm to 0.20 10^{-6} ml /Nm for FBP. Thus in comparison to the CBP, the FBP had the superior overall wear performance. The carbon fiber content in test specimens would account for FBP's excellent wear resistance [24]. The chances of a third-body contact across the sliding surfaces were reduced as a result, thus decreases abrasive wear that may have led to a high rate of material loss during the test.

3. 4. Effect of Sliding Distance When two brake pad materials are subjected to a constant speed of sliding 10 m/s and fixed nominal contact pressure of 0.4 MPa, The friction and temperature response concerning sliding distance is shown in Figure 7. The adherence of brake pad metal chips to the friction surface of the cast-iron disc is typically linked to a continual rise in the friction coefficient [25]. Both friction materials exhibit stability of coefficient of friction after 7 km, as shown in Figure

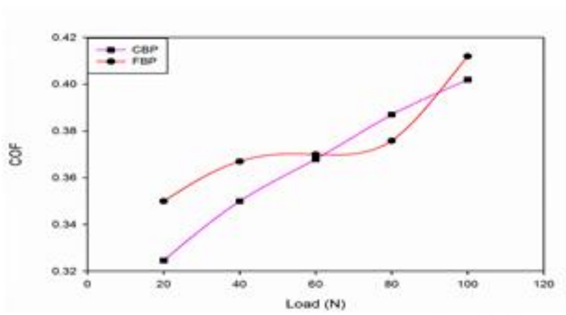

(a)

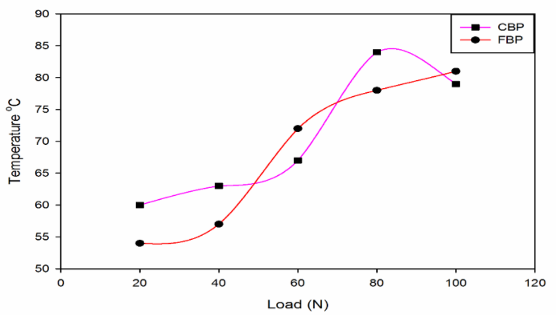

(b)

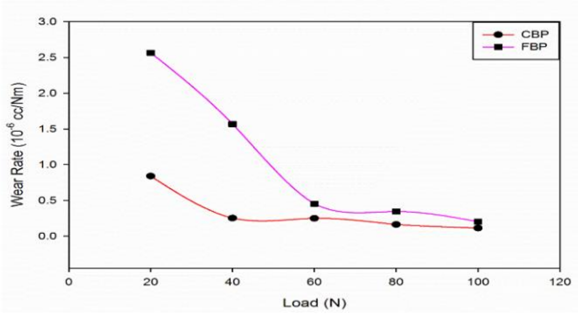

(c)

Figure 6. Variations in (a) coefficient of friction, (b) interface temperature, and (c) wear for FBP and CBP materials exposed to a constant sliding speed of 4 m/s for 300 seconds.

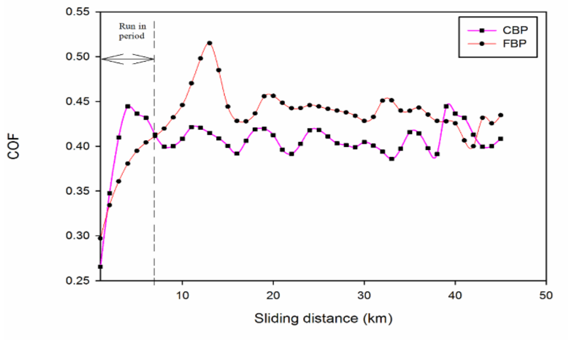

(a)

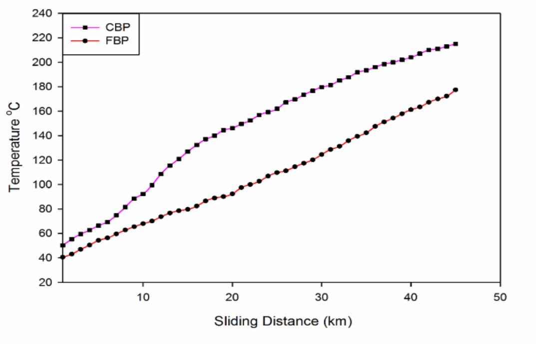

(b)

Figure 7. Changes in (a) coefficient of friction and (b) temperature for CBP and FBP materials at varied sliding distances under dry sliding conditions: 10 m/s and 0.4 MPa

7(a).The range of COF lies in 0.26 to 0.44 for CBP and lies in 0.39 to 0.51 for FBP respectively. This is due to a homogeneous transfer of the film on the surface of rotor disc, which explains the determined value of steady friction performance at higher temperatures, as shown in Figure 7. When the sliding distance was increased, all of the test specimens saw a consistent rise in temperature, as seen in Figure 7(b) maximum rise in temperature for CBP was observed to 215 °C and for FBP temperature rise was up to 177.4 °C. This is due to the specimens slide against the grey CI disc continually, a process known as adhesive dry sliding.

3. 5. SEM Analysis The different reinforcing stages were identified and found to be equally distributed, demonstrating the fabricated brake pad's homogeneity. Figure 8 depicts the microstructure of FBP, which shows tiny cracks that have little effect on the coefficient of friction or wear. Wear debris in the shape of plates was discovered, indicating good wear resistance.

The micrographs of the worn surface of CBP showed more pulled-out fiber, greater debonding of the fiber matrix, and substantial degradation in filler matrix bonding as shown in Figure 9. Roughness and specific wear rate are increased as a result of the pulled-out fibers [26]. Low wear resistance is indicated by fine spherical wear debris.

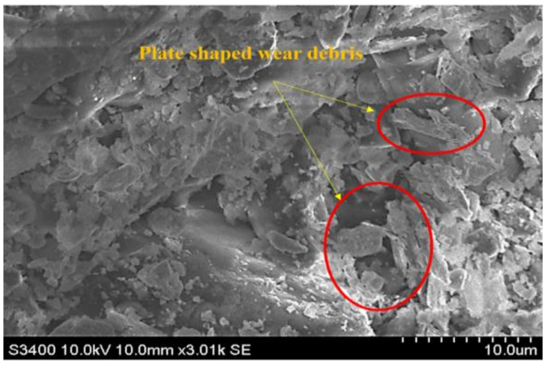

Figure 8. Microstructure of FBP

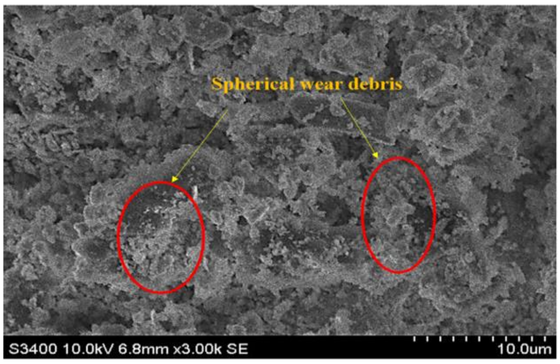

Figure 9. Microstructure of CBP

4. CONCLUSIONS

In a dry sliding test, the impact of speed of sliding, nominal contact pressure, and distance of sliding on friction coefficient (COF), wear rate, and temperature for FBP and CBP were investigated. The findings of this research and evaluation are listed below.

1. The influence of sliding speed on COF revealed an 'increasing-steady state decreasing' pattern for all materials. In comparison to CBP, FAB has the greatest COF (0.439). The lower COF went to CBP (0.341). As the temperature rose, frictional heating caused the COF of all materials to decrease. When the speed of sliding was more than 6 m/s, however, the wear rate for all materials decreased. this may be due to the creation of a transfer layer that shields the brake pad from fast wear.
2. The results revealed that FAB had the highest COF under normal load, and that it increased with the load.
3. Meanwhile, FBP had the fewest fluctuations and CBP had shown lower COF (0.35). In other words, FAB worked well under the influence of varying normal load since friction materials are anticipated to maintain a consistent COF (0.41) over a wide range of braking situations. When the normal load rose, the wear performance of both friction materials followed the sequence CBP > FBP, with FBP exhibiting strong wear resistance and a steady COF.
4. FAB was also successful in stabilizing the friction coefficient. for a large sliding distance (42 km).
5. At higher contact temperatures, Frictional performance is significantly influenced by the layer formed on the friction surface, which enhances the stability of the friction coefficient, as a result, improves fade resistance.
6. Physical and mechanical properties exhibited by FAB are much better than CBP. As a result, it is directly equivalent to CBP material**,** which contains asbestos and has excellent frictional properties.

5. REFERENCES

1. M. Akhondizadeh, M. fooladi Mahani, S. H. Mansouri, M. Rezaeizadeh, " A New Procedure of Impact Wear evaluation of Mill Liner", ***Ineternational Journal of Engineering, Transactions A: Basics***., Vol. 28, No. 4, (2015), 593-598.
2. D. Mehra, M. M. Mahapatra, and S. P. Harsha, "Effect of wear parameters on dry abrasive wear of RZ5-TiC in situ composite," ***Industrial Lubrication and Tribology***, Vol. 70, No. 2, (2018), 256-263, doi: 10.1108/ILT-12-2016-0306.
3. T. R. Jaafar, N. I. Ismail, M. F. Ismail, and E. A. Othman, "Influence of steel fibres on friction behaviours with respect to speed, pressure and temperature ***Industrial Lubrication and Tribology***, Vol. 69, No. 3, (2017), 420-424, doi: 10.1108/ILT-09-2016-0230.
4. N. Aranganathan, V. Mahale, and J. Bijwe, "Effects of aramid fiber concentration on the friction and wear characteristics of non-asbestos organic friction composites using standardized braking tests," ***Wear***, Vol. 354-355, (2016), 69-77, doi: 10.1016/j.wear.2016.03.002.
5. T. Singh and A. Patnaik, "Performance assessment of lapinus-aramid based brake pad hybrid phenolic composites in friction braking," ***Archives of Civil and Mechanical Engineering***., Vol. 15, No. 1, (2015), 151-161, doi: 10.1016/j.acme.2014.01.009.
6. C. Capela, S. E. Oliveira, and J. A. M. Ferreira, "Mechanical behavior of high dosage short carbon fiber reinforced epoxy composites," ***Fibers and Polymers***, Vol. 18, No. 6, (2017), 1200-1207, doi: 10.1007/s12221-017-7246-0.
7. F. Ahmadijokani, Y. Alaei, A. Shojaei, M. Arjmand, and N. Yan, "Frictional behavior of resin-based brake composites: Effect of carbon fibre reinforcement," ***Wear***, Vol. 420-421, (2019), 108-115, doi: 10.1016/j.wear.2018.12.098.
8. N. W. Khun, H. Zhang, L. H. Lim, C. Y. Yue, X. Hu, and J. Yang, "Tribological properties of short carbon fibers reinforced epoxy composites," ***Friction***, Vol. 2, No. 3, (2014), 226-239, doi: 10.1007/s40544-014-0043-5.
9. S. Y. Yang Yang, S.Y., Lin, W.N., Huang, Y.L., Tien, H.W., Wang, J.Y., Ma, C.C.M., Li, S.M. and Wang, Y.S., "Synergetic effects of graphene platelets and carbon nanotubes on the mechanical and thermal properties of epoxy composites," ***Carbon,*** Vol. 49, No. 3, (2011), 793-803, doi: 10.1016/j.carbon.2010.10.014.
10. U. V. Saindane, S. Soni, and J. V. Menghani, "Studies on mechanical properties of brake friction materials derived from carbon fibres reinforced polymer composite," ***Materials. Today Proceedings***., (2021), doi: 10.1016/j.matpr.2021.04.079.
11. P. Thiyagarajan, "Controlling the Hardness and Tribological Behaviour of Non-asbestos Brake Lining Materials for Automobiles," ***Carbon Letters***, Vol. 5, No. 1, (2004), 6-11,
12. M. Ünaldı and R. Kuş, "The Determination of the Effect of Mixture Proportions and Production Parameters on Density and Porosity Features of Miscanthus Reinforced Brake Pads by Taguchi Method," ***International Journal of Automotive Engineering and Technologies***, Vol. 7, No. 1, (2018), 48-57, doi: 10.18245/ijaet.438047.
13. S. D. 50 on permanence properties ASTM committe on D-20 on plastics, "Standard test Method for Water Absorption of Plastics," American Society for Testing and Materials. (1995).
14. Japan Industrial standard, "Test procedures of Porosity for Brake Linings and Pad Formulations. JIS D 4418." (1996).
15. K. W. Liew and U. Nirmal, "Frictional performance evaluation of newly designed brake pad materials," ***Materials and Design***, Vol. 48, (2013), 25-33, doi: 10.1016/j.matdes.2012.07.055.
16. C. Menapace, M. Leonardi, V. Matějka, S. Gialanella, and G. Straffelini, "Dry sliding behavior and friction layer formation in copper-free barite containing friction materials," ***Wear***, Vol. 398-399, (2018), 191-200, doi: 10.1016/j.wear.2017.12.008.
17. Sellami, M. Kchaou, R. Elleuch, A. L. Cristol, and Y. Desplanques, "Study of the interaction between microstructure, mechanical and tribo-performance of a commercial brake lining material," ***Materials and Design***, Vol. 59, (2014), 84-93, doi: 10.1016/j.matdes.2014.02.025.
18. A. Shojaei, M. Arjmand, and A. Saffar, "Studies on the friction and wear characteristics of rubber-based friction materials containing carbon and cellulose fibers," ***Journal of Materials Science***, Vol. 46, No. 6, (2011), 1890-1901, doi: 10.1007/s10853-010-5022-2.
19. L. Wei, Y. S. Choy, C. S. Cheung, and D. Jin, "Tribology performance, airborne particle emissions and brake squeal noise of copper-free friction materials," ***Wear***, (2020), 448-449. doi: 10.1016/j.wear.2020.203215.
20. W. Österle, Dörfel, I., Prietzel, C., Rooch, H., Cristol-Bulthé, A.L., Degallaix, G. and Desplanques, Y., "A comprehensive

microscopic study of third body formation at the interface between a brake pad and brake disc during the final stage of a pin-on-disc test," ***Wear***, Vol. 267, No. 5-8, (2009), 781-788, doi: 10.1016/j.wear.2008.11.023.

21. N. S. M. EL-Tayeb and K. W. Liew, "On the dry and wet sliding performance of potentially new frictional brake pad materials for automotive industry," ***Wear***, Vol. 266, No. 1-2, (2009), 275-287, doi: 10.1016/j.wear.2008.07.003.
22. N. Elzayady and R. Elsoeudy, "Microstructure and wear mechanisms investigation on the brake pad," ***Journal of Materials Research and Technology***, Vol. 11, (2021), 2314-2335, doi: 10.1016/j.jmrt.2021.02.045.
23. R. J. Moffat, "Describing the uncertainties in experimental results," ***Experimental Thermal and Fluid Science***, Vol. 1, No. 1, (1988), 3-17, doi: 10.1016/0894-1777(88)90043-X.
24. O. J. Gbadeyan, K. Kanny, and T. P. Mohan, "Influence of the multi-walled carbon nanotube and short carbon fibre composition on tribological properties of epoxy composites," ***Tribology-Materials, Surfaces & Interfaces***, Vol. 11, No. 2, (2017), 59-65, doi: 10.1080/17515831.2017.1293763.
25. K. W. Hee and P. Filip, "Performance of ceramic enhanced phenolic matrix brake lining materials for automotive brake linings," ***Wear***, Vol. 259, No. 7-12, (2005), 1088-1096, doi: 10.1016/j.wear.2005.02.083.
26. ÖZtüRk, F. Arslan, and S. Öztürk, "Effects of different kinds of fibers on mechanical and tribological properties of brake friction materials," ***Tribology Transactions***, Vol. 56, No. 4, (2013), 536-545, doi: 10.1080/10402004.2013.767399.

Persian Abstract

لنت ترمز نقش مهمی در کنترل وسایل نقلیه و ماشین آلات وبعد ایمنی دارد. همیشه نیاز به یک ماده کاربردی جدید با خواص بهبود یافته نسبت به موارد موجود وجود دارد. این مطالعه تحقیقاتی به منظور توسعه یک ماده جدید لنت ترمز متشکل از نانوکامپوزیت پلیمری برای افزایش ویژگیهای فیزیکی ، مکانیکی و اصطکاکی در مقایسه با مواد لنت ترمز موجود انجام شد. در این مطالعه ، نمونه های نانوکامپوزیت پلیمری توسعه داده شد و خواص فیزیکی آنها یعنی چگالی ، جذب آب ، روغن و تخلخل مورد ارزیابی قرار گرفت. سختی مکانیکی نمونه های توسعه یافته با سختی سنج ویکر برآورد شد. ویژگی های اصطکاک نمونه ها و مقادیر سایش با پین یا دستگاه دیسک تعیین می شود. رفتار لغزشی خشک با انجام آزمایشات متعدد با سرعت لغزش در بازه ۲–۱۰ متر بر ثانیه مورد بررسی قرار گرفت و بار از ۲۰ نیوتن به ۱۰۰ نیوتن تغییر کرد تا در مورد تأثیر سرعت ، تأثیر فشار تماس اسمی و اثر لغزش بحث شود. فاصله بر روی پارامترهای اصطکاک و دما مورفولوژی نمونه های آماده شده لنت ترمز با میکروسکوپ الکترونی روبشی مشخص شد. میکروگراف های الکترونی روبشی سطوح لنت ترمز نشان داد که بقایای سایش و فلات های مختلف به طور قابل توجهی بر ویژگی های اصطکاک تأثیر می گذارد. نمونه های توسعه یافته به همراه نمونه های تجاری مقاومت بسیار خوبی در برابر جذب آب و روغن نشان می دهند. نتایج بدست آمده برای نمونه های لنت ترمز نانوکامپوزیت پلیمری ارزیابی شده ، پتانسیل آنها را برای کاربردهای لنت ترمز نشان می دهد.

International Journal of Engineering

Journal Homepage: www.ije.ir

Taguchi-grey Relational Analysis for Optimizing the Compressive Strength and Porosity of Metakaolin-based Geopolymer

S. A. J. Al-Sultani*, I. A. Disher Al-Hydary, M. A. Ahmed Al-Dujaili

Department of Ceramics Engineering and Building Materials, Faculty of Materials Engineering, University of Babylon, Babylon, Iraq

PAPER INFO

Paper history:
Received 07 July 2021
Received in revised form 20 September 2021
Accepted 23 September 2021

Keywords:
Geopolymer
Multi Response Problems
Taguchi Method
Grey Relational Analysis
Metakaolin

ABSTRACT

Geopolymer is a promising eco-friendly material that can be produced with a variety of physical and mechanical properties through alerting the processing parameters. Obtaining Geopolymer with high compressive strength and high porosity may make this material a preferred candidate for many thermal and physicochemical applications. This research aims to identify the set of the processing parameters that yield such as these Geopolymer materials. Taguchi method combined with Grey relational analysis has been used to solve this multi-response trouble. The analysis and the experimental results showed that it is possible to achieve this aim by using a low amount of hydrogen peroxide as a foaming agent, a low amount of yeast as a catalyst, and a low amount of vegetable oil as a stabilizer. Furthermore, the polymerization time elapses before adding the foaming agent is found to be an important processing parameter. Also, the experimental results showed that high porosity and adequate compressive strength can be obtained at the same geopolymer body by choosing the suitable values of the processing parameters. Moreover, it has been found that the use of yeast as the catalyst and the polymerization time is important processing parameters. Also, it has been noticed that the amount of the vegetable oil, which is used as a stabilizer, should be kept in low values to obtain the optimal compressive strength and porosity.

***doi**: 10.5829/ije.2021.34.11b.15*

1. INTRODUCTION

Joseph Davidovits is considered the first to formulate the geopolymer term in1970s [1]. Geopolymers refer to the three-dimensional aluminosilicates cementitious material that can be produced by the precipitation, polycondensation and dissolution of the aluminosilicates origin [2]. Geopolymer has a typically amorphous or semi-crystalline structure with aluminum and silicon sites tetrahedrally coordinated. The geopolymer structure consists of a polymeric Si–O–Al framework [3]. geopolymers can be consolidated at room temperature and, for selected applications, can be used at high temperatures up to 1200°C [4].

Geopolymer materials have an advantage over the Portland cement-based binders which cause the emission of very large amounts of carbon dioxide. Fly ash, waste glass and slag were used as raw materials for the geopolymer which can decrease the carbon emission from these binder materials [3-6]. Metakaolin-based geopolymers are supposed as ‘‘model-system” without the drawbacks inserted by using fly ash, slag, and other alternative starting materials which include several difficult-to-characterize amorphous phases [7].

Geopolymer is an intrinsically porous material with a small pore size and variable pore shape. The synthesis of highly porous geopolymer generally involves the addition of blowing agents to the geopolymer paste, such as hydrogen peroxide (H_2O_2), metallic powders (aluminum and zinc). The addition of these agents in the geopolymer synthesis process affects the polymerization kinetics as well as the rheology of the produced paste [8-17].

In the production of lightweight geopolymers, Hydrogen peroxide has been widely used as a chemical foaming agent. In a highly alkaline environment of

*Corresponding Author Institutional Email: aldujailimohammed@gmail.com (S. A. J. Al-Sultani)

Please cite this article as: S. A. J. Al-Sultani, I. A. Disher Al-Hydary, M. A. Ahmed Al-Dujaili, Taguchi-grey Relational Analysis for Optimizing the Compressive Strength and Porosity of Metakaolin-based Geopolymer, International Journal of Engineering, Transactions B: Applications, Vol. 34, No. 11, (2021) 2525-2533

geopolymer, hydrogen peroxide decomposition can be an unlimited reaction resulting in a porous material with undesirable coarse voids [18]. The bubbles of the gas inclosed within the material extend and generate voids. The volume expansion of this material is rely on the amount of oxygen result in the following reaction [2].

$H_2O_2 \rightarrow H_2O + ½ O_2$

The high alkalinity catalyzed the hydrogen peroxide decomposition [19], and the solution of sodium silicate is known to stabilize the decomposition reaction through decreasing and slowing down the reaction [18].

Many processing factors can affect the structure and the properties of the geopolymer porous materials, such as the content and type of foam agents/stabilizer, the design of mix proportion, the quality of raw materials. Of special importance is the stabilizer which could limit the surface free energy of the bubble and increase the toughness of the bubble. This is reducing the burst and coalesce of bubble offering a great effect on the stability of pore in geopolymer porous materials [20- 22].

The stablizers (surfactants) like Tween 80, protein, and vegetable oils are classified in the hydrophilic group and have been used in the production of porous geopolymers. The vegetable oils is one of the interesting stablizers because of their low cost and availability. The reaction between highly alkaline solution of geopolymer and vegetable oils, by a saponification reaction, result in the interconnect porous structure [23, 24].

It is well known that the pores inside the material reduces the mechanical strength of the geopolymer [25, 26]. On the other hand, in the many applications were desired to have a material that combines high porosity and high mechanical strength. Such material can be used, for example, as load bearing thermal insulator, load bearing light weight material and highly porous catalyst or adsorbent that can be used under high pressure conditions. As per our review, a study that combines the optimization of both porosity and mechanical strength is not reported in the literatures.

The main target of this research is to improve both porosity and the compressive strength of metakaolin-based geopolymer. Taguchi method was adopted to design the experiments depend on the orthogonal analysis method. Based on the Taguchi-Grey relational multi-responses analysis method, the optimal mix proportion of the geopolymer was obtained.

The constraction industry through using of less polluting technology to the environment is already imminent and more had to do. Usually it can only consider single quality characteristics. While, Grey Relational Analysis (GRA) is usually employed to deal with the multi-quality characteristics [26]. This is because, GRA is a normalization evaluation technique to solve a complicated multi-performance characteristics optimization effectively [27]. It can be used with Taguchi method to solve the multi response problems. According to our review, Grey relational method is not well reported in the litearetuer to be used in the multi-responses analysis in the field of geopolymers except in the work of Prusty and Pradhan [28]. They were used Taguchi-Grey relational analysis to investigate and optimize the effect of ground granulated blast furnace slag replacement, water to geopolymer solids ratio, molarity of NaOH solution, binder content and Na_2SiO_3 to NaOH solution ratio on setting time, workability and compressive strength of fly ash-based geopolymer concrete [28]. However, it is well documented that it has been utilized to optimize many other products and processes, these includes literature [29-33].

In the current work, three common factors were selected to design the experiments including, the concentration of hydrogen peroxide, the quantity of hydrogen peroxide and the quantity of vegetable oil as stabilizer. These factors were commonly studied in the field of geopolymers and their influnce on the properties of the geopolymer are well documented in many studies [21, 24]. Furthermore, for the first time, two additional factors were studied in the current study; these are (i) the time of polymerization elapse before adding the hydrogen peroxide to the produced geopolymer paste prior to casting, (ii) the amount of yeast added to the mix which has been used to catalyze the decomposition of the hydrogen peroxide to produce pores. The first factor i.e the time of polymerization, is expected to affect the pore size, pore shape and the distribution of the pores along with geopolymer body; this is due to its effect on the viscosity of the geopolymer paste. The later factor, i.e. the amount of yeast, is chosen to have a controllable factor that affect the decomposition of hydrogen peroxide rather than the uncontrollable factors of the alkalinity and the amount of sodium silicates, which have fixed values based on the preselected composition of the geopolymer, that have been optimized in our previous work [34].

Five levels, having strongest impact on the performance of the specimens, for each of the five factors were selected in the design of the experiments based on primary rough experiments. The lower and the upper values of a given level were chosen through rejecting the values that produce a geopolymer body with: (i) very low mechanical strength, due to high porosity or large pore size or (ii) very low porosity due to low expansion upon adding the foaming agent. This information was obtained from this test is very useful in understanding how the strength of materials involved in natural application [35].

2. EXPERIMENTAL WORK

2. 1. Design of Experiments An efficient approach for the optimizing a single quality response issues is Taguchi method [36]. However, through these days, many operations were performed, manufactured products have more than one quality response of main interest [37]. Thus; traditional Taguchi method does not able to solve such multi-objective optimization problems. Taguchi method shared with Grey relational analysis to solve the more complicated multi response problems [38].

In this technique, orthogonal experimental design, adopting Taguchi method, it was used to design the experiments. GRA was used to combine the multi responses into a single effective response. Then, Taguchi method was used to analyze that the single effective response and suggest the values of the experimental parameters that are expected to achieve optimal responses.

Relay on the orthogonality, orthogonal experimental design chooses several representative points from the comprehensive experiments; these points have constant waste and similarity. The level in the orthogonal analysis refers to the specific conditions for each factor to be compared. The factors are parameters that affect the properties of product.

In the current study, the five factors and their corresponding levels are shown in Table 1. According to Taguchi method, the L_{25} ($5^{\wedge 5}$) orthogonal test scheme should be used in the experiments with the details given in Table 2.

TABLE 1. Five factors and five levels of orthogonal test design

Level \ Factor	A	B	C	D	E
1	10	0.1	0.2	0	0.1
2	20	0.2	0.4	30	0.2
3	30	0.3	0.6	60	0.3
4	40	0.4	0.8	90	0.4
5	50	0.5	1.0	120	0.5

where A: Concentration of H_2O_2%, B: Quantity of the yeast (g), C: Quantity of H_2O_2 (ml), D: Polymerization time (min) and E: Quantity of vegetable oil (ml).

TABLE 2. Orthogonal test scheme L25 ($5^{\wedge 5}$)

Experiment No.	A	B	C	D	E
1	10	0.1	0.2	0	0.1
2	10	0.2	0.4	30	0.2
3	10	0.3	0.6	60	0.3
4	10	0.4	0.8	90	0.4
5	10	0.5	1.0	120	0.5
6	20	0.1	0.4	60	0.4
7	20	0.2	0.6	90	0.5
8	20	0.3	0.8	120	0.1
9	20	0.4	1.0	0	0.2
10	20	0.5	0.2	30	0.3
11	30	0.1	0.6	120	0.2
12	30	0.2	0.8	0	0.3
13	30	0.3	1.0	30	0.4
14	30	0.4	0.2	60	0.5
15	30	0.5	0.4	90	0.1
16	40	0.1	0.8	30	0.5
17	40	0.2	1.0	60	0.1
18	40	0.3	0.2	90	0.2
19	40	0.4	0.4	120	0.3
20	40	0.5	0.6	0	0.4
21	50	0.1	1.0	90	0.3
22	50	0.2	0.2	120	0.4
23	50	0.3	0.4	0	0.5
24	50	0.4	0.6	30	0.1
25	50	0.5	0.8	60	0.2

2. 2. Materials and Methods Metakaolin can be obtained by the calcination of kaolin clay at 750°C for 3 hours in the air atmosphere via using heating rate of 5ºC/ min. The Kaolin was supplied from Dwaikhla, a local area in the western desert of Iraq. Sodium silicate ($Na_2SiO_3.5H_2O$, Thomas Barker), sodium hydroxide (NaOH, Thomas Barker), silica gel ($SiO_2.nH_2O$, Thomas Barker), hydrogen peroxide (50%-H_2O_2, Thomas Barker) were used as received without further treatment or purification. Instant yeast and sun flower vegetable oil were supplied from local market, they were used as a catalyst and stabilizing agent, respectively to synthesize the porous geopolymer.

Na_2O. Al_2O_3. $3.8SiO_2$. xH_2O formula describes the composition of the geopolymer synthesized in the current study. This formula and the processing parameters, including the amount of water of 11ml per 10.73g of metakaolin, the mixing time of 5 min and the sodium silicates to sodium hydroxide ratio of 3.02, were obtained from our previous study on the optimization of the composition and the processing parameters of geopolymer, as illustrated elsewhere with more details [34].

In this study the alkaline liquid is a solution of sodium hydroxide, sodium silicate and silica gel. Firstly, water is introduced in the beaker , then sodium hydroxide have been added to the required amount of water. Then, the silicate salt was added, while the solution was heated to 80°C and agitated at 600 rpm. After all silicates salt is disolved, silica gel was added to the solution , then stirred for one hour. Later, a desired quantity of water was added to compensate the water lost because of the vapoization, the solution was left to be cooled naturally to room temperature. The metakaolin was added to the cold solution, and mixed using a mechanical mixer at a fixed agitation rate (3550 rpm) for sufficient mixing time. After that, the alkaline solution is cooled to room temperature. Finally, the hydrogen peroxide, yeast and vegetable oil were added to the solution, after the desired polymerization time to form the geopolymer paste.

For molding the pastes of geopolymer, the molds made of PVC plastic were used. The molds were kept in the lab conditions at a temperature of 23°C± 2 for one day and then de-molded. These specimens have been cured at the room temperature for 28 days before testing. Figure 1 display the fractured surface of the samples obtained according to the pre-mentioned preparation method.

The compressive strength of the sample, having a height to diameter ratio of 2 was obtained via the compressive test, by using universal test machine. The water absorption, porosity and density of the produced samples were measured via using Archimedes method. Each measurement in this study is the average of three measurements.

2. 3. Optimization The experimentally obtained compressive strength and porosity values were transformed into a signal-to-noise (S/N) ratio. The value of S/N ratio mention the dissipation around the required results and includes, three types of performance characteristics: higher-the-better, lower-the-better and nominal-the-better. In this study, the S/N ratio of the higher-the-better was used, as it is desired to obtain a higher compressive strength and higher porosity, and calculated using Equation (1):

$$(S/N)_{ij} = -10\log\left(\frac{1}{n}\sum_{i=1}^{n}\frac{1}{y_{ij}{}^2}\right) \quad (1)$$

where; n is the number replications and yij is the experimental value of ith experiment for the jth response.

In order to spread out the data evenly, and measure it into an acceptable range for further analysis the (S/N) ratio were normalized [39] using Equation (2), to obtain

Figure 1. Porous geopolymer samples with different porosity

Zij which represents the normalized value of S/N ratio for the larger is better.

$$Z_{ij} = \frac{y_{ij}-\min(y_{ij})}{\max(y_{ij})-\min(y_{ij})}; i = 1,2,\ldots n; j = 1,2,\ldots n \quad (2)$$

According to GRA, Equation (3) was used to calculate of the deviation sequences (Δ):

$$\Delta = \left(Z_{max} - Z_{ij}\right); i = 1,2,\ldots.,m; j = 1,2,\ldots,n \quad (3)$$

where; Zmax is the maximum value of response Z_{ij}:the current value of the response

Equation (4) was used to calculate the grey relational coefficient (GRC) and Equation (5) was used to calculate the grey relational grade (GRG).

$$GRC_{ij} = \frac{\min(\Delta)+\lambda\max(\Delta)}{\Delta_{ij}+\lambda\max(\Delta)}; i = 1,2,,m; j = 1,2,,n \quad (4)$$

$$GRG_i = \sum_{j=1}^{n}\varphi_j GRC_{ij} \;\; ; i = 1,2,\ldots..,m \quad (5)$$

where: φj is the normalized non-negative coefficient assigned to the jth response with the sum of all φj is equal to 1, and Δij is the difference between the optimum value of the normalized S/N ratio, λ is the identification coefficient that ranges from 0 to 1 , the ith normalized S/N ratio value for the jth response. While, in the equation numerator, max(Δ) is means the largest optimum value of the normalized and max(Δ) is mean the smallest optimum value of the normalized. In this study all the responses (characteristics) are equally weighted.

3. RESULTS AND DISCUSSION

3. 1. Grey-based Taguchi Optimization Results For compressive strength and porosity, the average value of the experimentally obtained results are given in Table 3.

TABLE 3. Experimental results for the compressive strength and the porosity

Experiment No.	Compressive strength (MPa)	Porosity (%)
1	66.95	30.67
2	50.34	31.91
3	33.60	30.83
4	25.56	21.57
5	21.39	9.52
6	30.20	26.29
7	19.94	16.84
8	6.12	24.35
9	9.99	34.51
10	6.32	19.58
11	7.37	28.26
12	3.09	59.43

13	3.51	65.76
14	24.41	35.00
15	12.40	21.64
16	2.76	74.66
17	6.28	65.25
18	2.65	84.10
19	5.95	31.06
20	4.39	41.09
21	8.85	80.12
22	10.66	60.98
23	4.57	42.02
24	7.69	65.00
25	2.76	76.18

This raw data can be transformed into S/N ratio by using Equation (1). According to L_{25} orthogonal array the corresponding S/N ratio values for experimental parametric setting are summarized in Table 4.

The normalized values of the S/N ratio, calculated according to equation 2, are given in Table 5.

TABLE 4. Signal-to-noise (S/N) ratio values for the compressive strength and the porosity

Experiment No.	(S/N) ratio (compressive strength)	(S/N) ratio (Porosity)
1	36.52	29.73
2	34.04	30.08
3	30.53	29.78
4	28.15	26.68
5	26.60	19.58
6	29.60	28.39
7	25.99	24.53
8	15.74	27.73
9	19.99	30.76
10	16.01	25.84
11	17.35	29.02
12	9.79	35.48
13	10.91	36.36
14	27.75	30.88
15	21.87	26.71
16	8.82	37.46
17	15.96	36.29
18	8.46	38.49
19	15.49	29.84
20	12.85	32.27
21	18.94	38.07
22	20.56	35.70
23	13.19	32.47
24	17.72	36.26
25	8.82	37.64

TABLE 5. Normalized S/N ratio values for the compressive strength and the porosity

Experiment No.	Normalized S/N (Compressive strength)	Normalized S/N (Porosity)
1	1.00	0.54
2	0.91	0.56
3	0.79	0.54
4	0.70	0.38
5	0.65	0.00
6	0.75	0.47
7	0.62	0.26
8	0.26	0.43
9	0.41	0.59
10	0.27	0.33
11	0.32	0.49
12	0.05	0.84
13	0.09	0.89
14	0.69	0.59
15	0.48	0.38
16	0.01	0.94
17	0.27	0.88
18	0.00	1.00
19	0.25	0.54
20	0.16	0.67
21	0.37	0.98
22	0.43	0.85
23	0.17	0.68
24	0.33	0.88
25	0.01	0.95

The grey relation coefficients for the normalized S/N ratios, which were calculated according to Equation 4, are given in Table 6. These values are corresponding to a value of λ equal to 0.5 for the compressive strength, as well as the porosity. Next, by Equation 5, the grey relational grade could be computed. Finally, these grades were examined for optimizing the multi response parameter, design problem via Taguchi method.

The S/N ratio plot of grey relational coefficient, which combines the compressive strength and the porosity with respect to concentration of H_2O_2, quantity of the yeast, quantity of H_2O_2, polymerization time, and quantity of oil is shown in Figure 2, for a λ value of 0.5. It can be easily seen that the optimal parameter conditions are (A_5, B_1, C_1, D_3 and E_2). The subscript number indicates the level of the factor at which the optimal response could be obtained.

Similarly, the optimal multi response parameter can be obtained for the different values of λ as given in Table 7. Therefore, it can be seen that the suggested optimal conditions were similar for the some different values of λ; this indicates that Taguchi method is not sensitive for the minor changes in the values of λ. Moreover,

TABLE 6. Grey relational coefficients and grey grade values for λ values of 0.5

Experiment No.	GRC_{1j}	GRC_{i2}
1	1	0.52
2	0.85	0.53
3	0.70	0.52
4	0.63	0.44
5	0.59	0.33
6	0.67	0.48
7	0.57	0.40
8	0.40	0.47
9	0.46	0.55
10	0.41	0.43
11	0.42	0.49
12	0.34	0.76
13	0.35	0.82
14	0.62	0.55
15	0.49	0.45
16	0.34	0.90
17	0.41	0.81
18	0.33	1.00
19	0.40	0.52
20	0.37	0.60
21	0.44	0.96
22	0.47	0.77
23	0.38	0.61
24	0.43	0.81
25	0.34	0.92

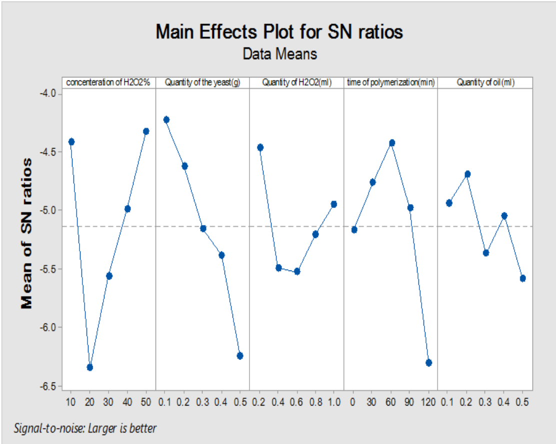

Figure 2. Effect of process parameters on the grey relational coefficient of geopolymer for λ value of 0.5

TABLE 7. Optimal parameter levels for different values of λ for compressive strength and porosity

λ Compressive strength	λ Porosity	A	B	C	D	E
0.1	0.9	10	0.1	0.2	0	0.1
0.2	0.8	10	0.1	0.2	60	0.1
0.3	0.7	10	0.1	0.2	60	0.1
0.4	0.6	10	0.1	0.2	60	0.2
0.5	0.5	50	0.1	0.2	60	0.2
0.6	0.4	50	0.1	0.2	60	0.2
0.7	0.3	50	0.1	0.2	60	0.2
0.8	0.2	50	0.1	0.2	90	0.2
0.9	0.1	50	0.1	0.2	90	0.2

according to the analysis of variance was found that the factor E, corresponding to the quantity of vegetable oil has a lowest rank among the studied factors. Keeping these in mind, one can reduce the number of the suggested optimal conditions to four experiments only, with the S/N ratio plot of grey relational coefficient given in Figure 3, as optimal parameter is given in Table 8.

These conditions were verified experimentally in the confirmation experiments. It is important to note that all the suggested optimal conditions have common low values of the factors B and C corresponding to the quantity of yeast and hydrogen peroxide, respectively. This indicates that these low values are necessary to achieve the optimal results regardless the values of the other parameters.

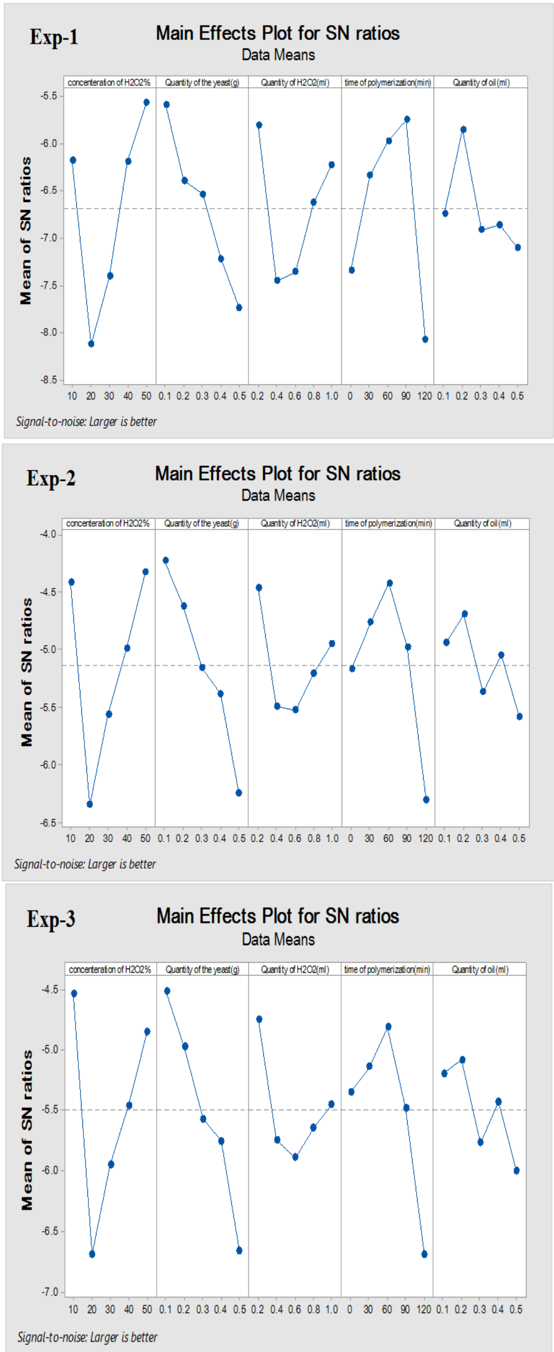

Figure 3. influence of process parameters on compressive strength and porosity of geopolymer for different values of λ

TABLE 8. Suggested optimal conditions for combined optimal compressive strength and porosity

Experiment Code	A	B	C	D	E
Exp-1	50	0.1	0.2	90	0.2
Exp-2	50	0.1	0.2	60	0.2
Exp-3	10	0.1	0.2	60	0.2
Exp-4	10	0.1	0.2	0	0.1

3. 2. Confirmation Experiments

Emphasization experiments were carried out to the validate that the suggested optimal circumstances, can enhance of the compressive strength and porosity for the geopolymer. The experimental results to the four emphasization experiments performed at the optimal settings of process parameters. They have exposured that the responses can be enhanced effectually via suggested optimal circumstances as given in Table 9. It could be observed that the obtained values for the compressive strength and porosity from the confirmation tests, especially for Exp-3, combined high values of compressive strength, as well as porosity. These values are superior as compared with that obtained in Table 3 of the current study, also, they are superior to that reported for the metakaolin-based geopolymer in the literatures [2, 21, 23, 40, 41] as summarized in Table 10.

TABLE 9. Compressive strength and porosity obtained for the confirmation experiments

Experiment	Compressive strength (MPa)	Porosity (%)
Exp-1	15.66	26.30
Exp-2	11.42	38.90
Exp-3	88.30	22.00
Exp-4	66.95	30.67

TABLE 10. Compressive strength and porosity reported in many literature for the metakaolin-based geopolymer

Reference	Compressive Strength (Mpa)	Porosity (%)
[2]	0.26 - 5.9	28 - 83
[21]	0.3 - 11.6	66 - 83
[23]	3.64 - 7.60	62.5
[20]	1.45	82
[24]	0.35 - 56.5	50 - 86

4. CONCLUSIONS

The goal of the present work was to optimize both compressive strength and the porosity of geopolymer using Taguchi method, with the help of Grey relational analysis. It was found that this route of the optimization is suitable to fulfill the aim. However, the analysis showed that Taguchi method is not sensitive toward the minor changes in the identification coefficient λ of the grey relation alanalysis. Nevertheless, the experimental results showed that high porosity and adequate compressive strength can be obtained at the same geopolymer body by choosing the suitable values of the processing parameters. Moreover, it was found that the use of yeast as a catalyst and the polymerization time are important processing parameters. Also, it was noticed that the amount of the vegetable oil, which is used as a stabilizer, should be kept in low values to obtain the optimal compressive strength and porosity.

5. FUTUR WORK

According to the obtained results from the current study, the study proposes the following future works: 1) Studying the influence of utilizing higher potassium communicate on the characterisations of the geopolymer. 2) Studying the influence of dissimilar parameters on the improvement of compressive strength on the characterisations of fly ash based geopolymer higher potassium contact.

6. REFERENCES

1. L. A. Alves, A. Nogueira, E. Vazquez, and S. de Barros, "A bibliographic historical analysis on geopolymer as a substitute for portland cement," ***Key Engineering Materials***, Vol. 834, (2020), 127-131, doi.org/10.4028/www.scientific.net/KEM.834.127
2. S. Petlitckaia and A. Poulesquen, "Design of lightweight metakaolin based geopolymer foamed with hydrogen peroxide," *Ceramics International*, Vol. 45, No. 1, (2019), 1322-1330, doi.org/10.1016/j.ceramint.2018.10.021
3. V. Ducman and L. Korat, "Characterization of geopolymer fly-ash based foams obtained with the addition of Al powder or H_2O_2 as foaming agents," ***Materials Characterization***, Vol. 113, (2016), 207-213, doi.org/10.1016/j.matchar.2016.01.019
4. R. B. E. Boum et al., "Thermal behaviour of metakaolin-bauxite blends geopolymer: microstructure and mechanical properties," ***SN Applied Sciences***, Vol. 2, No. 8, (2020), 1-12, doi.org/10.1007/s42452-020-3138-9
5. Bobirică, C., Orbeci, C., Bobirică, L., Palade, P., Deleanu, C., Pantilimon, C.M., Pîrvu, C. and Radu, I.C.,, "Influence of red mud and waste glass on the microstructure, strength, and leaching behavior of bottom ash-based geopolymer composites," ***Scientific Reports***, Vol. 10, No. 1, (2020), 1-12, doi.org/10.1038/s41598-020-76818-4
6. L. N. Assi, K. Carter, E. Deaver, and P. Ziehl, "Review of availability of source materials for geopolymer/sustainable concrete," ***Journal of Cleaner Production***, Vol. 263, (2020), 121477, doi.org/10.1016/j.jclepro.2020.121477
7. K. Yan, Y. Guo, Z. Ma, Z. Zhao, and F. Cheng, "Quantitative analysis of crystalline and amorphous phases in pulverized coal fly ash based on the Rietveld method," ***Journal of Non-Crystalline Solids***, Vol. 483, No. 1, (2018), 37-42, doi.org/10.1016/j.jnoncrysol.2017.12.043
8. R. M. Novais, G. Ascensão, L. H. Buruberri, L. Senff, and J. A. Labrincha, "Influence of blowing agent on the fresh- and hardened-state properties of lightweight geopolymers," ***Materials & Design,*** Vol. 108, (2016), 551-559, doi.org/10.1016/j.matdes.2016.07.039
9. A. N. Khattak, M. A. M. Khraisheh, and S. Gul, "Porosity control of self-supported geopolymeric membrane through hydrogen peroxide and starch additives Porosity control of self-supported geopolymeric membrane through hydrogen peroxide and starch additives," ***Desalination and Water Treatment,*** Vol. 152, (2019), 10-15, DOI: 10.5004/dwt.2019.23895
10. N. Lertcumfu, K. Kaewapai, P. Jaita, R. Sanjoom, G. Rujijanagul, and T. Tunkasiri, "Synergistic effect of animal oil or butter and hydrogen peroxide on physical and mechanical properties of porous alumino-siliceous materials," ***ScienceAsia***, Vol. 46 S, No. 1, (2020), 58-65, doi:10.2306/scienceasia1513-1874.2020.S008
11. N. B. Singh, "Fly ash-based geopolymer binder: A future construction material," ***Minerals***, Vol. 8, No. 7, (2018), doi.org/10.3390/min8070299
12. F. Rizal, A. P. Pratama, Khamistan, A. Fauzi, Syarwan, and A. Azka, "Effect of H_2O_2 as the Foaming Agent on the Geopolymer Mortar using Curing of Room Temperature," IOP Conference Series: Materials Science and Engineering, Vol. 854, No. 1, (2020), DOI: 10.1088/1757-899X/854/1/012022
13. N. A. Jaya, L. Yun-Ming, H. Cheng-Yong, M. M. A. B. Abdullah, and K. Hussin, "Correlation between pore structure, compressive strength and thermal conductivity of porous metakaolin geopolymer," ***Construction and Building Materials,*** Vol. 247, (2020), p. 118641, doi.org/10.1016/j.conbuildmat.2020.118641
14. Qin Shuai, Zhonghui Xu, Zhengzhen Yao, Xiaoyue Chen, Zao Jiang, Xi Peng, Ran An, Yu Li, Xin Jiang and Han Li "Fire resistance of phosphoric acid-based Geopolymer foams fabricated from Metakaolin and hydrogen peroxide," ***Materials Letters,*** Vol. 263, (2020), 1-4, doi.org/10.1016/j.matlet.2019.127228
15. U. Anggarini, S. Pratapa, V. Purnomo, and N. C. Sukmana, "A comparative study of the utilization of synthetic foaming agent and aluminum powder as pore-forming agents in lightweight geopolymer synthesis," ***Journal of Open Chemistry,*** Vol. 17, No. 1, (2019), 629-638, DOI:10.1515/chem-2019-0073
16. S. Yan, F. Zhang, X. Feng, J. Kong, B. Wang, and J. Yang, "Effect of high temperature on the mechanical properties of hierarchical porous cenosphere/geopolymer composite foams," Journal of Applied Ceramic Technology, Vol. 18, No. 3, (2021), 817-829, doi.org/10.1111/ijac.13681
17. E. Kränzlein, H. Pöllmann, and W. Krcmar, "Metal powders as foaming agents in fly ash based geopolymer synthesis and their impact on the structure depending on the Na /Al ratio," ***Cement and Concrete Composites***, Vol. 90, (2018), 161-168,
18. A. Hajimohammadi, T. Ngo, P. Mendis, T. Nguyen, A. Kashani, and J. S. J. van Deventer, "Pore characteristics in one-part mix geopolymers foamed by H_2O_2: The impact of mix design," ***Materials & Design,*** Vol. 130, No. 15, (2017), 381-391, doi.org/10.1016/j.matdes.2017.05.084
19. Pantongsuk, T., Kittisayarm, P., Muenglue, N., Benjawan, S., Thavorniti, P., Tippayasam, C., Nilpairach, S., Heness, G. and Chaysuwan, D., "Effect of hydrogen peroxide and bagasse ash additions on thermal conductivity and thermal resistance of geopolymer foams," ***Materials Today Communication***, Vol. 26, (2021), p. 102149, doi.org/10.1016/j.mtcomm.2021.102149
20. Y. Cui, D. Wang, J. Zhao, D. Li, S. Ng, and Y. Rui, "Effect of calcium stearate based foam stabilizer on pore characteristics and thermal conductivity of geopolymer foam material," ***Journal of Building Engineering***, Vol. 20, (2018), 21-29, doi.org/10.1016/j.jobe.2018.06.002
21. C. Bai, T. Ni, Q. Wang, H. Li, and P. Colombo, "Porosity, mechanical and insulating properties of geopolymer foams using vegetable oil as the stabilizing agent," ***Journal of the European Ceramic Society***, Vol. 38, No. 2, (2018), 799-805, doi.org/10.1016/j.jeurceramsoc.2017.09.021
22. C. Bai and P. Colombo, "High-porosity geopolymer membrane supports by peroxide route with the addition of egg white as surfactant," ***Ceramics International***, Vol. 43, No. 2, (2017), 2267-2273, doi.org/10.1016/j.ceramint.2016.10.205
23. N. Lertcumfu, K. Kaewapai, P. Jaita, T. Tunkasiri, S. Sirisoonthorn, and G. Rujijanagul, "Effects of olive oil on physical and mechanical properties of ceramic waste-based geopolymer foam," Journal of Reinforced Plastics and

Composites, Vol. 39, No. 3-4, (2020), 111-118, doi.org/10.1177/0731684419896852

24. Qiao, Y., Li, X., Bai, C., Li, H., Yan, J., Wang, Y., Wang, X., Zhang, X., Zheng, T. and Colombo, P., "Effects of surfactants/stabilizing agents on the microstructure and properties of porous geopolymers by direct foaming," ***Journal of Asian Ceramic Societies,*** Vol. 9, No. 1, (2021), 412-423, doi.org/10.1080/21870764.2021.1873482
25. E. D. Van Rest and D. J. Cowden, "Statistical Methods in Quality Control.," ***Applied Statistics.***, Vol. 7, No. 3, (1958), p. 202, doi.org/10.1177/0008068319570306
26. M. A. A. Al-Dujaili, I. A. D. Al-Hydary, and Z. Z. Hassan, "Optimizing the Properties of Metakaolin-based (Na, K)-Geopolymer Using Taguchi Design Method," ***International Journal of Engineering, Transactions A: Basics,*** Vol. 33, No. 4, (2020), 631-638, Doi:10.5829/IJE.2020.33.04A.14
27. E. Arıcı, E. Çelik, and O. Keleştemur, "An analysis of the engineering properties of mortars containing corn cob ash and polypropylene fiber using the Taguchi and Taguchi-based Grey Relational Analysis methods," ***Case Studies in Construction Materials***, Vol. 15, (2021), e00652. doi.org/10.1016/j.cscm.2021.e00652
28. J. K. Prusty and B. Pradhan, "Multi-response optimization using Taguchi-Grey relational analysis for composition of fly ash-ground granulated blast furnace slag based geopolymer concrete," ***Construction and Building Materials***, Vol. 241, (2020), p. 118049, doi.org/10.1016/j.conbuildmat.2020.118049.
29. H. M. Hsu, A. Cheng, S. J. Chao, J. R. Chang, L. W. Teng, and S. C. Chen, "The grey relational analysis of quality investigation of concrete containing solar PV cells," 4th International Conference on Engineering and Innovative Materials (ICEIM 2015), Section: Materials Science and Engineering, Vol. 27, No. MATEC Web of Conferences, Article No. 01006, 1-4, (2015). doi.org/10.1051/matecconf/20152701006
30. O. Keleştemur and E. Arıcı, "Analysis of some engineering properties of mortars containing steel scale using Taguchi based grey method," ***Journal of Building Engineering,*** Vol. 29, p. 101015, 2020. https://doi.org/10.1016/j.jobe.2019.101015
31. S. C. Yaragal, B. C. Kumar, and K. Mate, "Optimization of ferrochrome slag as coarse aggregate in concretes," ***Computers and Concrete,*** Vol. 23, No. 6, (2019), 421-431, DOI: http://dx.doi.org/10.12989/cac.2019.23.6.421
32. S. Zhang, W. Qiao, Y. Wu, Z. Fan, and L. Zhang, "Multi-Response Optimization of Ultrafine Cement-Based Slurry Using the Taguchi-Grey Relational Analysis Method," Materials, MDPI, Vol. 14, No. 1, (2021), 1-23, **doi.org/10.3390/ma14010117**
33. M. T. Çöğürcü and M. Uzun, "The Taguchi optimization of mechanical and durability properties of accelerator added concrete," ***Journal of Polytechnic,*** Vol. 0900, 0-2, 2021. DOI: 10.2339/politeknik.857525
34. Z. Z. H. M. A. Ahmed Al-dujaili, I. A. Disher Al-hydary, "Experimental Improvment of Geopolymer-Cement Properties Using Taguchi Method," University of Babylon, 2019.
35. M. R. Marakia , H. Tagimalek, M. Azargomanb, H. Khatamic , M. Mahmoodib . Experimental Investigation and Statistical Modeling of the Effective Parameters in Charpy Impact Test on AZ31 Magnesium Alloy with V-shape Groove Using Taguchi Method, ***International Journal of Engineering, Transactions C: Aspetcs***, Vol. 33, No. 12, (2020), 2521-2529, DOI: 10.5829/ije.2020.33.12c.13
36. A. Khezrloo, M. Tayebi, A. Shafiee, and A. Aghaie, "Evaluation of compressive and split tensile strength of slag based aluminosilicate geopolymer reinforced by waste polymeric materials using Taguchi method," ***Materials Research Express***, Vol. 8, No. 2, (2021), DIO: 10.1088/2053-1591/abe101/meta
37. M. I. Qazi, M. Abas, R. Khan, W. Saleem, C. I. Pruncu, and M. Omair, "Experimental investigation and multi-response optimization of machinability of AA5005H34 using composite desirability coupled with PCA," ***Metals (Basel)***, Vol. 11, No. 2, (2021), 1-24, doi.org/10.3390/met11020235
38. J. B. Saedon, N. Jaafar, and M. Azman, "Multi-objective optimization of titanium alloy through orthogonal array and grey relational analysis in WEDM," ***Procedia Technology***, Vol. 15, (2014), 832-840, DOI: 10.1016/j.protcy.2014.09.057
39. V. Rajput, S. S. Pundir, M. Goud, and N. M. Suri, "Multi-Response Optimization of ECDM Parameters for Silica (Quartz) Using Grey Relational Analysis," Silicon, Vol. 13, No. 5, (2021), 1619-1640, doi.org/10.1007/s12633-020-00538-7
40. M. Sayed, R. A. Gado, S. M. Naga, P. Colombo, and H. Elsayed, "Influence of the thermal treatment on the characteristics of porous geopolymers as potential biomaterials," M***aterials Science and Engineering: C***, Vol. 116, (2020), 111171. doi.org/10.1016/j.msec.2020.111171
41. H. Cheng-Yong, L. Yun-Ming, M. M. A. B. Abdullah, and K. Hussin, "Thermal Resistance Variations of Fly Ash Geopolymers: Foaming Responses," ***Scientific Report***, Vol. 7, (2017), 1-11, DOI: 10.1038/srep45355

Persian Abstract

چکیده

ژئوپلیمر یک ماده سازگار با محیط زیست است که می تواند با پارامترهای پردازش با انواع خواص فیزیکی و مکانیکی تولید شود. به دست آوردن ژئوپلیمر با مقاومت فشاری بالا و تخلخل زیاد ممکن است این ماده را برای بسیاری از کاربردهای حرارتی و فیزیکوشیمیایی به عنوان کاندیدای مطلوب تبدیل کند. هدف این تحقیق شناسایی مجموعه ای از پارامترهای پردازشی است که مانند این مواد ژئوپلیمر تولید می کند. روش تاگوچی همراه با تحلیل رابطه خاکستری برای حل این مشکل چند پاسخ استفاده شده است. تجزیه و تحلیل و نتایج تجربی نشان داد که می توان با استفاده از مقدار کم پراکسید هیدروژن به عنوان عامل کف کننده ، مقدار کم مخمر به عنوان کاتالیزور و مقدار کم روغن نباتی به عنوان تثبیت کننده به این هدف دست یافت. علاوه بر این ، زمان پلیمریزاسیون قبل از افزودن عامل کف کننده به عنوان یک پارامتر مهم پردازش سپری می شود. همچنین ، نتایج تجربی نشان داد که با انتخاب مقادیر مناسب پارامترهای پردازش ، می توان تخلخل بالا و مقاومت فشاری کافی را در یک جسم ژئوپلیمری یکسان بدست آورد. علاوه بر این ، مشخص شده است که استفاده از مخمر به عنوان کاتالیزور و زمان پلیمریزاسیون پارامترهای مهم پردازش است. همچنین ، توجه شده است که مقدار روغن نباتی ، که به عنوان تثبیت کننده استفاده می شود ، باید در مقادیر کم نگه داشته شود تا مقاومت فشاری و تخلخل مطلوب به دست آید.

IJE TRANSACTIONS B: Applications Vol. 34, No. 11, (November 2021) 2534-2544

International Journal of Engineering

Journal Homepage: www.ije.ir

A New Wide Tunability MEMS Based Variable Capacitor using Two Separate Electro-static Vertical Comb Drive Actuators

M. Ghalandarzadeh, S. Afrang*

Electrical Engineering Department, Faculty of Engineering, Urmia University, Urmia, Iran

PAPER INFO

Paper history:
Received 06 September 2020
Received in revised form 23 September 2021
Accepted 01 October 2021

Keywords:
MEMS
Variable Capacitors
Tunability
Electrostatic
Vertical Comb Drives
Pull-in

ABSTRACT

This paper presents a new MEMS variable capacitor to achieve high stable region and extremely wide tunability. The idea is based on increasing the stable region in the gap between the plates of the capacitor. It is done by combining the functionality of two different vertical comb drive actuator sets to takeover a unity air gap variation. The design of the structure is carried out so that the performance of these two actuator sets is fully independent without any destructive or damaging effect on each other. The advantage of this scheme is that adding the second mechanism of actuation does not change the overall structure thickness compared with when the structure uses a single actuation mechanism. Therefore, the tunability increases sharply. Aluminum is the structural material used for the design. Comb actuators are widely used as MEMS motors due to their long range of linear motion, low power consumption and ease of fabrication. A full review of electrostatic actuator portion is done. The structure is calculated using MATLAB software. To verify, the calculated results were compared with simulated results using Intellisuite software. The natural frequency is 1.173 KHz. According to calculation and simulation results the achieved minimum tuning range is 2300%.

***Doi**: 10.5829/ije.2021.34.11b.16*

1. INTRODUCTION

MEMS-based variable capacitors are used as key building blocks in many wireless communication applications, such as tunable filters, voltage-control oscillators, matching networks and phase shifters [1-4]. Commercially available solid-state varactors such as p-n junction diodes and Schottky diodes offer wide tuning range, small size and very fast tuning speed [5]. However, they suffer from low power handling, low Q-factor and non-linearity effect.

Compared to semiconductor varactors, MEMS variable capacitors have the potential for an extended tuning range, higher linearity and high quality factor [6-12], along with the reduction in weight, size, and cost of communication systems. According to working principle, the popular actuators for MEMS variable capacitors can be mainly classified into three categories, which include electrothermal, piezo-electric, and electrostatic actuators. Thermally and piezoelectrically actuated devices provide great motion control. Very linear variable capacitors can be obtained this way, and a few have been reported [13-16]. However, some of the major concerns are the hysteresis in actuation motion, power consumption, and response time. On the other hand, electrostatic actuation remains an attractive method for actuation the tuning capacitors due to virtually nonexistent current loss, high energy density, low power consumption and high-quality factors and large force that can be generated on the microscale [17, 18].

Micromachined variable capacitors generally fall in two categories those that vary the area and those that vary gap [17, 19]. Often, gap-tuning capacitors are constructed from two surface-micromachined electrostatically actuated parallel plates, one being movable and controlled by an applied voltage and the other being fixed [20-23]. The main problem in the electrostatic type variable capacitor is the pull in instability. This

*Corresponding Author Institutional Email: s.afrang@urmia.ac.ir (S. Afrang)

Please cite this article as: M. Ghalandarzadeh, S. Afrang, A New Wide Tunability MEMS Based Variable Capacitor using Two Separate Electro-static Vertical Comb Drive Actuators, International Journal of Engineering, Transactions B: Applications, Vol. 34, No. 11, (2021), 2534-2544

phenomenon limits the range of tuning [24-29]. The movable plate can only be actuated one third of the initial gap distance; beyond this value, the two plates will snap together. This phenomena can be explained by the mechanical instability between electrostatic forces and restoring forces of the varactor structure, which causes the upper plate to snap down when it reaches one-third of the air gap [2, 13]. In this case, the maximum theoretical tuning ratio is only 1.5:1. Although, techniques that increase the tuning range have been reported, they often do not have tuning ratios large enough for many RF applications, and furthermore, have increased process complexity. Recently, several approaches have been reported to enhance the tuning range of variable capacitors. The approaches involve either parallel plate capacitors and actuators [30-34] or interdigitate capacitors with comb drive actuation mechanisms [10, 35]. The parallel-plate capacitor with electro-static actuation that is preferable due to its high self-resonance, high quality factor, low power consumption and the interdigitated capacitors that have a linear respose, but exhibit a low selfresonance and low quality factor.

Comb drive structures can be widely used in electrostatically actuated MEMS devices. In this paper, we present a surface-micromachined variable capacitor that employs two sets of comb drive actuators to vertically displace parallel plate capacitors. The main aim of this article is to introduce a new structure to achieve variable capacitor with large tuning range using electrostatic actuators. In the comb drive electrostatic actuators, the pull in instability occurs later than conventional parallel plate electrostatic actuators [36]. A particular type of a comb drives are made vertically and are known as vertically comb drives. As mentioned, we lose nearly half of the air gap because of the phenomenon of pull-in.

We have proposed a new structure to overcome this problem, and achieve very large tuning range. Based on the proposed structure, we have introduced two steps of displacement. At the first step or phase I, half of the desired displacement is done by the first group of vertical comb drive actuators. this step will stop when it comes to pull in instability point. Then at the second step or phase II and for the first time, the other half of the desired displacement becomes realized by the second group of vertical comb drive actuators. In fact, using the second group of comb drives, the first pull-in point is eradicated and we were able to capture the entire air gap to obtain maximum tuning range. Therefore, the tuning range of the variable capacitor is sharply increased.

2. DEVICE STRUCTURE

The schematic diagram of the proposed structure is shown in Figures 1 (Top view) and 2 (Button view).

The structure consists of two sets of movable and fix comb drives (the outer side), four sets of movable and fix comb drives (the inner side), four fixed-guided end beams as springs (the outer side), four fixed-guided end beams as springs (the inner side), two stoppers, frame, four anchors and two parallel plates as_the desired capacitor.

The anchors are 4 in number and in the corners of the structure. The upper part of the structure, including the frame, outer springs, inner springs, outer comb drives, inner comb drives and up capacitor plate are all held in a suspended state on these anchors at a certain distance from the bottom structure. The anchors are connected from the bottom to the substrate and from the top to the external springs.

The lower plate of the capacitor is fixed to the substrate and upper plate is suspended by inner fixed-guided end beams. The plates are precisely opposite each other and at a distance as a gap (g) from each other.

The movable plate together with fixed plate makes the proposed variable capacitor. The frame is the interface between the outer and the inner springs. Outer springs from the side of guided-end and the inner springs are attached to the fix frame.

As shown in Figure 3, the outer movable combs are connected to the bottom of the frame and they move

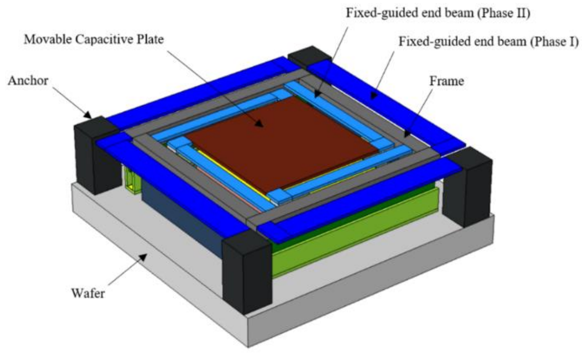

Figure 1. The schematic of the proposed variable capacitor (Top view)

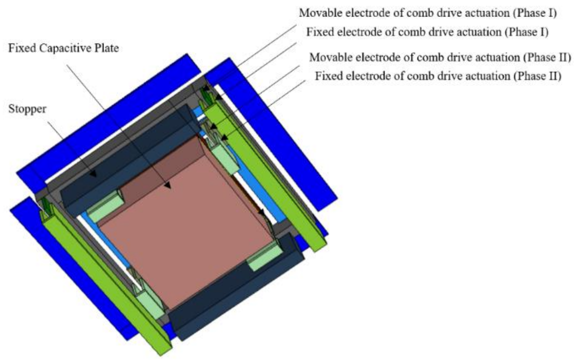

Figure 2. The schematic of the proposed variable capacitor (Button view)

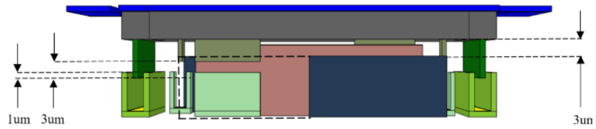

Figure 3. Location of inner and outer comb drive actuators

downward by the external springs, whereas, the inner movable combs are placed under the guided-end side of the inner springs and moved downward by the inner springs. The two stoppers are located at the bottom of the other sides of the frame.

The proposed variable capacitor has a wide range of capacitive variation. In order to realize this, two separate electrostatic actuation mechanisms are used.

In phase I, by applying voltage to the external comb actuators, the frame together with inner spring and upper capacitor plate is moved downward by the outer springs. After $\frac{g}{2}$ displacement, the frame stop by the stoppers. At this moment, the first displacement mechanism ends. If we assume that the air gap between the front end of external comb drives is g in the initial state, then at the end of phase I this distance has reached $\frac{g}{2}$.

In general, when the actuation voltage is applied to the comb drives, the electrostatic force generated in the comb drives moves the upper plate downward. This generated electrostatic force is more linear than the conventional electrostatic force, produced by the parallel-plate actuator. Moreover, this technique postpones the pull-in behavior compared to conventional parallel plate capacitors. Therefore, allows the movable plate to continue moving down linearly and consequently increase the tunability range of the variable capacitor. In the pull in point the equivalent stiffness of the structure becomes zero and leads the system to an unstable condition by undergoing to a saddle node bifurcation. In the proposed structure, by placing objects under the frame and thus stopping the displacement mechanism, we prevent the structure from entering this critical process.

In phase II, by applying voltage to the inner comb actuators, the upper capacitor plate continues moving downward by the inner springs.

In this case, when the inner comb drives are reached the critical point of the inner comb drive pull-in, at the same time the top capacitance plate will also travel the desired air gap (g/2) and touches the dielectric layer on the button capacitive plate. It is the maximum displacement rate of the top capacitive plate in phase II.

3. DESIGN

The aim of this research is to introduce two separate sets of electrostatic comb drives as vertical actuators to create variable capacitor with maximum tuning range. Figure 4 shows the total comb drive shape. As shown in this figure, when the voltage is applied, the movable comb will be displaced in the Z direction due to the fringing fields created in the comb. The capacitance between electrically conductive combs is expressed as:

$$c_{comb-drive} = N\varepsilon_0 l(z+b_0)\left(\frac{1}{g-y}+\frac{1}{g+y}\right) \quad (1)$$

For equal distance between the plates the capacitance is expressed as:

$$c_{comb-drive} = N\varepsilon_0 l(z+b_0)\left(\frac{2}{g}\right) \quad (2)$$

In Equation (2), 'N' indicates the number of combs, 'l' refers to the comb-length, 'b_0' is the initial overlap, 'g' is the adjacent gap size, 'z' is the vertical displacement amplitude along the z axis and 'y' represents the transversal displacement along the y axis. The energy stored in the capacitor is:

$$u_c = \frac{1}{2}C_{comb-drive}(z)V^2 \quad (3)$$

On the other hand, the electrostatic force applied to the comb drive is found by considering the power delivered to a time dependent capacitance and is given in the literature [37-39]:

$$f_z = \frac{d(w=u_c)}{dz} \quad (4)$$

By substitution:

$$F_{z1} = F_f = \frac{d\left(\frac{1}{2}C_{comb-drive}(z)V^2\right)}{dz} = \frac{1}{2}V^2\frac{dC_{comb-drive}(z)}{dz} = \frac{1}{2}V^2\frac{d\left[N\varepsilon_0 l(z+b_0)\left(\frac{2}{g}\right)\right]}{dz} = \frac{1}{2}V^2\left(\frac{2}{g}N\varepsilon_0 l\right) = \frac{N\varepsilon_0 l}{g}V^2 \quad (5)$$

The movable electrode on ground potential will be displaced in the z direction due to the fringe fields created in the comb. There is another capacitor which consists of the capacitor plate formed by the front end of the movable fingers and of the parallel part of the fixed electrode in front of it. This capacitance is expressed as:

$$C_{parallel-plate}(z) = 2N\varepsilon_0\frac{A}{(d-z)} \quad (6)$$

where 'A', 'N' and 'd' are the electrostatic area, number of fingers, and initial distance of the front ends of the

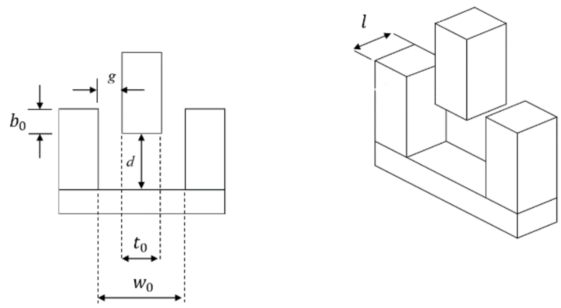

Figure 4. Schematic of comb drive structure

fingers if no actuation occurs and 'z' refers to the displacement in the z direction, respectively. The capacitor named by parallel plate capacitor does not have same electrodes. If we consider the electrostatic area of the front end of the movable fingers by $A_1 = l \times t_0$, and the parallel part area of the fixed electrode in front of movable electrode by $A_2 = l \times w_0$, then the capacitance is expressed as:

$$C_{parallel-plate}(z) = 4N\varepsilon_0 \frac{A_1 A_2}{(d-z)(A_1+A_2)} \tag{7}$$

The corresponding parallel plate electrostatic force is given by:

$$F_{z2} = F_p = \frac{1}{2}\frac{dC_{parallel-plate}(z)}{dz}V^2 = \frac{1}{2}\frac{d}{dz}[2N\varepsilon_0 l \frac{A}{(d-z)}]V^2 = \frac{1}{2}2N\varepsilon_0 lA \frac{d}{dz}\left[\frac{1}{(d-z)}\right]V^2 = \frac{N\varepsilon_0 lA}{(d-z)^2}V^2 \tag{8}$$

For an actuator in equilibrium, two types of electrostatic forces can be considered. The total electrostatic force in the comb drive is expressed as:

$$F_e = F_z = F_{z1} + F_{z2} = F_f + F_p = \frac{N\varepsilon_0 l}{g}V^2 + \frac{N\varepsilon_0 lA}{(d-z)^2}V^2 \tag{9}$$

If the movable electrode is displaced, following the Hooke's law, the reaction force F_s, is generated:

$$F_s = k_z(d-z) \tag{10}$$

In this equation 'k_z' refers to equivalent spring constant in the 'z' direction. The springs used for both phases of proposed structure are of fixed-guided end type (Figure 5). Corresponding equation of this spring constant that is due to four fixed-guided end beams is given by Rebeiz [40]:

$$k_z = 4\frac{Ewt^3}{l^3} \tag{11}$$

where, 'w', 't' and 'l' are width, thickness and length of the beams, respectively. In this equation 'k_z' refers to equivalent spring constant in the 'z' direction. Now, for the set of outer springs, we 're going to have k_{z1}.

$$k_{z1} = 4\frac{Ew_1 {t_1}^3}{{l_1}^3} \tag{12}$$

where, 'w_1', 't_1' and 'l_1' are width, thickness and length of the beams, respectively. In this equation 'k_{z1}' refers to equivalent spring constant in the 'z' direction; the spring constant is due to four outer fixed-guided end beams. These beams connect frame to anchors. And for the set of inner springs, k_{z2}.

$$k_{z2} = 4\frac{Ew_2 {t_2}^3}{{l_2}^3} \tag{13}$$

where, 'w_2', 't_2' and 'l_2' are width, thickness and length of the beams, respectively. In this equation 'k_{z2}' refers to equivalent spring constant in the 'z' direction; the spring constant is due to four inner fixed-guided end beams. These beams connect top capacitance plate to frame. We will now apply the final Equations (9) and (10) in the presented plan.

As mentioned in the description of the structure in the previous section, the proposed variable capacitor is designed to have two separate phases of motion and and we also need to remember that the movement in each phase will be made by the specific comb drive actutors of that phase.

So, we can name the total electrostatic force in the outer combs (phase I) drive with F_{e1}:

$$F_{e1} = F_{f1} + F_{p1} = \frac{N\varepsilon_0 l_1}{g}{V_1}^2 + \frac{N\varepsilon_0 l_1 A_1}{(d-z)^2}{V_1}^2 \tag{14}$$

and subsequent, the reaction force with F_{s1}:

$$F_{s1} = k_{z1}(d-z) \tag{15}$$

Also these forces are F_{e2}:

$$F_{e2} = F_{f2} + F_{p2} = \frac{N\varepsilon_0 l_2}{g}{V_2}^2 + \frac{N\varepsilon_0 l_2 A_2}{(d-z)^2}{V_2}^2 \tag{16}$$

and F_{s2}:

$$F_{s2} = k_{z2}(d-z) \tag{17}$$

for the inner combs (phase II), respectively.

In equilibrium and by equating the applied electrostatic force (9) with the mechanical restoring force (10) the actuation voltage is achieved.

$$V = \sqrt{\frac{K_Z(d-z)}{\frac{N\varepsilon_0 h}{g} + 2N\varepsilon_0 \frac{A_1 A_2}{(d-z)^2(A_1+A_2)}}} \tag{18}$$

Large tuning ratio together with low actuation voltage are the main goals of the proposed structure. The main parameter in determining the initial capacitance is its air-gap. Large tuning ratio requires large air-gap. For this reason 6μm air-gap is considered. On the other hand, low actuation voltage requires low spring constant together with small air-gap between the comb plates, long comb length and large area by considering Equation (18). Geometrical parameters in Table 1 satisfy our mentioned goals. Based on the parameters in Table 1 the outer and inner spring constant and by considering the equations 11, 12 and 13 are 0.11 and 0.72 N/m, respectively. The corresponding voltages due to these spring constants are 4 and 11V, respectively. To verify, the calculated results are again calculated using MATLAB software, and then simulated using Intellisuite software in the next section.

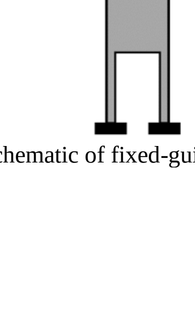

Figure 5. Schematic of fixed-guided end beam

4. CALCULATION AND SIMULATION RESULTS

As discussed in the previous section, the moving of the top capacitor plate to the bottom plate is done in two phases, phases I and II. For both phases, the calculated results for the proposed structure are again calculated using MATLAB software. Then, to validate the structure is simulated using Intellisuite software.

Materials and geometrical parameters of the structure is indicated in Table 1.

TABLE 1. Materials and geometrical parameters

Parameters	Value
Young's modulus (Al)	74 GPa
Yield strength (Al)	310 MPa
Variable capacitor area	280um×280um
Movable capacitor plate thickness	2 um
Initial air gap of variable capacitor	6 um
Length of stopper	392 um
Width of stopper	40 um
Thickness of stopper	10 um
External dimension of frame	436um×436um
Width of frame	40um
Thickness of frame	6um
Parameters of Phase I	**Value**
Length of fixed-guided end beams	480 um
Width of fixed-guided end beams	40 um
Thickness of fixed-guided end beams	1 um
Length of combs	480 um
Width of combs	3 um
Thickness of combs	7 um
Number of Movable Combs	8
Initial distance of the front ends of the fingers	6 um
Lateral air gap between fingers	1 um
Parameters of Phase II	**Value**
Length of fixed-guided end beams	340 um
Width of fixed-guided end beams	43 um
Thickness of fixed-guided end beams	1 um
Length of combs	80 um
Width of combs	3 um
Thickness of combs	7 um
Nmber of Movable Combs	20
Initial distance of the front ends of the fingers (at the end of Phase I)	6 um
Lateral air gap between fingers	1 um

Now we consider phase I. Figure 6 shows calculation results of movable capacitor plate displacement versus applied voltage. It should be noted again, that the voltage is applied to the combs. These combs are connected to the capacitor movable plate. As it is seen from the figure, the total capacitor movable plate displacement and corresponding voltage before snapping is 3.6μm and 3.6V, respectively. To verify, the proposed structure is simulated using Intellisuite software. Figure 7 shows simulation result of the structure.

As it is seen, the calculation results is approximately the same as the simulation results. Figure 8 shows the maximum displacement (3μm) of the movable plate due to the required applied voltage. At this point the frame is stopped as a result of the collision with the stopper. Therefore, phase I displacement mechanism ends. Figures 9 and 10 show calculated and simulated results of capacitance versus different applied voltages in phase I. As it is seen, the calculation result is approximately the same as the simulation result.

Figure 11 shows induced stress in the structure due to applied voltage and consequently the displacement of movable section.

If the voltage is removed, the mentioned stress is also removed. There is another stress due to fabrication process. This stress is named by "residual stress". Figures 12 and 13 show the effect of 20 MPa and 40 MPa residual stresses on the applied voltage. As it is seen the pull-in voltage is increased.

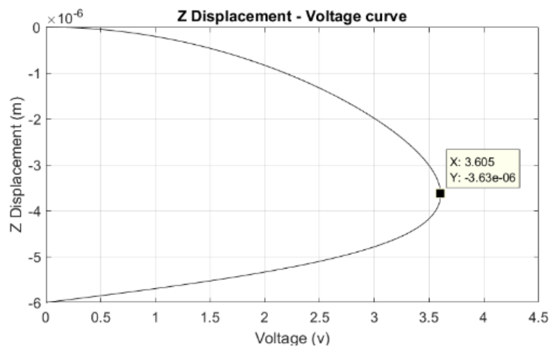

Figure 6. Calculated result of movable capacitor plate versus applied voltages (phase I)

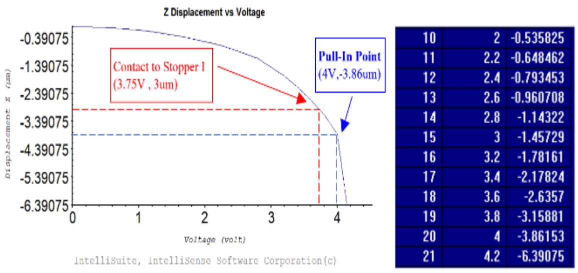

Figure 7. Simulated result of movable capacitor plate versus applied voltages (phase I)

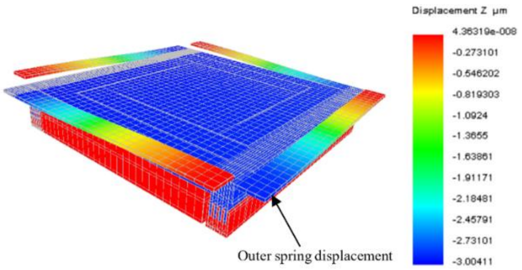

Figure 8. Maximum displacement of capacitor movable plate in phase I

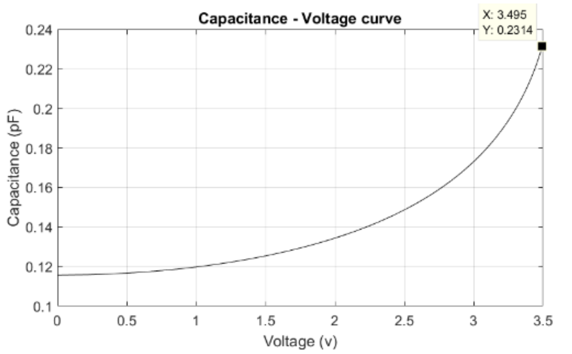

Figure 9. Calculated result of capacitance versus different applied voltages (phase I)

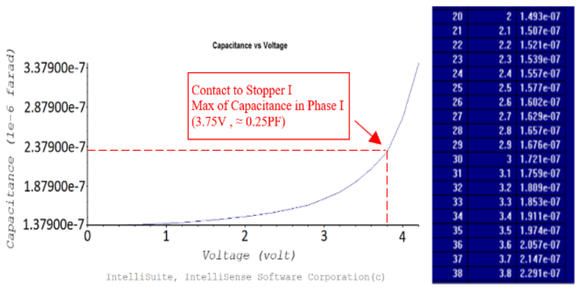

Figure 10. simulated result of capacitance versus different applied voltages (phase I)

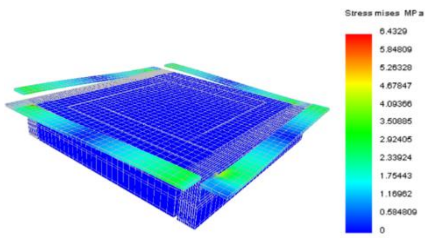

Figure 11. Stress mises_Residual Stress=0Mpa (phase I)

Figure 14 shows the effect of only stress on the air gap. As it is seen, simulation result show 0.02 µm capacitor plate displacement due to residual stress. The effect of mentioned displacement in the initial (minimum) capacitance is negligible.

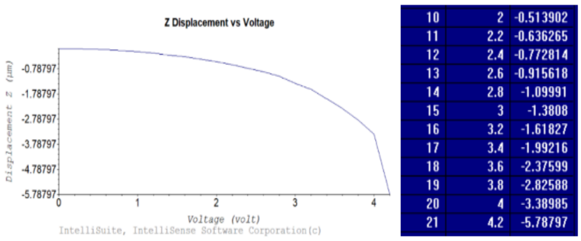

Figure 12. Simulated result of movable capacitor plate versus applied voltages_Residual Stress=20MPa (phase I)

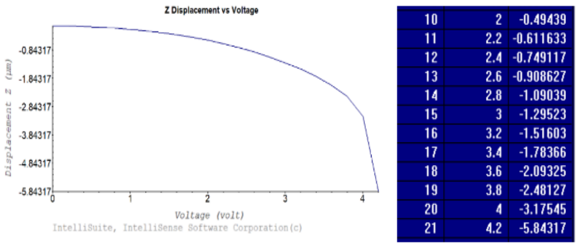

Figure 13. Simulated result of movable capacitor plate versus applied voltages_Residual Stress=40MPa (phase I)

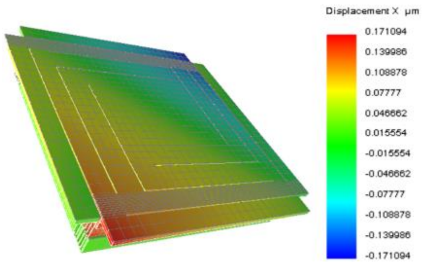

Figure 14.a Displacement along the x-axis due to Residual Stress=40Mpa in phase I

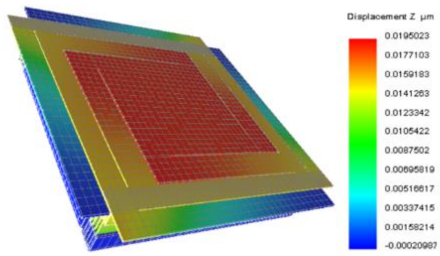

Figure 14.b Displacement along the z-axis due to Residual Stress=40Mpa in phase I

Now we consider phase II. Figure 15 shows calculation results of the movable capacitor plate displacement versus applied voltage. It should be noted again, that the voltage is applied to the combs. These combs are connected to the capacitor movable plate. As it is seen from the figure, the total capacitor movable plate displacement and corresponding voltage before snapping is 3.6µm and 12.33V, respectively. To verify, the proposed structure is simulated using Intellisuite software. Figure 16 shows simulation result of the structure. As it is seen, calculation result is approximately the same as the simulation result.

Figure 17 shows the maximum displacement (3μm) of the movable plate due to 63rd required applied voltage in phase II. At this point, the movable plate is stopped because of the collision with the dielectric layer on the capacitor fixed plate. Therefore, Phase II displacement mechanism ends. Figures 18 and 19 show calculated and simulated results of capacitance versus different applied voltages in phase II. As it is seen, the calculation result is approximately the same as the simulation result.

Figure 20 shows induced stress in the structure due to applied voltage and consequently the displacement of movable section. If the voltage is removed, the mentioned stress is also removed. Figures 21 and 22 show the effect of 20 and 40 MPa residual stresses on the applied voltage. As it is seen the pull-in voltage is increased.

Figure 23 shows the effect of residual stress on the structure in phase II. Simulation result show 0.124 μm and 0.028 μm capacitor plate displacement due to residual stress in the y and z direction respectively. As it can be seen, the effect of mentioned displacement in the initial capacitance (Z direction) is small.

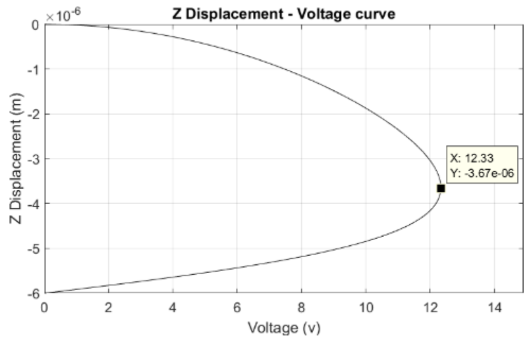

Figure 15. Calculation result of movable capacitor plate versus applied voltages (phase II)

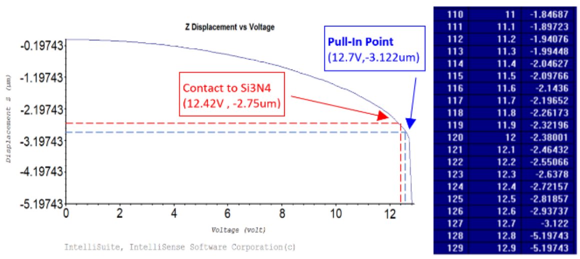

Figure 16. Simulation result of movable capacitor plate versus applied voltages (phase II)

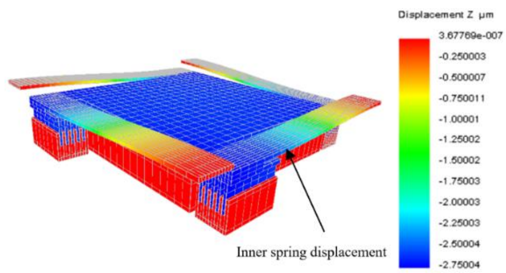

Figure 17. Maximum displacement of the capacitor movable plate in phase II

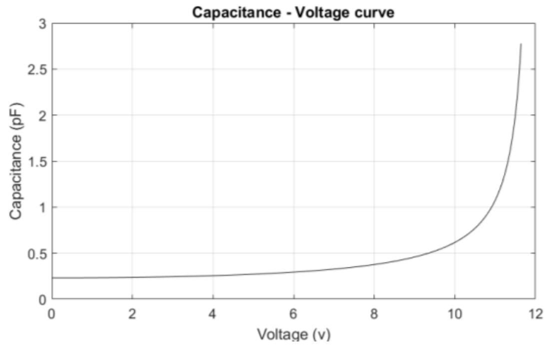

Figure 18. Calculated result of capacitance versus different applied voltages (phase II)

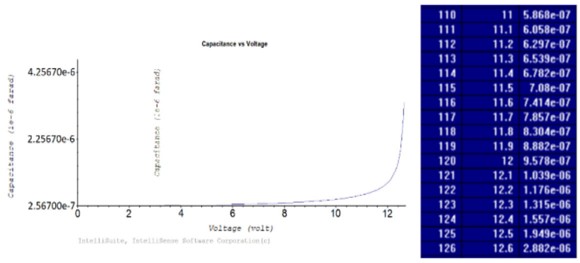

Figure 19. Simulated result of capacitance versus different applied voltages (phase II)

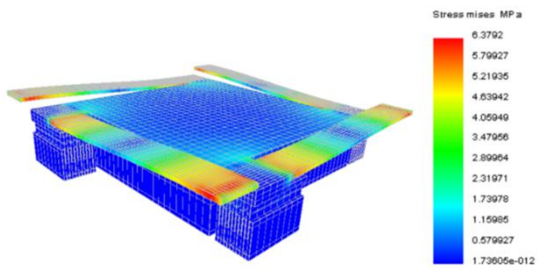

Figure 20. Stress mises (phase II)

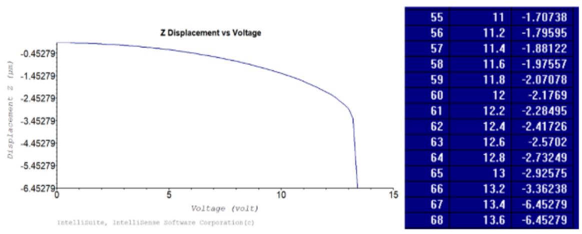

Figure 21. Simulated result of movable capacitor plate versus applied voltages_Residual Stress=20MPa (phase II)

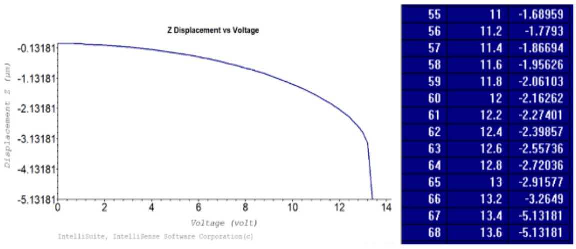

55	11	-1.68959
56	11.2	-1.7793
57	11.4	-1.86694
58	11.6	-1.95626
59	11.8	-2.06103
60	12	-2.16262
61	12.2	-2.27401
62	12.4	-2.39857
63	12.6	-2.55736
64	12.8	-2.72036
65	13	-2.91577
66	13.2	-3.2649
67	13.4	-5.13181
68	13.6	-5.13181

Figure 22. Simulated result of movable capacitor plate versus applied voltages_Residual Stress=40MPa (phase II)

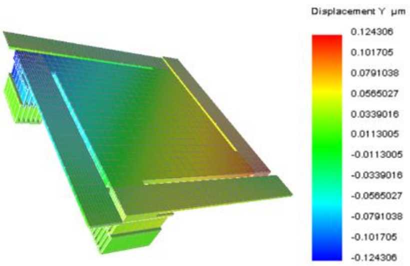

Figure 23.a Displacement due to Residual Stress=40Mpa in phase II - y direction

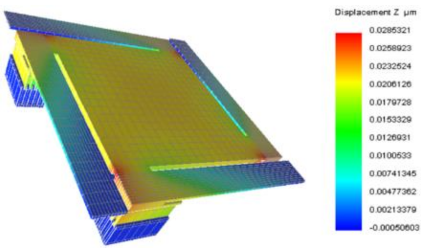

Figure 23.b Displacement due to Residual Stress=40Mpa in phase II - z direction

5. TUNING RANGE AND COMPARISON

The tuning range for a capacitor is the ratio of the difference between the maximum and minimum capacitance to its minimum capacitance that is expressed in percentage and is as follows:

$$Tuning\ \ range = \frac{C_{\max} - C_{\min}}{C_{\min}} \times 100 \tag{19}$$

The calculated results of minimum and maximum capacitance from Figures 9 and 20 are 0.12Pf and 2.9Pf, respectively. The tuning range related to these capacitances is 2316%. To verify, the simulation is done. The simulated results of minimum and maximum capacitance from Figures 10 and 21 are 0.137 and 3.4 Pf, respectively. The tuning range related to these capacitances is 2380%.

Table 2 summarizes the comparison between our proposed structure and the one plate moveable counterpart. This comparison is based on some important specifications such as tuning range, initial capacitance, actuation voltage and the effective capacitor size.

6. PROPOSED FABRICATION PROCESS

Fabrication steps of the proposed structure are shown in Figure 24. At first a high resistance substrate (SiO_2) is selected to prevent electrical connection between the different parts of the structure. Then, 0.1 μm layer of Al is deposited by sputtering and patterned to define lower plate of capacitor, anchors of external fixed-guided end beams, stoppers and outer and inner fixed combs as shown in Figure 24a. Next, a 0.1 μm silicon–nitride as a dielectric layer is deposited and patterned as shown in Figure 24b. In the third step a 6 μm polyimide 2526 as a sacrificial layer is deposited and patterned, to define inner and outer fixed combs by aluminum electroplating (Figure 24c). Then 1 μm aluminum is deposited by sputtering and patterned to create outer movable combs and overlap region of outer fixed and movable combs. Also the growth of the inner fixed combs is done (Figure 24d). To create the same level the other area in step four is filled with polyimide 2526. In the next step, 2 μm polyimide 2562 as a sacrificial layer and as a mold for aluminum electroplating is deposited, patterned and electroplated to define lower plate of capacitor, stoppers, outer movable combs and anchors of fixed-guided end beams (Figure 24e). Then 1 μm aluminum is deposited by sputtering and patterned to create inner movable combs, lower plate of capacitor, outer movable combs and anchors (Figure 24f). Then a 2 μm polyimide 2526 as a sacrificial layer and as a mold for aluminum

TABLE 2. MEMS variable capacitor performance comparison with the previously published variable capacitor

References No.	Tuning Rang	Initial Capacitance	Cmax	Actuation Volltage
[21]	41 %	0.3 PF	---	5.5 V
[6]	309 %	0.077 PF	0.238 PF	---
[22]	320 %	3 PF	---	13 V
[36]	242 %	1.955 PF	6.693 PF	9 V
[30]	207 %	24.5 fF	75.6 fF	40 V
[16]	286 %	0.498 PF	4.103 PF	28 V
[23]	240 %	15 PF	---	3.5 V
[20]	300 %	1.33PF	---	1.36 V
This Work (calculation)	2316 %	0.12 PF	2.9 PF	12.33V (without residual stress)
This Work (simulation)	2380%	0.137 PF	3.4 PF	12.42V (without residual stress)

electroplating is deposited patterned and electroplated to define lower plate of variable capacitor, inner and outer movable combs, and anchors (Figure 24g). Next, a 0.25 μm silicon–nitride as a dielectric layer is deposited and patterned as shown in Figure 24h. Then, a 1 μm polyimide 2526 as a sacrificial layer and as a mold for aluminum electroplating is deposited patterned and electroplated to define inner and outer movable combs and anchors (Figure 24i). In the tenth step a 3 μm polyimide 2526 as a sacrificial layer is deposited and patterned, to define frame by aluminum electroplating. The growth of the combs is done for the last time, while the growth of anchors continues (Figure 24j). Then 1 μm aluminum is deposited by sputtering and patterned to create frame, up electrode of movable combs and anchors (Figure 24k). Then 1 μm aluminum is deposited by sputtering and patterned to create frame, anchors and interconnection between up electrode of movable combs (Figure 24l). Then 1 μm aluminum is deposited by sputtering and patterned to create upper plate of variable capacitor, frame, outer fixed-guided end beams, inner fixed-guided end beams and anchors (Figure 24m). Finally, isotropic plasma ashing is used to remove sacrificial layer (Figure 24n).

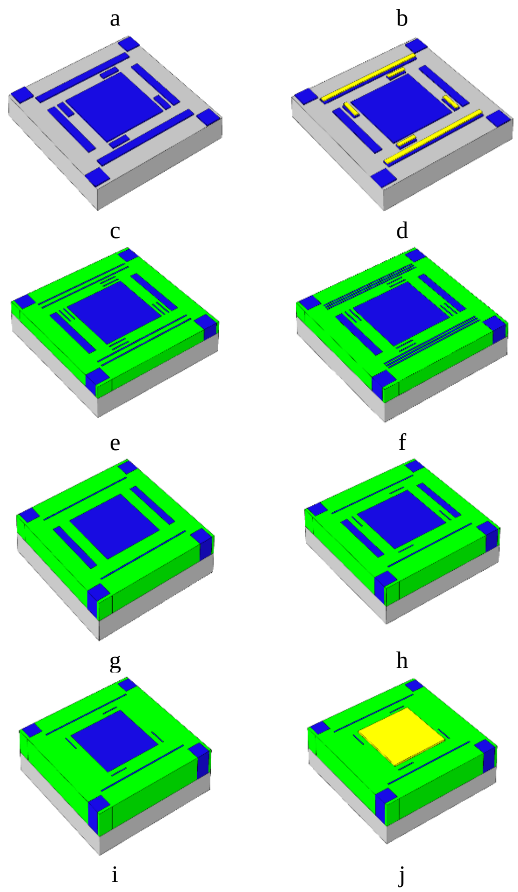

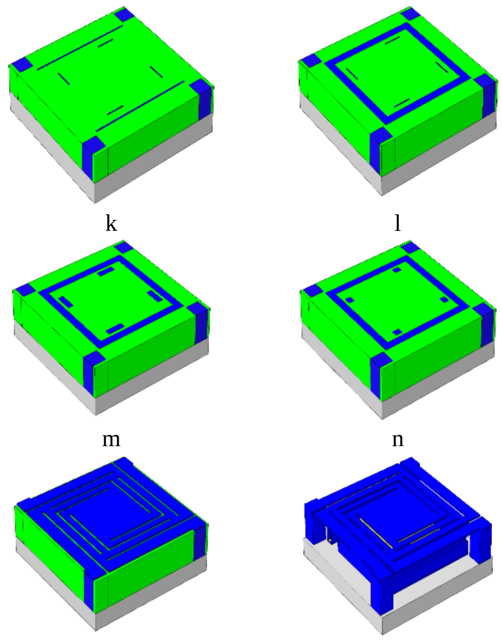

Figure 24. Schematic of proposed fabrication process

7. CONCLUSION

A new structure of MEMS variable capacitor was proposed to achieve maximum capacitance variation. It was accomplished by two independent displacement phases. In each phase, half of the desired final displacement was done and it was realized by special vertical comb drive actuators of that phase. In the second phase of displacement and for the first time, we introduced a new method in which the movable comb drive actuators are connected to the bottom of the guided end side of the inner guided end beams. Therefore, for the second mechanism of displacement, there is no need to increase the additional structure. The proposed structure was designed and then tested with MATLAB software. To verify, the structure was simulated using Intellisuite software. The achieved minimum tuning range and maximum applied voltage in the proposed structure is 2300% and 12.42V respectively.

8. REFERENCES

1. Dec, A. and Suyama, K., "Microwave mems-based voltage-controlled oscillators", ***IEEE Transactions on Microwave Theory and Techniques***, Vol. 48, No. 11, (2000), 1943-1949. DOI: 10.1109/22.883875

2. Khodapanahandeh, M., Mirzajani, H. and Ghavifekr, H.B., "A novel electrostatically actuated high q rf mems tunable capacitor for uhf applications", in Electrical Engineering (ICEE), Iranian Conference on, IEEE. (2018), 11-16. DOI: 10.1109/ICEE.2018.8472482

3. Rebeiz, G.M., Tan, G.-L. and Hayden, J.S., "Rf mems phase shifters: Design and applications", ***IEEE Microwave Magazine***, Vol. 3, No. 2, (2002), 72-81. DOI: 10.1109/MMW.2002.1004054

4. Saberhosseini, S.S., Ganji, B.A., Koohsorkhi, J. and Ghorbani, A., "Design and simulation of a variable mems capacitor for tunable hmsiw resonator", ***IET Circuits, Devices & Systems***, Vol. 14, No. 5, (2020), 707-712. doi: 10.1049/iet-cds.2019.0511

5. Reinke, J.R., "Cmos-mems variable capacitors for reconfigurable rf circuits", Carnegie Mellon University, Ph.D. Thesis (2011),

6. Gong, Z., Liu, H., Guo, X. and Liu, Z., "Optimization of a mems variable capacitor with high linearity and large tuning ratio", ***Microsystem Technologies***, Vol. 24, No. 7, (2018), 3169-3178. doi.org/10.1007/s00542-018-3844-z

7. Gupta, P., Singh, P. and Srivastava, P., "Design and analysis of rf mems varactor for extended tuning range", in 2013 International Conference on Control, Computing, Communication and Materials (ICCCCM), IEEE. (2013), 1-4. DOI: 10.1109/ICCCCM.2013.6648915

8. Mobki, H., Rashvand, K., Afrang, S., Sadeghi, M.H. and Rezazadeh, G., "Design, simulation and bifurcation analysis of a novel micromachined tunable capacitor with extended tunability", ***Transactions of the Canadian Society for Mechanical Engineering***, Vol. 38, No. 1, (2014), 15-29. doi.org/10.1139/tcsme-2014-0002

9. Mohabbatian, N., Abbaspour-Sani, E. and Ghasemzadeh, M., "An electrostatic tunable rf mems capacitor with improved quality factor", in 2014 22nd Iranian Conference on Electrical Engineering (ICEE), IEEE. (2014), 422-427. DOI: 10.1109/IranianCEE.2014.6999577

10. Nguyen, H., Hah, D., Patterson, P.R., Piywattanametha, W., Wu, M.C. and Chao, R., "A novel mems tunable capacitor based on angular vertical comb drive actuators", in Solid-State Sensor, Actuator and Microsystems Workshop, Citeseer. (2002), 277-280.

11. Rijks, T.G., Van Beek, J., Steeneken, P., Ulenaers, M., De Coster, J. and Puers, R., "Rf mems tunable capacitors with large tuning ratio", in 17th IEEE International Conference on Micro Electro Mechanical Systems. Maastricht MEMS 2004 Technical Digest, IEEE. (2004), 777-780. DOI: 10.1109/MEMS.2004.1290700

12. Teymoori, M.M., Ahangarkolaei, J.M. and Sangrody, R.A., "Investigation and comparison of two movable plates electrostatic mems tunable capacitors", ***International Journal of Electronics Communication and Computer Engineering,*** Vol. 6, No. 3, (2015). 404-408.

13. Feng, Z., Zhang, W., Su, B., Harsh, K.F., Gupta, K., Bright, V. and Lee, Y., "Design and modeling of rf mems tunable capacitors using electro-thermal actuators", in 1999 IEEE MTT-S International Microwave Symposium Digest (Cat. No. 99CH36282), IEEE. Vol. 4, (1999), 1507-1510. DOI: 10.1109/MWSYM.1999.7802401

14. Lee, C.-Y. and Kim, E.S., "Piezoelectrically actuated tunable capacitor", ***Journal of Microelectromechanical Systems***, Vol. 15, No. 4, (2006), 745-755. DOI: 10.1109/JMEMS.2006.878886

15. Mehran, M., Rotani, E.Z., Shirazi, A.D.M. and Hakimi, A., "An electro-thermal mems variable capacitor", in 2020 28th Iranian Conference on Electrical Engineering (ICEE), IEEE. Vol., No. Issue, (2020), 1-5. DOI: 10.1109/ICEE50131.2020.9260576

16. Shahi, M., "Development of tunable mems capacitor with dual-mode deformation to improve tunability and linearity", Southern Illinois University at Edwardsville, (2021), M.Sc. Thesis

17. Nguyen, H.D., Hah, D., Patterson, P.R., Chao, R., Piyawattanametha, W., Lau, E.K. and Wu, M.C., "Angular vertical comb-driven tunable capacitor with high-tuning capabilities", ***Journal of Microelectromechanical Systems***, Vol. 13, No. 3, (2004), 406-413. DOI: 10.1109/JMEMS.2004.828741

18. Steeneken, P., Rijks, T.G., Van Beek, J., Ulenaers, M., De Coster, J. and Puers, R., "Dynamics and squeeze film gas damping of a capacitive rf mems switch", ***Journal of Micromechanics and Microengineering***, Vol. 15, No. 1, (2004), 176.

19. Li, Z. and Tien, N.C., "A high tuning-ratio silicon-micromachined variable capacitor with low driving voltage", in Proc. Solid-State Sensor and Actuator Workshop. (2002), 2-6.

20. Ashoori, M. and Nabovati, H., "Wide tuning range and high quality factor mems variable capacitor with two movable plates in 0.18 µm cmos technology", ***Majlesi Journal of Mechatronic Systems***, Vol. 3, No. 4, (2014). 25-31.

21. Lee, H.S., Yoon, Y.J., Choi, D.-H. and Yoon, J.-B., "High-q, tunable-gap mems variable capacitor actuated with an electrically floating plate", in 2008 IEEE 21st International Conference on Micro Electro Mechanical Systems, IEEE. (2008), 180-183. DOI: 10.1109/MEMSYS.2008.4443622

22. Li, X., Xia, Y., Liu, J., Yin, L., Liu, Y., Fang, D. and Zhang, H., "Tunable rf mems capacitor for wireless communication", in 2009 International Conference on Optical Instruments and Technology: MEMS/NEMS Technology and Applications, International Society for Optics and Photonics. Vol. 7510, (2009), 751002. https://doi.org/10.1117/12.845903

23. Rais-Zadeh, M., Samarao, A., Monajemi, P. and Ayazi, F., "Low-voltage large-value tunable capacitors using selfaligned harpss", in 2008 IEEE 21st International Conference on Micro Electro Mechanical Systems, IEEE. (2008), 319-322. DOI: 10.1109/MEMSYS.2008.4443657

24. Al-Ghamdi, M., Khater, M., Abdel-Rahman, E. and Nepomuceno, E., "Quasi-static pull-in: An instability in electrostatic actuators", ***Scientific Reports***, Vol. 10, No. 1, (2020), 1-8. doi.org/10.1038/s41598-020-61534-w

25. Azizi, A., Fard, N.M., Mobki, H. and Arbi, A., "Bifurcation behaviour and stability analysis of a nano-beam subjected to electrostatic pressure", ***Applied and Computational Mathematics***, Vol. 7, No. 1-2, (2018), 1-11.

26. Razeghi A., B. Azizollah Ganji; A. Abdipour; R. A. Jafari-Talookolaei., "A Novel Metamaterial Microelectromechanical Systems Phase Shifter with High Phase Shift and High Bandwidth", ***International Journal of Engineering***, ***Transactions B: Applications,*** Vol. 32, No. 8, (2019) 1163-1168 doi: 10.5829/ije.2019.32.08b.12

27. Pratiher, B., "Electrostatically driven mems resonator: Pull-in behavior and non-linear phenomena", Nonlinear Systems: Theoretical Aspects and Recent Applications, (2020), 241.

28. Rezazadeh, G., Rashvand, K. and Madinei, H., "Effect of length-scale parameter on pull-in voltage and natural frequency of a micro-plate", ***International Journal of Engineering, Transactions C: Aspects***, Vol. 27, No. 3, (2014), 375-384. doi: 10.5829/idosi.ije.2014.27.03c.04

29. Zhang, W.-M., Yan, H., Peng, Z.-K. and Meng, G., "Electrostatic pull-in instability in mems/nems: A review", ***Sensors and Actuators A: Physical***, Vol. 214, (2014), 187-218. doi.org/10.1016/j.sna.2014.04.025

30. Afrang, S., Mobki, H., Sadeghi, M.H. and Rezazadeh, G., "A new mems based variable capacitor with wide tunability, high linearity and low actuation voltage", ***Microelectronics Journal***, Vol. 46, No. 2, (2015), 191-197. doi.org/10.1016/j.mejo.2014.11.006

31. Bakri-Kassem, M. and Mansour, R., "High tuning range parallel plate mems variable capacitors with arrays of supporting beams", in 19th IEEE international conference on micro electro mechanical systems, IEEE. (2006), 666-669. DOI: 10.1109/MEMSYS.2006.1627887

32. McFeetors, G. and Okoniewski, M., "Performance and operation of stressed dual-gap rf mems varactors", in 2006 European Microwave Conference, IEEE. (2006), 1064-1067. DOI: 10.1109/EUMC.2006.281117

33. Mobki, H., Sadeghi, M.H., Afrang, S. and Rezazadeh, G., "On the tunability of a mems based variable capacitor with a novel structure", ***Microsystem Technologies***, Vol. 17, No. 9, (2011), 1447-1452. doi.org/10.1007/s00542-011-1327-6

34. Rezazadeh, G. and Mobki, H., "Application of thau observer for fault detection of micro parallel plate capacitor subjected to nonlinear electrostatic force", ***International Journal of Engineering, Transactions B: Applications***, Vol. 28, No. 2, (2015), 270-276. doi: 10.5829/idosi.ije.2015.28.02b.13

35. Borwick, R.L., Stupar, P.A., DeNatale, J.F., Anderson, R. and Erlandson, R., "Variable mems capacitors implemented into rf filter systems", ***IEEE Transactions on Microwave Theory and Techniques***, Vol. 51, No. 1, (2003), 315-319. DOI: 10.1109/TMTT.2002.806519

36. Afrang, S. and Nematkhah, N., "A new mems based variable capacitor using electrostatic vertical comb drive actuator and auxiliary cantilever beams", ***Microsystem Technologies***, Vol. 25, No. 9, (2019), 3317-3327. DOI: 10.1109/TMTT.2002.806519

37. Chen, C. and Lee, C., "Design and modeling for comb drive actuator with enlarged static displacement", ***Sensors and Actuators A: Physical***, Vol. 115, No. 2-3, (2004), 530-539. doi.org/10.1016/j.sna.2004.04.052

38. Jaecklin, V., Linder, C., De Rooij, N. and Moret, J., "Micromechanical comb actuators with low driving voltage", ***Journal of Micromechanics and Microengineering***, Vol. 2, No. 4, (1992), 250.

39. Legtenberg, R., Groeneveld, A. and Elwenspoek, M., "Comb-drive actuators for large displacements", ***Journal of Micromechanics and Microengineering***, Vol. 6, No. 3, (1996), 320.

40. Rebeiz, G.M., "Rf mems: Theory, design, and technology, John Wiley & Sons, (2004).

Persian Abstract

چکیده

این مقاله یک خازن متغییر بر پایه فن آوری MEMS برای رسیدن به یک ناحیه پایدار بزرگ و قابلیت تنظیم وسیع را ارائه می کند. ایده کار بر اساس افزایش ناحیه پایدار در فاصله هوایی بین صفحات خازنی است که با ترکیب عملکرد دو مجموعه محرک شانه ای عمودی انجام می گیرد تا به تغییرات فاصله هوایی واحد غلبه شود. طراحی ساختار به صورتی است که عملکرد این دو مجموعه محرک، کاملا مستقل از یکدیگر و بدون تداخل و یا تخریب روی هم انجام شود. برتری طرح در این است که اضافه کردن مکانیزم دوم تحریک، ضخامت کلی ساختار را تغییر نمی دهد در مقایسه با حالتی که ساختار فقط از یک مکانیزم تحریک استفاده می کند. بنابراین قابلیت تنظیم شدیدا افزایش می یابد. ماده پایه مورد استفاده برای طراحی، آلومینیوم است. محرک های شانه های به صورت وسیع به عنوان موتورهای MEMS بکار برده می شوند، به علت محدوده وسیع حرکت خطی، مصرف توان پایین و سادگی فرآیند ساخت آنها. یک بررسی کامل از محرک های الکترواستاتیک انجام شده است. ساختار با استفاده از نرم افزار MATLAB محاسبه شده است. برای تایید، نتایج محاسبه شده با نتایج شبیه سازی حاصل شده از نرم افزار Intellisuit مقایسه شده است. فرکانس طبیعی ساختار 1.173KHz می باشد. مطابق با نتایج محاسبات و شبیه سازی، محدوده تنظیم بدست آمده 2300% است.

IJE TRANSACTIONS B: Applications Vol. 34, No. 11, (November 2021) 2545-2556

International Journal of Engineering

Journal Homepage: www.ije.ir

Extreme Learning Machine Based Pattern Classifiers for Symbolic Interval Data

N. Emami*[a], M. Kuchaki Rafsanjani[b]

[a] *Department of Computer Science, Faculty of Engineering and Basic Sciences, Kosar University of Bojnord, Iran*
[b] *Department of Computer Science, Faculty of Mathematics and Computer, Shahid Bahonar University of Kerman, Kerman, Iran*

PAPER INFO

Paper history:
Received 28 April 2021
Received in revised form 11 September 2021
Accepted 28 September 2021

Keywords:
Interval Data
Classification
Extreme Learning Machine
Data Analysis

ABSTRACT

Interval data are usually applied where inaccuracy and variability must be considered. This paper presents a learning method for Interval Extreme Learning Machine (IELM) in classification. IELM has two steps similar to well known ELM. At first weights connecting the input and the hidden layers are generated randomly and in the second step, ELM uses the Moore–Penrose generalized inverse to determine the weights connecting the hidden and output layers. In order to use Moore–Penrose generalized inverse for determining second layer weights in IELM, this paper proposes four classification methods to handle symbolic interval data based on ELM. The first one uses a midpoint of intervals for each feature value then it applies a classic ELM. The second one considers each feature value as a pair of quantitative features and implements a conjoint for classic extreme learning machine. The third one represents interval features by their vertices and performs a classic extreme learning machine as well. The fourth one takes each interval as a pair of quantitative features after that two separated classic extreme learning machines are performed on these features and combines the results accordingly. Algorithms are tested on the synthetic and real datasets. A synthetic dataset is applied to determine the number of hidden layer nodes in an IELM. The classification error rate is considered as a comparison criterion. The error rate obtained for each proposed methods is 19.167%, 15% , 6.536% and 18.333% respectively. Experiments demonstrate the usefulness of these classifiers to classify symbolic interval data.

doi*: 10.5829/ije.2021.34.11b.17*

NOMENCLATURE

a^L	Lower limit of interval	L	Hidden nodes
a^U	Upper limit of interval	w_i	First layer weight vector
a^M	Midpoint of interval	β_i	Second layer weight vector
k	Positive scalar	b_i	Bias
K	Number of classes	G(.)	Activation function
F	Increasing function	H	Hidden layer output matrix of the neural network
i/j	Index	$\hat{\beta}$	βapproximation
N	Number of sample	H^+	Moore-Penrose inverse of matrix H.
x_i	The ith sample	f_{ij}^L	The lower limit of the jth feature of the ith sample
t_j	The jth target	f_{ij}^U	The upper limit of the jth feature of the ith sample
o_j	The jth output	f_{ij}^M	The midpoint of the jth feature of the ith sample
p	Number of features	γ_i	Length of interval

1. INTRODUCTION

In real-life situations, there is imprecise and incompleteness in the feature values [1-6]. It is suitable to apply interval feature value for data [7-11]. Interval data offer a way of representing the available information where uncertainty or variability must be taken into account [12]. Analyzing and modeling for interval data have raised in the field of Symbolic Data Analysis (SDA) [13]. It is introduced as a new domain in multivariate analysis, pattern recognition and

*Corresponding Author Institutional Email: nasibeh.emami@kub.ac.ir (N. Emami)

Please cite this article as: N. Emami, M. Kuchaki Rafsanjani, Extreme Learning Machine Based Pattern Classifiers for Symbolic Interval Data, International Journal of Engineering, Transactions B: Applications, Vol. 34, No. 05, (2021) 2545-2556

artificial intelligence scope. SDA aims to provide suitable methods (clustering, factorial techniques, decision trees, etc.) for managing aggregated data described by multi-valued variables, where the cells of the data table contain the sets of categories, intervals or weight (probability) distributions [14,15].

Several clustering methods have been proposed for interval data. A fuzzy clustering method is used for analyzing interval-valued data which is introduced by D'Urso et al. [16]. A preferential interval-valued fuzzy c-means algorithm for remotely sensed imagery classification is presented by Feng et al. [17]. A method for dealing with hierarchical clustering for interval-valued data has been proposed by Galdino and Maciel [18]. A new interval possibilistic fuzzy c-means (IPFCM) clustering method is proposed for clustering symbolic interval data [19]. A multivariate outlier detection method for interval data is proposed by Silva et al. [20] that makes use of a parametric approach to model the interval data. A simulation study demonstrates the usefulness of the robust estimates for outlier detection, and new diagnostic plots allow gaining deeper insight into the structure of real world interval data. A robust partitioning fuzzy clustering algorithm for interval-valued data based on adaptive city-block distance that takes into account the relevance of the variables according to the boundaries is proposed [21]. This distance changes at each iteration of the algorithm and is different from one cluster to another. The method optimizes an objective function by alternating three steps to compute the representatives of each group, the fuzzy partition, and the relevance weights for the interval-valued variables for each boundary is investigated.

Several supervised classification methods are directed toward developing efficient tools related to interval data. A symbolic classifier as a region-oriented approach for the quantitative, categorical, interval, and categorical multi-valued data was introduced by Rizo Rodríguez and de Assis Tenório de Carvalho [22]. This approach is an adaptation of the concept of mutual neighbors to define the concepts of mutual neighbors between symbolic data and Mutual Neighbourhood Graph (MNG) between groups. At the end of the learning step, the symbolic description of each group is obtained through the use of an approximation of a MNG and a symbolic join operator. In order to reduce the complexity of the learning step without compromising the classifier performance with regarding to the prediction accuracy another MNG approximation is proposed [23]. A region-oriented approach in which each region is determined by the convex hull of the objects belonging to a class was introduced by D'Oliveira et al. [24]. A generalization of binary decision trees to predict the class membership of symbolic data is presented in literature [25]. A novel approach by Singh and Huang [26], in order to solve the problems of classification and decision-making by employing the interval-valued fuzzy sets, rough sets and granular computing (GrC) concepts. A novel approach which is introduced in literature [27] is a generalization of probabilistic neural network for interval data processing that can be used in classifying interval information. Generalized multi-perceptions to work with interval data are mentioned in literature [28]. The fuzzy radial basis function network to work with symbolic data was introduced by mali and Mitra [29]. A lazy-learning approach that extends K-Nearest Neighbor classification to modal and interval data is stated in literature [30]. A new model from multilayer perceptron based on interval arithmetic where inputs and outputs are considered as interval values but weights and biases are considered as single-values introduced in literature [12]. Different pattern classifiers for interval data based on the logistic regression methodology have been presented by De Souza et al. [31].

Lately, the Extreme Learning Machine (ELM) has been proposed by Huang [32-34]. It is derived from the single-hidden layer feed forward neural networks (SLFNs) and has an input and hidden layer. There are two steps for computing weights in ELM. In the first step, the weights are generated randomly between the input and hidden layer. The second step applies the Moore–Penrose generalized inverse to specify the weights connecting between the hidden and output layer.

We proposed four ELM based pattern classifiers for symbolic interval data. Inputs are vectors with interval components and output are crisp. Also, the weights and biases are real numbers. The first one uses the midpoint of intervals for each feature and uses a classic ELM. The second one considers each feature values as a pair of quantitative features and applies a conjoint classic ELM. The third one is represented by its vertices and performes classic ELM. The fourth one takes each interval as a pair of quantitative features and then it performes two separate classic ELM on these features and combines the results in suitable way. The main contributions of this paper are:

- Classification of aggregated data described by multi-valued features.
- Providing some ways in which interval data can be compatible for Moore-Penrose inverse calculation in the second layer of ELM.
- Reducing the classification error rate.

The rest of the paper is organized as follows: section 2 points out some important preliminaries, section 3 introduces proposed pattern classifiers for interval data based on ELM. The performance of these classifiers is based on the prediction error rate Experimental data and results have been presented in section 4 and the performance results on the car interval dataset are shown. Disscussion over the proposed methods can be found in section 5. Finally, section 6 concludes the paper.

2. PRELIMINARIES

This section describes preliminaries about interval arithmetic and original ELM.

2. 1. Interval Arithmatic Interval arithmetic was early introduced as a technique for considering uncertainty, inaccuracy or variability. It works by expressing every uncertainty quantity as a range of possible values. The size of this range (or interval) expresses the uncertainty associated with the quantity [7, 35, 36]. An interval number A is a closed interval $[a^L, a^U] \subset$ R of all real numbers that including the end points a^L and a^U, such that $a^L \ll a^u$. If $a^L = a^u$ then interval is called to be degenerated, thin or even point interval. Let interval number $A = [a^L, a^U] and\ B = [b^L, b^U] \subset R$. Intervals are produced for each arithmetic operation in Equations (1)-(6).

$$[a^L, a^U] + [b^L, b^U] = [a^L + b^L, a^U + b^U] \quad (1)$$

$$[a^L, a^U] - [b^L, b^U] = [a^L - b^L, a^U - b^U] \quad (2)$$

$$[a^L, a^U] \times [b^L, b^U] = [\min(a^L b^L, a^L b^u, a^U b^L, a^U b^U), \max(a^L b^L, a^L b^u, a^U b^L, a^U b^U)] \quad (3)$$

$$k \times [a^L, a^U] = [ka^L, ka^U] \quad (4)$$

$$F([a^L, a^U]) = [F(a^L), F(a^U)] \quad (5)$$

$$a^M = \frac{a^L + a^U}{2} \quad (6)$$

2. 2. Extreme Learning Machine (ELM) The mathematical modeling of the ELM describes here [33]. Consider N arbitrary samples(x_i, t_i),where $x_i = [x_{i1}, x_{i2}, \dots, x_{ip}]^T \in R^p$and $t_i = [t_{i1}, t_{i2}, \dots, t_{im}]^T \in R^m$, a standard Single Layer Feed Forward Neural Network(SLFN) with L hidden nodes can approximate these N samples with zero error means $\sum_{j=1}^{L} \| o_j - t_j \| = 0$; i.e., there exist (w_i, b_i) and β_i such that

$$\sum_{i=1}^{L} \beta_i G(w_i, b_i, x_j) = t_j, \quad j = 1, \dots, N \quad (7)$$

Equation (7) can be written in compact form as $H\beta = T$ where

$$H = \begin{bmatrix} h(x_1) \\ \vdots \\ h(x_N) \end{bmatrix} = \begin{bmatrix} G(w_1, b_1, x_1) & \dots & G(w_L, b_L, x_1) \\ \vdots & \cdots & \vdots \\ G(w_1, b_1, x_N) & \dots & G(w_L, b_L, x_1) \end{bmatrix}_{N \times L}$$

$$\beta = \begin{bmatrix} \beta_1^T \\ \vdots \\ \beta_L^T \end{bmatrix}_{L \times m} \quad and \quad T = \begin{bmatrix} T_1^T \\ \vdots \\ T_N^T \end{bmatrix}_{N \times m}$$

The i[th] column of H is the i[th] hidden node output with respect to inputs $x_1, x_2, \dots, x_N$.

Figure 1 shows the overal scheme of ELM. weights are selected randomly in the input layer but weights in the hidden layer need to be adjusted based on the training samples. Therefore, we have the linear system $H\beta = T$ to find a least squares solution $\hat{\beta}$ such that

$$\|H\hat{\beta} - T\| = \min_{\beta} \|H\beta - T\| \quad (8)$$

The smallest norm least square solution of Equation (8) is $\hat{\beta} = H^+ T$.

3. PROPOSED ELM CLASSIFIERS FOR INTERVAL DATA

In this section, MELM, JELM, VELM and LUELM pattern classifiers based on ELM for interval data are presented. In all these methods, the weights are real. The first layer weights are selected randomly and the second layer weights are learned by training data. Afterwards, the learned weights are used to assign new samples to the classes.

Suppose $(x_i, t_i), i = 1, \dots, N,$ be a training symbolic sample set with K class labels. Sample i[th] presents by interval features $\{f_{i1}, f_{i2}, \dots . f_{ip}\}$ which $f_{ij} = [f_{ij}^L, f_{ij}^U]$ $, j = 1,2, \dots, p$ and a categorical discrete variable $t_i \in \{1,2, \dots K\}$.

Let p, $\widetilde{N}$ and m to be the number of neurons for the input, hidden and output layers, respectively. The weight vector connecting the input and the i[th] hidden layers is denoted by $w_i = [w_{i1}, w_{i2}, \dots, w_{ip}]^T \in R^p$ and $\beta_i = [\beta_{i1}, \beta_{i2}, \dots, \beta_{im}]^T \in R^m, i = 1,2, \dots, \widetilde{N}$ and b_i denotes the threshold of the i[th] hidden node for $i = 1,2, \dots, \widetilde{N}$. An activation function g(.) is used for the hidden and output layers.

3. 1. MELM This method uses the midpoint of the intervals in the representation of interval data. That means a feature $f_{ij} = [f_{ij}^L, f_{ij}^U]$ is represented by $f_{ij}^m = \frac{f_{ij}^L + f_{ij}^U}{2}$. Therefore each symbolic interval training sample i has a vector of p features midpoint $x_i^M = [f_{i1}^M, f_{i2}^M, \dots, f_{ip}^M]$ that are fed as an input to the network. Then weights are selected randomly in the input layer and the second layer weights are earned by solving the linear system $H\beta = T$. The smallest norm least square solution of the linear system is $\tilde{\beta} = H^+ T$. So $\tilde{\beta}$ coefficient learned by training samples is being applied in the classification of interval data. Algorithm1 summerises the proposed MELM.

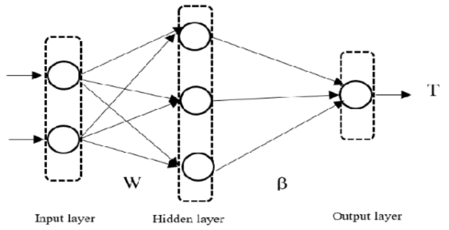

Figure 1. Overall Scheme of ELM

3. 2. JELM Here, pattern classifier is introduced which utilises the lower and upper bounds of the intervals conjointly. Sample interval training data are $x_i = [[f_{i1}^L, f_{i1}^U], [f_{i2}^L, f_{i2}^U], \dots, [f_{ip}^L, f_{ip}^U]]$. In order to consider the lower and upper bounds of the intervals conjointly, each sample has been represented by 2p feature values $x_i = [f_{i1}^L, f_{i1}^U, f_{i2}^L, f_{i2}^U, \dots, f_{ip}^L, f_{ip}^U]$. These vectors are being fed as inputs to the ELM.

The first layer weights are being produced randomly and for the second layer we need to solve the linear system $H\beta = T$. The smallest norm least square solution of the linear system comes from training samples and we have equation $\tilde{\beta} = H^+T$. After we find the approximate weights by training data, classification can be done. Algorithm 2 summerises the proposed JELM.

3. 3. VELM This subsection introduces a method based on ELM by employing the vertices of the hypercube for symbolic interval data. Suppose a symbolic interval vector is shown by $x_i = [[f_{i1}^L, f_{i1}^U], \dots, [f_{ip}^L, f_{ip}^U]]$ that have 2^p vertices in R^p space. It can be described by a matrix

$$M = \begin{pmatrix} f_{i1}^L & \cdots & f_{ip}^L \\ f_{i1}^L & \cdots & f_{ip}^U \\ \vdots & \ddots & \vdots \\ f_{i1}^U & \cdots & f_{i1}^L \\ f_{i1}^U & \cdots & f_{ip}^U \end{pmatrix}$$ of all the vertices of hypercube in R^p space. Therefore each symbolic interval training sample is a matrix $2^p \times p$ corresponds to all possible combinations of the limits of intervals. Class variable for each row of matrix M is similar to the original representation of the samples. If training sample dataset have N samples then the size of training sample becomes $N \times 2^p$ rows and p column in this representation.

For instance, let N=2, p=2 and suppose the sample $x_i = ([f_{i1}^L, f_{i1}^U], [f_{i2}^L, f_{i2}^U])$. matrix of vertices of the hyper cubes for this sample is:

$$M = \begin{pmatrix} f_{i1}^L & f_{i2}^L \\ f_{i1}^L & f_{i2}^U \\ f_{i1}^U & f_{i2}^L \\ f_{i1}^U & f_{i2}^U \end{pmatrix}$$ and the symbolic interval training dataset changed to a new dataset $$M = \begin{pmatrix} f_{11}^L & f_{12}^L & y_1 \\ f_{11}^L & f_{12}^U & y_1 \\ f_{11}^U & f_{12}^L & y_1 \\ f_{11}^U & f_{12}^U & y_1 \\ f_{21}^L & f_{22}^L & y_2 \\ f_{21}^L & f_{22}^U & y_2 \\ f_{21}^U & f_{22}^L & y_2 \\ f_{21}^U & f_{22}^U & y_2 \end{pmatrix}.$$

By constructing the M-matrix, the ELM inputs are prepared for the symbolic interval training data, and the weights of the first layer are randomly selected. Then the weights of the second layer are approximated by calculating the Moore-Penrose generalized inverse of H -matrix. Algorithm 3 summarises the proposed VELM.

3. 4. LUELM A pattern classifier for symbolic interval data based on ELM is defined by the lower and upper bounds of the interval separately. In this method, we will perform one ELM based on lower bounds and another ELM is based on the upper bounds. In each ELM, first layer weights are produced randomly and second layer weights are calculated by solving the linear system $H\beta = T$. So an approximation of β coefficient is $\tilde{\beta} = H^+T$.

In order to label the samples, the weighted average output of the networks is calculated and passed through the discretized function. Algorithm 4 summerises the proposed LUELM.

ALGORITHM 1: Pseudocode of MELM

MELM algorithm

Input: Given interval training set

$$x_i = ([[f_{i1}^L, f_{i1}^U], \dots, [f_{ip}^L, f_{ip}^U]], T_i), i = 1, .., N$$

Output: class label

1. Calculate the midpoint of intervals $x_i^M = [f_{i1}^M, .., f_{ip}^M] \in R^p$
2. Randomly assign the input weights w_i and bias b_i
3. Calculate the hidden layer output matrix H
4. Calculate the output weights matrix as $\hat{\beta} = H^+T$
5. Calculate the class label based on $\hat{\beta}$ coefficient

ALGORITHM 2: Pseudocode of JELM

JELM algorithm

Input: Given interval training set.

$$x_i = ([[f_{i1}^L, f_{i1}^U], \dots, [f_{ip}^L, f_{ip}^U]], T_i), i = 1, .., N$$

Output: class label

1. Consider lower and upper bounds of the intervals conjointly $x_i = [f_{i1}^L, f_{i1}^U, f_{i2}^L, f_{i2}^U, \dots, f_{ip}^L, f_{ip}^U] \in R^{2p}, i = 1, .., N$
2. Randomly assign the input weights w_i and bias b_i
3. Calculate the hidden layer output matrix H
4. Calculate the output weights matrix as $\hat{\beta} = H^+T$
5. Calculate the class label based on $\hat{\beta}$ coefficient

ALGORITHM 3: Pseudocode of VELM

VELM algorithm

Input: Given interval training set

$$x_i = ([[f_{i1}^L, f_{i1}^U], \dots, [f_{ip}^L, f_{ip}^U]], T_i), i = 1, .., N$$

Output: class label

1. Represent interval data by vertices of the hypercube $x_i \in R^p, i = 1, \dots N \times 2^p$
2. Randomly assign the input weights w_i and bias b_i
3. Calculate the hidden layer output matrix H

4. Calculate the output weights matrix as $\hat{\beta} = H^{+}T$
5. Calculate the class label based on $\hat{\beta}$ coefficient

4. EXPERIMENTAL AND RESULTS

In this section, the proposed methods for interval extreme learning machines have been applied for three examples. Example one is a synthetic interval data with a low degree of class overlapping. Example two is a synthetic interval data too; however, it has a moderate degree of class overlapping. These synthetic data sets are being used to determine the number of layers for each model. Example three is a real dataset.

Each synthetic interval data has three classes. One of the classes has an ellipse shape of size 200 and other classes have spherical shapes of size 150 and 100. Each class in these quantitative datasets was drawn according to two independent normal distributions. Each data point (z1, z2) of each one of this synthetic quantitative dataset is a seed of a vector of intervals (rectangle) defined as $([z_1 - \gamma_1/2\,, z_1 + \gamma_1/2], [z_2 - \gamma_2/2\,, z_2 - \gamma_2/2])$.

Example one is constructed according to the following parameters:
class1: $\mu_1 = 50\,,\ \mu_2 = 25, \delta_1^2 = 9\ and\ \delta_2^2 = 36$
class2: $\mu_1 = 45\,,\ \mu_2 = -2, \delta_1^2 = 25\ and\ \delta_2^2 = 25$
class3: $\mu_1 = 38\,,\ \mu_2 = 40, \delta_1^2 = 9\ and\ \delta_2^2 = 9$
It has low degree of class overlapping. Figures 2 and 3 display the quantitative and interval form of data in example one respectively.

Example two has moderate degree of class overlapping and it is constructed according to the following parameters:
class1: $\mu_1 = 50\,,\ \mu_2 = 25, \delta_1^2 = 9\ and\ \delta_2^2 = 36$
class2: $\mu_1 = 45\,,\ \mu_2 = 5, \delta_1^2 = 25\ and\ \delta_2^2 = 25$
class3: $\mu_1 = 45\,,\ \mu_2 = 40, \delta_1^2 = 9\ and\ \delta_2^2 = 9$
Figures 4 and 5 show the quantitative and interval form of data in example two, respectively [22].

Car dataset is a real symbolic interval dataset. It is widely used to compare classification methods of the literature of SDA [14, 15,31, 37-39]. It contains a total of 33 car models described by eight interval features included price, engine capacity, top speed, acceleration, step, length, width and height. The nominal variable of Car category places each car in two classes. Class

ALGORITHM 4: Pseudocode of LUELM

LUELM algorithm

Input: Given interval training set
$$x_i = (\left[[f_{i1}^L, f_{i1}^U], \dots, [f_{ip}^L, f_{ip}^U] \right], T_i), i = 1, .., N$$
Output: class label

Step one:
1. Consider the lower bounds of the interval
$$x_i = [f_{i1}^L, f_{i2}^L, \dots, f_{ip}^L] \in R^p, i = 1, .., N$$
2. Randomly assign the input weights w_i and bias b_i
3. Calculate the hidden layer output matrix H
4. Calculate the output weights matrix as $\hat{\beta} = H^{+}T$
5.

Step two:
6. Consider the upper bounds of the interval
$$x_i = [f_{i1}^U, f_{i2}^U, \dots, f_{ip}^U] \in R^p, i = 1, .., N$$
7. Randomly assign the input weights w_i and bias b_i
8. Calculate the hidden layer output matrix H
9. Calculate the output weights matrix as $\hat{\beta} = H^{+}T$

Step three:
10. Calculate the average of step one and two
11. Calculate the class label based on average $\hat{\beta}$ coefficient

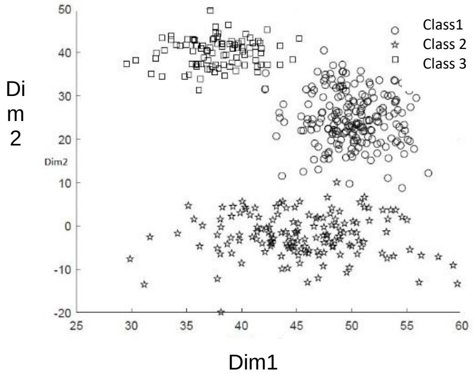

Figure 2. The quantitative form of data in example1

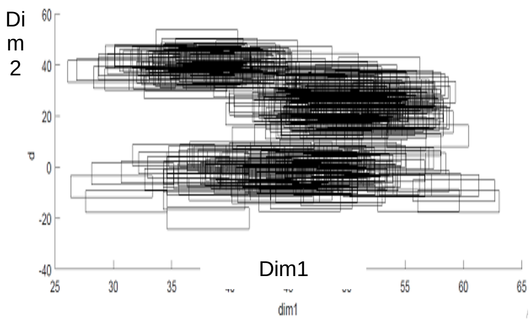

Figure 1. Interval form of data in example1

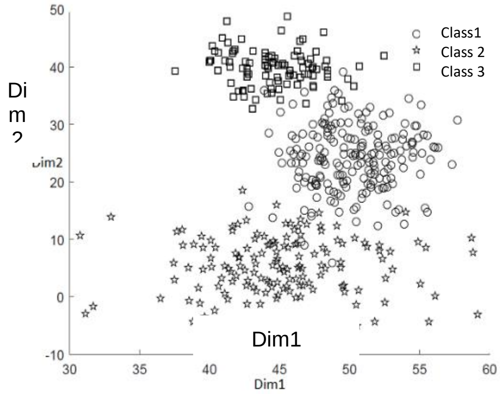

Figure 4. The quantitative form of data in example 2

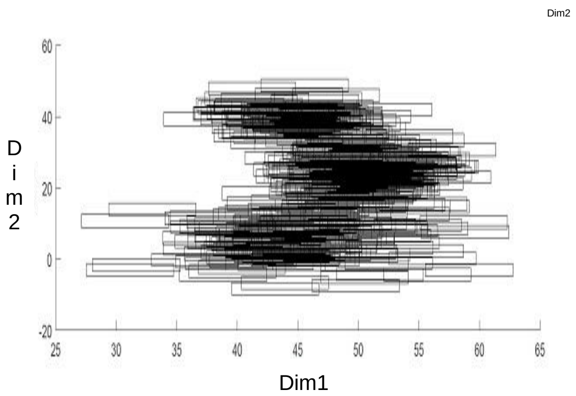

Figure 5. Interval form of data in example 2

one (Utilitarian and Berlina) has 18 car models and class two (Sporting and Luxury) has 13 car models. (see Table 1).

In order to evaluate the performance of the proposed classifiers, 75% of the original dataset is selected randomely as learning set and 25% of the original dataset is selected as test dataset.

The MELM, JELM, VELM and LUELM classifiers were applied to the synthetic interval example datasets one and two. The error rate of the classification is computed on the test data.The estimated error rate of classification corresponds to the average of the error rates is found among the 100 replications of the test set for each synthetic interval example datasets one and two.

The average classification error rate for each proposed classifier on synthetic interval example datasets one and two are shown in Tables 2 and 3 respectively. The standard deviation of the results is enclosed in parentheses. $\gamma_1 and\, \gamma_2$ are selected randomly from [1,10], [1,20], [1,30], [1,40], [1, 50] and the number of nodes in hidden layer (M) for each classifier is placed in a separate column. Interval data in this configuration shows lower degree of classification difficulty. Therefore, the best average rate of the JELM is slightly affected by the higher range of intervals.

TABLE 1. Car dataset feature and class values

	Price	Engine Capacity	Height	Category
Alfa 145	[27806, 33596]	[1370, 1910]	[143, 143]	Utilitarian
Alfa 156	[41593, 62291]	[1598, 2492]	[142, 142]	Berlina
Alfa 166	[64499, 88760]	[1970, 2959]	[142, 142]	Luxury
Aston Martin	[260500, 460000]	[5935, 5935]	[124, 132]	Sporting
.	.	.	.	.
.	.	.	.	.
.	.	.	.	.
passat	[39676, 63455]	[1595, 2496]	[146, 146]	Luxury

TABLE 2. Average classification error rate on synthetic interval examples one

Proposed methods	γ	Synthetic example one	
		M=5	M=7
MELM	[1,10]	1. 67(1.09)	12.92(27.69)
	[1,20]	1.82(1.32)	18.84(33.51)
	[1,30]	1.40(0.96)	16.34(29.05)
	[1,40]	1.11(0.80)	19.08(33.25)
	[1,50]	1.49(3.57)	18.10(28.15)
JELM	[1,10]	1.04(1.02)	0.48(0.69)
	[1,20]	1.85(1.78)	0.71(0.86)
	[1,30]	1.90(1.46)	0.48(0.80)
	[1,40]	1.61(1.88)	0.74(0.85)
	[1,50]	1.07(0.95)	0.71(0.83)
VELM	[1,10]	37.21(1.89)	34.79(1.99)
	[1,20]	39.72(3.33)	37.04(2.76)
	[1,30]	40.64(4.77)	32.30(2.29)
	[1,40]	42.30(2.85)	34.12(2.60)
	[1,50]	40.22(4.86)	37.96(4.76)
LUELM	[1,10]	2.5(1.18)	4.43(18.11)
	[1,20]	1.04(1.15)	1.16(1.10)
	[1,30]	5.18(13.46)	5.71(14.09)
	[1,40]	2.86(1.43)	7.05(14.41)
	[1,50]	3.27(1.58)	10.06(18.44)

TABLE 3. Average classification error rate on synthetic interval examples two

Proposed methods	γ	Synthetic example two	Synthetic example two
		M=5	M=7
MELM	[1,10]	8.57(2.63)	9.11(2.94)
	[1,20]	8.78(2.03)	20.68(26.00)
	[1,30]	8.93(2.30)	26.93(30.14)
	[1,40]	8.63(2.20)	26.96(28.72)
	[1,50]	9.11(2.94)	31.40(31.97)
JELM	[1,10]	8.63(2.89)	4.94(2.63)
	[1,20]	7.59(3.14)	4.32(2.10)
	[1,30]	8.96(4.15)	4.91(3.15)
	[1,40]	8.75(3.22)	6.70(2.46)
	[1,50]	8.39(3.44)	7.05(2.94)
VELM	[1,10]	37.70(3.46)	33.91(1.81)
	[1,20]	38.98(2.49)	34.07(2.23)
	[1,30]	36.09(2.06)	35.44(2.93)
	[1,40]	38.88(2.46)	35.81(4.00)
	[1,50]	38.03(4.02)	37.21(4.31)

	[1,10]	7.92(2.57)	16.67(27.93)
	[1,20]	7.20(2.39)	15.65(22.18)
LUELM	[1,30]	8.81(7.41)	14.88(18.10)
	[1,40]	7.20(4.10)	26.49(30.65)
	[1,50]	12.42(21.88)	22.56(25.48)

The worst average performance is obtained by the VELM that uses vertex to represent data. The size of data increases in VELM, therefore it is expected that as the size of data increments, the number of hidden nodes also becomes large. As a result the classification error rate in VELM with 7 nodes in hidden layer for synthetic example one and two is better than VELM with 5 nodes in hidden layer for synthetic example one and two.

Tables 2 and 3 show that MELM and LUELM with 5 nodes in the hidden layer produce better results than MELM and LUELM with 7 nodes in the hidden layer. JELM and VELM prefer 7 nodes in the hidden layer to lead to significant results. However, some high dimensional dot product operations appear in the training process. Eventually, it causes increasing of the computational complexity and training time.

In order to better demonstrate and compare the classification error rates of the proposed methods, the results are shown in Figures 6 to 13. The horizontal axis shows degree of classification difficulty and the vertical axis shows classification error rate on the proposed methods.

Figure 6 demonstrates MELM classification error rate on synthetic example one. It shows that as the degree of classification difficulty increases the results do not change significantly in MELM with 5 hidden nodes but, with the surge of neurons in the hidden layer, the classification error has an almost upward trend. Classification error rate on synthetic example one obtained from JELM is shown in Figure 7. Trends on Figure 7 illustrates that increasing the number of hidden layer neurons in JELM results in decreasing the average classification error rate. The trend of the average error rate based on the degree of classification difficulty is almost constant. Trends on VELM classification error rate on synthetic example one is demonstrated in Figure 8. In VELM, the number of data is increased, so when the number of hidden layer neurons increases, better results are obtained. The trend which is based on degree of classification difficulty is almost constant in this case.

Figure 9 illustrates the results on LUELM method. It shows that by increasing the number of hidden layer neurons, the classification error is increased and the degree of classification difficulty is related to an increasing trend.

Classification error rate diagram on synthetic example two is shown in Figure 10. Trends on this diagram show that the increasing in the degree of classification difficulty has no effect on the classification error rate of the MELM with 5 hidden nodes but it has an increasing effect on the classification error rate of the MELM with 7 hidden nodes. Figuer 11 illastrates JELM classification error rate in synthetic example two. This proposed method tends to have fewer neurons in the hidden layer, and the degree of classification difficulty of the data does not have much effects on the classification accuracy.

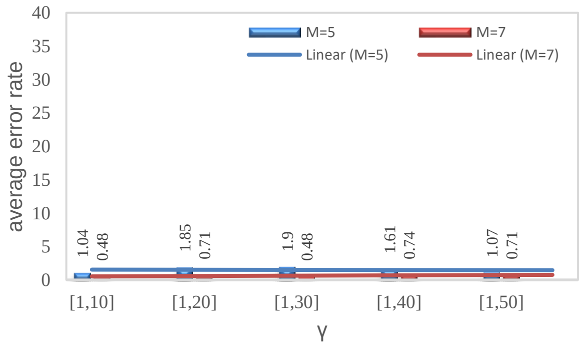

Figure 7. JELM classification error rate in synthetic example one

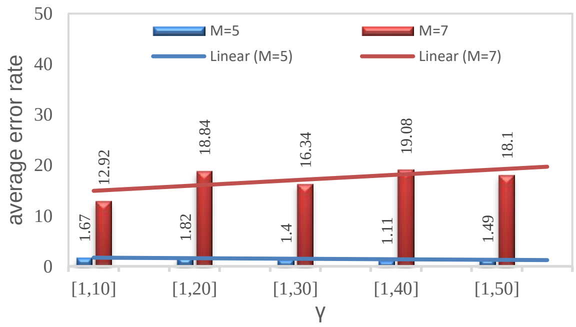

Figure 6. MELM classification error rate in synthetic example one

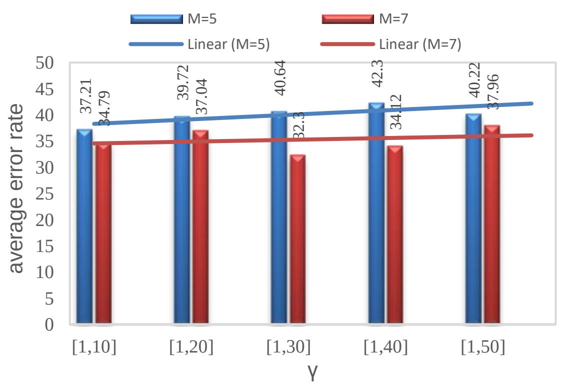

Figure 8. VELM classification error rate in synthetic example one

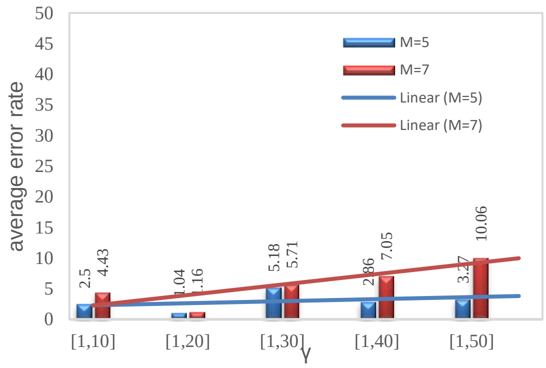

Figure 9. LUELM classification error rate in synthetic example one

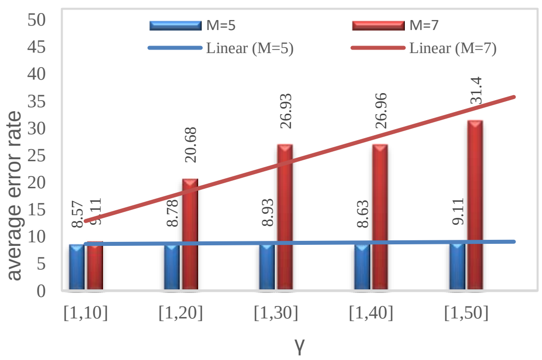

Figure 10. MELM classification error rate on synthetic example two

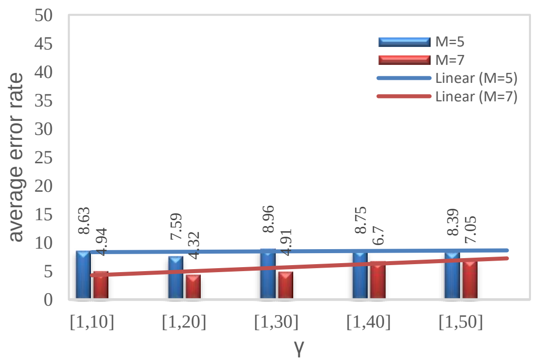

Figure 11. JELM classification error rate in synthetic example two

VELM classification error rate in synthetic example two is shown in Figure 12. Unlike other proposed algorithms in this paper, VELM offers interesting results. Here the best error rate is achieved for more neurons in hidden layer. As expected, with increasing the number of the data, the number of the hidden layer neurons increases. Also, the degree of classification difficulty of the data does not have significant effect on the VELM, but when VELM has a smaller number of neurons, the error increases along with increasing the degree of classification difficulty of the data.

Figure 13 illustrates LUELM classification error rate on synthetic example two. LUELM with 5 hidden neurons has significant error rate and it is as the degree of classification difficulty of the data. There is a slight increase in the average error rate, as the number of neurons increases, On the other hand, the classification error increases as the number of neurons increases.

The proposed methods are also tested on the a real Car dataset as an application. Data is divided into training and test data randomely such that 75% of the original dataset has been selected as the learning set and 25% of the original dataset has been selected as the test dataset Table 4 shows the results of the average error rate among the 100 replications of the proposed methods for the Car dataset. In real car dataset, MELM and LUELM with 5 neurons in the hidden layer demonstrate less error rate than MELM and LUELM with 7 neurons. Also the JELM and VELM with 7

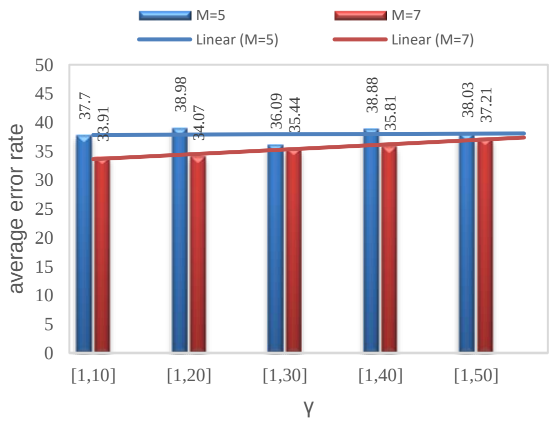

Figure 12. VELM classification error rate in synthetic example two

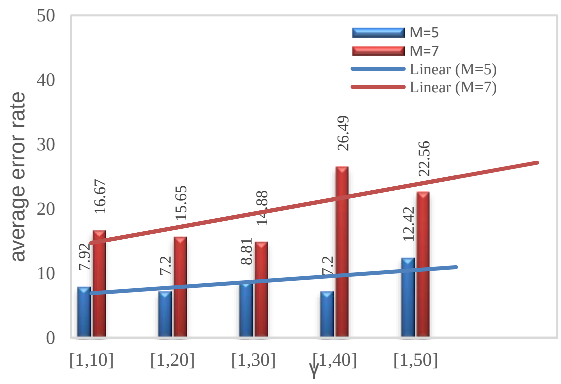

Figure 13. LUELM classification error rate in synthetic example two

neurons show less error rate than the JELM and VELMs with 5 neurons. Table 5 is created to compare average classification error rate on car dataset with previous works [31]. IDPCs methods are based on logistic regression (LR). Average error rate on Table 5 shows that proposed methods based on the ELM result in significant improvement and also among the proposed methods VELM has the best performance.

5. DISCUSSION

We tried to classify aggregated data described by multi-valued features. The essence of ELM is that the hidden layer of SLFNs does not need to be tuned. More specifically, this paper provides methods in which interval data can be compatible for Moore-Penrose inverse calculation in second layer of ELM and reduce classification error rate.

LR based methods and proposed algorithms have one problem in common: finding the optimum value for their parameters. an iterative optimization method is used in LR based methods to minimize the cost function, but the iterative optimization of network weights is avoided in proposed methods and they use the randomization and Pseudo inverse to determine the network. On the other hand the results show that proposed methods have a significant classification error rate than LR based methods.

TABLE 4. Average error rate for car dataset

Proposed methods	M=5	M=7
MELM	**19.17**	20.83
JELM	20.83	**15**
VELM	7.92	**6.54**
LUELM	**18.33**	19.58

TABLE 5. Comparing proposed methods with other methods on car dataset

Methods	Error rate(%)
IDPC_sp1(second application) [31]	57.57
IDPC_sp(first application) [31]	48.48
KNN [30]	45
IDPC_CSP [31]	36.36
IDPC_VSP(maxrule) [31]	36.4
IDPC_VSP(minrule) [31]	30.3
IDPC_VSP(averagerule) [31]	30.3
IDPC_pp [31]	27.2
MELM	19.1667
LUELM	18.3333
JELM	15
VELM	**6.5385**

Training Time Complexity in logistic regression, means solving the optimization problem. and it is estimated as $O(N \times p)$.

IDPC-CSP classifier that utilized mid-point representation has $O(N \times p)$ computational complexity.

In IDPC-SP classifiers, data are defined by the lower and upper bounds of the intervals conjointly. computational complexity for this method is: $O(N \times 2 \times p)$

In IDPC-VSP classifier Each symbolic interval training sample is a matrix $2^p \times p$ corresponding to all possible combinations of the limits of intervals. So, the size of input matrix is $p \times (2^p \times p \times N)$. Considering $\alpha = (2^p \times p)$ as a constant value. So, computational complexity of IDPC-VSP is $O(2 \times ((2^p \times p \times N \times p))$

IDPC-PP classifier is defined by the lower and upper bounds of the intervals separately. The analysis in this method consists of fitting two logistic binary regressions for each class. computational complexity for this method is sum of the computational complexity of lower bound and upper band based classifiers. So the estimation for computational complexity is $O(2 \times (N \times p))$.

There are two fundamental issues in neuro-computation: The first one is learning algorithm development and the second one is the network topology design. In fact, these two issues are closely related with each other. The learning ability of a neural network is not only a function of time, but also it is a function of the network structure.

A typical neural network contains an input layer, an output layer, and one or more hidden layers. The number of outputs and the number of inputs are usually fixed while the number of hidden layers and number of hidden neurons in each hidden layer are parameters that can be specified for each application [40].

ELM is a network which has a single hidden layer with L neurons. The time complexity of ELM is the sum of the calculations performed to obtain the weights between the input layer and the hidden layer and the weights between the hidden layer and the output layer. Assume that the size of the input matrix is $p \times N$ and the size of weights matrix between the input layer and the hidden layer is $L \times p$. In this case, the complexity of the matrix multiplication performed at this step is $O(L \times p \times N)$.

To calculate the weights in the second layer, ELM uses a Moore Penrose pseudo inverse that has a time complexity equal to $O(2 \times L \times N^2 + 2 \times L^3)$ for a matrix size of $L \times N$ and applying the common Singular Value Decomposition (SVD) method [41]. Therefore, the associate computational complexity can be estimated as: $O(L \times p \times N + 2 \times L \times N^2 + 2 \times L^3)$

The proposed methods in this paper have a structure similar to the original ELM however their representations are different from each other. In MELM method the size of the input matrix is $p \times N$. Therefore, computational complexity equals to the basice ELM.

JELM method represents the data in the size of $2p \times N$. As a result, its computational complexity is:

$O(L \times 2p \times N + 2 \times L \times N^2 + 2 \times L^3)$.

Each symbolic interval training sample is a matrix $2^p \times p$ corresponding to all possible combinations of the limits of intervals in VELM method. So the size of the input matrix is $p \times (2^p \times p \times N)$. Considering $\alpha = (2^p \times p)$ as a constant value. So, computational complexity of VELM is $O(L \times p \times \alpha N + 2 \times L \times N^2 + 2 \times L^3)$.

Input matrix in LUELM method is $p \times N$. In this method we have two networks which perform their calculations independently. Therefore, their computational complexity is added together and estimated as $O(2 \times (L \times p \times N + 2 \times L \times N^2 + 2 \times L^3))$.

6. CONCLUSION

In this paper, four new models of ELM are proposed to handle symbolic interval data. They have the architecture of a standard ELM with single-valued weights and biases, but the way interval data entered the network is different. In MELM, each interval is represented by the midpoints of intervals. JELM uses a pair of conjoint intervals. The vertices of intervals which has been used in VELM and LUELM is considered as the lower and upper bounds of the interval separately. Two Interval synthetic data and error rate criteria are used in order to determine the number of hidden layer nodes in each proposed pattern classifier model. The results show that MELM and LUELM produce significantly better results with five hidden layer nodes, while the JELM and VELM prefer seven hidden layer nodes to produce significant results. Proposed classifiers also used car interval dataset as a real synthetic dataset. Afterwards the results was compared with other methods and showed that the proposed methods have a better performance in comparison to other methods.

7. REFERENCES

1. Hira, Z. M., and Gillies, D. F., “A review of feature selection and feature extraction methods applied on microarray data”, ***Advances in Bioinformatics***, Vol. 2015, (2015). DOI: 10.1155/2015/198363
2. Dai, J., Liu, Y., Chen, j., and Liu, X., “Fast feature selection for interval-valued data through kernel density estimation entropy”, ***International Journal of Machine Learning and Cybernetics***, Vol. 11, (2020), 2607-2624. DOI: 10.1007/s13042-020-01131-5
3. Yang, L. f., Liu, C., Long, H., Ashfaq, R. A. R., He, Y. L., “Further improvements on extreme learning machine for interval neural network”, ***Neural Computing & Applications***, Vol. 29, (2018), 311-318. DOI: 10.1007/s00521-016-2727-4
4. Safaria, A., Hosseini, R., Mazinani, M., “A novel type-2 adaptive neuro fuzzy inference system classifier for modelling uncertainty in prediction of air pollution disaster”, ***International Journal of Engineering, Transactions B: Applications,*** Vol. 30, (2017), 1746-1751. DOI: 10.5829/ije.2017.30.11b.16
5. Mousavi, S. M., Makui, A., Raissic, S., Mojtahedic, S.M.H., “A multi-criteria decision-making approach with interval numbers for evaluating project risk responses”, ***International Journal of Engineering, Transactions B: Applications,*** Vol. 25, No. 2, (2012) 121-129. DOI: 10.5829/idosi.ije.2012.25.02b.05
6. Taheri, A. A., Taghilou, M., “Towards a Uncertainty Analysis in Thermal Protection using Phase-change Micro/Nano Particles during Hyperthermia”, ***International Journal of Engineering, Transactions A: Basics***, Vol. 34, No. 1, (2021), 263-271. DOI: 10.5829/ije.2021.34.01a.29
7. Moore, R. E., Interval analysis. Prentice-Hall, Englewood liffs, 1966.
8. Sunaga, T, “Theory of an interval algebra and its applications to numerical analysis”, ***Japan Journal of Industrial and Applied Mathematics***, Vol. 26, (2009), 125-143. DOI: https://doi.org/10.1007/BF03186528
9. Yeung, D. S., Ng, W. W.Y., Wang, D. F., Tsang, E. C. C., Wang, X. Z., “Localized generalization error model and its application to architecture selection for radial basis function neural network”, ***IEEE Transactions on Neural Networks***, Vol.18, (2007), 1294-1305. DOI: 10.1109/TNN.2007.894058
10. Tsang, E. C. C., Wang, X. Z and Yeung, D. S., “Improving learning accuracy of fuzzy decision trees by hybrid neural networks”, ***IEEE Transactions on Fuzzy Systems***, Vol. 8, (2000), 601-614. DOI: 10.1109/91.873583
11. Kameli, A., Javadian, N., Daghbandan, A., “Multi-period and Multi-objective Stock Selection Optimization Model Based on Fuzzy Interval Approach”, ***International Journal of Engineering, Transactions C: Aspects***, Vol. 32, (2019), 1306-1311. DOI: 10.5829/ije.2019.32.09c.11
12. Roque, A. M. S., Mate, C., Arroyo, J., and Sarabia, A. N., “IMLP: Applying multi-layer perceptrons to interval-valued data”, ***Neural Processing Letters***, Vol. 25, (2007), 157-169. DOI: 10.1007/s11063-007-9035-z
13. Bock, H. H., and Diday, E., Analysis of Symbolic Data: Exploratory Methods for Extracting Statistical Information from Complex Data. Springer: Berlin Heidelberg, 2000.
14. Carvalho, F. D. A. T. D., “Fuzzy c-means clustering methods for symbolic interval data”, ***Pattern Recognition Letters***, Vol. 28, (2007), 423-437. DOI: 10.1016/j.patrec.2006.08.014
15. Carvalho, F. d. A. T. d., Souza, R. M. C. R. d., and Bezerra, L. X. T., "A Dynamical Clustering Method for Symbolic Interval Data Based on A Single Adaptive Euclidean Distance," in 9th Brazilian Symposium on Neural Networks (SBRN'06), Ribeirao Preto, Brazil., (2006). DOI: 10.1109/SBRN.2006.2
16. D’Urso, P., Massari, R., Giovanni, L. D., Cappelli, C., “Exponential distance-based fuzzy clustering for interval-valued data”, ***Fuzzy Optimization and Decision Making,*** Vol. 16, (2017), 51-70. DOI: 10.1007/s10700-016-9238-8

17. Feng, G., Ni, M., Yan, W.,Xu, J., "A Preferential Interval-Valued Fuzzy C-Means Algorithm for Remotely Sensed Imagery Classification", ***International Journal of Fuzzy Systems***, Vol. 21, (2019), 2212-2222. DOI: 10.1007/s40815-019-00706-x

18. Galdino, S., Maciel, P., "hierarchical cluster analysis of interval-valued data using width of range euclidean distance", in IEEE Latin American Conference on Computational Intelligence (LA-CCI) 2019, (2019). DOI: 10.1109/LA-CCI47412.2019.9036754.

19. Jeng, I. T., Chen, C. M., Chang, S. C., Chuang, C. C., "IPFCM clustering algorithm under euclidean and hausdorff distance measure for symbolic interval data", ***International Journal of Fuzzy Systems,*** Vol. 21, (2019), 2102-219. DOI: 10.1007/s40815-019-00707-w

20. Silva, A. P. D., Filzmoser, P., Brito, P.," Outlier detection in interval data", ***Advances in Data Analysis and Classification***, Vol. 12, (2018), 785-822. DOI: 10.1007/s11634-017-0305-y

21. Rizo Rodríguez, S. I., de Assis Tenório de Carvalho, F., "A new fuzzy clustering algorithm for interval-valued data based on City-Block distance," in IEEE International Conference on Fuzzy Systems (FUZZ-IEEE), (2019). DOI: 10.1109/FUZZ-IEEE.2019.8859017.

22. Ichino, M., Yaguchi, H., Diday, E., A fuzzy symbolic pattern classifier. In: Ordinal and symbolic data analysis. Diday E., et al. (Eds.) Springer, Berlin, 1996.

23. De Carvalho, S. R. M. C., and Frery, A. C., "Symbolic approach to SAR image classification", in IEEE International Geoscience and Remote Sensing Symposium (IGARSS'99), Hamburg, Germany., (1999). DOI: 10.1109/IGARSS.1999.774617.

24. D'Oliveira, S., De Carvalho, F. A. T., Souza, R. M. C. R. D., "Classification of SAR Images Through a Convex Hull Region Oriented Approach", in 11th International Conference on Neural information processing, (2004). DOI: 10.1007/978-3-540-30499-9_118

25. Ciampi, A., Diday, E., Lebbe, J., Perinel, E., and Vignes, R., "Growing a tree classifier with imprecise data", ***Pattern Recognition Letters***, Vol. 21, (2000), 787-803. DOI: 10.1016/S0167-8655(00)00040-4

26. Singh, P., Huang, Y. P., "A four-way decision-making approach using interval-valued fuzzy sets, rough set and granular computing: a new approach in data classification and decision-making", ***Granular Computing***, Vol. 5, (2020), 397-409. DOI: 10.1007/s41066-019-00165-7

27. Kowalski, P. A., Kulczycki, P., "Interval probabilistic neural network", ***Neural Computing and Applications***, Vol. 28 (2017), 817-834. DOI: 10.1007/s00521-015-2109-3

28. Rossi, F., and Conan-Guez, B., "Multi-layer perceptrom interval data", In: Classification, Clustering, and Data Analysis. Studies in Classification, Data Analysis, and Knowledge Organization, Jajuga K., Sokołowski A., Bock H. H., (Eds.) Springer, Berlin, Heidelberg., (2002). DOI: 10.1007/978-3-642-56181-8_47

29. Mali, K., and Mitra, S. "Symbolic classification, clustering and fuzzy radial basis function network", ***Fyzzy Sets and Systems***, Vol. 152, (2005), 553-564. Doi: https://doi.org/10.1016/j.fss.2004.10.001

30. Appice, A., D'Amato, C., Esposito, F., and Malerba, D. "Classification of symbolic objects: A lazy learning approach", ***Intelligent Data Analysis***, Vol. 10, (2006), 301-324. DOI: 10.3233/IDA-2006-10402

31. De Souza, R. M. C. R., Queiroz, D. C. F. and Cysneiros, F. J. A., "Logistic regression-based pattern classifiers for symbolic interval data", ***Pattern Analysis and Applications,*** Vol. 14, (2011), 273-282. DOI: 10.1007/s10044-011-0222-1

32. Huang, G. B., Zhu, Q. Y., Siew, and C. K., "Extreme learning machine: theory and applications", ***Neurocomputing***, Vol. 70, (2006), 489-501. DOI: 10.1016/j.neucom.2005.12.126

33. Huang, G. B., Wang, D. H., and Lan, Y., "Extreme learning machines: A survey", ***International Journal of Machine Learning and Cybernetics***, Vol. 2, (2011), 107-122. DOI: 10.1007/s13042-011-0019-y

34. Huang, G., Zhou, H., Ding, X., and Zhang, R., "Extreme learning machine for regression and multiclass classification", ***IEEE Transactions on Systems, Man, and Cybernetics, Part B (Cybernetics)***, Vol. 42, (2012), 513-529. DOI: 10.1109/TSMCB.2011.2168604.

35. Chetwynd, D., Worden, K., and Manson., G., "An Application of Interval- Valued Neural Networks to a Regression Problem", in Proceedings of the Royal Society A, Mathematica, Physical and Engineering Sciences, (2006). DOI: https://doi.org/10.1098/rspa.2006.1717

36. Adam, S. P., Likas, A. C., and Vrahatis, M. N., "Evaluating generalization through interval-based neural network inversion", ***Neural Computing and Applications***, Vol. 31, (2019), 9241-9260. DOI: 10.1007/s00521-019-04129-5

37. Carvalho, F. A. T., Brito, P., and Bock., H. H., "Dynamic clustering for interval data based on L2 distance", ***Computational Statatistics***, Vol. 21, (2006), 231-250. DOI: https://doi.org/10.1007/s00180-006-0261-z

38. De Carvalho, J. T., Pimentel, L. X., Bezerra T., de Souza, R. M. C. R., "Clustering Symbolic Interval Data Based on a Single Adaptive Hausdorff Distance", in IEEE International Conference on Systems, Man and Cybernetics, Montreal, QC, Canada, (2007). DOI: 10.1109/ICSMC.2007.4413616.

39. De Souza, R. M. C. R., De Carvalho, F. A. T., Pizzato, D. F., "A Partitioning Method for Mixed Feature-Type Symbolic Data Using a Squared Euclidean Distance," in 29th Annual German Conference on Artificial Intelligence (KI2006), Bremen (Alemanha). Lecture notes on artificial intelligence—LNAI, vol 4314. Springer, Berlin, (2006). DOI: 10.1007/978-3-540-69912-5_20

40. Yu, H., "Network complexity analysis of multilayer feedforward artificial neural networks", ***Studies in Computational Intelligence***, Vol. 268, (2010), DOI: 10.1007/978-3-642-10690-3_3

41. Ahmadian, A. M., Zirwas, W., Ganesan, R. S., Panzner, B., "Low Complexity Moore-Penrose Inverse for Large CoMP Areas with Sparse Massive MIMO Channel Matrices", in IEEE 27th Annual International Symposium on Personal, Indoor, and Mobile Radio Communications (PIMRC), (2016), DOI: 10.1109/PIMRC.2016.7794773.

Persian Abstract

چکیده

داده‌های فاصله‌ای معمولاً در موقعیت‌هایی مورد استفاده قرار می‌گیرند که عدم صحت و تغییرپذیری وجود دارد. در این مقاله یادگیری شبکه عصبی ELM برای طبقه‌بندی داده‌های بازه‌ای ارائه شده است. IELM مانند ELM، دو مرحله دارد. در مرحله اول ، وزن‌های اتصال لایه ورودی و لایه پنهان به طور تصادفی تولید می‌شوند و در مرحله دوم، ELM برای تعیین وزن‌های بین لایه پنهان و لایه خروجی به کمک شبه معکوس، از روش Moore–Penrose استفاده می‌کند. در این مقاله چهار روش طبقه‌بندی برای مدیریت داده‌های فاصله‌ای مبتنی بر شبکه عصبی ELM پیشنهاد شده است. مورد اول از یک نقطه میانی فواصل برای هر مقدار ویژگی استفاده می‌کند سپس شبکه عصبی ELM کلاسیک طبقه‌بندی را انجام می‌دهد. مورد دوم هر مقدار ویژگی را به عنوان یک جفت ویژگی کمی در نظر می‌گیرد و از یک شبکه عصبی ELM کلاسیک برای طبقه‌بندی استفاده می‌کند. مورد سوم از طریق رئوس آن ویژگی‌های فاصله را نشان می‌دهد و همچنین یک شبکه عصبی ELM کلاسیک برای طبقه‌بندی بکار می‌رود. مورد چهارم هر بازه را به عنوان یک جفت ویژگی کمی در نظر می‌گیرد، بعد از آن دو شبکه عصبی ELM جداگانه بر اساس حد بالا و حد پایین آموزش می‌بینند و سپس نتایج را به طور مناسب ترکیب می‌کند. الگوریتم‌ها روی مجموعه داده‌های مصنوعی و واقعی آزمایش شده‌اند. مجموعه داده‌های مصنوعی برای تعیین تعداد گره‌های لایه پنهان در شبکه عصبی ELM اعمال می‌شود. میزان خطای طبقه‌بندی به عنوان معیار مقایسه در نظر گرفته شده است. میزان خطای به دست آمده برای هر چهار روش پیشنهادی به ترتیب ۱۹.۱۶۷٪ ، ۱۵٪ ، ۶.۵۳۶٪ و ۱۸.۳۳۳٪ است. آزمایش‌ها سودمندی این طبقه‌بندها را برای طبقه‌بندی داده‌های بازه‌ای نشان می‌دهد.

IJE TRANSACTIONS B: Applications Vol. 34, No. 11, (November 2021) 2557-2565

International Journal of Engineering

Journal Homepage: www.ije.ir

Flexural Strength and Behavioral Study of High-performance Concrete Beams using Stress-Block Parameters

A. I. A. Momin*[a], R. B. Khadiranaikar[b], A. A. Zende

[a] *Department of Civil Engineering, BLDEA's Vachana Pitamaha Dr. P.G Halakatti College of Engineering and Technology Vijayapur, Affiliated to VTU, Belagavi, Karnataka, India*
[b] *Department of Civil Engineering, Basaveshwar Engineering College, Bagalkot, Affiliated to VTU, Belagavi, Karnataka, India*

P A P E R I N F O

Paper history:
Received 18 August 2021
Received in revised form 13 September 2021
Accepted 23 September 2021

Keywords:
Concrete Structures
Strain
Experimental Testing
Structural Element
High-strength Concrete

A B S T R A C T

Most of the existing codes are using stress block parameters which were derived for normal strength concrete. Rectangular stress-block parameters used for normal strength concrete cannot be used safely for higher grade concrete like high-strength concrete (HSC). Hence, new stress-block parameters are established from the experimental investigations. Theses parameters can be made very much useful in the design of HPC members. Present research aims at behaviour study of HPC using stress block parameters. High performance concrete single span beams were tested under monotonic four-point bending. Considering the experimental stress-strain curves of HPC for grade 60, 80 and 100 MPa, an idealized stress block curve is established and the stress block parameters are derived. Based on the idealized stress block curve, the equations for ultimate moment of resistance, depth of neutral axis, limiting moment of resistance and maximum depth of neutral axis are proposed. Based on the observation of experimental load deformation curves, an ideal load deformation curve is proposed, which follows four significant events identified as, first cracking, yielding of reinforced steel, crushing of concrete with spalling of cover and ultimate failure. The predicted values compare well with the experimental values. The average location of the first crack observed was at 0.535 times the span of the beam from the left support of the observer in the tension zone.

doi: *10.5829/ije.2021.34.11b.18*

NOMENCLATURE

f_{ck}	Characteristic strength strength of concrete	ϵ_{cu}	Ultimate compressive strain
A_{st}	Area of tension steel	f_y	Characteristic strength of steel
ρ	Percentage of tension reinforcement	M_{ulim}	Limiting Moment of resistance
ρ_b	Balanced reinforcement	$M_{u,pred}$	The predicted ultimate moment of resistance
ρ/ρ_b	Longitudinal tension reinforcement ratio	$M_{u,exp}$	experimental ultimate moment
k_1, k_2 and k_3	Stress factor, Centroid factor and Area factor respectively	P_u	Ultimate load at failure of specimen
x_u	Depth of neutral axis	P_f	Load corresponding to first visible crack
$\overline{x}$	Depth of centre of compression from extreme compression fibre	δ_f	Deflection corresponding to first visible crack
C_u	Compressive force	ω_f	Crack width at failure
M_u	Ultimate moment of resistance	$\delta_{s,exp}$	Deflection at service load
b	Width of the section	$\omega_{s,exp}$	Crack width at service load
d	Depth of the section	T_u	Tension force
$\boldsymbol{\epsilon_c}$	Compressive strain at 85% of ultimate moment	$\boldsymbol{\epsilon_s}$	Tensile strain at 85% of ultimate moment

1. INTRODUCTION

The innovation in concrete technology has made use of concrete with increasing compressive strength and hence special type of concretes like High-Strength Concrete (HSC) and High-Performance Concrete (HPC) were developed. HPC exhibits improved properties for the required performance with long-term serviceability as

*Corresponding Author Institutional Email: cv.momin@bldeacet.ac.in (A. I. A. Momin)

Please cite this article as: A. I. A. Momin, R. B. Khadiranaikar, A. A. Zende, Flexural Strength and Behavioral Study of High-performance Concrete Beams using Stress-Block Parameters, International Journal of Engineering, Transactions B: Applications, Vol. 34, No. 05, (2021) 2557-2565

compared to conventional concrete and HSC, [1,2]. HPC has many advantages as compared to conventional concrete. HPC could also be advantageously used in the construction of columns, beams, slabs, piles etc. The use of HPC shall result in reduction of structure size, increases available space and also reduce the overall dead loads on the foundation of the structure. HPC can specially be used effectively for structures exposed to severe environments, because of low permeability and high resistance to various environmental factors [3,4]. The results of some of the researchers on conventional concrete in various design codes are not entirely applicable, which are limited to a maximum of 55 MPa strength. It is also not safe and adequate to use the results of conventional concrete having compressive strength less than 55 MPa for designing HPC beams. The flexural behavior of RC structures made of conventional strength concrete is limited due to excessive cracking and deflection, and the structures cast by conventional concrete may later be structurally inadequate. In case of HSC, both early and ultimate strength are higher as compared to conventional concrete. But the durability criteria are not addressed directly in HSC so that it may or may not yield higher durability. As compared to HSC, HPC has improved mechanical properties.

The flexural behavior of reinforced HPC is better compared to reinforced NSC or HSC. Hence, it is essential to investigate the behavior of HPC under flexure. A systematic investigation on the design recommendations of various codes for determination of strength of HPC beams in flexure is essential.

It is seen from the past literature that most of the standard codes are applicable to normal strength concrete, whereas, for higher grades of concrete these methods involving different stress block parameters cannot be extrapolated to use in the design. To study the flexural behavior of HSC, many researchers have proposed stress block parameters validating their experimental results and suggested some major modifications in different codes [5-8]. The stress block parameters are also proposed for special concrete like Geopolymer concrete (GPC) [9]. It is also not known that these stress block parameters proposed for HSC/GPC may or may not be applicable for HPC [10]. The ultimate strain of concrete as suggested by 441-R96 [11] is 0.003 whereas Eurocode-2 [12], Canadian code [13] and Indian Standard Code [14] limits it to 0.0035.

2. METHODOLOGY

The present study focuses on investigating the behaviour of single-span reinforced HPC beams experimentally tested under monotonic four-point bending test as shown in Figure 1. The HPC beams are rectangular in cross-section having width of 150mm and effective length of

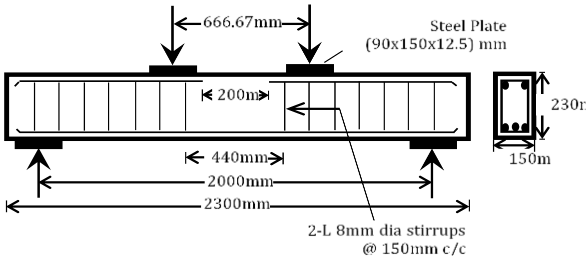

Figure 1. Details of the beam specimen

2000mm. The overall depth of the beam considered was 260mm for 60MPa and 100MPa and 300mm for 80MPa. A total of 12 beams as detailed in Table 1 of single span were cast by varying percentage of longitudinal tension steel, for three compressive strengths of concrete. In order to develop pure flexural behaviour in the beam section, stirrups are not provided between sections having constant moment [15-17]. These beams are grouped as 60SB1, 60SB2, 60SB3 and 60SB4 indicating M_{60} HPC beams, 80SB1, 80SB2, 80SB3 and 80SB4 indicating M_{80} HPC beams, 100SB1, 100SB2, 100SB3 and 100SB4 indicating M_{100} HPC beams.

Firstly, to study the behaviour of HPC beams, idealized stress block curve is established and the stress block parameters were derived. Based on the idealized stress block curve, the equations for ultimate moment of resistance, depth of NA, limiting moment of resistance and maximum depth of Neutral Axis (NA) are predicted for HPC. From the predicted equations, the flexural resistance and NA depth variation are determined and validated with the experimental values. The study also covers the variation of load deformation response and the crack pattern. The beam under investigation were designed using ACI-318 [18] in order to achive under reinforced section. The beams were loaded and tested as per IS:516-1959 [19]. The testing of beam specimens was carried out for pure flexure test using a loading frame of 2500 kN capacity. The beam at supports and at loading points is provided with steel plate of size 90mm x 150mm x 12.5mm for uniform distribution of stress. The linear variable differential transformer (LVDT's) of gauge length 30mm were attached at the centre of the specimen along the depth of the beam to locate the neutral axis and to measure strains. The deflections of the beam at the centre of the span were also measured by means of LVDT of gauge length 50mm supported over a stand. The load was applied through hydraulic jack and was measured through the load cell of capacity 500 kN. The data were recorded using 24-channel data logger.

3. STRESS BLOCK PARAMETERS

Different national codes have different stress block parameters and most of them deal with a compressive

TABLE 1. Details of HPC beam specimens in pure flexure for experimental program

Beam Designation	f_{ck}	Longitudinal Tension Steel (mm)	A_{st} (mm^2)	ρ	ρ_b	$\frac{\rho}{\rho_b}$
60SB1	83.89	2 # 12	226.19	0.78	4.76	0.16
60SB2	85.44	2 # 10+1# 12	270.16	0.93	4.85	0.19
60SB3	84.56	2 # 16+1# 10	480.66	1.69	4.80	0.35
60SB4	85.43	2 # 16+2# 10	559.20	1.97	4.84	0.40
80SB1	89.93	2 # 12 + 1# 10	304.72	0.77	5.10	0.15
80SB2	89.01	3 # 12	339.2	0.86	4.98	0.17
80SB3	87.76	2 # 10+1# 16	358.0	0.91	5.06	0.18
80SB4	89.31	2 # 12+1# 16	427.24	1.09	5.05	0.21
100SB1	105.65	2 # 12	226.19	0.78	5.99	0.13
100SB2	107.25	2#10 + 1# 12	270.16	0.93	6.08	0.15
100SB3	108.12	2 # 16+1# 10	480.66	1.69	6.13	0.27
100SB4	104.34	2 # 16+2# 10	559.20	1.97	5.92	0.33

strength less than 50 MPa. Therefore, an attempt made to derive the stress block parameters for HPC.

From the experimental data, an idealized stress block curve for HPC are established. To arrive at idealized stress block curve for HPC, three strength ranges of concrete are considered. From the behavior observed in experiments, literature survey and graphical representation for each grade of concrete as mentioned above, best fitting polynomial curves were drawn for each grade of concrete as shown in Figure 2. From these curves an idealized stress block curve is derived, which is as shown in the Figure 3. The coefficients such as k_1, k_3 and k_2 corresponds to stress factor, area factor and centroid factor, respectively. The value of k_1 is considered on the basis of average of values of stress at ultimate strain and its approximation was verified by literature survey [10]. There is no significant difference in the approximation and values available in the literature. The k_3 and k_2 are derived from assumed stress block and in most cases the approximation of their values holds phenomenally similar to most of literature study.

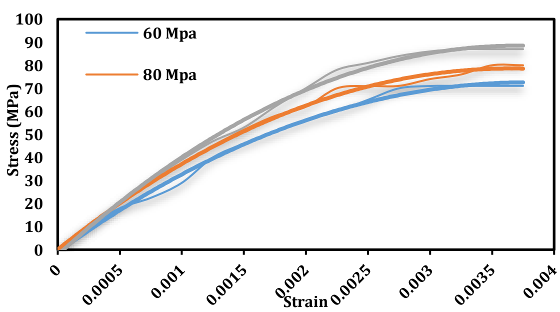

Figure 2. Stress-Strain Curve for HPC

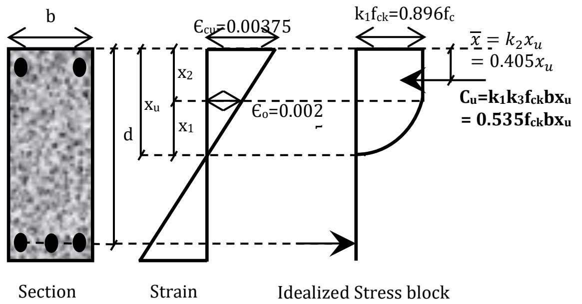

Figure 3. Equivalent Stress Block Parameters for Rectangular HPC Sections

Using the strain diagram, the depth x_1 and x_2 are found as

$$x_1 = \frac{2}{3}x_u \text{ and } x_2 = \frac{1}{3}x_u \tag{1}$$

The stress factor k_1 is the average of stresses under ultimate strain observed from experimental results conducted on three different grades of concrete and the area factor k_3 is found by determining the area of stress block and are given by Equation (2).

$$k_1 = 0.896 \text{ and } k_3 = 0.777 \tag{2}$$

The depth of centre of compression from extreme compression fibre is obtained by taking moment of area about extreme fibre as given in Equation (3).

$$\bar{x}=0.405x_u \tag{3}$$

Thus, from Equation (3), the centroid factor k_2 is given by Equation (4).

$$k_2 = 0.405 \tag{4}$$

Using the coefficients k_1, k_2, k_3 and considering partial safety factor of 1.3, the total compressive force is obtained as given in Equation (5).

$$C_u = 0.535 f_{ck} b x_u \tag{5}$$

The flexural strength of reinforced HPC beam section from the above stress block parameters is obtained by taking moment of C_u or T_u as given in Equation (6).

$$\begin{aligned} M_u &= 0.535 f_{ck} b x_u (d - 0.405 x_u) \\ M_u &= 0.87 f_y A_{st} d \left(1 - 0.658 \frac{A_{st} f_y}{f_{ck} b d}\right) \end{aligned} \tag{6}$$

Finally, the proposed equations and stress block parameters obtained as per the present study are summarized in Table 2.

TABLE 2. Proposed Equations and Stress block parameters

Parameter	Equation/ Value
Stress factor k_1	k_1=0.896
Centroid factor k_2	k_2=0.405
Area factor k_3	k_3=0.777

Flexural strength of reinforced HPC beam	$M_u = 0.535 f_{ck} b x_u (d - 0.405 x_u)$ $M_u = 0.87 f_y A_{st} d \left(1 - 0.658 \frac{A_{st} f_y}{f_{ck} b d}\right)$	
Depth of NA	$x_u = \frac{0.87 f_y A_{st}}{0.535 f_{ck} b}$	(7)
Limiting Moment of resistance	$M_{ulim} = 0.1934 f_{ck} b d^2$	(8)

4. ULTIMATE STRAIN OF CONCRETE IN COMPRESSION

To measure strain at extreme compression fibre, LVDT was attached at the extreme top fibre at the centre of the HPC beam specimens as shown in Figure 4. The ultimate strain of concrete as suggested by most of the design codes varies from 0.0028 to 0.0035 for strength up to 50 MPa. ACI 441-R96 [11] limits the strain to 0.0030 for both NSC and HSC, but it gives conservative moment capacity for HSC beams, up to 126 MPa strength [20]. As per the findings, the ultimate concrete strain for HSC varies between 0.002 to 0.004 or even higher [17]. The ultimate strain of concrete in compression obtained from the experimental tests is presented in Table 3 for HPC beam specimens for varying HPC strength and longitudinal reinforcement ratio. However, it can be observed from Figure 5, the ultimate strain of concrete obtained are much higher and above the range of specified strain values in Indian Standard Code, ACI code and Euro code. Most of the design codes limit the ultimate strain of concrete to 0.0035, since the ultimate strain of concrete is inversely proportional to compressive strength of concrete. ACI 441-R96 [11] limits the strain to 0.0030 for both NSC and HSC. However, it may not be conservative for higher strength of concrete [11].

This is because of the fact that, as the strength of the concrete increases, the concrete becomes more brittle, and hence takes lesser strain. [21-22]. But, the literature available related to HSC/ HPC are of the view that the ultimate strain is higher than the specified values in design codes. In the present investigation, the specimen tested provided the values much similar to that of available literature on HSC/ HPC. An average ultimate concrete strain of 0.0034, 0.00362 and 0.0038 was obtained for the three ranges of concrete considered in the present investigation.

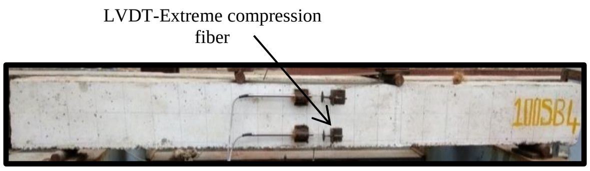

Figure 4. Beam specimen with LVDT to measure ultimate strain for HPC beam specimens

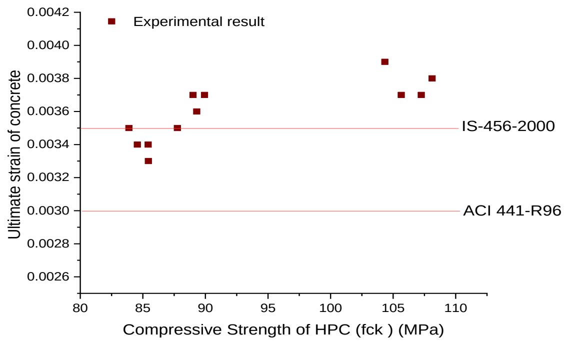

Figure 5. Ultimate strain of concrete for different strength of HPC

5. FLEXURAL RESISTANCE OF HPC BEAMS

The flexural resistance of single span HPC beam specimens tested was predicted by using the stress block parameters developed for HPC. The predicted ultimate moment of resistance ($M_{u,pred}$) determined from Equation (6), is validated with the experimental ultimate moment ($M_{u,exp}$). Table 3 provides the details of strength of concrete, section parameters, percentage of tension reinforcement, ultimate load at failure of specimen, neutral axis and ultimate moment from both experimental and theoretical observations.

The ratio of values of experimental ultimate moment of resistance and theoretical values are determined. It is observed that moment of resistance calculated from stress block curve varies between 0.8 to 1.02 times of experimental values of ultimate moment at failure. Figure 6 indicates the variation of M_u/M_{exp} ratio with varying percentages of tension reinforcement and characteristic

TABLE 3. Flexural Test results for HPC beam specimens

Beam Designation	D (mm)	ϵ_{cu}	Pu (kN)	x_u (mm)	$M_{u,exp}$ (kN-m)	$M_{u,pred}$ (kN-m)	$M_{u,pred}/M_{u,exp}$
60SB1	191	0.0035	71	15.23	23.67	18.95	0.80
60SB2	192	0.0033	85	17.86	28.33	22.62	0.80
60SB3	189	0.0034	124	32.10	41.53	38.34	0.92
60SB4	189	0.0034	145	36.96	48.50	44.10	0.91
80SB1	261	0.0037	117	19.14	39.30	34.97	0.89
80SB2	261	0.0035	127	21.53	42.33	38.79	0.92
80SB3	262	0.0036	121	23.05	40.33	41.01	1.02
80SB4	261	0.0037	150	27.02	50.13	48.42	0.97
100SB1	191	0.0037	71	12.09	23.83	19.08	0.80
100SB2	192	0.0037	84	14.23	28.17	22.80	0.81
100SB3	189	0.0038	144	25.11	48.23	38.95	0.81
100SB4	189	0.0039	154	30.27	51.53	44.79	0.87

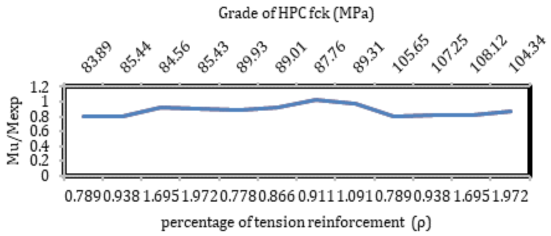

Figure 6. Variation of M_u/M_{exp} with percentage of tension reinforcement and grade of concrete for HPC beam specimens

strength of concrete. The variation of ratio M_u/bd^2 with the percentage of tension reinforcement for both predicted and experimental moment of resistance for first grade of HPC is shown in Figure 7. It can be observed that the variation closely matches the predicted moment of resistance determined from the stress block parameters developed for the HPC. Similar variation is observed for other two strengths.

6. LOAD DEFLECTİON VARIATION

The experimental load vs deflection curves are presented in Figures 8-10. It was observed that the deformation capacity for some of HPC beams decreased as tension steel reinforcement increased at approximately the same load level.

Thus, it can be proposed that, ductility can be increased by decreasing the tension steel reinforcement as the longitudinal steel reinforcement ratio dominates more than concrete strength. An ideal load-deformation curve considering all the beam specimens is proposed as shown in Figure 11. This curve shows an idealized behaviour of all HPC beams with four distinct segments [23] separated by four significant events, which occurred during the experimental work. These are denoted as A, B, C and D in the ideal curve identified as first cracking, yielding of reinforced steel, crushing of concrete with spalling of cover and ultimate failure, respectively. The

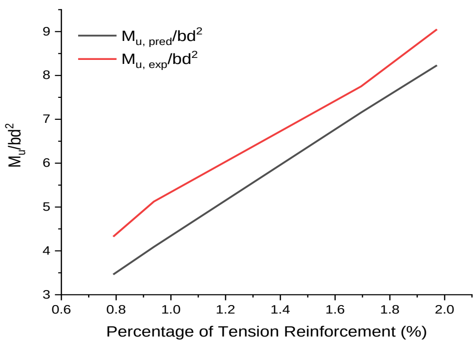

Figure 7. Variation of M_u/bd^2 with percentage of tension reinforcement for M_{60} grade HPC beam specimens

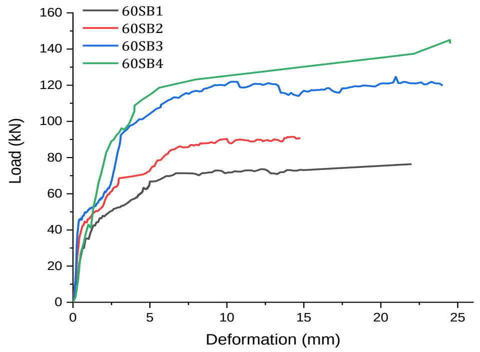

Figure 8. Load-deflection curve for M_{60} grade

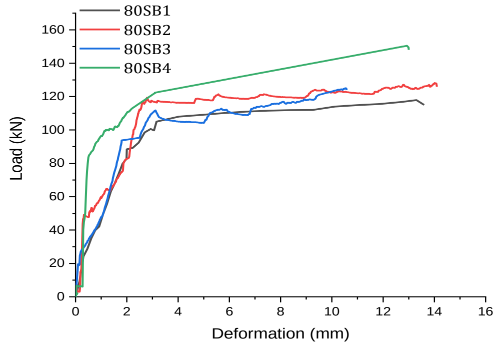

Figure 9. Load-deflection curve for M_{80} grade

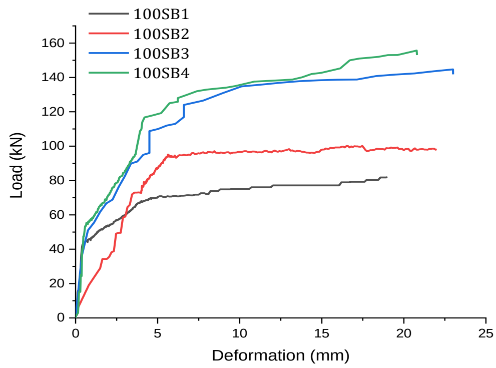

Figure 10. Load-deflection curve for M_{100} grade

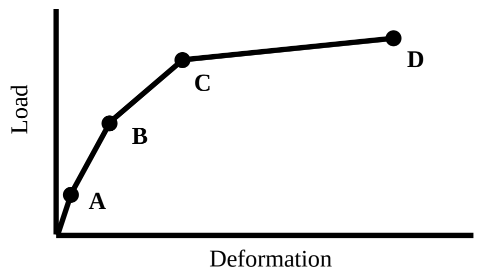

Figure 11. Ideal load-deflection curve for HPC beam specimens

zones A and B are due to the reduced beam stiffness while the other two zones cause reduction in the load applied. A similar behaviour is observed in all the beams. The beam models selected for experimental testing designed as under-reinforced were actually under-reinforced after experimental testing.

The load, deflection and location corresponding to first visible crack and the deflection at failure observed from the experimental testing of beams are presented in Table 4. The location of the first crack is measured with respect to the left support of the observer. It is observed that the load corresponding to first visible crack increased with an increase in the percentage of longitudinal tension steel for the same grade of HPC. The load corresponding to first visible crack also increased for HPC beam specimens. It was also observed that the first crack started in the constant moment zone for all the beam specimens with the average location of 0.535 L from the left support of the observer in the tension zone. Based on the results of Table 4 and from the crack pattern observed for all the beam specimens tested experimentally, the failure started in the tension zone with an average of 81.56% of ultimate load for HPC beam specimens. The first cracking load increased with an increase in the longitudinal reinforcement ratio. On further loading, the crack propagated due to yielding of reinforcing steel followed by crushing of concrete with spalling of cover in compression zone and finally the load carrying capacity was lost with formation of network of cracks.

7. CRACK PROPAGATION

The crack pattern and failure modes of HPC beams tested for all the three grades of concrete are shown in Figures 12 to 14. After applying the load on the test specimens, a few hair cracks were observed first and as the load increased, the first crack appeared in the centre of the specimens at the average location of 0.535 L from the left support. These cracks appeared at the bottom fibres and propagated diagonally towards the top fibres and support. As the load increased, the cracks started propagating towards the supports due to increased shear stress. Many researchers have observed the similar natured of propagation of cracks on high strength beams [23, 25]. As the frequency of loading increased, the micro cracks appeared on the beams fall to macro cracks with crack-width at failure load reaching up to 2.6 mm for the specimen 60SB3.

TABLE 4. Flexural Test results for HPC beam specimens

Beam Designation	P_f (kN)	δ_f (mm)	Location	ω_f (mm)	$\delta_{s,\,exp}$ (mm)	$\omega_{s,\,exp}$ (mm)
60SB1	66.7	5.00	0.465 L	2.7	1.29	0.45
60SB2	71.4	4.75	0.640 L	2.5	1.42	0.40
60SB3	109	5.70	0.389 L	2.6	2.68	0.45
60SB4	115	5.60	0.677 L	2.1	2.95	0.30
80SB1	105	3.16	0.340 L	2.3	1.77	0.35
80SB2	117	3.30	0.370 L	2.4	1.80	0.35
80SB3	95.3	2.50	0.380 L	2.2	1.45	0.35
80SB4	122	3.10	0.670 L	2.0	0.70	0.30
100SB1	70.3	5.00	0.735 L	1.6	0.41	0.25
100SB2	94.0	6.22	0.660 L	1.4	2.75	0.35
100SB3	124	6.60	0.410 L	1.3	3.13	0.25
100SB4	128	6.23	0.680 L	1.7	3.34	0.30

(a) 60SB1

(b) 60SB1

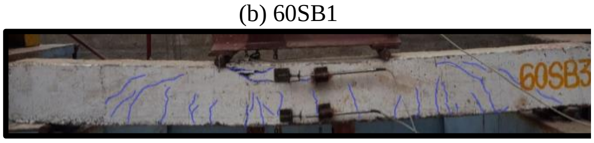

(c) 60SB3

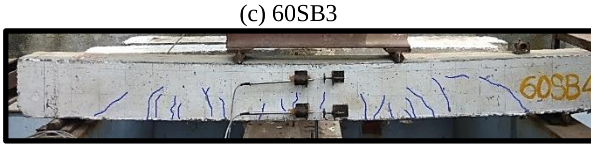

(d) 60SB4

Figure 12. Crack pattern and failure modes for M_{60} grade

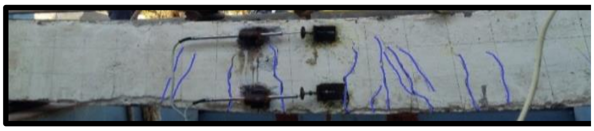
(a) 80SB1

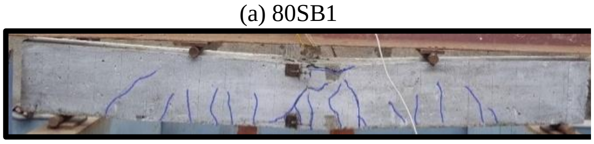
(b) 80SB2

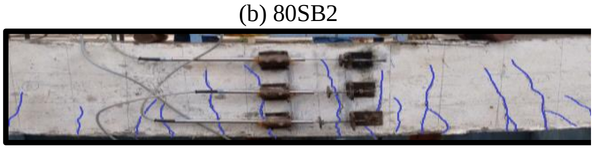
(c) 80SB3

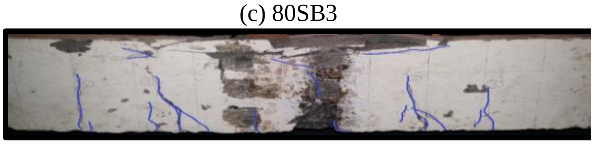
(d) 80SB4

Figure 13. Crack pattern and failure modes for M_{80} grade

(a) 100SB1

(b) 100SB2

(c) 100SB3

(d) 100SB4

Figure 14. Crack pattern and failure modes for M_{100} grade

To obtain the service loads, factor of safety of 1.70 is adopted for the ultimate experimental load [17-18] and the corresponding deflections are obtained. The service load deflections for the tested HPC beams varied from 1.29 to 2.95, 0.70 to 1.80 and 0.41 to 3.34 for strength of 60, 80 and 100 MPa, respectively. The observed deflections are in the range of 0.41 mm to 3.34 mm and are based on only short-term loadings without considering the factors such as shrinkage and creep. The width of the cracks observed at service load during experimental testing ranges from 0.25 to 0.45. The width of the cracks is within the limits as suggested by the design codes at service loads i.e., 2 mm to 5 mm [18].

8. CRACK WIDTH

The crack widths observed during the experimental testing at ultimate load are presented in Table 4. During the testing programme, it was observed that all the HPC beams showed vertical cracks or flexural cracks before to failure. The propagation of cracks outside the pure bending zone were also similar to flexural cracks. From Table 4, it is clear that, as the strength of concrete increases the crack widths reduce due to brittle nature of concrete. However, the variation in the crack width was marginal for varying longitudinal tension reinforcement ratio. Hence, strength of the concrete dominated more than the longitudinal tension reinforcement ratio influencing the crack width. The crack widths of HPC beams can be controlled by the longitudinal tension reinforcement. Increase in the usage of mineral admixtures in concrete while producing HPC makes the concrete dense resulting in a stronger interface zone which reduces the cracks [26].

9. DEFLECTION AND CRACK WIDTHS AT SERVICE LOADS

The mid-span deflection and crack width at service load from experimental test observations are noted and are presented in Table 4.

10. NEUTRAL AXIS DEPTH VARIATION

To study the NA depth variation of HPC, strain-distribution was obtained experimentally at tension reinforcement and at compression zone of concrete. The obtained NA depth from the experimental study is shown in Table 5.

The NA depth was obtained at 85% of ultimate moment. It can be seen from the Table 5, that as the tensile reinforcement ratio increases, the depth of NA also increases for HPC. Considering the cracking load given in Table 4, it was observed that the depth of NA was at mid depth approximately before cracking and just after cracking, the NA depth decreased. At a later stage the NA depth tends to remain the same or decreased slightly. Further, to study the behaviour of NA depth for HPC in more detail, different comparisons were made. The predicted value from the equivalent stress block parameters developed for HPC using Equation (7), is presented in Table 5. From the experimental and predicted results, it can be observed that a lower tensile reinforcement assures a ductile failure for HPC beams for all the three grades of concrete. It can be observed that the experimental NA depth lies in between 0.086 to 0.155 and predicted NA depth lies in between 0.080 to 0.160 for HPC beam specimens. Thus, they are in the same

TABLE 5. Flexural Test results for HPC beam specimens

Beam Designation	X_{pred}/d	X_{exp}/d	$\frac{x_{exp}/d}{x_{umax}/d}$	ϵ_c	ϵ_s
60SB1	0.080	0.086	0.20	0.0030	0.03146
60SB2	0.093	0.097	0.22	0.0028	0.02600
60SB3	0.170	0.181	0.41	0.0029	0.01303
60SB4	0.196	0.188	0.43	0.0029	0.01244
80SB1	0.073	0.082	0.19	0.0031	0.03539
80SB2	0.082	0.096	0.22	0.0030	0.02805
80SB3	0.088	0.091	0.21	0.0031	0.03050
80SB4	0.104	0.108	0.24	0.0031	0.02605
100SB1	0.063	0.069	0.16	0.0031	0.04257
100SB2	0.074	0.076	0.17	0.0031	0.03850
100SB3	0.133	0.137	0.31	0.0032	0.02037
100SB4	0.160	0.155	0.35	0.0033	0.01812

range of, which clarifies that the predicted stress block parameters suit the variation of NA depth for HPC. Many of the researchers have obtained an ultimate strain of more than 0.0035 and as per the present investigation an ultimate strain of 0.00375 was considered for the development of stress block parameters to evaluate the predicted NA depth.

11. CONCLUSIONS

Following conclusions are drawn from the experimental investigations carried out on HPC beams produced using locally mineral admixtures

1. The values obtained for ultimate strain from the experimental results are in line with the literature available on HSC. However, most of the design codes suggest values in the range of 0.003 to 0.0036. The ultimate strains of HPC beams strengths investigated seem to be reasonable with these codes.
2. Rectangular stress-block parameters used for NSC cannot be used safely for higher-grade concrete like HPC. Hence, new stress-block parameters are established from the experimental investigations. Theses parameters can be used in the design of HPC members.
3. Considering the experimental stress-strain curves of HPC for the concrete strengths considered, an idealized stress-block curve is proposed. The equation for moment of resistance of reinforced HPC beams (Equation 6) is derived using the idealized stress block. The moment of resistance of the HPC beam specimens predicted using the proposed equation agree quite closely (12.33% variation) with the experimental flexural strength.
4. Based on experimental load deformation curves, an ideal load-deformation curve is proposed (Figure 11), which follows four significant events identified as, first cracking, yielding of reinforced steel, crushing of concrete with spalling of cover and ultimate failure.
5. The deformation capacity for some of HPC beams decreased as tension steel reinforcement increased at approximately the same load level. Thus, it can be proposed that, ductility can be increased by decreasing the tension steel reinforcement as the longitudinal steel reinforcement ratio dominates more than concrete strength.
6. The width of the cracks observed at service loads during experimental testing was found in between 0.25 to 0.45, and are within the limits as suggested by the design codes. The provisions in some of the design codes overestimate the crack width at service load.
7. The depth of NA for HPC beams increases with increase in the tensile reinforcement ratio. Hence, a lower tensile reinforcement assures a ductile failure for HPC beams for all the three grades of concrete considered.
8. The NA depth are in the same range of (4.65% variation), which clarifies that the predicted stress block parameters suits the variation of NA depth for HPC beams considered.

12. REFERENCES

1. P.C Aitcin, "The durability characteristics of high-performance concrete: A review", ***Cement and Concrete Composites***, Vol. 25, No. 4-5 (2003), 409-420, doi: 10.1016/S0958-9465(02)00081-1
2. M. Madhkhan, P. Saeidian, "Mechanical Properties of Ultra High-Performance Concrete Reinforced by Glass Fibers under Accelerated Aging", ***International Journal of Engineering, B: Applications,*** Vol. 34, No. 05, (2021) 1074-1084, doi: 10.5829/ije.2021.34.05b.01.
3. H. R. Darvishvand, S. A. Haj Seiyed Taghia, M. Ebrahimi, "Utilizing the Modified Popovics Model in Study of Effect of Water to Cement Ratio, Size and Shape of Aggregate in Concrete Behavior", ***International Journal of Engineering, B: Applications***, Vol. 34, No. 02, (2021) 393-402, doi: 10.5829/ije.2021.34.02b.11.
4. S. Yasin Mousavi, A. Tavakkoli, M. Jahanshahi, A. Dankoub, "Performance of High-strength Concrete Made with Recycled Ceramic Aggregates", ***International Journal of Engineering, Transactions C: Aspects***, Vol. 33, No. 6, (2020), 1085-1093, doi: 10.5829/ije.2020.33.06c.05.
5. Togay Ozbakkaloglu, and Murat Saatcioglu, "Rectangular stress block for high-strength concrete", ***ACI Structural Journal***, Vol. 101, No. 4, (2004), 475-483, doi: 10.14359/13333.
6. Karthik, Madhu M., and John B. Mander, "Stress-block parameters for unconfined and confined concrete based on a unified stress-strain model", ***Journal of Structural Engineering***, Vol. 137, No. 2, (2010), 270-273, doi: 10.1061/(ASCE)ST.1943-541X.0000294.
7. Abdeldayem, H., Mohamed Hamdy, M., Brahim, B., "Assessing stress-block parameters in designing circular high-strength concrete members reinforced with FRP bars", ***Journal of Structural Engineering***, Vol. 144, No. 10, (2018), doi: /10.1061/(ASCE)ST.1943-541X.0002173.
8. Singh, B., Patel, V., Ojha, P. N., Arora, V. V., "Analysis of stress block parameters for high strength concrete", ***Journal of Asian Concrete Federation,*** Vol. 6, No. 1, (2020), 1-9, doi: 10.18702/acf.2020.6.6.1.
9. Tran, Tung & Pham, Thong, Hao, Hong, "Rectangular Stress-block Parameters for Fly-ash and Slag Based Geopolymer Concrete", ***Structures***, Vol. 19, (2019), 143-155, doi: 10.1016/j.istruc.2019.01.006.
10. Oztekin, Ertekin, Selim Pul, and Metin Husem, "Determination of rectangular stress block parameters for high performance concrete", ***Engineering Structures***, Vol. 25, No. 3, (2003), 371-376, doi: 10.1016/S0141-0296(02)00172-4.
11. "State of the Art Report on High-Strength Concrete Columns", ACI 441R-1996. American Concrete Institute.
12. "Design of Concrete Structures", Eurocode-2 (1999), European Committee for Standardization, Brussels.
13. "Design of concrete structures", A23.3-94, Canadian Standard Association, Rexdale, Ontario, Canada.
14. "Indian standard code of practice for plain and reinforced concrete for general building construction", IS 456 :2000. Bureau of Indian Standards, New Delhi.
15. Z. R. Aljazaeri, Z. Al-Jaberi, "Numerical Study on Flexural Behavior of Concrete Beams Strengthened with Fiber Reinforced Cementitious Matrix Considering Different Concrete Compressive Strength and Steel Reinforcement Ratio",

International Journal of Engineering, Transactions A: Basics, Vol. 34, No. 04, (2021), 793-802, doi: 10.5829/ije.2021.34.04a.05

16. M. Hajsadeghi, M. Jalali, C. Seong Chin, T. Zirakian, M. Bahrebar, "Flexural Characteristics of Fibre Reinforced Concrete with an Optimised Spirally Deformed Steel Fibre", ***International Journal of Engineering, Transactions C: Aspects***, Vol. 34, No. 6, (2021), 1390-1397, doi: 10.5829/ije.2021.34.06c.01
17. P.S. Kumar, M.A. Mannan, V.J. Kurian and H. Achuytha, "Investigation on the flexural behaviour of high-performance reinforced concrete beams using sandstone aggregates", ***Building and Environment***, Vol. 42, No. 7, (2007), 2622-2629, doi.org/10.1016/j.buildenv.2006.06.015.
18. "Building Code Requirements for Reinforced Concrete", ACI 318-1995, American Concrete Institute, Detroit.
19. "Flexural Strength Test of Concrete", IS 516-1959. Bureau of Indian Standards, New Delhi.
20. M. A. Rashid and M. A. Mansur, "Reinforced High-Strength Concrete Beams in Flexure", ***ACI Structural Journal***, Vol. 102, No. 3, (2005), 462-471.
21. "State of the Art Report on High-Strength Concrete", ACI 363R-1992, American Concrete Institute, Detroit.
22. "High Strength Concrete, State of the Art Report", FIP-CEB (1990), CEB Bulletin information No. 197, FIP State of the Art Report SR 90/1, Thomas Telford Ltd, London.
23. A.A. Momin and R.B. Khadiranaikar, "Experimental and Finite Element Analysis of 80 MPa Two-Span High-Performance Concrete Beam Under Flexure", ***Sustainable Construction and Building Materials***, Vol-25, Chapter-35, (2019), 381-396, doi: 10.1007/978-981-13-3317-0_35.
24. Samir A. Ashour, "Effect of compressive strength and tensile reinforcement ratio on flexural behavior of high-strength concrete beams", ***Engineering Structures***, Vol. 22, No. 5, (2000), 413-423, doi: 10.1016/S0141-0296(98)00135-7.
25. Swamy, R. N. and Anand, K. L, "Structural behavior of high strength concrete beams", ***Building Science***, Vol. 9, No. 2, (1974), 131-141, doi: 10.1016/0007-3628(74)90010-3.
26. Yang EI, Morita S and Seong TY, "Effect of axial restraint on mechanical behavior of high-strength concrete beams", ***ACI Structural Journal***, Vol. 97, No. 5, (2000), 751-756, doi: 10.14359/8810.

Persian Abstract

چکیده

اکثر کدهای موجود از پارامترهای بلوک تنش استفاده می کنند که برای بتن مقاومتی معمولی استخراج شده است. پارامترهای بلوک تنش مستطیلی که برای بتن مقاومتی معمولی استفاده می شود نمی تواند به طور ایمن برای بتن های درجه بالاتر مانند بتن با مقاومت بالا (HSC) استفاده شود. بنابراین ، پارامترهای جدید بلوک تنش از تحقیقات تجربی ایجاد شده است. این پارامترها می توانند در طراحی اعضای HPC بسیار مفید واقع شوند. هدف پژوهش حاضر مطالعه رفتار HPC با استفاده از پارامترهای بلوک تنش است. تیرهای دهانه بتنی با عملکرد بالا تحت خم یکنواخت چهار نقطه ای آزمایش شدند. با درنظر گرفتن منحنی های تنش-کرنش HPC برای درجه ۶۰ ، ۸۰ و ۱۰۰ مگاپاسکال، منحنی بلوک تنش ایده آل ایجاد شده و پارامترهای بلوک تنش مشتق می شوند. بر اساس منحنی بلوک تنش ایده آل ، معادلات لحظه نهایی مقاومت ، عمق محور خنثی ، لحظه محدود کننده مقاومت و حداکثر عمق محور خنثی ارائه شده است. بر اساس مشاهده منحنی های تغییر شکل بار، یک منحنی تغییر شکل بار ایده آل پیشنهاد می شود که چهار رویداد مهم را شناسایی می کند که عبارتند از: اولین ترک خوردگی ، تسلیم فولاد مسلح ، خرد شدن بتن با جوش خوردن پوشش و شکست نهایی. مقادیر پیش بینی شده به خوبی با مقادیر تجربی مقایسه می شود. مکان متوسط اولین ترک مشاهده شده ۰.۵۳۵ برابر طول پرتو از سمت چپ ناظر در منطقه کشش بود.

AIMS AND SCOPE

The objective of the International Journal of Engineering is to provide a forum for communication of information among the world's scientific and technological community and Iranian scientists and engineers. This journal intends to be of interest and utility to researchers and practitioners in the academic, industrial and governmental sectors. All original research contributions of significant value focused on basics, applications and aspects areas of engineering discipline are welcome.

This journal is published in three quarterly transactions: Transactions A (Basics) deal with the engineering fundamentals, Transactions B (Applications) are concerned with the application of the engineering knowledge in the daily life of the human being and Transactions C (Aspects) - starting from January 2012 - emphasize on the main engineering aspects whose elaboration can yield knowledge and expertise that can equally serve all branches of engineering discipline.

This journal will publish authoritative papers on theoretical and experimental researches and advanced applications embodying the results of extensive field, plant, laboratory or theoretical investigation or new interpretations of existing problems. It may also feature - when appropriate - research notes, technical notes, state-of-the-art survey type papers, short communications, letters to the editor, meeting schedules and conference announcements. The language of publication is English. Each paper should contain an abstract both in English and in Persian. However, for the authors who are not familiar with Persian, the publisher will prepare the latter. The abstracts should not exceed 250 words.

All manuscripts will be peer-reviewed by qualified reviewers. The material should be presented clearly and concisely:

- *Full papers* must be based on completed original works of significant novelty. The papers are not strictly limited in length. However, lengthy contributions may be delayed due to limited space. It is advised to keep papers limited to 7500 words.
- *Research* notes are considered as short items that include theoretical or experimental results of immediate current interest.
- *Technical notes* are also considered as short items of enough technical acceptability with more rapid publication appeal. The length of a research or technical note is recommended not to exceed 2500 words or 4 journal pages (including figures and tables).

Review papers are only considered from highly qualified well-known authors generally assigned by the editorial board or editor in chief. Short communications and letters to the editor should contain a text of about 1000 words and whatever figures and tables that may be required to support the text. They include discussion of full papers and short items and should contribute to the original article by providing confirmation or additional interpretation. Discussion of papers will be referred to author(s) for reply and will concurrently be published with reply of author(s).

INSTRUCTIONS FOR AUTHORS

Submission of a manuscript represents that it has neither been published nor submitted for publication elsewhere and is result of research carried out by author(s). Presentation in a conference and appearance in a symposium proceeding is not considered prior publication.

Authors are required to include a list describing all the symbols and abbreviations in the paper. Use of the international system of measurement units is mandatory.

- On-line submission of manuscripts results in faster publication process and is recommended. Instructions are given in the IJE web sites: www.ije.ir-www.ijeir.info
- Hardcopy submissions must include MS Word and jpg files.
- Manuscripts should be typewritten on one side of A4 paper, double-spaced, with adequate margins.
- References should be numbered in brackets and appear in sequence through the text. List of references should be given at the end of the paper.
- Figure captions are to be indicated under the illustrations. They should sufficiently explain the figures.
- Illustrations should appear in their appropriate places in the text.
- Tables and diagrams should be submitted in a form suitable for reproduction.
- Photographs should be of high quality saved as jpg files.
- Tables, Illustrations, Figures and Diagrams will be normally printed in single column width (8cm). Exceptionally large ones may be printed across two columns (17cm).

PAGE CHARGES AND REPRINTS

The papers are strictly limited in length, maximum 6 journal pages (including figures and tables). For the additional to 6 journal pages, there will be page charges. It is advised to keep papers limited to 3500 words.

Page Charges for Papers More Than 6 Pages (Including Abstract)	
For International Author ***	**$55 / per page**
For Local Author	**100,000 Toman / per page**

AUTHOR CHECKLIST

- Author(s), bio-data including affiliation(s) and mail and e-mail addresses).
- Manuscript including abstracts, key words, illustrations, tables, figures with figure captions and list of references.
- MS Word files of the paper.

International **J**ournal of **E**ngineering, P.O. Box 13145-1659, Tehran, I.R. Iran
Materials and Energy Research Center, 5 Ahuramazda St., Alvand Ave., Argentina Sq., Tehran, Islamic Republic of Iran
www.merc.ac.ir - www.emerc.ac.ir